Université de Liège

Laboratoire de Pathologie expérimentale

GIGA-Cancer

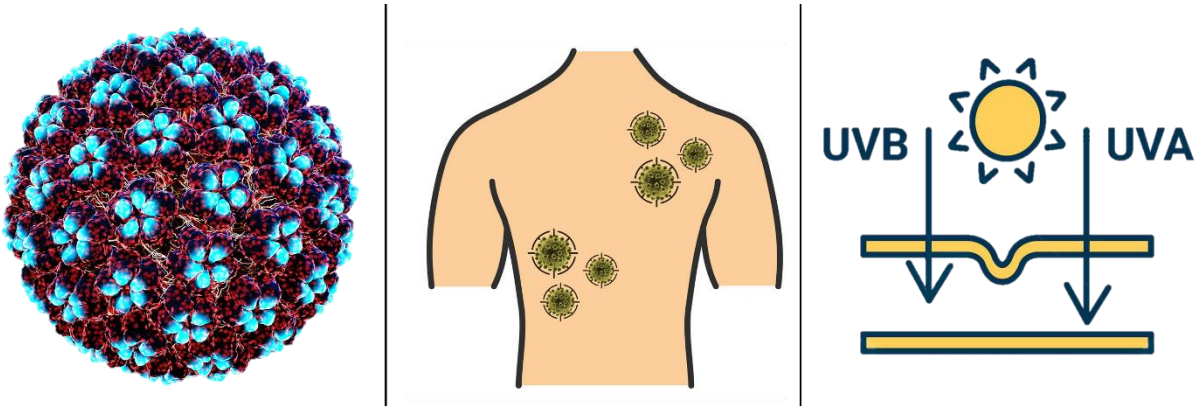

Décrypter les questions non résolues de longue date liées aux infections à α/β papillomavirus: focus sur la maladie de Bowen et l'adénocarcinome endocervical

Thèse soumise par Thomas Lerho en soutien à la candidature au doctorat en Sciences Biomédicales et Pharmaceutiques

Promoteurs : Dr Pascale Hubert et Dr Michaël Herfs

Année académique 2023-2024

MEMBRES DU JURY

Membres du comité de thèse

Dr. Christophe DEROANNE (President, Uliege)

Dr. Yvette HABRAKEN (Secrétaire, Uliege)

Dr. Julien HANSON (Uliege)

Évaluateurs externes

Dr. Nicolas Gillet (Unamur)

Dr. Thibault Kervarrec (Université de Tours)

Promoteurs

Dr. Michaël Herfs (Uliege)

Dr. Pascale Hubert (Uliege)

Remerciements

En terminant cette thèse, je tourne la page de ma "vie" académique, et je ne pouvais pas la conclure sans exprimer ma profonde gratitude envers les personnes qui m'ont permis de réaliser ce parcours du combattant.

Madame, Messieurs les membres du jury, je tiens à exprimer ma reconnaissance envers chacun d'entre vous pour votre engagement et votre contribution à cette thèse. Votre expertise dans vos domaines respectifs a enrichi mon travail de manière significative, et les commentaires constructifs que j'ai reçus m'ont permis de voir mon projet sous un angle nouveau et d'améliorer la qualité de ma recherche. Je tiens également à exprimer ma gratitude pour le temps que vous avez consacré à lire et à évaluer ma thèse. Votre implication dans ce processus a été une source d'inspiration et a renforcé ma conviction dans l'importance de mon travail.

Michael, ta passion pour la recherche a été une source d'inspiration constante tout au long de ces 4 années. Ton implication dans ce projet et ton dévouement à l'excellence ont créé un environnement stimulant et propice à l'apprentissage. Chaque jour passé au sein du laboratoire a été une leçon inestimable, façonnant ma compréhension du monde académique et de la recherche. Ta nature chaleureuse, ton humour contagieux et ta gentillesse ont rendu cette expérience de doctorat non seulement éducative mais aussi enrichissante sur le plan humain.

Pascale, ton énergie solaire a illuminé chaque jour passé dans le laboratoire. Ta présence bienveillante et ta capacité à écouter attentivement ont créé un environnement de travail unique, empreint de compassion et d'empathie. Je tiens à te remercier tout particulièrement pour m'avoir permis de tenir le coup jusqu'au bout. Ton encouragement constant a été la motivation dont j'avais besoin dans les moments difficiles, et ta confiance en moi a été un véritable moteur pour atteindre l'excellence.

En me donnant l'opportunité de réaliser mon doctorat dans votre laboratoire, vous m'avez non seulement permis de découvrir ce que je voulais faire de ma vie future, mais vous m'avez également offert la chance de grandir en tant que chercheur et en tant que personne. Je suis reconnaissante de la confiance que vous m'avez accordée et du soutien constant que vous m'avez apporté durant tout le projet de recherche.

Pour toutes les personnes dont je n'ai pas parlé, qu'il s'agisse d'amour, d'amis, de famille, de collègues, ou peut-être même de tout cela à la fois, et qui ont contribué de près ou de loin à cette thèse, MERCI infiniment. Vous avez tous eu un impact important dans ma vie, et c'est grâce à vous que j'en suis là aujourd'hui. Je vous prépare un discours mémorable dont vous m'en direz des nouvelles. Patientez encore un peu, ça arrive incessamment sous peu <3.

Table des matières

Abréviations :

5-LOX	*5-lipoxygenase*
8-oxoG	*8-oxoguanine*
ADP	Adénosine diphosphate
AK	Kératose actinique
APE1	*Apurinic/apyrimidinic endonuclease 1*
ATP	Adénosine triphosphate
BD	Maladie de Bowen
BER	Réparation par excision de base
BM	Membrane basale
LR-HPV	Papillomavirus humain à bas risque
CBM	Motif de liaison à la cycline
CDK	Kinase cycline dépendante
CIRC	Centre international de recherche sur le cancer
CK2	*Casein kinase 2*
Co-IP	Co-immunoprécipitation
CPD	Dimères cyclobutyliques de pyrimidine
CS	Syndrome de Cockayne
CSC	Carcinome épidermoïde/spinocellulaire
DAB	*3,3'-Diaminobenzidine*
DMEM	*Dulbecco's modified eagle medium*
DNMT1	*DNA methyltransferase 1*
E2BS	*E2 binding sites*
E6AP	*E6 ubiquitin-protein ligase*
ECM	Matrice extracellulaire
EGFR	Récepteur du facteur de croissance épidermique
EORTC	Organisation européenne pour la recherche et le traitement du cancer
EV	Épidermodysplasie verruciforme
EZH2	*Enhancer of zeste homolog 2*
FBS	Sérum de veau fœtal
GC-NER	Réparation génomique globale par excision de nucléotides
GPCA	*Gaussia princeps luciferase Protein Complementation Assay*
HOCl	Acide hypochloreux
HPV	Papillomavirus humain
HR	Voie de réparation de la recombinaison homologue
HR-HPV	Papillomavirus humain à haut risque
HSIL	Lésions de haut grade
HSPG	Protéoglycane de sulfate d'héparane
IKKβ	*IκB kinase beta*
kDa	kiloDalton
KLK8	*Kallikrein-8*

LCR	Région régulatrice non codante
MAML1	*Mastermind-like protein 1*
MRN	Mre11-Rad50-Nbs1
ND10	Domaine nucléaire 10
NER	Réparation par excision de nucléotides
NES	Signal d'exportation nucléaire
NLR	Rapport de luminescence normalisée
NLS	Signal de localisation nucléaire
NOX	*NADPH oxydase*
OBSL1	*Obscurine-like 1*
OGG1	8-oxoguanine glycosylase
OMS	Organisation mondiale de la santé
ORF	Cadre de lecture ouvert
PBM	*PDZ-Binding Motifs*
Pb	Paire de base
PCNA	*Proliferating cell nuclear antigen*
PD-1	*Programmed cell Death protein 1*
PML	*Promyelocytic leukemia bodies*
Pol-α	ADN polymérase-α
PUA	*3'phospho-α,β-unsaturated aldehyde*
PUFA	Acide gras polyinsaturé
PUVA	Psoralène et UVA
RFC	Facteur de réplication C
RLU	Luminescence relatives
ROS	Espèce réactive de l'oxygène
RPA	Protéine de réplication A
SMC	Protéine de maintenance structurale des chromosomes
SNX17	*Sorting nexin 17*
SOD	Superoxydes dismutases
TC-NER	Réparation couplée à la transcription par excision de nucléotides
TFBS	Site de liaison pour les facteurs de transcription
TopoI	ADN topoisomérases de type 1
TTD	Trichothiodystrophie
UV	Rayon ultraviolet
UVA	Rayon ultraviolet A
UVB	Rayon ultraviolet B
VLP	Particules pseudo-virales
XP	*Xeroderma pigmentosum*

Résumé

À ce jour, plus de 400 génotypes de papillomavirus humains (HPV) ont été méthodiquement caractérisés et classés en cinq genres distincts, à savoir les genres alpha, bêta, gamma, mu et nu. Néanmoins, au cours des trois dernières décennies, la majeure partie des investigations concernant les HPV, dépassant 90 %, s'est essentiellement focalisée sur les génotypes du genre alpha, en particulier l'HPV16 et 18, qui sont les deux souches prédominantes responsables du cancer du col de l'utérus. Toutefois, les β-HPV, identifiés pour la première fois dans les années 80 et comprenant plus de 68 génotypes, suscitent de plus en plus d'intérêt. Cet intérêt accru est principalement motivé par des preuves convaincantes suggérant que certains β-HPV, tels que HPV5, 8, 38 et 49, pourraient contribuer au développement de carcinomes épidermoïdes cutanés en potentialisant les effets néfastes des rayonnements ultraviolets. Cependant, de nombreuses questions à la fois conceptuelles et translationnelles restent en suspens. Par exemple, quel est le pourcentage de carcinomes épidermoïdes qui ont pour origine les β-HPV ? Parmi les 68 génotypes de β-HPV répertoriés jusqu'à présent, lesquels favorisent réellement le développement du cancer et peuvent être détectés dans les lésions (pré)néoplasiques ? Comment s'opère la synergie entre les rayons UV et ces virus ? L'objectif de cette thèse est de répondre à ces questions.

Dans la première partie de cette thèse, une cohorte constituée de 162 échantillons de maladie de Bowen a été assemblée, représentant ainsi l'une des cohortes les plus imposantes jamais rassemblées pour cette lésion précancéreuse. Une analyse virologique approfondie, basée sur trois statuts viraux distincts (α-HPV, β-HPV et HPV-), a été exécutée. Cette analyse a également porté sur l'évaluation de la proportion de lésions qui présentent une infection transcriptionnellement active et productive. Les résultats ont révélé que les lésions de Bowen positives pour les α-HPV sont principalement localisées dans les régions gynécologiques, tandis que la grande majorité des β-HPV ont été identifiés au sein des lésions exposées aux rayons ultraviolets (UV), ce qui est cohérent avec leur affinité pour les tissus cutanés.

La seconde phase de ce projet s'est penchée sur les mécanismes sous-jacents à la synergie entre les rayons UV et les β-HPV. Pour cela, un screening à haut débit a été réalisé en vue d'identifier d'éventuelles nouvelles interactions directes entre les oncoprotéines virales E6 et E7 des HPV5, 8, 38 et 49, et une liste des protéines participant aux mécanismes de réparation de l'ADN de la cellule hôte, incluant environ 80 % des protéines impliquées dans ces processus. La méthode employée, à savoir la GPCA, met en évidence des interactions directes entre deux protéines par le biais d'une émission de luminescence. Au total, 40 cibles ont été identifiées comme interagissant soit avec E6, soit avec E7, ou les deux simultanément. Parmi ces cibles, 22 ont été confirmées par co-immunoprécipitation, consolidant ainsi l'hypothèse que le virus altère les mécanismes de réparation du génome dans la cellule hôte et participe ainsi, en synergie avec les UV, au développement de lésions (pré)cancéreuses.

Abstract

To date, more than 400 genotypes of human papillomaviruses (HPV) have been characterized and classified into five distinct genera: alpha, beta, gamma, mu and nu. However, over the past three decades, over 90% of research on HPV has been predominantly focused on alpha genotypes, particularly HPV16 and HPV18, the two predominant strains responsible for cervical cancer. Nonetheless, β-HPV, identified for the first time in the 1980s and encompassing more than 68 genotypes, have been gaining increasing attention. This heightened interest is primarily driven by compelling evidence suggesting that certain β-HPV, such as HPV5, 8, 38, and 49, may contribute to the development of cutaneous squamous cell carcinomas by potentiating the deleterious effects of ultraviolet radiation. However, numerous conceptual and translational questions remain unanswered. For instance, what is the percentage of squamous cell carcinomas that can be attributed to β-HPV? Among the 68 β-HPV genotypes identified to date, which ones genuinely promote cancer development and can be detected in (pre)neoplastic lesions? How does the synergy between UV radiation and these viruses operate? The aim of this thesis is to address these questions.

In the first part of this thesis, a cohort composed of 162 Bowen's disease samples has been collected, representing one of the largest cohorts ever gathered for this precancerous condition. A comprehensive virological analysis, based on three distinct viral statuses (α-HPV, β-HPV, and HPV-), was conducted. This analysis also included an assessment of the proportion of lesions that exhibit transcriptionally active and productive infections. The results revealed that Bowen's disease lesions positive for α-HPV are primarily located in gynecological regions, while the majority of β-HPV have been identified within lesions exposed to ultraviolet (UV) radiation, which is consistent with their affinity for cutaneous tissues.

The second phase of this project delved into the mechanisms underlying the synergy between UV radiation and β-HPV. For this purpose, a high-throughput screening was conducted to identify potential novel direct interactions between the viral oncoproteins E6 and E7 of HPV5, 8, 38, and 49, and proteins participating in DNA repair mechanisms of the host cell, covering approximately 80% of the proteins involved in these processes. The method employed, known as GPCA, highlights direct interactions between two proteins through luminescence emission. In total, 40 targets were identified as interacting with either E6, E7, or both simultaneously. Among these targets, 22 were confirmed through co-immunoprecipitation, thereby reinforcing the hypothesis that the virus alters genome repair mechanisms within the host cell and, in synergy with UV, contributes to the development of (pre)cancerous lesions.

Le papillomavirus humain (HPV)

A. Généralités

La famille des Papillomaviridae est un groupe diversifié de virus ubiquitaires, capables d'infecter la peau et les muqueuses d'un large éventail d'espèces telles que les oiseaux, les poissons, les reptiles et les mammifères (bovidés, canidés, marsupiaux ainsi que l'être humain).[1] Actuellement, plus de 650 papillomavirus ont été identifiés, parmi lesquels 448 ont spécifiquement co-évolué pour infecter et persister au sein de la population humaine (contre 226 chez les animaux).[2] Cette spécificité explique notamment pourquoi on retrouve très rarement des infections inter-espèces.[3]

Les papillomavirus sont de petits virus (d'environ 55 nm) constitués d'une molécule d'ADN bicaténaire circulaire, qui varie entre 5500 et 8500 paires de bases (pb), contenue dans une capside icosaédrique non enveloppée. Cet ADN code généralement pour 6 protéines précoces (E1, E2, E4, E5, E6 et E7) impliquées dans la réplication virale et la prolifération cellulaire, ainsi que pour 2 protéines tardives (L1 et L2) impliquées dans l'entrée du virus, la formation de la capside, mais également dans la classification des papillomavirus (Figure 1).[4]

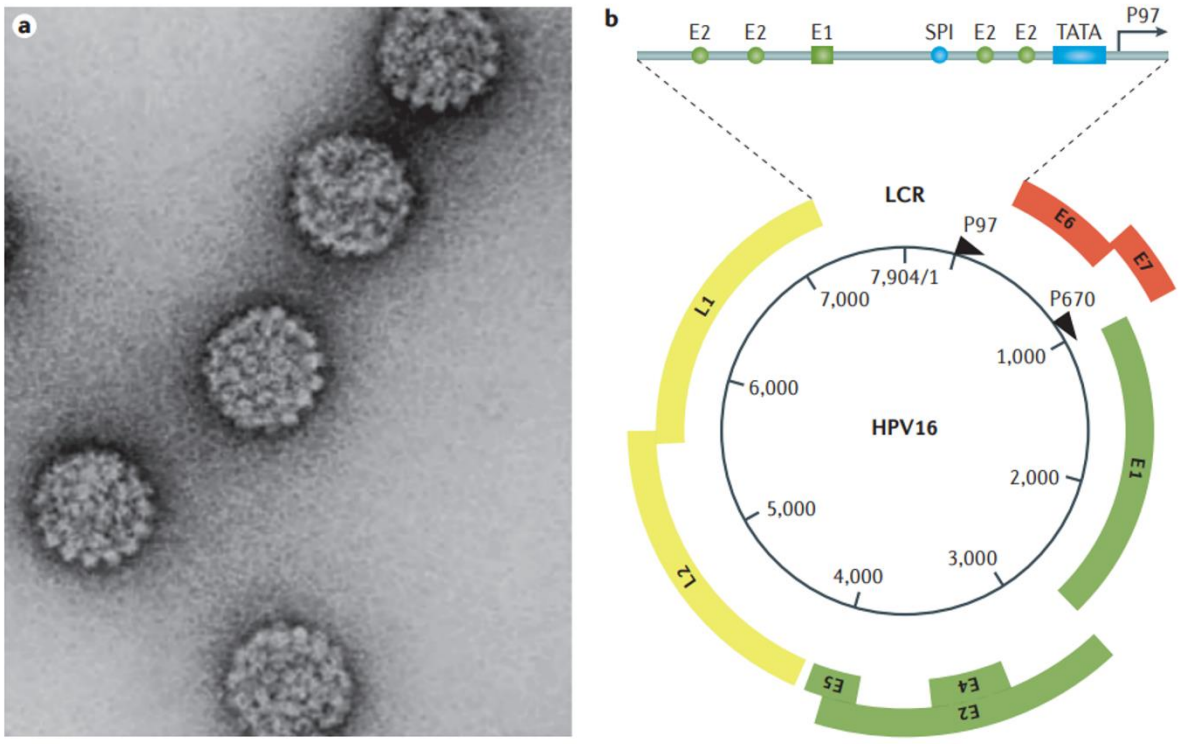

Figure 1 : **Structure et organisation d'un papillomavirus humain et de son génome**. a) Particules d'HPV observées à l'aide d'un microscope électronique à transmission. b) Structure génomique de l'HPV16, observation de l'organisation de l'ADN bicaténaire circulaire composé de 8 cadres de lecture codant pour les protéines précoces (E, en vert et rouge) et tardives (L, en jaune), contrôlées par le promoteur précoce p97 et le promoteur tardif p670 (flèches noires). La région régulatrice non codante (LCR) est une région qui contient l'origine de réplication, ainsi que des séquences de contrôle post-transcriptionnelles qui contribuent à l'expression des gènes viraux (Schiffman et al., 2016).

B. Classification

En 2004, le Docteur De Villiers a proposé un tout nouveau système de classification des HPV, basé sur la séquence nucléotidique du gène L1 (codant pour la protéine majeure de la capside). Ce système, validé par l'International Committee on Taxonomy of Viruses, propose de classer les virus en genres, espèces, types et sous-types en fonction du pourcentage d'homologie du gène L1.[5] En effet, la séquence de L1 est hautement conservée et peut être alignée pour tous les HPV connus.[6]

Dès lors, on considère que deux HPV appartiennent à un genre différent lorsque leur séquence L1 présente moins de 43 % d'homologie. En effet, pour être classés dans le même genre, ils doivent présenter une homologie comprise entre 43 % et 60 %. Lorsque deux HPV, d'un même genre, possèdent entre 60 et 70 % d'homologie, on parle d'espèce. De plus, ces espèces peuvent également être classées en type lorsqu'elles partagent entre 71 et 89 % d'homologie, en sous-types lorsque la séquence diffère de moins de 10 %, et sont considérées comme des variants lorsqu'ils présentent moins de 2 % de différence d'homologie (Figure 2).[5,7]

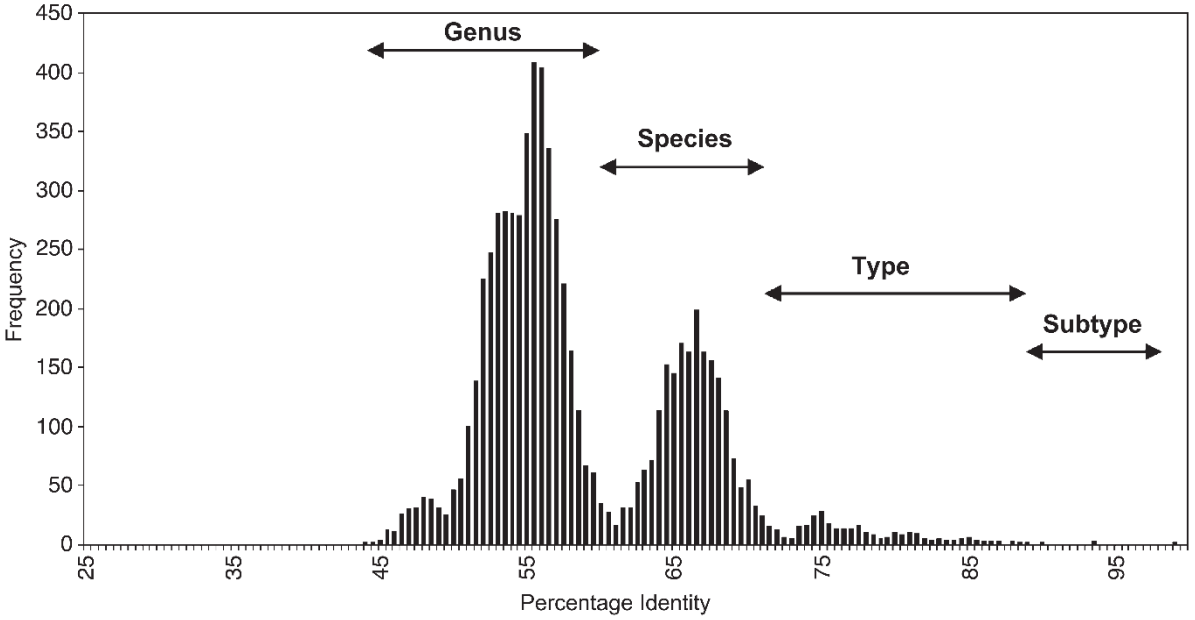

Figure 2 : **Distribution des génotypes de 118 HPV basée sur la comparaison des séquences nucléotidiques du gène codant pour la protéine virale L1 (% d'identité par paire)** (de Villiers *et al.*, 2004).

Parmi les 442 génotypes d'HPV actuellement recensés par le PapillomaVirus Episteme (PaVE), on retrouve cinq genres : 66 Alphapapillomavirus (α-HPV), 68 Betapapillomavirus (β-HPV), 302 Gammapapillomavirus (γ-HPV), 5 Mupapillomavirus (μ-HPV) et 1 Nupapillomavirus (ν-HPV) (Figure 3).[2,8]

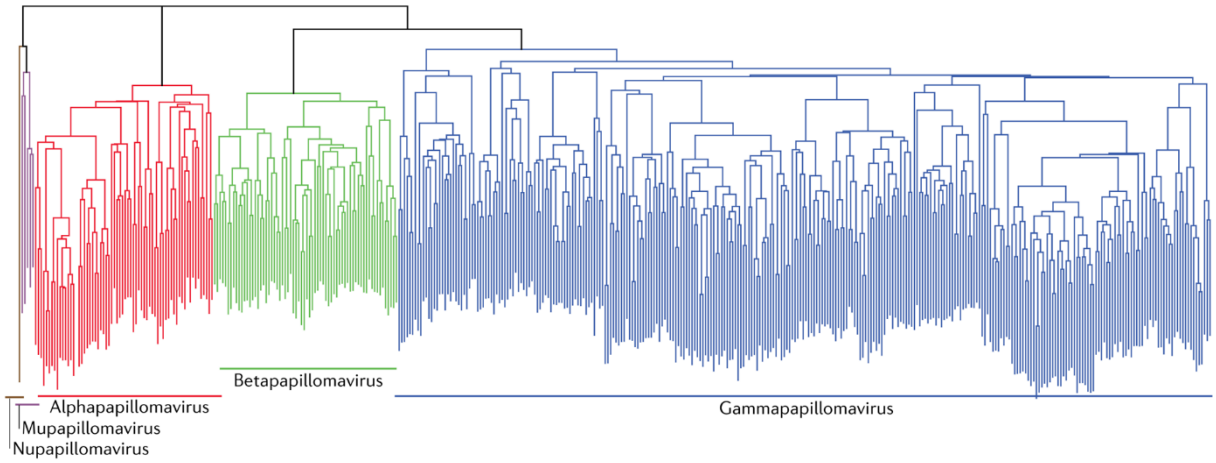

Figure 3 : **Arbre phylogénétique représentant les 442 papillomavirus humains référencés au sein du PapillomaVirus Episteme** (McBride, 2022).

Outre le pourcentage d'homologie du gène L1 (qui reste la méthode de classification principale des HPV), deux autres caractéristiques peuvent être prises en compte pour classer les papillomavirus : le tropisme et la pathogénicité.[9]

En effet, à l'exception des α-HPV, qui possèdent également une affinité pour les muqueuses orales et génitales, tous les papillomavirus humains ont un tropisme cutané. Néanmoins, certaines études récentes commencent à contredire ce dogme. Les équipes des docteurs Anna Rosa Garbuglia et Giuseppe Borzacchiello ont mis en évidence une certaine dualité dans le tropisme des papillomavirus. Leurs travaux ont démontré la présence de bêta et gamma-HPV (qui, jusqu'à récemment, n'étaient retrouvés qu'au niveau de la peau) au niveau de certaines muqueuses, comme par exemple les muqueuses anales et buccales.[10,11]

En ce qui concerne la pathogénicité des papillomavirus, cette caractéristique a principalement été utilisée pour classer les α-HPV muqueux en 2 catégories : les α-HPV à haut risque (HR-HPV) et à bas risque (LR-HPV).

Selon l'Organisation mondiale de la santé (OMS), 13 HR-HPV (à savoir les HPV 16, 18, 31, 33, 35, 39, 45, 51, 52, 56, 58, 59 et 68) possèdent un potentiel oncogène et sont à l'origine d'un certain pourcentage des cancers du col utérin (≃99.9%), du vagin (≃80%), de la vulve (≃50%), de l'anus (≃90%), de l'oropharynx (≃50%) et du pénis (≃50%). Les deux plus connus sont l'HPV 16 et l'HPV 18 en raison de leur rôle prédominant (≃70%) dans le développement du cancer du col. De plus, bien que peu d'études épidémiologiques aient été réalisées, une dizaine d'HPV sont classés comme phylogénétiquement oncogènes (HPV 26, 30, 34, 53, 61, 66, 67, 69, 70, 73, 82, 85, 91 et 103).[12,13]

Inversement, les LR-HPV (comme l'HPV 6, 11, 42 et 44, pour n'en citer que quelques-uns) sont responsables de lésions bénignes, notamment des verrues cutanées et des papillomatoses respiratoires. Ces infections ne causent pas de cancer et, dans la majorité des cas, disparaissent d'elles-mêmes sans traitement.[14,15]

Pendant longtemps, les chercheurs ont uniquement parlé de pathogénicité pour les α-HPV muqueux, sans prendre en considération les autres genres d'HPV. Pourtant, bien que la majorité des β-HPV soient responsables d'infections asymptomatiques et considérés comme faisant partie intégrante de la flore cutanée,[16,17] l'implication de ceux-ci dans le développement de cancers de la peau chez des patients atteints d'épidermodysplasie verruciforme (EV) est bien connue depuis les années 1980.[18,19] Qui plus est, le fait que 90 % des cancers cutanés retrouvés chez des patients EV soient associés à l'HPV 5 et 8 a permis à l'OMS de les classer comme potentiellement oncogènes.[20,21]

Les HPV 5 et HPV 8 ne sont pas les seuls β-HPV pouvant avoir un impact négatif pour l'homme. Au début des années 2000, plusieurs recherches ont démontré que l'HPV 38, au même titre que l'HPV 49, est capable d'immortaliser des kératinocytes humains primaires.[22,23] De surcroît, l'équipe du Docteur Tommasino a démontré que l'HPV 38 peut, en association avec les UVB, favoriser le développement de carcinomes épidermoïdes (CSC) de manière significative.[24] Cette information a d'ailleurs été confortée par une méta-analyse qui a démontré que certains β-HPV sont associés à une augmentation du risque de CSC chez des personnes immunocompétentes, qualifiant même les β-HPV de facteur de risque (Tableau 1).[25]

	HPV5	HPV8	HPV15	HPV17	HPV20	HPV24	HPV36	HPV38
Augmentation du risque	40%	39%	25%	34%	38%	26%	23%	36%

Tableau 1 : **Implication de différents génotypes de β-HPV dans l'induction de carcinome spinocellulaire chez des patients immunocompétents**.

Néanmoins, l'implication des β-HPV dans la carcinogenèse cutanée n'est pas unanimement reconnue et fait encore l'objet de nombreux débats. En effet, le docteur Strickley a récemment mis en évidence que l'immunité des lymphocytes T contre les HPV commensaux, chez des individus immunocompétents, empêche le développement de CSC en détectant les antigènes viraux et en stimulant ainsi la réponse immunitaire.[26]

À l'heure actuelle, les données scientifiques récoltées ne nous permettent pas de déterminer le poids des β-HPV dans l'équilibre risque/bénéfice. C'est pourquoi nous avons décidé de focaliser notre attention sur ceux-ci au cours de ce travail.

Nous pourrions également nous interroger sur les autres genres d'HPV tels que les γ-HPV qui constituent plus de la moitié des papillomavirus pouvant infecter l'homme.[27] Toutefois, n'étant pas le sujet de cette thèse, je n'entrerai pas dans les détails de cette thématique.

C. Les β-HPV

1. Généralités

Identifiés pour la première fois dans les années 80, les β-HPV (au nombre de 68) forment le deuxième plus grand groupe de papillomavirus, juste après les γ-HPV et leurs 302 membres.[28] Considérés comme faisant partie intégrante de la flore cutanée en raison de leur acquisition dès les premiers jours après la naissance (*via* une transmission intrafamiliale) et de leur implication dans des infections cutanées asymptomatiques, les β-HPV ont souvent été négligés et mis de côté au profit des α-HPV, qui ont longtemps été considérés comme les seuls HPV présentant une capacité oncogénique.[29,30]

Contrairement aux α-HPV, le génome des β-HPV est dépourvu du gène E5 dans la région codante, ne s'intègre pas, possède une région LCR plus courte de 300 à 500 pb, ainsi qu'un mode de fonctionnement un peu différent des oncoprotéines E6/E7 (Figure 4).[31–33] Le génome des β-HPV étant un peu différent de celui des α-HPV, nous allons nous attarder dessus et essayer de décortiquer son fonctionnement. Bien que les α-HPV ne soient pas le sujet de cette thèse, plusieurs parallèles seront effectués entre ceux-ci et les β-HPV.

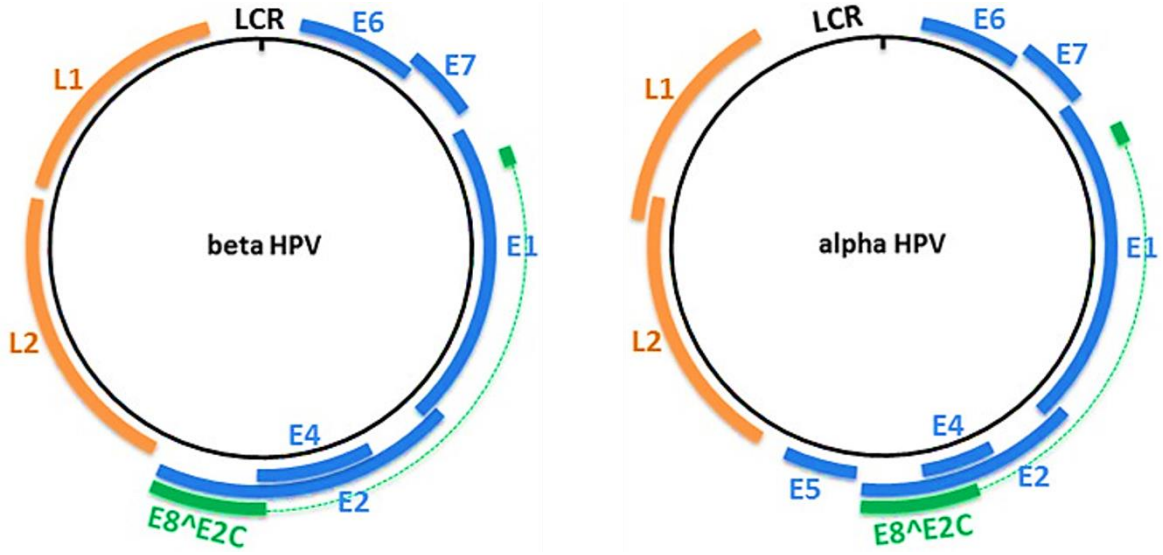

Figure 4 : **Organisation du génome des β-HPV et α-HPV**. Le génome circulaire d'ADN double brin est représenté par un cercle noir. Les positions des gènes précoces et tardifs sont représentées respectivement en bleu et en orange. La protéine de fusion E8, exprimée par les deux genres d'HPV, est quant à elle représentée en vert. La région LCR fait référence à la région régulatrice non codante (Gheit, 2019).

2. Le génome des β-HPV

Le génome des β-HPV, semblable à celui des α-HPV, est organisé en 3 régions distinctes (Tableau 2) :

- La région régulatrice non codante, située entre les cadres de lecture ouverts (ORF) L1 et E6, qui contient des promoteurs viraux et des éléments régulateurs impliqués dans la transcription de l'ADN viral, ainsi que l'origine de réplication Ori.
- La région codante précoce, exprimée tôt dans le cycle infectieux (dans les couches inférieures et moyennes de l'épiderme), qui code pour les protéines E1, E2, E4, E6 et E7 impliquées dans l'expression virale, la réplication/survie cellulaire ainsi que l'évasion immunitaire.
- La région codante tardive qui code pour les protéines de capside majeures (L1) et mineures (L2), exprimées dans les couches supérieures de l'épithélium pluristratifié.[34]

Gene products	Alpha HPV features	Beta HPV features
LCR	• Also called upstream regulatory region (URR), contains the early promoter and regulatory element involved in viral DNA replication and transcription	
E6	• Required for the maintenance of the cancer phenotype • Required for stable episomal maintenance	• Not required for the maintenance of the cancer phenotype • Inhibition of UV radiation-induced damage repair • Hampers the differentiation of HPV8-expressing keratinocytes by targeting the PDZ domain-containing protein syntenin 2 • Interacts with Notch pathway and promote the transformation process of the infected keratinocytes
	• Deregulation of cell cycle • Inhibition of apoptosis • Cell polarity, migration and attachment • The PDZ domain-binding motif of E6 proteins regulates HPV life cycle • Upregulation of the hTERT promoter activity	
E7	• Required for the maintenance of the cancer phenotype • Required for stable episomal maintenance	• Not required for the maintenance of the cancer phenotype • E7 from HPV38 shows the ability to counteract p53-mediated apoptosis by inducing accumulation of the p73 isoform, ΔNp73
	• Deregulation of cell cycle • Inhibition of apoptosis	
E5	• Not required for the maintenance of the oncogenic phenotype • Increases the immortalization effects of HPV16 E6 and E7 • Promotes tumor cell motility and cancer metastasis • Promotes cell-cycle progression • Inhibition of apoptosis	• The E5 ORF is lacking
E8^E2	• Acts as a transcriptional repressor, and represses E1/E2-dependent replication of the viral origin	
E1	• Viral DNA replication	
E2	• Ensure the segregation of the viral genome during cell division	
E4	• Contributes to efficient productive replication in differentiating cells	
L1	• Major capsid protein	
L2	• Minor capsid protein • L2 is required for an efficient trafficking of the viral genome to the nucleus • L2 mediates the viral genome delivery to the nuclear domain (ND10)	

Tableau 2 : **Caractéristiques principales et fonctions des protéines codées par les gènes précoces et tardifs des α-HPV et β-HPV** (Gheit, 2019).

i. Région régulatrice non codante (LCR)

La région régulatrice non codante est une région située entre les ORF des protéines virales L1 et E6 qui ne code pour aucune protéine. Cette région, qui représente entre 5 et 10% du génome, joue un rôle dans la régulation de la réplication et de la transcription virale grâce à l'origine de réplication (Ori) et aux éléments cis (promoteurs) et trans (facteurs de transcription) (Figure 5). Elle est également capable, avec l'aide d'amplificateurs spécifiques (*enhancers*), d'influencer le tropisme des HPV (muqueux ou cutanés). [35,36]

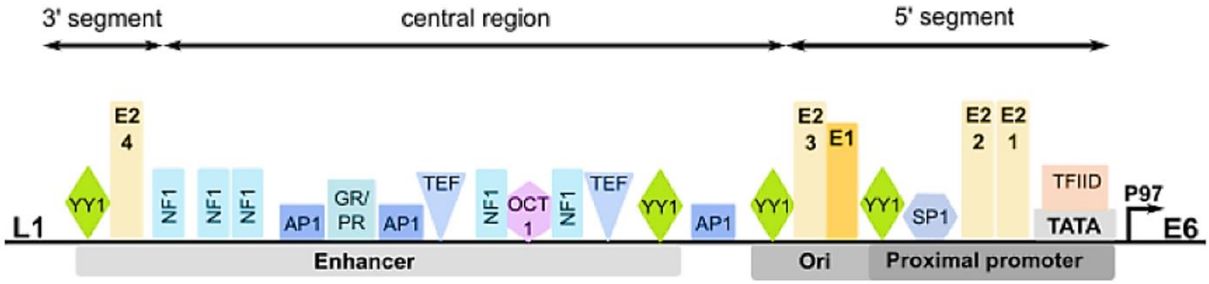

Figure 5 : **Structure schématique de la région LCR d'un α-HPV**. La région centrale et le segment 3' ont été agrandis afin de visualiser plus clairement les sites de liaison des protéines E1 et E2 ainsi que les sites de liaison des facteurs de transcription les plus importants. Il est important de noter que seuls quelques sites de liaison sont illustrés dans cette représentation, car il existe de nombreux autres sites de liaison connus (Warowicka *et al.*, 2022).

Pourtant, malgré le rôle capital de la LCR, son implication dans les β-HPV est très peu décrite en comparaison avec les α-HPV. Nous allons donc aborder les 4 différences qui existent entre les HPV au niveau de la LCR, à savoir :

- La taille
- Le nombre et la position des sites de liaison pour la protéine virale E2 (E2BS)
- Le nombre de site de liaisons pour les facteurs de transcription (TFBS)
- La localisation des promoteurs

La région LCR des β-HPV est deux fois plus petite que celle des α-HPV. Bien que cette différence soit importante, aucune hypothèse n'a été avancée pour l'expliquer et nous ne connaissons pas encore son impact.[37]

En ce qui concerne le nombre de sites de liaison pour la protéine E2 (E2BS), les β-HPV possèdent entre 4 et 5 sites E2BS, comparé aux 4 des α-HPV (Figure 6).[35] De plus, ces sites ne sont pas localisés aux mêmes endroits dans les deux types d'HPV, ce qui peut entraîner des différences de niveau de transcription. En effet, E2 peut réguler positivement ou négativement la transcription de l'oncoprotéine E6. Cette régulation dépend de la position des sites E2BS le long de la région LCR. Dans les HPV muqueux (α-HPV), on peut observer la présence de 2 sites E2BS situés à proximité du promoteur de l'oncoprotéine E6. Dans une telle configuration, E2 interfère (par encombrement stérique) avec la liaison des facteurs de transcription cellulaires SP1 et TBP, agissant ainsi comme un répresseur.[38,39] En revanche, dans la LCR des HPV cutanés (β-HPV), les sites de liaison sont situés plus loin du promoteur d'E6, ce qui conduit à une activation globale de la transcription par E2.[40,41]

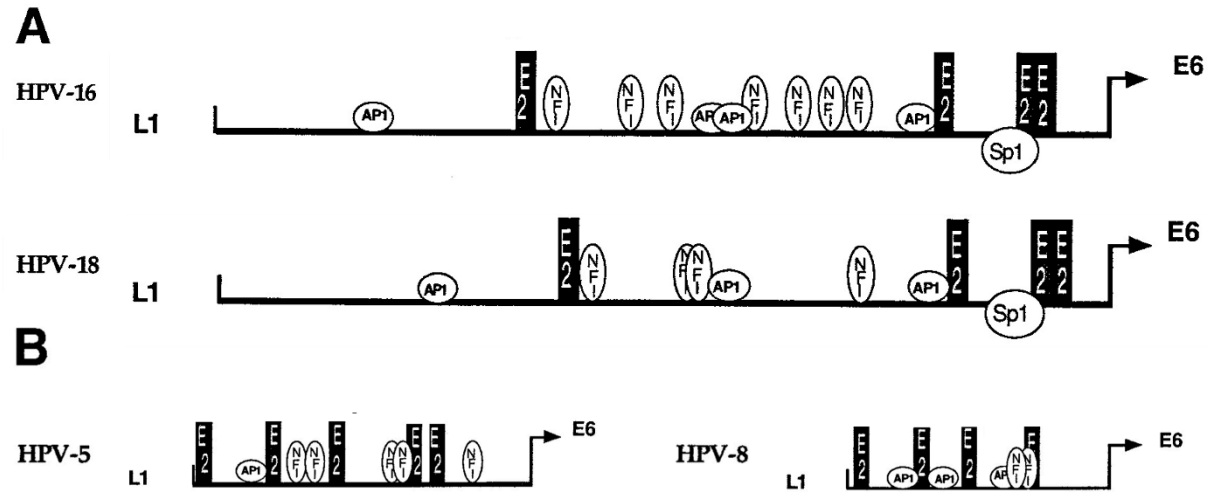

Figure 6 : **Sites de liaison pour la protéine E2 des α-HPV (HPV16 et 18) et β-HPV (HPV5 et 8) ainsi que les facteurs cellulaires AP-1, NFI et Sp1 dans la région régulatrice non codante**. Les barres horizontales représentent la LCR, située entre L1 et E6 (adapté de Sailaja *et al.*, 1999).

Quelques différences peuvent également être observées lorsque l'on se penche sur le nombre de sites de liaison pour les facteurs de transcription (TFBS) présents dans la région régulatrice non codante des β-HPV. En effet, contrairement aux α-HPV, il existe beaucoup moins de sites de liaison. On peut citer, par exemple chez les HPV5/8, l'absence du site de liaison pour SP-1 qui joue un rôle dans la transcription des oncoprotéines E6 chez les α-HPV, ainsi que l'absence du facteur de transcription TEF-1. Cependant, à l'heure actuelle, nous ne sommes pas en mesure de dire si cette différence est due à un manque de connaissances concernant cette région chez les β-HPV, ou s'il existe réellement moins de sites de liaison pour les facteurs de transcription.[37,42,43] Malgré cela, les β-HPV possèdent tout de même des TFBS en commun avec les α-HPV, tels que les facteurs de transcription AP-1, NF-I, OCT-1, *etc*. Cependant, leur localisation et leur nombre diffèrent de ceux des α-HPV (Tableau 3). Une fois de plus, le manque de connaissances concernant la LCR ne nous permet pas de comprendre l'impact de ces variations.

	α-HPV			β-HPV
Facteur de transcription	HPV16	HPV18	HPV6	HPV8
AP-1	+	+	+	+
C/EBP		+		+
E2F		+		
NF-Y		+	+	+
OCT-1	+	+	+	+
YY1	+			

Tableau 3 : **Sites de liaison des facteurs de transcriptions, prédit *in silico via* MATCH en utilisant TRANSFAC, retrouvés chez les HPV 6, 8, 16 et 18**. Certains d'entre eux sont communs à tous les papillomavirus, tels que AP-1 ou Oct-1, tandis que d'autres sont spécifiques à un génotype ou à un genre d'HPV, tels que E2F ou YY1 (adapté de García-Vallvé *et al.*, 2006).

Une autre différence majeure peut être observée lorsque l'on se penche sur la localisation des promoteurs précoces et tardifs parmi les deux genres d'HPV (Figure 7). Très peu de différences sont retrouvées pour le promoteur précoce, qui semble être actif tout au long du cycle viral et responsable de l'expression des oncoprotéines E6/E7.[44,45] En effet, que ce soit chez l'HPV8 ou chez l'HPV16, le promoteur précoce est retrouvé en amont du gène E6, en P175 pour l'HPV8 et en P97 pour l'HPV16.[46,47] En revanche, la position des promoteurs tardifs, régulés en fonction de la différenciation cellulaire et jouant un rôle dans l'expression des protéines virales (E1, E2, E4, L1 et L2), diverge.[48] Chez l'HPV8, le promoteur tardif est localisé dans la région LCR, en P7535, tandis que chez l'HPV16, il n'est pas retrouvé dans la LCR mais bien dans l'ORF de l'oncoprotéine E7, en P670.

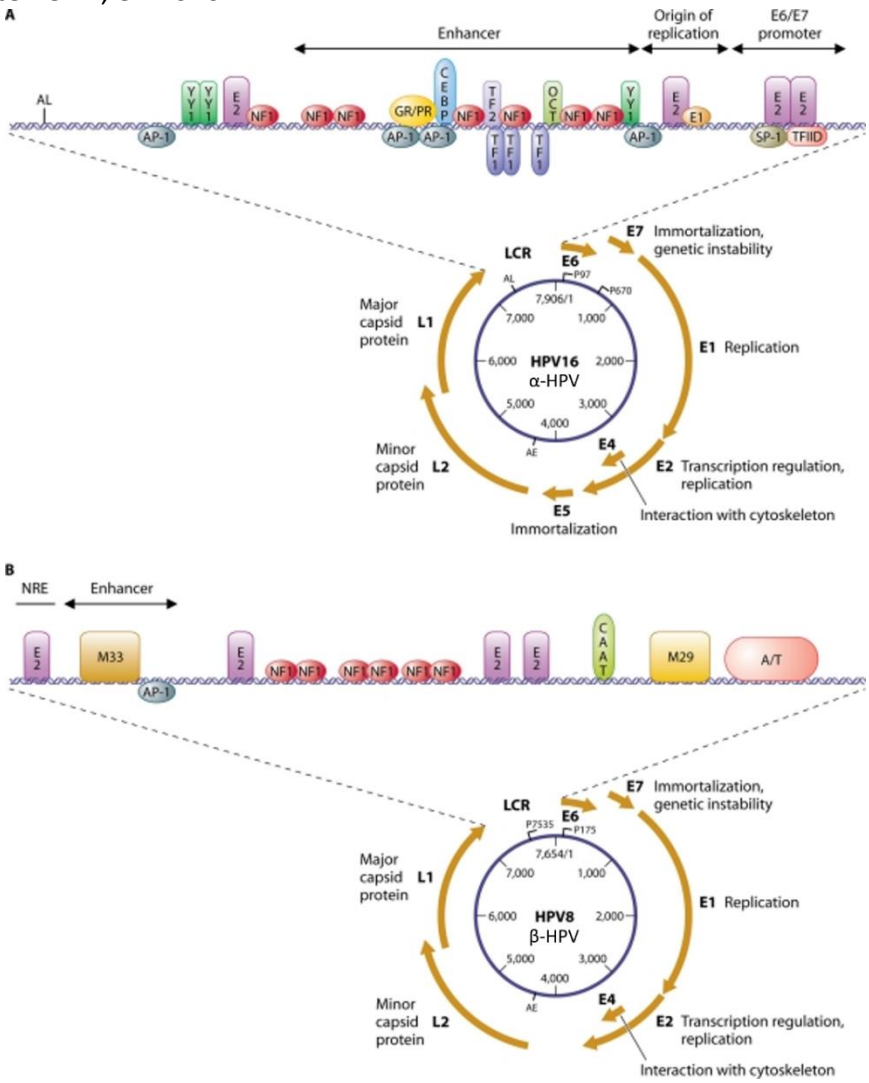

Figure 7 : **Organisation génétique des génomes de l'HPV16 (A) et l'HPV8 (B)**. Les principales fonctions des gènes précoces (E) et tardifs (L) sont mentionnées. Pour l'HPV16, les promoteurs (P97 et P670) ainsi que les sites de polyadénylation précoce (AE) et tardif (AL) sont indiqués. Pour l'HPV8, les promoteurs précoces (P175) et tardifs (P7535) sont mentionnés. En haut de la figure, une représentation schématique de la région LCR permet d'observer la localisation des sites E2BS (E2), les différents sites d'interactions avec les protéines cellulaires (YY1, NF1, AP1, GR/PR, CEBP, TEF1, TEF2, OCT-1, Sp1 et TFIID) ainsi que la taille de la LCR. De plus, deux motifs conservés spécifiques aux β-HPV (M33 qui est un activateur transcriptionnel constitutif pour le promoteur tardif de HPV8 et M29 qui régule à la baisse le promoteur précoce d'HPV8 en interagissant avec IRF5.2) sont présentés dans la LCR de HPV8 (Lazarczyk *et al.*, 2009).

ii. Les protéines nécessaires pour la réplication et l'amplification virales (E1 et E2)

Les protéines E1 et E2 constituent les deux premières protéines virales essentielles à la réplication et à la libération du virus.[49]

Elles jouent un rôle crucial dans les processus de transcription et de réplication de l'ADN, ainsi que dans la partition du génome viral. De plus, elles subissent une régulation complexe par le biais de diverses modifications post-traductionnelles telles que l'acétylation, la phosphorylation et la sumoylation.[50,51]

- E1

La protéine E1, codée par l'ORF le plus grand et le plus conservé (environ 600 acides aminés) du génome des HPV, est composée de trois domaines principaux, chacun ayant une fonction distincte et cruciale. Ces domaines sont le domaine régulateur N-terminal, le domaine de liaison à l'ADN et le domaine hélicase (Figure 8).[52]

- Le domaine N-terminal contient le signal de localisation nucléaire (NLS) ainsi que le signal d'exportation nucléaire (NES), qui sont responsables du transport de la protéine E1 entre le cytoplasme et le noyau. De plus, ce domaine comporte un motif de liaison à la cycline (CBM) qui interagit avec les cyclines A et E, formant un complexe avec la kinase cycline dépendante (CDK) 2, ainsi que des sites de phosphorylation pour CDK2 et d'autres kinases.[53,54]
- Le domaine de liaison à l'ADN reconnaît spécifiquement les séquences proches de l'origine de réplication virale, qui est ensuite liée par le domaine hélicase pour former un complexe en forme de beignet autour de l'ADN viral.[55]
- Le domaine hélicase, dépendant de l'ATP, joue un rôle crucial dans l'auto-assemblage de la protéine E1 et le déroulement de l'ADN viral afin d'initier le processus de réplication.[56] En tant qu'hélicase réplicative qui orchestre la copie fidèle de l'épisome viral dans le noyau des cellules infectées, E1 est durant tout le développement des HPV, la protéine virale, tous génotype confondu, la plus conservée.[57]

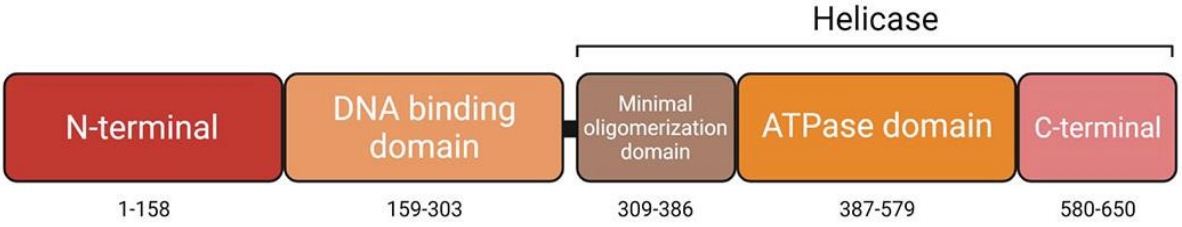

Figure 8 **: Schéma structurel des domaines de la protéine virale E1**. Ce schéma illustre les 3 domaines fonctionnels de E1, à savoir le domaine N-terminal, le domaine de liaison à l'ADN (DBD), ainsi que le domaine hélicase. Le domaine hélicase est composé du domaine d'oligomérisation minimal, du domaine ATPase et de l'extrémité C-terminale (Baedyananda *et al.*, 2022).

Comme mentionné précédemment, la protéine E1 est la seule à posséder une activité enzymatique (l'hélicase) qui joue un rôle essentiel dans l'amplification de l'épisome viral au sein des cellules infectées.[58] Pour ce faire, la protéine E1 s'assemble en un double hexamère, forme enzymatiquement active, qui se lie spécifiquement à l'origine de réplication virale (Ori) et déroule l'ADN viral dans le sens 3' → 5', amorçant ainsi le processus de réplication.[59] En plus de son activité d'hélicase, la protéine E1 interagit également avec plusieurs facteurs spécifiques de l'hôte, tels que l'ADN polymérase α-primase (Pol α-prim), la topoisomérase I (TopoI) et la protéine de réplication A (RPA), afin de coordonner l'assemblage d'un réplisome fonctionnel nécessaire à la réplication bidirectionnelle du génome viral (Figure 9).[60]

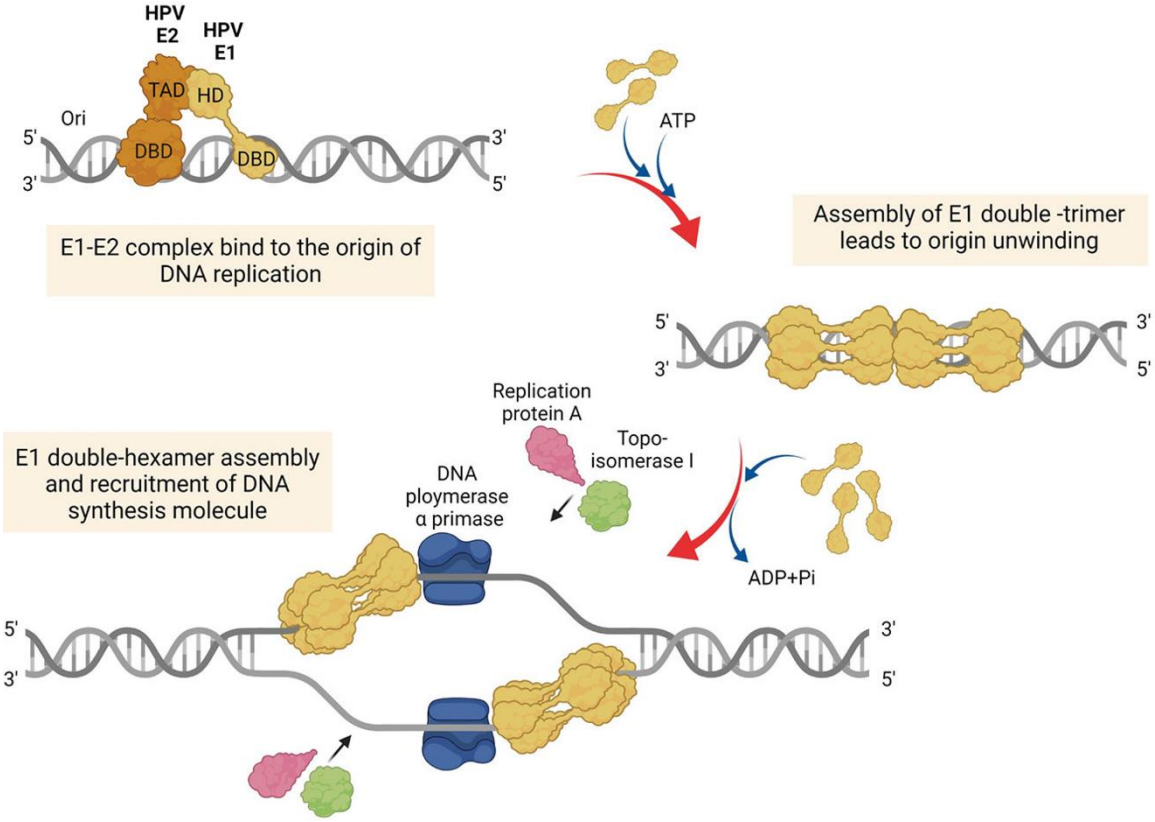

Figure 9 : **Initiation de la réplication de l'ADN de l'HPV**. Initialement, E1, pour pouvoir se lier à l'origine de réplication virale, forme un complexe avec E2. Par la suite, des protéines E1 supplémentaires sont recrutées pour s'assembler en tant que double trimère puis double hexamère. Ces assemblages permettent de dérouler l'ADN afin d'initier la réplication, *via* le recrutement de facteurs de réplication de l'hôte (Baedyananda *et al.*, 2022).

Par ailleurs, des études récentes ont suggéré une possible implication de la protéine E1 dans la cancérogenèse. En effet, E1 serait capable de déréguler l'expression de gènes impliqués dans la survie cellulaire. Dans des cellules surexprimant HPV16 E1, plusieurs gènes hôtes impliqués dans la synthèse des protéines (RPL36A), le métabolisme (ALDOC), la réponse immunitaire (ISG20), les dommages à l'ADN (ATR, BRCA1 et CHK1) et la prolifération cellulaire (CREB5, HIF1A, NFKB1, PIK3CA, JMJDIC, TSC22D3, FOXO3) ont montré une régulation significativement à la baisse.[61]

De plus, plusieurs études ont mis en évidence un rôle potentiel de E1 dans l'instabilité génétique, une caractéristique propre au cancer. Pour faciliter la réplication virale, E1 est capable d'induire des dommages à l'ADN, activant ainsi les voies de signalisation ATR/ATM et engageant la machinerie de réparation de l'ADN cellulaire. Une accumulation de protéines impliquées dans ladite voie, telles que γH2AX, ATR-interacting protein (ATRIP) et la topoisomerase IIβ-binding protein 1 (TopBP1), a d'ailleurs été observée dans les centres réplicatifs viraux.[62–64]

Pour finir, E1 joue également un rôle dans l'évasion immunitaire. Par exemple, HPV18 E1 peut moduler l'expression de gènes impliqués au niveau des récepteurs toll-like, des interférons et de l'apoptose, permettant ainsi à l'infection virale de persister en évitant une réponse immunitaire innée. [65,66]

Il est donc possible que la protéine E1 joue un rôle pertinent dans la carcinogenèse. Cependant, des études plus approfondies et spécifiquement axées sur la fonction de la protéine E1 dans la carcinogenèse cervicale doivent encore être réalisées, étant donné que seules quelques études se sont penchées sur ce sujet (Figure 10).

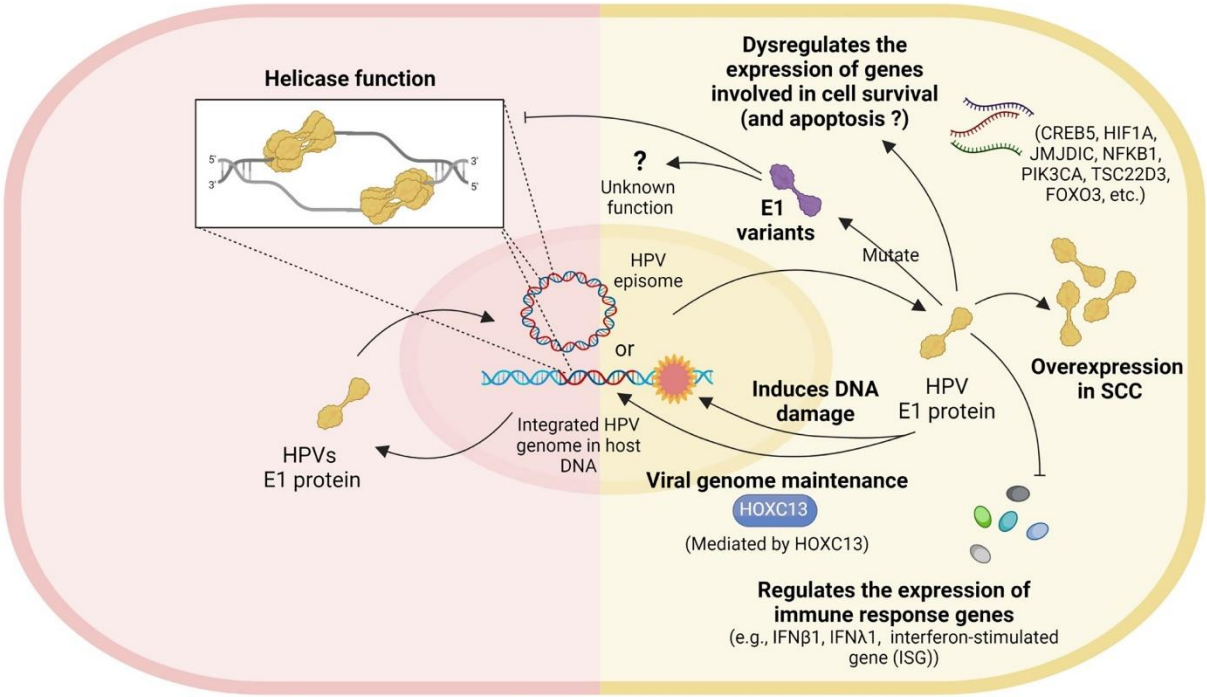

Figure 10 : **Schéma récapitulatif des rôles de la protéine virale E1**. Le panneau de gauche de cette figure met en évidence la fonction bien connue de la protéine E1 en tant qu'hélicase. Le panneau de droite met en évidence les rôles potentiels de la protéine E1 dans la cancérogenèse cervicale. Ces rôles comprennent la dérégulation de l'expression des gènes impliqués dans la survie cellulaire, la mutation ainsi que la surexpression de E1, l'induction des dommages à l'ADN, la maintenance du génome viral et la régulation de l'expression des gènes de la réponse immunitaire (Baedyananda *et al.*, 2022).

- E2

La protéine virale E2, principalement présente sous la forme d'un hétérodimère, se compose d'un domaine transactivateur à l'extrémité N-terminale et d'un domaine de liaison/dimérisation à l'extrémité C-terminale. Ces deux domaines sont reliés par une séquence de liaison flexible appelée charnière, dont la longueur et la composition varient en fonction du génotype de l'HPV (Figure 11). [67]

La protéine E2 des papillomavirus humains joue un rôle crucial dans la régulation de la transcription, l'initiation de la réplication de l'ADN et la partition du génome viral, ce qui en fait un acteur essentiel dans le cycle de vie viral.

En effet, la protéine E2 joue un rôle majeur dans la régulation de la transcription. À cet égard, elle peut :

- Recruter des facteurs cellulaires au niveau du génome viral pour activer ou réprimer les processus transcriptionnels.[68,69]
- Se lier spécifiquement à des motifs de séquence présents dans le génome viral, appelés sites de liaison E2 (E2BS), pour activer ou réprimer la transcription en fonction du site de liaison et des facteurs cellulaires associés.[70]
- Entraver stériquement la liaison des facteurs cellulaires, tels que Sp1 et TFIID, aux éléments promoteurs proximaux du génome viral.[71]
- Réprimer la transcription des oncoprotéines E6 et E7 en recrutant des facteurs, tels que Brd4 et SMCX, qui sont impliqués dans l'organisation et la dynamique de la chromatine, notamment en compactant celle-ci afin qu'elle soit moins accessible.[72,73]

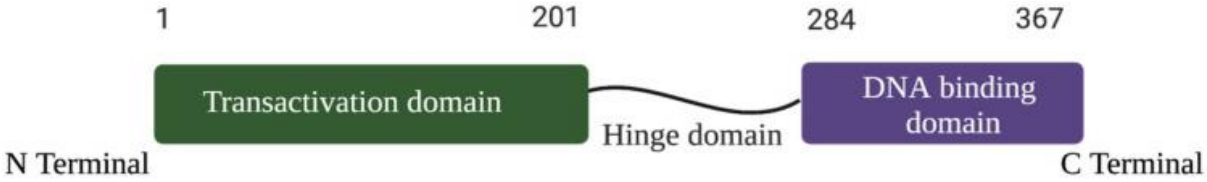

Figure 11 : **Structure schématique de la protéine virale E2 et de ses domaines respectifs, le domaine de transactivation, la région charnière et le domaine de liaison à l'ADN** (Evande *et al.*, 2023).

Mais ce n'est pas tout, E2 participe également à l'initiation de la réplication de l'ADN viral en facilitant le chargement de l'hélicase E1 sur l'origine de réplication. Cette origine de réplication contient un site de liaison E1, une région riche en A/T et au moins un site de liaison E2 (E2BS). C'est grâce à ce site de liaison que E2 améliore et soutient les fonctions de E1. [74–76] Il convient de noter que le mode de fonctionnement de E2 diffère légèrement entre les papillomavirus β et α (voir paragraphe sur le LCR).

De plus, E2 est capable de former un complexe avec la protéine L2, ce qui lui permet d'être colocalisée dans les domaines nucléaires 10 (ND10) où se déroulent les processus de transcription et de réplication virales précoces. Au sein de ces domaines, E2 joue également un rôle dans le processus d'empaquetage du génome viral.[77,78]

Enfin, grâce à son domaine transactivateur et aux sites E2BS, E2 établit un lien entre le génome viral et les chromosomes de l'hôte lors de la mitose, ce qui facilite la rétention, la maintenance et la partition du génome viral.[79]

En tant que protéine multifonctionnelle, E2 recrute également de nombreuses protéines cellulaires pour assurer ses fonctions. Grâce à ces interactions multiples (comme par exemple la caspase 8, p300, CBP, NRIP, *etc*), E2 peut également influencer des phénomènes tels que l'apoptose, le cycle cellulaire, l'importation nucléaire et la dégradation des protéines, en plus de son rôle majeur dans la régulation de la transcription, l'initiation de la réplication de l'ADN et la partition du génome viral.[80–83]

iii. Les protéines oncogènes (E6 et E7)

Les oncoprotéines virales E6 et E7, bien qu'elles ne possèdent pas d'activité enzymatique propre, sont capables d'interagir avec de nombreuses protéines de l'hôte afin de moduler la prolifération et la différenciation cellulaire, favorisant ainsi le cycle de vie viral.[84]

Les deux principales protéines virales responsables de l'activité oncogène des HPV sont les oncoprotéines E6 et E7. Bien que leur organisation structurelle soit à peu près similaire, de légères différences fonctionnelles peuvent être observées entre les β-HPV et les α-HPV. C'est sur ce point que nous allons porter notre attention par la suite.[85]

Il est à noter que l'oncoprotéine E5 n'est pas retrouvée dans les β-HPV (à l'exception de l'HPV14) et ne joue qu'un rôle mineur dans l'oncogénicité des α-HPV.[86]

- E6

L'oncoprotéine E6 des β-HPV, tout comme celle des α-HPV, est une petite protéine basique composée d'environ 150 acides aminés. Elle contient deux paires de motifs CXXC, capables d'adopter une conformation structurelle dénommée doigt de zinc (Figure 12).[87] Cette conformation particulière joue un rôle clé chez les HPV car elle leur permet d'interagir avec des protéines contenant le motif LxxLL, telles que l'ubiquitine ligase E3 (E6AP) ou encore la protéine 1 de type Mastermind (MAML1), pour n'en citer que quelques-unes.[88,89]

On peut toutefois noter que le motif de liaison aux PDZ (PBM) n'est retrouvé qu'au niveau de la région C-terminale des α-HPV, où il impacte l'organisation et la croissance cellulaire en interagissant avec des protéines de jonction telles que FRMPD2, PATJ, DLG1, *etc*, ainsi qu'avec des acteurs des voies de signalisation de TGF-β (TIP2/GIPC) et de PI3K/AKT (NHERF1).[90–93] Ce motif structurel, que l'on ne retrouve que chez les α-HPV à haut risque, est même considéré comme une signature moléculaire du potentiel oncogène de la protéine virale E6.[94]

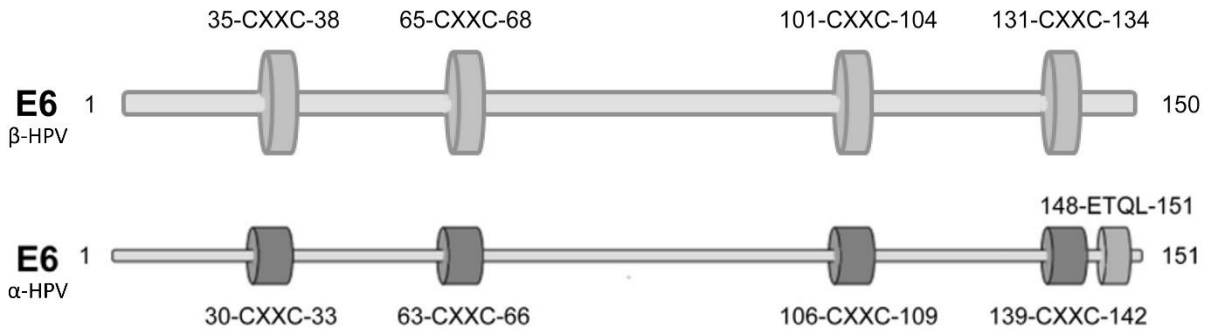

Figure 12 : **Structure schématique de l'oncoprotéine E6 des β-HPV et α-HPV**. La position de plusieurs motifs d'acides aminés importants pour leur structure et leurs fonctions est mise en évidence. Quel que soit le genre d'HPV, l'oncoprotéine E6 comprend quatre motifs CXXC, qui ont la capacité de former des complexes en doigt de zinc. Cependant, l'oncoprotéine E6 des α-HPV possède également un motif de liaison PDZ consensus (ETQL) à l'extrémité C-terminale (adapté de Tommasino, 2014 et 2017).

Malgré cette grande similitude structurelle, l'interactome de l'oncoprotéine E6 des β-HPV diffère de celui des α-HPV. En effet, le mode de fonctionnement des β-HPV est spécifique au génotype, contrairement aux α-HPV où l'on retrouve un schéma fonctionnel similaire dans la grande majorité de leurs génotypes. Actuellement, les fonctions les mieux caractérisées chez les β-HPV sont celles impliquées dans la régulation de la réponse apoptotique suite à différents types de stress cellulaires (Figure 13).[85,87]

Tout d'abord, l'oncoprotéine E6 des β-HPV est capable d'altérer l'expression des gènes régulés par p53 en utilisant trois mécanismes différents :

- En premier lieu, certains β-HPV (comme HPV38 et 92) sont capables de stabiliser p53 par une interaction directe, tandis que d'autres (comme HPV17) le font de manière indirecte[95]
- Ensuite, l'oncoprotéine E6 de l'HPV49 interagit avec E6AP, favorisant ainsi l'ubiquitination de p53 et sa dégradation par le protéasome[96]
- Enfin, certains β-HPV (comme HPV23) se lient à HIPK2 pour empêcher la phosphorylation (et donc l'activation) de p53 [97]

Mais ce n'est pas tout, *via* E6, les β-HPV sont également capables de modifier le fonctionnement de p300, une histone acétyltransférase qui régule la transcription *via* le remodelage de la chromatine, de deux manières distinctes :

- D'une part, les β-HPV tels que HPV5 et 8 sont capables de dégrader p300, à l'aide du protéasome, suite à une interaction directe forte avec cette protéine. La dégradation de p300 entraîne une diminution significative des niveaux de protéine ATR, qui est un acteur clé dans la signalisation des dommages causés par les rayons UV[98,99]
- D'autre part, les β-HPV tels que HPV38 peuvent, *via* une interaction directe faible, interagir avec p300. Cette interaction empêche l'acétylation de p53 et inhibe ainsi son activité transcriptionnelle[100]

Cela entraîne une inhibition de la différenciation cellulaire et une diminution de l'efficacité de la réparation des dommages à l'ADN. [101]

De plus, l'oncoprotéine E6 des β-HPV est capable d'interagir avec BAK pour inhiber la réponse apoptotique. Dans ce processus, E6 peut interagir soit avec E6AP (HPV8) soit avec HERC1 (HPV5) pour dégrader BAK à l'aide du protéasome.[102,103]

Un autre aspect crucial à considérer réside dans la capacité de l'oncoprotéine E6 de certains β-HPV à rendre une cellule immortelle. C'est particulièrement le cas pour E6 des HPV38 et 49, qui forment un complexe avec E6AP et NFX1-91, entraînant une augmentation significative du taux d'ARNm de hTERT et donc une immortalisation cellulaire.[96,104]

Enfin, une caractéristique inhérente à l'oncoprotéine E6 des β-HPV réside dans sa capacité à interagir avec MAML1, qui est un élément central du complexe de régulation de la voie de signalisation Notch. Les protéines E6 des HPV8, 17 et 38 sont capables de se lier spécifiquement au motif LxxLL situé à l'extrémité C-terminale de MAML1, ce qui induit une répression de l'activité transcriptionnelle de Notch. Étant donné l'implication de Notch dans la promotion de la sortie du cycle cellulaire et la différenciation cellulaire, son inactivation est bénéfique pour l'accomplissement du cycle viral.[105–107]

Toutes les interactions protéiques mentionnées précédemment, à l'exception de MAML1 qui est spécifique à l'oncoprotéine E6 des β-HPV, sont également observées chez les α-HPV. La distinction principale réside dans l'interaction moins complexe entre les α-HPV et p53. En effet, contrairement aux β-HPV qui présentent trois modes d'interaction distincts avec p53 (en fonction du génotype), les α-HPV à haut risque, en se liant à E6AP, induisent la dégradation de p53.[85] Pour le reste, les modalités d'interaction entre les deux genres viraux ne diffèrent pas.[108–113]

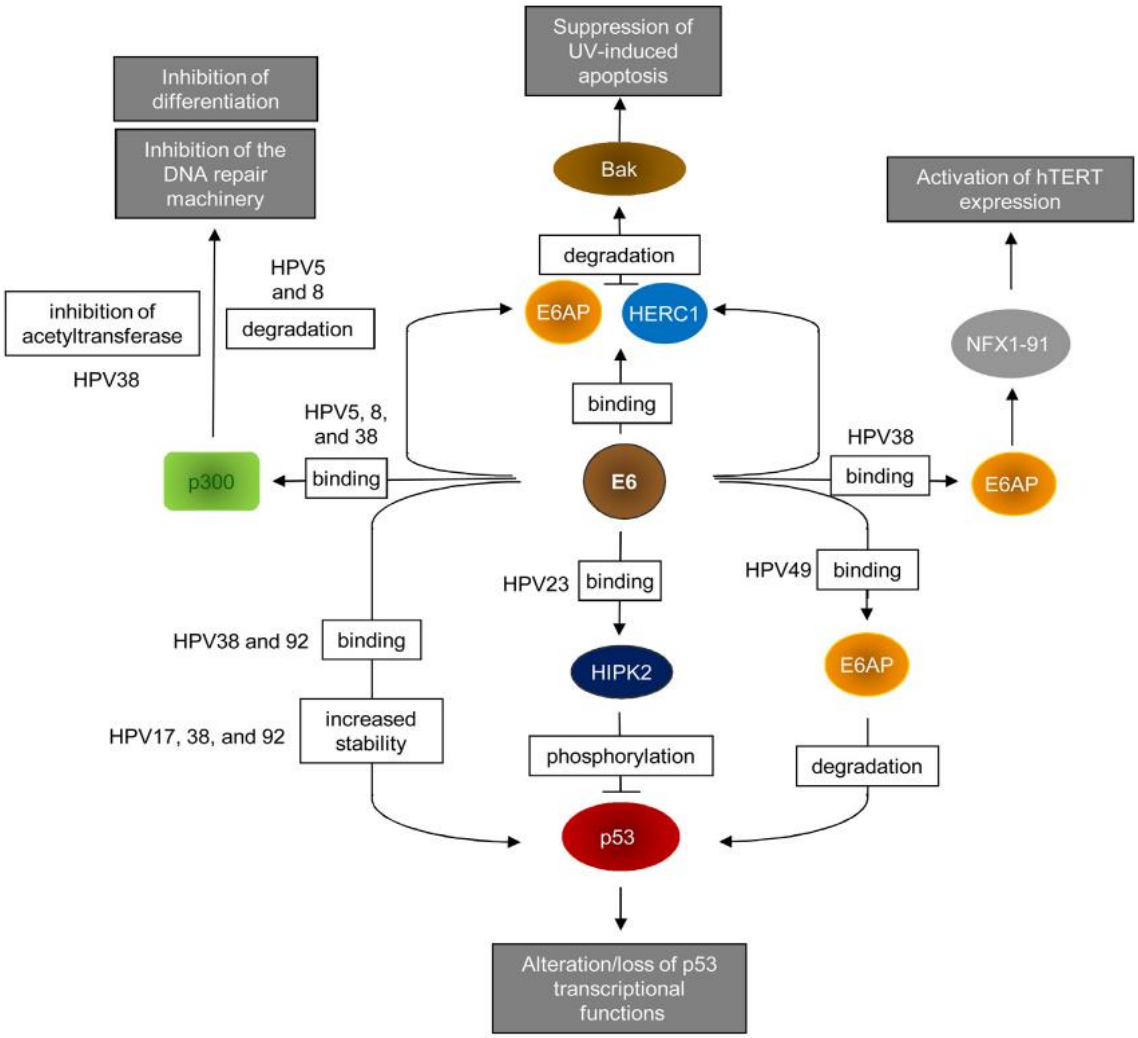

Figure 13 : **Représentation non exhaustive des différentes cibles de l'oncoprotéine E6 des β-HPV ainsi que les conséquences induites par ces interactions**. Les cases en gris foncé décrivent les événements spécifiques déclenchés par les différentes oncoprotéines E6 (Tommasino, 2017).

- E7

L'oncoprotéine E7 des β-HPV partage des caractéristiques similaires à celle des α-HPV. Elle est composée d'environ 100 acides aminés et peut être divisée en trois régions distinctes connues sous le nom de CR1, CR2 et CR3 (Figure 14).[85]

La région CR2 renferme le motif LXCXE, essentiel pour l'interaction avec pRb ainsi que ses protéines associées, p107 et p130. Cependant, contrairement aux α-HPV, les β-HPV ne possèdent pas de site de phosphorylation spécifiquement ciblé par la caséine kinase 2 (CK2).[87,114]

En outre, la région CR3, similaire aux α-HPV, contient deux motifs de liaison au zinc qui jouent un rôle crucial dans la formation d'homodimères et/ou de tétramères, ainsi que dans la stabilité des protéines.[115] Il convient toutefois de noter qu'aucune étude n'a évalué si ces propriétés étaient également préservées pour l'oncoprotéine E7 des β-HPV.

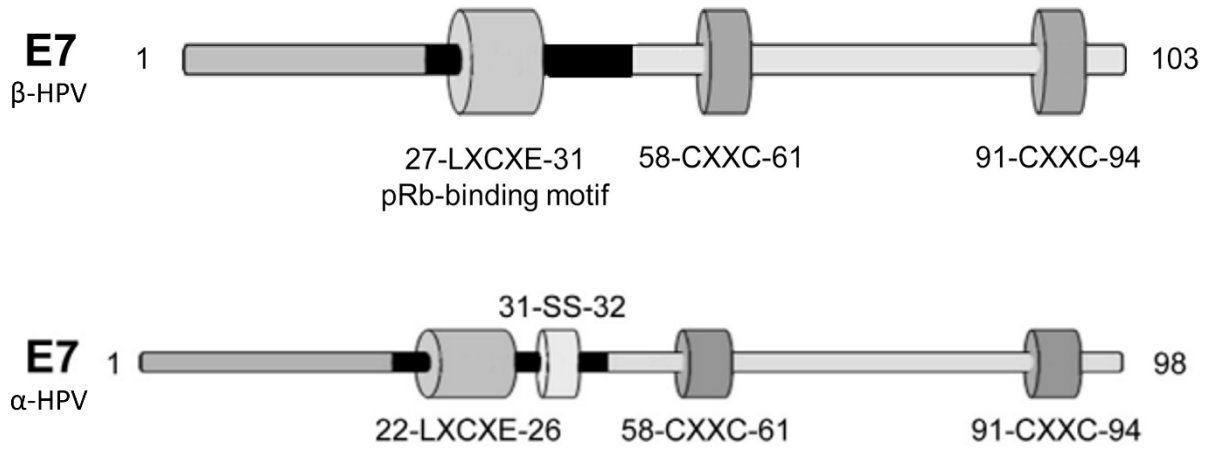

Figure 14 : **Structure schématique de l'oncoprotéine E7 des β-HPV et α-HPV**. La position de plusieurs motifs d'acides aminés importants pour leur structure et leurs fonctions est mise en évidence. Quel que soit le genre d'HPV, l'oncoprotéine E7 comprend deux motifs CXXC, qui ont la capacité de former des complexes en doigt de zinc. De plus, le domaine de liaison à pRb (LXCXE) est également présent chez les deux genres d'HPV (adapté de Tommasino, 2014 et 2017).

L'une des caractéristiques les plus étudiées de l'oncoprotéine E7 réside dans sa capacité à interagir avec pRb. Cette protéine joue un rôle essentiel dans la régulation du cycle cellulaire en contrôlant l'expression de divers gènes. pRb régule négativement, par association directe, l'activité des membres de la famille E2F (E2F1–3), maintenant la cellule dans un état de quiescence. Cependant, lors de la division cellulaire, les kinases cycline-dépendantes favorisent la phosphorylation de pRb. La phosphorylation excessive de pRb induit la libération des facteurs de transcription E2F, ce qui favorise l'expression de gènes impliqués dans la régulation de la division cellulaire, tels que les gènes codant pour les cyclines A et E.[116]

Chez les β-HPV, il a été constaté que l'oncoprotéine E7 est capable de se lier à la forme hyper-phosphorylée de pRb avec une affinité variable. Les études ont montré que les HPV5 et 8 interagissent faiblement avec pRb, tandis que l'HPV38 interagit de manière plus intense avec cette protéine. [22,23,117] Cette interaction perturbe ainsi le complexe pRb/E2F1-3 et favorise la division cellulaire.

L'oncoprotéine E7 est également impliquée dans la modulation de l'expression des gènes régulés par p53.[118] Dans le cas spécifique de l'HPV38, il a été observé qu'il peut induire l'accumulation d'une forme particulière de p53 dans le noyau, qui est phosphorylée uniquement aux niveaux des sérines 15 et 392. Cette forme spécifique de p53 est recrutée par un promoteur interne du gène p73, ce qui conduit à l'expression de la forme tronquée de δNp73α, une protéine qui agit comme un antagoniste de la voie p53/p73.[119]

Pour finir, l'oncoprotéine E7 de l'HPV38 favorise, par un mécanisme encore inconnu, la translocation nucléaire de l'IκB kinase beta (IKKβ), qui à son tour interagit et phosphoryle δNp73α au niveau de la sérine 422, augmentant ainsi sa stabilité. Cette augmentation de la stabilité de δNp73α favorise la formation d'un complexe inhibiteur comprenant deux enzymes épigénétiques, l'ADN méthyltransférase 1 (DNMT1) et l'enhancer of zeste homolog 2 (EZH2), qui se lient à un sous-ensemble de promoteurs régulés par p53. [118] De plus, il est important de noter que l'HPV38, par le biais de δNp73α, régule positivement l'expression de hTERT, un gène impliqué dans l'immortalité cellulaire (Figure 15).[120]

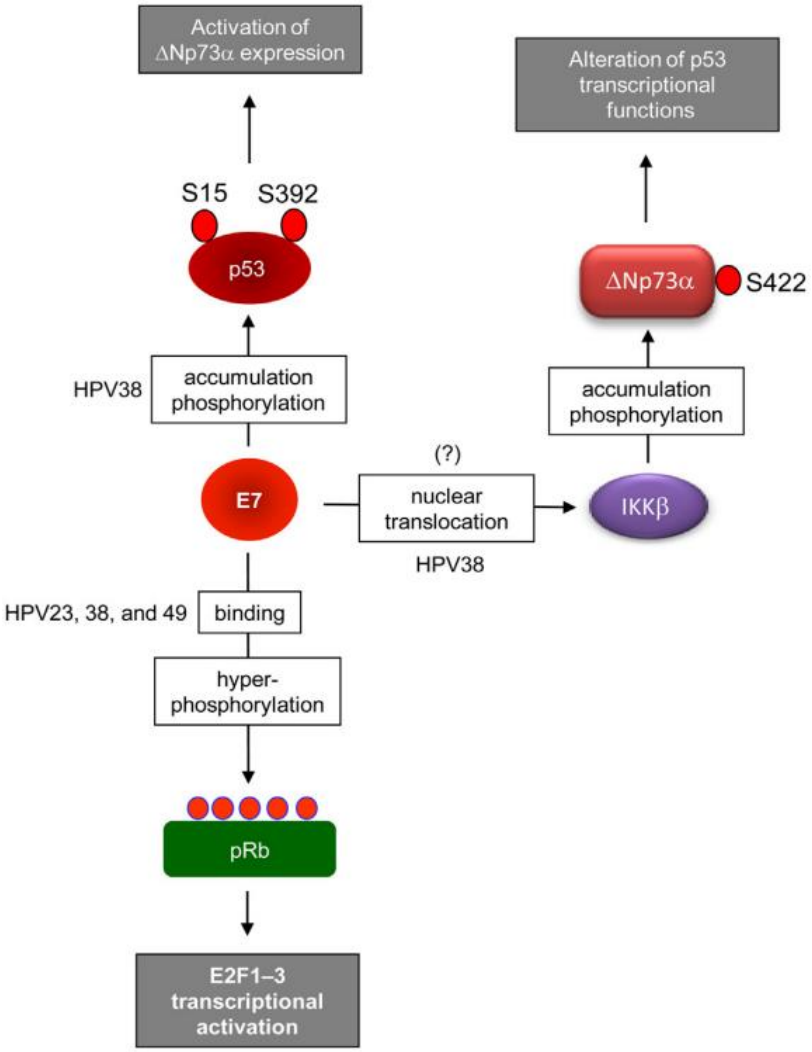

Figure 15 : **Représentation non exhaustive des différentes cibles de l'oncoprotéine E7 des β-HPV ainsi que les conséquences induites par ces interactions**. Les cases en gris foncé décrivent les événements spécifiques déclenchés par les différentes oncoprotéines E7 (Tommasino, 2017).

Contrairement aux β-HPV, les propriétés biologiques de l'oncoprotéine E7 des α-HPV ont été étudiées plus en détail. En effet, l'HPV16 a la capacité d'induire la dégradation de pRb en formant un complexe avec la culline 2.[121] Cependant, le mécanisme de dégradation impliqué pour les autres α-HPV n'est pas encore connu.

En outre, l'oncoprotéine E7 de l'HPV16 démontre une capacité d'interaction avec deux protéines, à savoir p107 et p130, qui sont impliquées dans la répression d'autres membres de la famille E2F (E2F4 et E2F5) ainsi que dans l'activation des histones désacétylases. Ces protéines jouent un rôle crucial dans la régulation de l'expression des gènes.[116,122] Des études antérieures ont démontré que E7 HPV16 est capable de déstabiliser p130, entraînant ainsi une altération de l'inhibition des complexes E2F.[123]

En plus de son interaction avec les membres de la famille E2F, l'oncoprotéine E7 est capable de perturber le cycle cellulaire en se liant directement à deux inhibiteurs de CDK, à savoir p21WAF1/CIP1 et p27KIP1. Cette liaison empêche p21WAF1/CIP1 et p27KIP1 de contenir le cycle cellulaire.[124,125]

Par ailleurs, l'HPV16 peut aussi interagir directement avec le complexe cycline A/CDK2. L'oncoprotéine E7, en interagissant avec les sous-unités de la cycline, stimule CDK2, qui se lie ensuite à la cycline A ou E.[126]

Il convient de prendre en compte que les oncoprotéines E6 et E7 des α et β-HPV, en plus de leurs interactions majeures mentionnées précédemment, interagissent avec un vaste réseau de protéines de l'hôte, qui leur permettent d'altérer plusieurs processus cellulaires, notamment [127–132] :

- L'échappement immunitaire, qui permet aux cellules infectées d'éviter la reconnaissance et la destruction par le système immunitaire (*via* l'inhibition directe des voies médiées par TLR9, en régulant à la baisse la transcription de celui-ci, ainsi que l'inhibition de IRF3, empêchant l'induction de l'IFN-β)
- L'apoptose, où les oncoprotéines interfèrent avec les voies de signalisation qui régulent la mort cellulaire programmée (voir ci-dessus)
- La différenciation, où elles perturbent les mécanismes responsables de la maturation cellulaire (notamment *via* l'interaction entre E6/E7 et MAML1, PTPN14 et TGFβ)
- Le métabolisme, où elles influencent les processus métaboliques cellulaires (*via* la dégradation de p53 ce qui a pour effet de réduire l'expression de TIGAR et HIF1 par exemple)
- Le cycle cellulaire, où elles altèrent la régulation du cycle cellulaire et favorisent la prolifération cellulaire incontrôlée (voir ci-dessus)
- La polarité cellulaire, où elles perturbent l'organisation spatiale des cellules (*via* leurs interactions avec les membres de la famille MAGUK)
- L'immortalisation, où elles induisent une durée de vie prolongée des cellules infectées
- Les voies de réparation de l'ADN (notamment BER et NER, impliqués dans la réparation des dommages à l'ADN induit par les UV), où elles modifient les mécanismes de réparation de l'ADN, conduisant à l'accumulation de mutations génétiques

Ces exemples soulignent l'impact étendu des interactions des oncoprotéines E6 et E7 sur divers processus cellulaires, ce qui contribue, *in fine*, au développement et à la progression du cancer induit par les HPV.

iv. Les protéines de la capside (L1 et L2)

L1 et L2 sont les 2 protéines virales nécessaires pour assurer la formation de la capside, c'est d'ailleurs pour cette raison qu'on les retrouve chez tous les HPV connus.[49] L1 et L2, dénommées respectivement protéine majeure et mineure de la capside, jouent un rôle important dans l'entrée du virus, la formation de la capside ainsi que la libération du virion.

- L1

L1 est une protéine d'environ 55 kDa qui a la capacité de s'auto-assembler spontanément en particules pseudo-virales (VLP). Plus précisément, L1 peut s'assembler en une structure pentamérique qui constitue l'unité de base de la capside, connue sous le nom de capsomère.[133,134] La capside, quant à elle, est composée de 72 capsomères qui lui confère une structure icosaédrique noueuse grâce à la formation de liaisons disulfures entre les extrémités N et C terminales de L1 (Figure 16).[135,136]

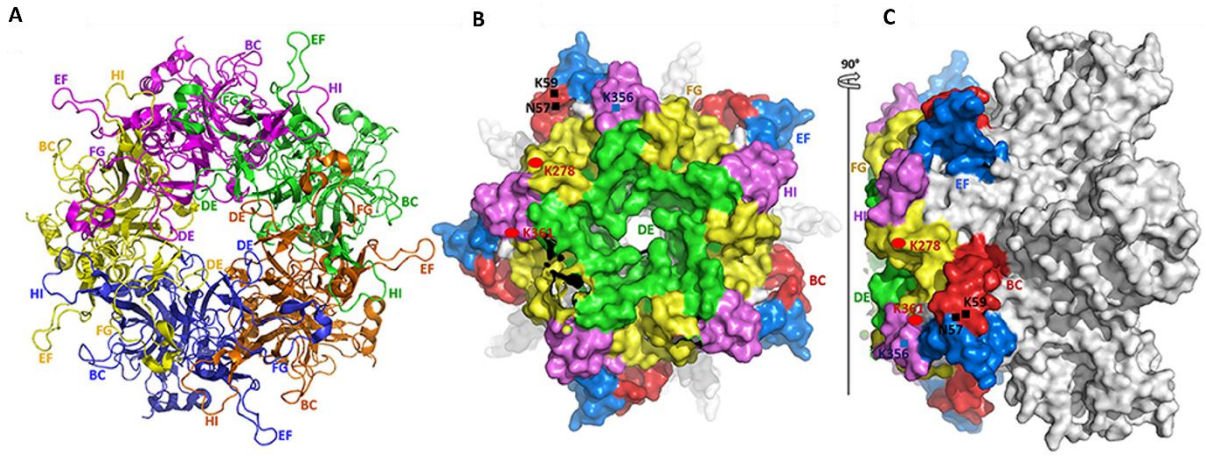

Figure 16 : **Représentation structurale de la protéine virale L1 de l'HPV**. A) Représentation de la structure principale des monomères L1, représentés par différentes couleurs, dans le capsomère. Les boucles BC, DE, EF, FG et HI sont clairement représentées. B et C) Conformation de la surface selon différentes perspectives (vue de dessus et vue latérale), mettant en évidence chaque boucle ainsi que certains sites de liaison aux protéoglycanes d'héparane-sulfate (HSPG) riches en lysine (K) (Kombe Kombe *et al.*, 2021).

Étant donné que L1 constitue l'ensemble de la surface externe de la capside, elle joue un rôle majeur dans le mécanisme d'entrée du virus. Conformément à l'article du Dr Day, l'interaction avec les chaînes de sulfate d'héparane des protéoglycanes (HSPG) et les kératinocytes, se fait principalement par l'intermédiaire de la protéine L1. [137]

En effet, ce mécanisme dépend de la liaison entre L1 et les HSPG présentes à la fois sur la membrane cellulaire et dans la matrice extracellulaire (ECM). [138,139] Cette interaction entraîne un léger changement conformationnel au niveau de la structure de la capside, médié par la cyclophiline B, qui expose la région N-terminale de la protéine mineure de la capside, appelée L2, à la surface de la particule virale. [140]

Cette exposition permet à une protéase, appelée furine, de cliver L2 au niveau de la membrane basale (BM) des kératinocytes basaux. Ce clivage induit un changement conformationnel supplémentaire qui permet au virion de se lier à un récepteur secondaire, l'intégrine α6β4 aidée par les tétraspanines CD63 et CD151, situé à la surface des kératinocytes. [141–143]

- L2

L2 est une protéine d'environ 70 kDa qui se localise au niveau des cavités centrales des capsomères (pentamères de L1). Chaque capsomère peut contenir 1 protéine L2, bien que parfois certaines cavités puissent être vides et que le rapport 1/5 (L2/L1) puisse ne pas être respecté (Figure 17).[144,145]

Cette protéine joue un rôle crucial dans le cycle de vie du papillomavirus humain. Bien que sa contribution lors de l'entrée du génome viral dans la cellule hôte soit limitée, L2 joue un rôle essentiel dans le transport du génome viral.[146,147] En formant un complexe avec E2, la protéine virale L2 facilite le transport de l'ADN viral vers le noyau cellulaire, plus spécifiquement vers le domaine nucléaire 10, où les processus de transcription et de réplication virales précoces se déroulent.[148–150]

Pour finir, les protéines L1 et L2 participent à l'encapsidation des génomes nouvellement répliqués, ce qui entraîne la libération de virions dans les couches superficielles lors de la desquamation.[151–153]

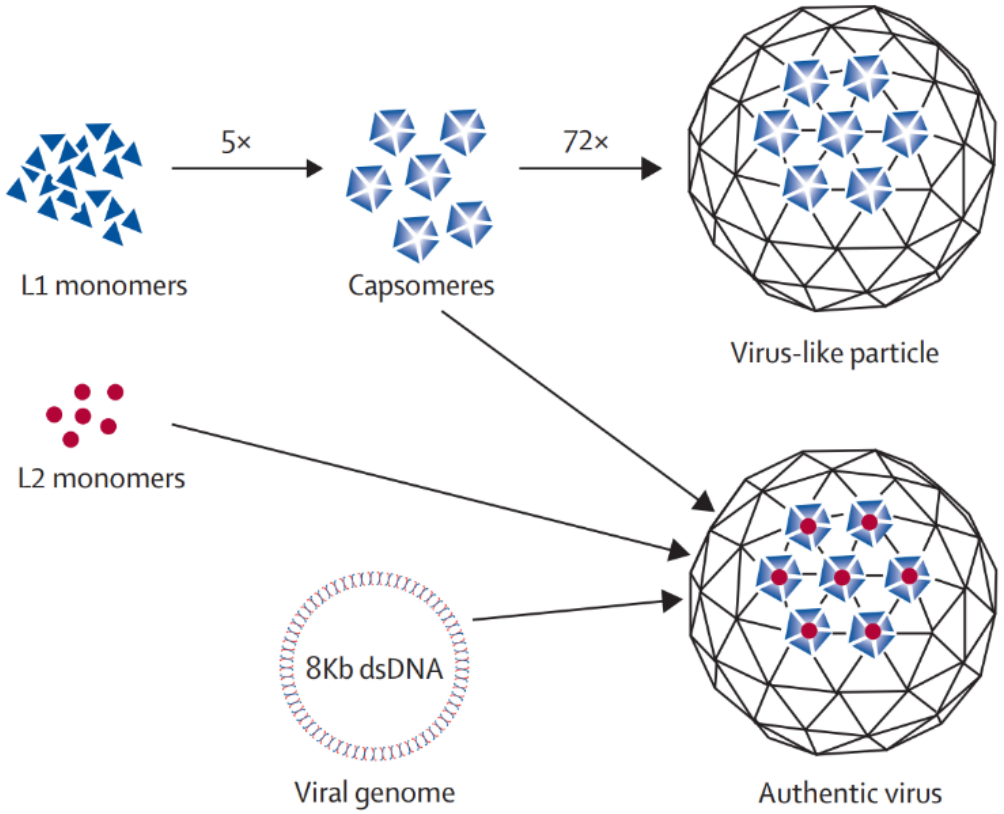

Figure 17 : **Structure et organisation de la capside du papillomavirus humain** (Schiller *et al.*, 2015).

v. Les protéines de fusion (E4 et E8)

Les protéines de fusion issues de l'épissage de l'ARNm codé par l'ORF de E2 sont considérées comme ayant un rôle moins crucial dans le cycle de vie du virus. En effet, elles contribuent à faciliter ce cycle en réprimant l'activité transcriptionnelle du virus, en limitant la réplication de son génome et en favorisant sa libération.

- E4

E4 est une protéine de fusion codée par le domaine charnière de l'ORF de E2. Cette protéine de fusion, appelée E1^E4, est synthétisée à partir d'un ARNm épissé, où le codon d'initiation et les premiers acides aminés proviennent de l'ORF E1 (Figure 18).[154] Dans le cycle de réplication virale, E4 joue un rôle lors des derniers stades. Initialement indétectable dans la cellule hôte, son expression est activée lorsque la cellule hôte déclenche l'activation tardive du promoteur viral.[155]

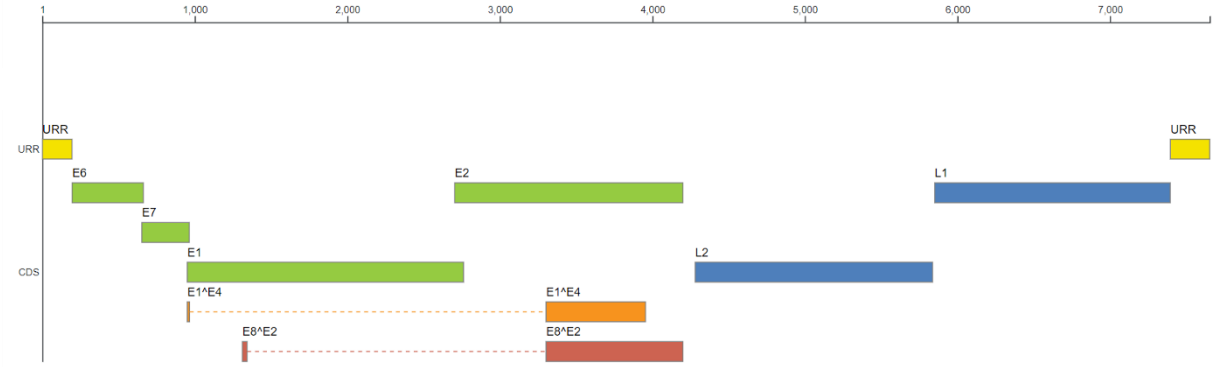

Figure 18 : **Organisation génomique des protéines de fusion E4 et E8** (PAVE, 2023).

Bien que les fonctions de E4 au cours du cycle de vie viral soient encore peu connues, des études récentes ont révélé que E4 contient un motif appelé "cluster de leucines" près de son extrémité N-terminale, qui joue un rôle crucial dans son association avec la kératine. L'effet de E4 sur les cytokératines se traduit par une réorganisation généralement observée à la périphérie cellulaire, facilitant ainsi la libération et/ou la transmission du virus. [156]

Par ailleurs, il est important de souligner que l'extrémité C-terminale de la protéine E4 interagit également avec les cytokératines de type 1 et 2 (notamment la 8, 13 et 18 pour ne citer qu'eux). Le motif appelé "*beta-aggregation*", situé à cette extrémité, permet à la protéine E4 de s'auto-associer, formant ainsi des structures qui présentent une similarité avec les fibres amyloïdes. Cette capacité d'auto-association joue un rôle important au niveau de l'organisation de la cellule hôte, notamment le réseau de cytokératine. [157] La capacité de E4 à perturber l'organisation de la kératine confirme son rôle dans la libération virale. [158] Pour finir, la détection d'E4, par immunohistochimie, uniquement dans les couches épithéliales médianes et supérieures souligne son importance dans les derniers stades du cycle de vie viral. [159,160]

De plus, des études récentes ont également révélé que E4 pourrait retarder la progression du cycle cellulaire à la phase G2 en inhibant l'activité de CDK1/cycline B. Des expériences ont montré que les cellules épithéliales exprimant E4 des HPV16, 18 ou 1 subissent un arrêt de la croissance cellulaire en phase G2 en raison de l'inhibition de l'accumulation nucléaire de la protéine cycline/CDK1 dans le noyau.[161]

Il convient également de noter que E4 est spécifique aux genres de papillomavirus. En effet, la structure qu'elle forme dans la cellule infectée ainsi que le moment où ces structures apparaissent ne seraient pas le même pour les β-HPV ou les α-HPV. Par exemple, les β-HPV se caractérisent par l'apparition d'inclusions cytoplasmiques dans les couches épithéliales inférieures à moyennes (couches épineuses). [162] La composition précise de ces structures cytoplasmiques n'est pas encore connue, mais des analyses suggèrent qu'elles pourraient être principalement constituées de E4, et que la présence abondante de E4 dans les lésions cutanées est probablement due à la présence de ces structures.[163] Ces inclusions cytoplasmiques sont considérées comme un contributeur majeur à l'effet cytopathique.[164]

- E8

E8 est une protéine de fusion codée par l'ORF de E2. Cette protéine, connue sous le nom d'E8^E2, est synthétisée à partir d'un ARNm épissé comprenant le domaine C-terminal et la région charnière de E2, qui sont reliés à un peptide de 10 à 13 résidus appelé E8 (dérivé du gène codant pour la protéine virale E1 située en amont) (Figure 19). Au cours du cycle viral, E8^E2 joue un rôle prépondérant dans la phase de maintien en tant que répresseur de la transcription et de la réplication virales. En effet, grâce à son domaine C-terminal, E8 interagit avec les génomes viraux et réprime l'activité transcriptionnelle virale et la réplication du génome en recrutant des complexes corépresseurs cellulaires tels que NCoR/SMRT-HDAC3.[165–167]

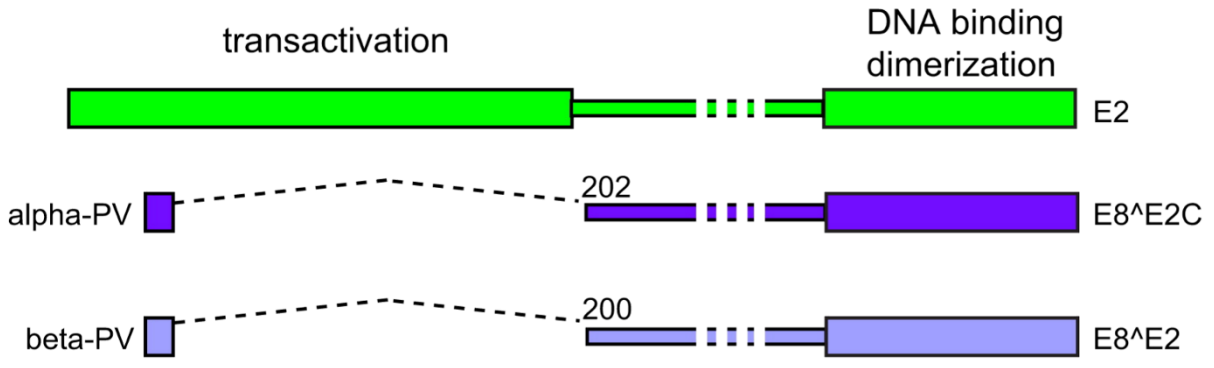

Figure 19 : **Structure et organisation de la protéine de fusion virale E8**. Les deux domaines conservés de la protéine E2, codés par tous les HPV, sont représentés en vert en haut. La région entre les domaines est de longueur variable et s'appelle la région charnière. En bleu, nous pouvons observer E8, parfois considérée comme une forme répressive de E2, présente chez les α-HPV et les β-HPV (McBride, 2013).

D. Cycle viral

Comme précédemment mentionné, quel que soit le genre, les HPV infectent et se répliquent dans les épithéliums muqueux et/ou cutanés de leurs hôtes. Ces épithéliums sont stratifiés et comprennent une couche basale de cellules auto-renouvelables qui se divisent symétriquement pour maintenir la couche basale et asymétriquement pour générer des cellules filles qui composent les couches différenciées de l'épithélium. [34] Cette caractéristique est exploitée par le cycle de vie des HPV, qui établit un réservoir d'infection persistante dans les cellules basales auto-renouvelables tout en générant uniquement des virions dans les cellules différenciées en phase terminale. Les virions sont ensuite libérés dans l'environnement sous forme de squames (cellules mortes) qui se détachent de la surface de l'épithélium. Cette stratégie permet une infection persistante de faible niveau dans les cellules auto-renouvelables, tout en limitant l'infection productive aux cellules différenciées en phase terminale, favorisant ainsi l'infection à long terme et l'évasion immunitaire (Figure 20). [28]

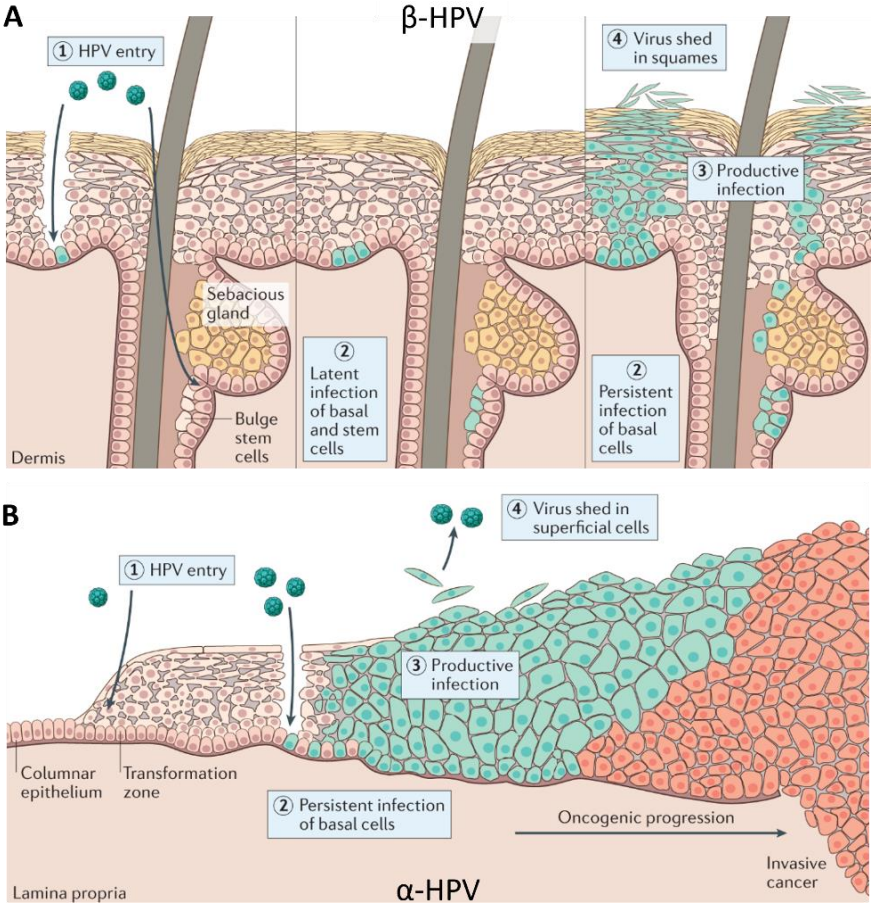

Figure 20 : **Cycle infectieux des β-HPV (A) et α-HPV (B)**. Quel que soit le genre d'HPV, le virus pénètre dans l'épithélium par une microfissure et/ou *via* les cellules de la zone de transition (1), et établit une infection persistante dans les cellules basales et/ou les cellules souches en division (2). Au fur et à mesure que les cellules infectées se différencient, la phase productive de l'infection virale est activée, avec amplification de l'ADN viral et synthèse des protéines de capside (3). Le virus est libéré de la surface de l'épithélium dans des squames exfoliantes ou des cellules superficielles (4). Cependant, les infections par les α-HPV à haut risque peuvent devenir chroniques et éventuellement subir une progression oncogène (cellules orange foncé). Ces cellules ne se différencient pas et ne produisent pas de virus et, dans un petit nombre de cas, peuvent évoluer vers un cancer invasif (McBride, 2022).

Le cycle de vie des HPV est basé sur la différenciation cellulaire. À chaque étape, les protéines de la cellule hôte sont détournées et manipulées pour faciliter le cycle de vie viral. Les HPV sont capables d'induire des dommages à l'ADN dans les cellules différenciées qui normalement ont quitté le cycle cellulaire, ce qui active plusieurs voies de signalisation et permet le recrutement de protéines nécessaires à la réplication virale. [168]

Outre la différentiation cellulaire, l'infection par les HPV est également limitée par le tropisme, c'est-à-dire la spécificité d'infection pour certains types d'épithélium en fonction du genre d'HPV. Actuellement, les chercheurs pensent que le tropisme n'est pas déterminé par les récepteurs viraux d'entrée, mais plutôt par la capacité de chaque virus à transcrire l'ARN dans différents types de kératinocytes. [169]

Indépendamment du tropisme, le cycle de vie des papillomavirus humains reste similaire quel que soit le genre d'HPV. Il comprend plusieurs étapes complexes, à savoir l'entrée du virus, la phase d'établissement, la phase de maintenance, la phase de prolifération cellulaire, la phase d'amplification du génome viral, la phase d'assemblage et de libération du virus, et enfin l'intégration du virus.

Ce cycle viral est bien décrit pour les cellules épithéliales pluristratifiées de l'exocol, mais il reste une grande énigme pour les cellules glandulaires de l'endocol. Pourtant, l'infection des cellules monostratifiées glandulaires du col de l'utérus par des HPV à haut risque est connue depuis longtemps, bien que cela soit parfois omis par les épidémiologistes. En effet, notre méta-analyse réalisée en 2023 a démontré que les HPV sont retrouvés dans ≃80% des adénocarcinomes du col de l'utérus, ce qui souligne leur rôle majeur dans cette pathologie (voir article en annexe). Cependant, malgré son implication majeure dans cette cancérisation glandulaire, le cycle viral au sein des cellules glandulaires reste méconnu et les informations qui vont suivre se rapporteront exclusivement aux HPV infectant les kératinocytes.

1. Entrée du virus

Pour amorcer l'infection d'un épithélium stratifié, le virion doit accéder à la couche cellulaire basale en division. Cela se produit généralement à la suite de microtraumatismes qui exposent les protéoglycanes de sulfate d'héparane présentes dans la membrane basale. Il convient également de noter que, en plus des kératinocytes de la couche basale, les β-HPV ont également la capacité d'infecter les cellules souches situées dans le renflement du follicule pileux.[170]

Avant même d'interagir avec la membrane basale, la capside virale peut être influencée par la présence de la laminine 3-2-2, un récepteur spécifique, ainsi que par la kallikréine 8 (KLK8), une protéase présentes dans la matrice extracellulaire (Figure 21). Alors que la laminine 3-2-2 joue un rôle transitoire en tant que récepteur extracellulaire favorisant le transfert du virion vers les cellules basales, la KLK8, en clivant la protéine L1, modifie la structure de la capside et facilite l'exposition de la protéine L2. Ce processus joue un rôle essentiel dans le mécanisme d'entrée du virus. [171,172]

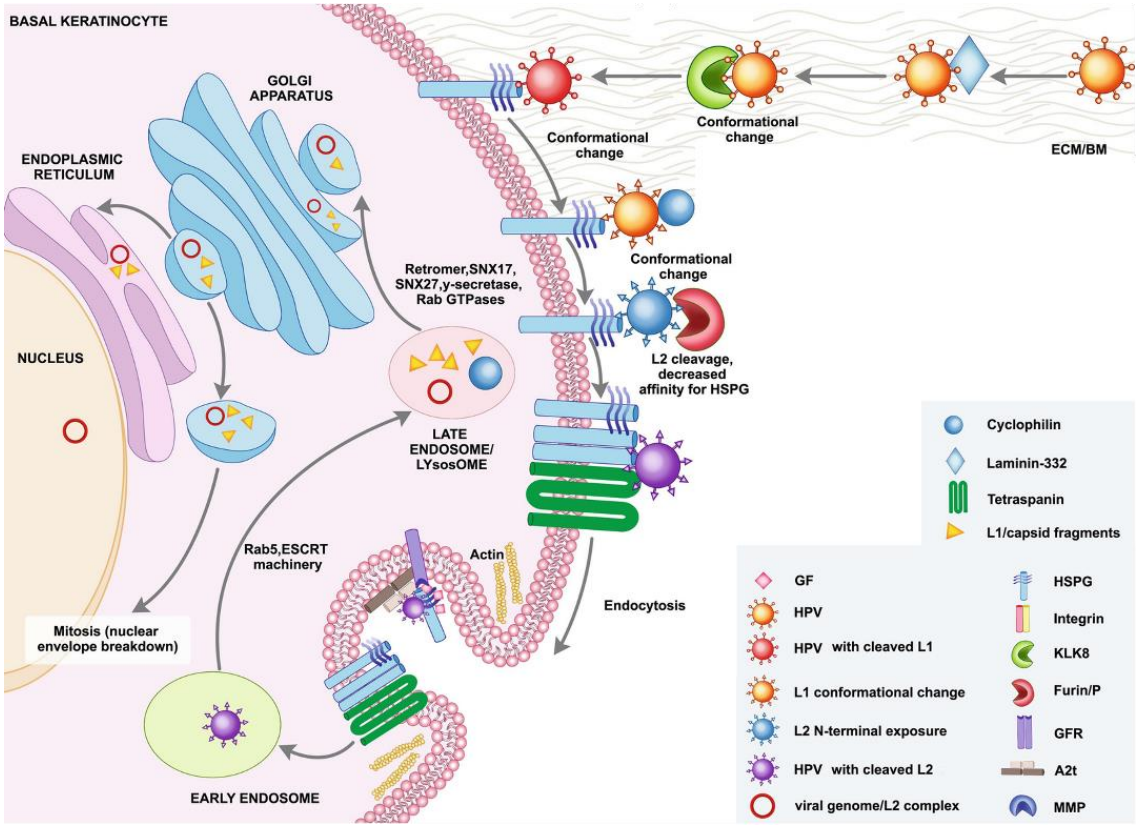

Figure 21 : **Liaison, entrée et transport des HPV dans les kératinocytes**. Pour initier le processus d'entrée, l'HPV se lie à la laminine 3-2-2 et KLK8 présents dans l'ECM ou la BM. Cette interaction induit un changement de structure du virus, *via* le clivage par KLK8. Ce changement permet à l'HPV d'interagir avec les HSPG et les cyclophilines présents sur la surface de la membrane cellulaire. Les cyclophilines induisent un second changement, permettant à l'HPV d'être clivé par une furine. Ce clivage permet au virion d'être internalisé *via* une macropinocytose dépendante de l'actine. Une fois dans la cellule, le virion circule à travers différents organites, notamment grâce aux protéines SNX et Vps, jusqu'à atteindre le noyau (Zhu, 2022)

Lorsque le virion interagit finalement avec la membrane basale, la protéine L1 se lie aux protéoglycanes de sulfate d'héparane, telles que les syndécans 1 ou 4, ce qui entraîne un changement de conformation de la capside et expose la protéine L2 à la surface de celle-ci. L'exposition de la protéine L2 permet à une protéase (la furine) de la cliver, ce qui provoque un second changement de conformation et permet aux virus d'interagir avec un récepteur secondaire situé à la surface des kératinocytes. (Voir paragraphe sur la protéine L1).[173–175]

Ce récepteur secondaire joue un rôle crucial dans le processus d'internalisation du virion dans la cellule hôte. Bien que le complexe exact de ce récepteur reste à déterminer, plusieurs candidats potentiels ont été identifiés, notamment les intégrines α6β4, l'annexine A2, le récepteur du facteur de croissance épidermique (EGFR) et les tétraspanines CD9, CD63 et CD151.[176–178] La liaison de L2 à ce complexe initie la voie de signalisation de l'EGFR, qui joue un rôle dans la phosphorylation du complexe A2t. Cette phosphorylation, par le biais de microdomaines lipidiques, permet l'internalisation du virion.[176,179]

Pour finir, une étude menée par l'équipe du Dr Florin a révélé que des éléments du réseau cytosquelettique, tels que l'obscurine-like 1 (OBSL1), co-localisaient avec les protéines L2, L1 et CD151. Toutefois, son rôle précis dans l'internalisation du virion doit encore être élucidé.[180]

En ce qui concerne le processus d'endocytose proprement dit, la plupart des recherches suggèrent qu'il est similaire à la macropinocytose, qui pourrait être actine dépendant / clathrine, dynamine et radeau lipidique (cholestérol, flotillines, cavéoline) indépendante. En effet, l'HPV16 à recours à un processus d'internalisation qui possède des caractéristiques propres à la macropinocytose telles que la forte dépendance à l'actine, aux récepteurs de tyrosine kinases, aux voies de signalisation PKC et PAK-1, ainsi qu'à l'échangeur Na+/H+. En plus de ces caractéristiques propres à la macropinocytose, les HPV sont également indépendants du cholestérol, requièrent des GTPases et utilisent des vésicules plus petites, ce qui ne correspond pas aux caractéristiques typiques de la macropinocytose.[181,182]

Cependant, il convient de noter que ces informations sont spécifiques à certains types de HPV et doivent être interprétées avec prudence. Le milieu scientifique continue de débattre de ce phénomène d'internalisation génotype dépendant. D'autres mécanismes d'internalisation, tels que l'endocytose dépendante de la cavéoline ou de la clathrine, ont également été décrits dans divers articles scientifiques.[174]

Une fois à l'intérieur de la cellule, le virus doit atteindre le noyau, où se trouve la machinerie de réplication, afin de répliquer son génome et produire davantage de virus. Pour ce faire, le virus utilise le complexe rétromère pour favoriser son transport rétrograde du cytoplasme vers le réseau trans-Golgi/réticulum endoplasmique.[183]

Dans un premier temps, le virus est acheminé vers un endosome précoce qui évolue en un endosome tardif. À l'intérieur de cet endosome tardif, la capside virale subit un désassemblage en raison de l'acidité de l'environnement, de l'action de cyclophiline et de la γ-sécrétase, entraînant la dissociation des protéines de capside L1 et L2.[184,185]

Ensuite, le complexe rétromère, un complexe hétéropentamérique composé d'un dimère de nexines (SNX1, SNX2, SNX5 et SNX6) et d'un trimère de protéines vacuolaires (Vps26, Vps29 et Vps35), facilite le transport du complexe L2-ADN viral (ainsi que certaines protéines L1 résiduelles) contenu dans l'endosome vers le réseau trans-Golgi.[186,187]

Ce processus implique également un complexe multiprotéique analogue au rétromère appelé *retriever*, ainsi que la sorting nexin 17 (SNX17), une protéine adaptatrice qui, par son interaction avec L2, joue un rôle majeur dans le désassemblage de la capside et la dissociation de L1 et L2. [188–190]

Une fois le réseau trans-Golgi atteint, le complexe L2-ADN viral doit être acheminé vers le noyau. Cela nécessite que la cellule conserve son potentiel de réplication et soit engagée dans le cycle cellulaire, en pré-mitose. En effet, pour pouvoir entrer dans le noyau, le complexe L2-ADN viral doit attendre que l'enveloppe nucléaire soit perturbée, ce qui se produit pendant la prophase. Une fois que la prophase a commencé, le génome viral se dissocie du réseau trans-Golgi, s'aligne le long des microtubules pour se colocaliser avec les centrosomes, puis avec les chromosomes condensés.[191,192]

À l'intérieur du noyau, L2 facilite la ‘’livraison’’ du génome viral au domaine nucléaire 10, également connu sous le nom de promyelocytic leukemia bodies (PML), où se déroulent la transcription et la réplication virales précoces. De plus, L2 est capable de modifier la composition du domaine nucléaire 10 en libérant ou dégradant l'antigène nucléaire Sp100, un composant de ND10 impliqué dans l'inhibition de la transcription et de la réplication virales.[148,193]

2. Amplification du génome

Comme mentionné précédemment, le cycle de réplication des HPV est étroitement lié à la différenciation de l'épithélium infecté. De plus, contrairement aux kératinocytes basaux, seuls les kératinocytes différenciés présentent une charge virale élevée, ce qui permet au virus d'échapper au système immunitaire, car ces cellules sont relativement moins surveillées par l'immunité. [194]

La réplication virale peut être divisée en trois phases principales : l'amplification initiale, la phase d'établissement et de maintenance, et l'amplification végétative (Figure 22).

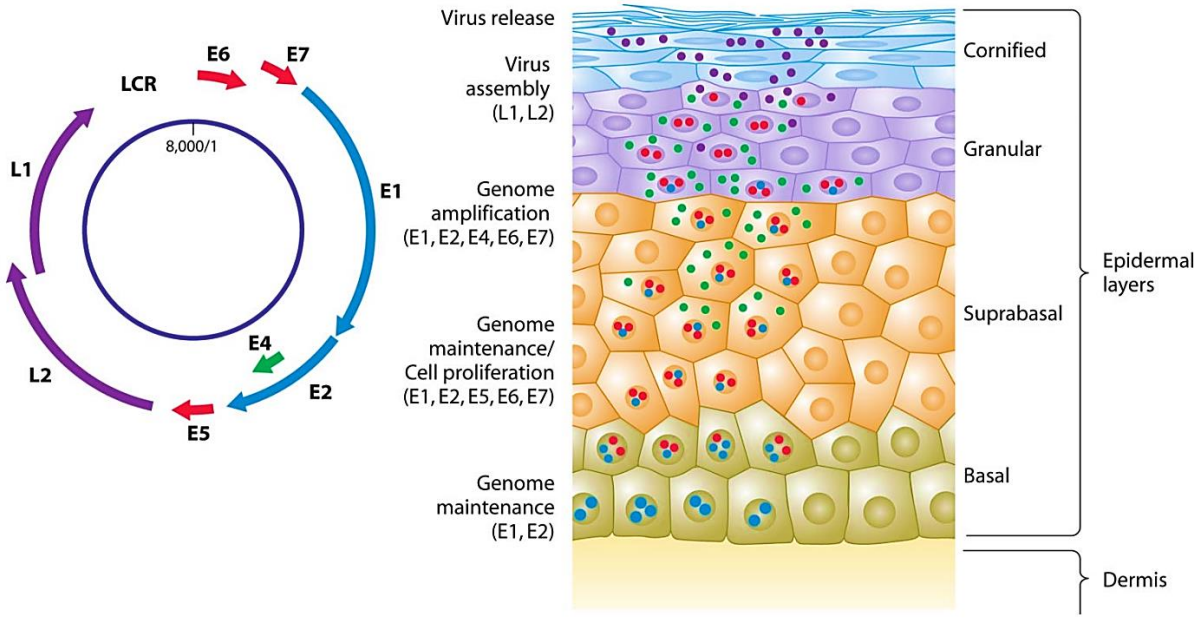

Figure 22 : **Organisation du génome et du cycle viral des HPV**. À gauche, le génome d'un α-HPV est représenté par un cercle bleu. Les ORF codant pour les protéines précoces (E1 et E2 en bleu clair, E4 en vert, et E5, E6 et E7 en rouge) sont exprimés très tôt au cours des étapes du cycle viral (couche basale, suprabasale et granulaire), contrairement aux ORF codant pour les protéines tardives (L1 et L2 en mauve) qui ne sont exprimées qu’à la toute fin du cycle viral (couche granulaire et cornée). À droite, les différentes couches cellulaires sont représentées avec des couleurs distinctes : vert pour la couche basale, orange pour les couches suprabasales, mauve pour les couches granulaires et bleu pour la couche cornée. L'expression des protéines virales à travers les cellules des différentes couches de l’épiderme est représentée à l'aide de points dont la couleur correspond à celle de l'ORF codant pour la protéine. De plus, les différentes étapes du cycle viral sont également représentées, notamment la phase de maintenance, la phase d'amplification et la phase de libération du virion (Lazarczyk *et al.*, 2009).

i. Amplification initiale

La première phase du cycle viral, appelée amplification initiale, vise à maintenir un nombre constant de copies épisomales du génome viral (environ 50 à 100 copies par cellule). En effet, ces génomes viraux sont maintenus à un faible nombre de copies dans les cellules auto-renouvelables et sont répartis entre les cellules filles grâce à des interactions avec les chromosomes mitotiques de l'hôte.[195]

Les protéines virales E1 et E2, associées à la machinerie de réplication de l'ADN de l'hôte, jouent un rôle essentiel dans cette phase d'amplification initiale. [196] Une fois entré dans le noyau, le processus de réplication de l'ADN viral est initié par la liaison de la protéine E2 à des sites spécifiques appelés E2BS, situés dans la région LCR. Cette liaison est cruciale pour le cycle des HPV, car elle permet le recrutement et la liaison de l'hélicase E1 à l'origine de réplication virale. [197]

En plus de son rôle en tant qu'hélicase, la protéine E1 peut servir de plateforme pour le recrutement de protéines cellulaires impliquées dans la réplication de l'ADN, telles que pol-α, RPA, TopoI et Brd4. Par exemple, E1 interagit avec pol-α pour faciliter le processus d'amorçage de la réplication. Elle peut également interagir avec RPA pour favoriser le chargement de RPA sur l'ADN monocaténaire, empêchant ainsi l'ADN simple brin de se replier sur lui-même. De plus, E1 peut interagir avec TopoI pour guider cette protéine vers l'ADN double brin, où elle joue un rôle important lors du processus de réplication (Figure 9). [60,198]

Enfin, la protéine de fusion E8, en interagissant avec le complexe répresseur NCoR/SMRT-HDAC3, régule l'amplification du génome viral, contribuant ainsi au maintien d'un faible nombre de copies virales par cellule.[199,200]

ii. Phase d'établissement et de maintenance

Après l'amplification initiale, la phase de maintenance est initiée afin d'assurer un nombre constant de copies du génome viral, en tant que génome extrachromosomique, dans le noyau des cellules basales indifférenciées, favorisant ainsi une infection persistante.

Au cours de cette phase, il est essentiel de garantir une ségrégation adéquate des génomes viraux lors de la division cellulaire, ce qui est connu sous le nom d'ancrage chromosomique. Cette étape cruciale dépend de E2 et Brd4, qui facilitent l'ancrage du génome viral aux chromosomes de la cellule hôte. En effet, E2 peut se lier à la fois à l'ADN viral (*via* son domaine de liaison à l'ADN) et aux chromosomes de l'hôte (*via* son domaine N-terminal). [79,201] Des études ont d'ailleurs montré une colocalisation d'E2 et de Brd4, suggérant une interaction potentielle entre ces deux protéines. [202] E2 peut également interagir avec les protéines de maintenance structurale des chromosomes (SMC), SMC5 et SMC6, pour améliorer la stabilité du génome viral. [203]

Outre les protéines E1 et E2, les oncoprotéines E6 et E7 sont également nécessaires pour maintenir de manière stable le génome épisomal. [204,205]

iii. Amplification végétative

L'étape d'amplification végétative, également appelée productive, se produit dans les cellules différenciées de l'épithélium stratifié et conduit à la production de nouveaux virions. [206] Étant donné que l'amplification du génome viral nécessite des conditions cellulaires favorisant la prolifération cellulaire et donc la réplication de l'ADN, les HPV ont développés des stratégies pour empêcher l'arrêt du cycle cellulaire et les signaux d'apoptose.

Cette fois-ci tout le génome du papillomavirus va être impliqué, à commencer par les oncoprotéines E6 et E7 qui jouent un rôle clé dans cette étape en inactivant les protéines suppresseurs de tumeurs, notamment p53 et pRb. Cela garantit que les cellules infectées restent actives et progressent vers la phase S du cycle cellulaire. De plus, les oncoprotéines E6 et E7 des α-HPV sont capables d'interagir avec certaines protéines impliquées dans les voies de réparation de l'ADN, et de les recruter au niveau de leur foyer de réplication virale, afin de favoriser celle-ci. Par exemple, E7 est capable d'activer les voies ATM, Chk1 et Chk2 dans les couches différenciées de l'épithélium pour recruter les protéines impliquées dans la recombinaison homologue (HR) et favoriser la réplication virale (voir paragraphe E6 et E7). [62,168]

En plus de E6 et E7, les protéines virales E4 et E5 (uniquement pour les α-HPV) contribuent également à une réplication productive efficace (voir paragraphe E4). [207]

De plus, l'activation du promoteur tardif, situé dans la région LCR pour les β-HPV et dans la région E7 pour les α-HPV, favorise l'expression de E1 et E2, ce qui entraîne une forte augmentation du nombre de copies virales. [208] Ces promoteurs tardifs induisent également l'expression des protéines de capside L1 et L2, qui seront impliquées dans la dernière phase du cycle viral, la formation et la libération du virus dans les couches superficielles de l'épithélium [153]

3. Formation et libération du virus

Dans la dernière étape du cycle viral, la capside est assemblée autour du génome viral, suivi de la libération du virion grâce à la desquamation des kératinocytes. Les acteurs principaux de ce processus sont les protéines de capside L1 et L2 ainsi que le génome viral.

L'assemblage de la capside se déroule à l'intérieur du noyau où se trouve le génome viral. Les protéines de capside L1 et L2 peuvent se rendre dans le noyau grâce à leur séquence de localisation nucléaire ainsi que des facteurs de transport tels que les caryophérines et Hsp70. [209–211] Une fois dans le noyau, la capside va pouvoir s'assembler autour du génome viral. L'interaction entre L1 et L2 semble être régulée par la sumoylation de L2, qui inhibe les interactions avec L1. [212] De plus, la nucléophosmine, une protéine cellulaire, interagit avec la protéine L2 pour favoriser l'assemblage correct des capsides infectieuses. [213]

Quant à l'incorporation du génome viral dans la capside virale, ce processus n'est malheureusement pas entièrement compris. Contrairement à d'autres génomes viraux, les HPV ne possèdent pas de signaux d'encapsidation spécifiques. Les protéines L1 et L2 contiennent des séquences chargées positivement à leurs extrémités N et/ou C terminales, qui se lient à l'ADN de manière indépendante de la séquence, probablement par des interactions ioniques avec le squelette phosphate de l'ADN. [214,215] Cette absence de signaux d'encapsidation permet aux HPV d'emballer efficacement une variété d'ADN double brin, indépendamment du génome du papillomavirus, tant que la taille du génome ne dépasse pas 8 kb. [216] L'incorporation du génome viral pourrait se produire grâce à un mécanisme de discrimination de taille encore non élucidé, cette hypothèse nécessite toutefois d'être confirmée.[217,218]

Une fois que la capside est assemblée autour du génome viral, le gradient redox fourni par les couches supérieures de l'épithélium en différenciation favorise la formation de ponts disulfure entre les molécules de L1, ce qui entraîne la maturation de la capside. Cette étape de maturation solidifie la capside du virus pour qu'elle puisse résister à la digestion par les protéases. [219,220]

Pour terminer, étant donné que les HPV sont des virus non lytiques, ils doivent profiter de la desquamation de l'épithélium pour être libérés. Selon la théorie actuelle, l'augmentation d'expression de la protéine E4 pourrait déstabiliser la structure kératinique, fragilisant ainsi la couche cornée et entraînant la desquamation des kératinocytes.[221]

E. Épidémiologie

La pathogénicité induite par les HPV est principalement dépendante des différents genres d'HPV impliqués. Certains virus sont capables de provoquer des infections asymptomatiques et peuvent être considérés comme faisant partie de notre microbiote normal, en particulier la majorité des β-HPV au sein de la flore cutanée. D'autres, tels que les α-HPV à faible risque, provoquent des lésions bénignes telles que des verrues ou des papillomes, tandis que certains HPV peuvent induire des lésions qui peuvent évoluer vers un cancer invasif après une infection à long terme, notamment les α-HPV à haut risque.

Bien que cette thèse se concentre principalement sur les β-HPV, il est nécessaire d'aborder un minimum l'épidémiologie des α-HPV. L'infection par les α-HPV est actuellement considérée comme l'infection sexuellement transmissible la plus courante, touchant environ 75% de la population sexuellement active au cours de sa vie. [222] En plus des lésions bénignes mentionnées précédemment, les α-HPV favorisent également le développement de certains cancers, au point d'être considérés comme des facteurs étiologiques. Par exemple, le cancer du col de l'utérus est associé à 99,99% avec les α-HPV, suivi de l'anus (≃90%), du vagin (≃80%), du pénis (≃50%), de l'oropharynx (≃50%) et de la vulve (≃50%), présentant ainsi une prévalence variable en fonction du site de développement du cancer.

Une étude menée par le Centre International de Recherche sur le Cancer (CIRC) a révélé qu'en 2018, les α-HPV étaient responsables de 690 000 cas de cancer, représentant environ 4 à 5% de tous les cancers dans le monde (Tableau 4). Bien que ces chiffres n'aient pas été mis à jour, il est probable qu'ils continuent d'augmenter, soulignant l'importance de la vaccination. En effet, plus des deux tiers des cancers associés aux HPV surviennent dans les pays ‘’moins développés’’, où le dépistage et la vaccination sont moins disponibles. [223–225]

	Men		Women		Total	
	New cases	New cases attributable to infectious pathogens	New cases	New cases attributable to infectious pathogens	New cases	New cases attributable to infectious pathogens
Human papillomavirus						
Cervix uteri carcinoma*	..	..	570 000	570 000	570 000	570 000
Oropharyngeal carcinoma	110 000	34 000	26 000	8100	140 000	42 000
Oral cavity cancer	190 000	3900	91 000	2000	280 000	5900
Larynx cancer*	150 000	3600	22 000	≤1000	180 000	4100
Anus squamous cell carcinoma	9900	9900	19 000	19 000	29 000	29 000
Penis carcinoma*	34 000	18 000	..	..	34 000	18 000
Vagina carcinoma*	..	..	18 000	14 000	18 000	14 000
Vulva carcinoma*	..	..	44 000	11 000	44 000	11 000

Tableau 4 : **Nombre d'infections attribuables aux α-HPV, en fonction du sexe et du site d'infection** (adapté de De Martel *et al.*, 2020).

Concernant les β-HPV, actuellement, nous disposons de très peu d'informations et il est difficile d'établir des conclusions solides. Comme mentionné précédemment, la majorité des β-HPV sont responsables d'infections asymptomatiques. Cependant, chez les patients immunodéficients, qui présentent un risque de développer un carcinome épidermoïde cutané de 40 à 100 fois plus élevé, on observe une prévalence nettement plus élevée de β-HPV par rapport aux patients immunocompétents. De plus, jusqu’à 90% des cancers cutanés observés chez les patients atteints d’épidermodysplasie verruciforme sont associés aux HPV 5 et 8. [226–228]

Malgré l'accumulation de données suggérant une possible implication des β-HPV dans le développement des carcinomes épidermoïdes cutanés, aucune équipe de recherche n'a encore réussi à détecter la présence de β-HPV dans ces cancers. En effet, les β-HPV ne semblent pas s'intégrer dans le génome de l'hôte, ce qui rend leur détection dans les cellules cancéreuses très difficiles. De plus, la dédifférenciation cellulaire apparaissant durant la cancérisation empêche très certainement la persistance des infections épisomales. Par conséquent, cela rend donc quasiment impossible la démonstration du rôle des β-HPV dans le développement du carcinome cutané en analysant les lésions tardives/invasives. Dès lors, plusieurs scientifiques ont été contraints de se concentrer sur l'étude de lésions précancéreuses, telles que la kératose actinique ou la maladie de Bowen, pour contourner ce problème.[229,230]

Le fait que les β-HPV ne s'intègrent pas dans le génome de l'hôte a conduit à l'élaboration de l'hypothèse du "*hit and run*" (Figure 23). Selon cette hypothèse, les HPV seraient impliqués dans l'initiation de la carcinogenèse, mais pas dans sa progression ultérieure. En effet, il se pourrait que les β-HPV favorisent l'accumulation de mutations induites par les UV, ce qui est appelé le "*hit*". Cependant, une fois que des mutations touchent des oncogènes ciblés par les β-HPV, tels que p53 ou Notch, l'expression des protéines virales devient superflue pour le développement des cellules cancéreuses. De plus, la différenciation cellulaire étant perturbée au sein des cellules cancéreuses, les β-HPV vont quitter ces cellules, on parle de ''run''. En effet, les HPV dépendent de la différenciation cellulaire afin d'accomplir leur cycle viral.[231,232]

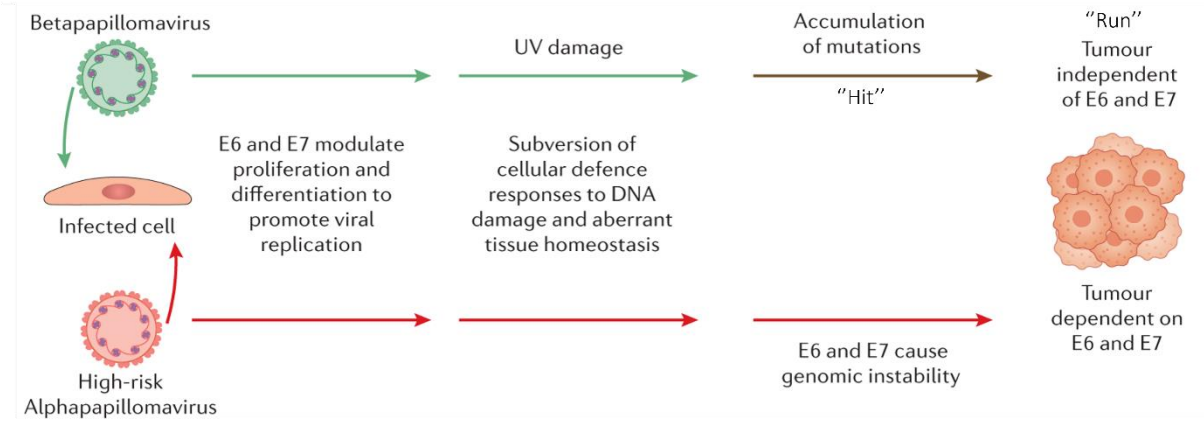

Figure 23 : **Théorie du ''hit and run'' des β-HPV dans la carcinogenèse cutanée**. Que ce soit les α-HPV ou les β-HPV, le virus est capable de moduler la prolifération et la différenciation des cellules hôtes afin de favoriser la réplication virale. Dans les cellules infectées par des β-HPV, les défenses cellulaires sont dérégulées et les cellules accumulent des mutations médiées par les UV, on parle de ''*hit*''. Lorsque les mutations touchent des gènes oncogènes (tels que les gènes suppresseurs de tumeurs) qui altèrent le fonctionnement normal des cellules, l'expression des gènes viraux devient superflue pour le développement du carcinome cutané, on parle de ''*run*''. Ce mécanisme de fonctionnement diffère des α-HPV, qui doivent continuellement dégrader p53 et pRb pour que le cancer subsiste (adapté de McBride 2021).

Afin de mieux appréhender le processus d'accumulation de mutations provoqué par les rayonnements ultraviolets ainsi que la corrélation entre ces rayonnements, les β-HPV et le cancer de la peau, nous allons désormais explorer notre deuxième sujet majeur : les UV et la carcinogenèse cutanée.

Les rayons ultraviolets (UV)

A. Généralités

Les rayons ultraviolets (UV), découverts en 1801 par Johann Wilhelm Ritter, sont des rayonnements électromagnétiques de longueur d'onde inférieure à celle de la lumière visible. Ils se divisent en trois types, à savoir les UVA, UVB et UVC, classés en fonction de leur activité biologique et de leur pouvoir de pénétration cutané (Figure 24). En effet, les rayonnements UV de plus longue longueur d'onde ont moins d'énergie (et sont donc moins nocifs), mais pénètrent plus profondément dans la peau (jusqu'au derme). En revanche, les rayonnements UV de plus courte longueur d'onde ont plus d'énergie et sont donc plus dangereux pour l'organisme, mais pénètrent moins profondément dans la peau (épiderme uniquement). Concernant les effets néfastes des UV ; ceux-ci comprennent les brûlures, le vieillissement prématuré de la peau, les lésions oculaires ainsi que les cancers cutanés. [233,234]

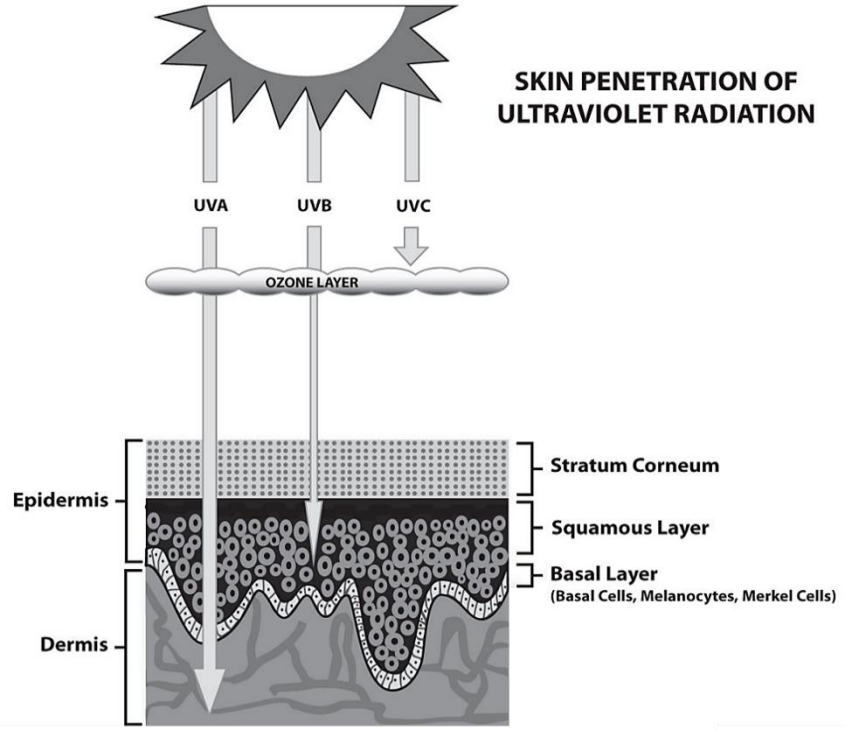

Figure 24 : **Types de rayonnement ultraviolet et pénétration cutanée** (Watson *et al.*,2016).

Les rayonnements UVA, avec une longueur d'onde comprise entre 315 et 400 nm, représentent près de 95% du rayonnement UV atteignant la surface de la Terre. Ils peuvent pénétrer dans les couches profondes de la peau, notamment le derme, et sont responsables du vieillissement prématuré de la peau en dégradant les fibres de collagène et d'élastine. De plus, les rayonnements UVA sont également capables de favoriser le développement de cancers cutanés en induisant la formation de dimères de pyrimidine et en générant des espèces réactives de l'oxygène (ROS) à l'intérieur des cellules. [235,236] Des études suggèrent également que les rayonnements UVA peuvent potentialiser la toxicité cellulaire des rayonnements UVB en ayant une activité immunosuppressive et en endommageant les systèmes de réparation de l'ADN. [237,238]

Les rayonnements UVB, quant à eux, ont une longueur d'onde comprise entre 280 et 315 nm, ce qui leur confère une forte activité biologique. Toutefois, ils ne pénètrent que dans les couches superficielles de la peau (l'épiderme). Outre les coups de soleil, les rayonnements UVB produisent également de grandes quantités de ROS dans les cellules cutanées, favorisant ainsi à long terme le développement de carcinomes cutanés. Bien que les rayonnements UVB ne représentent que 5% des rayonnements UV atteignant la surface terrestre, leur potentiel cancérigène est 100 fois plus élevé que celui des UVA. [239,240]

Enfin, Les rayonnements UVC, avec une longueur d'onde comprise entre 100 et 280 nm, sont théoriquement les plus nocifs. Cependant en pratique, ils sont complètement filtrés par la couche d'ozone et n'atteignent pas la surface de la Terre. [241]

Pour terminer, plusieurs facteurs peuvent influencer la quantité d'UV atteignant la surface de la Terre et, par conséquent, leur impact sur notre santé :

- L'épaisseur de la couche d'ozone dans l'atmosphère stratosphérique, qui agit comme un bouclier contre les UV [242,243]
- L'heure de la journée et les saisons, qui affectent la distance parcourue par les UV et l'angle de pénétration de ceux-ci [244]
- La latitude et l'altitude, qui influencent également la distance que les UV doivent parcourir [245]
- Les conditions météorologiques, telles que le brouillard, la brume et les nuages, qui peuvent réduire les niveaux d'UV [233]

B. Altérations générées par les UV

Les rayonnements UV sont largement reconnus comme étant l'agent étiologique principal dans le développement des cancers de la peau. [246] En effet, les UVA et UVB induisent des dommages à l'ADN, un stress oxydatif et une immunosuppression, qui jouent un rôle crucial dans la carcinogenèse cutanée. Les dimères de pyrimidine et les espèces réactives de l'oxygène (ROS) générés par les UV sont particulièrement impliqués dans ces mécanismes. Ces altérations au niveau de l'ADN et des défenses cellulaires peuvent favoriser l'accumulation de mutations et le développement de cellules cancéreuses.[247,248]

1. Dimères de pyrimidine

Les dimères de pyrimidine sont des altérations moléculaires de l'ADN résultant d'une réaction photochimique entre des résidus adjacents de thymine ou de cytosine sur le même brin d'ADN. Ces lésions, qui impliquent des liaisons covalentes, sont provoquées par les rayonnements UVA et UVB, les UVB ayant un rendement 100 fois plus élevé que les UVA. On distingue trois types de dimères de pyrimidine : les dimères cyclobutyliques de pyrimidine (CPD), les photoproduits 6-4 et l'isomère de Dewar (Figure 25). [249–251]

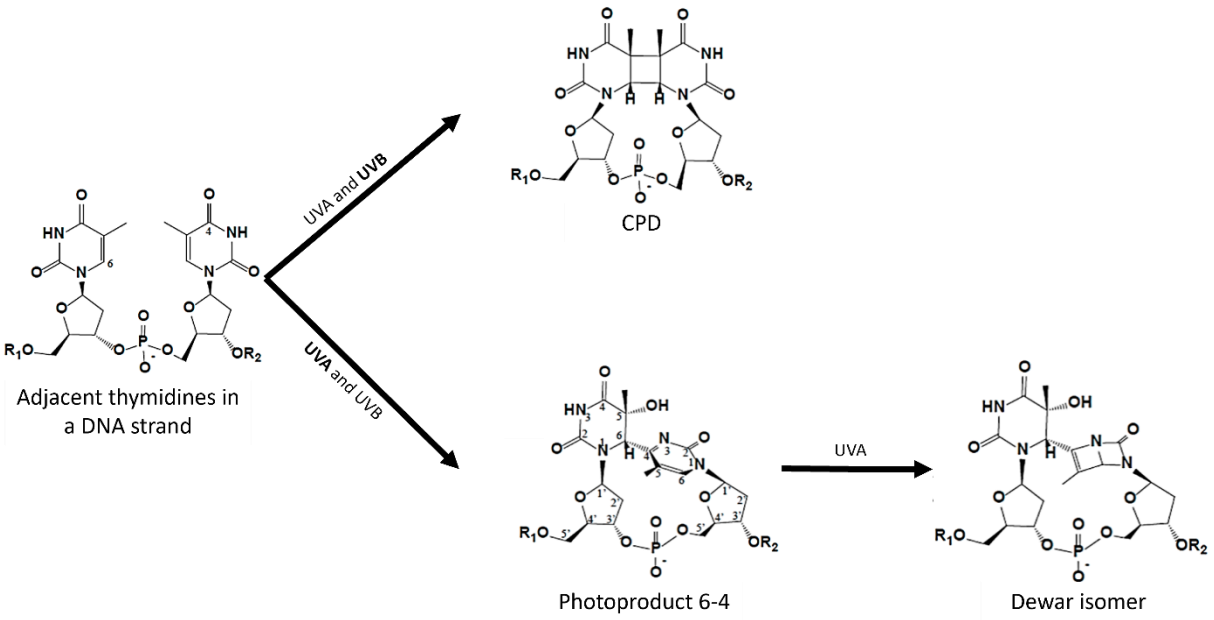

Figure 25 : **Schéma illustrant les altérations de l'ADN induites par les rayonnements UVA et UVB**. Le rayonnement prédominant responsable de la formation de cette lésion est représenté en gras (adapté de Yokoyama *et al.*, 2014)

Les dimères cyclobutyliques de pyrimidine se forment lorsque deux pyrimidines adjacentes subissent l'ouverture de leurs doubles liaisons C5=C6, formant ainsi une structure en anneau à quatre atomes de carbone. Ces altérations représentent environ 75% des dimères de pyrimidine et sont responsables d'une distorsion d'environ 7 à 9° par rapport à la conformation initiale de l'ADN (Figure 26). [252,253]

Les photoproduits 6-4 résultent de la formation d'un pont stable entre les positions C6 et C4 de deux pyrimidines adjacentes. Ces altérations sont environ quatre fois moins fréquentes que les CPD, mais elles sont plus mutagènes car elles induisent une distorsion de 44° de l'ADN par rapport à sa conformation initiale (Figure 26). [254,255] La distorsion plus importante induite par les photoproduits 6-4 (par rapport aux CPD) facilite la détection par les différents acteurs impliqués dans les voies de réparation de l'ADN. Par conséquent, les photoproduits 6-4 sont réparés plus rapidement que les CPD, qui persistent plus longtemps dans la structure de l'ADN.[256,257]

Le troisième et dernier type de dimère de pyrimidine est l'isomère de Dewar, qui résulte de l'isomérisation réversible du photoproduit 6-4 lors d'une exposition ultérieure aux rayonnements UV dont la longueur d'onde est supérieure à 290 nm. Cette altération provoque une flexion hélicoïdale d'environ 21° (Figure 26). [258,259]

Que ce soit les CPD, les photoproduits 6-4 ou l'isomère de Dewar, ces altérations ont été décrites par la communauté scientifique comme des lésions prémutagènes en raison de leur interférence avec la progression des ADN polymérases (δ et ε) lors de la réplication et de l'ARN polymérase 2 lors de la transcription. [260] Pour contrer ces altérations, notre organisme a mis en place un mécanisme de réparation, à savoir la voie de réparation par excision de nucléotides (NER), qui sera examinée plus en détail par la suite. Cependant, il peut arriver que la réparation ne soit pas possible et que ces altérations deviennent mutagènes. L'accumulation de telles altérations dans des gènes, notamment les gènes suppresseurs de tumeurs tels que *TP53*, favorise le développement du cancer. [261]

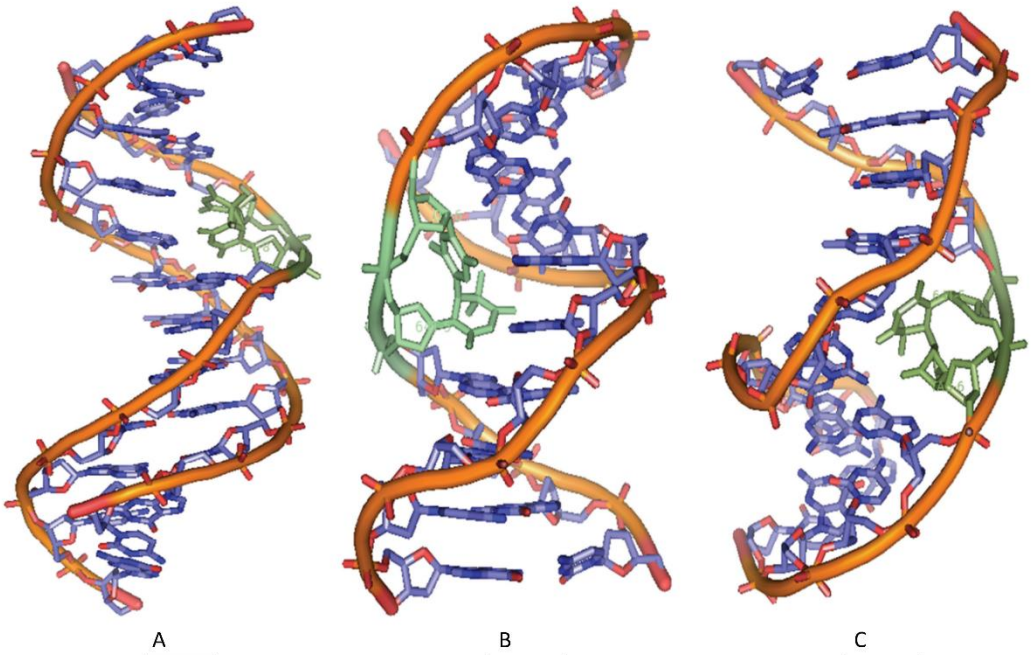

Figure 26 : **Représentation 3D de l'ADN montrant les altérations (en vert) induites par les UV**. Les CPD (A), les photoproduits 6-4 (B) et les isomères de Dewar (C) sont illustrés. Les atomes d'hydrogène ne sont pas affichés. (Rastogi *et al.*, 2010)

2. Espèce réactives de l'oxygène (ROS)

Les espèces réactives de l'oxygène sont des entités chimiques oxygénées, telles que des radicaux libres ou des peroxydes, caractérisées par la présence d'électrons de valence non appariés, qui leur confère une grande réactivité chimique. Parmi ceux-ci figurent l'anion superoxyde $O_2^{\bullet -}$, le peroxyde d'hydrogène H_2O_2, et le radical hydroxyle $OH^{\bullet}$ (Figure 27).[262]

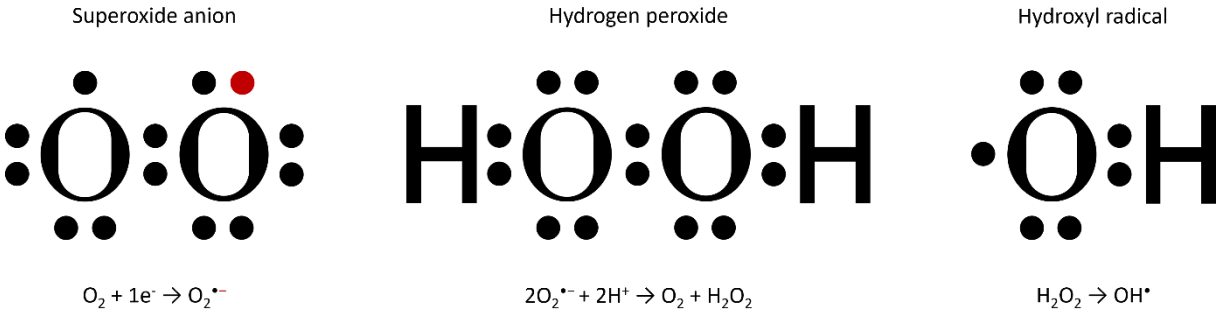

Figure 27 : **Représentation schématique de la structure de Lewis des principaux ROS ainsi que la réaction chimique responsable de leurs formations**.

Avant d'examiner comment les espèces réactives de l'oxygène induisent des dommages cellulaires, il est essentiel de se pencher sur leur mécanisme de production. Les ROS d'origine endogène sont principalement générées pendant le processus de respiration cellulaire et d'explosion oxydative (Figure 28). En outre, les ROS peuvent également être d'origine exogène, lorsque leur formation est stimulée par divers agents tels que le tabac, l'alimentation ou les rayonnements UV.[263]

En ce qui concerne les ROS endogènes, leur production peut survenir au cours de la phosphorylation oxydative, un processus qui se déroule dans les mitochondries et qui convertit l'adénosine diphosphate (ADP) en adénosine triphosphate (ATP), une forme d'énergie directement utilisable par la cellule. La phosphorylation oxydative implique le transfert d'électrons de molécules réductrices à des oxydants le long d'une chaîne de transport d'électrons, générant ainsi une cascade de réactions d'oxydoréduction successives qui libèrent progressivement l'énergie des électrons. Finalement, l'oxygène agit comme le dernier accepteur d'électrons le long de cette chaîne. [264] En conditions normales, l'oxygène est réduit pour produire de l'eau. Cependant, une petite fraction d'$O_2^{\bullet -}$ est générée, environ 1 à 5% des électrons sont détournés au niveau des complexes I et III de la chaîne de transport d'électrons pour former l'anion superoxyde. Ce dernier est généralement converti par les superoxydes dismutases (SOD) mitochondriales en H_2O_2, qui à son tour peut être converti en eau par l'action de la catalase, ou en $OH^{\bullet}$ par la réaction de Fenton ($Fe^{2+}_{(aq)} + H_2O_2 \rightarrow Fe^{3+}_{(aq)} + OH^-_{(aq)} + OH^{\bullet}$). [265,266]

En ce qui concerne l'explosion oxydative, elle est réalisée par les enzymes de la famille NADPH oxydases (NOX), et implique la libération rapide de ROS. Cette famille de NOX est constituée de 7 membres, à savoir NOX1-5 et DUOX1-2. [267,268] Ces enzymes comportent entre 6 et 7 sous-unités, dont les sous-unités membranaires NOX2 (gp91phox) et p22phox, ainsi que les sous-unités régulatrices cytoplasmiques p40phox, p47phox, p67phox et la GTPase Rac1. Les NOX sont des protéines transmembranaires retrouvées chez certaines cellules immunitaires telles que les macrophages, les neutrophiles et les éosinophiles, où elles facilitent la dégradation de particules ou de bactéries internalisées. Elles sont également présentes dans des cellules qui ne sont pas liées au système immunitaire telles que les cellules endothéliales, les hépatocytes, les myocytes striés ou encore les neurones, où elles peuvent influencer certaines voies de signalisation en inhibant des phosphatases ou en activant des kinases.[269]

La principale différence, cruciale pour la signalisation redox, est que le complexe NOX des cellules non immunitaires est constitutivement actif, produisant constamment un niveau très faible de ROS. En effet, ces NOX sont capables de produire de l'$O_2^{\bullet -}$, *via* la sous-unité catalytique NOX, qui s'active lorsque les sous-unités cytoplasmiques sont assemblées. Les électrons de NADPH sont transférés à l'oxygène pour produire l'$O_2^{\bullet -}$, qui est ensuite converti en H_2O_2 par l'action d'une superoxyde dismutase. Une fois généré, l'H_2O_2 va pouvoir être convertis en $OH^{\bullet}$ *via* la réaction de fenton ou en acide hypochloreux (HOCL). [270,271]

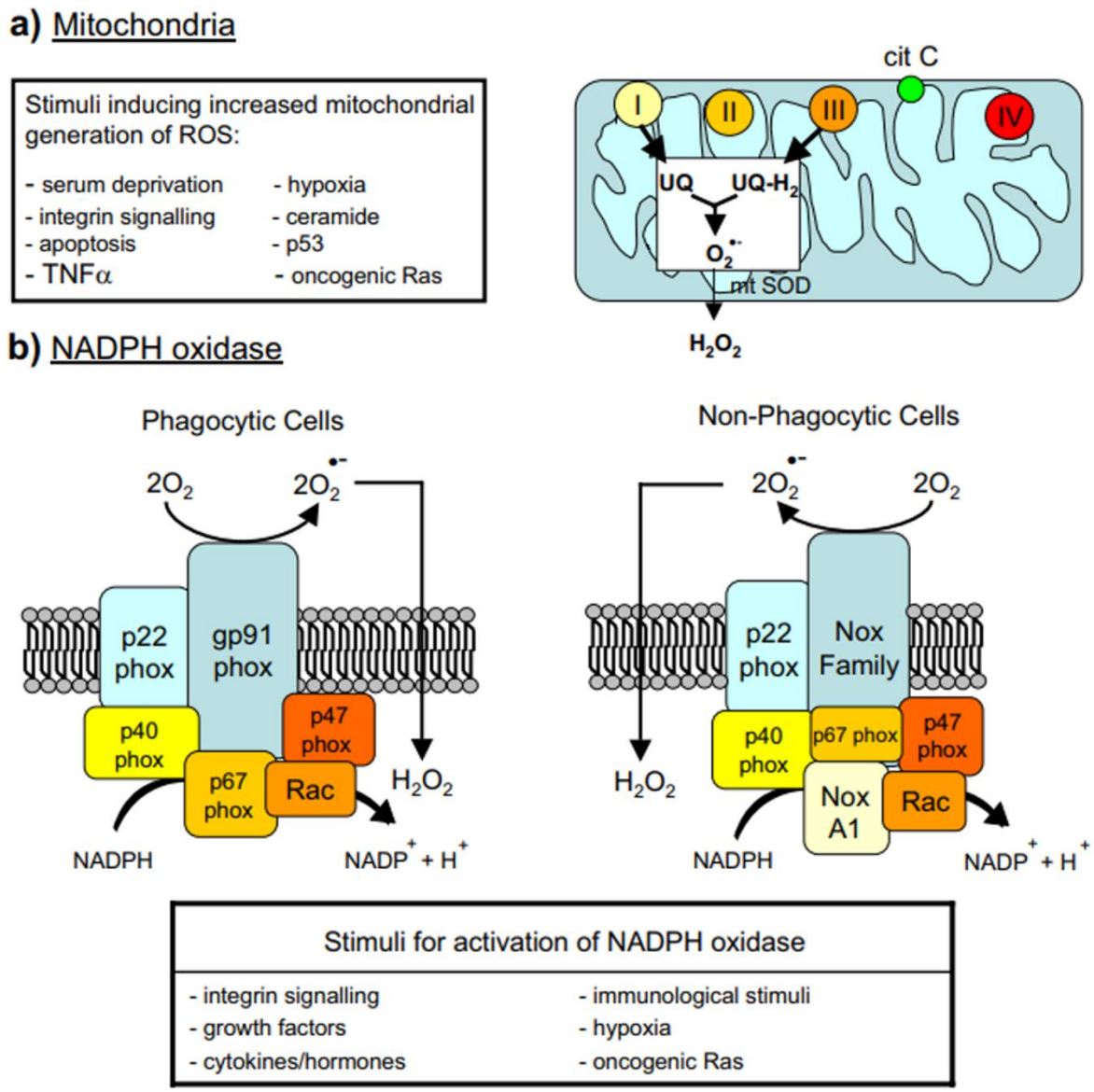

Figure 28 : **Sources endogènes de ROS comprenant la respiration cellulaire, l'explosion oxydative ainsi que l'oxydation des acides gras** (Novo *et al.*, 2008).

En ce qui concerne les ROS exogènes, elles peuvent être engendrées par l'exposition aux UV. Les UV induisent la formation de diverses espèces réactives de l'oxygène telles que $O_2^{\bullet -}$, $OH^{\bullet}$ et H_2O_2, grâce à différents mécanismes impactant directement les composants cellulaires ou par le biais de la photosensibilisation. Il est à souligner que les rayonnements UV ont la capacité de diminuer l'expression de la protéine kinase C (PKC), ce qui résulte en une augmentation de la production de ROS. De plus, des études ont démontré que les UV causent des dommages à l'ADN, notamment par la formation de 8-oxoguanine (8-oxoG), un marqueur des altérations oxydatives de l'ADN. Bien qu'il ait été proposé que la 8-oxoG générée par les UV se forme par un mécanisme impliquant $^1O_2$, ce marqueur est généralement associé au radical hydroxyle. Enfin, il convient de noter que les rayonnements UV ont également la capacité d'endommager l'ADN mitochondrial, compromettant ainsi la chaîne de transport d'électrons et induisant, par conséquent, la production de ROS. [272–275]

L'alcoolisme et le tabagisme ont également été associés au stress oxydatif et, par conséquent, à diverses maladies. La consommation d'alcool, qu'elle soit aiguë ou chronique, entraîne une augmentation des ROS, en partie due à l'acétaldéhyde formé comme produit du métabolisme de l'éthanol. L'acétaldéhyde altère l'homéostasie du calcium et augmente la production de ROS, ce qui peut entraîner un stress du réticulum endoplasmique. De plus, l'alcool est capable d'élever les niveaux de fer dans le corps, contribuant ainsi à la réaction de Fenton et à la production du radical hydroxyle. [276,277]

D'autre part, la fumée de cigarette, composée de plus de 5 000 substances chimiques et agents oxydants, génère environ 10^{14} - 10^{16} radicaux libres par bouffée. En présence de fer, la demi-quinone du goudron peut générer des $OH^{\bullet}$ et du H_2O_2. [278,279]

Enfin, on sait que des régimes alimentaires caractérisés par une consommation excessive de graisses saturées, de sucres raffinés et de protéines animales, ainsi qu'une faible consommation de fibres d'origine végétale, augmentent la carbonylation des protéines et les produits de peroxydation des lipides, tout en réduisant l'état de défense antioxydante, ce qui entraîne un stress oxydatif. De plus, des études ont rapporté que la présence constante de substrats oxydables au repos (comme le glucose et le galactose) entraîne une diminution de la phosphorylation oxydative, augmentant ainsi la probabilité qu'un plus grand nombre d'électrons s'échappent de la chaîne respiratoire, ce qui contribue à la génération de ROS. Par ailleurs, le fer alimentaire ainsi que le cuivre sont connus pour générer des $OH^{\bullet}$ par la réaction de Fenton (Figure 29). [280,281]

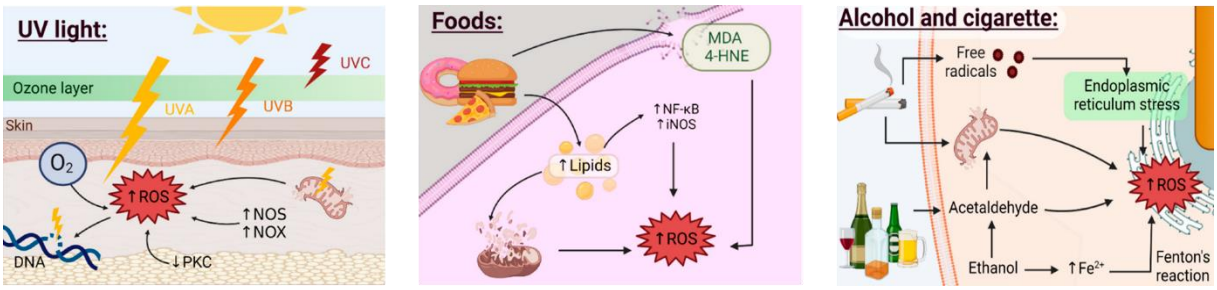

Figure 29 : **Sources exogènes de ROS, comprennent l'exposition à des facteurs externes tels que les radiations ultraviolettes, les aliments, ainsi que les substances comme l'alcool et le tabac** (Aranda-Rivera *et al.*, 2022).

Dans un contexte biologique, les ROS sont des sous-produits inévitables du métabolisme normal de l'oxygène. D'ailleurs, ils jouent un rôle crucial dans la signalisation cellulaire et l'homéostasie, étant considérés comme intrinsèques au fonctionnement cellulaire. Cependant, les ROS peuvent également causer des dommages irréversibles à l'ADN en oxydant et en altérant certains composants cellulaires, principalement les macromolécules qui composent notre organisme. Ces altérations entravent ainsi leur capacité à remplir leurs fonctions d'origine. Ainsi, les ROS manifestent une dualité, agissant à la fois de manière bénéfique et néfaste pour notre organisme, en fonction de l'équilibre entre leur production et leur élimination, au bon moment et au bon endroit. [282,283]

En effet, la quantité de ROS considérée comme néfaste dépend du type de cellule/tissu et de l'espèce réactive de l'oxygène qui s'accumule spécifiquement. Parmi les trois types de ROS mentionnés précédemment, le radical hydroxyle est le plus néfaste pour notre organisme. Son temps de demi-vie très court (de l'ordre de 10^{-9} secondes) en fait un électrophile excessivement réactionnel, ce qui lui permet de réagir rapidement avec les macromolécules de notre organisme. [284]

En revanche, l'anion superoxyde et le peroxyde d'hydrogène sont relativement neutres et stables (avec des temps de demi-vie plus longs), ce qui permet à l'organisme d'utiliser différents mécanismes pour s'en débarrasser. Par exemple, les enzymes antioxydantes telles que la superoxyde dismutase peuvent réduire l'anion superoxyde en peroxyde d'hydrogène, qui peut à son tour être réduit en eau par des catalases et certaines peroxydases. De plus, certaines vitamines telles que la A, C et E, ainsi que certaines protéines comme la lactoferrine et la ferritine, peuvent également contrer les effets délétères du stress oxydatif et maintenir l'homéostasie redox (Figure 30).[285–287]

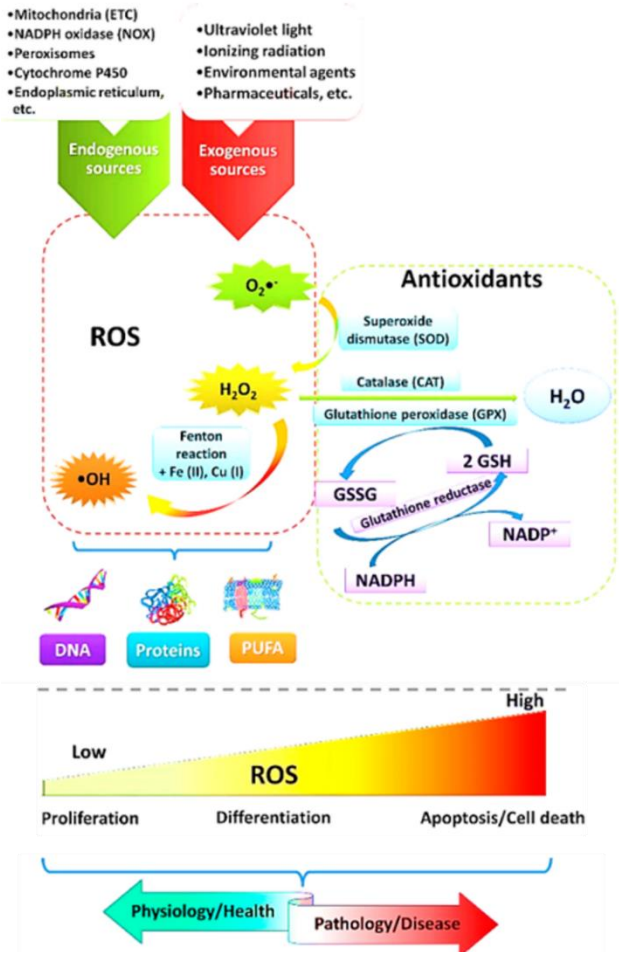

Figure 30 : **Génération d'espèces réactives de l'oxygène et leur impact sur les cellules**. Ce schéma simplifié illustre les sources exogènes et endogènes de ROS, ainsi que les mécanismes antioxydants qui ajustent l'équilibre des niveaux de ROS. En fonction des concentrations, les ROS influencent différents facteurs de transcription, enzymes et/ou autres protéines, induisant des voies de signalisation qui garantissent un bon fonctionnement cellulaire et, de manière générale, une bonne santé. En revanche, des niveaux élevés de ROS conduisent aux dommages irréversibles des macromolécules. Selon les concentrations, les ROS ont un impact sur les fonctions cellulaires telles que la prolifération, la différenciation et l'apoptose (Milkovic *et al.*, 2019).

La plupart du temps, notre corps peut se débarrasser des ROS et maintenir un certain équilibre risque/bénéfice. Malheureusement, il arrive parfois que cet équilibre penche du côté risque et que les ROS deviennent incontrôlables, provoquant ainsi l'oxydation de certaines protéines, lipides, sucres et acides nucléiques. Lorsque cela se produit, notre organisme déclenche des processus de réparation pour corriger ces dommages. C'est notamment le cas lorsque les dimères de pyrimidine et les ROS endommagent l'ADN. Ces lésions sont détectées par notre organisme, qui active alors les voies de réparation de l'ADN, que nous allons examiner plus en détail ci-dessous. [288]

C. Mécanisme de réparation contre les UV

Comme évoqué précédemment, les UV sont capables de provoquer des altérations de l'ADN en induisant la formation de dimères de pyrimidine et d'espèces réactives de l'oxygène. Les dimères de pyrimidine, engendrés par les UVA et les UVB, entraînent des déformations variables au sein de la structure de l'ADN. Parallèlement, les ROS, générés principalement par les UVA, peuvent oxyder les bases de l'ADN (dans 70% des cas) ainsi que les sucres (dans 30% des cas). L'une des altérations les plus fréquentes concerne la guanine, qui se transforme en 8-oxoguanine. D'ailleurs, comme nous avons pu le voir précédemment, cette modification est si courante qu'elle est utilisée comme marqueur pour détecter si la cellule a subi un stress oxydatif ou non. [289]

Pour contrer ces types d'altérations, notre organisme a mis en place des mécanismes spécifiques de réparation, à savoir la voie de réparation par excision de nucléotide (NER) pour les dimères de pyrimidine, et la voie de réparation par excision de base (BER) pour les ROS (Figure 31).[290]

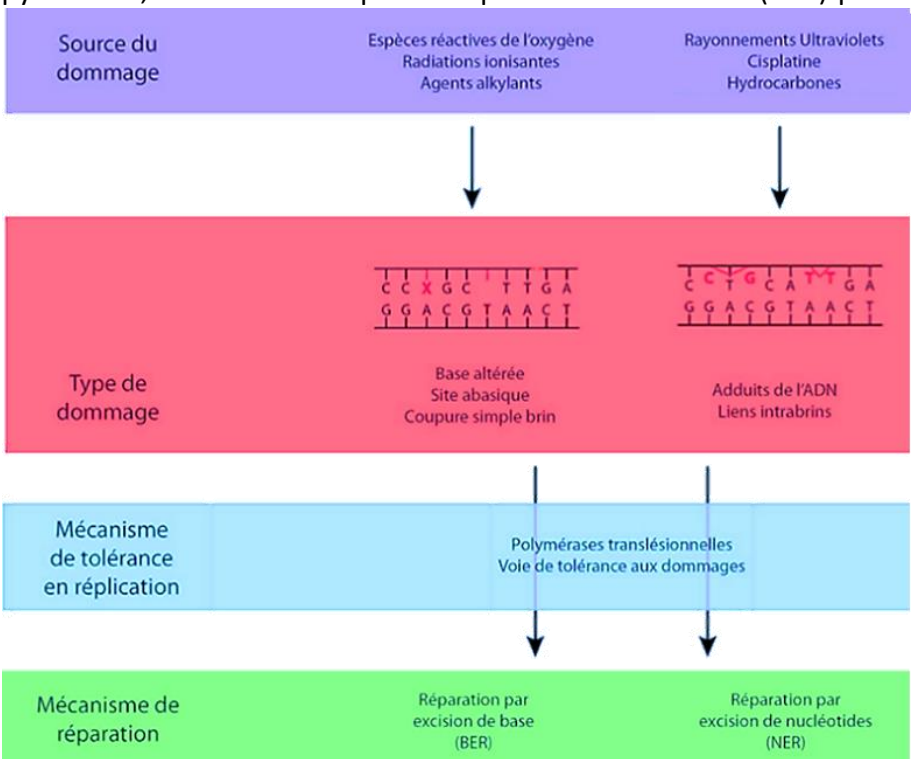

Figure 31 : **Synthèse des altérations de l'ADN les plus fréquentes, susceptibles d'être induites par des agents nocifs exogènes ou endogènes. Le mécanisme de réparation présumé, impliqué dans chaque type de lésion est également mentionné** (Adapté de Houtgraaf *et al.*, 2006).

Avant d'examiner en détail le processus de réparation par excision de nucléotide, il est essentiel de comprendre que la reconnaissance des lésions de l'ADN déclenche une voie de signalisation qui optimise les conditions, notamment en arrêtant le cycle cellulaire pour permettre la réparation des dommages. Cette reconnaissance diffère selon la nature de la cassure, simple ou double brin (Figure 32).[291]

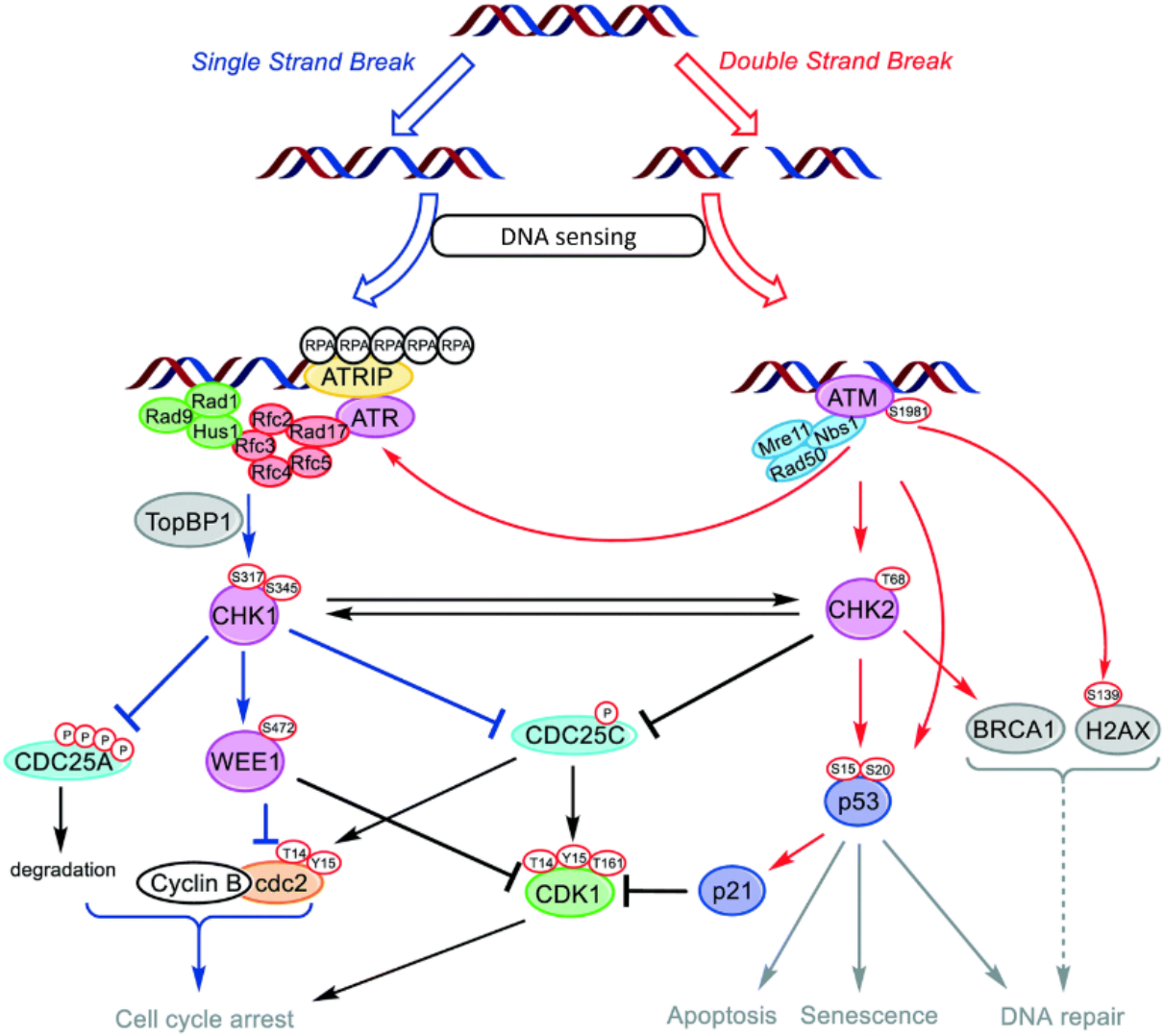

Figure 32 : **Transducteurs des voies de réparation des dommages à l'ADN**. Les transducteurs ATR et ATM sont activés en réponse aux cassures d'ADN simple brin ou double brin, respectivement. Une fois activés, ATR phosphoryle la protéine effectrice CHK1, entraînant le recrutement de facteurs de réparation de l'ADN et l'arrêt du cycle cellulaire, ainsi que la phosphorylation d'une série de protéines impliquées dans la réparation. De manière similaire, l'ATM activé phosphoryle des effecteurs tels que CHK2, entraînant l'activation de facteurs supplémentaires en aval. Ces deux voies jouent un rôle clé dans l'arrêt du cycle cellulaire, permettant à la cellule de réparer les dommages à l'ADN, ou de déclencher la sénescence/apoptose lorsque la réparation est impossible (Ronco *et al.*, 2017).

Pour les lésions simple brin, RPA joue un rôle crucial en stabilisant la zone d'ADN monocaténaire et en se liant spécifiquement à ATRIP, qui est capable de recruter spécifiquement la kinase ATR.[292]

ATR doit ensuite être activé par un ensemble de protéines, notamment le complexe Rad9-Rad1-Hus1 (9-1-1) et le complexe Rad17-Rfc2-5. En outre, Rad9 peut lier TopBP1 pour faciliter son rapprochement avec ATR, favorisant ainsi son activation.[293,294] Une fois activé, ATR phosphoryle Chk1 avec l'aide de la claspin, amorçant ainsi une cascade de signalisation qui aboutit à l'arrêt du cycle cellulaire et au recrutement de protéines nécessaires à la réparation des dommages à l'ADN.[295] De plus, ATR peut également être recruté par ATM, comme nous le verrons par la suite, pour faciliter la réparation des cassures double brin. Dans ce cas, ATM et ATR participent à la réponse aux dommages de l'ADN "lente", pouvant éventuellement déclencher p53 dans les cellules saines, entraînant ainsi l'arrêt du cycle cellulaire ou l'apoptose.[296]

En ce qui concerne les lésions double brin, elles sont initialement détectées par le complexe hétérotrimérique Mre11-Rad50-Nbs1 (MRN). Ce complexe recrute ensuite ATM au site de la cassure, formant ainsi un foyer nucléaire.[297] ATM est activé par dédimérisation causée par une autophosphorylation (S367, S1893 et S1981) et une acétylation (Tips60).[298] Une fois activé, ATM phosphoryle l'histone H2AX, un variant de l'histone H2A, sur la sérine 139. Cette phosphorylation de H2AX permet la formation du complexe H2AX-MDC1, qui recrute divers effecteurs (par exemples : BRCA1, 53BP1, ...) impliqués dans l'arrêt du cycle cellulaire, l'activation des points de contrôle du cycle cellulaire et la réparation des dommages à l'ADN.[299,300] De plus, ATM phosphoryle Chk2 sur la thréonine 68, qui à son tour phosphoryle p53 sur les sérines 15 et 20. Une fois phosphorylée, p53 active p21, ce qui entraîne l'arrêt du cycle cellulaire en inhibant CDK1. En outre, Chk2 inhibe CDC25, entraînant l'inhibition de CDK2-cycline E et CDK1-cycline B, renforçant ainsi l'effet d'arrêt du cycle cellulaire induit par l'inhibition de CDK1.[301,302]

1. La voie de réparation par excision de nucléotide (NER)

La voie de réparation par excision de nucléotide constitue un mécanisme essentiel de défense contre les lésions qui déforment de manière significative l'ADN, en particulier les dimères de pyrimidine tels que les CPD et les photoproduits 6-4, qui peuvent se transformer en isomères de Dewar. Ce processus de réparation implique plusieurs étapes coordonnées. [303]

Initialement, la reconnaissance des lésions se produit par des facteurs de reconnaissance qui se lient à la région endommagée de l'ADN. Ensuite, des hélicases contribuent à l'ouverture du duplex d'ADN en amont et en aval du site lésé, tandis que des endonucléases spécifiques réalisent des coupures en 5' et en 3' du brin endommagé. Une fois le segment excisé, une ADN polymérase utilise le brin non endommagé comme matrice pour synthétiser le brin excisé. Enfin, une ADN ligase se charge de relier le fragment d'ADN restauré. [304]

Chez les eucaryotes, on distingue deux sous-voies de NER, la réparation génomique globale par excision de nucléotides (GC-NER) et la réparation couplée à la transcription par excision de nucléotides (TC-NER). La GC-NER a donc un processus plus lent de détection du dommage comparé à la TC-NER, ciblant spécifiquement les régions en cours de transcription active. Bien que ces sous-voies diffèrent dans leur mécanismes de reconnaissance des lésions de l'ADN, elles partagent le même processus d'excision, de réparation et de ligature des dommages (Figure 33). [305]

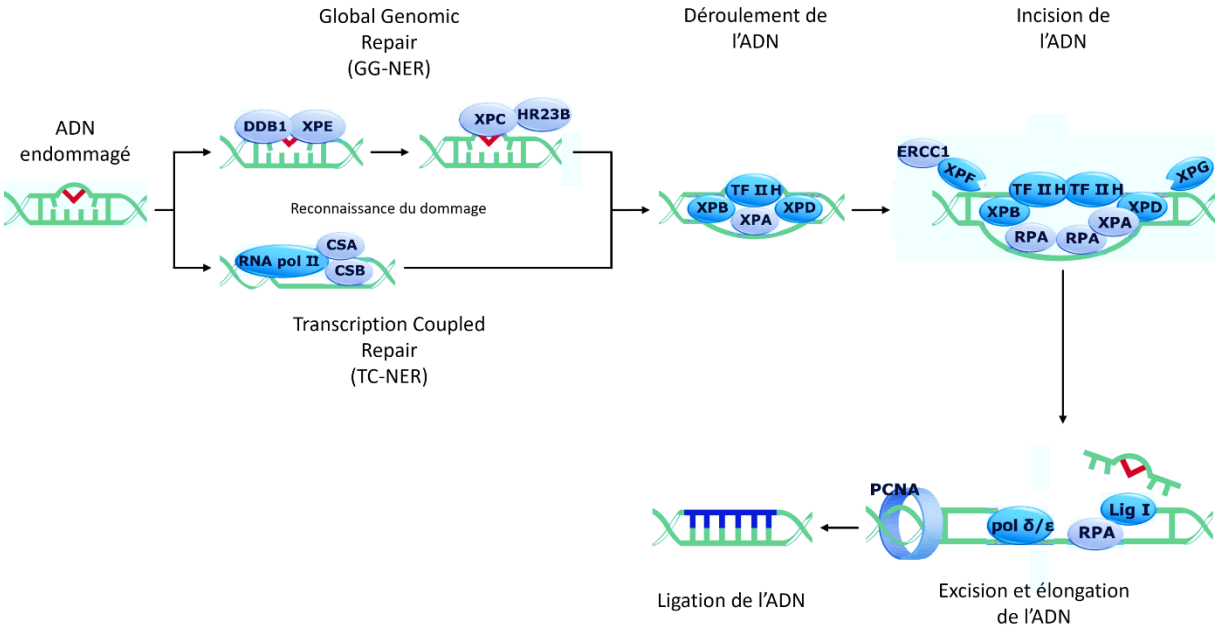

Figure 33 : **Représentation schématique des différentes étapes de la voie de réparation par excision de nucléotide, à savoir la reconnaissance du dommage, le déroulement de l'ADN, la formation du complexe de pré-incision et l'incision, l'excision et l'élongation de l'ADN et pour finir la ligation de celui-ci**. (Adapté de GeneTex.com).

La GC-NER est capable de détecter les lésions d'ADN grâce à deux systèmes de reconnaissance qui agissent en collaboration [306,307] :

- Le complexe XPC/HR23B/CETN2 interagit spécifiquement avec les photoproduits 6-4, recrutant ensuite l'hélicase TFIIH pour former le complexe de pré-incision
- De même, le complexe DDB1/DDB2 (ou UV-DDB) se lie fortement aux photoproduits 6-4 et modérément aux CPD. De plus, il est capable de recruter XPC/HR23B/CETN2 sur le site endommagé

En revanche, la TC-NER repose sur l'ARN polymérase II. Lorsqu'un dommage survient, cette enzyme se bloque, entraînant l'arrêt du complexe basal de la transcription. Une fois à l'arrêt, deux protéines vont être recrutées [308,309] :

- La protéine dénommée, *Cockayne syndrome B* (CSB) qui permet à l'ARN polymérase II de reculer de quelques nucléotides, libérant ainsi la zone pour l'intervention des enzymes de réparation et retardant/arrêtant l'activité de l'ARN polymérase
- La protéine *Cockayne syndrome A* (CSA) qui assure le recrutement de l'hélicase TFIIH et la formation du complexe de pré-incision

Le complexe TFIIH, composé de 7 protéines centrales (XPB, XPD et GTF2H1-5), interagit avec le complexe ''*CdK activating kinase*'' (CDK7, MAT1 et la cycline H) *via* XPD, formant ainsi le complexe de pré-incision. Une fois recruté, TFIIH, *via* XPB et XPD, se lie à l'ADN et joue son rôle d'hélicase en dénaturant la double hélice sur une étendue de 22 à 30 nucléotides, créant ainsi une région de transcription, appelée ''bulle'' de transcription. En même temps, TFIIH, *via* la sous-unité *CdK activating kinase* va induire la phosphorylation de l'ARN polymérase II et sa dissociation avec le promoteur. Pour terminer, TFIIH, *via* GTF2H4 et GTF2H5, recrute XPA, une protéine à doigt de zinc nécessaire au recrutement du complexe XPF/ERCC1. [310–313]

Le complexe endonucléase XPF/ERCC1, en collaboration avec l'endonucléase XPG recrutée par la ''bulle'' de transcription et TFIIH, réalise le clivage de la lésion au niveau du brin 5' pour XPF et 3' pour XPG. Pendant cette étape, RPA se lie au brin non endommagé à l'intérieur de la ''bulle'' de transcription, le protégeant ainsi des endonucléases et l'empêchant de former des structures en épingle à cheveux. De plus, RPA assure un positionnement adéquat du complexe XPF/ERCC1 et XPG au niveau de la lésion pour assurer un clivage correct. [314,315]

Une fois que la séquence de 22 à 30 nucléotides est excisée, XPG recrute le facteur de réplication C (RFC) qui charge le ''*proliferating cell nuclear antigen*'' (PCNA) sur le brin d'ADN. Cela permet aux ADN polymérases (δ et ε) d'effectuer la synthèse d'ADN complémentaire. Enfin, les ADN ligase I ou l'ADN ligase III, couplée à XRCC1, scellent les brins pour achever le processus de NER. [316,317]

2. La voie de réparation par excision de base (BER)

La voie de réparation par excision de base représente un mécanisme essentiel de défense contre les lésions oxydatives, qui peuvent être induites par le métabolisme cellulaire ou les UV, sans provoquer de déformations significatives de l'ADN. Ce processus de réparation est rapide et implique une coordination de plusieurs étapes. [318]

Initialement, la reconnaissance des altérations est assurée par une ADN glycosylase qui élimine la base endommagée, générant ainsi un site abasique (site AP). Par la suite, ce site AP est sujet à un clivage *via* différents mécanismes, impliquant soit l'ADN glycosylase elle-même, soit une endonucléase. Une fois le site AP éliminé, les extrémités 3' et 5' du brin d'ADN sont ''nettoyées'' grâce à diverses enzymes, permettant à une ADN polymérase d'utiliser le brin non endommagé comme matrice pour synthétiser le fragment retiré. Enfin, une ADN ligase se charge de relier le fragment d'ADN restauré. [319]

La voie du BER présente deux sous-voies, à savoir la *short patch* BER et la *long patch* BER, qui diffèrent en termes de longueur du segment à resynthétiser ainsi que des facteurs cellulaires impliqués tout au long du processus (Figure 34). [320]

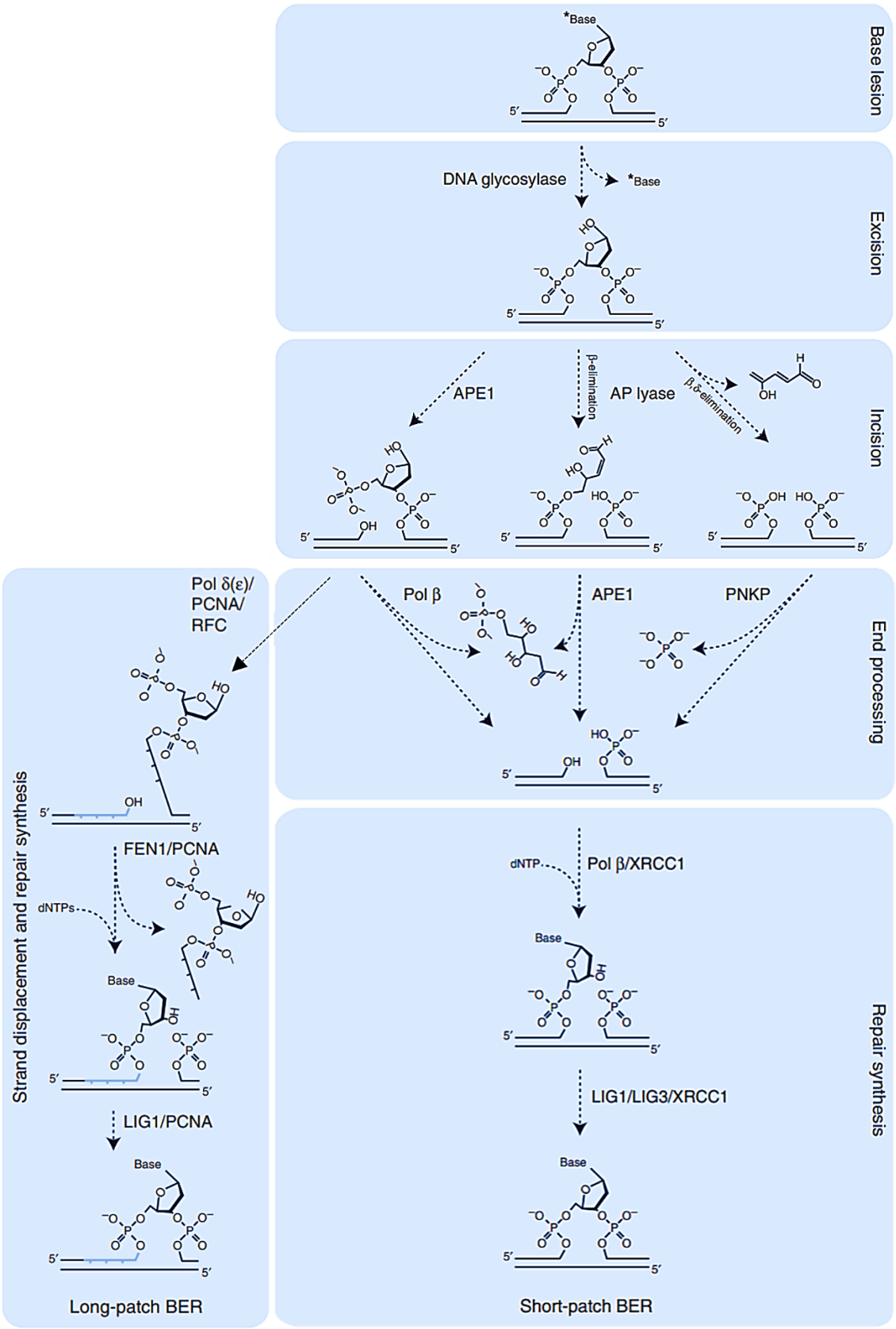

Figure 34 : **Voie de réparation par excision de base (BER)**. Le BER peut être réalisé par deux sous-voies, la *short patch* et la *long patch*, qui diffèrent l'une de l'autre à partir de l'excision et du "nettoyage" du site abasique. Malgré cette différence, le processus de réparation se déroule en 5 étapes principales, quelle que soit la sous-voie utilisée. Ces 5 étapes sont la reconnaissance et l'excision de la base, le clivage du site AP, le nettoyage du site AP, la synthèse de réparation et la ligature du fragment synthétisé (Krokan *et al.*, 2013)

La *short patch* BER est amorcée par une ADN glycosylase capable de détecter des lésions spécifiques présentes dans le brin d'ADN. En effet, diverses ADN-glycosylases existent, chacune reconnaissant sélectivement un type précis d'altération. Par exemple, la 8-oxoguanine glycosylase (OGG1) cible les guanines oxydées en C8 suite à une exposition aux UV, tandis que SMUG1 reconnaît la 5-hydroxyuracile, une cytosine produite lors de la désamination oxydative de la cytosine par des ROS.[321]

Une fois la lésion reconnue, l'ADN glycosylase clive la liaison N-glycosidique entre la base altérée et le désoxyribose, libérant ainsi la base altérée dans le milieu et générant un site abasique. [322]

Après la formation du site AP, deux types d'enzymes peuvent hydrolyser la liaison phosphodiester entre un désoxyribonucléotide normal et un désoxyribonucléotide dépourvu de base nucléique, c'est-à-dire le site AP, afin de permettre son élimination (Figure 35) [323] :

- Une ADN glycosylase bifonctionnelle, telle qu'OGG1, qui clive non seulement la liaison N-glycosidique entre la base altérée et le désoxyribose, mais qui est également capable de cliver le site AP *via* une β-élimination ou une β-δ élimination. La β élimination se produit au niveau de la liaison phosphodiester de l'extrémité 3', générant une extrémité 3' contenant un aldéhyde α, β-insaturé et une extrémité 5' contenant un phosphate. Si l'ADN glycosylase reste en contact avec le site AP suffisamment longtemps, la β élimination est complétée par une δ élimination, convertissant ainsi l'extrémité 3' aldéhyde α, β-insaturé en 3' phosphate.
- L'endonucléase AP1 (APE1) qui clive le site AP du côté 5', produisant ainsi une extrémité 3' contenant un hydroxyle et une extrémité 5' contenant un désoxyribose phosphate.

Une fois le site AP éliminé, le nettoyage des extrémités 3' et 5' est assuré par différentes enzymes en fonction de l'enzyme qui a excisé le site AP (Figure 35) [324] :

- Lorsque l'ADN glycosylase bifonctionnelle génère une extrémité 3' aldéhyde α, β-insaturé par β-élimination, l'endonucléase APE1 est responsable de son nettoyage et génère une extrémité 3' hydroxyle.
- Lorsque l'ADN glycosylase bifonctionnelle génère une extrémité 3' phosphate par β-δ élimination, la phosphatase PNKP est impliquée dans son nettoyage et produit une extrémité 3' hydroxyle.
- Lorsque l'endonucléase génère une extrémité 5' désoxyribose phosphate, l'ADN polymérase β, par le biais de son activité de lyase, réalise son nettoyage et génère une extrémité 5' phosphate.

Une fois les extrémités nettoyées, l'ADN polymérase β est placée au niveau de l'extrémité 3' hydroxyle par XRCC1, une protéine d'échafaudage, permettant ainsi une synthèse précise de la base manquante en utilisant le brin non endommagé comme matrice. [325]

Enfin, pour conclure le processus de *short patch* BER, l'ADN ligase I/III, également associée à XRCC1, scelle le brin d'ADN. [326]

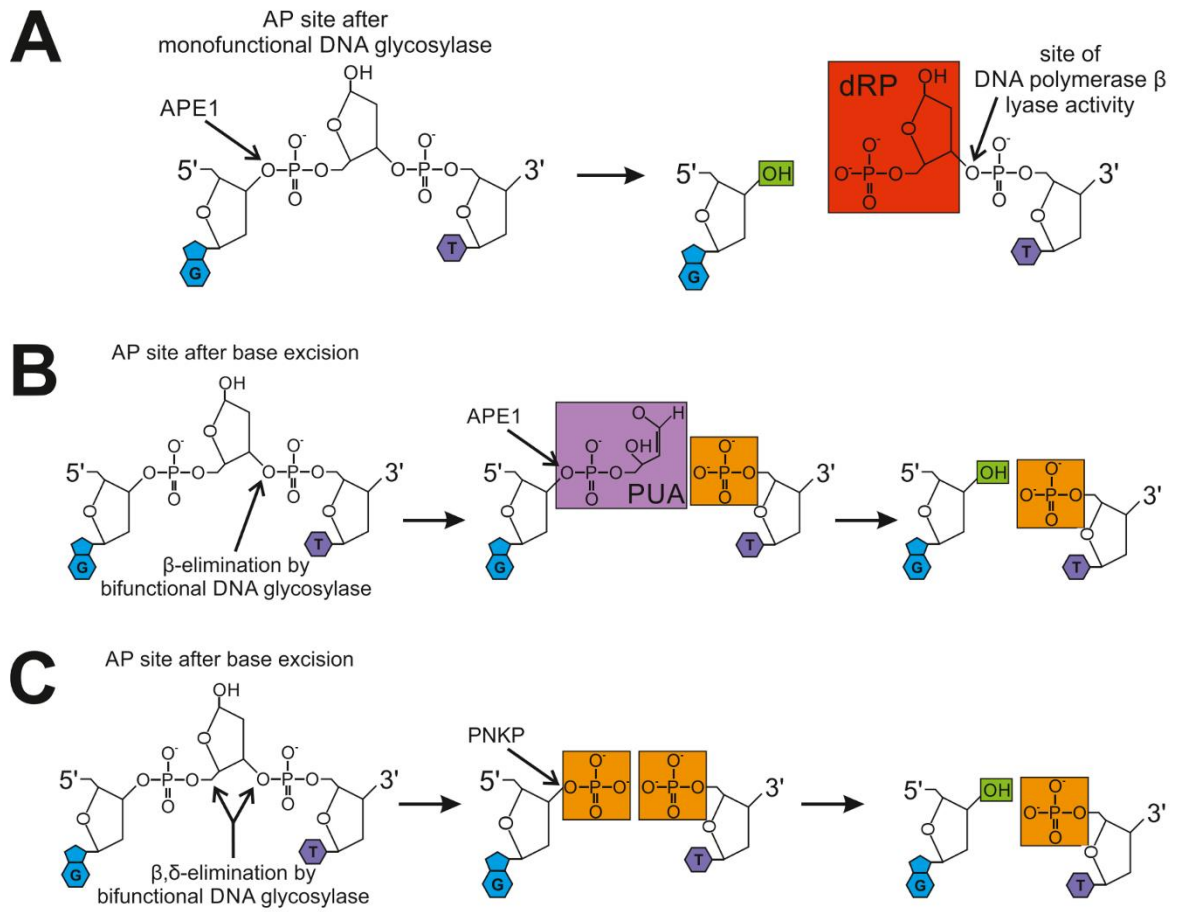

Figure 35 : **Clivage du site AP et nettoyage des extrémités 3' et 5'**. A) Les ADN glycosylases monofonctionnelles excisent uniquement la base endommagée de l'ADN, générant un site AP. Ensuite, le complexe de réparation APE1 clive le site AP, créant une rupture dans le brin d'ADN. Cette rupture contient une extrémité 3' hydroxyle et une extrémité 5' désoxyribose phosphate. L'activité lyase de l'ADN polymérase β vient nettoyer l'extrémité 5', générant ainsi une extrémité 5' phosphate. B) Les ADN glycosylases bifonctionnelles, en plus d'éliminer la base d'ADN endommagée, peuvent effectuer une β élimination qui clive le site AP au niveau de la liaison phosphodiester de l'extrémité 3'. Cela laisse une rupture dans le brin d'ADN, contenant une extrémité 3' aldéhyde α, β-insaturé et une extrémité 5' phosphate. Ensuite, l'enzyme APE1 intervient pour nettoyer l'extrémité 3', générant ainsi une extrémité 3' hydroxyle. C) Les ADN glycosylases bifonctionnelles peuvent également effectuer une β-δ élimination qui génère une rupture dans le brin d'ADN, contenant des extrémités 3' phosphate et 5' phosphate. L'enzyme PNKP intervient ensuite pour nettoyer l'extrémité 3', générant une extrémité 3' hydroxyle (Parsons *et al.*, 2023).

Dans le cas de la *long patch* BER, la détection et l'élimination de la lésion sont similaires à celles de la *short patch*. Cependant, le clivage du site AP est réalisé exclusivement par APE1, ce qui signifie que l'ADN glycosylase responsable de la détection de la lésion est une ADN glycosylase monofonctionnelle, comme SMUG1 par exemple. Une fois le site AP clivé, RFC intervient pour ouvrir et positionner PCNA au niveau du site abasique de l'ADN. Après avoir été chargé sur l'ADN, PCNA joue un rôle crucial en tant que facteur de processivité pour les ADN polymérases δ et ε. Ces dernières synthétisent alors un nouveau fragment d'une longueur variant entre 2 à 8 nucléotides. De plus, PCNA stimule également l'endonucléase FEN1 pour qu'elle puisse inciser le polynucléotide destiné à être remplacé par le brin nouvellement synthétisé. Enfin, la ligase I, également activée par le PCNA, effectue la suture des extrémités et achève ainsi le processus de *long patch* BER. [327–329]

D. UV et altérations cutanées

Les UV ont divers effets sur la peau, dont la plupart sont malheureusement néfastes. Cependant, il existe quelques effets positifs, notamment dans le traitement de certaines maladies telles que le psoriasis, le vitiligo et le lupus vulgaire, grâce à la PUVA-thérapie. Cette approche médicale associe le psoralène, un photosensibilisant et agent mutagène, avec la photothérapie par rayonnement UVA. Ensemble, les UVA et le psoralène induisent un effet pro-apoptotique, caractérisé par l'accumulation de pontages inter-brins entre deux brins d'ADN d'un même chromosome, ainsi qu'un effet anti-inflammatoire. [330,331]

Cependant, les effets négatifs des UV sont également importants. Ils peuvent déclencher une cascade de cytokines et de médiateurs vasoactifs, en plus de causer des lésions à l'ADN, conduisant à une réponse inflammatoire que l'on appelle communément ''coups de soleil''. [332] Une autre conséquence significative de l'exposition, prolongée cette fois-ci, aux UV est le photovieillissement de la peau. Celui-ci se manifeste par une perte d'élasticité, des rides profondes et des zones d'hyper/hypopigmentation au niveau de la peau. L'élastose actinique, principalement observée au niveau du derme réticulaire, est l'une des caractéristiques les plus courantes du photovieillissement. Elle est caractérisée par une diminution du nombre de fibres de collagène ainsi qu'une accumulation de fibres élastiques anormales et épaisses associées à des protéines, telles que la fibronectine ou la fibrilline. [333,334] Par ailleurs, les UV peuvent entraîner une accumulation de kératinocytes épidermiques responsables de l'épaississement de l'épiderme, appelée hyperkératose, afin de mieux résister aux effets néfastes des UV. [335] De plus, les UV peuvent créer un état d'immunotolérance ou d'immunosuppression favorisant l'infection persistante de virus, notamment le papillomavirus humain. [336,337]

Outre ces conséquences, les UV peuvent également présenter des risques plus graves pour notre organisme. Des études ont montré que 90 à 95% des cancers de la peau survenant chez les populations blanches étaient attribuables aux rayons UV, qui sont ainsi considérés comme le principal facteur de risque des cancers cutanés. [338] Le développement de ces cancers est principalement dû à l'effet mutationnel des UV qui sont capables, *via* les dimères de pyrimidine et les ROS, de provoquer environ 61 mutations/Mb dans les carcinomes spinocellulaires et 13 mutations/Mb dans les mélanomes, entraînant à terme une croissance incontrôlée et la formation de tumeurs. [339,340]

Il est également crucial de noter l'existence de diverses conditions pathologiques, que nous avons désignées comme des "précurseurs du cancer cutané", qui favorisent le développement de cancers cutanés. Parmi ces précurseurs figurent des syndromes héréditaires génétiques résultant d'anomalies sur un ou plusieurs chromosomes, ainsi que des lésions précancéreuses se caractérisant par un état anormal où des cellules prolifèrent de manière incontrôlée au sein d'une zone géographiquement limitée. [341,342]

1. Précurseurs du cancer cutané

Comme exposé précédemment, les précurseurs du cancer cutané se répartissent en deux grandes catégories : les syndromes héréditaires génétiques résultant de mutations génétiques et les lésions précancéreuses caractérisées par une atypie cellulaire et une prolifération anarchique sans pour autant franchir la membrane basale.

Parmi la très grande diversité de syndromes génétiques, notre attention se focalise sur ceux qui impactent les gènes impliqués dans les voies de réparation de l'ADN, en particulier la NER et la BER. Ces deux voies sont fondamentales pour réparer les dommages causés à l'ADN par les rayonnements UV. Trois syndromes héréditaires génétiques sont reliés à des mutations dans les gènes de la voie NER : le xeroderma pigmentosum (XP), le syndrome de Cockayne (CS) et la trichothiodystrophie (TTD). Parmi ceux-ci, seul le XP a un impact sur le développement de cancers cutanés, c'est pourquoi nous n'examinerons pas en détail les deux autres syndromes. Concernant la voie BER, certaines enzymes sont vitales et leur absence entraîne le décès de l'embryon, expliquant l'absence de syndrome héréditaire humain spécifiquement associé à la BER. [343–345]

En ce qui concerne les lésions précancéreuses, compte tenu du rôle hypothétique des β-HPV dans le développement des carcinomes épidermoïdes cutanés, nous avons choisi de concentrer notre attention sur les deux lésions précancéreuses susceptibles de progresser vers ce type de cancer, à savoir la kératose actinique et la maladie de Bowen.[346]

i. Syndrome héréditaires génétiques

- Le xeroderma pigmentosum (XP)

Initialement décrit en 1874 par Moritz Kaposi, le xeroderma pigmentosum, connu sous le nom de maladie des "enfants de la Lune", est une génodermatose autosomique récessive touchant 1 personne sur 250.000 en Europe et aux États-Unis, ainsi qu'une personne sur 40.000 en Asie. [347,348] Ce syndrome est caractérisé par des mutations au sein des gènes impliqués dans la réparation de l'ADN par excision de nucléotides, la principale voie de réparation des dommages causés par les dimères de pyrimidines (principalement induits par les UV). En l'absence d'un NER fonctionnel, les mutations induites par les UV s'accumulent au fil des divisions cellulaires et engendrent des anomalies dans l'ADN, qui peuvent être responsable de la cancérisation. [349,350] Ces patients sont exposés à un risque significativement élevé de développer des carcinomes épidermoïdes/basocellulaires ou des mélanomes malins, avec des risques respectifs multipliés par environ 10.000 et 2.000 fois. De plus, XP est associé à des tumeurs malignes de la surface oculaire, notamment le carcinome épidermoïde, le carcinome basocellulaire et le mélanome, avec un risque relatif accru d'environ 2.000 fois. [351,352]

Cliniquement, XP se manifeste par une photosensibilité accrue, des changements pigmentaires cutanés ainsi que des lésions oculaires liées aux UV, un risque accru de tumeurs cutanées/oculaires et, dans certains cas, une dégénérescence neurologique progressive. [353] La peau des patients atteints vieillit prématurément, se caractérisant par une atrophie, des rides, une télangiectasie (dilatation des capillaires de la peau ou des muqueuses), des lentigos précoces (taches de vieillesse), une poïkilodermie (atrophie épidermique, télangiectasies, pigmentation brune ou dépigmentation), une kératose actinique ainsi que des brûlures et des cloques suite à une exposition minimale au soleil (Figure 36). [354–356]

Environ 90% des patients atteints de XP présentent des atteintes oculaires au niveau des parties antérieures de l'œil (conjonctive, cristallin, cornée et paupières) qui sont particulièrement sensibles aux effets néfastes des rayons UV. Les manifestations ophtalmologiques incluent la photophobie (sensibilité à la lumière), le blépharospasme (fermeture ou clignement excessif et involontaire des paupières), et des lésions de la conjonctive (néovascularisation, xérose, mélanose). D'autres manifestations ophtalmologiques comprennent également des irrégularités du bord des paupières, une pigmentation accrue des paupières avec perte de cils, un trichiasis (mauvais alignement des cils), une blépharite (inflammation du bord de la paupière), une cataracte, une ulcération cornéenne, *etc*. [357,358]

Pour finir, la neurodégénérescence progressive, observée chez environ 25 % des patients, se manifeste par des troubles cognitifs, la perte auditive progressive, le retard de la parole, l'ataxie (troubles de la coordination des mouvements et de l'équilibre), la diminution des réflexes, des convulsions, *etc*. Cette dégénérescence peut être attribuée à une perte neuronale dans le cerveau et le cervelet, potentiellement causée par le stress oxydatif endommageant l'ADN des neurones affectés. [351,359]

Figure 36 : **Exemple du xeroderma pigmentosum chez un enfant de 17 ans** (Sharquie *et al.*, 2022).

Le diagnostic de XP doit être envisagé chez les patients qui présentent une photosensibilité accrue ainsi que des manifestations cutanées, ophtalmologiques et neurologiques caractéristiques (comme évoqué précédemment). Cependant, il est important de noter que certains individus atteints peuvent ne pas montrer les brûlures cutanées typiques. Dans ce cas, le diagnostic peut être établi lors de l'apparition de lésions (pré)cancéreuses cutanées. [360]

Pour confirmer le diagnostic de XP et le distinguer d'autres affections présentant des symptômes similaires, des méthodes telles que la dermoscopie, l'histologie et l'analyse de l'ADN cutané par biopsie sont utilisées. Sur le plan histologique, le XP se caractérise par une augmentation de la mélanine et des mélanocytes dans la couche basale de l'épiderme, une hyperkératose, un infiltrat lymphocytaire dans le derme supérieur, une atrophie et/ou une élastose du derme, des télangiectasies et une atypie des kératinocytes. Le diagnostic génétique quant à lui consiste à identifier la mutation présente dans l'un des gènes responsables du XP. [361,362]

Il est à noter que le terme "xeroderma pigmentosum" englobe actuellement 8 syndromes génétiques distincts (Tableau 5). Selon la mutation spécifique en cause, certains types de XP sont plus enclins aux maladies oculaires et à la neurodégénérescence progressive. [363]

Type	Fréquence	Symptôme cutanés	Symptômes ophtalmologiques	Symptômes neurologiques	Gène touché
XPA	25%	Grave	Modéré	Grave	XPA
XPB	Rare	Grave	Modéré	Grave	XPB/ERCC3
XPC	25%	Modéré	Grave	Modéré	XPC
XPD	15%	Grave	Modéré	Grave	XPC/ERCC2
XPE	Rare	Modéré	Grave	Modéré	XPE/DDB2
XPF	6%	Modéré	Modéré	Grave	XPF/ERCC4
XPG	6%	Grave	Modéré	Grave	XPG/ERCC5
Variant	20-30%	Modéré	Grave	Modéré	POLH

Tableau 5 : **Liste des différents types de xeroderma pigmentosum ainsi que des symptômes et gènes associés.**

La détection précoce revêt une importance cruciale afin de mettre en place des mesures de protection le plus tôt possible, visant à atténuer les complications induites par les rayons UV. En l'absence de mesures de protection adéquates, la peau des individus atteints de ce syndrome peut manifester des lésions photosensibles telles que la dépigmentation, l'hyperpigmentation, les lentigos, les télangiectasies, les kératoses actiniques et l'atrophie, pouvant également évoluer vers des cancers cutanés. Les yeux et les paupières sont également extrêmement sensibles, avec plus de 40 % des patients souffrant de blépharospasme (contractions involontaires et répétées des muscles des paupières) et de photophobie. D'autres altérations, dont des érythèmes, des anomalies de pigmentation, l'opacification de la cornée et des lésions cancéreuses des paupières, sont fréquentes. En conséquence, l'espérance de vie des patients atteints est réduite, atteignant généralement seulement 20 à 30 ans. [347,364]

À l'heure actuelle, il n'existe pas de traitement spécifique pour ce syndrome autosomique récessif. Par conséquent, la prévention des complications revêt une importance primordiale pour cette maladie potentiellement mortelle. La stratégie la plus efficace consiste à protéger l'ensemble du corps des rayonnements UV. Cela implique de limiter les sorties en plein jour et d'éviter l'exposition aux sources émettant des UV, notamment certaines lampes. Lors des sorties, le port de vêtements amples, de gants et de chapeaux à larges bords, ainsi que l'application régulière de crèmes solaires à indice de protection élevé, sont des mesures essentielles. Un suivi médical régulier, comprenant des consultations pédiatriques, dermatologiques, ophtalmologiques et neurologiques, est indispensable pour traiter rapidement toute complication pouvant survenir. [363]

Par ailleurs, bien qu'il n'y ait pas encore de traitement formellement établi, plusieurs options thérapeutiques sont en cours d'exploration. Des traitements expérimentaux tels que le *T4 endonucléase-V*, le *vismodegib* et le *nicotinamide* ont montré des résultats prometteurs dans la gestion du XP. [365,366]

ii. Lésions précancéreuses

Parmi les principales lésions précancéreuses, on retrouve la kératose actinique (AK) et la maladie de Bowen (BD), qui affectent la peau, ainsi que la leucoplasie, qui se développe au niveau de la muqueuse buccale (Figure 37). Jusqu'à présent, aucun lien n’a été démontré entre la leucoplasie et les HPV, contrairement à la kératose actinique et à la maladie de Bowen où des hypothèses sur l'implication des HPV dans leur développement sont de plus en plus nombreuses. Pour cette raison, nous allons nous concentrer sur ces deux derniers types de lésions précancéreuses, en mettant particulièrement l'accent sur la maladie de Bowen, qui, contrairement à la kératose actinique, est largement moins étudiée et donc moins connue dans la littérature scientifique. [367,368]

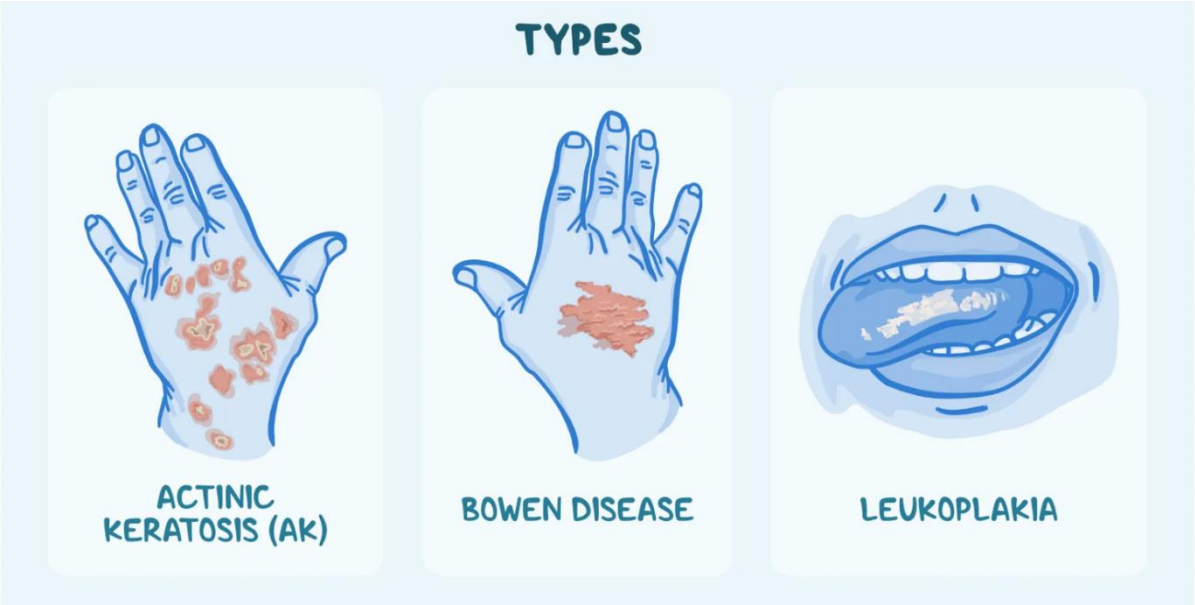

Figure 37 : **Représentation schématique des différents types de lésions précancéreuses cutanées UV-dépendantes** (Adapté de Osmosis.org)

- Kératose actinique (AK)

La kératose actinique est une lésion précancéreuse courante, se classant au troisième rang des affections cutanées les plus fréquemment traitées par les dermatologues. En Australie, par exemple, elle affecte entre 40% et 60% de la population. [369,370] Elle se caractérise par l'épaississement de la couche cornée de l'épiderme (aussi appelé hyperkératose), causé par une réplication anarchique des kératinocytes dans une zone cutanée chroniquement endommagée par l'exposition aux UV. Typiquement, les AK se localisent sur les zones du corps soumises à une exposition solaire importante, comme le cuir chevelu, le visage, les oreilles, le cou, les dos des mains, les avant-bras et la poitrine. [371]

Cliniquement, les AK se présentent généralement sous la forme de petites plaques rosées ou rougeâtres, squameuses et d'épaisseur variable, accompagnées d'une rougeur environnante (Figure 38). En outre, elles sont particulièrement remarquables en raison de leur texture rappelant celle du papier de verre, contrairement aux lésions de Bowen que nous aborderons par la suite. Les lésions ont un diamètre qui varie généralement entre 2 et 6 mm et sont souvent associées à des signes de dommages solaires, tels que des altérations pigmentaires, des rides et des ecchymoses. Selon leurs caractéristiques cliniques, les AK peuvent être classées en trois catégories [372] :

- Grade I : Facilement visible et légèrement palpable.
- Grade II : Facilement visible et palpable.
- Grade III : Très visible et hyperkératosique.

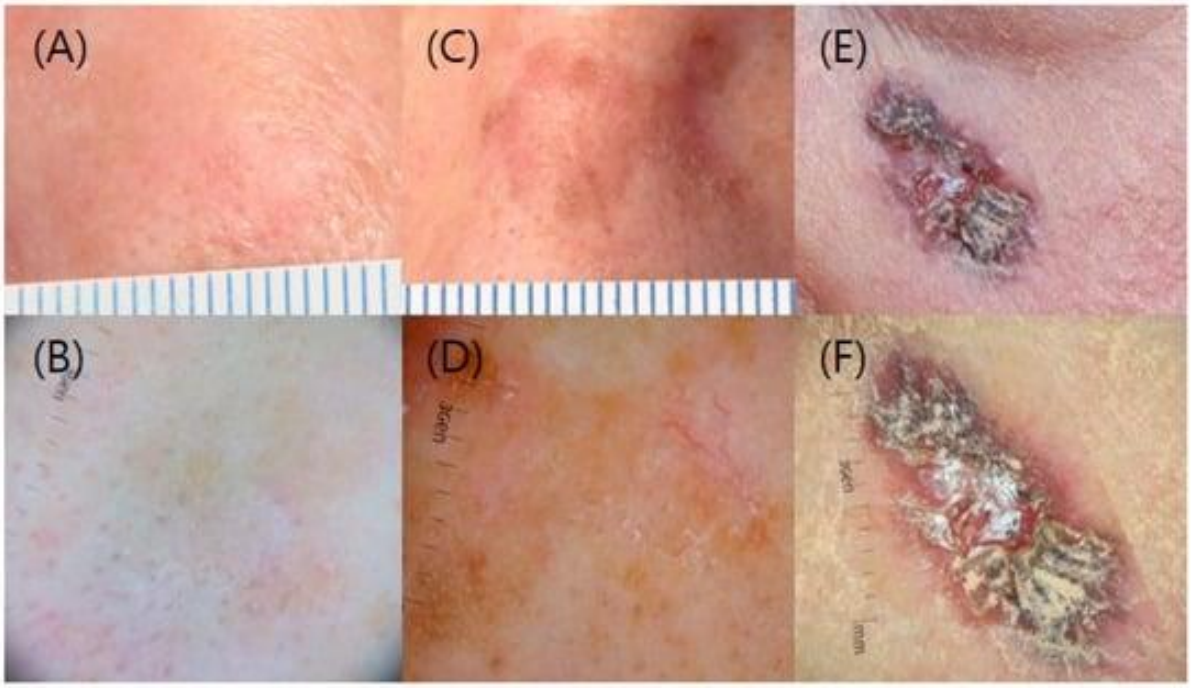

Figure 38 : **Classement clinique et dermoscopique d'une kératose actinique**. A/B) grade 1. C/D) grade 2. E/F) grade 3 (Ah Yoo *et al.*, 2022).

Bien que généralement asymptomatiques, les AK peuvent parfois être douloureuses, prurigineuses, saignantes ou provoquer une sensation de picotement ou de brûlure. [373]

Le principal facteur de risque impliqué dans la formation des AK est le rayonnement ultraviolet, qui induit notamment des mutations dans le gène suppresseur de tumeur p53. La dérégulation de la voie p53 entraîne une prolifération incontrôlée des kératinocytes, pouvant progresser vers une kératose actinique et éventuellement un cancer de la peau si la lésion n'est pas surveillée. [374,375]

Par ailleurs, plusieurs études suggèrent que les HPV jouent également un rôle dans le développement des AK. Une étude publiée en 2005 a démontré la présence d'HPV dans 80% des biopsies d'AK (20/25) ainsi qu'une charge virale élevée dans la moitié de ces cas. Ces résultats démontrent l'effet synergique existant entre les AK, qui fournissent un environnement propice au virus *via* la prolifération et la différenciation anormales des kératinocytes, et des HPV, qui stimulent la prolifération cellulaire *via* leurs protéines virales. [231,376] D'autres facteurs de risque tels que l'immunosuppression, les antécédents de cancer épithéliaux, le nombre de AK, l'âge, le genre, le type de peau, les genodermatoses ainsi que la calvitie méritent également d'être mentionnés. [377–379]

Le diagnostic de la kératose actinique est généralement établi par un examen clinique approfondi combinant l'observation visuelle et le toucher. Dans certains cas, une biopsie peut être nécessaire, notamment lorsque la lésion est de grande taille, épaisse ou saigne, afin d'écarter la possibilité d'un cancer de la peau. La surveillance étroite des AK est importante car elles peuvent régresser (dans environ 15 à 60% des cas), persister sans changement structurel ou évoluer vers un carcinome épidermoïde cutané (CSC) dans 0,25% à 20% des cas. [380–382]

Actuellement, il n'existe pas de méthode fiable basée sur des critères cliniques ou histologiques permettant de prédire avec certitude si une AK subira une transformation cancéreuse ou non. En conséquence, il est recommandé d'opter pour un traitement adéquat pour tous les cas de kératose actinique, en tenant compte d'une évaluation approfondie de l'espérance de vie du patient, de ses comorbidités, de ses préférences individuelles, de son mode de vie ainsi que des caractéristiques cliniques de la lésion (Tableau 6).

Patient factors	Lesion factors	Treatment factors
– Immune suppression	– Site	– Lesion- or field-directed
– Comorbidities	(e.g., face, scalp, lower lip, limbs)	– Application by patient or by medical staff
– Medications	– Clinical consistency	– Duration of application
– Patient preference	(e.g., thickness of keratinization)	– Side effects
– Treatment compliance	– Size of lesion and of affected area	– Availability of equipment
		(e.g., laser, red-light lamp)
		– Cost

Tableau 6 : **Liste de facteurs influençant le choix du traitement de la kératose actinique** (Gutzmer *et al.*, 2019).

Pour le traitement de la kératose actinique, une large gamme d'options thérapeutiques est disponible. Parmi celles-ci, les médicaments topiques tels que les crèmes au fluorouracile ou à l'imiquimod sont recommandés pour les zones où plusieurs AK sont présentes, car ils peuvent être facilement appliqués pour traiter une zone étendue. D'autres procédures comme la cryothérapie utilisant de l'azote liquide à une température de -195,8°C, la thérapie photodynamique en combinaison avec des photosensibilisants tels que l'acide δ-aminolévulinique ou le *methyl aminolévulinate*, la thérapie au laser au dioxyde de carbone, le dermo-*peeling* à l'aide d'acide trichloroacétique ou d'acide glycolique, ainsi que la chirurgie peuvent également être envisagés. Une fois la lésion soignée, un suivi régulier du patient est essentiel pour détecter toute nouvelle lésion qui pourrait apparaitre. Cela permet de prendre des mesures préventives en cas de récidive et de surveiller attentivement la santé de la peau du patient. [373,383]

- Maladie de Bowen (BD)

Initialement décrit par M. Bowen en 1912 comme un carcinome *in situ* se développant dans des zones non exposées aux rayons UV (comme le mollet et la fesse), la maladie de Bowen se caractérise par une lésion cutanée affectant toute l'épaisseur de l'épiderme, présentant un taux de prolifération faible et une hyperkératose généralement de type parakératosique. Toutefois, de nos jours, l'OMS et la majorité de la communauté scientifique utilisent le terme "maladie de Bowen" pour décrire un carcinome *in situ* présentant des caractéristiques d'hyperkératose (et notamment parakératosique), sans prendre en considération sa localisation anatomique. C'est pourquoi, dans le cadre de cette étude, nous utiliserons le terme générique "maladie de Bowen" pour caractériser ces lésions cutanées, qu'elles proviennent de zones exposées au soleil ou non.

Outre l'épiderme cutané, cette affection peut également affecter certaines muqueuses chez l'homme, comme le gland et le prépuce interne, on parle alors d'érythroplasie de Queyrat. En raison du tropisme spécifique de l'érythroplasie de Queyrat et des connaissances approfondies (vis-à-vis des HPV) sur cette altération cutanée, nous accorderons une attention restreinte à ce sujet par la suite, afin de concentrer notre analyse sur la maladie de Bowen cutanée dite "classique". [384,385]

Cliniquement, la maladie de Bowen se présente le plus souvent sous la forme d'une plaque squameuse et érythémateuse, à croissance lente et aux contours bien définis. La composante squameuse de la lésion est généralement teintée de jaune ou de blanc et peut s'éliminer facilement, exposant une zone associée à un degré variable de rougeur, allant du rose à un érythème rouge saumon vif. Les lésions ont généralement une surface nivelée, qui peut présenter des croûtes, une hyperkératose ou des fissures. Contrairement à la kératose actinique, dont la taille est généralement réduite à quelques millimètres, la maladie de Bowen peut s'étendre sur plusieurs centimètres, selon la durée de l'affection (Figure 39). Malgré leur tendance à être asymptomatiques, certaines lésions de Bowen peuvent occasionner des démangeaisons. Sur base de ces caractéristiques, une classification en trois catégories distinctes de la maladie de Bowen a été proposée pour la première fois en 2015 [386] :

- Le type classique de la maladie de Bowen, caractérisé par la présence d'un motif vasculaire atypique (vaisseaux en épingle à cheveux glomérulaires), d'écailles blanchâtres et d'un réseau vasculaire rosâtre.
- Le type pigmenté de la maladie de Bowen, caractérisé par une pigmentation sans structure (couvrant plus de 50 % de la surface) ainsi que des bandes pigmentées et des croûtes.
- Le type partiellement pigmenté de la maladie de Bowen, marqué par une région blanche rosâtre sans structure, des points ou des globules gris, des vaisseaux en épingle à cheveux glomérulaires et pointillés associés à des zones écailleuses blanchâtres superposées. Dans ce cas, la pigmentation ne dépasse pas 50 % de la surface.

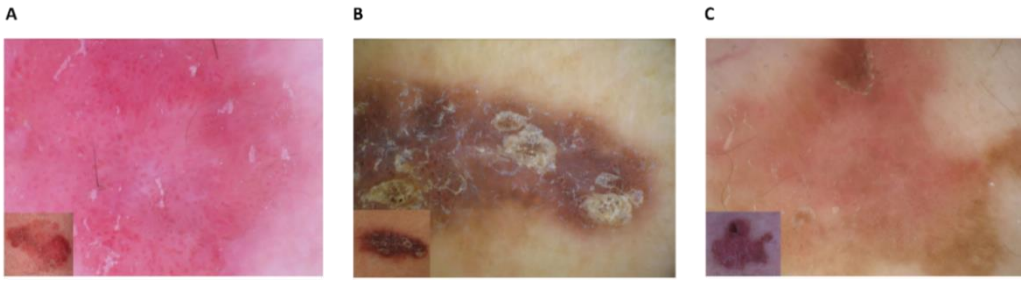

Figure 39 : **Classification clinique et dermatoscopique d'une maladie de Bowen**. A) BD classique. B) BD pigmenté. C) BD partiellement pigmenté (Payapvipapong *et al.*, 2015).

Divers facteurs étiologiques, certains partagés avec la kératose actinique, contribuent à la genèse de la maladie de Bowen. Parmi ces facteurs figurent l'immunosuppression, l'âge, le type de peau, le sexe, l'exposition à l'arsenic, les dermatoses inflammatoires (comme le lupus) ainsi que l'exposition aux rayons ultraviolets (UV), considérés comme le principal facteur de risque en raison de leur rôle dans la mutation génique, notamment du gène suppresseur de tumeur *TP53*. [387,388]

De plus, de manière similaire à la kératose actinique, plusieurs études ont suggéré que les HPV pourraient constituer un facteur de risque pour l'érythroplasie de Queyrat. La toute première étude, datant de 1983, a révélé que 80% de ces lésions de Bowen gynécologiques étaient positives pour le HPV16. Ces résultats ont depuis été corroborés par d'autres recherches. [389,390] Cependant, les informations concernant l'implication des HPV dans les lésions de Bowen cutanées sont limitées. C'est pourquoi notre attention s'est portée majoritairement sur ces lésions cutanées, examinant la présence et l'impact de l'ensemble des α-HPV et β-HPV. [391,392]

Depuis l'introduction du système de classification de la maladie de Bowen en 2015, les caractéristiques cliniques observables par dermoscopie sont suffisantes pour établir le diagnostic. Cependant, en cas de manifestations moins typiques, une biopsie excisionnelle suivie d'une évaluation histologique doivent être entreprises pour confirmer ou exclure cette pathologie. D'un point de vue histologique, les lésions de Bowen présentent des kératinocytes atypiques s'étendant sur toute l'épaisseur de l'épiderme sans perturber la jonction dermo-épidermique. Ces kératinocytes exhibent une activité mitotique intense, un pléomorphisme marqué et de volumineux noyaux. En outre, des phénomènes d'hyperkératose et, parfois de parakératose (noyaux présents dans l'épiderme corné), caractéristiques spécifiques de la maladie de Bowen, peuvent être observés. [393]

Malgré sa croissance généralement lente, il est essentiel de surveiller attentivement ces lésions précancéreuses et de les traiter, car dans 3 à 5% des cas, elles peuvent évoluer vers un carcinome épidermoïde invasif, comportant un risque d'environ 5% de métastases. [394]

Pour le traitement de la maladie de Bowen, les modalités thérapeutiques sont similaires à celles de la kératose actinique, avec parfois l'ajout de radiothérapie locale. Le choix du traitement dépendra de critères tels que la taille de la lésion, son emplacement, son épaisseur, le nombre de lésions, l'âge du patient, l'état immunitaire, les comorbidités, la prise concomitante de médicaments et les préférences du patient (Figure 40). [395,396]

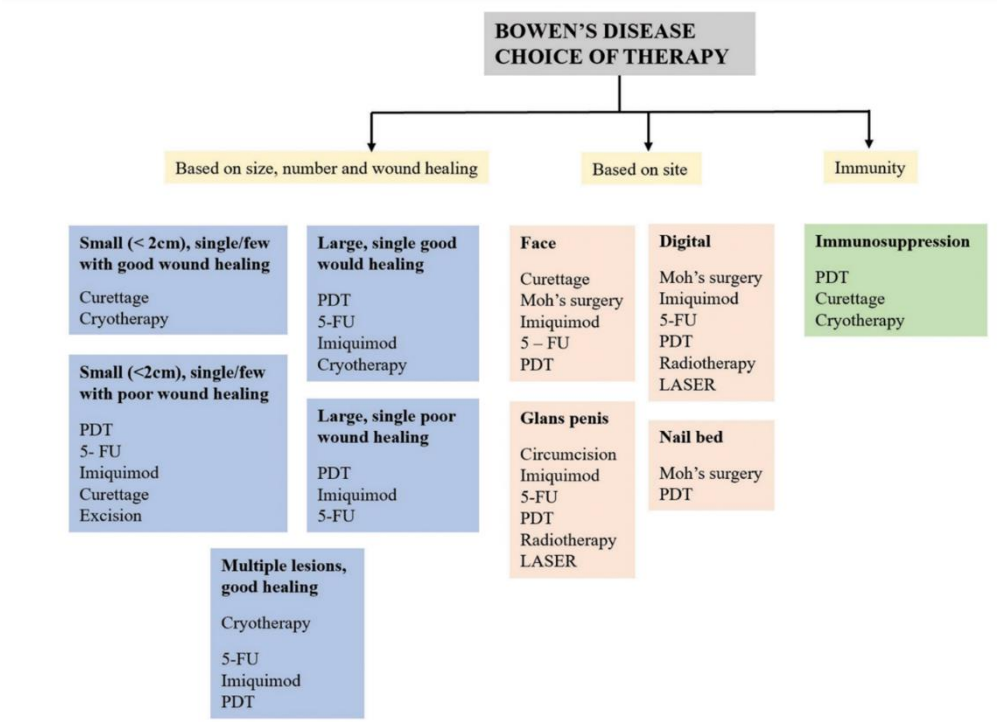

Figure 40 : **Représentation schématique des *Guidelines* à suivre pour le traitement d'une lésion de Bowen** (Palaniappan *et al.*, 2022).

2. Lésions cancéreuses

Comme nous l'avons vu précédemment, il existe des cas où des syndromes génétiques peuvent favoriser le développement de cancers, tout comme certaines lésions précancéreuses peuvent évoluer en cancer. Concernant la peau, on distingue trois types de cancers différents : le carcinome spinocellulaire et le carcinome basocellulaire, qui émergent à partir des kératinocytes, ainsi que le mélanome, qui prend naissance à partir des mélanocytes (Tableau 7). [397–402]

	Carcinome spinocellulaire	Carcinome basocellulaire	Mélanome
Incidence	≃20%	≃70%	≃10%
Cellule d'origine	Kératinocytes superficiels	Kératinocytes basaux	Mélanocytes
Croissance	Rapide	Lente	Rapide
Potentiel métastatique	≃5%	≃0%	≃5-40%
Mortalité	≃2-5%	≃0%	≃6-70%
Implication des HPV	Oui	Non	Non

Tableau 7 : **Principales caractéristiques des carcinomes cutanés.**

Jusqu'à présent, le rôle potentiel des HPV dans le développement de cancers cutanés a été principalement associé au carcinome spinocellulaire. C'est pourquoi nous allons nous concentrer exclusivement sur ce type de cancer dans la suite de notre introduction. [403,404]

i. Carcinome épidermoïde/spinocellulaire (CSC)

Le carcinome épidermoïde cutané, également désigné sous le terme de carcinome spinocellulaire, est caractérisé par la pénétration des kératinocytes atypiques au-delà de la membrane basale. Bien que prédominant dans les régions cutanées exposées au rayonnement solaire, ce type de carcinome peut émerger à partir de lésions précancéreuses ou se manifester de manière spontanée. Cette variante de carcinome constitue environ 20% de l'ensemble des cancers cutanés à l'échelle mondiale, se positionnant ainsi en tant que second type de cancer cutané le plus répandu après le carcinome basocellulaire (70%). Malgré un pronostic généralement favorable, une proportion d'environ 5% des cas connaît une évolution vers des métastases ganglionnaires, entraînant dans 1,5% des cas un décès associé à cette pathologie. [405,406]

Démontrant une prévalence quatre fois supérieure à celle du mélanome et cinq fois supérieure à celle du cancer du poumon, le CSC se caractérise par une charge mutagène plus élevée que d'autres cancers fréquents. [407,408] Cette augmentation substantielle des mutations, principalement imputables aux UV, conjuguée à des altérations cellulaires additionnelles, contribue à l'évolution d'une région cutanée à travers des stades progressifs de dysplasie, culminant en la transformation en CSC. Parmi les gènes fréquemment mutés, nous pouvons citer [408–411] :

- Le gène *TP53*, altéré dans une fourchette allant de 55% à 95% des CSC, confère aux cellules tumorales la capacité de résister à l'apoptose
- Le gène *CDKN2A*, qui code pour les protéines p16 et p14ARF, assume un rôle prépondérant dans la régulation du cycle cellulaire et la maîtrise de la prolifération cellulaire
- *NOTCH1/2*, muté dans plus de 75% des cas de CSC, représente un gène suppresseur de tumeur qui orchestre la régulation de la différenciation des kératinocytes épidermiques ainsi que leur croissance. NOTCH1 est caractérisé par une expression à travers l'épaisseur totale de l'épiderme, tandis que l'expression de NOTCH2 se localise principalement au niveau de la couche basale de l'épiderme
- Le gène *RAS*, altéré dans 12% à 20% des CSC, opère au sein des voies de signalisation RAF-MEK-ERK et PI3K-AKT-mTOR, jouant un rôle crucial dans la transduction des signaux cellulaires, *via* les voies RAF–MEK–ERK et PI3K–AKT–mTOR, et influençant directement la croissance cellulaire

D'un point de vue clinique, le CSC se manifeste généralement par une lésion squameuse, souvent pigmentée, de teinte chair, rose ou brune (Figure 41). De plus, des altérations pouvant être détectées par dermoscopie sont observées au niveau de ses vaisseaux sanguins, se présentant sous la forme de motifs en pointillés, en boucles ou encore en serpentins. Ses symptômes peuvent varier entre l'absence de manifestations, des sensations de prurit, des ulcérations ou des douleurs. Enfin, des symptômes neuropathiques locaux tels que l'engourdissement, la sensation de brûlure, la paresthésie ou la paralysie sont associés à l'invasion périnerveuse caractéristique de certains CSC. [412,413]

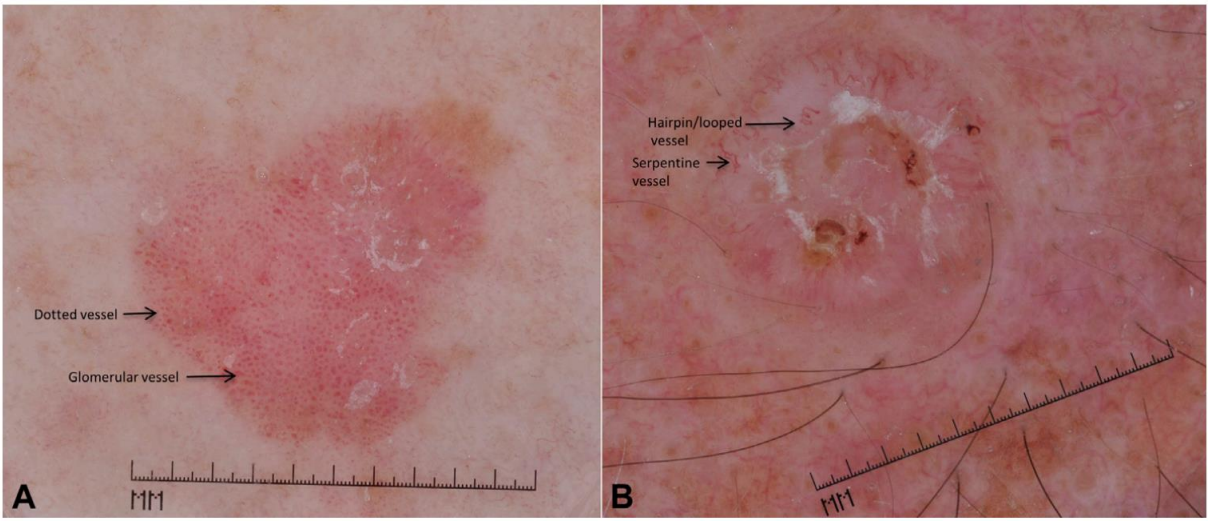

Figure 41 : **Observation macroscopique d'un carcinome spinocellulaire**. A) Carcinome spinocellulaire présentant des vaisseaux en pointillés et glomérulaires. B) Carcinome spinocellulaire présentant des vaisseaux en épingle à cheveux et en serpentins (Que *et al.*, 2017)

D'un point de vue histologique, les CSC peuvent être classés en 3 grades en fonction de leur degré de différenciation :

- Bien différencié, les kératinocytes sont légèrement agrandis et présentent un cytoplasme abondant teinté de rose vitreux à éosinophile. Les ponts intercellulaires sont souvent visibles. On observe généralement une kératinisation, qui se manifeste sous la forme d'une accumulation de kératinocytes bien différenciés, formant une structure centrale appelée « perle de kératine ». Les marges de ces lésions tendent à être bien circonscrites avec une apparence lobulée
- Modérément différencié : Ce grade présente des caractéristiques intermédiaires entre les formes bien et peu différenciées. Les kératinocytes montrent des degrés variables d'atypie nucléaire et d'atypie architecturale
- Peu différencié : Les lésions peu différenciées montrent un motif fortement infiltrant. Les kératinocytes présentent une atypie nucléaire marquée, avec des noyaux pléomorphes et hyperchromatiques, ainsi que de nombreuses figures mitotiques atypiques. La kératinisation est peu fréquente voire absente

La classification histologique prend en compte des caractéristiques telles que le degré de kératinisation, l'atypie nucléaire et l'architecture de la tumeur (bien circonscrit versus infiltrant) pour déterminer le grade du CSC (Figure 42). Cette classification en grade permet d'évaluer la différenciation et l'agressivité de la tumeur. [413,414]

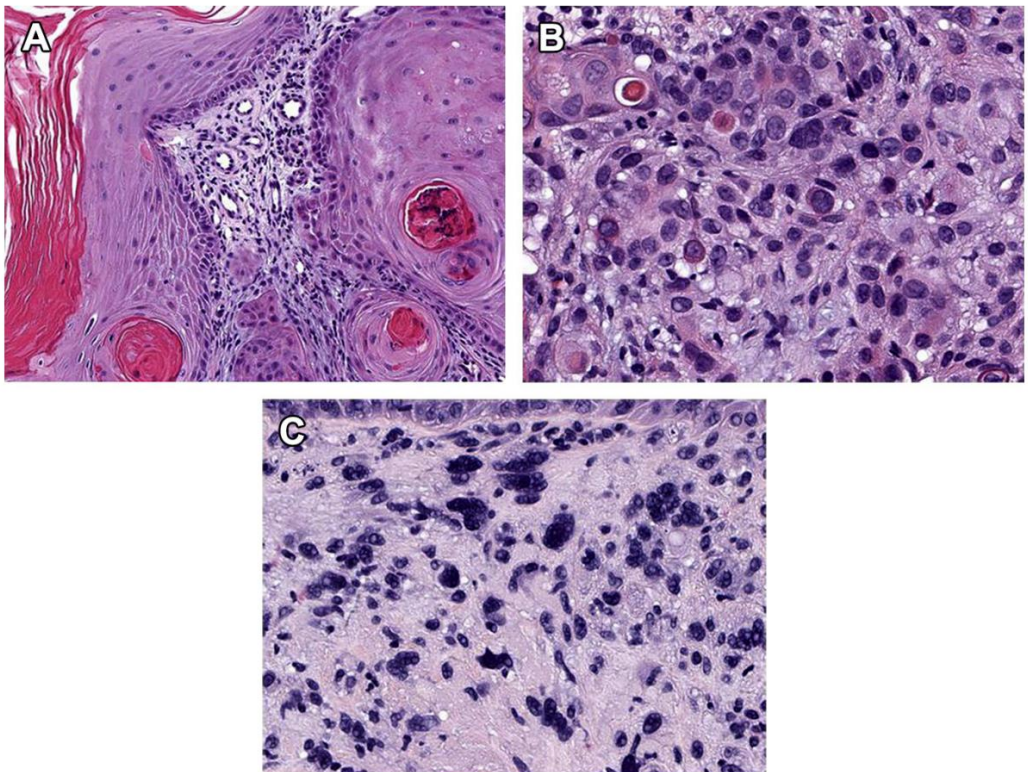

Figure 42 : **Histologie du carcinome spinocellulaire**. A) Bien différencié, la tumeur montre des ‘’nids’’ de kératinocytes matures avec un faible rapport nucléaire/cytoplasmique et des ‘’amas’’ de kératine. B) Modérément différencié, la tumeur montre un pléomorphisme cellulaire, peu ou pas d’amas de kératine et des cellules avec des atypies cellulaires plus importantes. C) Peu différencié, la tumeur présente un schéma infiltrant et des kératinocytes hautement atypiques avec des noyaux pléomorphes, hyperchromatiques et peu ou pas de kératinisation (Parekh *et al.*, 2017)

En ce qui concerne les facteurs de risque les plus importants, ils sont, bien évidemment, proches de ceux décrits pour la kératose actinique et la maladie de Bowen, [415,416] :

- L'exposition aux UV, qui provoque des lésions au niveau de l'ADN cellulaire
- L'âge avancé, les individus plus âgés étant davantage susceptibles de développer un CSC
- Le genre, avec les hommes présentant un risque trois fois plus élevé de développer un CSC que les femmes
- Le type de peau, les peaux claires étant beaucoup plus vulnérables que les peaux foncées
- L'immunosuppression, les personnes ayant subi une transplantation d'organe et soumises à une immunosuppression présentent un risque considérablement accru de CSC, avec des taux de 65 à 250 fois supérieurs (en fonction du nombre et du type d’agents immunosuppresseurs utilisés) à ceux observés pour les individus immunocompétents

- La présence de précurseurs du carcinome épidermoïde cutané, tels que la kératose actinique, la maladie de Bowen et le xeroderma pigmentosum

Ces facteurs de risque contribuent de manière significative à l'apparition et au développement du carcinome épidermoïde cutané et doivent être pris en compte dans les stratégies de prévention et de dépistage.

De plus, il est important de noter que l'immunosuppression peut également créer une prédisposition aux infections qui, à leur tour, favorisent la carcinogenèse du CSC. Cette corrélation est soulignée par la présence accrue d'ADN d'HPV chez les patients immunodéprimés atteints de CSC. Notamment, des études ont révélé que les HPV16 et 18 pouvaient stimuler le développement de cancers péri unguéaux et anogénitaux. En outre, certaines souches de β-HPV pourraient également être impliquées dans la carcinogenèse précoce en potentialisant les dommages causés par les UV. [417,418]

Par ailleurs, d'autres facteurs de risque moins fréquents peuvent également contribuer à la genèse du CSC. Parmi ceux-ci, on peut citer les expositions environnementales à des agents tels que l'arsenic, les hydrocarbures aromatiques polycycliques, les nitrosamines et les agents alkylants. De plus, l'exposition aux radiations ionisantes ainsi que le traitement par des inhibiteurs de BRAF, tels que le vémurafénib et le dabrafénib, ont été identifiés comme pouvant favoriser le développement de CSC. [419–421] Ces éléments soulignent la complexité des facteurs de risque qui interagissent pour influencer la carcinogenèse du CSC, mettant en lumière la nécessité d'une approche multifactorielle dans la compréhension et la prévention de ce cancer cutané.

Concernant le diagnostic, il est établi à l'aide d'une biopsie cutanée réalisée à une profondeur adéquate, permettant ainsi au pathologiste d'évaluer des paramètres tels que la profondeur d'invasion, l'atteinte périnerveuse ou lymphovasculaire, la différenciation cellulaire et la continuité avec l'épiderme supérieur. Dans certains cas, une évaluation des ganglions lymphatiques locaux et de la glande parotide peut également être nécessaire. Par ailleurs, une évaluation de l'atteinte nerveuse doit être effectuée, en observant notamment la présence de douleurs neurologiques ou de paralysie. [422]

Une fois le diagnostic établi, le carcinome spinocellulaire peut être classé en tant que CSC à faible risque ou à haut risque (Tableau 8). Cette classification oriente les choix thérapeutiques qui seront mis en œuvre. En effet, des directives spécifiques sont disponibles pour guider la prise en charge clinique, parmi lesquelles figurent les recommandations du *National Comprehensive Cancer Network* (NCCN) et de l'Organisation Européenne pour la Recherche et le Traitement du Cancer (EORTC). [423,424] Ces approches de classification et de traitement permettent de personnaliser la prise en charge du CSC en fonction du risque associé, améliorant ainsi les résultats cliniques et la qualité de vie des patients concernés.

	Tumour diameter	Location	Depth/level of invasion	Histologic features	Surgical margins	Immune status
Low risk	Less than 2 cm	Sun exposed sites (except ear/lip)	Less than 6 mm/ invasion above subcutaneous fat	Well-differentiated Common variant or verrucous	Clear	Immuno-competent
High risk	More than 2 cm	Ear/lip Non-sun exposed sites (sole of foot) SCC arising in radiation sites, scars, burns or chronic inflammatory conditions Recurrent SCCs	More than 6 mm/ invasion beyond subcutaneous fat	Moderately, or poorly differentiated grade Acantholytic, spindle, or desmoplastic subtype Perineural invasion	Incomplete excision	Immunosuppressed (organ transplant recipients, chronic immunosuppressive disease or treatment)

Tableau 8 : **Facteurs pronostiques du carcinome spinocellulaire** (Stratigos *et al.*, 2015)

Conformément aux directives établies par le NCCN et l'EORTC, les stratégies de traitement pour les CSC à faible risque impliquent en première ligne une excision standard avec des marges cliniques de 4 à 6 mm, suivie d'une évaluation postopératoire des marges. En cas de marges positives, des options supplémentaires telles qu'une ré-excision ou une chirurgie de Mohs peuvent être envisagées, en fonction de la localisation de la lésion. Dans le cas de petites tumeurs situées dans des zones non pileuses, le curetage et l'électrodessication peuvent être indiqués. Pour les CSC à risque élevé, les recommandations privilégient la chirurgie micrographique de Mohs. Cette procédure consiste en l'excision du tissu cancéreux suivi d'une analyse histopathologique immédiate afin de déterminer si l'excision est adéquate. Si nécessaire, des excisions supplémentaires sont réalisées pour assurer l'élimination complète du tissu cancéreux. La chirurgie de Mohs présente un taux de récidive de seulement 3%, comparé aux 8-10% associés à une chirurgie conventionnelle. Bien que la chirurgie demeure l'approche privilégiée dans la prise en charge du CSC, il peut y avoir des situations où certains patients ne sont pas candidats à une intervention chirurgicale. [425]

Lorsque la chirurgie n'est pas possible, une radiothérapie locale primaire peut être envisagée. Dans certains cas, des traitements topiques tels que des crèmes contenant du 5-fluorouracile ou des agonistes du TLR7, comme l'imiquimod, représentent également des alternatives pour les lésions précancéreuses ou les CSC *in situ*. [426]

Pour finir, au cours de la dernière décennie d'autres stratégies thérapeutiques ont été testées. C'est notamment le cas des inhibiteurs du récepteur du facteur de croissance épidermique (EGFR) tels que le cetuximab ou le panitumumab (des anticorps monoclonaux ciblant le domaine extracellulaire du récepteur), ainsi que le gefitinib ou l'afatinib (qui bloquent l'activité de la tyrosine kinase et inhibent les voies cellulaires en aval). En effet, le rôle essentiel de l'EGFR, impliqué dans la régulation de la prolifération, de la migration, de la survie, de la résistance à l'apoptose et de la différenciation, en fait une cible thérapeutique intéressante.

Parallèlement, l'immunothérapie a également émergé comme une approche thérapeutique pour certains patients atteints d'un CSC. Cette approche comprend notamment l'utilisation d'inhibiteurs du récepteur de mort cellulaire programmée 1 (PD-1), tels que le cemiplimab ou le pembrolizumab. Le récepteur PD-1 est exprimé à la surface de diverses cellules immunitaires, dont les lymphocytes T, les lymphocytes B, les monocytes, les cellules NK et les cellules dendritiques. En interagissant avec ses ligands, PD-L1 et PD-L2, présents notamment à la surface des cellules tumorales, PD-1 déclenche un signal inhibiteur qui compromet la fonction des lymphocytes T activés, conduisant *in fine* à l'épuisement immunitaire. Bien que ces nouvelles approches thérapeutiques soient encore en phase de développement et/ou d'évaluation, elles ouvrent de nouvelles perspectives pour le traitement des patients atteints de CSC. Il est prévu qu'elles soient progressivement intégrées dans les stratégies de prise en charge du CSC, élargissant ainsi les options thérapeutiques disponibles. [427,428]

E. Altérations cutanée et génétique

L'identification des altérations génomiques au sein des lésions (pré)cancéreuses cutanées représente une tâche complexe, en grande partie en raison du niveau significatif de mutation observé dans les kératinocytes, résultant de l'exposition aux rayons ultraviolets (UV). En effet, la charge mutationnelle observée dans les kératoses actiniques et la maladie de Bowen exposés aux UV, atteint approximativement 44 mutations par mégabase, contre 50 pour les CSC.[429–431]

Chaque processus mutationnel peut être influencé par divers mécanismes, notamment les erreurs de réparation de l'ADN, l'exposition à des facteurs environnementaux tels que les UV ou la fumée de tabac, ainsi que des anomalies dans la réplication de l'ADN. Ces processus génèrent des signatures mutationnelles distinctes, englobant des substitutions de bases, des insertions et suppressions de petites tailles (indels), des réarrangements génomiques, et des variations dans le nombre de copies chromosomiques. Ces signatures mutationnelles ont été initialement caractérisées en 2013, sur base de 7.042 cancers, par le Dr Alexandrov.[432,433]

Parmi ces signatures, certaines substitutions de base uniques (SBS) retrouvées au sein des lésions (pré)cancéreuses (kératose actinique, maladie de Bowen et CSC) ont attirés notre attention, en particulier les signatures mutationnelles 2 (C→T) et 13 (C→G), attribuées à l'activité de la famille APOBEC (plus spécifiquement à l'APOBEC3A/B, supposées être les principales responsables de la majorité des mutations dans le cancer humain). De plus, les signatures 7a/b (C→T), liées à une exposition aux UV, ont également retenu notre attention. Ces signatures pourraient résulter de l'un des deux principaux photoproduits UV connus, à savoir les dimères cyclobutyliques de pyrimidine ou les photoproduits 6-4. Cependant, aucune preuve concluante ne soutient actuellement cette hypothèse, et le photoproduit responsable de SBS7a/b reste incertain. [434–437]

Pour finir, d'autres signatures mutationnelles sont retrouvées dans ces lésions (pré)cancéreuses cutanées, notamment la signature 4 (C→A), associée à la fumée de cigarettes, ainsi que les signatures 5 et 19, dont l'étiologie semble liée à l'âge mais demeure incertaine à ce jour (Tableau 9). [438,439]

Bien sûr, étant donné que l'accumulation de connaissances sur les signatures mutationnelles est un processus relativement récent, de nombreuses lacunes subsistent et méritent une exploration approfondie dans les années à venir.

Signature mutationnelle	Kératose actinique	Maladie de Bowen	Carcinome épidermoïde
1	V	V	V
2	V		V
4	V		
5	V	V	
7a	V	V	V
7b	V	V	V
13	V		V
19	V		V

Tableau 9 : **Principales signatures mutationnelles observées au sein des lésions (pré)cancéreuses étudiées dans le cadre de cette thèse**

L'influence de ces diverses signatures mutationnelles peut varier en fonction des gènes affectés. Parmi les gènes ayant un impact majeur sur le développement des lésions (pré)cancéreuses cutanées, citons [440–443]:

- *NOTCH 1/2/3*, qui régule le développement cellulaire et la différenciation cellulaire.
- *KNSTRN*, jouant un rôle crucial au début de l'anaphase et dans la ségrégation des chromosomes pendant la mitose.
- *TP53*, qui contrôle l'arrêt du cycle cellulaire, la sénescence, la réparation de l'ADN et l'apoptose.
- *FAT1*, perturbant la voie de signalisation Wnt/β-caténine et favorisant l'expression accrue de CDK6 via l'activation de la voie Hippo.
- *KMT2C*, jouant un rôle essentiel dans la régulation de l'expression génique en modifiant les histones grâce à son activité d'histone méthyltransférase.
- *PIK3CA*, participant à la survie et la croissance cellulaire, ainsi qu'à la régulation du cytosquelette.
- *CDKN2A*, codant pour p16INK4a et p14ARF, deux protéines qui contrôlent indirectement les activités de p53 et pRB.
- *HRAS*, jouant un rôle central dans la transmission des signaux mitogènes.
- *TGF-β*, impliqué dans la prolifération, la différenciation cellulaire, et l'apoptose via la voie SMAD.
- ...

Cette énumération recense les principaux gènes agissant en tant que "drivers" dans le carcinome épidermoïde cutané. Comme indiqué dans le Tableau 10, il est à noter que de nombreux autres gènes interviennent également dans le processus de développement de cette pathologie.[444,445]

	Peau exposée aux UV	Kératose actinique	Maladie de Bowen	Carcinome épidermoïde
Mutations ''*driver*''	NOTCH 1-3 FAT1 TP53 KNSTRN	NOTCH 1-3 KNSTRN TP53 FAT1 KMT2C PIK3CA CDKN2A RB1	NOTCH 1-3 KNSTRN TP53 FAT1 KMT2C PIK3CA CDKN2A RB1	NOTCH 1-3 FAT1 TP53 KNSTRN KMT2C PIK3CA CDKN2A RB1 ABI3BP IMPA1 HRAS TGF-β
Changements épigénétiques		Méthylation du promoteur CDKN2A et hyperméthylation de CDH1 et IGFBP3	Méthylation du promoteur CDKN2A et hyperméthylation de CDH1 et IGFBP3	Hyperméthylation du promoteur de FOXE1
Augmentation de la signalisation (activation, surexpression, amplification)		SFKs Bcl-2 EGFR	SFKs Bcl-2 EGFR c-myc STAT-3 TNC FSCN1 SERPINB1	SFKs Bcl-2 EGFR c-myc STAT-3 B-1 Integrin MMP Ras VEGF MMP2 MMP7 MMP12 TNC FSCN1 SERPINB1 ACTN1 RAB31
Diminution de la signalisation (désactivation, répression transcriptionnelle ou traductionnelle, suppression de gène)	NOTCH	NOTCH p53	NOTCH p53 Srcasm PKCδ E-cadherin COL3A1	NOTCH p53 Srcasm PKCδ E-cadherin P-cadherin COL1A1 COL3A1 CD36

Tableau 10 **: Principaux gènes impliqués dans la progression du carcinome épidermoïde cutané**

F. UV, HPV et cancer de la peau

En 2011, l'équipe dirigée par le Dr Tommasino a réalisé une expérience dans le but de démontrer l'implication potentielle des β-HPV dans la carcinogenèse cutanée (Figure 43). Ils ont exposé trois groupes de souris (deux groupes de souris transgéniques exprimant les oncoprotéines E6 et E7 de l'HPV38 sous la dépendance du promoteur de la kératine 14, ainsi qu'un groupe de souris témoin FVB/N) à des rayons UVB pendant 30 semaines. À l'issue de cette période d'irradiation, la majorité des souris transgéniques ont développé des carcinomes épidermoïdes cutanés, contrairement aux souris témoins. [446]

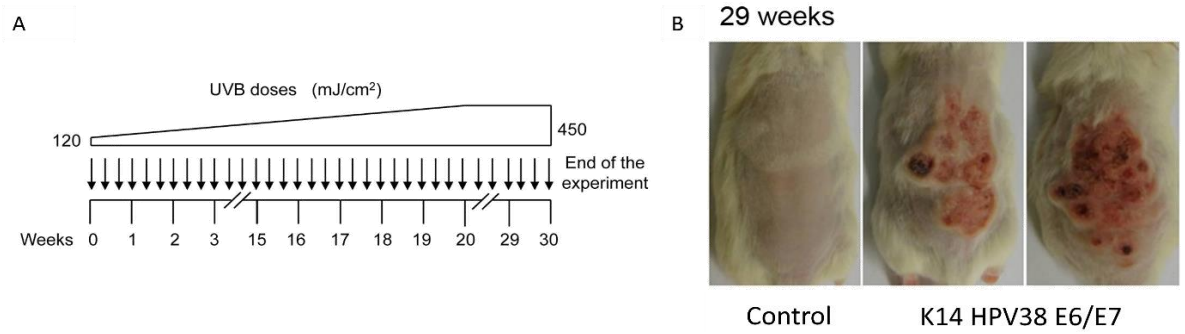

Figure 43 : **Développement tumorale chez les souris transgéniques (K14 HPV38 E6/E7) après une irradiation aux UVB**. A) Représentation schématique de la procédure expérimentale d'irradiation. B) Photos représentatives de la peau dorsale des souris témoins et transgéniques après avoir été exposées aux UVB pendant 30 semaines.

Cette étude scientifique a permis d'émettre l'hypothèse suivante (Figure 44). Dans des conditions physiologiques, les rayons UV induisent des altérations dans l'ADN des kératinocytes. Les dommages causés par les UV peuvent entraîner soit l'arrêt du cycle cellulaire et la réparation des altérations, soit l'apoptose si les dommages sont irréparables. Chez les patients immunodéprimés, le potentiel de réplication des β-HPV est plus important. En effet, en raison d'un affaiblissement du système immunitaire, les β-HPV ne sont plus aussi bien ‘’contrôlés’’, ce qui leur permet de perturber l'arrêt du cycle cellulaire. Cette altération favorise l'accumulation/non réparation des mutations induites par les UV, qui avec le temps, peut conduire à la transformation cancéreuse.[447–449]

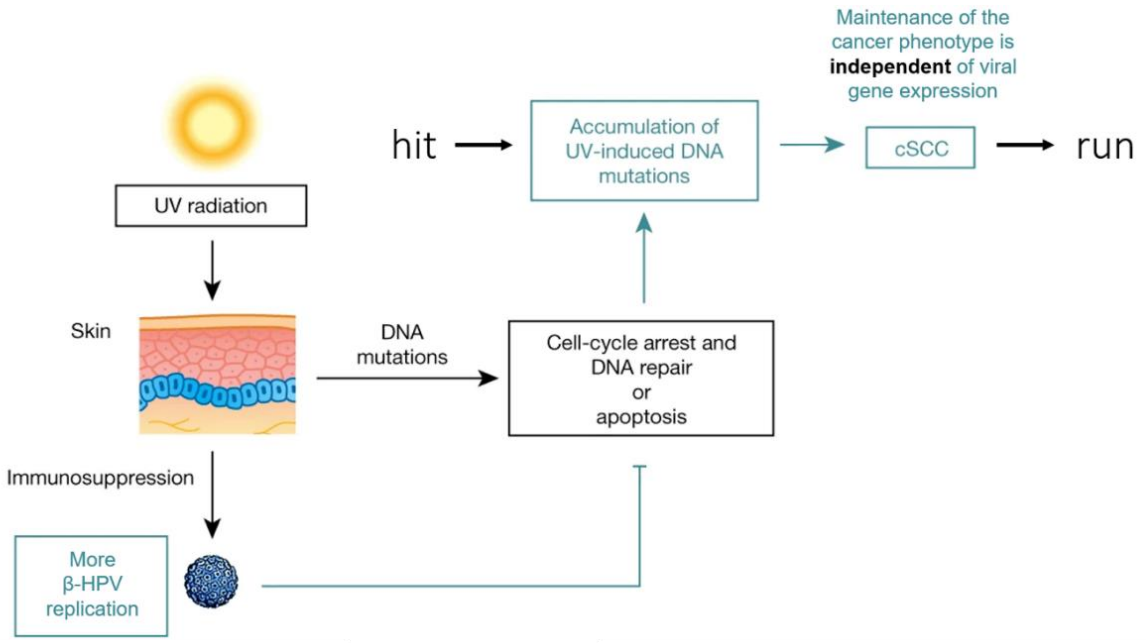

Figure 44 : **Implication des β-HPV dans la carcinogenèse cutanée**. Dans des conditions physiologiques, les UV peuvent induire des mutations dans l'ADN des kératinocytes. Les dommages causés par les UV entraînent soit l'arrêt du cycle cellulaire et la réparation des mutations de l'ADN, soit l'apoptose si les dommages à l'ADN sont irréparables. Cependant, chez les patients immunodéprimés où la charge virale des β-HPV est plus importante, les oncoprotéines E6 et E7 des β-HPV peuvent altérer l'arrêt du cycle cellulaire et favoriser la survie des cellules dont l'ADN est endommagé. Au fil du temps, l'accumulation de mutations dans des gènes oncogènes peut se produire (hit). Ces altérations génétiques perturbent le fonctionnement normal des cellules et l'expression des gènes viraux devient superflue pour le développement du carcinome cutané (run) (adapté de Lambert *et al.*, 2020).

En complément de ces informations, nous avons formulé l'hypothèse selon laquelle les β-HPV, en plus de leur capacité à perturber l'arrêt du cycle cellulaire, pourraient également détourner la machinerie de réparation de l'ADN à leur avantage. En effet, ce dernier phénomène serait nécessaire pour permettre une réplication virale sans erreur. Par le biais de ces deux mécanismes, les β-HPV pourraient favoriser activement le développement de carcinomes épidermoïdes cutanés. Ainsi, il est possible de considérer cette relation entre les β-HPV, les UVB et le carcinome épidermoïde cutané comme un "triangle amoureux" qui mérite une attention particulière dans les recherches futures.

Objectifs

Au cours des trois dernières décennies, la grande majorité des recherches sur les papillomavirus humains (plus de 90%), se sont concentrées principalement sur les génotypes du genre alpha, en particulier HPV16 et 18, les deux souches responsables de la majorité des cancers du col de l'utérus. Cependant, les β-HPV, identifiés pour la première fois dans les années 80 et comprenant actuellement 68 génotypes, suscitent un intérêt croissant. Cette augmentation d'intérêt est principalement motivée par des preuves convaincantes suggérant que certains HPV de type bêta (5, 8, 38 et 49) pourraient contribuer au développement de carcinomes épidermoïdes cutanés en potentialisant les effets délétères des rayonnements ultraviolets. Néanmoins, de nombreuses questions, à la fois conceptuelles et translationnelles, restent en suspens. Par exemple, parmi les 68 génotypes de β-HPV répertoriés jusqu'à présent, lesquels favorisent effectivement le développement du cancer et peuvent être détectés dans les lésions précancéreuses ? De plus, comment s'opère la synergie entre les rayons UV et ces virus ?

Dans le cadre de ce projet, notre première démarche consiste à caractériser d'un point de vue virologique la maladie de Bowen. À cette fin, une cohorte comprenant 162 échantillons tissulaires a été assemblée, constituant l'une des cohortes les plus importantes jamais rassemblées pour cette lésion précancéreuse. Outre cette caractérisation virologique, nous souhaitons également évaluer l'activité transcriptionnelle ainsi que le potentiel reproductif des β-HPV au sein de cette lésion précancéreuse.

La deuxième phase de ce projet se concentre sur les mécanismes sous-jacents à la synergie entre les rayons UV et les β-HPV. À cet effet, un screening à haut débit (GPCA) a été réalisé pour identifier de nouvelles interactions directes potentielles entre les oncoprotéines virales E6 et E7 des HPV5, 8, 38 et 49, et une liste des protéines participant aux mécanismes de réparation de l'ADN de la cellule hôte, incluant environ 80% des protéines impliquées dans ces processus. Une fois identifiées par GPCA, ces cibles seront confirmées par Co-IP afin d'assurer la validité de ces interactions.

Matériel et méthodes

A. Collecte des échantillons tissulaires de patients atteints de la maladie de Bowen

Afin d'explorer le potentiel rôle des papillomavirus humains (HPV) dans la pathogenèse de la maladie de Bowen, une série de 162 échantillons tissulaires (comprenant des biopsies et des résections chirurgicales), préalablement inclus en paraffine, a été méthodiquement récupérée à la Biobanque de l'Hôpital Universitaire de Liège, en Belgique. De plus, une confirmation du diagnostic a été réalisée par des pathologistes expérimentés.

Ces blocs tissulaires ont ensuite été coupés au moyen d'un microtome, à une épaisseur de 5µm, et déposés sur des lames Superfrost Plus (Thermo Scientific) pour permettre la réalisation de marquages immunohistochimiques, d'hybridations *in situ* et de RNAscope. De plus, des fragments tissulaires (copeaux) ont été soigneusement disposés dans des tubes Eppendorf afin d'extraire l'ADN et ensuite détecter la présence d'HPV par le biais du *Luminex HPV Assay*.

Au sein de cette cohorte de 162 échantillons de tissus, 29 sont originaires de régions gynécologiques (la vulve, le prépuce, le sillon inter fessier et le pénis), 56 proviennent de zones cutanées exposées au soleil (à savoir le crâne, le cou, la nuque, la poitrine, les bras et avant-bras et le dos des mains) et 77 sont attribuables à des zones désignées comme ''autres'', c'est-à-dire non classifiées comme gynécologiques ou exposées au soleil. Ces catégories vont servir de fondement pour les analyses comparatives ultérieures, impliquant les marquages immunohistochimiques, les hybridations *in situ*, le RNAscope ainsi que le génotypage d'HPV.

Il importe de souligner que cette étude a été rigoureusement validée par le comité d'éthique institutionnel, se voyant octroyer une approbation en date du 24/03/2020 sous la référence #2020/77.

B. Immunohistochimie

Plusieurs analyses immunohistochimiques ont été exécutées afin de détecter la présence de protéines d'intérêt ($p16^{INK4a}$, Ki67, p53, caspase 3, CD45 et L1) au sein de nos échantillons tissulaires.

Les échantillons inclus en paraffine ont été préalablement soumis à une série d'étapes de déparaffinage et de réhydratation, comprenant les séquences suivantes :

1) Deux bains successifs de 5 minutes dans du xylène (100%)
2) Deux bains de 2 minutes dans de l'éthanol (100%)
3) Un bain d'1 minute dans de l'éthanol (95%)
4) Un bain de 5 minutes dans une solution de méthanol (100%) + 4,5% de peroxyde d'hydrogène (visant à inhiber l'activité des peroxydases endogènes)
5) Deux bains de 2 minutes dans de l'éthanol (70%)
6) Deux bains successifs de 2 minutes dans de l'eau distillée

La restauration des épitopes a ensuite été entreprise, impliquant l'incubation préalable des lames soit dans du tampon citrate à 10 mM/pH6 (Sigma-Aldrich), soit dans une solution d'EDTA à 1 mM/pH9 (Invitrogen), pendant 11 minutes à 120°C au moyen d'une marmite à pression ou 23 minutes dans un four à micro-ondes fonctionnant à 500 Watts.
Par la suite, les sites de liaison non spécifiques ont été neutralisés en utilisant la solution de blocage *Animal-Free Blocking Solution* (Dako).
Une fois le blocage terminé, les échantillons tissulaires ont été soumis à une incubation avec les anticorps primaires appropriés, durant une heure à température ambiante, suivie d'une exposition aux anticorps secondaires (conjugués au système streptavidine-HRP) pendant 30 minutes, toujours à température ambiante (Tableau 11).

Enfin, les lames ont été mises en contact avec le réactif chromogène 3,3'-Diaminobenzidine (DAB), qui provient du kit *SignalStain® DAB Substrate* (Cell Signaling), pendant 10 minutes à température ambiante. Par la suite, une contre-coloration à l'hématoxyline a été réalisée pendant 30 secondes. Les lames sont finalement montées avec une lamelle couvre objet à l'aide du kit *VectaMount mounting* et la détection du signal est réalisée à l'aide d'un microscope optique.

Protéine d'intérêt	Référence	Firme	Clone	Dilution	Espèce	Démasquage
$p16^{INK4a}$	ENZ-ABS377	Enzo	/	1/100	Souris	Citrate/micro-onde
Ki67	790-4286	Ventana	30-9	Prêt à l'emploi	Lapin	EDTA/micro-onde
p53	800-2912	Ventana	DO-7	Prêt à l'emploi	Souris	Citrate/marmite à pression
Caspase 3	#9661	Cell Signaling	Asp175	1/200	Lapin	Citrate/micro-onde
L1	M3528	Dako	K1H8	1/100	Souris	EDTA/marmite à pression
CD45	760-4279	Ventana	2B11 & PD7/26	1/4	Souris	EDTA/marmite à pression
Anti-lapin	K4003	Dako	/	Prêt à l'emploi	Chèvre	/
Anti-souris	K4001	Dako	/	Prêt à l'emploi	Chèvre	/

Tableau 11 : **Récapitulatif des anticorps employés pour les analyses immunohistochimiques**.

C. Évaluation des immunomarquages

Une évaluation visuelle et arbitraire a été effectuée pour attribuer un score aux marqueurs $p16^{INK4a}$, Ki67, p53, L1, caspase 3, d'élastose actinique et d'hyperkératose parakératosique (Tableau 12).

	Processus de quantification des immunohistochimies			
$p16^{INK4a}$	Négatif	*Patchy* (dispersé)	Basal	Diffus
Ki67	<25%	26-50%	51-75%	>75%
p53	Non aberrant (1-50%)		Aberrant (0% ou >50%)	
Caspase 3	Négatif		Positif	
Élastose actinique	Négatif		Positif	
Hyperkératose parakératosique	Négatif		Positif	
L1	Négatif		Positif	
CD45	Nombre de cellules positives par mm^2			

Tableau 12 : **Méthode de classification des différents paramètres analysés dans cette étude**.

En parallèle, une quantification informatisée a été entreprise pour le marquage anti-CD45 à l'aide du logiciel QuPath-0.4.3 (Figure 45). Dans ce contexte, les lames ont d'abord été numérisées à l'aide du scanner Pannoramic 250 (Sysmex) pour obtenir des images à haute résolution de l'ensemble des échantillons. Ensuite, une délimitation manuelle de la lésion précancéreuse a été réalisée sur les images numérisées, au moyen du logiciel QuPath. Finalement, le logiciel QuPath a été utilisé pour détecter et compter de manière automatisée les cellules positives pour CD45 au sein de la lésion précancéreuse. Un nombre de cellules positives par mm^2 a ainsi été obtenu pour chaque lésion.

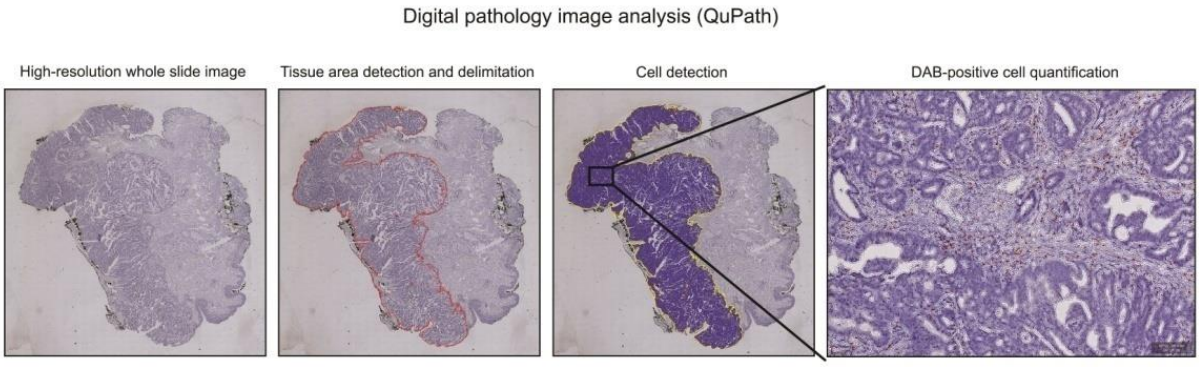

Figure 45 : **Représentation de la délimitation d'une zone d'intérêt et de la quantification des cellules positives présentes au sein d'une biopsie par le logiciel QuPath-0.4.3** (Herfs *et al.*, 2018).

D. Extraction d'ADN

L'extraction de l'ADN a été réalisée en utilisant les copeaux tissulaires présents dans des tubes Eppendorf, au moyen du kit *NucleoSpin DNA FFPE XS* de Macherey-Nagel (référence : 740980.250).

Pour débuter le processus, l'échantillon est déparaffiné durant une période de 3 minutes à une température de 60°C, à l'aide du *Paraffin Dissolver* inclus dans le kit.

Ensuite, le tissu est digéré durant toute la nuit, à une température de 56°C, par la protéinase K (22.4 mg/ml), ce qui a pour effet de libérer l'ADN contenu dans le tissu.

Avant d'effectuer la récupération de l'ADN, une étape d'incubation de 30 minutes à une température de 90°C dans le *D-Link Buffer* est entreprise. Cette solution renferme des sels inorganiques à un pH de 4.5-5, lesquels ont pour fonction d'éliminer les liaisons croisées formées au niveau de l'ADN au cours de l'étape de digestion par la protéinase K.

Par la suite, l'ADN est récupéré sur une colonne de silice et soumis à une centrifugation de 30 secondes à 2000g. Par le biais de deux lavages à l'aide d'un tampon supplémenté d'éthanol, la colonne est soigneusement nettoyée. Chaque lavage est suivi d'une centrifugation à 11 000g pour se débarrasser des métabolites et macromolécules résiduels contenus dans l'échantillon.

Pour finir, l'ADN est élué grâce à un tampon d'élution (5 mM Tris/HCl, pH 8) et centrifugé pendant 30 secondes à 11.000g. Les échantillons sont ensuite dosés à l'aide d'un spectrophotomètre, *NanoDrop ND-1000* de la marque Isogen Life Science, après quoi l'ADN est conservé à une température de -20°C.

E. Luminex HPV Assay

Après avoir réalisé l'extraction de l'ADN de nos échantillons, une analyse de génotypage d'HPV a été entreprise en utilisant la méthode *Luminex HPV Assay*. Cette approche combine une PCR multiplexe avec une hybridation spécifique. Elle repose sur l'association entre, d'une part, les amplicons issus de la PCR et, d'autre part, des sondes ciblant spécifiquement les HPV d'intérêt (Figure 46). Ces sondes sont fixées sur des billes de polystyrène qui sont intrinsèquement colorées avec des fluorophores distincts (Luminex Corp). Cette coloration unique permet d'utiliser plus d'une centaine de billes présentant des spectres d'absorption spécifiques.

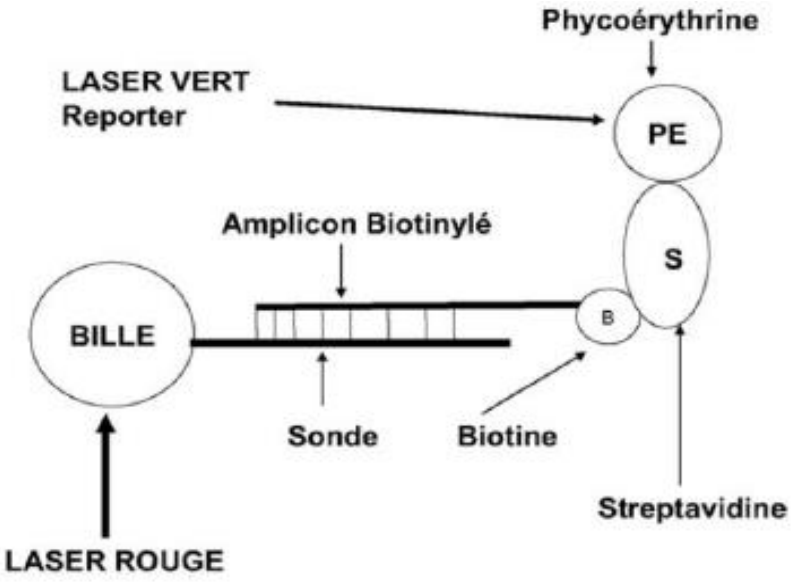

Figure 46 : **Représentation schématique du processus d'hybridation utilisé dans le cadre de l'exécution du *Luminex HPV Assay***. Les amplicons de l'oncoprotéine E7, préalablement amplifiés via une PCR multiplexe, sont associés au complexe biotine/streptavidine/phycoérythrine. Par la suite, ces amplicons s'hybrident avec des sondes spécifiques correspondant à des séquences d'HPV cibles, lesquelles sont liées à des billes fluorescentes (Moalic et al., 2004).

Dans un premier temps, l'ADN subit une amplification par PCR multiplex, utilisant des sondes spécifiques de l'oncoprotéine E7 des HPV cibles, associées au complexe biotine-streptavidine-phycoérythrine (Figure 47).

Les amplicons ainsi générés sont ensuite dénaturés et mis en contact avec des sondes spécifiques à chaque HPV cible, liées à des billes fluorescentes. Après hybridation spécifique entre les amplicons et les sondes, les plaques 96 puits sont soumises à des lavages pour éliminer les sondes non liées.

Enfin, le complexe amplicon/sonde est analysé à l'aide de deux lasers : le premier révèle la fluorescence émise par les billes et le second révèle la fluorescence émise par la phycoérythrine du complexe biotine-streptavidine-phycoérythrine présent dans les amplicons générés durant la PCR multiplex.

Cette méthode est actuellement la plus sensible et spécifique pour le génotypage d'HPV. Elle permet la détection de 21 α-HPV (HPV6, 11, 16, 18, 26, 31, 33, 35, 39, 45, 51, 52, 53, 56, 58, 59, 66, 68, 70, 73 et 82) ainsi que 46 β-HPV (HPV5, 8, 9, 12, 14, 15, 17, 19, 20, 21, 22, 23, 24, 25, 36, 37, 38, 47, 49, 75, 76, 80, 92, 93, 96, 98, 99, 100, 104, 105, 107, 110, 111, 113, 115, 118, 120, 122, 124, 143, 145, 150, 151, 152, 159 et 174) en même temps. De plus, pour vérifier le bon déroulement de la technique, la β-globine est utilisée comme contrôle interne. Cette méthode a été exécutée par l'équipe du Dr. Tarik Gheit (IARC-WHO, Lyon, France).

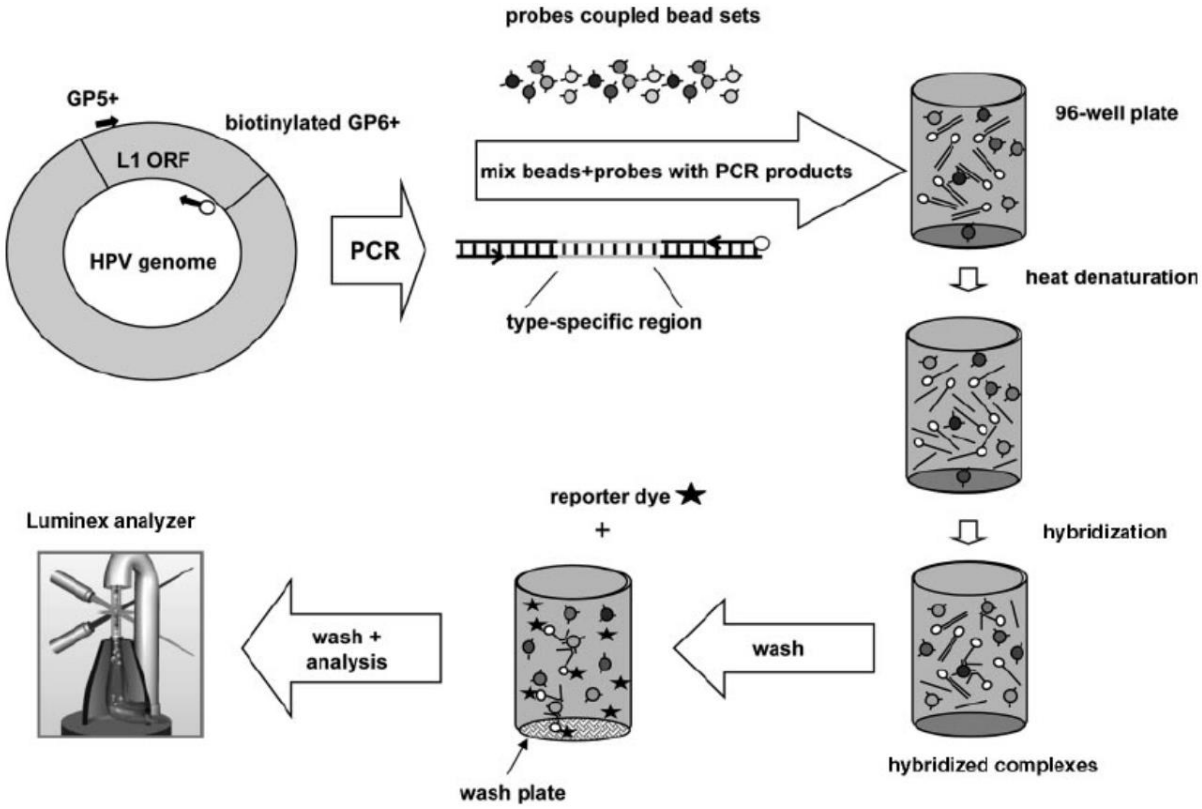

Figure 47 **: Représentation schématique du génotypage d'un HPV d'intérêt via la méthode du *Luminex HPV Assay*** (Schmitt *et al.*, 2006)

F. Hybridation *in situ*

Les résultats du génotypage des α-HPV obtenus à partir du *Luminex HPV Assay* ont été confirmés par une technique d'hybridation *in situ*. Dans cette démarche, le cocktail de sondes simple brin *INFORM HPV III family 16* provenant de Ventana a été utilisé. Ces sondes sont complémentaires à des séquences spécifiques d'ADN appartenant aux α-HPV de haut risque 16, 18, 31, 33, 35, 39, 45, 51, 52, 56, 58 et 66. La détection a été réalisée au moyen de la phosphatase alcaline, une enzyme capable de catalyser la déphosphorylation d'un substrat chimique ajouté à l'échantillon, le kit *iView Blue Plus* de Ventana Medical Systems, ce qui a engendré une coloration chromogénique à l'endroit de l'hybridation.

Il convient de souligner que cette technique d'hybridation *in situ* a été réalisée au sein du département d'Anatomie et Cytologie pathologiques du Centre Hospitalier Universitaire de Liège, en Belgique.

G. RNAscope

Le RNAscope est une technique ''améliorée'' d'hybridation *in situ* qui permet de détecter et de localiser des molécules d'ARN spécifiques au sein de cellules ou de tissus. Dans notre cas, nous avons utilisé cette méthode pour détecter l'ARN de certains HPV d'intérêt afin de déterminer s'ils étaient toujours transcriptionnellement actifs.

Cette technique repose sur l'hybridation en tandem de deux sondes indépendantes, appelées ‘’sondes en Z’’. La partie inférieure du ‘’Z’’ est composée d'une région de 18 à 25 bases qui est complémentaire à l'ARN cible. La partie supérieure du ‘’Z’’ est une séquence de 14 bases qui interagit par complémentarité avec le préamplificateur (Figure 48).

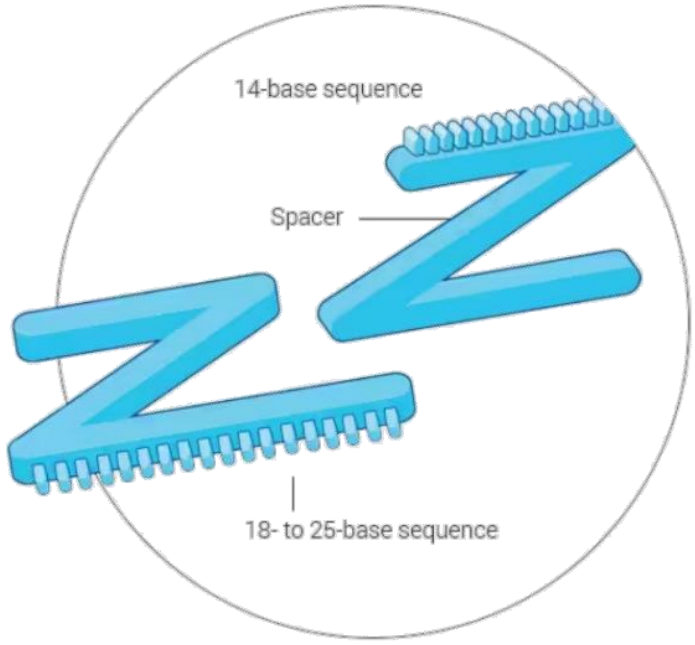

Figure 48 : **Schéma illustrant une ‘’sonde en Z’’**. Cette sonde est composée de trois parties distinctes : une région de 18 à 25 paires de bases qui se lie à une région spécifique de l'ARN, un *spacer*, et une région de 14 paires de bases qui se lie à un préamplificateur (ACD, 2023).

Une fois que les ‘’sondes en Z’’ se sont hybridées avec l'ARN d'intérêt et le préamplificateur, des amplificateurs se lie aux multiples sites de liaison présents sur le préamplificateur.

Enfin, des sondes marquées, contenant une molécule fluorescente ou une enzyme chromogène, se lient aux multiples sites de liaison présents sur chaque amplificateur (Figure 49).

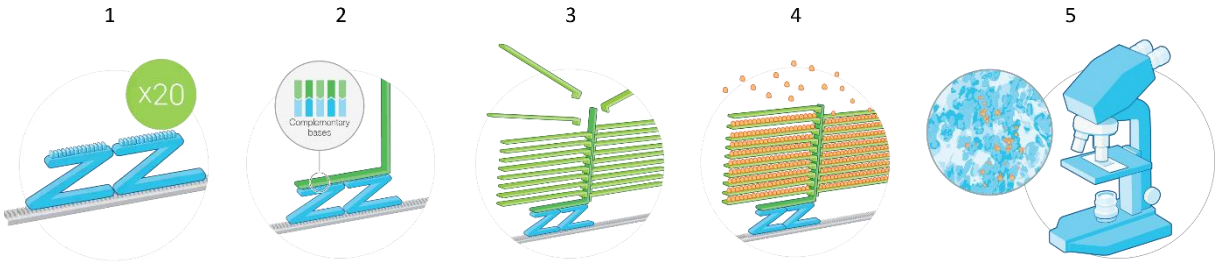

Figure 49 : **Schéma illustrant les différentes étapes du RNAscope**. 1) Hybridation des deux ‘’sondes Z’’ avec la séquence d'ARN d'intérêt. 2) Hybridation du préamplificateur avec les ‘’deux sondes Z’’. 3) Liaison des amplificateurs aux multiples sites du préamplificateur. 4) Liaison des sondes marquées aux divers sites des amplificateurs. 5) Analyse à l'aide d'un microscope optique ou à fluorescence (Adapté d'ACD, 2023)

Le protocole proprement dit commence par le déparaffinage des lames, contenant les échantillons de tissu d'intérêt, *via* les étapes suivantes :

- Deux bains successifs de 5 minutes dans du xylène (100%).
- Deux bains de 1 minute dans de l'éthanol (100%).

Après avoir déparaffiné les lames, elles sont séchées pendant 5 minutes à température ambiante. Ensuite, une solution d'H_2O_2 (fournie par le kit RNAscope 2.5 HD Assay—BROWN) est appliquée sur le tissu pendant 10 minutes à température ambiante, pour bloquer les peroxydases endogènes.

La restauration des épitopes a ensuite été entreprise, impliquant l'incubation préalable des lames dans le *target retrieval* fournit par le kit pendant 15 minutes à 95°C dans un bain marie. Ensuite, une solution de protéase plus (fournie par le kit) est appliquée pendant 30 minutes à 40°C pour préparer les échantillons à l'hybridation.

Les lames sont ensuite mises en contact avec les ‘’sondes en Z’’ spécifiques aux HPV 5 et 8, pendant 2 heures à 42°C. Pour finir, une cascade de 10 amplificateurs de signal est utilisée à température ambiante ou à 42°C pendant 15 ou 30 minutes, selon l'amplificateur utilisé. Entre chaque étape, les lames sont lavées 3 fois pendant 1 minute avec une solution de *Wash Buffer* (fournie avec le kit RNAscope 2.5 HD Assay—BROWN).

Le système de détection utilisé est la peroxydase de raifort couplée à la DAB, qui produit une coloration brune. Cette étape est réalisée pendant 10 minutes à température ambiante. Ensuite, une contre-coloration à l'hématoxyline est effectuée pendant 30 secondes.

Enfin, les lames sont montées avec une lamelle couvre-objet en utilisant le kit VectaMount mounting, et la détection du signal est réalisée à l'aide d'un microscope optique.

La technique du RNAscope a été réalisée en utilisant le kit *RNAscope® 2.5 HD Assay - BROWN* (ACD biotechne brand) selon les recommandations du fournisseur. Nous avons choisi d’utiliser cette technique car elle est connue pour sa grande sensibilité et sa spécificité élevée. En effet, la méthode repose sur l'hybridation en tandem de deux sondes indépendantes pour amplifier sélectivement les signaux spécifiques à la cible. En outre, l'utilisation de préamplificateurs, d'amplificateurs et de sondes contribue à sa grande sensibilité.

H. Génération de la banque de plasmides

Dans le but d'explorer plus en détail l'interactome des β-HPV, notamment en relation avec les protéines impliquées dans les voies de réparation de l'ADN, une méthode appelée *Gaussia princeps luciferase Protein Complementation Assay* (*GPCA*) a été utilisée. Avant de procéder à la mise en œuvre de cette méthode, qui sera détaillée ultérieurement, la création d'une librairie de plasmides codant pour des protéines d’intérêts (les oncoprotéines E6/E7 de β-HPV et les protéines impliquées dans les voies de réparation de l'ADN) s'est avérée nécessaire.

Cette construction a été réalisée en utilisant deux plasmides, à savoir pSpica-N1 et pSpica-N2 (dérivés du plasmide pCiNeo), qui permettent respectivement l'expression des morceaux de protéine Gluc1 et Gluc2 de la *gaussia princeps luciferase* (Figure 50), ces plasmides nous ont été gentiment fournis par le Dr Murielle Masson (Université de Strasbourg, France). Il est important de mentionner que ces régions complémentaires de la luciférase sont reliées aux extrémités N-terminales des protéines d'intérêt générées grâce à une séquence ''charnière'' flexible constituée de 20 acides aminés.

Les plasmides pSpica-N1 finaux, qui expriment les gènes codant pour les protéines participant aux mécanismes de réparation de l'ADN, ont été conçus au sein de notre laboratoire. Dans cette démarche, les ORF des protéines impliquées dans les différentes voies de réparation de l'ADN ont été obtenues à partir de l'ORFéome 7.1 et 8.1 (Harvard Medical School, Boston, USA). Une copie de ces banques de séquences se trouve dans le laboratoire du Dr. Jean-Claude Twizère de l'Université de Liège, en Belgique. Ces séquences, originellement hébergées dans le vecteur d'entrée pDONR223, ont été transférées dans le plasmide pSpica-N1 à l'aide du système de clonage *Gateway* (Figure 51).

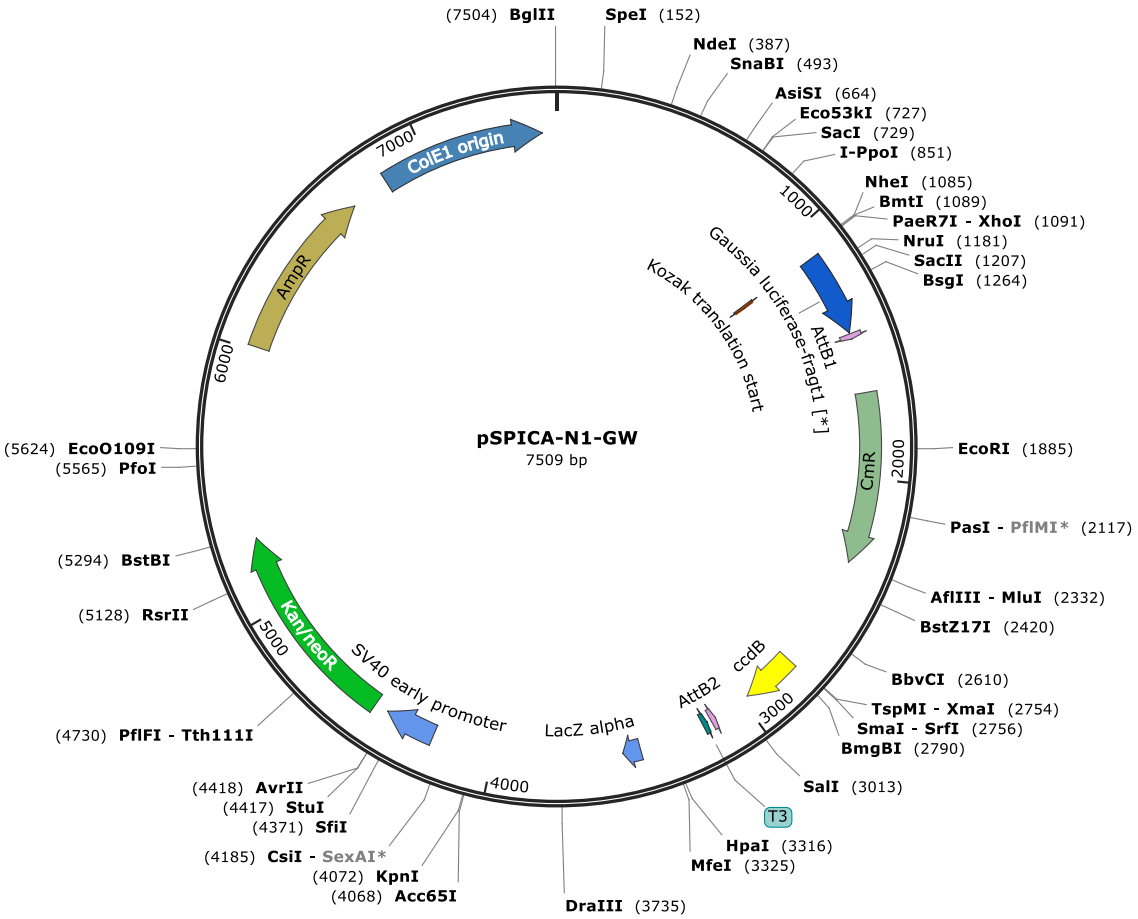

Figure 50 : **Schéma illustrant le plasmide pSPICA-N1**. Le gène Gaussia Luciferase-fragt1 est représenté par une flèche en bleu foncé, codant pour la première moitié de la luciférase de la Gaussia princeps. L'antigène grand T du SV40 est indiqué par une flèche en bleu clair, tandis que le gène de résistance à l'ampicilline est représenté par une flèche en brun clair. De plus, les sites AttB1 et AttB2, essentiels pour l'introduction d'un gène d'intérêt dans le plasmide par la technologie Gateway, sont également marqués par une flèche en rose (SnapGene Viewer, 2023).

La procédure de transfert consiste à combiner 150ng du plasmide pSpica-N1 CCDB, 150ng du plasmide pDONR223 contenant l'ORF ciblé, et 0,9 µl de l'enzyme BP (ThermoFisher), au sein d'un Eppendorf de 1,5 ml. Ensuite, ces Eppendorf ont été incubés pendant 4 heures à température ambiante (25°C).

Après l'incubation, 2µl de la solution précédente (Spica-N1 + pDONR223 + BP) ont été transférés dans un nouvel Eppendorf de 1,5 ml, auquel 40µl de bactéries compétentes DH5α (également fournie par le Dr. Jean-Claude Twizère) ont été ajoutés. Les Eppendorfs ont ensuite été placés sur glace pendant 30 minutes, puis immergés dans un bain-marie à 42°C pendant 20 secondes, suivi d'un retour sur la glace pendant 2 minutes.

Une fois ces étapes achevées, 1 ml de milieu LB (composé de 10 g de Tryptone, 5 g d'extrait de levure et 10 g de NaCl par litre d'eau distillée) a été ajouté aux Eppendorfs. Ils ont ensuite été agités pendant 1 heure à une vitesse de 200 RPM et à 37°C.

Après cette étape, les Eppendorfs ont été centrifugés pendant 15 minutes à 3000 RPM et le surnageant a été éliminé. Pour finir, le culot cellulaire a été resuspendu dans 200 µl de milieu LB et ensuite étalé sur une gélose de LB contenant de l'ampicilline (100mg/ml). Les géloses ont été incubées toute la nuit à 37°C.

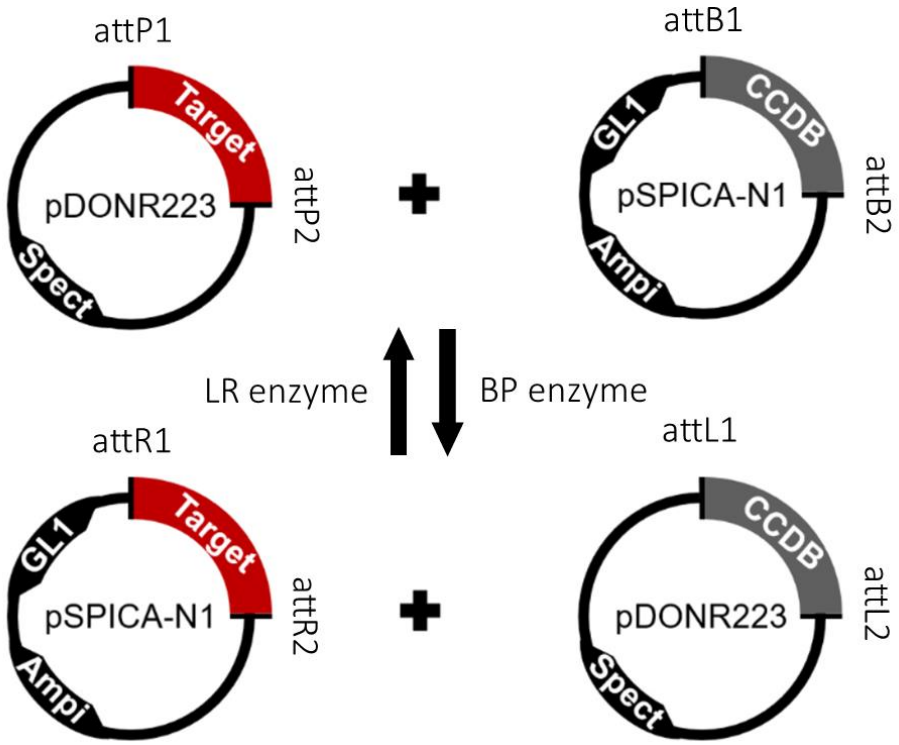

Figure 51 : **Représentation schématique du système de clonage Gateway**. Le plasmide pDONR223, renfermant le gène d'intérêt, est mixé avec le plasmide pSpica-N1, portant la moitié de la luciférase de la *Gaussia princeps* ainsi qu'une cassette CCDB. L'enzyme BP, ajoutée dans le mélange, induit la coupure des plasmides aux sites AttB1/AttB2 et AttP1/AttP2. Cette étape facilite l'insertion du gène d'intérêt depuis le pDONR223 vers le pSpica-N1. Inversement, l'enzyme LR peut être utilisée pour revenir à la situation de départ si nécessaire. Ce système de clonage Gateway est couramment utilisé en biologie moléculaire pour faciliter le transfert et la manipulation de gènes et de fragments d'ADN entre différents vecteurs ou plasmides.

Après incubation, les colonies ayant poussé sur les géloses de sélection ont été remises en suspension dans un tube de culture de 14 ml contenant du LB + de l'ampicilline (100 mg/ml) qui ont par la suite été déposés dans un incubateur à 37°C pendant 24 heures.

Enfin, l'ADN a été extrait des bactéries en suivant les instructions du fournisseur du kit *NucleoSpin® Plasmid EasyPure* (Macherey Nagel). Une fois le plasmide final récupéré, il a été envoyé à la plateforme de séquençage de l'Université de Liège pour nous assurer que la séquence d'intérêt a bien été insérée dans le plasmide pSpica-N1 et que celui-ci continue d'exprimer la moitié de la luciférase de la Gaussia Princeps. Pour cela, nous avons utilisé l'amorce suivante : 5'-CAG CTC TTA AGG CTA GAG TAC-3' (Neo univ Forward). Ainsi, une librairie de 200 plasmides codant pour les protéines impliquées dans les voies de réparation de l'ADN a été générée.

Les plasmides pSpica-N2 finaux, exprimant les oncoprotéines E6 ou E7 des HPV 5, 8, 38 et 49, ont été générés de la même manière.

I. Culture cellulaire

La lignée cellulaire HEK-293T, dérivée de cellules rénales embryonnaires humaines et fournies par le Dr Yves Jacobs de l'Institut Pasteur, a été sélectionnée pour notre étude. Le choix de cette lignée repose non seulement sur leur croissance fiable, mais également sur leur expression de l'antigène T du virus SV40, permettant la réplication épisomique des plasmides transfectés contenant l'origine de réplication du SV40. Cette particularité favorise l'amplification des plasmides transférés et l'expression prolongée des produits géniques d'intérêt.

La culture de cette lignée s'effectue dans un milieu de culture *Dulbecco's Modified Eagle Medium High glucose* (DMEM) provenant de chez ThermoFisher, auquel sont ajoutés 10% de sérum de veau fœtal (FBS) ainsi que 1% de gentamicine.

J. *Gaussia princeps* luciferase Protein Complementation Assay (*GPCA*)

Comme mentionné précédemment, la *GPCA* a été employée dans le but d'approfondir notre compréhension de l'interactome des protéines virales E6 et E7 des β-HPV avec les protéines de la cellule hôte participant aux mécanismes de réparation de l'ADN. Cette méthode de criblage à haut débit dispose d'une sensibilité remarquable, capable de détecter même des interactions très faibles. Néanmoins, cette sensibilité élevée peut engendrer des faux positifs et ainsi altérer la spécificité de la méthode. En outre, cette méthode ne met en évidence que des interactions directes, les acteurs supplémentaires dans l'interaction ne sont pas détectés.

C'est pourquoi nous avons choisi d'utiliser la *GPCA* pour effectuer un criblage initial des interactions potentielles. Par la suite, nous avons validé les interactions positives au moyen de la co-immunoprécipitation (Co-IP), une méthode plus spécifique dont nous aborderons les détails plus loin. Cette approche séquentielle nous permet de tirer avantage de la puissance de la *GPCA* tout en contrôlant les résultats par une méthode de confirmation utilisée plus communément.

Vingt-quatre heures avant la transfection, $3x10^4$ cellules HEK-293T, par puits, ont été ensemencées dans une plaque à fond plat Costar 96 puits (Corning Life Sciences).

Le jour suivant, les cellules ont été transfectées avec 100 ng de pSpica-N2 (contenant l'oncoprotéine E6 ou E7 des HPV5, 8, 38 ou 49) et 100 ng de pSpica-N1 (contenant une séquence codante pour une des nombreuses protéines d'intérêt impliquées dans les voies de réparation de l'ADN) en utilisant le PEImax (Polysciences) comme agent de transfection.

Après une période de 24 heures, les cellules ont été rincées au PBS et incubées pendant 30 minutes à température ambiante avec le tampon de lyse de Renilla (E2820, Promega). Par la suite, 50 µl de réactif de substrat de luciférase ont été ajoutés dans chaque puits, suivi directement de la mesure de l'activité de la luciférase pendant 10 secondes à l'aide d'un luminomètre microplaque Centro LB960 (Berthold Technologies).

Pour conclure, les résultats ont été exprimés sous forme de rapport de luminescence normalisée (NLR). Le NLR a été calculé en divisant la luminescence relative (RLU) par la somme des valeurs des témoins (Figure 52).

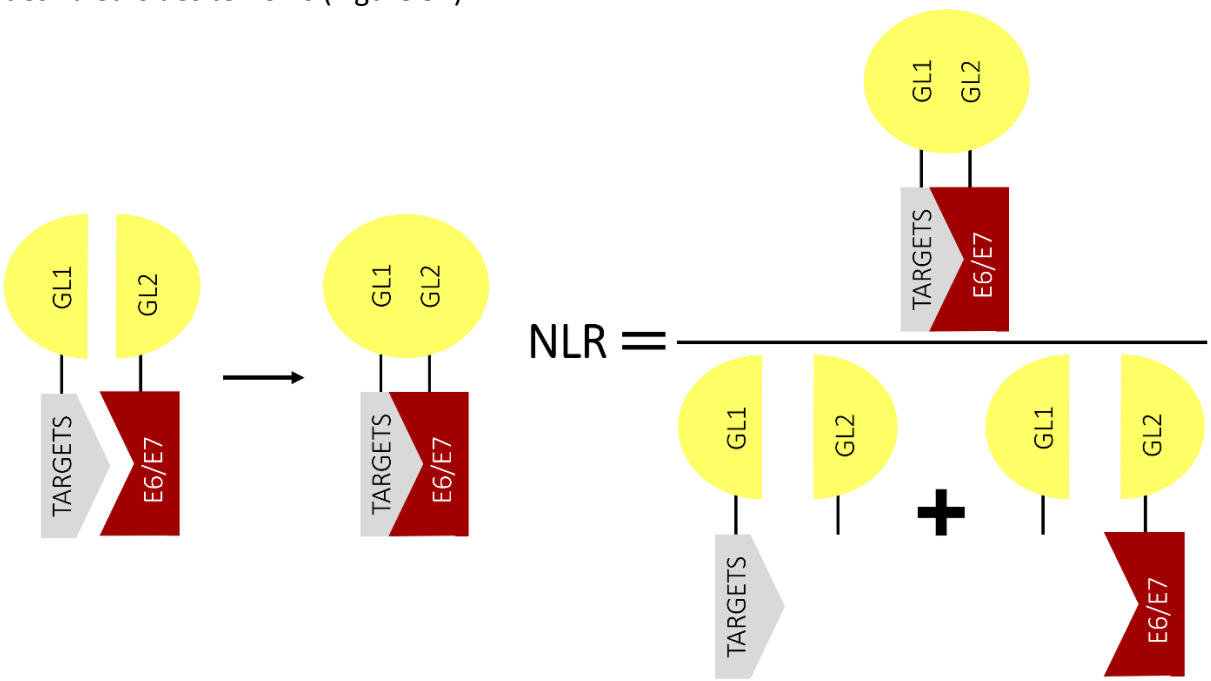

Figure 52 : **Illustration de la méthode de criblage à haut débit de *GPCA***. La protéine hôte et la protéine pathogène sont toutes deux fusionnées à des moitiés complémentaires de la luciférase de *Gaussia princeps*. Lorsque les deux protéines interagissent de manière binaire, l'activité de la luciférase est induite car les deux moitiés des protéines de luciférase sont à proximité et cette dernière est alors fonctionnelle. La luminescence est calculée à partir d'un ratio de luminescence normalisé (NLR).

K. Co-IP

Comme précédemment exposé, nous avons opté pour une approche de Co-IP afin de confirmer les résultats obtenus par *GPCA*. Il est important de noter que ces deux méthodes présentent des avantages et des limites propres, justifiant ainsi leur utilisation conjointe pour obtenir une compréhension plus holistique des mécanismes sous-jacents lors de l'infection par les β-HPV.

La première phase implique la construction d'un plasmide pCineo-3xFLAG contenant l'oncoprotéine E6 ou E7 de l'HPV8, permettant l'incorporation d'une étiquette 3xFLAG à l'extrémité N-terminale des oncoprotéines virales. Cette tâche a été accomplie en suivant le même protocole que celui employé pour la création de la banque de plasmides, à l'exception de l'utilisation de 0,9µl de l'enzyme LR (ThermoFisher) à la place de l'enzyme BP (Figure 51 et Figure 53).

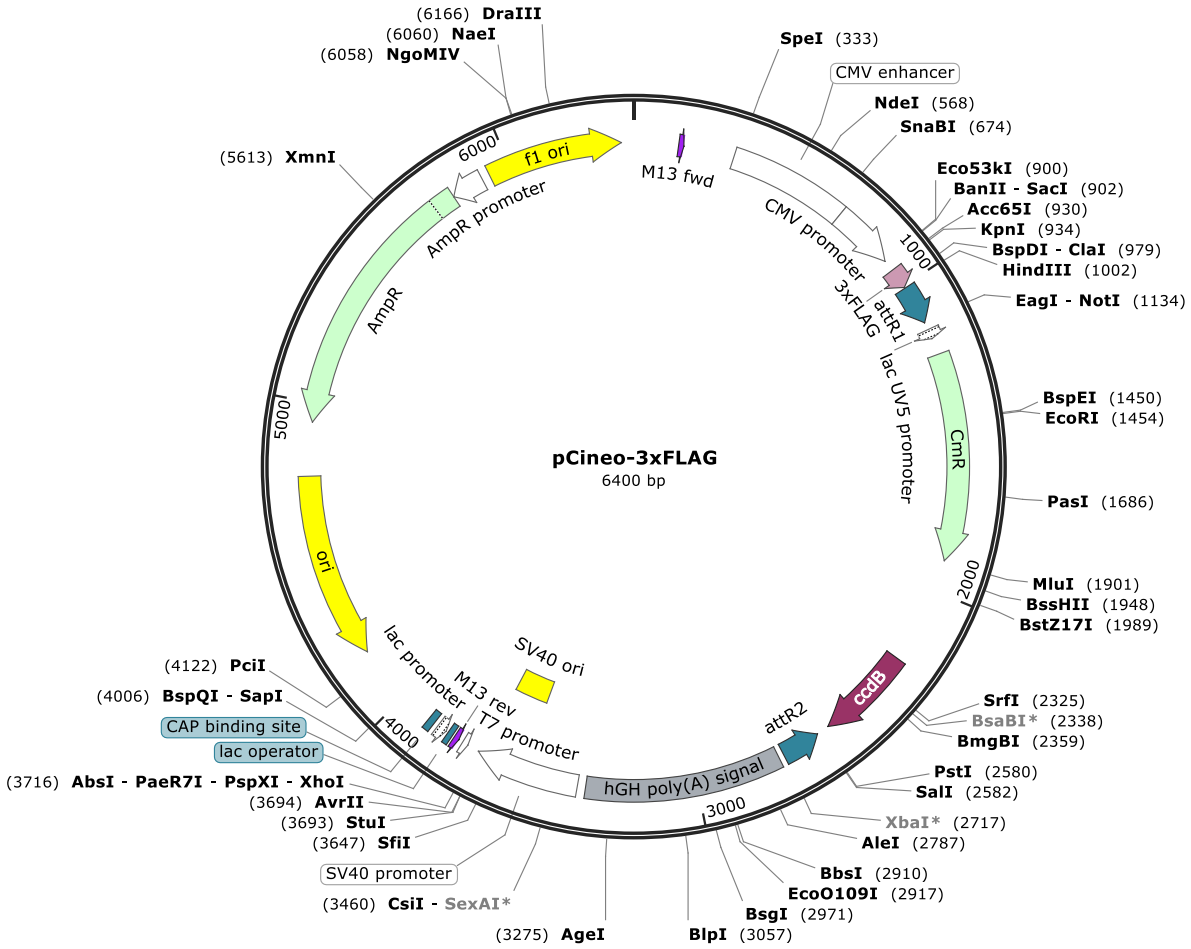

Figure 53 : **Schéma illustrant le plasmide pCineo-3xFLAG**. Le gène 3xFLAG est représenté par une flèche en mauve clair. L'origine de réplication du SV40 est indiqué par un rectangle jaune, tandis que le gène de résistance à l'ampicilline est représenté par une flèche en vert clair. De plus, les sites AttR1 et AttR2, essentiels pour l'introduction d'un gène d'intérêt dans le plasmide par la technologie Gateway, sont également marqués par une flèche en turquoise (SnapGene Viewer, 2023).

Concernant la Co-IP, 24 heures avant la transfection, $4x10^5$ cellules HEK-293T, par puits, ont été ensemencées dans une plaque de 6 puits à fond plat. Le jour suivant, les cellules ont été transfectées avec 1,5 µg de plasmide pCineo-3xFLAG (contenant HPV8 E6, HPV8 E7 ou vide) ainsi que 1,5 µg de pSpica-N1 (contenant la séquence codante pour une des multiples protéines d'intérêt reliées aux voies de réparation de l'ADN), utilisant le PEImax (Polysciences) en tant qu'agent de transfection.

Au bout de 24 heures post-transfection, les cellules ont été récupérées, rincées au PBS et soumises à une incubation de 30 minutes sur glace dans un tampon de lyse (50 mM de Tris-HCl à pH 7,4, 150 mM de NaCl, 1 mM d'EDTA, 1 % de Triton X-100 et l'inhibiteurs de protéases P3). Ensuite, après une centrifugation de 30 minutes à 18.900g à 4°C, 98 µl du surnageant ont été collectés et mis à incuber, à 4°C, toute la nuit avec 30 µl de billes magnétiques anti-Flag M2 (Sigma-Aldrich), préalablement lavées 5 fois avec du tampon TBS (50mM de Tris pH 7,4 et 150 mM de NaCl). Par ailleurs, un échantillon de 2 µl de surnageant a été conservé dans 18 µl de tampon Laemmli (62,5 mM Tris HCl pH8, 10 % Glycerol, 2% SDS, cocktail inhibiteur de protéase, phosphostop, Eau milliQ) en vue d'une analyse ultérieure des protéines totales.

Une fois l'incubation avec les billes magnétiques anti-Flag M2 achevée, celles-ci ont subi un lavage ultérieur de 5 cycles avec du TBS contenant un inhibiteur de protéases (P3). Ensuite, les billes ont été éluées dans 20 µl de tampon Laemmli. Les billes ont finalement été chauffées à 99°C pendant 10 minutes, puis un Western blot classique a été réalisé.

Les 20 µl de protéines totales et de protéines d'intérêt ont été déposés sur un gel de polyacrylamide avec un pourcentage adapté au poids moléculaire de la protéine analysée. Après une migration de 1 heure et 30 minutes à 120V, les protéines ayant migré sur le gel ont été transférées sur une membrane de PVDF durant 1 à 1 heure et 30 minutes (en fonction du poids moléculaire de la protéine) en utilisant un tampon de transfert contenant 20% de méthanol.

Les membranes de PVDF ont ensuite été bloquées avec du TBS-T (TBS + 0,1% de Tween) contenant 5% de lait pendant 1 heure à température ambiante, suivie d'une incubation nocturne avec l'anticorps *Polyclonal Rabbit Anti Gluc* (Invitrogen, PA1-181) à une dilution de 1/4000.

Le jour suivant, après trois lavages de 10 minutes avec du TBS-T (TBS +0,1% de Tween), les membranes ont été incubées pendant 1 heure avec un anticorps secondaire anti-lapin (Invitrogen, G2123) à une dilution de 1/3000. À la fin de l'incubation, les membranes ont subi trois lavages supplémentaires de 10 minutes avec du TBS-T avant d'être mis en contact avec un système de chimiluminescence (substrat Pierce ECL, Thermo Fisher Scientific) afin de révéler les bandes protéiques sur le système d'imagerie *Amersham ImageQuant 800* (Cytiva).

L. Analyses statistiques

Le test du χ^2 et le one way ANOVA-Bonferroni ont été employés pour comparer les données d'immunohistochimie entre chaque groupe. Les différences sont considérées comme significatives lorsque la p-valeur est inférieure à 0,05.

En ce qui concerne les analyses statistiques utilisé pour la *GPCA*, elles ont été effectuées en utilisant le logiciel GraphPad Prism 8. Dans ces analyses, la distribution normale a été évaluée à l'aide du score d'asymétrie et la détection des valeurs aberrantes a été réalisée à l'aide de la méthode ROUT avec un Q=5%.[450] Concernant les Co-IP, le logiciel ImageJ a été utilisé pour quantifier les bandes protéiques. L'équation décrite dans la Figure 54 nous a permis d'obtenir un score d'enrichissement de signal pour chaque potentielle interaction.

$$\text{Score} = \frac{IP/I \ \text{(E6/E7)}}{IP/\text{I} \ \text{(Empty)}}$$

Figure 54 : **Équation du score d'enrichissement**. IP= intensité de la Co-IP. I= intensité de l'input total (protéine totale).

Références

1. Bravo, I. G., de Sanjosé, S. & Gottschling, M. The clinical importance of understanding the evolution of papillomaviruses. *Trends Microbiol* **18**, 432–438 (2010).

2. Van Doorslaer, K. *et al.* PaVE: THE PAPILLOMAVIRUS EPISTEME. vol. 45 pave.niaid.nih.gov. (2023).

3. Bravo, I. G. & Felez-Sanchez, M. Papillomaviruses: Viral evolution, cancer and evolutionary medicine. *Evol Med Public Health* **2015**, 32–51 (2015).

4. Schiffman, M. *et al.* Carcinogenic human papillomavirus infection. *Nat Rev Dis Primers* **2**, (2016).

5. de Villiers, E.-M., Fauquet, C., Broker, T. R., Bernard, H.-U. & zur Hausen, H. Classification of papillomaviruses. *Virology* **324**, 17–27 (2004).

6. Bernard, H.-U. *et al.* Classification of papillomaviruses (PVs) based on 189 PV types and proposal of taxonomic amendments. *Virology* **401**, 70–79 (2010).

7. Bzhalava, D., Eklund, C. & Dillner, J. International standardization and classification of human papillomavirus types. *Virology* **476**, 341–344 (2015).

8. Van Doorslaer, K. *et al.* The Papillomavirus Episteme: a major update to the papillomavirus sequence database. *Nucleic Acids Res* **45**, D499–D506 (2017).

9. Villiers, E. De. Cross-roads in the classification of papillomaviruses. *Virology* **445**, 2–10 (2013).

10. Sias, C. *et al.* Alpha , Beta , gamma human PapillomaViruses (HPV) detection with a different sets of primers in oropharyngeal swabs , anal and cervical samples. *Virol J* **16**, 1–10 (2019).

11. Altamura, G., Tommasino, M. & Borzacchiello, G. Cutaneous vs. Mucosal Tropism: The Papillomavirus Paradigm Comes to an "and". *Front Microbiol* **11**, (2020).

12. IARC Working Group on the Evaluation of Carcinogenic Risks to Humans. *Biological agents, a review of human carcinogens*. *IARC monographs on the evaluation of carcinogenic risks to humans* vol. 100 (B) (World Health Organization, 2012).

13. Bouvard, V. *et al.* A review of human carcinogens—Part B: biological agents. *Lancet Oncol* **10**, 321–322 (2009).

14. de Sanjose, S. *et al.* Human papillomavirus genotype attribution in invasive cervical cancer: a retrospective cross-sectional worldwide study. *Lancet Oncol* **11**, 1048–1056 (2010).

15. HPV and Cancer. *national cancer institute* https://www.cancer.gov/about-cancer/causes-prevention/risk/infectious-agents/hpv-and-cancer (2021).

16. Antonsson, A., Karanfilovska, S., Lindqvist, P. G. & Hansson, B. G. General acquisition of human papillomavirus infections of skin occurs in early infancy. *J Clin Microbiol* **41**, 2509–2514 (2003).

17. Hsu, Y.-C. *et al.* Shared and persistent asymptomatic cutaneous human papillomavirus infections in healthy skin. *J Med Virol* **81**, 1444–1449 (2009).

18. Lutzner, M. A., Blanchet-Bardon, C. & Orth, G. Clinical Observations, Virologic Studies, and Treatment Trials in Patients wih Epidermodysplasia Verruciformis, a Disease Induced by Specific Human Papillomaviruses. *J Invest Dermatol* **83**, 18–25 (1984).

19. Ostrow, R. S. *et al.* Human papillomavirus DNA in cutaneous primary and metastasized squamous cell carcinomas from patients with epidermodysplasia verruciformis (Southern blot hybridization/metastasis/warts). *Medical Sciences Minnesota* **79**, 19–37 (1982).

20. Dell'Oste, V. *et al.* High β-HPV DNA Loads and Strong Seroreactivity Are Present in Epidermodysplasia Verruciformis. *Journal of Investigative Dermatology* **129**, 1026–1034 (2009).

21. Bouvard, V. *et al. A review of human carcinogens--Part B: biological agents. The lancet oncology* vol. 10 (2009).

22. Cornet, I. *et al.* Comparative Analysis of Transforming Properties of E6 and E7 from Different Beta Human Papillomavirus Types. *J Virol* **86**, 2366–2370 (2012).

23. Caldeira, S. *et al.* The E6 and E7 Proteins of the Cutaneous Human Papillomavirus Type 38 Display Transforming Properties. *J Virol* **77**, 2195–2206 (2003).

24. Viarisio, D. *et al.* E6 and E7 from beta hpv38 cooperate with ultraviolet light in the development of actinic keratosis-like lesions and squamous cell carcinoma in mice. *PLoS Pathog* **7**, (2011).

25. Chahoud, J. *et al.* Association between β-genus human papillomavirus and cutaneous squamous cell carcinoma in immunocompetent individuals-a meta-analysis. *JAMA Dermatol* **152**, 1354–1364 (2016).

26. Strickley, J. D. *et al.* Immunity to commensal papillomaviruses protects against skin cancer. *Nature* **575**, 519–522 (2019).

27. McBride, A. A. & Hurt, D. PaVE: THE PAPILLOMAVIRUS EPISTEME. pave.niaid.nih.gov.

28. McBride, A. A. Human papillomaviruses: diversity, infection and host interactions. *Nature Reviews Microbiology* vol. 20 95–108 Preprint at https://doi.org/10.1038/s41579-021-00617-5 (2022).

29. Weissenborn, S. J., De Koning, M. N. C., Wieland, U., Quint, W. G. V. & Pfister, H. J. Intrafamilial Transmission and Family-Specific Spectra of Cutaneous Betapapillomaviruses. *J Virol* **83**, 811–816 (2009).

30. Antonsson, A. *et al. The Ubiquity and Impressive Genomic Diversity of Human Skin Papillomaviruses Suggest a Commensalic Nature of These Viruses*. *JOURNAL OF VIROLOGY* vol. 74 http://www.ncbi.nlm.nih.gov/blast/blast.cgi (2000).

31. Sankovski, E., Männik, A., Geimanen, J., Ustav, E. & Ustav, M. Mapping of Betapapillomavirus Human Papillomavirus 5 Transcription and Characterization of Viral-Genome Replication Function. *J Virol* **88**, 961–973 (2014).

32. Jan Weissenborn, S. *et al. Human Papillomavirus-DNA Loads in Actinic Keratoses Exceed those in Non-Melanoma Skin Cancers*. (2005).

33. Viarisio, D., Gissmann, L. & Tommasino, M. Human papillomaviruses and carcinogenesis: well-established and novel models. *Current Opinion in Virology* vol. 26 56–62 Preprint at https://doi.org/10.1016/j.coviro.2017.07.014 (2017).

34. Gheit, T. Mucosal and cutaneous human papillomavirus infections and cancer biology. *Frontiers in Oncology* vol. 9 Preprint at https://doi.org/10.3389/fonc.2019.00355 (2019).

35. Sailaja, G., Watts, R. M. & Bernard, H.-U. *Many different papillomaviruses have low transcriptional activity in spite of strong epithelial specific enhancers*. *Journal of General Virology* vol. 80 (1999).

36. Park, J. S. *et al.* Neoplastic change of squamo-columnar junction in uterine cervix and vaginal epithelium by exogenous estrogen in HPV-18 URR E6/E7 transgenic mice. *Gynecol Oncol* **89**, 360–368 (2003).

37. Sankovski, E., Männik, A., Geimanen, J., Ustav, E. & Ustav, M. Mapping of Betapapillomavirus Human Papillomavirus 5 Transcription and Characterization of Viral-Genome Replication Function. *J Virol* **88**, 961–973 (2014).

38. Demeret, C., Desaintes, C., Yaniv, M. & Thierry, F. O. Different Mechanisms Contribute to the E2-Mediated Transcriptional Repression of Human Papillomavirus Type 18 Viral Oncogenes. *J Virol* **71**, 9343–9349 (1997).

39. Dostatni, N. *et al.* The functional BPV-1 E2 trans-activating rotem can act as a repressor y preventing formation of the initiation complex. *Genes Dev* 1657–1671 (1991).

40. Mistry, N., Simonsson, M. & Evander, M. Transcriptional activation of the human papillomavirus type 5 and 16 long control region in cells from cutaneous and mucosal origin. *Virol J* **4**, (2007).

41. Guido, M. C., Zamorano, R., Garrido-Guerrero, E., Garigli02~, P. & Garcia-Carranc~, A. Early promoters of genital and cutaneous human papillomaviruses are differentially regulated by the bovine papillomavirus type 1 E2 gene product. *Journal of General Virology* **73**, 1395–1400 (1992).

42. Muller, M. & Demeret, C. The HPV E2-Host Protein-Protein Interactions: A Complex Hijacking of the Cellular Network. *Open Virol J* **6**, 173–189 (2012).

43. García-Vallvé, S., Iglesias-Rozas, J. R., Alonso, Á. & Bravo, I. G. Different papillomaviruses have different repertoires of transcription factor binding sites: Convergence and divergence in the upstream regulatory region. *BMC Evol Biol* **6**, (2006).

44. Ozbun, M. A. & Meyers, C. *Characterization of Late Gene Transcripts Expressed during Vegetative Replication of Human Papillomavirus Type 31b*. *JOURNAL OF VIROLOGY* vol. 71 (1997).

45. Graham, S. V. The human papillomavirus replication cycle, and its links to cancer progression: A comprehensive review. *Clin Sci* **131**, 2201–2221 (2017).

46. Stubenrauch, F., Malejczyk, J., Fuchs,' And, P. G. & Pfister`*, H. Late Promoter of Human Papillomavirus Type 8 and Its Regulation. *J Virol* **66**, 3485–3493 (1992).

47. Smotkin, D. & Wettsteintt, F. 0. Transcription of human papillomavirus type 16 early genes in a cervical cancer and a cancer-derived cell line and identification of the E7 protein (viral DNA integration/plasmid/virus-cell hybrid transcripts/fusion protein/early viral protein). *Proc. Natl. Acad. Sci* **83**, 4680–4684 (1986).

48. Grassmann, K., Rapp, B., Maschek, H., Petry, K. U. & Iftner, A. T. Identification of a Differentiation-Inducible Promoter in the E7 Open Reading Frame of Human Papillomavirus Type 16 (HPV-16) in Raft Cultures of a New Cell Line Containing High Copy Numbers of Episomal HPV-16 DNA. *J Virol* **70**, 2339–2349 (1996).

49. Van Doorslaer, K. & McBride, A. A. Molecular archeological evidence in support of the repeated loss of a papillomavirus gene. *Sci Rep* **6**, (2016).

50. Wu, Y. C., Roark, A. A., Bian, X. L. & Wilson, V. G. Modification of papillomavirus E2 proteins by the small ubiquitin-like modifier family members (SUMOs). *Virology* **378**, 329–338 (2008).

51. Sekhar, V. & McBride, A. A. Phosphorylation Regulates Binding of the Human Papillomavirus Type 8 E2 Protein to Host Chromosomes. *J Virol* **86**, 10047–10058 (2012).

52. Bergvall, M., Melendy, T. & Archambault, J. The E1 proteins. *Virology* **445**, 35–56 (2013).

53. Leng Xiao, X. & Wilson, V. G. *Genetically defined nuclear localization signal sequence of bovine papillomavirus E1 protein is necessary and sufficient for the nuclear localization of El-fl-galactosidase fusion proteins*. *Journal of General Virology* vol. 75 (1994).

54. Yu, J.-H., Lin, B. Y., Deng, W., Broker, T. R. & Chow, L. T. Mitogen-Activated Protein Kinases Activate the Nuclear Localization Sequence of Human Papillomavirus Type 11 E1 DNA Helicase To Promote Efficient Nuclear Import. *J Virol* **81**, 5066–5078 (2007).

55. Enemark, E. J. & Joshua-Tor, L. Mechanism of DNA translocation in a replicative hexameric helicase. *Nature* **442**, 270–275 (2006).

56. Hughes, F. J. & Romanos, M. A. *El protein of human papillomavirus is a DNA helicase/ ATPase*. *Nucleic Acids Research* vol. 21 (1993).

57. Baedyananda, F., Sasivimolrattana, T., Chaiwongkot, A., Varadarajan, S. & Bhattarakosol, P. Role of HPV16 E1 in cervical carcinogenesis. *Frontiers in Cellular and Infection Microbiology* vol. 12 Preprint at https://doi.org/10.3389/fcimb.2022.955847 (2022).

58. Berg, M. & Stenlund, A. *Functional Interactions between Papillomavirus E1 and E2 Proteins*. *JOURNAL OF VIROLOGY* vol. 71 (1997).

59. Wilson, V. G., West, M., Woytek, K. & Rangasamy, D. *Papillomavirus E1 Proteins: Form, Function, and Features*. *Virus Genes* vol. 24 http://www.ncbi.nlm.nih.gov/Structure/cdd/wrpsb.cgi (2002).

60. Loo, Y.-M. & Melendy, T. Recruitment of Replication Protein A by the Papillomavirus E1 Protein and Modulation by Single-Stranded DNA. *J Virol* **78**, 1605–1615 (2004).

61. Baedyananda, F., Chaiwongkot, A., Varadarajan, S. & Bhattarakosol, P. HPV16 E1 dysregulated cellular genes involved in cell proliferation and host DNA damage: A possible role in cervical carcinogenesis. *PLoS One* **16**, (2021).

62. Reinson, T. *et al.* Engagement of the ATR-Dependent DNA Damage Response at the Human Papillomavirus 18 Replication Centers during the Initial Amplification. *J Virol* **87**, 951–964 (2013).

63. Fradet-Turcotte, A. *et al.* Nuclear Accumulation of the Papillomavirus E1 Helicase Blocks S-Phase Progression and Triggers an ATM-Dependent DNA Damage Response. *J Virol* **85**, 8996–9012 (2011).

64. Sakakibara, N., Mitra, R. & McBride, A. A. The Papillomavirus E1 Helicase Activates a Cellular DNA Damage Response in Viral Replication Foci. *J Virol* **85**, 8981–8995 (2011).

65. Castillo, A. *et al.* A systems biology analysis of the changes in gene expression via silencing of HPV-18 E1 expression in HeLa cells. *Open Biol* **4**, (2014).

66. Castro-Muñoz, L. J. *et al.* The Human Papillomavirus (HPV) E1 protein regulates the expression of cellular genes involved in immune response. *Sci Rep* **9**, (2019).

67. Giri, I. & Yaniv, M. *Structural and mutational analysis of E2 trans-activating proteins of papillomaviruses reveals three distinct functional domains*. *The EMBO Journal* vol. 7.

68. Stubenrauch, F., Leigh, I. M. & Pfister, A. H. *E2 Represses the Late Gene Promoter of Human Papillomavirus Type 8 at High Concentrations by Interfering with Cellular Factors*. *JOURNAL OF VIROLOGY* vol. 70 (1996).

69. Hou, S. Y., Wu, S.-Y., Zhou, T., Thomas, M. C. & Chiang, C.-M. *Alleviation of Human Papillomavirus E2-Mediated Transcriptional Repression via Formation of a TATA Binding Protein (or TFIID)-TFIIB-RNA Polymerase II-TFIIF Preinitiation Complex*. *MOLECULAR AND CELLULAR BIOLOGY* vol. 20 (2000).

70. Dong, G., Broker, T. R. & Chow, L. T. *Human papillomavirus type 11 E2 proteins repress the homologous E6 promoter by interfering with the binding of host transcription factors to adjacent elements*. *JOURNAL OF VIROLOGY* (1994).

71. Tan, S.-H., Louis, ', Leong, E.-C., Walker, P. A. & Bernard', H.-U. *The Human Papillomavirus Type 16 E2 Transcription Factor Binds with Low Cooperativity to Two Flanking Sites and Represses the E6 Promoter through Displacement of Spl and TFIID*. *JOURNAL OF VIROLOGY* (1994).

72. Wu, S. Y. *et al.* Brd4 links chromatin targeting to HPV transcriptional silencing. *Genes Dev* **20**, 2383–2396 (2006).

73. Smith, J. A. *et al.* Genome-wide siRNA screen identifies SMCX, EP400, and Brd4 as E2-dependent regulators of human papillomavirus oncogene expression. *Proc Natl Acad Sci U S A* **107**, 3752–3757 (2010).

74. Sanders, C. M. & Stenlund, A. Transcription factor-dependent loading of the E1 initiator reveals modular assembly of the papillomavirus origin melting complex. *Journal of Biological Chemistry* **275**, 3522–3534 (2000).

75. Sanders, C. M. & Stenlund, A. *Recruitment and loading of the E1 initiator protein: an ATP-dependent process catalysed by a transcription factor*. *The EMBO Journal* vol. 17 (1998).

76. Ustav, E., Ustav, M., Szymanski, P. & Stenlund, A. *The bovine papillomavirus origin of replication requires a binding site for the E2 transcriptional activator (DNA replication/transcription factor)*. *Biochemistry* vol. 90 (1993).

77. Day, P. M., Roden, R. B. S., Lowy, D. R. & Schiller, J. T. *The Papillomavirus Minor Capsid Protein, L2, Induces Localization of the Major Capsid Protein, L1, and the Viral Transcription/Replication Protein, E2, to PML Oncogenic Domains*. *JOURNAL OF VIROLOGY* vol. 72 (1998).

78. Day, P. M., Baker, C. C., Lowy, D. R. & Schiller, J. T. Establishment of papillomavirus infection is enhanced by promyelocytic leukemia protein (PML) expression. *PNAS* **101**, 14252–14257 (2004).

79. Bastien, N. & McBride, A. A. Interaction of the papillomavirus E2 protein with mitotic chromosomes. *Virology* **270**, 124–134 (2000).

80. Muller, M. & Demeret, C. The HPV E2-Host Protein-Protein Interactions: A Complex Hijacking of the Cellular Network. *Open Virol J* **6**, 173–189 (2012).

81. McBride, A. A. Replication and Partitioning of Papillomavirus Genomes. in *Advances in Virus Research* vol. 72 155–205 (2008).

82. Bellanger, S., Ling Tan, C., Zhen Xue, Y., Teissier, S. & Thierry, F. *Tumor suppressor or oncogene? A critical role of the hu-man papillomavirus (HPV) E2 protein in cervical cancer progression*. *J Cancer Res* vol. 1 www.ajcr.us/ (2011).

83. McBride, A. A., Sakakibara, N., Stepp, W. H. & Jang, M. K. Hitchhiking on host chromatin: How papillomaviruses persist. *Biochimica et Biophysica Acta - Gene Regulatory Mechanisms* vol. 1819 820–825 Preprint at https://doi.org/10.1016/j.bbagrm.2012.01.011 (2012).

84. McLaughlin-Drubin, M. E., Meyers, J. & Munger, K. Cancer associated human papillomaviruses. *Current Opinion in Virology* vol. 2 459–466 Preprint at https://doi.org/10.1016/j.coviro.2012.05.004 (2012).

85. Tommasino, M. The human papillomavirus family and its role in carcinogenesis. *Seminars in Cancer Biology* vol. 26 13–21 Preprint at https://doi.org/10.1016/j.semcancer.2013.11.002 (2014).

86. Venuti, A. *et al.* Papillomavirus E5: The smallest oncoprotein with many functions. *Molecular Cancer* vol. 10 Preprint at https://doi.org/10.1186/1476-4598-10-140 (2011).

87. Tommasino, M. The biology of beta human papillomaviruses. *Virus Research* vol. 231 128–138 Preprint at https://doi.org/10.1016/j.virusres.2016.11.013 (2017).

88. Brimer, N., Drews, C. M. & Vande Pol, S. B. Association of papillomavirus E6 proteins with either MAML1 or E6AP clusters E6 proteins by structure, function, and evolutionary relatedness. *PLoS Pathog* **13**, (2017).

89. Zanier, K. *et al.* Structural basis for hijacking of cellular LxxLL motifs by papillomavirus E6 oncoproteins. *Science (1979)* **339**, 694–698 (2013).

90. Belotti, E. *et al.* The human PDZome: A gateway to PSD95-disc large-zonula occludens (PDZ)-mediated functions. *Molecular and Cellular Proteomics* **12**, 2587–2603 (2013).

91. Storrs, C. H. & Silverstein, S. J. PATJ, a Tight Junction-Associated PDZ Protein, Is a Novel Degradation Target of High-Risk Human Papillomavirus E6 and the Alternatively Spliced Isoform 18 E6*. *J Virol* **81**, 4080–4090 (2007).

92. Favre-Bonvin, A., Reynaud, C., Kretz-Remy, C. & Jalinot, P. Human Papillomavirus Type 18 E6 Protein Binds the Cellular PDZ Protein TIP-2/GIPC, Which Is Involved in Transforming Growth Factor β Signaling and Triggers Its Degradation by the Proteasome. *J Virol* **79**, 4229–4237 (2005).

93. Accardi, R. *et al.* E6 and E7 from Human Papillomavirus Type 16 Cooperate To Target the PDZ Protein Na/H Exchange Regulatory Factor 1. *J Virol* **85**, 8208–8216 (2011).

94. Ganti, K. *et al.* The human papillomavirus E6 PDZ binding motif: From life cycle to malignancy. *Viruses* vol. 7 3530–3551 Preprint at https://doi.org/10.3390/v7072785 (2015).

95. White, E. A. *et al.* Comprehensive Analysis of Host Cellular Interactions with Human Papillomavirus E6 Proteins Identifies New E6 Binding Partners and Reflects Viral Diversity. *J Virol* **86**, 13174–13186 (2012).

96. Cornet, I. *et al.* Comparative Analysis of Transforming Properties of E6 and E7 from Different Beta Human Papillomavirus Types. *J Virol* **86**, 2366–2370 (2012).

97. Muschik, D. *et al.* Cutaneous HPV23 E6 prevents p53 phosphorylation through interaction with HIPK2. *PLoS One* **6**, (2011).

98. Giampieri, S. & Storey, A. Repair of UV-induced thymine dimers is compromised in cells expressing the E6 protein from human papillomaviruses types 5 and 18. *Br J Cancer* **90**, 2203–2209 (2004).

99. Wallace, N. A., Robinson, K., Howie, H. L. & Galloway, D. A. HPV 5 and 8 E6 Abrogate ATR activity resulting in increased persistence of UVB induced DNA damage. *PLoS Pathog* **8**, 41 (2012).

100. Muench, P. *et al.* Cutaneous papillomavirus E6 proteins must interact with p300 and block p53-mediated apoptosis for cellular immortalization and tumorigenesis. *Cancer Res* **70**, 6913–6924 (2010).

101. Wallace, N. A., Robinson, K., Howie, H. L. & Galloway, D. A. β-HPV 5 and 8 E6 Disrupt Homology Dependent Double Strand Break Repair by Attenuating BRCA1 and BRCA2 Expression and Foci Formation. *PLoS Pathog* **11**, 1–24 (2015).

102. Underbrink, M. P., Howie, H. L., Bedard, K. M., Koop, J. I. & Galloway, D. A. E6 Proteins from Multiple Human Betapapillomavirus Types Degrade Bak and Protect Keratinocytes from Apoptosis after UVB Irradiation. *J Virol* **82**, 10408–10417 (2008).

103. Holloway, A., Simmonds, M., Azad, A., Fox, J. L. & Storey, A. Resistance to UV-induced apoptosis by β-HPV5 E6 involves targeting of activated BAK for proteolysis by recruitment of the HERC1 ubiquitin ligase. *Int J Cancer* **136**, 2831–2843 (2015).

104. Bedard, K. M., Underbrink, M. P., Howie, H. L. & Galloway, D. A. The E6 Oncoproteins from Human Betapapillomaviruses Differentially Activate Telomerase through an E6AP-Dependent Mechanism and Prolong the Lifespan of Primary Keratinocytes. *J Virol* **82**, 3894–3902 (2008).

105. Wu, L. *et al.* MAML1, a human homologue of Drosophila Mastermind, is a transcriptional co-activator for NOTCH receptors. *Nat Genet* **26**, 484–489 (2000).

106. Brimer, N., Lyons, C., Wallberg, A. E. & Vande Pol, S. B. Cutaneous papillomavirus E6 oncoproteins associate with MAML1 to repress transactivation and NOTCH signaling. *Oncogene* **31**, 4639–4646 (2012).

107. Rangarajan A *et al.* Notch signaling is a direct determinant of keratinocyte growth arrest and entry into differentiation. *EMBO J* **20**, 3427–3436 (2001).

108. Scheffner, M., Werness, B. A., Huibregtse, J. 54, Levine, A. J. & Howley', P. M. *The E6 Oncoprotein Encoded by Human Papillomavirus Types 16 and 18 Promotes the Degradation of ~53*. *Cell* vol. 63 (1990).

109. Scheffner, M., Huibregtse,', J. M., Vierstra, P. D. & Howley', P. M. *The HPV-16 E6 and EG-AP Complex Functions as a Ubiquitin-Protein Ligase in the Ubiquitination of ~53*. *Cell* vol. 75 (1993).

110. Martinez-Zapien, D. *et al.* Structure of the E6/E6AP/p53 complex required for HPV-mediated degradation of p53. *Nature* **529**, 541–545 (2016).

111. Patel, D. *et al. The E6 protein of human papillomavirus type 16 binds to and inhibits co-activation by CBP and p300. The EMBO Journal* vol. 18 (1999).

112. Thomas, M. & Banks, L. Inhibition of Bak-induced apoptosis by HPV-18 E6. *Oncogene* 2943–2954 (1998).

113. Gewin, L., Myers, H., Kiyono, T. & Galloway, D. A. Identification of a novel telomerase repressor that interacts with the human papillomavirus type-16 E6/E6-AP complex. *Genes Dev* **18**, 2269–2282 (2004).

114. Barbosa, M. S. *et al. The region of the HPV E7 oncoprotein homologous to adenovirus E1a and SV40 large T antigen contains separate domains for Rb binding and casein kinase 11 phosphorylation*. *The EMBO Journal* vol. 9 (1990).

115. Mcintyre, M. C., Frattini, M. G., Grossman, S. R. & Laimins, L. A. *Human Papillomavirus Type 18 E7 Protein Requires Intact Cys-X-X-Cys Motifs for Zinc Binding, Dimerization, and Transformation but Not for Rb Binding*. *JOURNAL OF VIROLOGY* (1993).

116. Dimova, D. K. & Dyson, N. J. The E2F transcriptional network: Old acquaintances with new faces. *Oncogene* vol. 24 2810–2826 Preprint at https://doi.org/10.1038/sj.onc.1208612 (2005).

117. Yamashita T, Segawa K, Fujinaga Y, Nishikawa T & Fujinaga K. Biological and biochemical activity of E7 genes of the cutaneous human papillomavirus type 5 and 8. *Oncogene* **8**, 2433–2441 (1993).

118. Saidj, D. *et al.* Oncoprotein E7 from Beta Human Papillomavirus 38 Induces Formation of an Inhibitory Complex for a Subset of p53-Regulated Promoters. *J Virol* **87**, 12139–12150 (2013).

119. Accardi, R. *et al.* Skin human papillomavirus type 38 alters p53 functions by accumulation of ΔNp73. *EMBO Rep* **7**, 334–340 (2006).

120. Gabet, A.-S. *et al.* Impairment of the telomere/telomerase system and genomic instability are associated with keratinocyte immortalization induced by the skin human papillomavirus type 38. *The FASEB Journal* **22**, 622–632 (2008).

121. Huh, K. *et al.* Human Papillomavirus Type 16 E7 Oncoprotein Associates with the Cullin 2 Ubiquitin Ligase Complex, Which Contributes to Degradation of the Retinoblastoma Tumor Suppressor. *J Virol* **81**, 9737–9747 (2007).

122. Cobrinik, D. Pocket proteins and cell cycle control. *Oncogene* **24**, 2796–2809 (2005).

123. Zhang, B., Chen, W. & Roman, A. The E7 proteins of low-and high-risk human papillomaviruses share the ability to target the pRB family member p130 for degradation. *PNAS* **103**, 437–442 (2005).

124. Jones, D. L., Alani, R. M. & Mü Nger, K. The human papillomavirus E7 oncoprotein can uncouple cellular differentiation and proliferation in human keratinocytes by abrogating p21 Cip1-mediated inhibition of cdk2. *Genes Dev* 2101–2111 (1997).

125. Zerfass-Thome K *et al.* Inactivation of the cdk inhibitor p27KIP1 by the human papillomavirus type 16 E7 oncoprotein. *Oncogene* **13**, 2323–2330 (1996).

126. He, W., Staples, D., Smith, C. & Fisher, C. Direct Activation of Cyclin-Dependent Kinase 2 by Human Papillomavirus E7. *J Virol* **77**, 10566–10574 (2003).

127. Vande Pol, S. B. & Klingelhutz, A. J. Papillomavirus E6 oncoproteins. *Virology* **445**, 115–137 (2013).

128. Poirson, J. *et al.* Mapping the interactome of HPV E6 and E7 oncoproteins with the ubiquitin-proteasome system. *FEBS Journal* **284**, 3171–3201 (2017).

129. Bruyere, D. *et al.* Human papillomavirus E6/E7 oncoproteins promote radiotherapy-mediated tumor suppression by globally hijacking host DNA damage repair. *Theranostics* **13**, 1130–1149 (2023).

130. Hasan, U. A. *et al.* The Human papillomavirus type 16 E7 oncoprotein induces a transcriptional repressor complex on the Toll-like receptor 9 promoter. *Journal of Experimental Medicine* **210**, 1369–1387 (2013).

131. da Silva Cardeal, L. B. *et al.* HPV16 oncoproteins induce MMPs/RECK-TIMP-2 imbalance in primary keratinocytes: Possible implications in cervical carcinogenesis. *PLoS One* **7**, (2012).

132. Grabowska, A. K. & Riemer, A. B. The Invisible Enemy – How Human Papillomaviruses Avoid Recognition and Clearance by the Host Immune System. *Open Virol J* **6**, 249–256 (2012).

133. Baker, T. S. *et al.* Structures of bovine and human papillomaviruses, analysis by cryoelectron microscopy and three-dimensional image reconstruction. *Biophys J* **60**, 1445–1456 (1991).

134. Doorbar, J. *et al.* The biology and life-cycle of human papillomaviruses. *Vaccine* vol. 30 Preprint at https://doi.org/10.1016/j.vaccine.2012.06.083 (2012).

135. Modis T, L.Trus B & C.Harrison S. Atomic model of the papillomavirus capsid. *EMBO J* **21**, 4754–4762 (2002).

136. S.Chen X, L.Garcea R, Goldberg I, Casii G & C.Harrison S. Structure of Small Virus-like Particles Assembled from the L1 Protein of Human Papillomavirus 16. *Mol Cell* **5**, 557–567 (2000).

137. Day, P. M., Lowy, D. R. & Schiller, J. T. Heparan Sulfate-Independent Cell Binding and Infection with Furin-Precleaved Papillomavirus Capsids. *J Virol* **82**, 12565–12568 (2008).

138. Selinka, H.-C. *et al.* Inhibition of Transfer to Secondary Receptors by Heparan Sulfate-Binding Drug or Antibody Induces Noninfectious Uptake of Human Papillomavirus. *J Virol* **81**, 10970–10980 (2007).

139. Buck, C. B., Day, P. M. & Trus, B. L. The papillomavirus major capsid protein L1. *Virology* **445**, 169–174 (2013).

140. Bronnimann, M. P. *et al.* Furin Cleavage of L2 during Papillomavirus Infection: Minimal Dependence on Cyclophilins. *J Virol* **90**, 6224–6234 (2016).

141. Richards, R. M., Lowy, D. R., Schiller, J. T. & Day, P. M. Cleavage of the papillomavirus minor capsid protein, L2, at a furin consensus site is necessary for infection. *PNAS* **103**, 1522–1527 (2006).

142. Kines, R. C., Thompson, C. D., Lowy, D. R., Schiller, J. T. & Day, P. M. The initial steps leading to papillomavirus infection occur on the basement membrane prior to cell surface binding. *PNAS* **106**, 20458–20463 (2009).

143. Scheffer, K. D., Berditchevski, F. & Florin, L. The tetraspanin CD151 in papillomavirus infection. *Viruses* vol. 6 893–908 Preprint at https://doi.org/10.3390/v6020893 (2014).

144. Lambris, J. D., Back N, Cohen I, Lajtha A & Paoletti R. *Advances in Experimental Medicine and Biology*. vol. 726 (2021).

145. Pereira, R., Hitzeroth, I. I. & Rybicki, E. P. Insights into the role and function of L2, the minor capsid protein of papillomaviruses. *Archives of Virology* vol. 154 187–197 Preprint at https://doi.org/10.1007/s00705-009-0310-3 (2009).

146. Doorbar, J. & Gallimore, P. H. *Identification of Proteins Encoded by the L1 and L2 Open Reading Frames of Human Papillomavirus Ia*. *JOURNAL OF VIROLOGY* (1987).

147. Popa, A. *et al.* Direct Binding of Retromer to Human Papillomavirus Type 16 Minor Capsid Protein L2 Mediates Endosome Exit during Viral Infection. *PLoS Pathog* **11**, (2015).

148. Florin, L., Schäfer, F., Sotlar, K., Streeck, R. E. & Sapp, M. Reorganization of nuclear domain 10 induced by papillomavirus capsid protein l2. *Virology* **295**, 97–107 (2002).

149. DiGiuseppe, S., Bienkowska-Haba, M. & Sapp, M. Human Papillomavirus Entry: Hiding in a Bubble. *J Virol* **90**, 8032–8035 (2016).

150. Becker, K. A., Florin, L., Sapp, C., Maul, G. G. & Sapp, M. Nuclear Localization but Not PML Protein Is Required for Incorporation of the Papillomavirus Minor Capsid Protein L2 into Virus-Like Particles. *J Virol* **78**, 1121–1128 (2004).

151. Day, P. M., Roden, R. B. S., Lowy, D. R. & Schiller, J. T. *The Papillomavirus Minor Capsid Protein, L2, Induces Localization of the Major Capsid Protein, L1, and the Viral Transcription/Replication Protein, E2, to PML Oncogenic Domains*. *JOURNAL OF VIROLOGY* vol. 72 (1998).

152. Florin, L. *et al.* Identification of a Dynein Interacting Domain in the Papillomavirus Minor Capsid Protein L2. *J Virol* **80**, 6691–6696 (2006).

153. Longworth, M. S. & Laimins, L. A. Pathogenesis of Human Papillomaviruses in Differentiating Epithelia. *Microbiology and Molecular Biology Reviews* **68**, 362–372 (2004).

154. Wang, X., Meyers, C., Wang, H.-K., Chow, L. T. & Zheng, Z.-M. Construction of a Full Transcription Map of Human Papillomavirus Type 18 during Productive Viral Infection. *J Virol* **85**, 8080–8092 (2011).

155. Yajid, A. I., Zakariah, M. A., Zin, A. A. M. & Othman, N. H. Potential role of E4 protein in human papillomavirus screening: A review. *Asian Pacific Journal of Cancer Prevention* vol. 18 315–319 Preprint at https://doi.org/10.22034/APJCP.2017.18.2.315 (2017).

156. Roberts, S., Ashmole, I., Rookes, S. M. & Gallimore, P. H. *Mutational Analysis of the Human Papillomavirus Type 16 E1 ∧ E4 Protein Shows that the C Terminus Is Dispensable for Keratin Cytoskeleton Association but Is Involved in Inducing Disruption of the Keratin Filaments*. *JOURNAL OF VIROLOGY* vol. 71 (1997).

157. McIntosh, P. B. *et al.* Structural Analysis Reveals an Amyloid Form of the Human Papillomavirus Type 16 E1 ∧ E4 Protein and Provides a Molecular Basis for Its Accumulation . *J Virol* **82**, 8196–8203 (2008).

158. Brown, D. R. *et al.* The human papillomavirus type 11 E1∧E4 protein is a transglutaminase 3 substrate and induces abnormalities of the cornified cell envelope. *Virology* **345**, 290–298 (2006).

159. Peh, W. L. *et al.* Life Cycle Heterogeneity in Animal Models of Human Papillomavirus-Associated Disease. *J Virol* **76**, 10401–10416 (2002).

160. Doorbar, J. The E4 protein; structure, function and patterns of expression. *Virology* **445**, 80–98 (2013).

161. Knight, G. L., Turnell, A. S. & Roberts, S. Role for Wee1 in Inhibition of G 2 -to-M Transition through the Cooperation of Distinct Human Papillomavirus Type 1 E4 Proteins . *J Virol* **80**, 7416–7426 (2006).

162. Egawa, K. New types of human papillomaviruses and intracytoplasmic inclusion bodies: a classification of inclusion warts according to clinical features, histology and associated HPV types. *British journal of Dermatology* **130**, 158–166 (1994).

163. Doorbar, J., Medcalf, E. & Napthine, S. *Analysis of HPV1 E4 Complexes and Their Association with Keratins in Vivo*. *VIROLOGY* vol. 218 (1996).

164. Rogel-Gaillard, C., Pehau-Arnaudet, G., Breitburd, oise & Orth, G. Cytopathic Effect in Human Papillomavirus Type 1-Induced Inclusion Warts: In Vitro Analysis of the Contribution of Two Forms of the Viral E4 Protein. *The Journal Of Inverstigative Dermatology* **101**, 843–851 (1993).

165. stubenrauch F., Hummel M., IFTNER T. & LAIMINS L.A. The E8ˆE2C Protein, a Negative Regulator of Viral Transcription and Replication, Is Required for Extrachromosomal Maintenance of Human Papillomavirus Type 31 in Keratinocytes. *J Virol* **74**, 1178–1186 (2000).

166. Straub, E., Fertey, J., Dreer, M., Iftner, T. & Stubenrauch, F. Characterization of the Human Papillomavirus 16 E8 Promoter. *J Virol* **89**, 7304–7313 (2015).

167. Kuehner F. & Stubenrauch F. Functions of Papillomavirus E8^E2 Proteins in Tissue Culture and In Vivo. *Viruses* **14**, 953–963 (2022).

168. Moody, C. A. & Laimins, L. A. Human papillomaviruses activate the ATM DNA damage pathway for viral genome amplification upon differentiation. *PLoS Pathog* **5**, (2009).

169. Hernandez-Alias, X., Benisty, H., Schaefer, M. H. & Serrano, L. Translational adaptation of human viruses to the tissues they infect. *Cell Rep* **34**, (2021).

170. Quint, K. D. *et al.* Human Beta-papillomavirus infection and keratinocyte carcinomas. *Journal of Pathology* **235**, 342–354 (2015).

171. Cerqueira, C., Samperio Ventayol, P., Vogeley, C. & Schelhaas, M. Kallikrein-8 Proteolytically Processes Human Papillomaviruses in the Extracellular Space To Facilitate Entry into Host Cells. *J Virol* **89**, 7038–7052 (2015).

172. Culp, T. D., Budgeon, L. R., Marinkovich, M. P., Meneguzzi, G. & Christensen, N. D. Keratinocyte-Secreted Laminin 5 Can Function as a Transient Receptor for Human Papillomaviruses by Binding Virions and Transferring Them to Adjacent Cells. *J Virol* **80**, 8940–8950 (2006).

173. Day, P. M. & Schelhaas, M. Concepts of papillomavirus entry into host cells. *Current Opinion in Virology* vol. 4 24–31 Preprint at https://doi.org/10.1016/j.coviro.2013.11.002 (2014).

174. Ozbun, M. A. & Campos, S. K. The long and winding road: human papillomavirus entry and subcellular trafficking. *Current Opinion in Virology* vol. 50 76–86 Preprint at https://doi.org/10.1016/j.coviro.2021.07.010 (2021).

175. Shafti-Keramat, S. *et al.* Different Heparan Sulfate Proteoglycans Serve asCellular Receptors for HumanPapillomaviruses. *J Virol* **77**, 13125–13135 (2003).

176. Taylor, J. R. *et al.* Heterotetrameric annexin A2/S100A10 (A2t) is essential for oncogenic human papillomavirus trafficking and capsid disassembly, and protects virions from lysosomal degradation. *Sci Rep* **8**, (2018).

177. Aksoy, P., Abban, C. Y., Kiyashka, E., Qiang, W. & Meneses, P. I. HPV16 infection of HaCaTs is dependent on β4 integrin, and α6 integrin processing. *Virology* **449**, 45–52 (2014).

178. Spoden, G. *et al.* Human Papillomavirus Types 16, 18, and 31 Share Similar Endocytic Requirements for Entry. *J Virol* **87**, 7765–7773 (2013).

179. Dziduszko, A. & Ozbun, M. A. Annexin A2 and S100A10 Regulate Human Papillomavirus Type 16 Entry and Intracellular Trafficking in Human Keratinocytes. *J Virol* **87**, 7502–7515 (2013).

180. Wüstenhagen, E. *et al.* The Cytoskeletal Adaptor Obscurin-Like 1 Interacts with the Human Papillomavirus 16 (HPV16) Capsid Protein L2 and Is Required for HPV16 Endocytosis. *J Virol* **90**, 10629–10641 (2016).

181. Schelhaas, M. *et al.* Entry of human papillomavirus type 16 by actin-dependent, clathrin- and lipid raft-independent endocytosis. *PLoS Pathog* **8**, (2012).

182. Bousarghin, L., Touzé, A., Sizaret, P.-Y. & Coursaget, P. Human Papillomavirus Types 16, 31, and 58 Use Different Endocytosis Pathways To Enter Cells. *J Virol* **77**, 3846–3850 (2003).

183. Xie, J., Zhang, P., Crite, M. & DiMaio, D. Papillomaviruses go retro. *Pathogens* vol. 9 Preprint at https://doi.org/10.3390/pathogens9040267 (2020).

184. Bienkowska-Haba, M., Williams, C., Kim, S. M., Garcea, R. L. & Sapp, M. Cyclophilins Facilitate Dissociation of the Human Papillomavirus Type 16 Capsid Protein L1 from the L2/DNA Complex following Virus Entry. *J Virol* **86**, 9875–9887 (2012).

185. Siddiqa, A., Broniarczyk, J. & Banks, L. Papillomaviruses and endocytic trafficking. *International Journal of Molecular Sciences* vol. 19 Preprint at https://doi.org/10.3390/ijms19092619 (2018).

186. Popa, A. *et al.* Direct Binding of Retromer to Human Papillomavirus Type 16 Minor Capsid Protein L2 Mediates Endosome Exit during Viral Infection. *PLoS Pathog* **11**, (2015).

187. Digiuseppe, S., Bienkowska-Haba, M., Guion, L. G. M., Keiffer, T. R. & Sapp, M. Human Papillomavirus Major Capsid Protein L1 Remains Associated with the Incoming Viral Genome throughout the Entry Process. *J Virol* **91**, 537–554 (2017).

188. McNally, K. E. *et al.* Retriever is a multiprotein complex for retromer-independent endosomal cargo recycling. *Nat Cell Biol* **19**, 1214–1225 (2017).

189. Bergant Marušič, M., Ozbun, M. A., Campos, S. K., Myers, M. P. & Banks, L. Human Papillomavirus L2 Facilitates Viral Escape from Late Endosomes via Sorting Nexin 17. *Traffic* **13**, 455–467 (2012).

190. Bergant, M., Peternel, Š., Pim, D., Broniarczyk, J. & Banks, L. Characterizing the spatio-temporal role of sorting nexin 17 in human papillomavirus trafficking. *Journal of General Virology* **98**, 715–725 (2017).

191. Aydin, I. *et al.* Large Scale RNAi Reveals the Requirement of Nuclear Envelope Breakdown for Nuclear Import of Human Papillomaviruses. *PLoS Pathog* **10**, (2014).

192. DiGiuseppe, S. *et al.* Incoming human papillomavirus type 16 genome resides in a vesicular compartment throughout mitosis. *Proc Natl Acad Sci U S A* **113**, 6289–6294 (2016).

193. Stepp, W. H., Meyers, J. M. & Mcbride, A. A. Sp100 Provides Intrinsic Immunity against Human Papillomavirus Infection. *mBio* **4**, (2013).

194. Moore, P. S. & Chang, Y. Why do viruses cause cancer? Highlights of the first century of human tumour virology. *Nature Reviews Cancer* vol. 10 878–889 Preprint at https://doi.org/10.1038/nrc2961 (2010).

195. Coursey, T. L. & McBride, A. A. Hitchhiking of Viral Genomes on Cellular Chromosomes. *Annu Rev Virol* **6**, 275–296 (2019).

196. McKinney, C. C., Kim, M. J., Chen, D. & McBride, A. A. Brd4 activates early viral transcription upon human papillomavirus 18 infection of primary keratinocytes. *mBio* **7**, (2016).

197. Sanders, C. M. & Stenlund, A. *Recruitment and loading of the E1 initiator protein: an ATP-dependent process catalysed by a transcription factor*. *The EMBO Journal* vol. 17 (1998).

198. Gauson, E. J. *et al.* Evidence Supporting a Role for TopBP1 and Brd4 in the Initiation but Not Continuation of Human Papillomavirus 16 E1/E2-Mediated DNA Replication. *J Virol* **89**, 4980–4991 (2015).

199. Dreer, M., van de Poel, S. & Stubenrauch, F. Control of viral replication and transcription by the papillomavirus E8^E2 protein. *Virus Research* vol. 231 96–102 Preprint at https://doi.org/10.1016/j.virusres.2016.11.005 (2017).

200. Dreer, M. *et al.* Interaction of NCOR/SMRT Repressor Complexes with Papillomavirus E8^E2C Proteins Inhibits Viral Replication. *PLoS Pathog* **12**, (2016).

201. Ilves, I., Kivi, S. & Ustav, M. *Long-Term Episomal Maintenance of Bovine Papillomavirus Type 1 Plasmids Is Determined by Attachment to Host Chromosomes, Which Is Mediated by the Viral E2 Protein and Its Binding Sites*. *JOURNAL OF VIROLOGY* vol. 73 (1999).

202. Cardenas-Mora, J., Spindler, J. E., Jang, M. K. & McBride, A. A. Dimerization of the Papillomavirus E2 Protein Is Required for Efficient Mitotic Chromosome Association and Brd4 Binding. *J Virol* **82**, 7298–7305 (2008).

203. Bentley, P., Tan, M. J. A., McBride, A. A., White, E. A. & Howley, P. M. The SMC5/6 Complex Interacts with the Papillomavirus E2 Protein and Influences Maintenance of Viral Episomal DNA. *J Virol* **92**, (2018).

204. Thomas, J. T., Hubert, W. G., Ruesch, M. N. & Laimins, L. A. *Human papillomavirus type 31 oncoproteins E6 and E7 are required for the maintenance of episomes during the viral life cycle in normal human keratinocytes*. *Biochemistry* vol. 96 www.pnas.org. (1999).

205. Lorenz, L. D., Rivera Cardona, J. & Lambert, P. F. Inactivation of p53 Rescues the Maintenance of High Risk HPV DNA Genomes Deficient in Expression of E6. *PLoS Pathog* **9**, (2013).

206. Maglennon, G. A., McIntosh, P. & Doorbar, J. Persistence of viral DNA in the epithelial basal layer suggests a model for papillomavirus latency following immune regression. *Virology* **414**, 153–163 (2011).

207. Fehrmann, F., Klumpp, D. J. & Laimins, L. A. Human Papillomavirus Type 31 E5 Protein Supports Cell Cycle Progression and Activates Late Viral Functions upon Epithelial Differentiation. *J Virol* **77**, 2819–2831 (2003).

208. Klumpp, D. J. & Laimins, L. A. Differentiation-Induced Changes in Promoter Usage for Transcripts Encoding the Human Papillomavirus Type 31 Replication Protein E1. *Virology* **257**, 239–246 (1999).

209. Zhou, J. *et al. Identification of the Nuclear Localization Signal of Human Papillomavirus Type 16 l-1 Protein*. *VIROLOGY* vol. 185 (1991).

210. Bird, G., O'Donnell, M., Moroianu, J. & Garcea, R. L. Possible Role for Cellular Karyopherins in Regulating Polyomavirus and Papillomavirus Capsid Assembly. *J Virol* **82**, 9848–9857 (2008).

211. Florin, L. *et al.* Nuclear Translocation of Papillomavirus Minor Capsid Protein L2 Requires Hsc70. *J Virol* **78**, 5546–5553 (2004).

212. Marušič, M. B., Mencin, N., Ličen, M., Banks, L. & Grm, H. Š. Modification of Human Papillomavirus Minor Capsid Protein L2 by Sumoylation. *J Virol* **84**, 11585–11589 (2010).

213. Day, P. M., Thompson, C. D., Pang, Y. Y., Lowy, D. R. & Schiller, J. T. Involvement of nucleophosmin (NPM1/B23) in assembly of infectious HPV16 capsids. *Papillomavirus Research* **1**, 74–89 (2015).

214. TouzÃ©, A. *et al.* The nine C-terminal amino acids of the major capsid protein of the human papillomavirus type 16 are essential for DNA binding and gene transfer capacity. *FEMS Microbiol Lett* **189**, 121–127 (2000).

215. Mehdaoui, S. EL *et al. Gene Transfer Using Recombinant Rabbit Hemorrhagic Disease Virus Capsids with Genetically Modified DNA Encapsidation Capacity by Addition of Packaging Sequences from the L1 or L2 Protein of Human Papillomavirus Type 16*. *JOURNAL OF VIROLOGY* vol. 74 (2000).

216. Buck, C. B., Pastrana, D. V., Lowy, D. R. & Schiller, J. T. Efficient Intracellular Assembly of Papillomaviral Vectors. *J Virol* **78**, 751–757 (2004).

217. Cerqueira, C. *et al.* A Cell-Free Assembly System for Generating Infectious Human Papillomavirus 16 Capsids Implicates a Size Discrimination Mechanism for Preferential Viral Genome Packaging. *J Virol* **90**, 1096–1107 (2016).

218. Cerqueira, C. & Schiller, J. T. Papillomavirus assembly: An overview and perspectives. *Virus Research* vol. 231 103–107 Preprint at https://doi.org/10.1016/j.virusres.2016.11.010 (2017).

219. Conway, M. J. *et al.* Tissue-Spanning Redox Gradient-Dependent Assembly of Native Human Papillomavirus Type 16 Virions. *J Virol* **83**, 10515–10526 (2009).

220. Buck, C. B., Thompson, C. D., Pang, Y.-Y. S., Lowy, D. R. & Schiller, J. T. Maturation of Papillomavirus Capsids. *J Virol* **79**, 2839–2846 (2005).

221. Brown, D. R. *et al.* The human papillomavirus type 11 E1ΛE4 protein is a transglutaminase 3 substrate and induces abnormalities of the cornified cell envelope. *Virology* **345**, 290–298 (2006).

222. IARC Working Group on the Evaluation of Carcinogenic Risks to Humans. *Biological agents, a review of human carcinogens*. *IARC monographs on the evaluation of carcinogenic risks to humans* vol. 100 (B) (World Health Organization, 2012).

223. Sung, H. *et al.* Global Cancer Statistics 2020: GLOBOCAN Estimates of Incidence and Mortality Worldwide for 36 Cancers in 185 Countries. *CA Cancer J Clin* **71**, 209–249 (2021).

224. Bruyere, D. *et al.* Treatment algorithm and prognostic factors for patients with stage I–III carcinoma of the anal canal: a 20-year multicenter study. *Modern Pathology* **34**, 116–130 (2021).

225. de Martel, C., Georges, D., Bray, F., Ferlay, J. & Clifford, G. M. Global burden of cancer attributable to infections in 2018: a worldwide incidence analysis. *Lancet Glob Health* **8**, e180–e190 (2020).

226. Dell'Oste, V. *et al.* High β-HPV DNA loads and strong seroreactivity are present in epidermodysplasia verruciformis. *Journal of Investigative Dermatology* **129**, 1026–1034 (2009).

227. Lindelo È F, B., Sigurgeirsson, B., Ga, H., Bel[2], È. & Stern[3], R. S. *Incidence of skin cancer in 5356 patients following organ transplantation*. *British Journal of Dermatology* vol. 143 (2000).

228. Harwood, C. A. *et al. Human Papillomavirus Infection and Non-Melanoma Skin Cancer in Immunosuppressed and Immunocompetent Individuals*. *J. Med. Virol* vol. 61 (2000).

229. Galati, L. *et al.* Detection of human papillomaviruses in paired healthy skin and actinic keratosis by next generation sequencing. *Papillomavirus Research* **9**, (2020).

230. Donà, M. G. *et al.* Comprehensive analysis of β- and γ-human papillomaviruses in actinic keratosis and apparently healthy skin of elderly patients. *British Journal of Dermatology* vol. 181 620–622 Preprint at https://doi.org/10.1111/bjd.17836 (2019).

231. Weissenborn, S. J. *et al.* Human papillomavirus-DNA loads in actinic keratoses exceed those in non-melanoma skin cancers. *Journal of Investigative Dermatology* **125**, 93–97 (2005).

232. Viarisio, D. *et al.* Beta HPV38 oncoproteins act with a hit-and-run mechanism in ultraviolet radiation-induced skin carcinogenesis in mice. *PLoS Pathog* **14**, (2018).

233. Narayanan, D. L., Saladi, R. N. & Fox, J. L. Ultraviolet radiation and skin cancer. *International Journal of Dermatology* vol. 49 978–986 Preprint at https://doi.org/10.1111/j.1365-4632.2010.04474.x (2010).

234. WHO. Ultraviolet radiation. https://www.who.int/news-room/fact-sheets/detail/ultraviolet-radiation (2022).

235. De Gruijl, F. R. Photocarcinogenesis: UVA vs. UVB Radiation. *Skin Pharmacol Appl Skin Physiol* **15**, 316–320 (2002).

236. De Gruijl F. Photocarcinogenesis- UVA vs UVB. in *methods in enzymology* vol. 319 359–366 (2000).

237. Halliday, G. M., Damian, D. L., Rana, S. & Byrne, S. N. The suppressive effects of ultraviolet radiation on immunity in the skin and internal organs: Implications for autoimmunity. *Journal of Dermatological Science* vol. 66 176–182 Preprint at https://doi.org/10.1016/j.jdermsci.2011.12.009 (2012).

238. De Gruijl, F. R., Van Kranen, H. J. & Mullenders, L. H. F. *UV-induced DNA damage, repair, mutations and oncogenic pathways in skin cancer*. *Journal of Photochemistry and Photobiology B: Biology* vol. 63 www.elsevier.com/locate/jphotobiol (2001).

239. Watson, M., Holman, D. M. & Maguire-Eisen, M. Ultraviolet Radiation Exposure and Its Impact on Skin Cancer Risk. *Seminars in Oncology Nursing* vol. 32 241–254 Preprint at https://doi.org/10.1016/j.soncn.2016.05.005 (2016).

240. WHO. Radiation: Ultraviolet (UV) radiation. https://www.who.int/news-room/questions-and-answers/item/radiation-ultraviolet-(uv) (2016).

241. Haigh, J. D. The Sun and the Earth's Climate Living Reviews in Solar Physics. *Living Rev. Solar Phys* **4**, (2007).

242. Kripke, M. L. Impact of Ozone Depletion on Skin Cancers. *J Dermatol Surg Oncol* **14**, 853–857 (1988).

243. Lautenschlager, S., Wulf, H. C. & Pittelkow, M. R. Photoprotection. *www.thelancet.com* **370**, (2007).

244. Hill D, White V, Marks R & Borland R. Changes in sun-related attitudes and behaviours, and reduced sunburn prevalence in a population at high risk of melanoma. *European Journal of Cancer Prevention* **2**, 447–456 (1993).

245. WHO. Radiation: Ultraviolet (UV) radiation and skin cancer. https://www.who.int/news-room/questions-and-answers/item/radiation-ultraviolet-(uv)-radiation-and-skin-cancer#:~:text=The%20incidence%20of%20malignant%20melanoma,for%20women%20and%20men%20respectively. (2017).

246. D'Orazio, J., Jarrett, S., Amaro-Ortiz, A. & Scott, T. UV radiation and the skin. *International Journal of Molecular Sciences* vol. 14 12222–12248 Preprint at https://doi.org/10.3390/ijms140612222 (2013).

247. Whiteman, D. C., Whiteman, C. A., Adeá, & & Green, L. C. Childhood sun exposure as a risk factor for melanoma: a systematic review of epidemiologic studies. *Cancer Causes and Control* **12**, 69–82 (2001).

248. Glanz, K., Buller, D. B. & Saraiya, M. Reducing ultraviolet radiation exposure among outdoor workers: State of the evidence and recommendations. *Environmental Health: A Global Access Science Source* vol. 6 Preprint at https://doi.org/10.1186/1476-069X-6-22 (2007).

249. Perdiz, D. *et al.* Distribution and repair of bipyrimidine photoproducts in solar UV-irradiated mammalian cells: Possible role of dewar photoproducts in solar mutagenesis. *Journal of Biological Chemistry* **275**, 26732–26742 (2000).

250. Courdavault, S. *et al.* Larger yield of cyclobutane dimers than 8-oxo-7,8-dihydroguanine in the DNA of UVA-irradiated human skin cells. *Mutation Research - Fundamental and Molecular Mechanisms of Mutagenesis* **556**, 135–142 (2004).

251. Douki, T., Reynaud-Angelin, A., Cadet, J. & Sage, E. Bipyrimidine photoproducts rather than oxidative lesions are the main type of DNA damage involved in the genotoxic effect of solar UVA radiation. *Biochemistry* **42**, 9221–9226 (2003).

252. Sinha, R. P. & Häder, D. P. UV-induced DNA damage and repair: A review. *Photochemical and Photobiological Sciences* **1**, 225–236 (2002).

253. Douki, T. & Cadet, J. Individual determination of the yield of the main UV-induced dimeric pyrimidine photoproducts in DNA suggests a high mutagenicity of CC photolesions. *Biochemistry* **40**, 2495–2501 (2001).

254. Rastogi, R. P., Richa, Kumar, A., Tyagi, M. B. & Sinha, R. P. Molecular mechanisms of ultraviolet radiation-induced DNA damage and repair. *Journal of Nucleic Acids* vol. 2010 Preprint at https://doi.org/10.4061/2010/592980 (2010).

255. Kimi, J. & Patel, D. Contrasting structural impacts induced by cis-syn cyclobutane dimer and (6-4) adduct in dna duplex decamers: implication in mutagenesis and repair activity. *Photochem Photobiol* **62**, 44–50 (1995).

256. Sugasawa, K. Regulation of damage recognition in mammalian global genomic nucleotide excision repair. *Mutation Research - Fundamental and Molecular Mechanisms of Mutagenesis* vol. 685 29–37 Preprint at https://doi.org/10.1016/j.mrfmmm.2009.08.004 (2010).

257. Thomas, D. C., Okumoto, D. S., Sancar, A. & Bohr, V. A. Preferential DNA repair of (6-4) photoproducts in the dihydrofolate reductase gene of Chinese hamster ovary cells. *Journal of Biological Chemistry* **264**, 18005–18010 (1989).

258. Lee, J. H., Hwang, G. S., Kim, J. K. & Choi, B. S. The solution structure of DNA decamer duplex containing the Dewar product of thymidylyl(3' → 5')thymidine by NMR and full relaxation matrix refinement. *FEBS Lett* **428**, 269–274 (1998).

259. Yamamoto, J., Hitomi, K., Todo, T. & Iwai, S. Chemical synthesis of oligodeoxyribonucleotides containing the Dewar valence isomer of the (6-4) photoproduct and their use in (6-4) photolyase studies. *Nucleic Acids Res* **34**, 4406–4415 (2006).

260. Voituriez, J. *et al. Nuclear Magnetic Resonance Studies of Cis-Syn, Trans-Syn, and 6-4 Photodimers of Thymidylyl(3'-5')thymidine Monophosphate and Cis-Syn Photodimers of Thymidylyl(3'-5')thymidine Cyanoethyl Phosphotriestert*. *Biochemistry* vol. 27 (1988).

261. Pearlman, D. A., Holbrook, S. R., Pirkle, D. H. & Kim, S.-H. Molecular Models for DNA Damaged by Photoreaction Holbrook is a staff scientist in the. *Science (1979)* **227**, 1304–1308 (1984).

262. Turrens, J. F. Mitochondrial formation of reactive oxygen species. *Journal of Physiology* vol. 552 335–344 Preprint at https://doi.org/10.1113/jphysiol.2003.049478 (2003).

263. Bhattacharyya, A., Chattopadhyay, R., Mitra, S. & Crowe, S. E. Oxidative Stress: An Essential Factor in the Pathogenesis of Gastrointestinal Mucosal Diseases. *Physiol Rev* **94**, 329–354 (2014).

264. Novo, E. & Parola, M. Redox mechanisms in hepatic chronic wound healing and fibrogenesis. *Fibrogenesis and Tissue Repair* vol. 1 Preprint at https://doi.org/10.1186/1755-1536-1-5 (2008).

265. Cadenas, E. & Davies, K. J. A. Mitochondrial Free Radical Generation, Oxidative Stress, And Aging. *Free Radic Biol Med* **29**, 222–230 (2000).

266. Halliwell B & Gutteridge J.M.C. *Free Radicals in Biology and Medicine*. (Oxford University Press, 2015).

267. Lambeth J.D. Nox Enzymes, ROS, and Chronic Disease: An Example ofAntagonistic Pleiotropy. *Free Radic Biol Med.* **43**, 332–347 (2007).

268. De Minicis, S. & Brenner, D. A. NOX in liver fibrosis. *Archives of Biochemistry and Biophysics* vol. 462 266–272 Preprint at https://doi.org/10.1016/j.abb.2007.04.016 (2007).

269. Bedard, K. & Krause, K.-H. The NOX Family of ROS-Generating NADPH Oxidases: Physiology and Pathophysiology. *Physiol Rev* **87**, 245–313 (2007).

270. Vignais, P. V. *The superoxide-generating NADPH oxidase: structural aspects and activation mechanism*. *CMLS, Cell. Mol. Life Sci* vol. 59 http://www.ncbi.nlm.nih.gov (2002).

271. Lambeth, J. D. NOX enzymes and the biology of reactive oxygen. *Nature Reviews Immunology* vol. 4 181–189 Preprint at https://doi.org/10.1038/nri1312 (2004).

272. Bossi, O. *et al.* UV irradiation increases ROS production via PKCδ signaling in primary murine fibroblasts. *J Cell Biochem* **105**, 194–207 (2008).

273. Ray, A. J., Turner, R., Nikaido, O., Rees, J. L. & Birch-Machin, M. A. The Spectrum of Mitochondrial DNA Deletions is a Ubiquitous Marker of Ultraviolet Radiation Exposure in Human Skin. *J Invest Dermatol* **115**, 674–679 (2000).

274. Kimeswenger, S. *et al.* Infrared A radiation promotes survival of human melanocytes carrying ultraviolet radiation-induced DNA damage. *Exp Dermatol* **25**, 447–452 (2016).

275. Wei, H., Cai, Q., Rahn, R. & Zhang, X. SINGLET OXYGEN INVOLVEMENT IN ULTRAVIOLET (254 NM) RADIATION-INDUCED FORMATION OF 8-HYDROXY-DEOXYGUANOSINE IN DNA. *Free Dacidal Biology & Medicine* **23**, 148–154 (1997).

276. Cui, J. *et al.* Acetaldehyde induces neurotoxicity in vitro via oxidative stress- And Ca2+ imbalance-mediated endoplasmic reticulum stress. *Oxid Med Cell Longev* **2019**, (2019).

277. Wu, D. & Cederbaum, A. I. Alcohol, Oxidative Stress, and Free Radical Damage. *Alcohol Research & Health* **27**, 277–284 (2003).

278. Baker, R. R., Massey, E. D. & Smith, G. An overview of the effects of tobacco ingredients on smoke chemistry and toxicity. *Food and Chemical Toxicology* **42**, 53–83 (2004).

279. Goel, R. *et al.* Highly Reactive Free Radicals in Electronic Cigarette Aerosols. *Chem Res Toxicol* **28**, 1675–1677 (2015).

280. Görlach, A. *et al.* Reactive oxygen species, nutrition, hypoxia and diseases: Problems solved? *Redox Biology* vol. 6 372–385 Preprint at https://doi.org/10.1016/j.redox.2015.08.016 (2015).

281. Jiang, S., Liu, H. & Li, C. Dietary Regulation of Oxidative Stress in Chronic Metabolic Diseases. *Foods* **10**, 1854 (2021).

282. Herb, M., Gluschko, A. & Schramm, M. Reactive Oxygen Species: Not Omnipresent but Important in Many Locations. *Front Cell Dev Biol* **9**, (2021).

283. Devasagayam TPA *et al.* Free Radicals and Antioxidants in Human Health: Current Status and Future Prospects. *Journal of The Association of Physicians of India* **52**, (2004).

284. Gligorovski, S., Strekowski, R., Barbati, S. & Vione, D. Environmental Implications of Hydroxyl Radicals (•OH). *Chem Rev* **115**, 13051–13092 (2015).

285. Mitra, S. *et al.* Impact of ROS generated by chemical, physical, and plasma techniques on cancer attenuation. *Cancers* vol. 11 Preprint at https://doi.org/10.3390/cancers11071030 (2019).

286. Kehrer, J. P. & Klotz, L. O. Free radicals and related reactive species as mediators of tissue injury and disease: Implications for Health. *Crit Rev Toxicol* **45**, 765–798 (2015).

287. Ighodaro, O. M. & Akinloye, O. A. First line defence antioxidants-superoxide dismutase (SOD), catalase (CAT) and glutathione peroxidase (GPX): Their fundamental role in the entire antioxidant defence grid. *Alexandria Journal of Medicine* **54**, 287–293 (2018).

288. Milkovic, L., Gasparovic, A. C., Cindric, M., Mouthuy, P. A. & Zarkovic, N. Short overview of ROS as cell function regulators and their implications in therapy concepts. *Cells* vol. 8 Preprint at https://doi.org/10.3390/cells8080793 (2019).

289. Ohno, M., Oka, S. & Nakabeppu, Y. Quantitative analysis of oxidized guanine, 8-oxoguanine, in mitochondrial DNA by immunofluorescence method. *Methods Mol Biol* **554**, 199–212 (2009).

290. Sample, A. & He, Y. Y. Mechanisms and prevention of UV-induced melanoma. *Photodermatology Photoimmunology and Photomedicine* vol. 34 13–24 Preprint at https://doi.org/10.1111/phpp.12329 (2018).

291. Houtgraaf, J. H., Versmissen, J. & van der Giessen, W. J. A concise review of DNA damage checkpoints and repair in mammalian cells. *Cardiovascular Revascularization Medicine* **7**, 165–172 (2006).

292. Zou, L. & Elledge, S. J. Sensing DNA damage through ATRIP recognition of RPA-ssDNA complexes. *Science (1979)* **300**, 1542–1548 (2003).

293. Mordes, D. A., Glick, G. G., Zhao, R. & Cortez, D. TopBP1 activates ATR through ATRIP and a PIKK regulatory domain. *Genes Dev* **22**, 1478–1489 (2008).

294. Delacroix, S., Wagner, J. M., Kobayashi, M., Yamamoto, K. I. & Karnitz, L. M. The Rad9-Hus1-Rad1 (9-1-1) clamp activates checkpoint signaling via TopBP1. *Genes Dev* **21**, 1472–1477 (2007).

295. Liu, S., Song, N. & Zou, L. The conserved C terminus of Claspin interacts with Rad9 and promotes rapid activation of Chk1. *Cell Cycle* **11**, 2711–2716 (2012).

296. Tibbetts, R. S. *et al.* A role for ATR in the DNA damage-induced phosphorylation of p53. *Genes Dev* **13**, 152–157 (1999).

297. Uziel T *et al.* Requirement of the MRN complex for ATM activation by DNA damage. *EMBO J* **22**, 5612–5621 (2003).

298. Bakkenist, C. J. & Kastan, M. B. DNA damage activates ATM through intermolecular autophosphorylation and dimer dissociation. *Nature* **421**, 499–506 (2003).

299. Cortez D, Wang Y, Qin J & Elledge S.J. Requirement of ATM-dependent phosphorylation of brca1 in the DNA damage response to double-strand breaks. *Science (1979)* **286**, 1162–1166 (1999).

300. Fradet-Turcotte, A. *et al.* 53BP1 is a reader of the DNA-damage-induced H2A Lys 15 ubiquitin mark. *Nature* **499**, 50–54 (2013).

301. Banin, S. *et al. Enhanced Phosphorylation of p53 by ATM in Response to DNA Damage*. *New Series* vol. 281 (1998).

302. Kciuk, M., Gielecińska, A., Mujwar, S., Mojzych, M. & Kontek, R. Cyclin-dependent kinases in DNA damage response. *Biochimica et Biophysica Acta - Reviews on Cancer* vol. 1877 Preprint at https://doi.org/10.1016/j.bbcan.2022.188716 (2022).

303. Sugasawa, K. Molecular mechanisms of DNA damage recognition for mammalian nucleotide excision repair. *DNA Repair* vol. 44 110–117 Preprint at https://doi.org/10.1016/j.dnarep.2016.05.015 (2016).

304. Marteijn, J. A., Lans, H., Vermeulen, W. & Hoeijmakers, J. H. J. Understanding nucleotide excision repair and its roles in cancer and ageing. *Nature Reviews Molecular Cell Biology* vol. 15 465–481 Preprint at https://doi.org/10.1038/nrm3822 (2014).

305. Kusakabe, M. *et al.* Mechanism and regulation of DNA damage recognition in nucleotide excision repair. *Genes and Environment* **41**, (2019).

306. Sugasawa, K. UV-induced ubiquitylation of XPC complex, the UV-DDB-ubiquitin ligase complex, and DNA repair. *Journal of Molecular Histology* vol. 37 189–202 Preprint at https://doi.org/10.1007/s10735-006-9044-7 (2006).

307. Gillet, L. C. J. & Schärer, O. D. Molecular mechanisms of mammalian global genome nucleotide excision repair. *Chemical Reviews* vol. 106 253–276 Preprint at https://doi.org/10.1021/cr040483f (2006).

308. Duan, M., Speer, R. M., Ulibarri, J., Liu, K. J. & Mao, P. Transcription-coupled nucleotide excision repair: New insights revealed by genomic approaches. *DNA Repair (Amst)* **103**, (2021).

309. Fousteri, M. & Mullenders, L. H. F. Transcription-coupled nucleotide excision repair in mammalian cells: Molecular mechanisms and biological effects. *Cell Research* vol. 18 73–84 Preprint at https://doi.org/10.1038/cr.2008.6 (2008).

310. Greber, B. J., Toso, D. B., Fang, J. & Nogales, E. The complete structure of the human TFIIH core complex. *Elife* **8**, 1–29 (2019).

311. Sugitani, N., Sivley, R. M., Perry, K. E., Capra, J. A. & Chazin, W. J. XPA: A key scaffold for human nucleotide excision repair. *DNA Repair* vol. 44 123–135 Preprint at https://doi.org/10.1016/j.dnarep.2016.05.018 (2016).

312. Fuss, J. O. & Tainer, J. A. XPB and XPD helicases in TFIIH orchestrate DNA duplex opening and damage verification to coordinate repair with transcription and cell cycle via CAK kinase. *DNA Repair* vol. 10 697–713 Preprint at https://doi.org/10.1016/j.dnarep.2011.04.028 (2011).

313. Hirose, Y. & Ohkuma, Y. Phosphorylation of the C-terminal domain of RNA polymerase II plays central roles in the integrated events of eucaryotic gene expression. *Journal of Biochemistry* vol. 141 601–608 Preprint at https://doi.org/10.1093/jb/mvm090 (2007).

314. Muniesa-Vargas, A., Theil, A. F., Ribeiro-Silva, C., Vermeulen, W. & Lans, H. XPG: a multitasking genome caretaker. *Cellular and Molecular Life Sciences* vol. 79 Preprint at https://doi.org/10.1007/s00018-022-04194-5 (2022).

315. Faridounnia, M., Folkers, G. E. & Boelens, R. Function and interactions of ERCC1-XPF in DNA damage response. *Molecules* vol. 23 Preprint at https://doi.org/10.3390/molecules23123205 (2018).

316. Lehmann, A. R. DNA polymerases and repair synthesis in NER in human cells. *DNA Repair* vol. 10 730–733 Preprint at https://doi.org/10.1016/j.dnarep.2011.04.023 (2011).

317. Paul-Konietzko, K., Thomale, J., Arakawa, H. & Iliakis, G. DNA Ligases I and III Support Nucleotide Excision Repair in DT40 Cells with Similar Efficiency. *Photochem Photobiol* **91**, 1173–1180 (2015).

318. Izumi, T. & Mellon, I. Base Excision Repair and Nucleotide Excision Repair. in *Genome Stability* 275–302 (Elsevier Inc., 2016). doi:10.1016/B978-0-12-803309-8.00017-3.

319. D'andrea alan D. DNA Repair Pathways and Human Cancer. in *The Molecular Basis of Cancer* vol. 4 47–66 (2015).

320. Carter, R. J. & Parsons, J. L. Base Excision Repair, a Pathway Regulated by Posttranslational Modifications. *Mol Cell Biol* **36**, 1426–1437 (2016).

321. Jacobs, A. L. & Schär, P. DNA glycosylases: In DNA repair and beyond. *Chromosoma* vol. 121 1–20 Preprint at https://doi.org/10.1007/s00412-011-0347-4 (2012).

322. Berti, P. J. & McCann, J. A. B. Toward a detailed understanding of base excision repair enzymes: Transition state and mechanistic analyses of N-glycoside hydrolysis and N-glycoside transfer. *Chemical Reviews* vol. 106 506–555 Preprint at https://doi.org/10.1021/cr040461t (2006).

323. Krokan, H. E. & Bjørås, M. Base excision repair. *Cold Spring Harb Perspect Biol* **5**, 1–22 (2013).

324. Parsons, J. L. & Grundy, G. J. The Base Excision Repair (BER) Pathway. in *Encyclopedia of Cell Biology (Second Edition)* vol. 1 541–551 (Elsevier, 2023).

325. Sobol, R. W. & Wilson, S. H. Mammalian DNA ,8-Polymerase in Base Excision Repair of Alkylation Damage. *Nucleic Acid Research and Molecular Biology* **68**, 57–74 (2001).

326. Nash, R. A., Caldecott, K. W., Barnes, D. E. & Lindahl, T. XRCC1 Protein Interacts with One of Two Distinct Forms of DNA Ligase III. *Biochemistry* **36**, 5207–5211 (1997).

327. Robertson, A. B., Klungland, A., Rognes, T. & Leiros, I. Base excision repair: The long and short of it. *Cellular and Molecular Life Sciences* vol. 66 981–993 Preprint at https://doi.org/10.1007/s00018-009-8736-z (2009).

328. Sattler, U., Frit, P., Salles, B. & Calsou, P. Long-patch DNA repair synthesis during base excision repair in mammalian cells. *EMBO Rep* **4**, 363–367 (2003).

329. Fortini, P. & Dogliotti, E. Base damage and single-strand break repair: Mechanisms and functional significance of short- and long-patch repair subpathways. *DNA Repair (Amst)* **6**, 398–409 (2007).

330. Matsumura, Y. & Ananthaswamy, H. N. Toxic effects of ultraviolet radiation on the skin. *Toxicology and Applied Pharmacology* vol. 195 298–308 Preprint at https://doi.org/10.1016/j.taap.2003.08.019 (2004).

331. Shenoi, S. & Prabhu, S. Photochemotherapy (PUVA) in psoriasis and vitiligo. *Indian J Dermatol Venereol Leprol* **80**, 497–504 (2014).

332. Clydesdale, G. J., Dandie, G. W. & Muller, H. K. Ultraviolet light induced injury: Immunological and inflammatory effects. *Immunology and Cell Biology* vol. 79 547–568 Preprint at https://doi.org/10.1046/j.1440-1711.2001.01047.x (2001).

333. Spiekstra, S. W., Breetveld, M., Rustemeyer, T., Scheper, R. J. & Gibbs, S. Wound-healing factors secreted by epidermal keratinocytes and dermal fibroblasts in skin substitutes. *Wound Repair and Regeneration* **15**, 708–717 (2007).

334. Huang, A. H. & Chien, A. L. Photoaging: a Review of Current Literature. *Current Dermatology Reports* vol. 9 22–29 Preprint at https://doi.org/10.1007/s13671-020-00288-0 (2020).

335. Coelho, S. G. *et al.* Short- and long-term effects of UV radiation on the pigmentation of human skin. in *Journal of Investigative Dermatology Symposium Proceedings* vol. 14 32–35 (Nature Publishing Group, 2009).

336. Schade, N., Esser, C. & Krutmann, J. Ultraviolet B radiation-induced immunosuppression: Molecular mechanisms and cellular alterations. *Photochemical and Photobiological Sciences* **4**, 699–708 (2005).

337. De Villiers E-M. Human papillomavirus infections in skin cancers. *Biomed and Pharmacother* **52**, 26–33 (1998).

338. Armstrong B.K & Kricker A. How much melanoma is caused by sun exposure. *Melanoma Res* **3**, 395–401 (1993).

339. Pickering, C. R. *et al.* Mutational landscape of aggressive cutaneous squamous cell carcinoma. *Clinical Cancer Research* **20**, 6582–6592 (2014).

340. De Gruijl F. Photocarcinogenesis UVA vs UVB. *Methods in Enzymology* **319**, 359–366 (2000).

341. Leiter U, Keim U & Garbe C. Epidemiology of Skin Cancer: Update 2019. in *Sunlight, Vitamin D and Skin Cancer* vol. 3 123–139 (2020).

342. Schmitt, J., Seidler, A., Diepgen, T. L. & Bauer, A. Occupational ultraviolet light exposure increases the risk for the development of cutaneous squamous cell carcinoma: A systematic review and meta-analysis. *British Journal of Dermatology* vol. 164 291–307 Preprint at https://doi.org/10.1111/j.1365-2133.2010.10118.x (2011).

343. Zghal, M., Fazaa, B., Abdelhak, S. & Mokni, M. Xeroderma pigmentosum. *Annales de Dermatologie et de Venereologie* vol. 145 706–722 Preprint at https://doi.org/10.1016/j.annder.2018.09.004 (2018).

344. Natale, V. & Raquer, H. Xeroderma pigmentosum-Cockayne syndrome complex. *Orphanet Journal of Rare Diseases* vol. 12 Preprint at https://doi.org/10.1186/s13023-017-0616-2 (2017).

345. Stefanini, M., Botta, E., Lanzafame, M. & Orioli, D. Trichothiodystrophy: From basic mechanisms to clinical implications. *DNA Repair* vol. 9 2–10 Preprint at https://doi.org/10.1016/j.dnarep.2009.10.005 (2010).

346. Ferrándiz, C. *et al. Precancerous Skin Lesions*. *Actas Dermosifiliogr* vol. 108 (2017).

347. Daya-Grosjean, L. Xeroderma Pigmentosum and Skin Cancer. in *Molecular Mechanisms of Xeroderma Pigmentosum* (eds. Ahmad S.I. & Hanaoka F) 19–27 (2008).

348. Abeti, R. *et al.* Xeroderma pigmentosum: overview of pharmacology and novel therapeutic strategies for neurological symptoms. *British Journal of Pharmacology* vol. 176 4293–4301 Preprint at https://doi.org/10.1111/bph.14557 (2019).

349. Friedberg, E. C. The discovery that xeroderma pigmentosum (XP) results from defective nucleotide excision repair. *DNA Repair (Amst)* **3**, 183–195 (2004).

350. Taylor, A. M. R. Neurodegeneration in xeroderma pigmentosum. *Brain* vol. 131 1967–1968 Preprint at https://doi.org/10.1093/brain/awn153 (2008).

351. Bradford, P. T. *et al.* Cancer and neurologic degeneration in xeroderma pigmentosum: Long term follow-up characterises the role of DNA repair. *J Med Genet* **48**, 168–176 (2011).

352. Leung, A. K. C., Barankin, B., Lam, J. M., Leong, K. F. & Hon, K. L. Xeroderma pigmentosum: An updated review. *Drugs Context* **11**, (2022).

353. Lehmann, A. R., McGibbon, D. & Stefanini, M. Xeroderma pigmentosum. *Orphanet J Rare Dis* **6**, (2011).

354. Bang, E. *et al.* Lentigo maligna in a patient with xeroderma pigmentosum, variant type: A case report with dermoscopic findings and review of the literature. *Photodermatology Photoimmunology and Photomedicine* vol. 36 401–404 Preprint at https://doi.org/10.1111/phpp.12568 (2020).

355. Tamura, D., Digiovanna, J. J., Khan, S. G. & Kraemer, K. H. Living with xeroderma pigmentosum: Comprehensive photoprotection for highly photosensitive patients. *Photodermatol Photoimmunol Photomed* **30**, 146–152 (2014).

356. Black, J. O. Xeroderma Pigmentosum. *Head Neck Pathol* **10**, 139–144 (2016).

357. Schelini, M. C. *et al.* Xeroderma Pigmentosum: Ocular Findings in an Isolated Brazilian Group with an Identified Genetic Cluster. *Journal of Opthalmology* 1–8 (2019).

358. Lim, R., Sethi, M. & Morley, A. M. S. Ophthalmic Manifestations of Xeroderma Pigmentosum: A Perspective from the United Kingdom. in *Ophthalmology* vol. 124 1652–1661 (Elsevier Inc., 2017).

359. Salomão, R. P. A., Pedroso, J. L. & Barsottini, O. G. P. Neurological manifestations of xeroderma pigmentosum due to XPA gene mutation. *Pract Neurol* **18**, 489–491 (2018).

360. Adam, M. P., Mirzaa, G. M. & Pagon, R. A. *Xeroderma Pigmentosum*. (2003).

361. Lucero R & Horowitz D. Xeroderma pigmentosum. *StatPearls* https://www.ncbi.nlm.nih.gov/books/NBK551563/ (2022).

362. Faria Licarião Rocha, L. K. *et al.* Dermoscopic features of 61 skin lesions in xeroderma pigmentosum patients: A cross-sectional study. *J Am Acad Dermatol* **86**, 1361–1362 (2022).

363. Piccione, M. *et al.* Xeroderma pigmentosum: General aspects and management. *J Pers Med* **11**, (2021).

364. Fassihi, H. Spotlight on 'xeroderma pigmentosum'. *Photochemical and Photobiological Sciences* vol. 12 78–84 Preprint at https://doi.org/10.1039/c2pp25267h (2013).

365. Lambert, W. C. & Lambert, M. W. Development of effective skin cancer treatment and prevention in xeroderma pigmentosum. *Photochemistry and Photobiology* vol. 91 475–483 Preprint at https://doi.org/10.1111/php.12385 (2015).

366. Chen, A. C. *et al.* A Phase 3 Randomized Trial of Nicotinamide for Skin-Cancer Chemoprevention. *New England Journal of Medicine* **373**, 1618–1626 (2015).

367. van der Waal, I. Oral leukoplakia, the ongoing discussion on definition and terminology. *Med Oral Patol Oral Cir Bucal* **20**, e685–e692 (2015).

368. Ferrándiz, C. *et al. Precancerous Skin Lesions*. *Actas Dermosifiliogr* vol. 108 (2017).

369. Green, A. C. Epidemiology of actinic keratoses. *Current Problems in Dermatology (Switzerland)* **46**, 1–7 (2015).

370. Nashan, D., Meiss, F. & Müller, M. Therapeutic strategies for actinic keratoses - A systematic review. *European Journal of Dermatology* vol. 23 14–32 Preprint at https://doi.org/10.1684/ejd.2013.1923 (2013).

371. Cramer, P. & Stockfleth, E. Actinic keratosis: where do we stand and where is the future going to take us? *Expert Opinion on Emerging Drugs* vol. 25 49–58 Preprint at https://doi.org/10.1080/14728214.2020.1730810 (2020).

372. Röwert-Huber, J. *et al.* Actinic keratosis is an early in situ squamous cell carcinoma: a proposal for reclassification. *British Journal of Dermatology* **156**, 8–12 (2007).

373. Dianzani, C. *et al.* Current therapies for actinic keratosis. *International Journal of Dermatology* vol. 59 677–684 Preprint at https://doi.org/10.1111/ijd.14767 (2020).

374. Javor, S. *et al.* P53 staining index and zonal staining patterns in actinic keratoses. *Arch Dermatol Res* **313**, 275–279 (2021).

375. Gutzmer, R. *et al.* Actinic Keratosis and Cutaneous Squamous Cell Carcinoma. *Dtsch Arztebl Int* **116**, (2019).

376. Mcbride, P., Neale, R., Pandeya, N. & Green, A. Sun-Related Factors, Betapapillomavirus, and Actinic Keratoses A Prospective Study. *Arch Dermatol* **143**, 862–868 (2007).

377. Flohil, S. C. *et al.* Prevalence of actinic keratosis and its risk factors in the general population: The rotterdam study. *Journal of Investigative Dermatology* **133**, 1971–1978 (2013).

378. Traianou, A. *et al.* Risk factors for actinic keratosis in eight European centres: A case-control study. *British Journal of Dermatology* **167**, 36–42 (2012).

379. Bouwes Bavinck, J. N. *et al.* Keratotic skin lesions and other risk factors are associated with skin cancer in organ-transplant recipients: A case-control study in the Netherlands, United Kingdom, Germany, France, and Italy. *Journal of Investigative Dermatology* **127**, 1647–1656 (2007).

380. Werner, R. N. *et al.* The natural history of actinic keratosis: A systematic review. *British Journal of Dermatology* vol. 169 502–518 Preprint at https://doi.org/10.1111/bjd.12420 (2013).

381. Quaedvlieg P.J.F, Tirsi E., Thissen M.R.T.M & Krekels G.A. Actinic keratosis how to differentiate the good from the bad one? *Eur J Dermatol* **16**, 335–339 (2006).

382. Callen, J. P., Bickers, D. R. & Moy, R. L. Actinic keratoses. *J Am Acad Dermatol* **36**, 650–653 (1997).

383. Worley, B. *et al.* Treatment of actinic keratosis: a systematic review. *Archives of Dermatological Research* vol. 315 1099–1108 Preprint at https://doi.org/10.1007/s00403-022-02490-5 (2023).

384. Bowen, J. T. PRECANCEROUS DERMATOSES : A STUDY OF TWO CASES OF CHRONIC ATYPICAL EPITHELIAL PROLIFERATION. *Arch Dermatol* **119**, 243–260 (1983).

385. Lanssens, S. & Ongenae, K. Dermatologic lesions and risk for cancer. *Acta Clin Belg* **66**, 177–185 (2011).

386. Payapvipapong, K. & Tanaka, M. Dermoscopic classification of Bowen's disease. *Australasian Journal of Dermatology* **56**, 32–35 (2015).

387. Morton, C. A., Birnie, A. J. & Eedy, D. J. British Association of Dermatologists' guidelines for the management of squamous cell carcinoma in situ (Bowen's disease) 2014. *British Journal of Dermatology* vol. 170 245–260 Preprint at https://doi.org/10.1111/bjd.12766 (2014).

388. Palaniappan, V. & Karthikeyan, K. Bowen's Disease. *Indian Dermatology Online Journal* vol. 13 177–189 Preprint at https://doi.org/10.4103/idoj.idoj_257_21 (2022).

389. Tenberg', H., Gissmann', L., Gross', G., Grussendorf-Conen3, E.-I. & Zur Hausen', H. *HUMAN PAPILLOMAVIRUS TYPE-16-RELATED DNA IN GENITAL BOWEN'S DISEASE AND IN BOWENOID PAPULOSIS*. *Int. f. Cancer* vol. 32 (1983).

390. Mishra, J. *et al.* Bowen's disease of vulva: A rare case of vulvar premalignant disorder. *Clin Cancer Investig J* **9**, 210 (2020).

391. Rubben, A., Malte Baron, J. & Grussendorf-Conen, E.-I. *Prevalence of human papillomavirus type 16-related DNA in cutaneous Bowen's disease and squamous cell cancer*. *INTERNATIONAL JOURNAL OF ONCOLOGY* vol. 9 (1996).

392. Kawashima M, Favre M, Obalek S, Jablonska S & Orth G. Premalignant lesions and cancers of the skin in the general population. *J Invest Dermatol* **95**, 537–542 (1990).

393. Paul Neagu, T., Ţigliş, M., Botezatu, D. & Enache, V. Clinical, histological and therapeutic features of Bowen's disease. *Rom J Morphol Embryol* **58**, 33–40 (2017).

394. Arlette, J., Arlette, J. P., Martin, F., Trotter, J. & Trotter, M. J. *Squamous cell carcinoma in situ of the skin: History, presentation, biology and treatment*. *Australasian Journal of Dermatology* vol. 45 (2004).

395. Bath-Hextall, F. J., Matin, R. N., Wilkinson, D. & Leonardi-Bee, J. Interventions for cutaneous Bowen's disease. *Cochrane Database of Systematic Reviews* vol. 2013 Preprint at https://doi.org/10.1002/14651858.CD007281.pub2 (2013).

396. Moreno, G., Chia, A. L. K., Lim, A. & Shumack, S. Therapeutic options for Bowen's disease. *Australasian Journal of Dermatology* vol. 48 1–10 Preprint at https://doi.org/10.1111/j.1440-0960.2007.00317.x (2007).

397. Gordon, R. Skin cancer: An overview of epidemiology and risk factors. *Semin Oncol Nurs* **29**, 160–169 (2013).

398. Dzwierzynski, W. W. Melanoma Risk Factors and Prevention. *Clinics in Plastic Surgery* vol. 48 543–550 Preprint at https://doi.org/10.1016/j.cps.2021.05.001 (2021).

399. Winge, M. C. G. *et al.* Advances in cutaneous squamous cell carcinoma. *Nature Reviews Cancer* vol. 23 430–449 Preprint at https://doi.org/10.1038/s41568-023-00583-5 (2023).

400. Scoggins, C. R. *et al.* Prognostic Information From Sentinel Lymph Node Biopsy in Patients With Thick Melanoma. *ARCH SURG* **145**, 622–627 (2010).

401. Rousseau, D. L. *et al.* Revised American Joint Committee on Cancer staging criteria accurately predict sentinel lymph node positivity in clinically node-negative melanoma patients. *Annals of Surgical Oncology* vol. 10 569–574 Preprint at https://doi.org/10.1245/ASO.2003.09.016 (2003).

402. Murali, R. *et al.* Sentinel lymph node biopsy in patients with thin primary cutaneous melanoma. *Ann Surg* **255**, 128–133 (2012).

403. Reuschenbach, M. *et al.* High-risk human papillomavirus in non-melanoma skin lesions from renal allograft recipients and immunocompetent patients. *Br J Cancer* **104**, 1334–1341 (2011).

404. Wang, J., Aldabagh, B., Yu, J. & Arron, S. T. Role of human papillomavirus in cutaneous squamous cell carcinoma: A meta-analysis. *J Am Acad Dermatol* **70**, 621–629 (2014).

405. Waldman, A. & Schmults, C. Cutaneous Squamous Cell Carcinoma. *Hematology/Oncology Clinics of North America* vol. 33 1–12 Preprint at https://doi.org/10.1016/j.hoc.2018.08.001 (2019).

406. Karia, P. S., Han, J. & Schmults, C. D. Cutaneous squamous cell carcinoma: Estimated incidence of disease, nodal metastasis, and deaths from disease in the United States, 2012. *J Am Acad Dermatol* **68**, 957–966 (2013).

407. Hammerman, P. S. *et al.* Comprehensive genomic characterization of squamous cell lung cancers. *Nature* **489**, 519–525 (2012).

408. Pickering, C. R. *et al.* Mutational landscape of aggressive cutaneous squamous cell carcinoma. *Clinical Cancer Research* **20**, 6582–6592 (2014).

409. Brown, V. L. *et al.* p16 INK4a and p14 ARF Tumor Suppressor Genes Are Commonly Inactivated in Cutaneous Squamous Cell Carcinoma. *J Invest Dermatol* **122**, 1284–1292 (2004).

410. Brash, D. E. *et al. A role for sunlight in skin cancer: UV-induced p53 mutations in squamous cell carcinoma (UV light/tumor suppressor genes)*. *Genetics* vol. 88 (1991).

411. South, A. P. *et al.* NOTCH1 mutations occur early during cutaneous squamous cell carcinogenesis. *Journal of Investigative Dermatology* **134**, 2630–2638 (2014).

412. Adams C, Thomas B & Bingham J. Cutaneous Squamous Cell Carcinoma With Perineural Invasion: A Case Report and Review of the Literature. *Cutis* **93**, 141–144 (2014).

413. Parekh, V. & Seykora, J. T. Cutaneous Squamous Cell Carcinoma. *Clinics in Laboratory Medicine* vol. 37 503–525 Preprint at https://doi.org/10.1016/j.cll.2017.06.003 (2017).

414. Que, S. K. T., Zwald, F. O. & Schmults, C. D. Cutaneous squamous cell carcinoma: Incidence, risk factors, diagnosis, and staging. *Journal of the American Academy of Dermatology* vol. 78 237–247 Preprint at https://doi.org/10.1016/j.jaad.2017.08.059 (2018).

415. Berg, D. & Otley, C. C. Skin cancer in organ transplant recipients: Epidemiology, pathogenesis, and management. *J Am Acad Dermatol* **47**, 1–20 (2002).

416. Gutzmer, R. *et al.* Actinic Keratosis and Cutaneous Squamous Cell Carcinoma. *Dtsch Arztebl Int* **116**, (2019).

417. Riddel, C., Rashid, R. & Thomas, V. Ungual and periungual human papillomavirus-associated squamous cell carcinoma: A review. *Journal of the American Academy of Dermatology* vol. 64 1147–1153 Preprint at https://doi.org/10.1016/j.jaad.2010.02.057 (2011).

418. Viarisio, D. *et al.* Beta HPV38 oncoproteins act with a hit-and-run mechanism in ultraviolet radiation-induced skin carcinogenesis in mice. *PLoS Pathog* **14**, (2018).

419. Su, F. *et al. RAS Mutations in Cutaneous Squamous-Cell Carcinomas in Patients Treated with BRAF Inhibitors*. *n engl j med* vol. 366 (2012).

420. Shore, R. E. *Radiation-Induced Skin Cancer in Humans*. *Medical and Pediatric Oncology* vol. 36 (2001).

421. Yu, H. S., Liao, W. T. & Chai, C. Y. Arsenic carcinogenesis in the skin. *Journal of Biomedical Science* vol. 13 657–666 Preprint at https://doi.org/10.1007/s11373-006-9092-8 (2006).

422. Firnhaber J. Basal Cell and Cutaneous Squamous Cell Carcinomas. *Am Fam Physician* **102**, 339–346 (2020).

423. National Comprehensive Cancer Network (NCCN). *NCCN Guidelines for Squamous Cell Skin Cancer V*. https://www.nccn.org/guidelines/guidelines-detail?category=1&id=1465 (2023).

424. Stratigos, A. *et al.* Diagnosis and treatment of invasive squamous cell carcinoma of the skin: European consensus-based interdisciplinary guideline. *Eur J Cancer* **51**, 1989–2007 (2015).

425. Corchado-Cobos, R., García-Sancha, N., González-Sarmiento, R., Pérez-Losada, J. & Cañueto, J. Cutaneous squamous cell carcinoma: From biology to therapy. *International Journal of Molecular Sciences* vol. 21 Preprint at https://doi.org/10.3390/ijms21082956 (2020).

426. Maubec, E. Update on the management of cutaneous squamous cell carcinoma. *Acta Dermato-Venereologica* vol. 100 309–317 Preprint at https://doi.org/10.2340/00015555-3498 (2020).

427. Bander, T. S., Nehal, K. S. & Lee, E. H. Cutaneous Squamous Cell Carcinoma: Updates in Staging and Management. *Dermatologic Clinics* vol. 37 241–251 Preprint at https://doi.org/10.1016/j.det.2019.03.009 (2019).

428. Villani, A., Potestio, L., Fabbrocini, G. & Scalvenzi, M. New Emerging Treatment Options for Advanced Basal Cell Carcinoma and Squamous Cell Carcinoma. *Advances in Therapy* vol. 39 1164–1178 Preprint at https://doi.org/10.1007/s12325-022-02044-1 (2022).

429. Alexandrov, L. B. *et al.* The repertoire of mutational signatures in human cancer. *Nature* **578**, 94–101 (2020).

430. Thomson, J. *et al.* The Genomic Landscape of Actinic Keratosis. *Journal of Investigative Dermatology* **141**, 1664-1674.e7 (2021).

431. Cozma, E. C., Banciu, L. M., Soare, C. & Cretoiu, S. M. Update on the Molecular Pathology of Cutaneous Squamous Cell Carcinoma. *International Journal of Molecular Sciences* vol. 24 Preprint at https://doi.org/10.3390/ijms24076646 (2023).

432. Alexandrov, L. B. *et al.* Signatures of mutational processes in human cancer. *Nature* **500**, 415–421 (2013).

433. Zheng, Q. *et al.* Whole-Exome and Transcriptome Analysis of UV-Exposed Epidermis and Carcinoma In Situ Reveals Early Drivers of Carcinogenesis. *Journal of Investigative Dermatology* **141**, 295-307.e13 (2021).

434. Lazo de la Vega, L. *et al.* Invasive squamous cell carcinomas and precursor lesions on UV-exposed epithelia demonstrate concordant genomic complexity in driver genes. *Modern Pathology* **33**, 2280–2294 (2020).

435. Biao, T. *et al.* From Bowen disease to cutaneous squamous cell carcinoma: eight markers were verified from transcriptomic and proteomic analyses. *J Transl Med* **20**, (2022).

436. Inman, G. J. *et al.* The genomic landscape of cutaneous SCC reveals drivers and a novel azathioprine associated mutational signature. *Nat Commun* **9**, (2018).

437. Chang, D. & Shain, A. H. The landscape of driver mutations in cutaneous squamous cell carcinoma. *NPJ Genom Med* **6**, (2021).

438. Sarin, K. Y. *et al.* Genome-wide meta-analysis identifies eight new susceptibility loci for cutaneous squamous cell carcinoma. *Nat Commun* **11**, (2020).

439. Lazar, A. D., Dinescu, S. & Costache, M. Deciphering the molecular landscape of cutaneous squamous cell carcinoma for better diagnosis and treatment. *Journal of Clinical Medicine* vol. 9 1–23 Preprint at https://doi.org/10.3390/jcm9072228 (2020).

440. Hedberg, M. & Seykora, J. T. Clarifying Progress on the Genomic Landscape of Actinic Keratosis. *Journal of Investigative Dermatology* vol. 141 1622–1624 Preprint at https://doi.org/10.1016/j.jid.2021.02.761 (2021).

441. Kim, Y. *et al.* Genome-wide association study of actinic keratosis identifies new susceptibility loci implicated in pigmentation and immune regulation pathways. *Commun Biol* **5**, (2022).

442. Wong, H. Y. *et al. Epidermal mutation accumulation in photodamaged skin is associated with skin cancer burden and can be targeted through ablative therapy*. (2023).

443. Kim, Y. S., Park, G. S., Bang, C. H. & Chung, Y. J. Genomic landscape of multiple Bowen's disease using whole-exome sequencing. *Journal of Dermatology* **50**, 397–400 (2023).

444. Bailey, P. *et al.* Driver gene combinations dictate cutaneous squamous cell carcinoma disease continuum progression. *Nat Commun* **14**, (2023).

445. Hedberg, M. L. *et al.* Molecular Mechanisms of Cutaneous Squamous Cell Carcinoma. *Int J Mol Sci* **23**, (2022).

446. Viarisio, D. *et al.* E6 and E7 from beta hpv38 cooperate with ultraviolet light in the development of actinic keratosis-like lesions and squamous cell carcinoma in mice. *PLoS Pathog* **7**, (2011).

447. Rollison, D. E., Viarisio, D., Amorrortu, R. P., Gheit, T. & Tommasino, M. An Emerging Issue in Oncogenic Virology: the Role of Beta Human Papillomavirus Types in the Development of Cutaneous Squamous Cell Carcinoma. *J Virol* **93**, (2019).

448. Tommasino, M. HPV and skin carcinogenesis. *Papillomavirus Research* vol. 7 129–131 Preprint at https://doi.org/10.1016/j.pvr.2019.04.003 (2019).

449. Strickley, J. D. *et al.* Immunity to commensal papillomaviruses protects against skin cancer. *Nature* **575**, 519–522 (2019).

450. Motulsky, H. J. & Brown, R. E. Detecting outliers when fitting data with nonlinear regression - A new method based on robust nonlinear regression and the false discovery rate. *BMC Bioinformatics* **7**, (2006).

451. Sano, T., Oyama, T., Kashiwabara, K., Fukuda, T. & Nakajima, T. *Expression Status of p16 Protein Is Associated with Human Papillomavirus Oncogenic Potential in Cervical and Genital Lesions*. *American Journal of Pathology* vol. 153 (1998).

452. Wood R & Lowery M. Human DNA Repair Genes. https://www.mdanderson.org/documents/Labs/Wood-Laboratory/human-dna-repair-genes.html (2020).

453. Patel, T., Morrison, L. K., Rady, P. & Tyring, S. Epidermodysplasia verruciformis and susceptibility to HPV. *Disease Markers* vol. 29 199–206 Preprint at https://doi.org/10.3233/DMA-2010-0733 (2010).

454. Tampa, M. *et al.* The Role of Beta HPV Types and HPV-Associated Inflammatory Processes in Cutaneous Squamous Cell Carcinoma. *J Immunol Res* **2020**, (2020).

455. Wieland, U., Kreuter, A. & Pfister, H. Human papillomavirus and immunosuppression. *Current Problems in Dermatology (Switzerland)* **45**, 154–165 (2014).

456. Schaper, I. D. *et al.* Development of Skin Tumors in Mice Transgenic for Early Genes of Human Papillomavirus Type 8. *Cancer Res* **65**, 1394–1400 (2005).

457. Minoni, L. *et al.* Transforming Properties of Beta-3 Human Papillomavirus E6 and E7 Proteins. *mSphere* **5**, (2020).

458. Rehm, T. M., Straub, E., Iftner, T. & Stubenrauch, F. Restriction of viral gene expression and replication prevents immortalization of human keratinocytes by a beta-human papillomavirus. *PNAS* **119**, 1–8 (2022).

459. Bzhalava, D., Guan, P., Franceschi, S., Dillner, J. & Clifford, G. A systematic review of the prevalence of mucosal and cutaneous human papillomavirus types. *Virology* **445**, 224–231 (2013).

460. Farzan, S. F. *et al.* Cutaneous alpha, beta and gamma human papillomaviruses in relation to squamous cell carcinoma of the skin: A population-based study. *Int J Cancer* **133**, 1713–1720 (2013).

461. Hasche, D. *et al.* The interplay of UV and cutaneous papillomavirus infection in skin cancer development. *PLoS Pathog* **13**, e1006723 (2017).

462. Arron, S. T., Ruby, J. G., Dybbro, E., Ganem, D. & Derisi, J. L. Transcriptome sequencing demonstrates that human papillomavirus is not active in cutaneous squamous cell carcinoma. *Journal of Investigative Dermatology* **131**, 1745–1753 (2011).

463. Ganzenmueller, T. *et al.* Next-generation sequencing fails to identify human virus sequences in cutaneous squamous cell carcinoma. *Int J Cancer* **131**, (2012).

464. Schneider, I., Lehmann, M. D., Kogosov, V., Stockfleth, E. & Nindl, I. Eyebrow hairs from actinic keratosis patients harbor the highest number of cutaneous human papillomaviruses. *BMC Infect Dis* **13**, 1–7 (2013).

465. Borgogna, C. *et al.* Improved detection reveals active β-papillomavirus infection in skin lesions from kidney transplant recipients. *Modern Pathology* **27**, 1101–1115 (2014).

466. Lambert, P., Munger, K., Rosl, F., Hasche, D. & Massomo, T. *Beta human papillomaviruses and skin cancer*. *Nature* vol. 575 (2020).

467. Neagu, N. *et al.* The role of HPV in keratinocyte skin cancer development: A systematic review. *Journal of the European Academy of Dermatology and Venereology* vol. 37 40–46 Preprint at https://doi.org/10.1111/jdv.18548 (2023).

468. Gross, G. & Pfister, H. Role of human papillomavirus in penile cancer, penile intraepithelial squamous cell neoplasias and in genital warts. *Med Microbiol Immunol* **193**, 35–44 (2004).

469. Tenberg', H., Gissmann', L., Gross', G., Grussendorf-Conen3, E.-I. & Zur Hausen', H. *HUMAN PAPILLOMAVIRUS TYPE-16-RELATED DNA IN GENITAL BOWEN'S DISEASE AND IN BOWENOID PAPULOSIS*. *Int. f. Cancer* vol. 32 (1983).

470. Nilsson, K., Svensson, S. & Landberg, G. Retinoblastoma protein function and p16INK4a expression in actinic keratosis, squamous cell carcinoma in situ and invasive squamous cell carcinoma of the skin and links between p16INK4a expression and infiltrative behavior. *Modern Pathology* **17**, 1464–1474 (2004).

471. Dorfer, S. *et al.* High-risk mucosal human papillomavirus infection in squamous cell carcinoma and bowen's disease of the hand. *Acta Derm Venereol* **99**, 462–463 (2019).

472. Willman, J. H., Heinz, D., Golitz, L. E. & Shroyer, K. R. Correlation of p16 and pRb expression with HPV detection in Bowen's disease. *J Cutan Pathol* **33**, 629–633 (2006).

473. De Graeff, P. *et al.* Factors influencing p53 expression in ovarian cancer as a biomarker of clinical outcome in multicentre studies. *Br J Cancer* **95**, 627–633 (2006).

474. Paul Neagu, T., Ţigliş, M., Botezatu, D. & Enache, V. Clinical, histological and therapeutic features of Bowen's disease. *Rom J Morphol Embryol* **58**, 33–40 (2017).

475. Idriss, M., Misri, R. & Böer-Auer, A. Orthokeratotic Bowen disease: a histopathologic, immunohistochemical and molecular study. *J Cutan Pathol* **43**, 24–31 (2016).

476. Wallace, N. A. Catching HPV in the Homologous Recombination Cookie Jar. *Trends in Microbiology* vol. 28 191–201 Preprint at https://doi.org/10.1016/j.tim.2019.10.008 (2020).

477. Hu, C. & Wallace, N. Beta HPV Deregulates Double-Strand Break Repair. *Viruses* vol. 14 Preprint at https://doi.org/10.3390/v14050948 (2022).

478. Hu, C. *et al.* Beta human papillomavirus 8E6 promotes alternative end-joining. *Elife* **12**, (2023).

479. Cornet, I. *et al.* Comparative Analysis of Transforming Properties of E6 and E7 from Different Beta Human Papillomavirus Types. *J Virol* **86**, 2366–2370 (2012).

480. Rual, J. F. *et al.* Towards a proteome-scale map of the human protein-protein interaction network. *Nature* **437**, 1173–1178 (2005).

481. Muller, M., Cassonnet, P., Favre, M., Jacob, Y. & Demeret, C. A comparative approach to characterize the landscape of host-pathogen protein-protein interactions. *J Vis Exp* (2013) doi:10.3791/50404.

482. Rao, V. S., Srinivas, K., Sujini, G. N. & Kumar, G. N. S. Protein-Protein Interaction Detection: Methods and Analysis. *Int J Proteomics* **2014**, 1–12 (2014).

483. Lin, J. S. & Lai, E. M. Protein–protein interactions: Co-immunoprecipitation. in *Methods in Molecular Biology* vol. 1615 211–219 (Humana Press Inc., 2017).

484. Rual, J. F. *et al.* Towards a proteome-scale map of the human protein-protein interaction network. *Nature* **437**, 1173–1178 (2005).

485. Kassam, S. N. & Rainbow, A. J. UV-inducible base excision repair of oxidative damaged DNA in human cells. *Mutagenesis* **24**, 75–83 (2009).

486. Taylor, E. M. *et al.* Xeroderma pigmentosum and trichothiodystrophy are associated with different mutations in the XPD (ERCC2) repairtranscription gene (nucleotide excision repairtranscription factor TFIIHUV irradiation). *Proc. Natl. Acad. Sci.* **94**, 8658–8663 (1997).

487. WeedaFt Reinier A van Ham, G. C., Vermeulen, W., Bootsma, D., van der Eb, A. J. & J Hoeijmakerst, J. H. *A Presumed DNA Helicase Encoded by ERCC-3 Is Involved in the Human Repair Disorders Xeroderma Pigmentosum and Cockayne's Syndrome*. *Cell* vol. 62 (1990).

488. Le, S. *et al.* Lynch syndrome and muir-torre syndrome: An update and review on the genetics, epidemiology, and management of two related disorders. *Dermatology Online Journal* vol. 23 Preprint at https://doi.org/10.5070/d32311037239 (2017).

489. Sheth, R., Menon, P. & Malik, D. A Case of Muir-Torre Syndrome. *Cureus* (2021) doi:10.7759/cureus.14582.

490. Poirson, J. *et al.* High-Risk Mucosal Human Papillomavirus 16 (HPV16) E6 Protein and Cutaneous HPV5 and HPV8 E6 Proteins Employ Distinct Strategies To Interfere with Interferon Regulatory Factor 3-Mediated Beta Interferon Expression. *J Virol* **96**, (2022).

491. Bortnik, V. *et al.* Loss of HPV type 16 E7 restores cGAS-STING responses in human papilloma virus-positive oropharyngeal squamous cell carcinomas cells. *Journal of Microbiology, Immunology and Infection* **54**, 733–739 (2021).

492. Golato, T. *et al.* Development of a Cell-Based Assay for Measuring Base Excision Repair Responses. *Sci Rep* **7**, (2017).

493. Piekna-Przybylska, D. Reporter assays for BER pathway. in *Methods in Molecular Biology* vol. 1999 145–160 (Humana Press Inc., 2019).

Annexes :

Premier auteur :

Reynders C, **Lerho T**, Goebel EA, Crum CP, Vandenput S, Beaudart C, Herfs M. Prevalence and genotype distribution of human papillomavirus in cervical adenocarcinoma (usual type and variants): A systematic review and meta-analysis. J Med Virol. 2023 Oct;95(10):e29190.

(doi: 10.1002/jmv.29190)

Co-auteur :

Bruyere D, Monnien F, Colpart P, Roncarati P, Vuitton L, Hendrick E, Lepinoy A, Luquain A, Pilard C, **Lerho T**, Molimard C, Maingon P, Arnould L, Bone-Lepinoy MC, Dusserre L, Martin L, Reynders C, Ancion M, Peiffert D, Leroux A, Hubert P, Delhorme JB, Ghnassia JP, Woronoff AS, Delvenne P, Prétet JL, Bosset JF, Peulen O, Mougin C, Valmary-Degano S, Herfs M. Treatment algorithm and prognostic factors for patients with stage I-III carcinoma of the anal canal: a 20-year multicenter study. Mod Pathol. 2021 Jan;34(1):116-130.

(DOI: 10.1038/s41379-020-0637-6)

Hubert P, Roncarati P, Demoulin S, Pilard C, Ancion M, Reynders C, **Lerho T**, Bruyere D, Lebeau A, Radermecker C, Meunier M, Nokin MJ, Hendrick E, Peulen O, Delvenne P, Herfs M. Extracellular HMGB1 blockade inhibits tumor growth through profoundly remodeling immune microenvironment and enhances checkpoint inhibitor-based immunotherapy. J Immunother Cancer. 2021 Mar;9(3):e001966.

(DOI: 10.1136/jitc-2020-001966)

Lebeau A, Bruyere D, Roncarati P, Peixoto P, Hervouet E, Cobraiville G, Taminiau B, Masson M, Gallego C, Mazzucchelli G, Smargiasso N, Fleron M, Baiwir D, Hendrick E, Pilard C, **Lerho T**, Reynders C, Ancion M, Greimers R, Twizere JC, Daube G, Schlecht-Louf G, Bachelerie F, Combes JD, Melin P, Fillet M, Delvenne P, Hubert P, Herfs M. HPV infection alters vaginal microbiome through down-regulating host mucosal innate peptides used by Lactobacilli as amino acid sources. Nat Commun. 2022 Feb 28;13(1):1076.

(DOI: 10.1038/s41467-022-28724-8)

Bruyere D, Roncarati P, Lebeau A**, Lerho T**, Poulain F, Hendrick E, Pilard C, Reynders C, Ancion M, Luyckx M, Renard M, Jacob Y, Twizere JC, Peiffer R, Peulen O, Delvenne P, Hubert P, McBride A, Gillet N, Masson M, Herfs M. Human papillomavirus E6/E7 oncoproteins promote radiotherapy-mediated tumor suppression by globally hijacking host DNA damage repair. Theranostics. 2023 Jan 31;13(3):1130-1149.

(DOI: 10.7150/thno.78091)

Modern Pathology (2021) 34:116–130
https://doi.org/10.1038/s41379-020-0637-6

ARTICLE

Treatment algorithm and prognostic factors for patients with stage I–III carcinoma of the anal canal: a 20-year multicenter study

Diane Bruyere[1] · Franck Monnien[2] · Prudence Colpart[2] · Patrick Roncarati[1] · Lucine Vuitton[3,4] · Elodie Hendrick[1] · Alexis Lepinoy[5] · Alexandra Luquain[2] · Charlotte Pilard[1] · Thomas Lerho[1] · Chloé Molimard[2] · Philippe Maingon[6,7] · Laurent Arnould[8] · Marie-Christine Bone-Lepinoy[5] · Laurence Dusserre[9] · Laurent Martin[10] · Celia Reynders[1] · Marie Ancion[1] · Didier Peiffert[11] · Agnès Leroux[12] · Pascale Hubert[1] · Jean-Baptiste Delhorme[13] · Jean-Pierre Ghnassia[14] · Anne-Sophie Woronoff[15] · Philippe Delvenne[1,16] · Jean-Luc Prétet[4,17] · Jean-François Bosset[18] · Olivier Peulen[19] · Christiane Mougin[4,17] · Séverine Valmary-Degano[2,4,20] · Michael Herfs[1]

Received: 14 May 2020 / Revised: 15 July 2020 / Accepted: 15 July 2020 / Published online: 29 July 2020

Abstract

Despite a growing incidence in developed countries and a recent improved understanding of its pathogenesis, anal cancer management has not evolved over the past decades and drug combination used as first-line regimen still largely depends on clinician preferences. Aiming at paving the way for precision medicine, a large cohort of 372 HIV-negative patients diagnosed over a 20-year time period with locally advanced anal carcinoma was collected and carefully characterized at the clinical, demographic, histopathologic, immunologic, and virologic levels. Both the prognostic relevance of each clinicopathological parameter and the efficacy of different concurrent chemoradiation strategies were determined. Overall, the incidence of anal cancer peaked during the sixth decade (mean: 63.4) and females outnumbered males (ratio: 2.51). After completion of treatment, 95 (25.5%) patients experienced progression of persistent disease or local/distant recurrence and 102 (27.4%) died during the follow-up period (median: 53.8 months). Importantly, uni-multivariate analyses indicated that both negative HPV/p16^{ink4a} status and aberrant p53 expression were far better predictors for reduced progression-free survival than traditional risk factors such as tumor size and nodal status. As for overall survival, the significant influences of age at diagnosis, p16^{ink4a} status, cTNM classification as well as both CD3^{+} and CD4^{+} T-cell infiltrations within tumor microenvironment were highlighted. Cisplatin-based chemoradiotherapy was superior to both radiotherapy alone and other concurrent chemoradiation therapies in the treatment of HPV-positive tumors. Regarding their HPV-uninfected counterparts, frequent relapses were observed, whatever the treatment regimen administered. Taken together, our findings reveal that current anal cancer management and treatment have reached their limits. A dualistic classification according to HPV/p53 status should be considered with implications for therapy personalization and optimization.

Introduction

With an estimated 48,500 new cases diagnosed worldwide in 2018 [1], the incidence of anal cancer has substantially raised since the early 80's [2]. Although less common than adenocarcinoma of the colon or rectum, both intraepithelial and invasive neoplasms of the anal canal are no longer considered as rare by most clinicians, pathologists, and epidemiologists. From a pathogenesis standpoint, anal cancer is undoubtedly more similar to lower gynecological tract tumors than it is to other gastrointestinal malignancies. Indeed, most (~85%) anal (pre)neoplastic lesions display a squamous differentiation [3], are caused by a carcinogenic human papillomavirus (HPV) infection and are related to

These authors contributed equally: Séverine Valmary-Degano, Michael Herfs

Supplementary information The online version of this article (https://doi.org/10.1038/s41379-020-0637-6) contains supplementary material, which is available to authorized users.

✉ Michael Herfs
M.Herfs@uliege.be

Extended author information available on the last page of the article

risk factors such as a high lifetime number of sexual partners or an immunocompromised status (e.g., HIV positivity) [4, 5].

Although surgery (especially to remove early-stage tumors such as superficially invasive lesions) or radiotherapy alone (with fragile patients or older than 80) are sometimes advisable, the vast majority of tumors arising from the anal canal are treated with a combination of chemotherapy and radiation. Concurrent 5-fluorouracil (5-FU)/mitomycin plus radiotherapy (45–59.4 Gy) has been constituting the preferred primary treatment option for patients with locally advanced anal carcinoma for several decades [6, 7]. Most patients who have experienced treatment failure undergo surgical excision (usually a salvage abdominoperineal resection), affecting their quality of life. Given that locoregional relapse is well-known to occur in ~35% of patients, some treatment alternatives using cisplatin or capecitabine (xeloda®) were tested [8–11]. Of note, several clinical trials evaluating immune checkpoint inhibitors (anti-PD-1, PD-L1, and/or CTLA-4) in patients with refractory or metastatic anal squamous cell carcinoma (SCC) are still ongoing (e.g., NCT02314169, NCT02919969) [12]. Despite some promising results (especially with cisplatin-based therapy) [11], conflicting results have been reported [9, 10]. The limited number of enrolled patients and/or the (too) wide eligibility criteria (e.g., absence of reliable tumor characterization, unknown HIV status) are very likely to explain these existing discrepancies. Indeed, potential risk factors such as HPV status and disruptive *TP53* mutations as well as the existence of two distinct subtypes of anal SCC with different cellular origin (squamous zone vs. transitional zone) were recently highlighted [13–15]. Moreover, the predictive value of some T-cell subsets (e.g., $CD8^+$ and $PD\text{-}1^+$) infiltrating tumor stroma was revealed in the context of other HPV-driven cancers (both head and neck and cervical SCC) [16–19]. Therefore, in an era of precision medicine, it is reasonable to think that not all anal cancer patients should be managed/treated in the same way.

The aim of our large retrospective study was (1) to identify HIV-negative non-metastatic anal cancer patients at high risk of recurrence/progression, (2) to define robust prognostic markers, (3) to determine the efficacy of different chemoradiotherapy regimens and, ultimately, (4) to pave the way for a future personalization of treatment algorithms.

Material and methods

Patient selection and clinical data retrieval

A total of 372 patients treated for primary stages I to III (according to the American Joint Committee on Cancer, 8th edition) anal SCC between January 1998 and December 2017 were selected. The consultations and treatments were taking place in five different University/Regional Medical Centers located in Belgium [Liege ($n = 83$)] or north-eastern France [Nancy ($n = 71$), Dijon ($n = 101$), Strasbourg ($n = 72$), Besançon ($n = 45$)]. Paraffin-embedded tissue specimens (biopsies or surgical resections) from each patient were retrieved from pathology archives and processed/archived in the Biobanks of the University Hospital of Liege or University Hospital of Besançon (BB-0033–00024) throughout the project. Both original diagnoses and tumor differentiation were confirmed by experienced pathologists (SV-D and PD). In order to avoid bias which could affect the analysis, patients with incomplete clinicopathological information, metastatic (stage IV) disease, or treated for a glandular neoplasm (anal adenocarcinoma or rectal tumor spreading downward within the anal canal) were excluded. Patients who directly received non-curative-intent treatments (palliative care), who were immunosuppressed (HIV-positive or transplant recipients) as well as patients diagnosed with a cancerous lesion entirely detected in the anal margin (defined by the presence of hair follicles and sweat glands) were not taken into consideration either. Clinicopathological information [gender, age at diagnosis, tumor size, nodal and HIV statuses, treatment details (surgical procedures, radiotherapy doses, chemotherapeutic agents) and follow-up data] was collected for all patients from personal health records. This study (data collection and experimental protocols) was approved by the institutional review board of the respective institutions (Belgium: #2020/51; France: #F1962-CAPINDEPTH).

Immunohistochemistry

After deparaffinization and rehydration in graded alcohols, the activity of endogenous peroxidases was blocked using 3% H_2O_2 in methanol for 5 min. Antigens were then retrieved in 10 mM citrate buffer (pH 6) (Sigma-Aldrich, St Louis, MO, USA) or in 10 mM Tris/1 mM EDTA solution (pH 9) (Invitrogen, Carlsbad, CA, USA) for 11 min at 120 °C in a pressure cooker. Before incubating the tissue sections with the primary antibodies for 1 h at room temperature, the non-specific binding sites were blocked using serum-free Protein Block reagent (Dako/Agilent Technologies, Glostrup, Denmark). The following antibodies were used for the primary reaction: anti-$p16^{ink4a}$ (clone E6H4; CINtec Histology-Roche, Basel, Switzerland), anti-p53 (clone DO-7; Ventana, Medical Systems, Tucson, AZ, USA), anti-cytokeratin 7 (CK7) (clone SP52; Ventana Medical Systems,), anti-Ki67 (clone 30–9; Ventana Medical Systems), anti-PD-1 (clone NAT105; Abcam, Cambridge, UK), anti-CD3 (clone 2GV6; Ventana Medical Systems), anti-CD4 (clone SP35; Ventana Medical Systems), anti-CD8 (clone SP57; Ventana Medical

Systems) and anti-carbonic anhydrase 9 (CA IX) (ab15086, Abcam). The secondary reaction (immunoperoxidase staining) was performed using the mouse/rabbit EnVision detection system (Dako) and positive cells were finally visualized using SignalStain DAB Substrate Kit (Cell Signaling, Danvers, MA, USA). Mouse and rabbit control IgGs (Santa Cruz Biotechnology, Santa Cruz, CA, USA) were used as negative controls.

Immunostaining assessment

All immunolabelled tissues were evaluated by independent investigators (senior pathologists) and the entire cancerous lesion was considered. As previously described [15, 20], $p16^{ink4a}$ and CK7 immunostainings were scored as positive when a diffuse immunoreactivity was detected in the large majority (>75%) of tumor cells. The detection of 1–49% cancer cells displaying a nuclear p53 expression was considered as non-aberrant. In contrast, p53 staining was classified as aberrant when 0% or ≥50% positive cells with moderate or strong intensity were observed [21]. The proliferation index (percentage of Ki67-positive cells) of a given tumor was stratified as follows: 0–25%, 26–50%, 51–75%, and >75%. Both the intensity (negative, low, moderate, or strong) and the extent (undetectable, 0–25%, 26–50%, 51–75%, and >75%) of CA IX immunostained tissues were assessed, according to an arbitrary scale. Regarding T-cell subpopulations ($CD3^+$, $CD4^+$, $CD8^+$, and $PD\text{-}1^+$) infiltrating tumor microenvironment, the number of positive cells per mm^2 was determined by computerized counts (QuPath 0.2.0 software for digital pathology image analysis) and verified by manual counting [22].

HPV genotyping

Following DNA extraction (QIAamp DNA FFPE Tissue Kit; Qiagen, Hilden, Germany), HPV genotyping of French samples was performed using the INNO-LiPA HPV Genotyping Extra test (Innogenetics, Gent, Belgium). The Abbott RealTime High-Risk HPV assay (Abbott, Wiesbaden, Germany) was used for characterizing HPV infections of tissue specimens collected in Belgium. Both assays allow the detection of all WHO/IARC-classified carcinogenic HPV genotypes (HPV16, 18, 31, 33, 35, 39, 45, 51, 52, 56, 58, and 59) and show equal performances (high sensitivity) with formalin-fixed tissues [23].

In situ hybridization

HPV infection was visualized and further confirmed on tissue sections by in situ hybridization. The INFORM HPV III Family 16 Probe cocktail (allowing the detection of HPV16, 18, 31, 33, 35, 39, 45, 51, 52, 56, 58, and 66) was used according to supplier's recommendations (Ventana Medical Systems).

Statistical analysis

GraphPad Prism 5 and R statistical software packages were used to conduct the statistical analyses. Differences were considered statistically significant when $p < 0.05$. Depending on the number of variables (two or more), the comparison of clinicopathological data between independent groups was performed using a Fisher's exact test or a χ^2 test. The Kaplan-Meier method was used to estimate both the overall (OS) and progression-free (PFS) survivals. The OS was calculated from the date of original diagnosis/biopsy to the date of death (from any cause). The events included in PFS were the progression of persistent diseases, recurrences at the local/primary site, and distant metastases. When a patient was still alive without event occurrence at last follow-up visit, this latter date was used as the end point. The survival distribution between separate groups was compared using a Log-rank (Mantel-Cox) test. The prognostic value [hazard ratio (HR) with 95% confidence interval (95% CI)] of each clinicopathological variable was determined in a univariate analysis. Potential risk factors with $p < 0.25$ in univariate analysis were incorporated in a subsequent multivariate analysis based on the Cox regression model. The analysis was then refined using a stepwise method with $p < 0.1$ for removal. The data were compared as follows: age: <60 vs. ≥60; gender: men vs. women; $HPV/p16^{ink4a}$ status: positive vs. negative; HPV infection: single vs. multiple; tumor origin: non-keratinazing squamous zone vs. transitional zone; proliferative index: <50% vs. >50%; p53 staining: non-aberrant vs. aberrant; tumor differentiation: well/moderate vs. poor/basaloid; $CD3^+$ cells: quarter (Q) 2/Q3/Q4 vs. Q1; $CD4^+$ cells: quarter Q2/Q3 vs. Q1/Q4; $CD8^+$ cells: >median vs. <median; $PD\text{-}1^+$ cells: Q2/Q3/Q4 vs. Q1; cT: T1/T2 vs. T3/T4; cN: N + vs. N-; Tumor stage: I-IIb vs. IIIa-IIIc.

Results

Study population: demographic and clinical features

After applying strict inclusion and exclusion criteria (i.e., HIV-negative, non-metastatic squamous diseases with both available tumor tissues and extensive clinicopathological data), 372 patients with stages I to IIIc anal carcinoma were selected. This cohort included four (4/372, 1.1%) superficially invasive SCC and one (1/372, 0.3%) verrucous carcinoma. The mean age was 63.4 years (ranged from 31 to 98) and females outnumbered males (female/male ratio: 2.51). Approximately 60% (225/368, 61.1%) of study

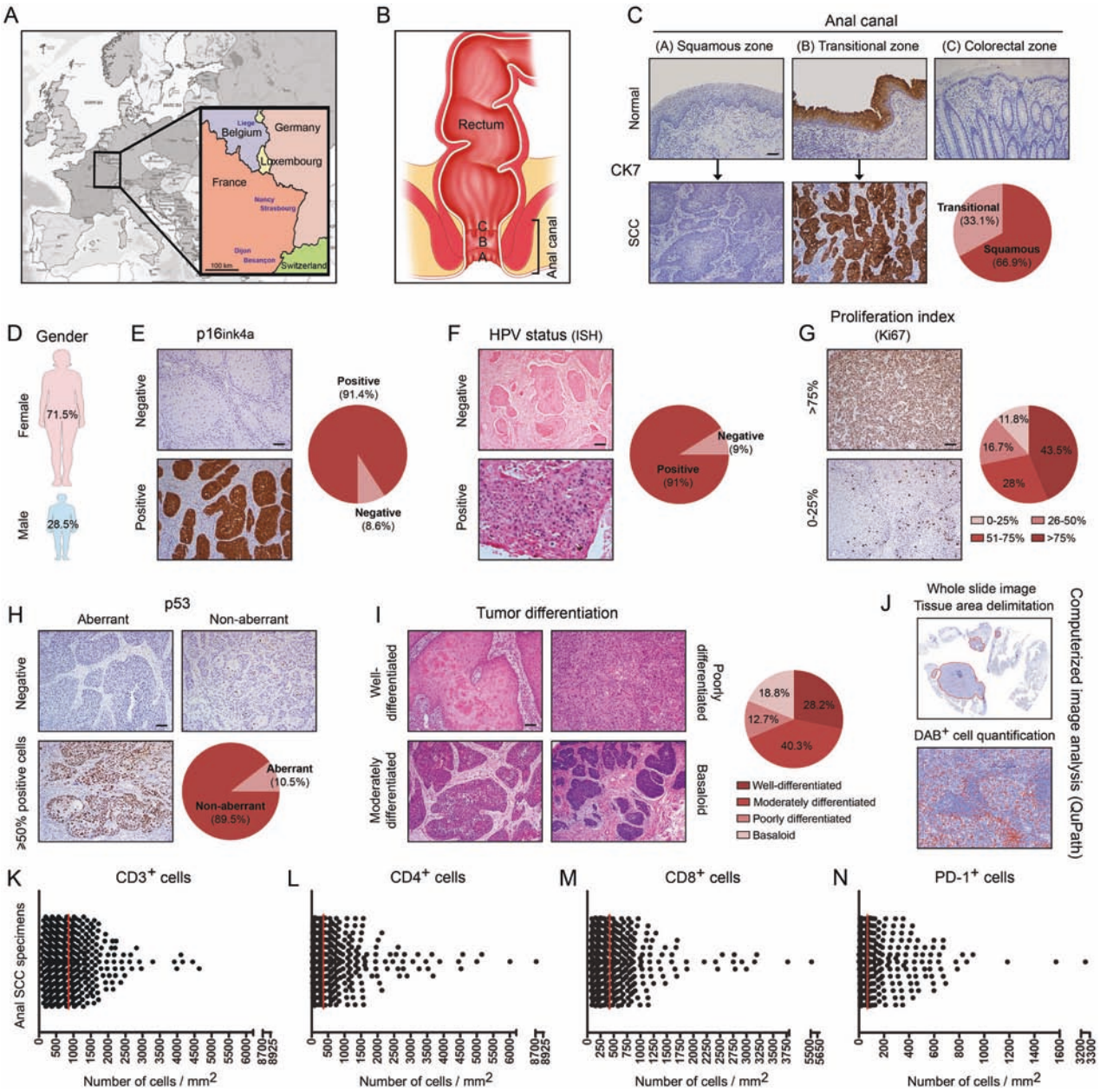

Fig. 1 Description, illustration, measurement of assessed clinicopathological variables, and general characteristics of the study population ($n = 372$). **a** University/regional hospitals participating in the present multicenter study. **b** Schematic representation of the lower gastrointestinal tract. **c** Histology of the different epithelial tissues (squamous, transitional "urothelium-like" and colorectal) lining the anal canal. The specific anti-CK7 immunoreactivity displayed by both the normal urothelium-like epithelium and neoplastic lesions arising from the transitional zone should be noticed. Based on CK7 expression, two region-specific subtypes of anal SCC (squamous vs. transitional) can be easily and precisely distinguished. **d** Percentage of anal canal cancers by gender. **e** $p16^{ink4a}$ expression, **f** HPV status, **g** proliferative index (percentage of Ki67-positive tumor cells), **h** p53 immunoreactivity, and **i** degree of differentiation exhibited by anal canal SCC. Note the diffuse $p16^{ink4a}$ immunoreactivity displayed by the large majority of neoplasms, in keeping with the carcinogenic HPV infection detected by both genotyping assay and in situ hybridization (ISH). **j** Illustration of the different steps followed for computerized DAB-positive immune cell quantification (QuPath). **k** $CD3^+$, **l** $CD4^+$, **m** $CD8^+$, and **n** $PD\text{-}1^+$ T-cell infiltration within tumor microenvironment was determined for each tissue specimen and the number of cells was reported to tumor area (mm^2). The median (in red) is shown. The scale bar represents 100 µm.

patients had no sign of spread to lymph nodes at diagnosis and patients were distributed among each discrete cancer staging category as follows: I: 17.8%; IIa: 33.1%; IIb: 5.5%; IIIa: 20.8%; IIIb: 4.4%; IIIc: 18.4%. Due to the lack of precise information regarding tumor size or nodal status, tumor stage was undetermined in 7 out of 372 (1.9%) patients. About two thirds (247/372, 66.4%) of patients were treated with combined chemoradiotherapy while most

Table 1 Demographic and patient characteristics according to disease recurrence/progression.

Characteristics	No recurrence/progression ($n = 277$) (74.46%)	Treatment failure ($n = 95$) (25.54%)	P value
Age at diagnosis (31–98 years)			$p = 0.718$
<60	115 (41.52%)	42 (44.21%)	
≥60	162 (58.48%)	53 (55.79%)	
Gender			$p = 0.236$
Male	74 (26.71%)	32 (33.68%)	
Female	203 (73.29%)	63 (66.32%)	
HPV status			$\mathbf{p < 0.0001}$
Negative	13 (4.69%)	19 (20%)	
Positive	252 (90.98%)	71 (74.74%)	
Undetermined	12 (4.33%)	5 (5.26%)	
HPV infection			$p = 1.00$
Single	234 (234/252, 92.86%)	66 (66/71, 92.96%)	
Multiple	18 (18/252, 7.14%)	5 (5/71, 7.04%)	
HPV genotypes			$p = 0.699$
HPV16	233 (233/252, 92.46%)	68 (68/71, 95.77%)	
HPV18	7 (7/252, 2.78%)	1 (1/71, 1.41%)	
Others	42 (42/252, 16.67%)	10 (10/71, 14.08%)	
p16ink4a staining			$\mathbf{p < 0.0001}$
Negative	12 (4.33%)	20 (21.05%)	
Positive	265 (95.67%)	75 (78.95%)	
Tumor origin (based on CK7 staining)			$p = 0.801$
Squamous zone	184 (66.43%)	65 (68.42%)	
Transitional zone	93 (33.57%)	30 (31.58%)	
Proliferative index (Ki67)			$p = 0.182$
≤25%	35 (12.64%)	9 (9.47%)	
26–50%	40 (14.44%)	22 (23.16%)	
51–75%	76 (27.43%)	28 (29.47%)	
>75%	126 (45.49%)	36 (37.90%)	
p53 status			$\mathbf{p = 0.011}$
Aberrant (0 or >50%)	22 (7.94%)	17 (17.89%)	
Non aberrant	255 (92.06%)	78 (82.11%)	
Tumor differentiation			$p = 0.597$
Well-differentiated	75 (27.08%)	30 (31.58%)	
Moderately differentiated	110 (39.71%)	40 (42.11%)	
Poorly differentiated	38 (13.72%)	9 (9.47%)	
Basaloid	54 (19.49%)	16 (16.84%)	
$CD3^+$ cells (median: 839.2 cells/mm^2)			$p = 0.895$
First quarter (<448.8 cells/mm^2)	68 (24.55%)	25 (26.31%)	
Second quarter (448.8–839.2 cells/mm^2)	72 (25.99%)	21 (22.11%)	
Third quarter (839.2–1306 cells/mm^2)	69 (24.91%)	24 (25.27%)	
Fourth quarter (>1306 cells/mm^2)	68 (24.55%)	25 (26.31%)	

Table 1 (continued)

Characteristics	No recurrence/progression ($n = 277$) (74.46%)	Treatment failure ($n = 95$) (25.54%)	P value
$CD4^+$ cells (median: 359.2 cells/mm^2)			$p = 0.556$
First quarter (<140.1 cells/mm^2)	71 (25.63%)	22 (23.16%)	
Second quarter (140.1–359.2 cells/mm^2)	68 (24.55%)	25 (26.32%)	
Third quarter (359.2–924.6 cells/mm^2)	73 (26.35%)	20 (21.05%)	
Fourth quarter (>924.6 cells/mm^2)	65 (23.47%)	28 (29.47%)	
$CD8^+$ cells (median: 421.1 cells/mm^2)			$p = 0.792$
First quarter (<235.6 cells/mm^2)	69 (24.91%)	24 (25.26%)	
Second quarter (235.6–421.1 cells/mm^2)	66 (23.83%)	27 (28.42%)	
Third quarter (421.1–739.8 cells/mm^2)	72 (25.99%)	21 (22.11%)	
Fourth quarter (>739.8 cells/mm^2)	69 (24.91%)	23 (24.21%)	
Unknown	1 (0.36%)		
PD-1^+ cells (median: 66.8 cells/mm^2)			$p = 0.966$
First quarter (<30.1 cells/mm^2)	68 (24.55%)	25 (26.32%)	
Second quarter (30.1–66.8 cells/mm^2)	69 (24.91%)	24 (25.26%)	
Third quarter (66.8–164.7 cells/mm^2)	71 (25.63%)	22 (23.16%)	
Fourth quarter (>164.7 cells/mm^2)	69 (24.91%)	24 (25.26%)	
cTNM			
cT			$\boldsymbol{p = 0.047}$
T1–T2	204 (73.65%)	59 (62.11%)	
T3–T4	71 (25.63%)	35 (36.84%)	
Unknown	2 (0.72%)	1 (1.05%)	
cN			$\boldsymbol{p = 0.029}$
N-	177 (63.90%)	48 (50.53%)	
N1	51 (18.41%)	17 (17.89%)	
N2	19 (6.86%)	13 (13.69%)	
N3	27 (9.75%)	16 (16.84%)	
Unknown	3 (1.08%)	1 (1.05%)	
cM			/
M−	277 (100%)	95 (100%)	
M+	0 (0%)	0 (0%)	
Tumor stage (AJCC 8th edition)			$\boldsymbol{p = 0.057}$
Stage I	55 (19.86%)	10 (10.53%)	
Stage IIa	93 (33.57%)	28 (29.47%)	
Stage IIb	16 (5.78%)	4 (4.21%)	

Table 1 (continued)

Characteristics	No recurrence/progression ($n = 277$) (74.46%)	Treatment failure ($n = 95$) (25.54%)	P value
Stage IIIa	56 (20.22%)	20 (21.05%)	
Stage IIIb	11 (3.97%)	5 (5.26%)	
Stage IIIc	41 (14.80%)	26 (27.37%)	
Stage IV	0 (0%)	0 (0%)	
Unknown	5 (1.80%)	2 (2.11%)	
Primary treatment			$p = 0.98$
Chemotherapy	0 (0%)	0 (0%)	
Radiotherapy	86 (31.05%)	29 (30.53%)	
Chemoradiotherapy	183 (66.06%)	64 (67.37%)	
Surgery	8 (2.89%)	2 (2.10%)	
Geographical location			$p = 0.585$
Besançon (France)	35 (12.64%)	10 (10.53%)	
Strasbourg (France)	58 (20.94%)	14 (14.74%)	
Nancy (France)	53 (19.13%)	18 (18.95%)	
Dijon (France)	73 (26.35%)	28 (29.47%)	
Liege (Begium)	58 (20.94%)	25 (26.31%)	

Bold values indicate statistically significant differences.

others (115/372, 30.9%) received 5 to 6 weeks of radiotherapy alone (45–59.4 Gy). The remaining patients (10/372, 2.7%) underwent primary surgery [local excision ($n = 9$) or abdominoperineal resection ($n = 1$)], most often (9/10, 90%) without neoadjuvant therapy. For these patients, the cTNM was concordant with the pTNM.

Study population: clinicopathological characterization

All clinicopathological variables assessed in this study as well as the overall results are shown in Fig. 1. Explaining the diffuse $p16^{ink4a}$ (surrogate biomarker for HPV infection) immunoreactivity displayed by the large majority of tumors (340/372, 91.4%), carcinogenic HPV infection was detected by both genotyping assay (INNO-LiPA or Abbott RealTime) and in situ hybridization in 91% (323/355) of tumor specimens. The concordance between high-risk HPV status and $p16^{ink4a}$ immunoreactivity was excellent (349/355, 98.3%). HPV16 was by far the most prevalent type (301/323, 93.2%) and multiple infections were relatively rare (23/323, 7.1%). All 17 (17/372, 4.6%) non-interpretable samples were fixed in Bouin's fluid. Largely correlated with mutated/deleted *TP53* [24], aberrant p53 expression (undetectable or ≥50% positive cells) was observed in a minority of neoplasms (39/372, 10.5%) but, importantly, was more frequently noticed in HPV/$p16^{ink4a}$-negative tumors (11/32, 34.4%) compared to their HPV-related counterparts (28/323, 8.7%). In most tumors (266/372, 71.5%), the percentage of proliferating (Ki67-positive) cells exceeded 50% and well to moderately differentiated cancers represented over two thirds (255/372, 68.5%) of specimens. Extremely specific and sensitive for categorizing anal SCC into two groups according to their cellular origin [15], semi-quantitative analysis of CK7 expression allowed to determine that neoplasms originating in the external non-keratinizing squamous mucosa (CK7 negative) were twice as frequent than tumors arising from the transitional zone (CK7 positive) (249/372, 66.9% vs. 123/372, 33.1%). Apart from 6 cases (6/32, 18.8%), all HPV-uninfected cancers (26/32, 81.2%) stained negative for CK7, in keeping with their development from the lower (squamous) part of the anal canal. Despite considerable interindividual variations, overall, high intratumoral densities of both $CD4^+$ (median: 359.2 cells/mm^2) and $CD8^+$ (median: 421.1 cells/mm^2) T cells were observed. As expected, the sum of these latter parameters was close to the absolute $CD3^+$ T-cell count (median: 839.2 cells/mm^2) determined in each sample, validating our computerized quantifications. PD-1^+ cells (median: 66.8 cells/mm^2) were less abundant within tumor microenvironment.

Risk factors predicting disease progression/recurrence

The median follow-up time was 53.8 months (range: 1.1–254 months). After completion of treatment, local recurrence/progression (in case of residual disease) occurred in 53 (53/372, 14.2%) patients and metastatic disease was diagnosed in 30 (30/372, 8.1%) patients. Twelve (12/372, 3.2%) patients experienced both local and distant recurrences. Among these latter, with the exception of 1 patient

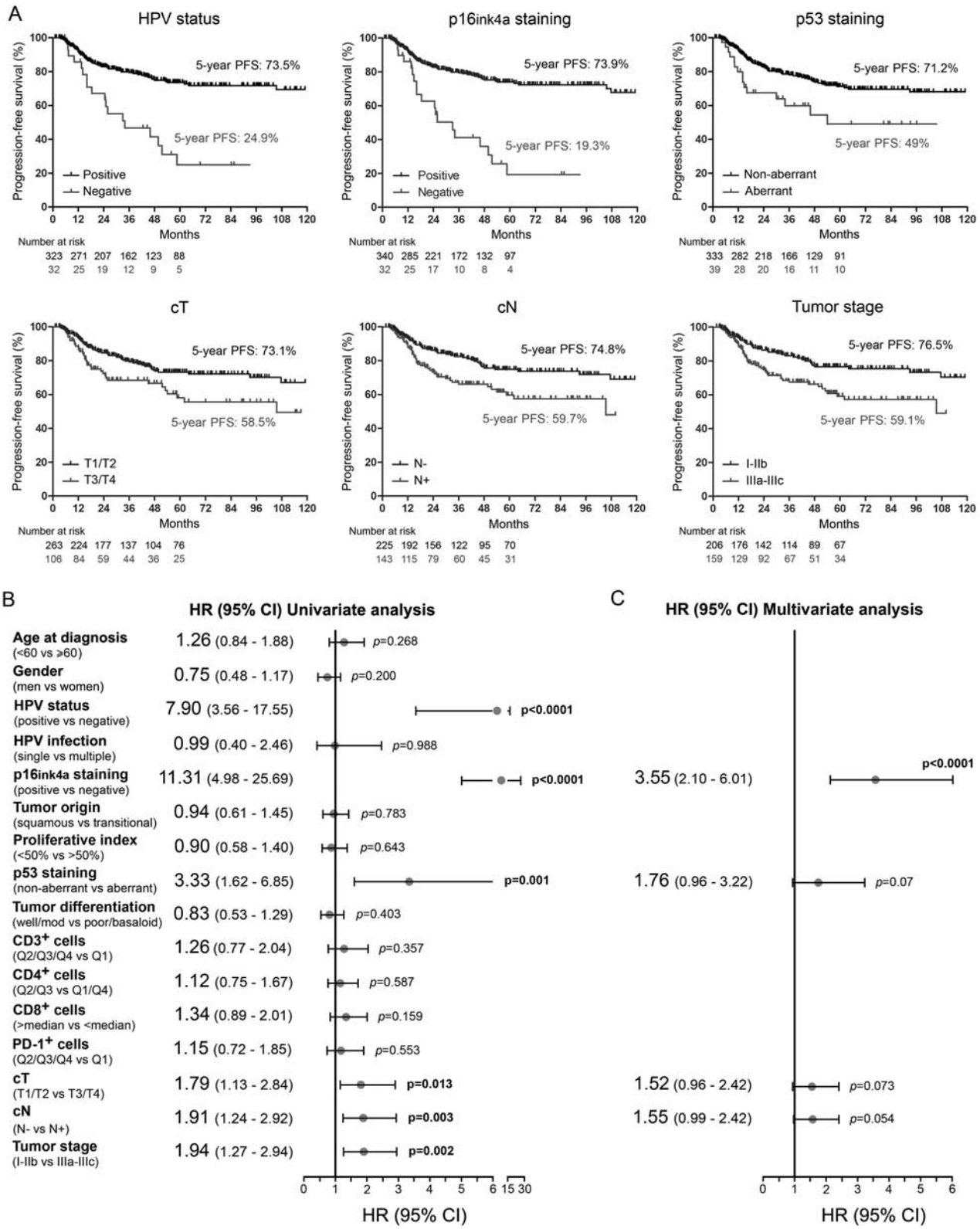

Fig. 2 Analysis of prognostic factors associated with progression-free survival. a Kaplan–Meier estimates of PFS according to significant risk factors highlighted in univariate analysis. Prognostic value of clinicopathological variables in univariate (**b**) and multivariate (**c**) analysis.

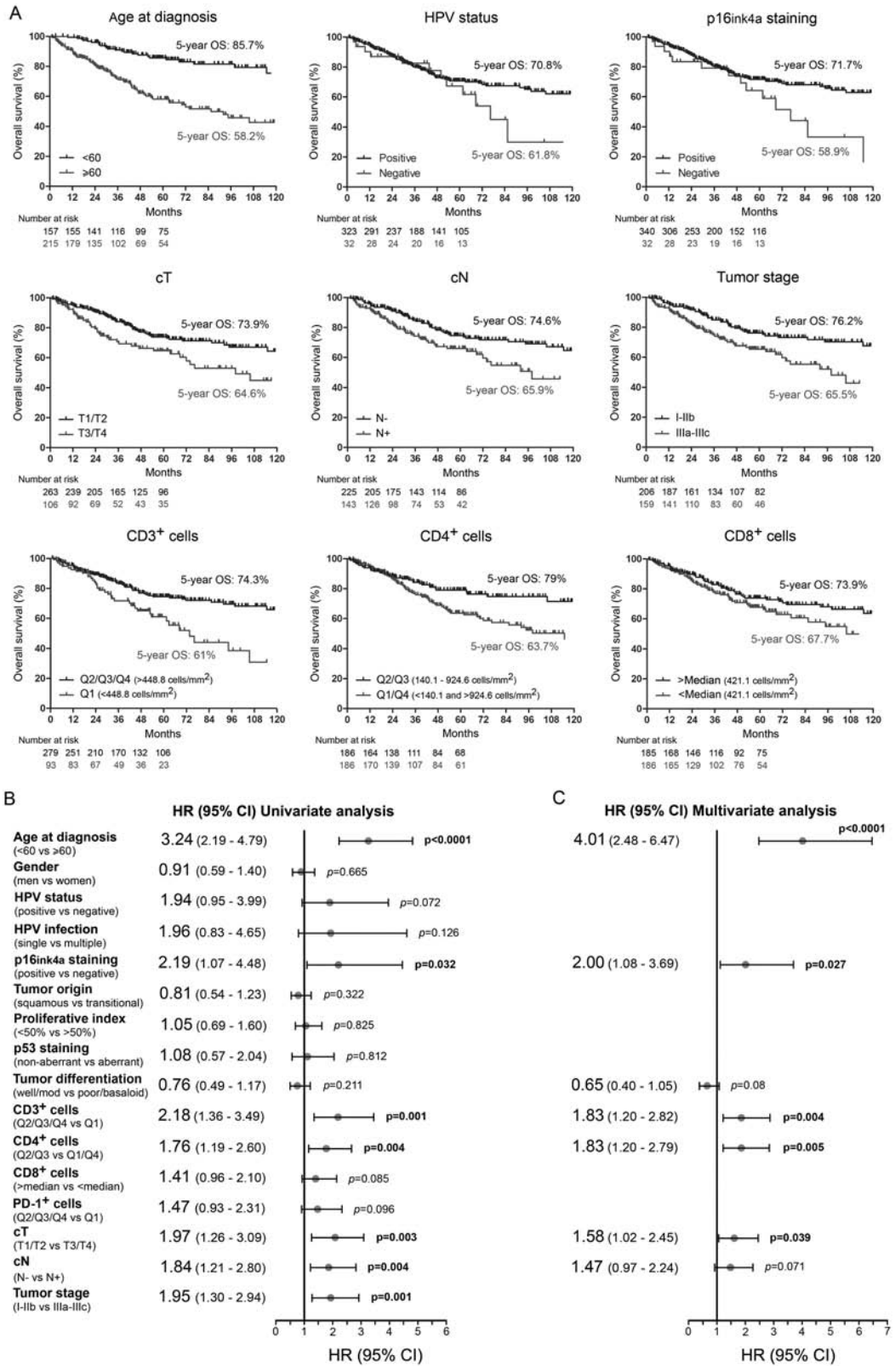

Fig. 3 Analysis of prognostic factors associated with overall survival. a Kaplan–Meier OS curves according to significant risk factors reported in univariate analysis (cut-off: $p < 0.1$). Prognostic value of clinicopathological variables in univariate (**b**) and multivariate (**c**) analysis.

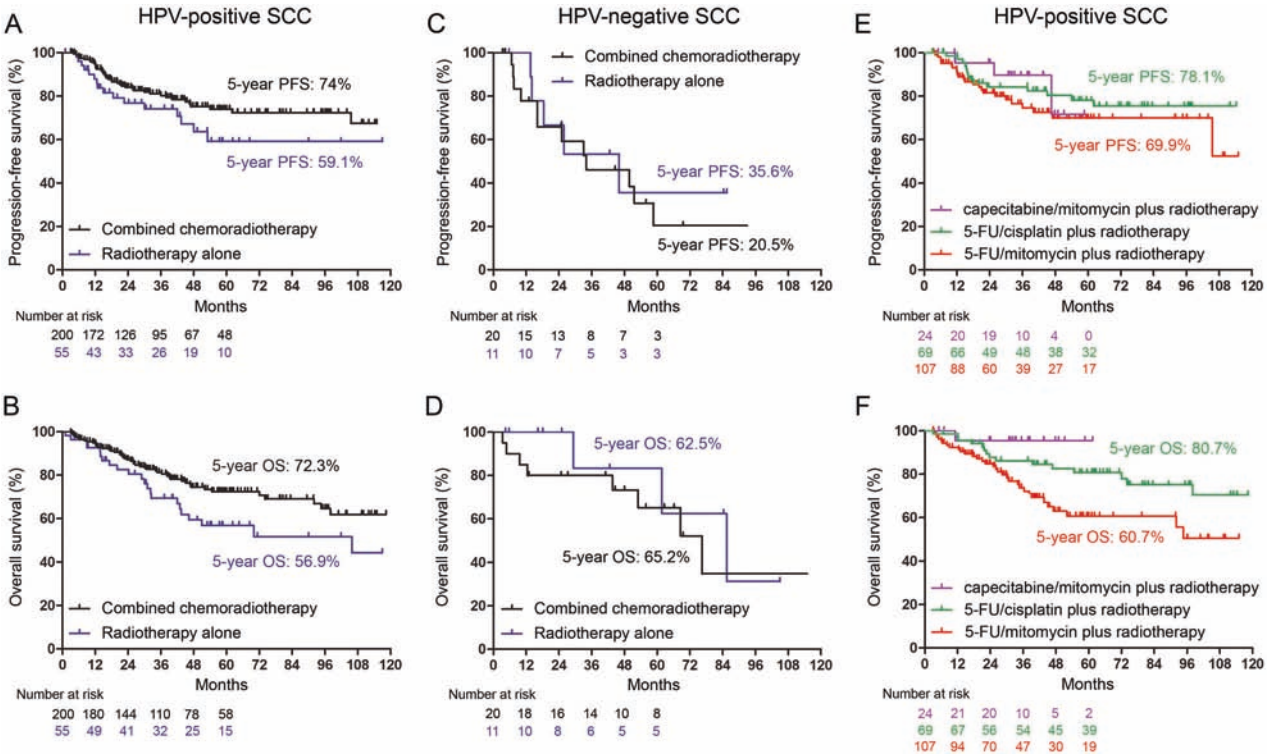

Fig. 4 Comparative efficacy of different treatment regimens. a, **c**, **e** PFS and **b**, **d**, **f** OS of patients with locally advanced (stage II-III) anal cancer according to treatment algorithms. All patients were subdivided into two groups based on their HPV status (HPV-positive vs. HPV-negative).

(1/12, 8.3%), locoregional relapse always preceded the detection of metastases (mostly in liver, lungs, and bone). The median time to local recurrence/progression and distant metastasis was 21.8 months and 25.9 months, respectively. Patient characteristics according to disease recurrence/progression are listed in Table 1. No statistical difference was noticed between the two groups in regard to age at diagnosis ($p = 0.718$), gender ($p = 0.236$), tumor origin (based on CK7 staining) ($p = 0.801$), proliferative index ($p = 0.182$), differentiation ($p = 0.597$), T-cell density ($CD3^+$, $p = 0.895$; $CD4^+$, $p = 0.556$; $CD8^+$, $p = 0.792$, $PD\text{-}1^+$, $p = 0.966$), primary treatment ($p = 0.98$) or hospital center where patients were treated ($p = 0.585$). In contrast, progressive or recurrent tumors were more often HPV/$p16^{ink4a}$-negative ($p < 0.0001$) with an aberrant p53 expression pattern ($p = 0.011$). In addition, local/distant recurrences occurred more frequently in patients diagnosed with neoplasms more than 5 cm wide ($p = 0.047$) manifesting an original lymphatic node involvement ($p = 0.029$) and, overall, in case of higher tumor stages ($p = 0.057$). Kaplan–Meier survival curves as well as both univariate and multivariate analyses for PFS are shown in Fig. 2. As opposed to 73.5% for HPV/$p16^{ink4a}$-positive cancers, importantly, 5-year PFS was only 24.9% and 19.3% for patients with HPV-uninfected [HR = 7.90; $p < 0.0001$] and $p16^{ink4a}$-negative (HR = 11.31; $p < 0.0001$) tumors, respectively. In univariate analysis, aberrant p53 staining (HR = 3.33; $p = 0.001$), high T-classification (T3/T4) (HR = 1.79; $p = 0.013$), lymph node positivity (HR = 1.91; $p = 0.003$) and advanced tumor stage (IIIa-IIIc) (HR = 1.94; $p = 0.002$) were also statistically related to poorer PFS. As shown in Fig. 2c, the multivariate analysis indicated that $p16^{ink4a}$ negative status ($p < 0.0001$) was a strong independent predictor for reduced PFS.

Prognostic factors for overall survival

During the follow-up period, 102 out of 372 (27.4%) patients died as a result of anal SCC or other causes (most notably old age). The OS (Kaplan–Meier curves) and the results of both univariate and multivariate analyses are shown in Fig. 3. In univariate analysis, the following clinicopathological factors were significantly associated with decreased OS: age at diagnosis (over 60) (HR = 3.24; $p < 0.0001$), $p16^{ink4a}$ negativity (HR = 2.19; $p = 0.032$), low intratumoral $CD3^+$ T-cell density (HR = 2.18; $p = 0.001$), low/high $CD4^+$ T-cell count (hormetic effect, Supplementary Fig. 1) (HR = 1.76; $p = 0.004$), high T-classification (T3/T4) (HR = 1.97; $p = 0.003$), positive nodal status (HR = 1.84; $p = 0.004$) and advanced tumor stage (IIIa-IIIc) (HR = 1.95; $p = 0.001$). Although patients with HPV-negative cancer tended to have a poorer OS compared to those treated for a HPV-positive tumor,

statistical significance was not reached (HR = 1.94; $p = 0.072$). A similar tendency was also reported in case of low densities of $CD8^+$ (HR = 1.41; $p = 0.085$) and $PD\text{-}1^+$ (HR = 1.47; $p = 0.096$) T cells within tumor microenvironment. As shown in Fig. 3c, patient age ($p < 0.0001$), $p16^{ink4a}$ negativity ($p = 0.027$), tumor size ($p = 0.039$) as well as both intratumoral $CD3^+$ ($p = 0.004$) and $CD4^+$ ($p = 0.005$) T-cell infiltrations were identified as independent prognostic factors for OS by multivariate analysis (Fig. 3c).

Efficacy of different treatment regimens

Out of 247 patients treated with chemoradiotherapy, 5-FU (750–1000 mg/m^2 on days 1–5 and 29–32)/mitomycin (10–12 mg/m^2 on day 1) was the predominantly used chemotherapeutic combination (133/247, 53.8%) followed by 5-FU/cisplatin (60–80 mg/m^2 on days 1 and 29 or 25 mg/m^2 weekly) (81/247, 32.8%) and capecitabine (2 × 825 mg/m^2 on radiation days)/mitomycin (25/247, 10.1%). The remaining patients (8/247, 3.2%) received only one anti-cancer agent or other drug cocktails such as mitomycin/cisplatin. Given the strong prognostic value of HPV status, and as routinely done with head and neck SCC for a decade [25, 26], anal cancer patients were sub-classified into two groups (HPV-positive vs. HPV-negative) and the efficacy of different combination drugs was assessed. As shown in Fig. 4a, b, combined chemoradiotherapy was superior to radiotherapy alone in the treatment of locally advanced (stage II-III) HPV-positive anal canal SCC [5-year PFS: 74% vs. 59.1% ($p = 0.084$); 5-year OS: 72.3% vs. 56.9% ($p = 0.089$)]. In contrast, although the total number of patients was relatively low, no benefit from the addition of chemotherapy to concurrent radiotherapy was observed with HPV-negative cancers and 5-year PFS was under 40% whatever the treatment administered (Fig. 4c). The efficacy of each individual chemoradiotherapy regimen was then assessed in the HPV-positive group. Evidence of improvement in both 5-year PFS (78.1% vs. 69.9%, $p = 0.201$) and OS (80.7% vs. 60.7%, $p = 0.024$) was observed with 5-FU/cisplatin compared to 5-FU/mitomycin chemoradiotherapy. As detailed in Supplementary Table 1, these latter results are unlikely to be explicated by differences in term of patient age, gender, HPV genotypes, tumor origin, proliferative index, p53 status, differentiation or cTNM/tumor stage classification. The low number of patients treated with capecitabine/mitomycin combined with radiotherapy does not allow to draw any conclusion regarding this treatment regimen.

Discussion

Based on a better understanding of cancer pathobiology, both the diagnosis and the subsequent management of most liquid and solid tumors have considerably evolved over the past decade, allowing a global improvement of patient outcome and quality of life. Although its incidence is increasing by 2–3% annually in high-income countries [2], anal carcinoma represents undoubtedly an exception. Indeed, treatment is still largely (if not exclusively) dictated by tumor staging and concurrent chemoradiotherapy has remained the gold standard of care for most (>90%) patients for almost 30 years [27]. This current situation is mainly explained by controversial results reported by earlier single-institution studies with limited sample sizes and/or containing poorly described patients with uncontrolled HIV infection (before the availability of highly active antiretroviral drugs). Aiming at in depth characterizing SCC arising from the anal canal, the present large multicenter cohort was first collected and the prognostic significance of various clinicopathological variables was explored. In agreement with half a dozen smaller studies published in the past few years [13–15, 28–31], HPV/$p16^{ink4a}$-negative status has been clearly shown as a robust predictor for unfavorable patient outcome. Similarly, aberrant p53 expression was also associated with poor response to treatment. Of note, in a weak proportion (<10%) of tumors, HPV infection and mutated *TP53* coexisted and, importantly, these latter neoplasms were associated with an intermediate prognosis [5-year PFS: 64.5% vs. 74.8% ($p = 0.048$)] (Fig. 5). Also mentioned in the context of both cervical and oropharyngeal cancers [32–34], these data further support the predictive value of *TP53* status in cancer patients undergoing chemoradiation-based therapy. Although no link between tumor origin and patient survival was observed in this larger study, the 2:1 ratio between the two region-specific subtypes of anal SCC (squamous zone vs. anal transitional zone) as well as the higher proportion of

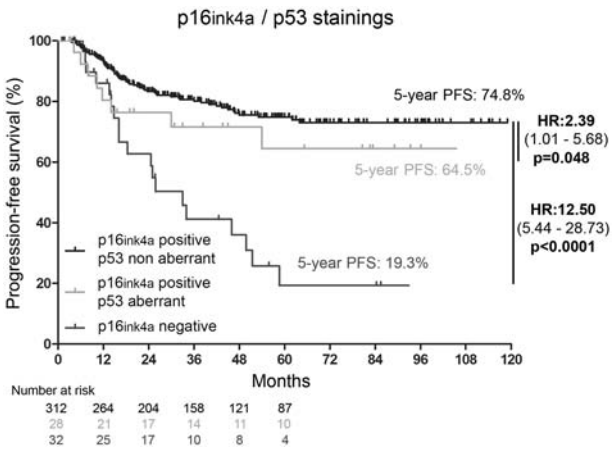

Fig. 5 Progression-free survival of anal cancer patients according to p16ink4a/p53 status. All patients were subdivided into three groups (p16ink4a-positive/p53 non aberrant vs. p16ink4a-positive/p53 aberrant vs. p16ink4a-negative). The intermediate prognosis of HPV-driven neoplasms displaying a mutated TP53 should be noticed.

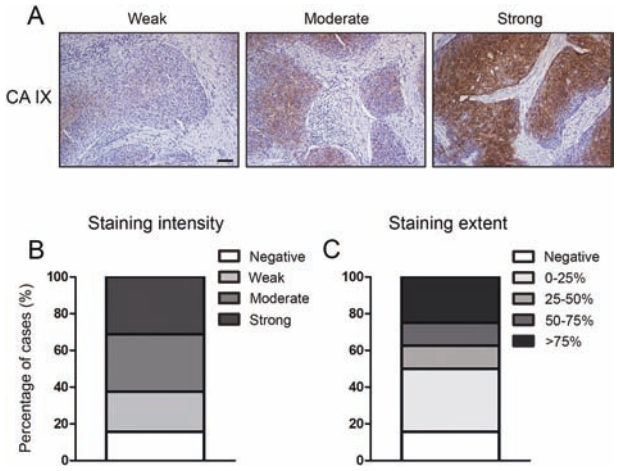

Fig. 6 Carbonic anhydrase IX, an endogenous hypoxia biomarker, expression in HPV-negative anal SCC. a Representative examples of anal cancer stained for CA IX. Semi-quantitative analysis of CA IX staining intensity (**b**) and extent (**c**) displayed by HPV-negative anal SCC ($n = 32$). The scale bar represents 100 µm.

HPV-uninfected neoplasms detected in the external part of the anal canal were confirmed. Interestingly, this latter result closely mimics the reported HPV prevalence for gynecological SCC (virtually all cervical cancers are HPV-positive whereas only about 75–80% vaginal neoplasms are etiologically related to HPV infection) [35].

Although never previously analyzed in anal cancers, the high densities of T-cell subsets within tumor microenvironment as well as the identification of $CD3^+$, $CD8^+$, and $PD\text{-}1^+$ tumor-infiltrating lymphocytes as favorable prognostic biomarkers were not really surprising given recent reports focusing on oropharynx [17–19]. The unexpected finding was the clear-cut beneficial effect of moderate densities of $CD4^+$ cells (Supplementary Fig. 1). Whether this hormetic effect is related to differences in T cell polarization (e.g., Th1, Th2, Th17, Treg) is unknown but, in view of its substantial prognostic value, single-cell RNA sequencing or flow cytometry analysis using enzymatically-dissociated fresh cancer biopsies certainly represent interesting perspectives.

Another striking finding in this study was the very high risk of disease progression and/or local/distant recurrence in patients with HPV-negative cancer, whatever the treatment regimen administered (chemoradiotherapy or radiotherapy alone). As commonly considered with oropharyngeal or vulvar tumors [25, 26], HPV-positive anal cancers and their HPV-negative counterparts represent undeniably two distinct entities and should, therefore, not be treated in the same way. The present data argues for a low radiosensitivity of HPV-uninfected SCC and, for lack of anything better, surgical resection could provide better outcomes. The use of hypoxia-activated pro-drugs (e.g., Nimorazole and Tirapazamine) alongside chemoradiotherapy could also be regarded as an attractive alternative [36]. Currently tested with head and neck SCC patients (NCT01950689), targeting hypoxia therapeutically might be efficient given that 27 out of 32 (84.4%) HPV-negative anal cancers displayed hypoxic areas, as supported by the expression of the endogenous hypoxia biomarker CA IX (Fig. 6).

The chemotherapeutic drug combination used as first line regimen for HPV-positive patients has been a matter of debate for a long time and is still mainly dependent on clinician preferences. Here, we showed that chemoradiation using 5-FU and cisplatin was superior to concurrent chemoradiotherapy involving 5-FU/mitomycin. Although our study is limited by its retrospective design and the toxicity profile between groups was not assessed, the present results intriguingly confirm the clinical success of cisplatin in the treatment of HPV-positive tumors. Indeed, cisplatin demonstrated clear benefits in terms of overall survival and reduced recurrences compared to other common chemotherapy regimens or targeted therapies (e.g., cetuximab) for both cervical and HPV-positive oropharyngeal cancer patients [37–39]. Although still not fully understood, recent evidences demonstrated that DNA damage pathways are hijacked by HPV E6/E7 oncoproteins to promote viral life cycle [40, 41]. Therefore, this latter phenomenon could represent the Achilles' heel of HPV-positive cancers and explain their high sensitivity to cisplatin-induced DNA single/double-strand breaks.

In conclusion, traditional prognostic factors such as tumor size and nodal status as well as treatment algorithms used since the mid-90's for non-metastatic anal SCC have clearly reached their limits. Based on both the present information and the literature on oropharyngeal, vaginal/vulvar and penile cancers accumulated during the last decade, anal cancer patients should be systematically separated into two groups according to HPV/$p16^{ink4a}$ status. In case of *TP53* mutation in HPV-driven cancer, a closer monitoring could be considered. The potential therapeutic benefit of cisplatin-based chemoradiotherapy or immune checkpoint inhibitors (e.g., anti-PD-1) compared to concurrent radiotherapy plus 5-FU and mitomycin would require further investigations. Finally, our results point to the crucial requirement to optimize current treatment and/or to investigate novel drugs/strategies for treating HPV-negative anal cancers.

Acknowledgements The authors thank their clinical colleagues at the University/Regional Medical Centers of Liege, Nancy, Dijon, Strasbourg and Besançon for helpful discussions. We also thank the Biobanks of the University of Liege and University Hospital of Besançon (biobank BB-0033–00024) as well as the GIGA-Immunohistochemistry Platform (University of Liege) for their assistance. We are also grateful to Dr Stephanie Gofflot, Raphael Thonon, Kamilia El Kandoussi, Tiffany Di Salvo and Hülya Kocadag for their technical assistance. DB, CP, TL, CR, and MA are Televie/FRIA fellows. EH is a Televie postdoctoral researcher. MH is a Research Associate at the FNRS.

Funding This work was supported in part by the Belgian Fund for Scientific Research [R.FNRS.4985 (MIS F.4520.20)], the University of Liege [Crédits Sectoriels de Recherche en Sciences de la Santé 2018–2019 (R.CFRA.3025 and R.CFRA.3238)], the Télévie [R. FNRS.4817 (PDR Televie 7.8507.19)], the Leon Fredericq Foundation and the French League against Cancer (Conférence de Coordination InterRégionale Est).

Author contributions MH designed the study; FM, PR, LV, ALe, ALu, PM, LA, M-CB-L, LD, LM, DP, AL, J-BD, J-PG, A-SW, PD, J-FB, and SV-D collected data/tissue specimens; DB, PR, EH, CP, TL, CR, MA, J-LP, and MH performed experiments; DB, FM, PC, ChlM, PH, PD, ChrM, SV-D, and MH interpreted the data and/or reviewed the samples; DB, OP, and MH performed the statistical analysis; DB and MH generated the Figures; MH wrote the paper. All authors had final approval of the submitted manuscript.

Compliance with ethical standards

Conflict of interest The authors declare that they have no conflict of interest.

Publisher's note Springer Nature remains neutral with regard to jurisdictional claims in published maps and institutional affiliations.

References

1. Bray F, Ferlay J, Soerjomataram I, Siegel RL, Torre LA, Jemal A. Global cancer statistics 2018: GLOBOCAN estimates of incidence and mortality worldwide for 36 cancers in 185 countries. CA Cancer J Clin. 2018;68:394–424.
2. Nelson RA, Levine AM, Bernstein L, Smith DD, Lai LL. Changing patterns of anal canal carcinoma in the United States. J Clin Oncol. 2013;31:1569–75.
3. Williams GR, Talbot IC. Anal carcinoma–a histological review. Histopathology. 1994;25:507–16.
4. Lin C, Franceschi S, Clifford GM. Human papillomavirus types from infection to cancer in the anus, according to sex and HIV status: a systematic review and meta-analysis. Lancet Infect Dis. 2018;18:198–206.
5. Colon-Lopez V, Shiels MS, Machin M, Ortiz AP, Strickler H, Castle PE, et al. Anal cancer risk among people with HIV infection in the United States. J Clin Oncol. 2018;36:68–75.
6. Bartelink H, Roelofsen F, Eschwege F, Rougier P, Bosset JF, Gonzalez DG, et al. Concomitant radiotherapy and chemotherapy is superior to radiotherapy alone in the treatment of locally advanced anal cancer: results of a phase III randomized trial of the European Organization for Research and Treatment of Cancer Radiotherapy and Gastrointestinal Cooperative Groups. J Clin Oncol. 1997;15:2040–9.
7. Flam M, John M, Pajak TF, Petrelli N, Myerson R, Doggett S, et al. Role of mitomycin in combination with fluorouracil and radiotherapy, and of salvage chemoradiation in the definitive nonsurgical treatment of epidermoid carcinoma of the anal canal: results of a phase III randomized intergroup study. J Clin Oncol. 1996;14:2527–39.
8. Meulendijks D, Dewit L, Tomasoa NB, van Tinteren H, Beijnen JH, Schellens JH, et al. Chemoradiotherapy with capecitabine for locally advanced anal carcinoma: an alternative treatment option. Br J Cancer. 2014;111:1726–33.
9. Ajani JA, Winter KA, Gunderson LL, Pedersen J, Benson AB,3rd, Jr Thomas CR. et al. Fluorouracil, mitomycin, and radiotherapy vs fluorouracil, cisplatin, and radiotherapy for carcinoma of the anal canal: a randomized controlled trial. JAMA. 2008;299:1914–21.
10. James RD, Glynne-Jones R, Meadows HM, Cunningham D, Myint AS, Saunders MP, et al. Mitomycin or cisplatin chemoradiation with or without maintenance chemotherapy for treatment of squamous-cell carcinoma of the anus (ACT II): a randomised, phase 3, open-label, 2 × 2 factorial trial. Lancet Oncol. 2013;14:516–24.
11. Matzinger O, Roelofsen F, Mineur L, Koswig S, Van Der Steen-Banasik EM, Van Houtte P, et al. Mitomycin C with continuous fluorouracil or with cisplatin in combination with radiotherapy for locally advanced anal cancer (European Organisation for Research and Treatment of Cancer phase II study 22011-40014). Eur J Cancer. 2009;45:2782–91.
12. Bian JJ, Almhanna K. Anal cancer and immunotherapy-are we there yet? Transl Gastroenterol Hepatol. 2019;4:57.
13. Serup-Hansen E, Linnemann D, Skovrider-Ruminski W, Hogdall E, Geertsen PF, Havsteen H. Human papillomavirus genotyping and p16 expression as prognostic factors for patients with American Joint Committee on Cancer stages I to III carcinoma of the anal canal. J Clin Oncol. 2014;32:1812–7.
14. Meulendijks D, Tomasoa NB, Dewit L, Smits PH, Bakker R, van Velthuysen ML, et al. HPV-negative squamous cell carcinoma of the anal canal is unresponsive to standard treatment and frequently carries disruptive mutations in TP53. Br J Cancer. 2015;112:1358–66.
15. Herfs M, Longuespee R, Quick CM, Roncarati P, Suarez-Carmona M, Hubert P, et al. Proteomic signatures reveal a dualistic and clinically relevant classification of anal canal carcinoma. J Pathol. 2017;241:522–33.
16. Shah W, Yan X, Jing L, Zhou Y, Chen H, Wang Y. A reversed CD4/CD8 ratio of tumor-infiltrating lymphocytes and a high percentage of CD4(+)FOXP3(+) regulatory T cells are significantly associated with clinical outcome in squamous cell carcinoma of the cervix. Cell Mol Immunol. 2011;8:59–66.
17. Badoual C, Hans S, Merillon N, Van Ryswick C, Ravel P, Benhamouda N, et al. PD-1-expressing tumor-infiltrating T cells are a favorable prognostic biomarker in HPV-associated head and neck cancer. Cancer Res. 2013;73:128–38.
18. Jung AC, Guihard S, Krugell S, Ledrappier S, Brochot A, Dalstein V, et al. CD8-alpha T-cell infiltration in human papillomavirus-related oropharyngeal carcinoma correlates with improved patient prognosis. Int J Cancer. 2013;132:E26–36.
19. Oguejiofor K, Hall J, Slater C, Betts G, Hall G, Slevin N, et al. Stromal infiltration of CD8 T cells is associated with improved clinical outcome in HPV-positive oropharyngeal squamous carcinoma. Br J Cancer. 2015;113:886–93.
20. Herfs M, Roncarati P, Koopmansch B, Peulen O, Bruyere D, Lebeau A, et al. A dualistic model of primary anal canal adenocarcinoma with distinct cellular origins, etiologies, inflammatory microenvironments and mutational signatures: implications for personalised medicine. Br J Cancer. 2018;118:1302–12.
21. de Graeff P, Hall J, Crijns AP, de Bock GH, Paul J, Oien KA, et al. Factors influencing p53 expression in ovarian cancer as a biomarker of clinical outcome in multicentre studies. Br J Cancer. 2006;95:627–33.
22. Bankhead P, Loughrey MB, Fernandez JA, Dombrowski Y, McArt DG, Dunne PD, et al. QuPath: open source software for digital pathology image analysis. Sci Rep. 2017;7:16878.
23. Kocjan BJ, Seme K, Poljak M. Comparison of the Abbott Real-Time High Risk HPV test and INNO-LiPA HPV Genotyping Extra test for the detection of human papillomaviruses in formalin-fixed, paraffin-embedded cervical cancer specimens. J Virol Methods. 2011;175:117–9.
24. Murnyak B, Hortobagyi T. Immunohistochemical correlates of TP53 somatic mutations in cancer. Oncotarget. 2016;7:64910–20.

25. Chow LQM. Head and neck cancer. N Engl J Med. 2020;382:60–72.
26. Mallen-St Clair J, Alani M, Wang MB, Srivatsan ES. Human papillomavirus in oropharyngeal cancer: the changing face of a disease. Biochim Biophys Acta. 2016;1866:141–50.
27. Ghosn M, Kourie HR, Abdayem P, Antoun J, Nasr D. Anal cancer treatment: current status and future perspectives. World J Gastroenterol. 2015;21:2294–302.
28. Mai S, Welzel G, Ottstadt M, Lohr F, Severa S, Prigge ES, et al. Prognostic relevance of HPV Infection and p16 overexpression in squamous cell anal cancer. Int J Radiat Oncol Biol Phys. 2015;93:819–27.
29. Rodel F, Wieland U, Fraunholz I, Kitz J, Rave-Frank M, Wolff HA, et al. Human papillomavirus DNA load and p16INK4a expression predict for local control in patients with anal squamous cell carcinoma treated with chemoradiotherapy. Int J Cancer. 2015;136:278–88.
30. Koerber SA, Schoneweg C, Slynko A, Krug D, Haefner MF, Herfarth K, et al. Influence of human papillomavirus and p16 (INK4a) on treatment outcome of patients with anal cancer. Radiother Oncol. 2014;113:331–6.
31. Soares PC, Abdelhay ES, Thuler LCS, Soares BM, Demachki S, Ferro GVR, et al. HPV positive, wild type TP53, and p16 overexpression correlate with the absence of residual tumors after chemoradiotherapy in anal squamous cell carcinoma. BMC Gastroenterol. 2018;18:30.
32. Westra WH, Taube JM, Poeta ML, Begum S, Sidransky D, Koch WM. Inverse relationship between human papillomavirus-16 infection and disruptive p53 gene mutations in squamous cell carcinoma of the head and neck. Clin Cancer Res. 2008;14:366–9.
33. Maruyama H, Yasui T, Ishikawa-Fujiwara T, Morii E, Yamamoto Y, Yoshii T, et al. Human papillomavirus and p53 mutations in head and neck squamous cell carcinoma among Japanese population. Cancer Sci. 2014;105:409–17.
34. Busby-Earle RM, Steel CM, Williams AR, Cohen B, Bird CC. p53 mutations in cervical carcinogenesis–low frequency and lack of correlation with human papillomavirus status. Br J Cancer. 1994;69:732–7.
35. de Martel C, Plummer M, Vignat J, Franceschi S. Worldwide burden of cancer attributable to HPV by site, country and HPV type. Int J Cancer. 2017;141:664–70.
36. Mistry IN, Thomas M, Calder EDD, Conway SJ, Hammond EM. Clinical advances of hypoxia-activated prodrugs in combination with radiation therapy. Int J Radiat Oncol Biol Phys. 2017;98:1183–96.
37. Mehanna H, Robinson M, Hartley A, Kong A, Foran B, Fulton-Lieuw T, et al. Radiotherapy plus cisplatin or cetuximab in low-risk human papillomavirus-positive oropharyngeal cancer (De-ESCALaTE HPV): an open-label randomised controlled phase 3 trial. Lancet. 2019;393:51–60.
38. Rose PG, Bundy BN, Watkins EB, Thigpen JT, Deppe G, Maiman MA, et al. Concurrent cisplatin-based radiotherapy and chemotherapy for locally advanced cervical cancer. N Engl J Med. 1999;340:1144–53.
39. Ryu SY, Lee WM, Kim K, Park SI, Kim BJ, Kim MH, et al. Randomized clinical trial of weekly vs. triweekly cisplatin-based chemotherapy concurrent with radiotherapy in the treatment of locally advanced cervical cancer. Int J Radiat Oncol Biol Phys. 2011;81:e577–81.
40. Anacker DC, Moody CA. Modulation of the DNA damage response during the life cycle of human papillomaviruses. Virus Res. 2017;231:41–9.
41. Spriggs CC, Laimins LA. Human papillomavirus and the DNA damage response: exploiting host repair pathways for viral replication. Viruses 2017;9:232–46.

Affiliations

Diane Bruyere[1] · Franck Monnien[2] · Prudence Colpart[2] · Patrick Roncarati[1] · Lucine Vuitton[3,4] · Elodie Hendrick[1] · Alexis Lepinoy[5] · Alexandra Luquain[2] · Charlotte Pilard[1] · Thomas Lerho[1] · Chloé Molimard[2] · Philippe Maingon[6,7] · Laurent Arnould[8] · Marie-Christine Bone-Lepinoy[5] · Laurence Dusserre[9] · Laurent Martin[10] · Celia Reynders[1] · Marie Ancion[1] · Didier Peiffert[11] · Agnès Leroux[12] · Pascale Hubert[1] · Jean-Baptiste Delhorme[13] · Jean-Pierre Ghnassia[14] · Anne-Sophie Woronoff[15] · Philippe Delvenne[1,16] · Jean-Luc Prétet[4,17] · Jean-François Bosset[18] · Olivier Peulen[19] · Christiane Mougin[4,17] · Séverine Valmary-Degano[2,4,20] · Michael Herfs[1]

[1] Laboratory of Experimental Pathology, GIGA-Cancer, University of Liege, 4000 Liege, Belgium

[2] Department of Pathology, University Hospital of Besançon, 25000 Besançon, France

[3] Department of Gastroenterology, University Hospital of Besançon, 25000 Besançon, France

[4] EA3181, University Bourgogne Franche-Comté, LabEx LipSTIC ANR-11-LABX-0021, 25000 Besançon, France

[5] Bourgogne Institute of Oncology, 21000 Dijon, France

[6] Department of Radiation Oncology, Georges-François Leclerc Center, 21000 Dijon, France

[7] Department of Radiation Oncology, La Pitié Salpêtrière University Hospital, Sorbonne University, 75013 Paris, France

[8] Department of Biology and Pathology of Tumors, Georges-François Leclerc Center, 21000 Dijon, France

[9] Pathology Center of Dijon (Cypath), 21000 Dijon, France

[10] Department of Pathology, University Hospital of Dijon, 21000 Dijon, France

[11] Department of Radiation Oncology, Lorraine Institute of Oncology, 54519 Vandœuvre-lès-Nancy, France

[12] Department of Pathology, Lorraine Institute of Oncology, 54519 Vandœuvre-lès-Nancy, France

[13] Department of Digestive Surgery, University Hospital of Strasbourg, 67200 Strasbourg, France

[14] Department of Pathology, Paul Strauss Center, 67000 Strasbourg, France

[15] Doubs and Belfort Territory Cancer Registry, University Hospital of Besançon, 25000 Besançon, France

[16] Department of Pathology, University Hospital of Liege, 4000 Liege, Belgium

[17] CNR Papillomavirus, University Hospital of Besançon, 25000 Besançon, France

[18] Department of Radiation Oncology, University Hospital of Besançon, 25000 Besançon, France

[19] Metastasis Research Laboratory, GIGA-Cancer, University of Liege, 4000 Liege, Belgium

[20] Department of Pathology, University Hospital of Grenoble-Alps, 38043 Grenoble cedex 9, France

Journal for ImmunoTherapy of Cancer

Extracellular HMGB1 blockade inhibits tumor growth through profoundly remodeling immune microenvironment and enhances checkpoint inhibitor-based immunotherapy

Pascale Hubert,[1] Patrick Roncarati,[1] Stephanie Demoulin,[1] Charlotte Pilard,[1] Marie Ancion,[1] Celia Reynders,[1] Thomas Lerho,[1] Diane Bruyere,[1] Alizee Lebeau,[1] Coraline Radermecker,[2,3] Margot Meunier,[2,3] Marie-Julie Nokin,[4] Elodie Hendrick,[1] Olivier Peulen,[4] Philippe Delvenne,[1,5] Michael Herfs [1]

To cite: Hubert P, Roncarati P, Demoulin S, *et al*. Extracellular HMGB1 blockade inhibits tumor growth through profoundly remodeling immune microenvironment and enhances checkpoint inhibitor-based immunotherapy. *Journal for ImmunoTherapy of Cancer* 2021;**9**:e001966. doi:10.1136/jitc-2020-001966

► Additional material is published online only. To view please visit the journal online (http://dx.doi.org/10.1136/jitc-2020-001966).

Accepted 10 February 2021

For numbered affiliations see end of article.

Correspondence to
Dr Michael Herfs;
M.Herfs@uliege.be

ABSTRACT

Background High-mobility group box 1 (HMGB1) is a multifunctional redox-sensitive protein involved in various intracellular (eg, chromatin remodeling, transcription, autophagy) and extracellular (inflammation, autoimmunity) processes. Regarding its role in cancer development/progression, paradoxical results exist in the literature and it is still unclear whether HMGB1 mainly acts as an oncogene or a tumor suppressor.

Methods HMGB1 expression was first assessed in tissue specimens (n=359) of invasive breast, lung and cervical cancer and the two distinct staining patterns detected (nuclear vs cytoplasmic) were correlated to the secretion profile of malignant cells, patient outcomes and the presence of infiltrating immune cells within tumor microenvironment. Using several orthotopic, syngeneic mouse models of basal-like breast (4T1, 67NR and EpRas) or non-small cell lung (TC-1) cancer, the efficacy of several HMGB1 inhibitors alone and in combination with immune checkpoint blockade antibodies (anti-PD-1/PD-L1) was then investigated. Isolated from retrieved tumors, 14 immune cell (sub)populations as well as the activation status of antigen-presenting cells were extensively analyzed in each condition. Finally, the redox state of HMGB1 in tumor-extruded fluids and the influence of different forms (oxidized, reduced or disulfide) on both dendritic cell (DC) and plasmacytoid DC (pDC) activation were determined.

Results Associated with an unfavorable prognosis in human patients, we clearly demonstrated that targeting extracellular HMGB1 elicits a profound remodeling of tumor immune microenvironment for efficient cancer therapy. Indeed, without affecting the global number of ($CD45^+$) immune cells, drastic reductions of monocytic/granulocytic myeloid-derived suppressor cells (MDSC) and regulatory T lymphocytes, a higher M1/M2 ratio of macrophages as well as an increased activation of both DC and pDC were continually observed following HMGB1 inhibition. Moreover, blocking HMGB1 improved the efficacy of anti-PD-1 cancer monoimmunotherapy. We also reported that a significant fraction of HMGB1 encountered within cancer microenvironment (interstitial fluids) is oxidized and, in opposite to its reduced isoform, oxidized HMGB1 acts as a tolerogenic signal in a receptor for advanced glycation endproducts-dependent manner.

Conclusion Collectively, we present evidence that extracellular HMGB1 blockade may complement first-generation cancer immunotherapies by remobilizing antitumor immune response.

INTRODUCTION

High-mobility group box 1 (HMGB1) was originally identified in the early 70s as an ubiquitous and abundant non-histone chromatin-binding protein.[1] Highly conserved (>95% identity) among all mammals, nuclear HMGB1 is involved in replication, gene expression, DNA repair and contributes actively to genome stability. Thirty years later, compelling data revealed the implication of HMGB1 in the pathogenesis of a variety of non-infectious, inflammatory/autoimmune disorders (eg, sepsis, rheumatoid arthritis, systemic lupus erythematosus, myositis),[2–5] supporting its additional role in immune responses. Actively secreted under inflammatory/stress conditions or passively released from any type of injured cells, HMGB1 triggers and amplifies these diverse inflammation-associated diseases through both stimulating proinflammatory cytokine synthesis (eg, tumor necrosis factor-α (TNFα), interleukin (IL)-1β, IL-6) and inducing immature immune cell activation and chemotaxis.[6–8] In addition to operate as an 'alarmin' via the receptor for advanced glycation endproducts (RAGE) and/or Toll-like receptor (TLR) 2, 4 and 9 signaling(s), extracellular HMGB1 may also regulate vascular growth and

axonal sprouting,[9 10] extending its activity well beyond its pro-inflammatory function. More recently, the crucial importance of redox status of three cysteine residues at positions 23, 45 and 106 in the regulation of HMGB1 cytokine activity was emphasized.[11–14] As a result, three redox forms of HMGB1 have been described: reduced, disulfide (Cys-23 and Cys-45 forming an intramolecular bond) and oxidized HMGB1. Of note, this latter form can be partially (Cys-106) or completely oxidized at the critical amino acids. Reduced and disulfide HMGB1 have been shown to have chemotactic and pro-inflammatory activity, respectively,[13] whereas reactive oxygen species (ROS)-dependent oxidation of HMGB1 at Cys-106 abrogates its immunostimulatory activity and contributes to apoptotic cell-mediated immunotolerance through still unknown mechanisms.[11] These opposite roles displayed by mutually exclusive forms of HMGB1 are likely to explain the paradoxical results collected over the years, especially in the context of cancer development. Although increasing evidence reports that HMGB1 could enhance drug resistance and contribute to tumor progression and metastasis,[15–20] a defective immunogenic cell death associated with a reduced efficacy of both anthracyclines and oxaliplatin following HMGB1 knockdown was also described.[21 22] Therefore, it remains unclear whether extracellular HMGB1 acts as a pro-tumor or a tumor-suppressor protein during carcinogenesis.[23]

In the past decade, immunotherapy using immune checkpoint inhibitors (especially drugs blocking the programmed cell death protein 1 (PD-1)and its ligand (PD-L1)) has raised considerable interest for treating patients with advanced (metastatic) cancers or unresponsive/resistant to targeted therapies. Despite tremendous clinical successes with some cancer (sub)types (eg, Merkel cell carcinoma, melanoma, microsatellite instability-high colorectal cancer) and the progressive increase of eligible patients for anti-PD-1/PD-L1 monoclonal antibodies (from ~1% in 2011 to >40% in 2018), the overall response rate to checkpoint immunotherapy remains modest for most cancers (12.46% in 2018 among US patients).[24] As an example, basal-like (also commonly called 'triple negative' due to the lack of expression of HER2 and nuclear hormone receptors) breast cancer has been shown to exhibit a high immunogenicity[25] but the proportion of responders did not exceed 15% in several phase I–II clinical trials,[26 27] reflecting that individual patient immunity is complex and, undoubtedly, leads to variability in response to treatment. Therefore, the combination of immune checkpoint inhibitors with standard cancer treatments (eg, chemotherapy) or drugs targeting another tumor-induced immune defect is frequently considered as a promising strategy for improving the efficacy of future therapies (without, hopefully, excessively increasing the incidence of immune-related adverse events).[28] In this regard, recent clinical data reported the beneficial effect of chemoimmunotherapy in the context of various solid tumors (eg, non-small-cell lung cancer and basal-like breast cancer).[29 30] The combination of two immunomodulatory drugs (the therapy concurrently targeting PD-1 and cytotoxic T-lymphocyte-associated protein 4 (CTLA-4) is, by far, the most vigorously examined) has also showed to improve both durable response rate and disease-free survival of responding patients compared with monotherapies.[31] However, of note is that the combinational approach of several immunoregulatory blockers can also cause antagonistic instead of synergistic effects (eg, concurrent immunotherapy using anti-PD-1 antibody and CD134/OX40 agonist).[32]

The present study aims at clearly determining whether targeting extracellular HMGB1 with both direct and indirect inhibitors may be efficient in cancer therapy. Particularly relevant for studying novel anticancer drugs with potential immunotherapeutic properties, several syngeneic mouse models were used and the tumor immune microenvironment was precisely characterized in each condition. The efficacy of HMGB1 inhibitors in combination with immune checkpoint blockade antibodies (anti-PD-1/PD-L1) was also assessed. Finally, the redox state of HMGB1 in tumor-extruded fluids as well as the influence of different forms on antigen presenting cell activation were determined.

MATERIALS AND METHODS

Tissue samples and clinical data retrieval

A total of 359 paraffin-embedded cancer specimens and 180 paired normal tissues from the same patients were retrieved from the Tissue Biobank of the University Hospital Center of Liege (Belgium). These tissue samples included 120 normal breast tissues, 40 HPV-negative ectocervical mucosae, 20 normal bronchial epithelia, 275 invasive breast tumors (35 luminal A, 31 luminal B, 37 HER2+ and 172 basal-like), 57 cervical squamous cell carcinomas (SCC) and 27 non-small-cell lung cancers (adenocarcinomas). All cases were re-examined by experienced histopathologists to confirm the diagnosis. Clinicopathological data (age at diagnosis, TNM classification, proliferation index, treatment details (surgery and/or (neo)adjuvant therapies) and follow-up data) for all women diagnosed with basal-like breast cancer were extracted from patient's medical records (online supplemental table 1).

Mouse and human cell cultures

The 4T1, 67NR (mouse basal-like breast cancer cells) and TC-1 (mouse lung cancer cells expressing HPV16 E6 and E7 oncoproteins) cells were kindly provided by Dr Nathalie Bendriss-Vermare (INSERM U1052, Claude Bernard Lyon 1 University, France) and Dr Sophie Hallez (Laboratory of Chemical Biology, Université Libre de Bruxelles, Belgium), respectively. These latter cell lines were maintained in Roswell Park Memorial Institute (RPMI) 1640 medium (Gibco, Thermo Fisher Scientific, Waltham, Massachusetts, USA) containing 10% fetal calf serum (Lonza, Basel, Switzerland), 1% non-essential amino acid (Gibco, 100X), 1 mM sodium pyruvate (Gibco), 2 mM L-glutamine (Gibco), 50 µM β-mercaptoethanol

(Gibco) and 1% penicillin-streptomycin (Gibco, 100X). Neu15 cells (kindly provided by Dr Nathalie Bendriss-Vermare) were cultured in RPMI 1640 supplemented with 10% fetal calf serum, 1% non-essential amino acids, 1 mM sodium pyruvate, 2 mM L-glutamine, 1% insulin-transferrin-selenium (Gibco, 100X) and 1% penicillin-streptomycin. Both EpRas and EpH4 (kindly provided by Professor Hartmut Beug, University of Vienna, Austria) as well as RAW264.7 cells were grown in Dulbecco's Modified Eagle Medium (DMEM) containing 10% fetal calf serum and supplied with 1% non-essential amino acids, 1 mM sodium pyruvate and 1% penicillin-streptomycin. Normal human mammary epithelial cells (HMEC and MCF10A) and human breast cancer cell lines (Luminal A: T-47D and MCF7; HER2+: SK-BR-3; basal-like: MDA-MB-468, BT-549, MDA-MB-231, MDA-MB-157, HCC70, HCC1143 and Hs578T) were obtained from the American Type Culture Collection (Manassas, Virginia, USA) or were kindly provided by Dr Akeila Bellahcene (Metastasis Research Laboratory, University of Liege, Belgium), Dr Christine Gilles (Laboratory of Tumor and Development Biology, University of Liege, Belgium) or Dr Alain Chariot (Laboratory of Medical Chemistry, University of Liege, Belgium). MDA-MB-231, HCC70 and HCC1143 were cultured in RPMI 1640 supplemented with 10% fetal calf serum, 1% non-essential amino acids, 1 mM sodium pyruvate, 50 µM β-mercaptoethanol and 1% penicillin-streptomycin. MCF7 and Hs578T were maintained in DMEM containing 10% fetal calf serum, 1% non-essential amino acids, 1 mM sodium pyruvate, 2 mM L-glutamine, 10 µg/mL insulin (Sigma Aldrich, Saint Louis, Michigan, USA) and 1% penicillin-streptomycin. MDA-MB-157 and MDA-MB-468 were grown in DMEM containing 10% fetal calf serum and supplied with 1% non-essential amino acids, 2 mM L-glutamine and 1% penicillin-streptomycin. HMEC cells were cultured in Mammary Epithelial Cell Growth Basal Medium (Lonza) containing all requested supplements and growth factors (0.25% bovine pituitary extract, 20 ng/mL epidermal growth factor (EGF), 5 µg/mL insulin, 0.2 µg/mL hydrocortisone, 30 µg/mL gentamicin and 15 ng/mL amphotericin B (Lonza)). MCF10A was maintained in 1:1 mixture of DMEM and Ham's F12 medium (Gibco) containing 5% horse serum (Sigma Aldrich), 1% non-essential amino acids, 0.5 µg/mL hydrocortisone, 2.5 mM L-glutamine, 20 ng/mL EGF, 0.1 µg/mL cholera toxin, 10 µg/mL insulin and 1% penicillin-streptomycin. T-47D cells were cultured in RPMI 1640 containing 10% fetal calf serum, 7.692 µg/mL insulin, 1% non-essential amino acids, 1 mM sodium pyruvate and 1% penicillin–streptomycin. SK-BR-3 cells were grown in McCoy 5A (Gibco) supplemented with 10% fetal calf serum, 1% non-essential amino acid, 1 mM sodium pyruvate and 1% penicillin-streptomycin. BT-549 cells were cultured in RPMI 1640 containing 10% fetal calf serum and supplied with 0.88 µg/mL insulin, 1% non-essential amino acids, 1 mM sodium pyruvate and 1% penicillin–streptomycin. All cell lines were authenticated by Short Tandem Repeat (STR) analysis (Eurofins Genomics, Ebersberg, Germany) and tested negative for mycoplasma contamination (MycoAlert Mycoplasma Detection Kit, Lonza).

Assessing HMGB1 inhibitor efficacy in vitro

The neutralizing activity of glycyrrhizin (direct HMGB1 inhibitor) (Sigma Aldrich) as well as RAGE antagonist peptide (RAP) (Merck Millipore, Burlington, Massachusetts, USA) and truncated N-terminal domain of HMGB1 (A box) (HMGBiotech, Milan, Italy) was indirectly determined through analyzing their ability to attenuate HMGB1-induced TNFα release by macrophages/monocytes. To do this, 4×10^5 murine RAW 264.7 macrophages per well of a twenty four-well plate were seeded in appropriate growth medium. Twenty-four hours later, the cells were stimulated with 1 µg/mL recombinant mouse HMGB1 (R&D systems, Minneapolis, Minnesota, USA) alone or in combination with inhibitors (several concentrations were tested). After 16 hours, TNFα level in cell culture supernatant was quantified using the mouse TNFα DuoSet ELISA purchased from R&D systems. In order to determine whether the dose range for each inhibitor also inhibited HMGB1 secreted by both lung (TC-1) and basal-like breast cancer cells (4T1, 67NR, EpRas) used in our in vivo models, similar experiments were performed in which the stimulation by recombinant HMGB1 was replaced by conditioned media from these latter cell lines (1×10^6 cells per well of a six-well plate for 48 hours in 2 mL of growth medium). As described in previous articles,[14 33] a similar procedure was used for analyzing the neutralizing effect of a polyclonal anti-HMGB1 antibody raised in rabbit (Eurogentec, Seraing, Belgium). Titer for this latter antibody was determined by immunoblotting.

For ethyl pyruvate (EP) (Sigma Aldrich), its inhibitory effect on HMGB1 secretion was determined by ELISA (HMGB1 Detection kit, Chondrex, Redmond, WA, USA). Forty-8 hours after adding EP (concentration range: 0.1–10 mM), conditioned medium from basal-like breast cancer cell lines was harvested and HMGB1 concentration was measured.

Syngeneic mouse models

C57BL/6J and BALB/c female mice aged 6–8 weeks (n=10 per condition) were used in the present study. Five$\times10^5$ 4T1, 1×10^6 67NR and 2×10^6 EpRas (in 300 µL appropriate growth medium) were orthotopically injected into the mammary fat pad of mice. Regarding TC-1 cells (8×10^5), they were subcutaneously injected (mouse flank). In some peculiar cases, a similar procedure was used with Nude RJ:ATHYM-Foxn1^{nu} mice (n=6 per condition). When tumor volume reached 50–100 mm^3, treatments with HMGB1 inhibitors alone or in combination with checkpoint blockade antibodies were initiated. One nM/kg glycyrrhizin, 10 µM/kg RAP, 500 µg/kg A box and 1 mM/kg EP were administrated by intraperitoneal (i.p.) injection at 3-day intervals for 3 weeks. Similar administration frequencies were used for both rabbit (8.6 mg/kg, Eurogentec) and mouse (5 mg/kg, clone 3E8,

Biolegend, San Diego, California, USA) anti-HMGB1 antibodies. When indicated (combination therapy), mice received 200 µg of in vivo plus monoclonal anti-mouse PD-1 (clone 29F.1A12, Bio X cell, West Lebanon, New Hampshire, USA) or 100 µg of antimouse PD-L1 (clone 10F.9G2, Bio X cell) antibody by i.p. injection at days 4, 7 and 11. Tumor size was monitored with a digital caliper (Thermo Fisher Scientific) every 2–3 days and mice were euthanized when the average tumor volume [(length × width^2)× ϖ /6] of the control group exceeded 1500 mm^3. Tumor growth inhibition index was calculated using the following formula: [1-(mean volume of treated tumors)/(mean volume of control tumors)] × 100%. Half of retrieved tumors were fixed in 10% formalin for 48 hours, embedded in paraffin and sections were subjected to immunohistochemical analysis. The other unfixed tumors were crudely dissected into small pieces, incubated with an enzymatic cocktail (1 mg/mL collagenase A (Sigma Aldrich) and 20 µg/mL DNase (Sigma Aldrich)) for 30 min at 37°C and then passed through a 70 µm pore size membrane filter (BD Biosciences, San Jose, California, USA). The cells were finally resuspended in phosphate-buffered saline (PBS) 3% BSA (Merck Millipore) before CD45$^+$ cell isolation and flow cytometry analysis (procedure and fluorochrome-conjugated antimouse antibodies detailed below). Due to mortality in some tumor-bearing mice treated with anti-PD-1 or anti-PD-L1 inhibitors, in order to have the same number of analyses per condition, some resected tumors were cut into halves (the first half was embedded in paraffin, while the immune cells were retrieved from the second part). The animals were bred in-house (GIGA-Mouse facility and Transgenics platform) or purchased from Janvier Labs (Le Genest-Saint-Isle, France) and the experiments were performed in strict compliance with the ethical rules/recommendations established by the Federation of European Laboratory Animal Sciences Associations.

Antibody-mediated granulocytic MDSC depletion in mice

Granulocytic MDSC were depleted by i.p. injection of 100 µg of ultra-LEAF purified anti-Ly6G antibody (clone 1A8, Biolegend) at day −1, 3 and 7. Promoting target cell phagocytosis through Fc-dependent opsonization and allowing a durable and controlled depletion,[34] mice were treated using a recently published double antibody-based strategy (100 µg anti-Ly6G+50 µg in vivo antirat kappa immunoglobulin light chain (clone MAR 18.5, Bio X cell)) during the second week of depletion (at days 11–12 and 15–16).

Flow cytometry (for in vivo experiments)

Flow cytometry analyses were performed using a FACSCanto II flow cytometer and collected data were analyzed with FACSDiva software, V.6.1.2 (BD Biosciences). Immune cells from digested tumors were first isolated using CD45 MicroBeads according to manufacturer's protocol (Miltenyi Biotec, Bergisch Gladbach, Germany). For precisely determining the number of CD45$^+$ cells per milligram of tumor, this latter positive selection was not performed in this particular case. In order to minimize non-specific binding, CD45$^+$ cells were then incubated with anti-CD16/CD32 antibody (clone 2.4G2, BD Biosciences). All cell surface reactions were performed at 4°C for 30 min. The fluorochrome-conjugated antimouse antibodies used in the present study are listed in online supplemental table 2. The permeabilization step allowing intracellular Foxp3 staining was performed according to the manufacturer's recommendations (eBioscience, Thermo Fisher Scientific). The following immune cell populations were analyzed: DC (CD45$^+$, CD11b$^+$, I-A/I-E^{high}, F4/80$^-$), pDC (CD45$^+$, CD11b^{int}, CD11c$^+$, BST2$^+$, Siglec H$^+$), CD4$^+$ T cells (CD45$^+$, CD3$^+$, CD4$^+$), CD8$^+$ T cells (CD45$^+$, CD3$^+$, CD8$^+$), monocytic MDSC (CD45$^+$, CD11b$^+$, I-A/I-E^{int}, Ly6G$^-$, Ly6C^{high}), granulocytic MDSC (CD45$^+$, CD11b$^+$, I-A/I-E^{int}, Ly6G$^+$, Ly6C$^-$), neutrophils (CD45$^+$, CD11b$^+$, I-A/I-E^{int}, Ly6G$^+$, Ly6C^{int}), M1 macrophages (CD45$^+$, CD11b$^+$, CD11c$^+$, F4/80$^+$, CD206$^-$), M2 macrophages (CD45$^+$, CD11b$^+$, CD11c$^-$, F4/80$^+$, CD206$^+$), CD4$^+$ T regulatory cells (CD45$^+$, CD3$^+$, CD4$^+$, CD25$^+$, FoxP3$^+$), CD8$^+$ T regulatory cells (CD45$^+$, CD3$^+$, CD8$^+$, CD25$^+$, FoxP3$^+$), NK cells (CD45$^+$, NKp46$^+$), B cells (CD45$^+$, CD19$^+$) and eosinophils (CD45$^+$, Ly6C$^-$, Siglec F$^+$). Of note, the proportion of DC is likely slightly overestimated (<2%) in some experiments given that the expression of F4/80 was not systematically evaluated. The activation status of DC and pDC was also determined by evaluating CD80, CD86, I-A/I-E, ILT3 and CD80, CD86, I-A/I-E, ICOSL, respectively. In order to properly segregate negative from positive cell populations, PMT voltages were set optimally. Cell fragments and debris were eliminated based on both forward-scatter and side-scatter values. Gating strategy is shown in online supplemental figure 1.

Assessing HMGB1 inhibitor toxicity in vivo

Eight-week-old female cancer-free BALB/c mice (n=5 per condition) were treated at 3-day intervals by i.p. injections of glycyrrhizin (1 nM/kg), RAP (10 µM/kg), A box (500 µg/kg) and EP (1 mM/kg) (similarly to what is done with the syngeneic mouse models). Mice were weighed every 2–3 days. After 3 weeks, mice were euthanized and lungs, heart, spleen, liver and kidneys were retrieved, weighed and then embedded in paraffin for histological evaluation. The levels of serum urea and alanine aminotransferase (ALT) were measured using a cobas 6000 analyzer (Roche, Basel, Switzerland).

Immunohistochemistry

Immunohistochemical analyses were performed using a standard protocol detailed previously.[35 36] Antigens were retrieved in 10 mM citrate (pH 6) (Sigma Aldrich) or EDTA (pH 9) (Zytomed Systems, Berlin, Germany) buffer. The primary antibodies used in the present study were as followed: anti-HMGB1 (clone 1D5, Abnova, Taipei City, Taiwan), anti-cleaved caspase 3 (clone C92-605, BD Biosciences), anti-CD31 (ab28364, Abcam, Cambridge, UK),

anti-CD3 (clone 2GV6, Ventana Medical Systems, Tucson, Arizona, USA), anti-Foxp3 (clone 236 A/E7; eBioscience, San Diego, California, USA), anti-CD68 (clone KP-1, Ventana Medical Systems), anti-CD206 (clone E2L9N, Cell Signaling Technology, Danvers, MA, USA), anti-PD-1 (clone NAT105, Abcam), anti-human PD-L1 (clone 28–8, Abcam) and anti-mouse PD-L1 (orb10162, Biorbyt, Cambridge, UK). The secondary reaction was performed using the mouse or rabbit Envision+system (Dako, Glostrup, Denmark) according to the manufacturer's recommendations. Positive cells were visualized using a 3,3'-diaminobenzidine (DAB) substrate (Cell Signaling Technology). Mouse or rabbit control IgGs (Santa Cruz Biotechnology, Santa Cruz, California, USA) were used as negative controls.

Assessment of immunohistochemical stainings

Experienced histopathologists evaluated the percentage of epithelial (normal or cancer) cells displaying a cytoplasmic HMGB1 immunoreactivity. Collected results were stratified as followed: negative, <10% and >10%. PD-L1 expression was considered as positive when membranous immunostaining was detected in ≥1% of cancer cells or inflammatory cells within tumor microenvironment. As previously described,[37–39] staining quantification for apoptotic (cleaved caspase 3^+) cancer cells as well as $CD3^+$, $Foxp3^+$, $CD68^+$, $CD206^+$ and PD-1^+ immune cells infiltrating the stroma surrounding tumor cells was performed by computerized counts (QuPath 0.2.0 open source software for digital pathology image analysis). Slides were scanned using 3 dimensional Histech Pannoramic scanner (Sysmex, Villepinte, France). The number of positive cells was reported to cancer area (mm^2). For CD31 immunoreactivity, QuPath software was also used (positive pixel count algorithm) and, as previously described,[40] the ratio of DAB-stained pixels to total cancer area was determined.

Generation of DC and pDC from human $CD34^+$ hematopoietic stem/progenitor cells and cocultures

Both DC and pDC were generated from $CD34^+$ cells isolated from cord blood samples using the MACS CD34 MicroBead kit (Miltenyi Biotec, Bergisch Gladbach, Germany). As previously described,[41] for the generation of DC, $CD34^+$ precursor cells were cultured for 7 days in the presence of 20 ng/mL human SCF (Peprotech, Cranbury, New Jersey, USA), 10 ng/mL TPO (Peprotech), 25 ng/mL Flt3L (Peprotech), 200 U/mL GM-CSF (Amoytop Biotech, Xiamen, China) and 100 U/mL IL-4 (ImmunoTools, Friesoythe, Germany). Regarding the production of pDC, $CD34^+$ cells were cultured for 21 days in the presence of 10 ng/mL TPO (Peprotech), 100 ng/mL Flt3L (Peprotech) and 20 ng/mL IL-3 (Peprotech). The detailed protocol was also previously described.[42] Where indicated, DC were treated with 3 µg/mL fully reduced, disulfide or terminally oxidized HMGB1 (HMGBiotech, Milan, Italy) for 1 day, followed by a lipopolysaccharide (LPS)-induced maturation (1 µg/mL, Sigma-Aldrich) for 24 hours. The procedure was identical with pDC except that maturation was induced by adding 12 µg/mL CpG ODN (Eurogentec) in the cell cultures for 24 hours. In selected experiments, an inhibitor of RAGE (10 µM RAP) or TLR4 (2 µM LPS-RS, Invitrogen, Carlsbad, California, USA) was added in the culture system. The expression of several maturation markers (CD40, CD80, CD83, CD86, HLA-DR, HLA-ABC and CCR7) was finally determined by flow cytometry (FACSCanto II flow cytometer, GIGA-in vitro imaging platform). The fluorochrome-conjugated anti-human antibodies used in this study are listed in online supplemental table 2.

Characterization of the redox state of released HMGB1 in tumor microenvironment

Mouse breast cancer cells (4T1, 67NR and EpRas) were orthotopically injected into the mammary fat pad of mice. When the volume reached 1000 mm^3, tumors were retrieved and soluble proteins/interstitial fluids were collected using a pressure-assisted innovative methodology (EXPEL) recently described.[43] In order to irreversibly freeze the redox state of HMGB1 molecules contained in tumor-extruded fluids, an alkylation step (50 mM iodoacetamide for 30 min at 25°C) was then directly conducted. Proteins were quantified using the Pierce BCA protein assay (ThermoFisher Scientific) and 15 µg were separated by electrophoresis on 10% polyacrylamide gels and transferred onto polyvinylidene difluoride membranes. After saturation with TBS-Tween 20 0.1% supplemented with 5% skim milk for 30 min, the membrane was incubated overnight at 4°C with anti-HMGB1 antibody (1/1000, A00066-1, Boster Biological Technology, Pleasanton, California, USA). After washing and incubation with the horseradish peroxidase (HRP)-conjugated anti-rabbit secondary antibody, the protein bands were detected by chemoluminescence and quantified using ImageJ software (National Institute of Health (NIH), Bethesda, Maryland, USA). As oxidized and reduced controls, recombinant HMGB1 was exposed to either 10 mM H_2O_2 or DTT for 1 hour and then alkylated.

Gene expression analysis

The expression of HMGB1, PD-1 (*PDCD1* gene) and PD-L1 (*CD274* gene) according to cancer subtypes, grades, lymph node and metastatic statuses was evaluated using the Molecular Taxonomy of Breast Cancer International Consortium (METABRIC) public dataset (Illumina HT-12 v3 platform for transcriptional profiling).[44 45] Breast cancers were categorized into the four current major molecular subtypes based on proliferative index (Ki67), hormone receptor expression (estrogen receptor (ER), progesterone receptor (PR)) and HER2 positivity: Luminal A (ER^+/PR^+, $HER2^-$, $Ki67^{low}$), Luminal B (ER^+/PR^+, $HER2^-$, $Ki67^{high}$ and ER^+/PR^+, $HER2^+$), HER2+ (ER^-/PR^-, $HER2^+$) and basal-like (ER^-/PR^-, $HER2^-$).

Metabolic extracellular flux analysis

Mouse basal-like breast cancer cells (10 000 cells per well) were seeded in Seahorse XFp mini-plates (Agilent, Santa Clara, California, USA) and analyzed using the mitochondrial stress test as previously described.[46] HMGB1 inhibitors were added in growth culture medium for 12 hours and removed before the assay. For the optimal measurement of both oxygen consumption (OCR) and extracellular acidification (ECAR), cells were maintained in unbuffered serum-free DMEM (pH 7.4) containing 1 mM pyruvate, 2 mM glutamine and 10 mM glucose during the assay. Cells were successively stressed with 1 µM oligomycin, 1 µM FCCP and 0.5 µM rotenone/antimycin A and collected results were normalized to cell number (evaluated by Hoechst).

HMGB1 measurement by ELISA

One×10^6 cells per well of a six-well plate were cultured in appropriate growth medium during 48 hours. Cell culture supernatant was then harvested and HMGB1 release by both human and mouse breast cancer cells was quantified by ELISA using the following commercially available kit: HMGB1 Detection kit (Chondrex). After 48 hours, the number of attached cells in each condition was also determined in order to normalize HMGB1 measurements (ng/mL per 10^6 cells).

ROS measurement

Mitochondrial ROS production by cancer cells was measured using CellROX Flow Cytometry kit (Life Technologies, Carlsbad, California, USA) according to the manufacturer's protocol. N-acetylcysteine (5 mM) and Tert-butyl hydroperoxide (100 µM) were used as negative and positive controls, respectively.

Cell proliferation and apoptosis/necrosis

Cell proliferation under indicated culture conditions was monitored for 6 days using live-cell imaging analysis (IncuCyte ZOOM system, Essen BioScience, Welwyn Garden City, UK). The percentage of apoptotic/necrotic cells was determined by annexin V-FITC and propidium iodide staining according to the manufacturer's recommendations (BD Biosciences). Results were acquired by flow cytometry (FACSCalibur flow cytometer, BD Biosciences).

Statistical analysis

Collected experimental data were analyzed using the GraphPad Prism V.8 software (San Diego, California, USA). The comparison of both patient characteristics and immunohistochemical variables (negative, <10% and >10% of cells exhibiting a cytoplasmic HMGB1 immunostaining) between independent groups was performed using a Fisher's exact test or a χ^2 test according to the number of variables. Two group comparisons were performed using (Welch-corrected) unpaired t-tests. Experiments containing more than two groups were compared using one-way analysis of variance (ANOVA), followed by Dunnett's multiple comparison test or Bonferroni post-test. Regarding METABRIC gene expression data, both graphs and statistical analyses (one-way ANOVA followed by Bonferroni post-test or unpaired t-test) were done using the open source statistical language R (V.3.5). Disease-free survival was defined as the time from the date of original biopsy/diagnosis to the date of local or distant recurrence (metastasis). The Kaplan-Meier method (with log-rank (Martel-Cox) test) was used. *p<0.05, **p<0.01, ***p<0.001 and ****p<0.0001.

RESULTS

HMGB1 is highly secreted by basal-like breast cancer cells and its cytoplasmic immunoreactivity is associated with both regulatory T (Treg) cell infiltration within tumor stroma and poor outcome

By using the METABRIC public dataset, the mRNA expression level of HMGB1 according to breast cancer molecular subtypes, histologic grades, nodal and metastatic statuses was first assessed. Although the statistical significance was reached between some cancer subtypes (basal-like vs LumA (p<0.001) or LumB (p<0.01)) and grades (grade 2 vs grade 3 (p<0.01)) (very likely due to the high number of analyzed samples), no obvious difference was observed (figure 1A). Kaplan-Meier analyses demonstrated no difference in 5-year patient survival according to HMGB1 gene expression either (online supplemental figure 2). A large cohort of both normal and neoplastic breast tissues was then examined by immunohistochemistry and, interestingly, two distinct HMGB1 staining patterns were identified: nuclear versus cytoplasmic (figure 1B). Whereas normal mammary glands always displayed a nuclear immunoreactivity, a cytoplasmic expression of HMGB1 (in up to 40% tumor cells) was detected in approximately half of analyzed breast cancer specimens (132/275, 48%). Similar results were collected in the context of other solid tumors (cervical SCC and non-small-cell lung cancer) (online supplemental figure 3A,B). As shown in figure 1C, diffuse cytoplasmic HMGB1 staining was more frequently observed in triple negative/basal-like cancers compared with their counterparts expressing HER2 (p<0.05) and/or hormone receptors (p<0.01). Remarkably, the prognostic value of this latter expression pattern was also highlighted. Indeed, patients with basal-like breast cancer displaying a cytoplasmic HMGB1 expression in either 0%–10% or >10% cells were significantly associated with an unfavorable outcome (figure 1D). As detailed in online supplemental table 1, these shorter disease-free survivals cannot be explained by differences in age at diagnosis, tumor size, nodal/metastatic status, tumor stage, proliferative index or treatment modality. Of note, a significant increased density of both $Foxp3^+$ Treg lymphocytes (102.6 vs 148.8 and 171.6 cells/mm^2) and $CD206^+$ M2 macrophages (533.4 vs 757.1 and 811.1 cells/mm^2) was noticed within tumor microenvironment of cytoplasmic HMGB1-positive cancers compared with basal-like neoplasms exhibiting exclusively a nuclear immunoreactivity (figure 1F). Quantified by computerized counts (figure 1E), the global

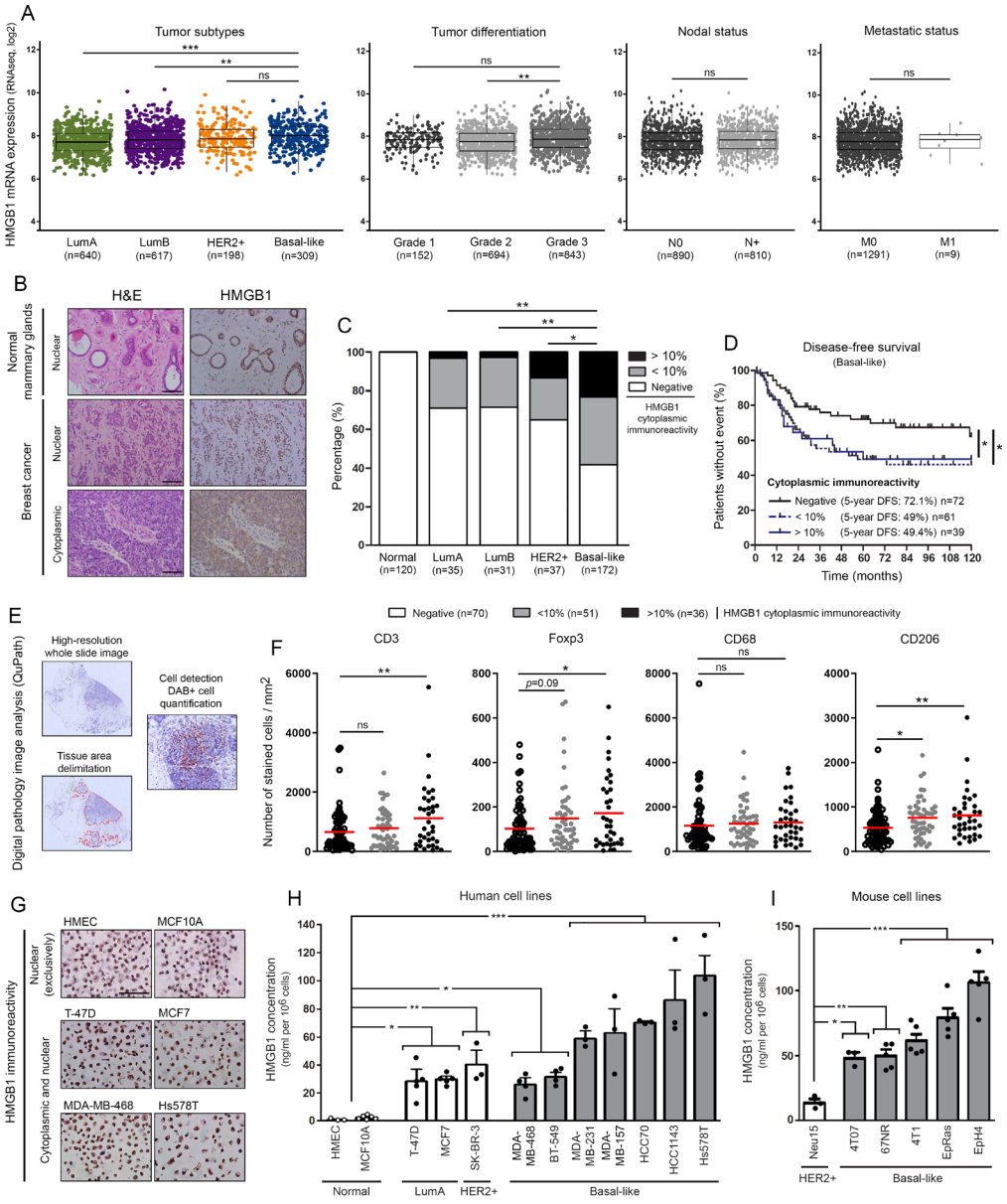

Figure 1 HMGB1 is highly secreted by basal-like breast cancer cells and its tumor-specific cytoplasmic expression is associated with immune tolerance and poor outcome. (A) The METABRIC dataset was used for analyzing HMGB1 expression level in breast cancers according to molecular subtypes, histologic grades, nodal and metastatic statuses. (B) Representative pictures of normal mammary glands and breast cancers stained for HMGB1. Note the two distinct HMGB1 staining patterns detected in tumor specimens: nuclear versus cytoplasmic. (C) Semiquantitative evaluation of cytoplasmic HMGB1 immunoreactivity (negative, 0%–10% or >10% positive cells) in both normal mammary glands (n=120) and neoplasms (LumA, n=35; LumB, n=31; HER2+, n=37; basal-like, n=172). (D) Disease-free survival of patients treated for basal-like breast cancer according to cytoplasmic HMGB1 expression (negative, n=72; 0%–10%, n=61; >10%, n=39). This latter parameter was clearly found to be an independent prognostic factor. (E) Illustration of the different steps for DAB-positive cell quantification using computerized image analysis (QuPath). (F) $CD3^+$, $Foxp3^+$, $CD68^+$ and $CD206^+$ cell infiltrations in microenvironment of basal-like breast tumors. Whereas the global number ($CD68^+$) did not significantly change, an increased density of $CD206^+$ M2 macrophages was detected in cytoplasmic HMGB1-positive cancers. A similar increase was also reported with $Foxp3^+$ Treg lymphocytes. the number of positive cells was reported to tumor area (mm^2). (G) Representative examples of normal (HMEC and MCF10A) and malignant cells (LumA: T-47D and MCF7; basal-like: MDA-MB-468 and Hs578T) stained for HMGB1. Note the exclusive nuclear immunoreactivity displayed by normal mammary cells. Secretion/release of HMGB1 analyzed by ELISA in (H) human and (I) mouse cell culture supernatants. High concentrations were especially detected in cell cultures derived from triple negative/basal-like tumors. The means±SEM (plus each individual data point) for at least three independent experiments are represented. The scale bar represents 100 µm. Asterisks indicate statistically significant differences (*p<0.05; **p<0.01; ***p<0.001). P values were determined using one-way ANOVA followed by Bonferroni post-test (A), unpaired t-test (A), χ^2 test (C), log-rank (Mantel-Cox) test (D) and one-way ANOVA followed by Dunnett's multiple comparison post-test (F, H, I). ANOVA, analysis of variance; HMGB1, high-mobility group box 1; METABRIC, Molecular Taxonomy of Breast Cancer International Consortium.

number of lymphocytes ($CD3^+$) also augmented (657 vs 1120 cells/mm^2) in case of diffuse (in >10% cancer cells) cytoplasmic HMGB1 expression. In contrast, the global number of macrophages ($CD68^+$) was quite similar for all the analyzed groups (1161, 1256 and 1309 cells/mm^2) (figure 1F). Immune cell densities were undetermined in 15 out of 172 (8.7%) basal-like breast cancer patients (mainly due to the lack of remaining slides). Confirming our ex vivo data, cytoplasmic staining pattern for HMGB1 was only detected in malignant cell lines (especially those derived from basal-like breast cancers) and associated to protein concentration in both human and mouse cell culture media (figure 1G–I). Given that the percentages of apoptotic/necrotic cells detected in vitro (online supplemental figure 4) did not correlate with the HMGB1 concentrations in culture supernatants, the differences measured by ELISA are likely related to the active secretion of HMGB1 rather than its passive release from injured cells.

Both direct and indirect HMGB1 inhibitors efficiently neutralize extracellular HMGB1 in vitro without affecting tumor cell proliferation/viability

In the last decade, different modes of inhibition for extracellular HMGB1 as well as several direct or indirect inhibitors have been highlighted (figure 2A). Consisting of the truncated N-terminal domain of HMGB1, A box has previously been shown to efficiently reverse established sepsis in vivo.[33] A box acts as a competitive antagonist of HMGB1 and, given the sequence similarity between both human and mouse HMGB1, it is presumed to elicit very low neutralizing immunological responses. Composed of 10 amino acids of the RAGE-binding domain of HMGB1, RAP competes with natural HMGB1 for a site on the extracellular domain of RAGE that is required for ligand-receptor interaction,[47] resulting in RAGE signaling pathway inhibition. Derived from the licorice plant (*Glycyrrhiza glabra*) and administered at high doses to patients with chronic hepatitis B or C infection, glycyrrhizin has been shown to have anti-inflammatory properties through binding directly to extracellular HMGB1 and, consequently, blocking its activity.[48] Regarding EP, a stable aliphatic esther of pyruvic acid, its ability both to inhibit HMGB1 release in a dose-dependent manner and subsequently ameliorate mouse models of inflammatory diseases (eg, colitis) was recently demonstrated by several research groups.[49 50] The importance of SIRT1/STAT signaling pathway inhibition in this mechanism was proposed.[50] In order to determine the effective concentration of glycyrrhizin, RAP and A box that inhibited HMGB1 activity by >80%, murine RAW 264.7 cells were stimulated with recombinant HMGB1 (synthesized in mouse tumor cells) alone or in the presence of each inhibitor. HMGB1-dependent TNFα secretion was then determined by ELISA. As shown in figure 2B, all three inhibitors neutralize very efficiently extracellular HMGB1. Similar results were obtained when the stimulation by recombinant HMGB1 was replaced by conditioned media from mouse tumor cells used in our in vivo models (figure 2C and online supplemental figure 5). To analyze the ability of EP to reduce HMGB1 release, this latter compound was directly added in mouse basal-like breast cancer cell cultures for 48 hours and HMGB1 concentrations were measured. As shown in figure 2D, a significant decrease was observed at a concentration as low as 1 mM. The effect of each HMGB1 inhibitor on cell metabolism, proliferation and apoptosis was then precisely assessed using Seahorse flux analyzer, IncuCyte live cell analyzing system and annexin V-propidium iodide staining assay, respectively (figure 2E–L and online supplemental figure 6). Whereas glycyrrhizin (1 nM), RAP (10 µM) and A box (0.5 µg/mL) did not affect these three cellular parameters, significant changes in both OCR and extracellular pH were observed with 5 and 10 mM EP (figure 2G–J), suggesting that high doses of this derivative of pyruvic acid alters cell energetic metabolism (glycolysis) (very likely by competing with endogenous pyruvate). Of note is that the metabolism, proliferation and apoptosis of tumor cells were not affected by the addition of 1 mM EP that has been shown above to be enough for exerting a significant inhibitory effect on HMGB1 release (figure 2D–L and online supplemental figure 6).

Extracellular HMGB1 blockade inhibits tumor growth in syngeneic mouse tumor models through activating adaptive immune responses

Next, we sought to determine whether extracellular HMGB1 blockade had antitumor effects in vivo. Three syngeneic mouse models of basal-like breast cancer (4T1, 67NR and EpRas) as well as one additional of non-small cell lung cancer (TC-1) were used (figure 3 and online supplemental figure 3). Due to the stable transfection of HPV16 E6 and E7, these latter cells are also frequently used as a model of cervical cancer. To mimic human disease closely, all breast cancer cell lines were orthotopically injected (into the mammary fat pad) and treatments with HMGB1 inhibitors (injections at 3-day intervals for 15–20 days) began when solid tumors (50–100 mm^3) were established. As commonly practiced, the concentration used in vivo for each HMGB1 inhibitor (glycyrrhizin (1 nM/kg), RAP (10 µM/kg), A box (500 µg/kg) and EP (1 mM/kg)) was extrapolated from our in vitro data (figure 2) by assuming that mol/L~mol/kg for compounds diluted in liquid solutions (PBS). Strikingly, in all four models, a significant decrease in tumor growth was observed with extracellular HMGB1 blockade (figure 3A and online supplemental figure 3D). Although having different modes of action, these four HMGB1 inhibitors displayed quite similar therapeutic antitumor activities. When collected data were pooled, mean tumor growth inhibitions of 38%, 46%, 49% and 31% were obtained for treated mice transplanted with 4T1, 67NR, EpRas and TC-1 cells, respectively. Importantly, this latter beneficial effect was not observed in immunocompromised Nude mice, indicating its dependence on the adaptive immune responses (figure 3B). When the

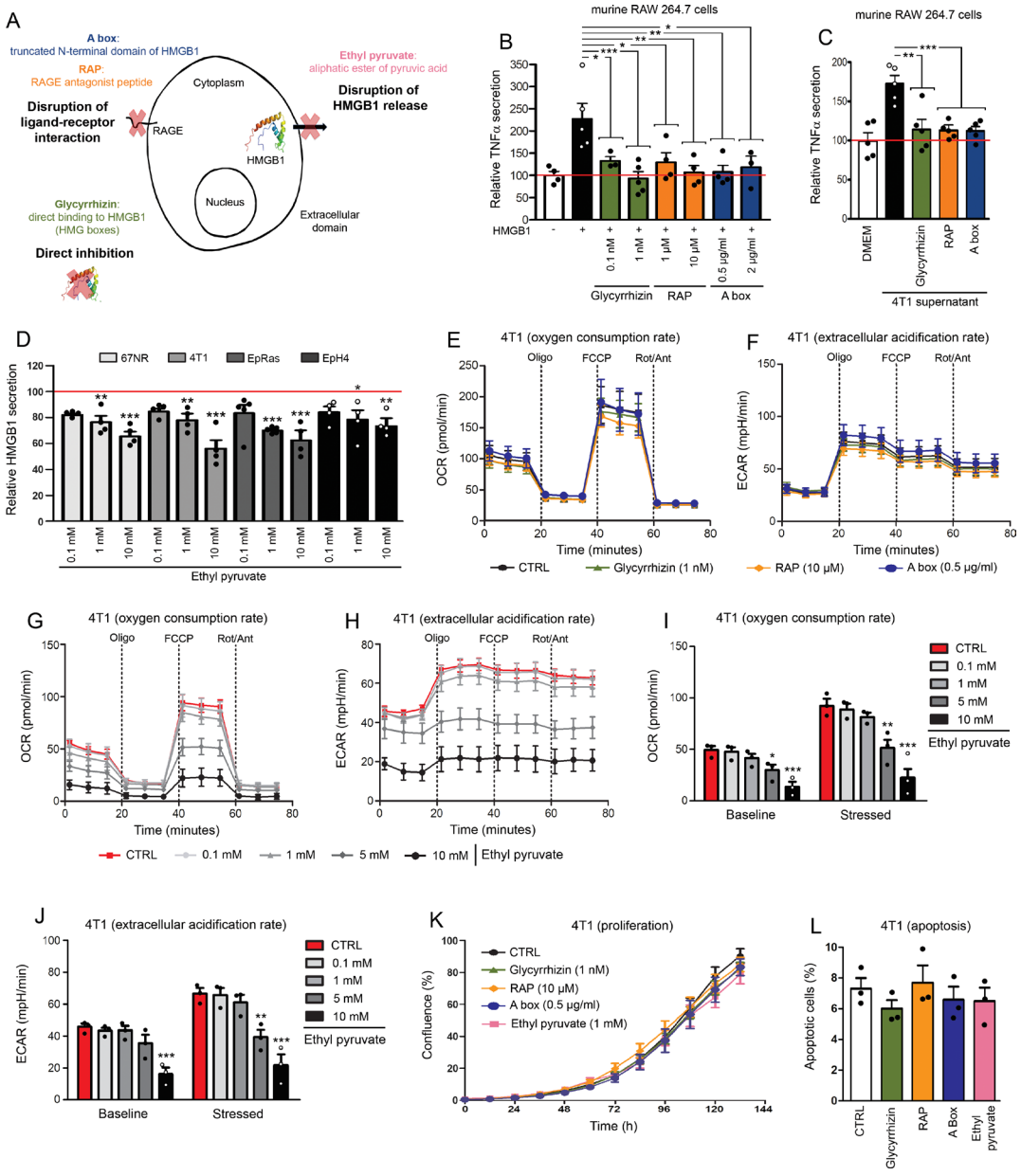

Figure 2 Glycyrrhizin, RAP, A box and EP exert efficient neutralizing effects on extracellular HMGB1 without altering tumor cell proliferation and apoptosis/necrosis. (A) Schematic representation of different modes of inhibition for extracellular HMGB1. Mouse RAW 264.7 cells were stimulated with recombinant HMGB1 (B) or conditioned media from 4T1 basal-like breast cancer cells (C) in the absence or presence of glycyrrhizin, RAP or a box (several concentrations were tested). Note the significant decrease of HMGB1-induced TNFα secretion when HMGB1 inhibitors were added in the cell cultures, indicating their efficient neutralizing effect. (D) EP was directly added in the culture medium of 4 different mouse basal-like breast cancer cell lines (4T1, 67NR, EpRas and EpH4). Forty-eight hours later, HMGB1 concentrations were determined by ELISA and the ability of EP to inhibit HMGB1 release in a dose-dependent manner was highlighted. (E) Oxygen consumption rate (OCR) and (F) extracellular acidification rate (ECAR) in 4T1 cells in the absence or presence of glycyrrhizin (1 nM), RAP (10 µM) and a box (0.5 µg/mL) were determined using Seahorse extracellular flux analyzer. No modification of OCR/ECAR was detected with these three HMGB1 inhibitors. (G) OCR and (H) ECAR in 4T1 cells following EP addition (concentration range: 0.1–10 mM). Histograms representing OCR (I) and ECAR (J) before (baseline) and after (stressed) oligomycin and FCCP addition in the absence or presence of EP. Both OCR and ECAR were strongly decreased with 5 and 10 mM EP. No significant change was detected with lower concentrations (0.1–1 mM). (K) Cell proliferation and (L) apoptosis of mouse 4T1 cells cultured without or with HMGB1 inhibitors (glycyrrhizin (1 nM), RAP (10 µM), a box (0.5 µg/mL) and EP (1 mM)) were determined using IncuCyte live cell analyzing system and annexin V-propidium iodide staining assay, respectively. No significant change was reported. The means±SEM (plus each individual data point) for at least three independent experiments are represented. Asterisks indicate statistically significant differences (*p<0.05; **p<0.01; ***p<0.001). P values were determined using one-way ANOVA, followed by Dunnett's multiple comparison post-test (B, C, D, I, J, K, L). ANOVA, analysis of variance; ECAR, extracellular acidification rate; EP, ethyl pyruvate; HMGB1, high-mobility group box 1; RAGE, receptor for advanced glycation endproducts; RAP, RAGE antagonist peptide; TNFα, tumor necrosis factor-α.

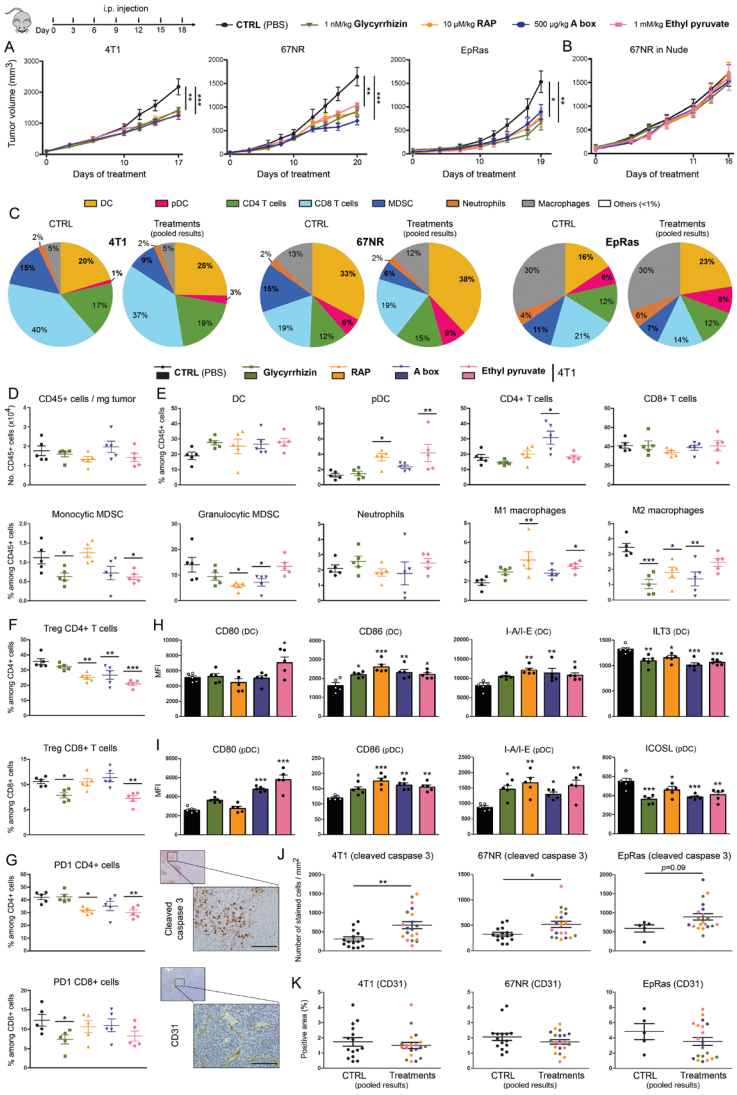

Figure 3 Extracellular HMGB1 blockade inhibits the growth of pre-established solid tumors in immunocompetent mice through activating anticancer immune responses. (A) Mouse basal-like breast cancer cells (4T1, 67NR and EpRas) were orthotopically injected into the mammary fat pad of immunocompetent BALB/c mice. Tumor-bearing mice were then treated at 3-day intervals with PBS (control) or HMGB1 inhibitors (glycyrrhizin (1 nM/kg), RAP (10 µM/kg), a box (500 µg/kg) and EP (1 mM/kg)). The mean tumor volumes±SEM are represented. (B) HMGB1 inhibitors were tested in nude mice implanted with 67NR cells. Note the absence of beneficial effect in these latter immunocompromised mice, indicating the dependence on the adaptive immune responses. (C) At day 17, 19 or 20 (depending on the analyzed cell line), tumors were harvested, $CD45^+$ immune cells were isolated and analyzed by flow cytometry. The proportions of each analyzed immune cell population in both control and treated groups (pooled results) are shown. Note the drastic reduction of MDSC following extracellular HMGB1 blockade. (D) Total number of ($CD45^+$) immune cells per milligram of tumor in both control and treated groups. (E) Scatter dot plots showing the percentage of each individual immune cell population (DC, PDC, $CD4^+$ and $CD8^+$ T cells, monocytic and granulocytic MDSC, neutrophils, M1 and M2 macrophages) among $CD45^+$ cells in the different treatment groups. an increased M1/M2 ratio of macrophages was observed in most HMGB1 inhibitor-treated tumors. The intratumoral immune cells were analyzed in five mice per condition. (F) Scatter dot plots illustrating the percentage of tumor-infiltrating Treg ($Foxp3^+$) $CD4^+$ and $CD8^+$ cells among total $CD4^+$ and $CD8^+$ populations in the different treatment groups. (G) Scatter dot plots illustrating the percentage of tumor-infiltrating PD-1^+ $CD4^+$ and PD-1^+ $CD8^+$ cells among total $CD4^+$ and $CD8^+$ populations in the treatment groups. The activation status of both DC (H) and PDC (I) in the different treatment groups was also determined by analyzing the expression of several cell surface markers (CD80, CD86, I-A/I-E, ILT3 and ICOSL). Data represent the mean fluorescent intensity (MFI)±SEM of 5 independent experiments in each group (each individual data point is shown). The number of apoptotic cancer cells (cleaved caspase 3^+) (J) as well as the density of blood vessels within tumor microenvironment ($CD31^+$) (K) were determined by computerized counting (using QuPath software). The number of cleaved caspase 3^+ cells and the percentage of $CD31^+$ pixels were reported to tumor area. The scale bar represents 100 µm. Asterisks indicate statistically significant differences (*p<0.05; **p<0.01; ***p<0.001). P values were determined using one-way ANOVA followed by Dunnett's multiple comparison post-test (A, B, D, E, F, G, H, I) and (Welch-corrected) unpaired t-test (J, K). ANOVA, analysis of variance; DC, dendritic cell; EP, ethyl pyruvate; HMGB1, high-mobility group box 1; i.p, intraperitoneal; MDSC, myeloid-derived suppressor cells; pDC, plasmacytoid DC; RAP, RAGE antagonist peptide.

average tumor volume reached 1500 mm^3 in the control group, $CD45^+$ cells were isolated from harvested tumors and both the number of immune cells per milligram of tumor and the percentage of each individual immune cell population (DC, pDC, $CD4^+$ and $CD8^+$ T cells, monocytic and granulocytic MDSC, neutrophils, M1 and M2 macrophages) among total $CD45^+$ cells were determined by flow cytometry in the different treatment groups. As shown in figure 3C and online supplemental figure 3E, it is interesting to notice that each syngeneic mouse model displays a specific immune environment dominated by $CD8^+$ T cells (4T1), DC (67NR) or macrophages (EpRas and TC-1). Despite minor variations (related to models and/or drugs used), four main observations were made in treated groups compared with the controls: (1) a diminution of both monocytic and granulocytic MDSC was observed following extracellular HMGB1 inhibition, (2) without affecting the global number of macrophages, a higher M1/M2 ratio was detected in treated tumors, (3) reduced proportions of Treg cells among total $CD4^+$/$CD8^+$ cells and 4) an increased activation of antigen-presenting cells (DC and pDC), as demonstrated by the higher expression of CD80, CD86, I-A/I-E associated to the lower presence of ILT3 (DC) or ICOSL (pDC) (figure 3D–I, online supplemental figures 3 and 7). To evaluate whether the strong reduction of intratumoral granulocytic MDSC actively participate to the beneficial (anti-tumor) effect of HMGB1 inhibitors, depletion experiments were performed. Importantly, anti-Ly6G antibody treatment significantly reduced tumor growth, mimicking the clinical effect of extracellular HMGB1 blockade (online supplemental figure 8). Beside the immune cell infiltration, the apoptosis of cancer cells as well as angiogenesis were also assessed in retrieved tumors by quantifying cleaved caspase 3^+ cells and CD31 expression (by computerized counts), respectively. Whereas no difference was observed for the density of blood vessels within tumor microenvironment (figure 3K), the number of apoptotic tumor cells was significantly higher (up to 2.2-fold increase) in treated cancers compared with control groups (figure 3J), indicating even more an enhancement of immune responses in vivo following extracellular HMGB1 blockade. Finally, no weight loss or sign of toxicity (determined by both the histological evaluation of several organs and the levels of serum urea and ALT) was observed with any of the HMGB1 inhibitors (online supplemental figure 9).

Extracellular HMGB1 blockade enhances therapeutic effectiveness of anti-PD-1 antibody in immunocompetent mice

The expression of the immune checkpoint receptor PD-1 and its ligand PD-L1 was first assessed in human breast specimens as well as in our syngeneic mouse models (4T1 and 67NR). As shown in figures 4A–C and 5A–D, both the mRNA and protein levels of PD-1/PD-L1 were significantly increased in triple negative/basal-like cancers compared with the other molecular breast cancer subtypes. Due to the absence of PD-L1 immunoreactivity in a substantial proportion of human samples (figure 5C,D), the reported differences were less evident with this latter protein compared with PD-1. Importantly, the cell surface expression of both proteins was revealed in harvested (untreated) 4T1/67NR tumors by flow cytometry (figures 3G and 5E), supporting the adequacy of our in vivo models for analyzing the anti-cancer efficacy of HMGB1 blockade and anti-PD-1/PD-L1 combination therapy. Detected on tumor and/or immune cells, it is interesting to notice that 4T1 and 67NR tumors displayed distinct PD-L1 expression profiles (mainly on inflammatory cells: 4T1 vs on cancer cells: 67NR) (figure 5E). As shown in figure 4D,E and online supplemental figure 10, the combination of anti-PD-1 antibody and HMGB1 inhibition (RAP and EP) was associated with increased numbers of apoptotic tumor cells as well as significantly higher tumor growth inhibitions compared with anti-PD-1 alone (49.5% vs 33% (4T1, p=0.12) and 61.5% *vs* 34% (67NR, p<0.05)) or each HMGB1 inhibitor used in monotherapy [49.5% vs 30% (4T1, p<0.05) and 61.5% vs 35% (67NR, p<0.01)]. As illustrated by these two latter parameters (figures 3A–D and 4D,E), anti-PD-1 and extracellular HMGB1 blockade displayed close efficacy in our immune-competent mouse models. Although the significance was not reached in all conditions, the addition of one HMGB1 inhibitor to anti-PD-1 antibody also resulted in a higher percentage of M1 macrophages, a reduction of intratumoral $Foxp3^+$ Treg cells and an increased activation of DC/pDC (figure 4G–J and online supplemental figure 11), suggesting even more that HMGB1 blockade boosts anti-PD1-mediated enhancement of (T cell) immune responses. Due to the strong antitumor effect of anti-PD-L1 monotherapy in our models, the benefit of the combination therapy was less marked (tumor growth inhibition observed with 4T1 tumor-bearing mice: 45% (anti-PD-L1) vs 58% (anti-PD-L1 plus RAP or EP)) or absent (67NR: 64% (anti-PD-L1) vs 59% (combination of anti-PD-L1 and HMGB1 inhibition)) (figure 5F–L, (online supplemental figures 10 and 12). Although anti-PD-L1 displayed impressive therapeutic effectiveness (with an elimination below palpable detection observed in 3 mice-bearing 67NR tumors], anti-PD-L1 treatment, however, was associated with rapid and fatal hypersensitivity reactions in ~30% of both 4T1 and 67NR tumor-bearing mice. Observed with anti-PD-1 as well, these latter reactions were mainly observed within 20–30 min after the third administration. As previously published,[51] one extra dose caused the mortality of virtually all animals (data not shown).

Oxidized HMGB1 is encountered in cancer microenvironment (interstitial fluids) and induces DC tolerogenicity in a RAGE-dependent manner

To further characterize the immunosuppressive activity of HMGB1 during cancer progression, the redox state as well as the impact on DC/pDC maturation of each HMGB1 isoform detected within the tumor extracellular

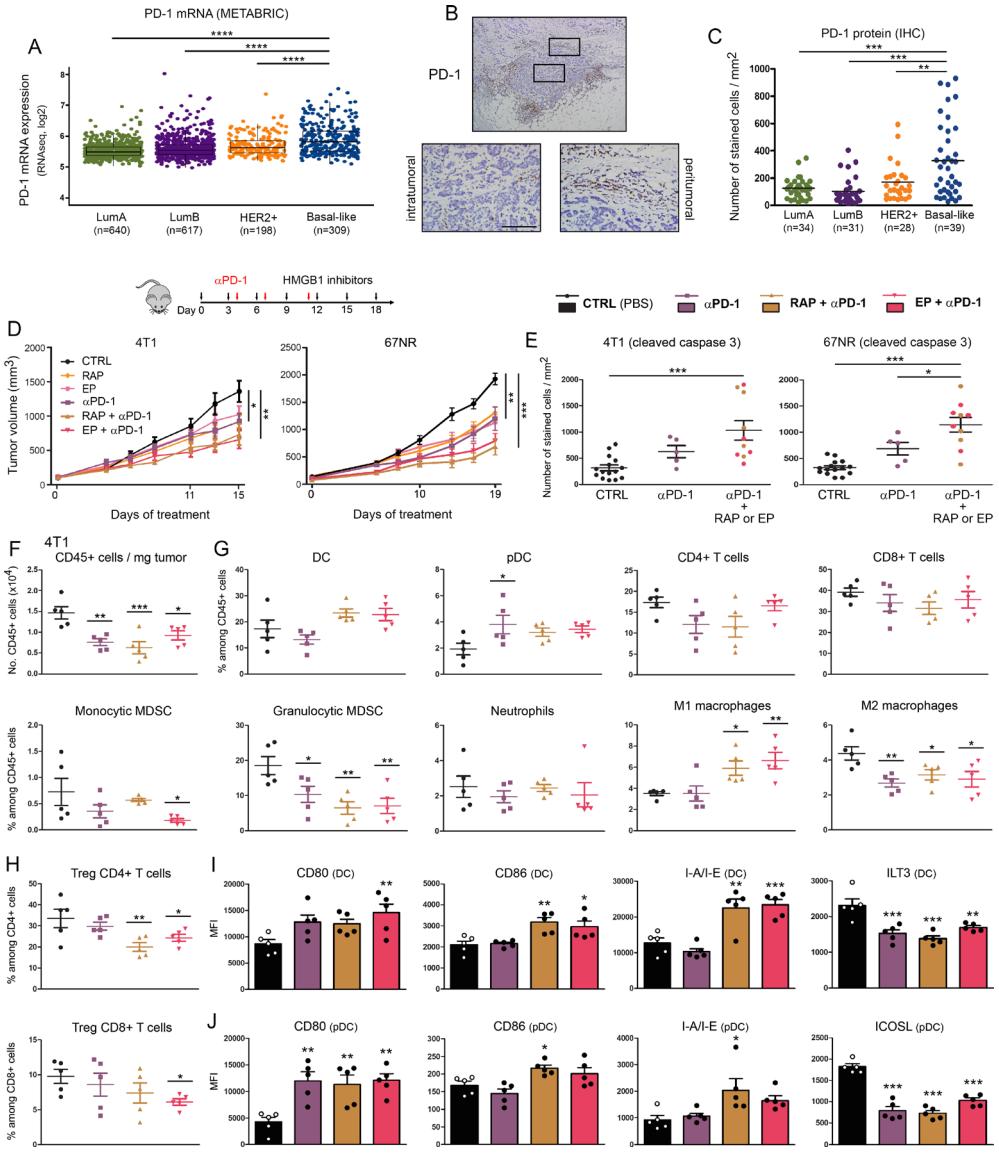

Figure 4 Extracellular HMGB1 blockade enhances anti-PD-1-induced inhibition of tumor growth in vivo. (A) PD-1 mRNA expression (*PDCD1* gene) in the four major molecular subtypes of breast cancer was determined using the METABRIC public dataset. (B) Representative example of breast cancer stained for PD-1. Positive cells were observed in the epithelial component of the tumor as well as in the stroma surrounding cancer cells. (C) PD-1$^+$ cell infiltration within tumor microenvironment was determined by computerized counting. Each point represents the number of positive cells/mm^2 for one independent tumor specimen. (D) Mouse breast cancer cells (4T1 and 67NR) were orthotopically injected into the mammary fat pad of immunocompetent BALB/c mice. Anti-PD-1 antibody was tested alone (i.p. injection of 200 µg at days 4, 7 and 11) and in combination with HMGB1 inhibitors (RAP (10 µM/kg) and EP (1 mM/kg), treatment at 3 day intervals). In parallel, the anticancer efficacy of these combination regimens was also compared with that displayed by each individual HMGB1 inhibitor used in monotherapy. The mean tumor volumes±SEM are represented. (E) The apoptotic cancer cells (cleaved caspase 3$^+$) were detected by immunohistochemistry and quantified using QuPath software. The number of positive cells was reported to tumor area (mm^2). (F) The total number of (CD45$^+$) immune cells per milligram of tumor was determined in the different treatment groups. (G) Scatter dot plots illustrating the percentage of each individual immune cell population (DC, PDC, CD4$^+$ and CD8$^+$ T cells, monocytic and granulocytic MDSC, neutrophils, M1 and M2 macrophages) among CD45$^+$ cells in both control and treated groups. Reduced densities of granulocytic MDSC as well as an increase of M1 macrophages were especially observed in case of combination therapy. The intratumoral immune cells were analyzed in five mice per condition. (H) Scatter dot plots showing the percentage of tumor-infiltrating Treg (Foxp3$^+$) CD4$^+$ and CD8$^+$ cells among total CD4$^+$ and CD8$^+$ populations in the different treatment groups. the activation status of DC (I) and pDC (J) was determined by flow cytometry. the expression of several surface markers (CD80, CD86, I-A/I-E, ILT3 and ICOSL) was analyzed. Data represent the mean fluorescent intensity (MFI)±SEM of 5 independent experiments in each group (each individual data point is shown). The scale bar represents 100 µm. Asterisks indicate statistically significant differences (*p<0.05; **p<0.01; ***p<0.001; ****p<0.0001). P values were determined using one-way ANOVA followed by Bonferroni post-test (A, C, E) or Dunnett's multiple comparison post-test (D, F, G, H, I, J). ANOVA, analysis of variance; DC, dendritic cell; HMGB1, high-mobility group box 1; METABRIC, Molecular Taxonomy of Breast Cancer International Consortium; MDSC, myeloid-derived suppressor cells; pDC, plasmacytoid DC; RAP, RAGE antagonist peptide.

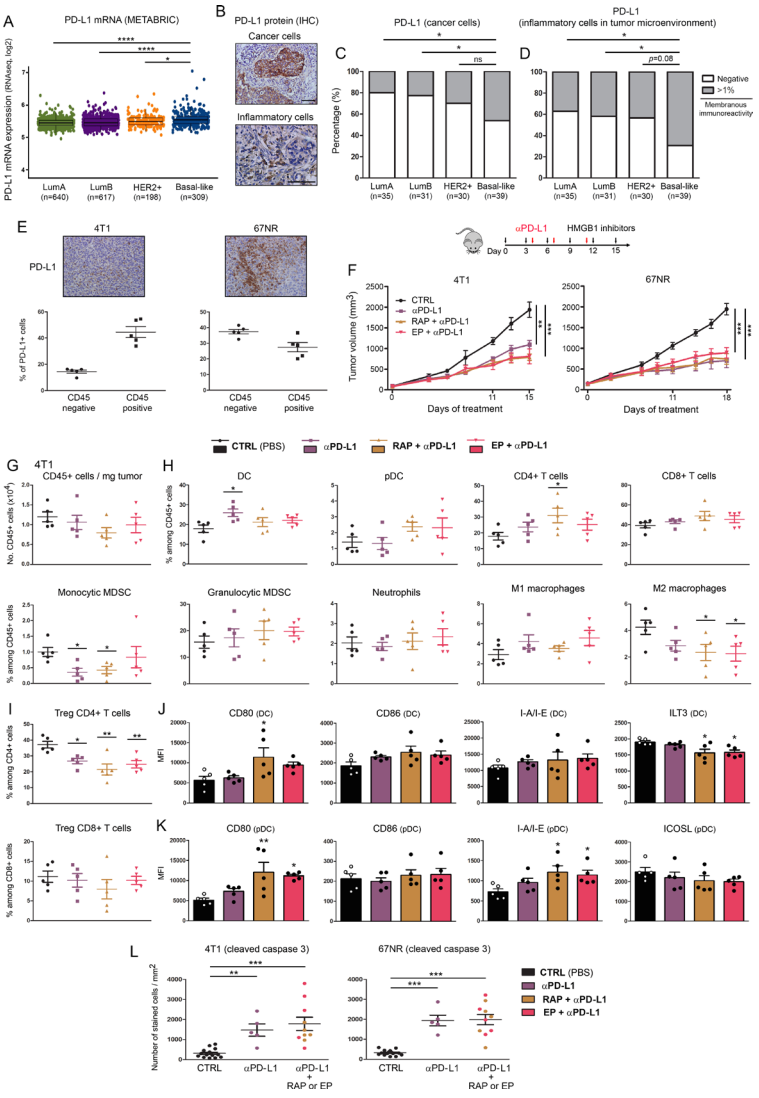

Figure 5 Combination of anti-PD-L1 with HMGB1 inhibitors strongly inhibits tumor growth in syngeneic mouse models of basal-like breast cancer. (A) mRNA level of PD-L1 (*CD274* gene) in the four major molecular subtypes of breast cancer was determined using the METABRIC public dataset. (B) Representative example of breast cancer stained for PD-L1. Positive signals were detected on cancer cells and/or on inflammatory cells within tumor microenvironment. Semiquantitative evaluation of PD-L1 immunoreactivity (negative or >1% membrane staining) displayed by cancer cells (C) or inflammatory cells infiltrating the tumor microenvironment (D). The analyzed cancer specimens were categorized into the four molecular subtypes of breast cancer (LumA, LumB, HER2$^+$ and basal-like). (E) The percentage of PD-L1$^+$ cells in both epithelial/cancer (CD45$^-$) and inflammatory (CD45$^+$) components of untreated harvested 4T1/67NR tumors was determined by flow cytometry. Note the distinct profile displayed by these two cell lines. (F) Mouse breast cancer cells (4T1 and 67NR) were orthotopically injected into the mammary fat pad of immunocompetent BALB/c mice. Anti-PD-L1 antibody was tested alone (i.p. injection of 100 µg at days 4, 7 and 11) and in combination with HMGB1 inhibitors (RAP (10 µM/kg) and EP (1 mM/kg), treatment at 3-day intervals). The mean tumor volumes±SEM are represented. (G) The total number of (CD45$^+$) immune cells per milligram of tumor was determined in the different treatment groups by flow cytometry. (H) Scatter dot plots illustrating the percentage of each individual immune cell population (DC, PDC, CD4$^+$ and CD8$^+$ T cells, monocytic and granulocytic MDSC, neutrophils, M1 and M2 macrophages) among CD45$^+$ cells in both control and treated groups. The intratumoral immune cell infiltration was analyzed in five mice per condition. (I) scatter dot plots showing the percentage of tumor-infiltrating Treg (Foxp3$^+$) CD4$^+$ and CD8$^+$ cells among total CD4$^+$ and CD8$^+$ populations in the different treatment groups. The activation status of DC (J) and pDC (K) was determined by flow cytometry. the expression of several surface markers (CD80, CD86, I-A/I-E, ILT3 and ICOSL) was assessed. Data represent the mean fluorescent intensity (MFI)±SEM of five independent experiments in each group (each individual data point is shown). (L) The apoptotic cancer cells (cleaved caspase 3$^+$) were detected by immunohistochemistry and quantified using QuPath software. The number of positive cells was reported to tumor area (mm^2). The scale bar represents 100 µm. Asterisks indicate statistically significant differences (*p<0.05; **p<0.01; ***p<0.001; ****p<0.0001). P values were determined using one-way ANOVA, followed by Bonferroni post-test (A, L), Fisher's exact test (C, D) and one-way ANOVA followed by Dunnett's multiple comparison post-test (F, G, H, I, J, K). ANOVA, analysis of variance; DC, dendritic cell; EP, ethyl pyruvate; HMGB1, high-mobility group box 1; i.p, intraperitoneal; METABRIC, Molecular Taxonomy of Breast Cancer International Consortium; pDC, plasmacytoid DC; RAP, RAGE antagonist peptide.

compartment were determined. Causing the oxidation of different types of macromolecules (eg, proteins, DNA and lipids), we first measured the production of mitochondrial ROS by both breast (4T1, 67NR, EpRas) and lung (TC-1) cancer cells. Consistent with the long-time observations that most tumors cells display an altered redox status,[52] the malignant cells used in this study have been shown to represent a major source of ROS (figure 6A,B). Using a novel innovative methodology (called EXPEL),[43] soluble proteins contained in tumor-extruded fluids were retrieved and directly alkylated in order to maintain their original redox state. As shown in figure 6C,D, all HMGB1 forms are encountered within tumor microenvironment with an approximate 2:1 reduced-disulfide/oxidized ratio. However, it is important to notice that the proportion of oxidized HMGB1 is very likely underestimated by the lower sensitivity displayed by the anti-HMGB1 antibody for this latter redox form (as indicated by control bands). To precisely determine the effect of each individual form of HMGB1 on antigen-presenting cell phenotype/functional activity, human DC were incubated with oxidized, reduced or disulfide HMGB1 for 24 hours and then stimulated for maturation (LPS during 24 hours). While disulfide HMGB1 displayed no activity on DC phenotype, the reduced and oxidized forms significantly induced the activation and tolerogenicity of DC, respectively (figure 6E). Similar results were obtained with pDC generated from human $CD34^+$ hematopoietic progenitor cells (online supplemental figure 13). Importantly, the tolerogenic properties of oxidized HMGB1 were significantly blocked by the inhibition of RAGE, leading to the complete restoration of DC activation (figure 6F). In contrast, TLR4 did not contribute to DC functional impairment in the presence of oxidized HMGB1 (figure 6F).

DISCUSSION

The role of HMGB1 in cancer progression has been a matter of debate for over ten years.[23] In this context, quite a few theoretical and translational questions remained unanswered. Does HMGB1 expression affect patient outcome? Is HMGB1 a promising target for cancer therapy or, in contrast, should we promote its cellular release? Does extracellular HMGB1 positively or negatively impact antitumor immune responses? Which redox form is detected in cancer microenvironment? In the present study, we first reported that active HMGB1 secretion/cytoplasmic immunoreactivity is both a specific trait of malignant cells (not detected in normal conditions) and a predictor for unfavorable prognosis in patients with locally advanced cancer. In an era of large-scale transcriptome analyses, it is interesting to notice that next-generation sequencing results did not highlight the predictive value of HMGB1 due to their unability to discriminate dual effects/locations of a same target. Lacking a leader sequence, HMGB1 has been shown to be actively secreted through lysosome-mediated exocytosis following its JAK/STAT1-regulated nuclear-cytoplasmic translocation.[53 54] Nevertheless, the upstream components of this non-classical secretory pathway are still largely unknown as well as the reasons why some cancer (sub)types highly secrete HMGB1 (and display large areas of HMGB1 cytoplasmic immunoreactivity) while others do not. These latter points certainly merit further investigations given the clear protumor activity of HMGB1 demonstrated here in vivo.

Using several syngeneic mouse models of basal-like or lung cancer, both direct and indirect extracellular HMGB1 blockade significantly resulted in tumor growth inhibition. In each case, the antitumor effect of HMGB1 inhibitors was only detected 7–10 days following the first injection. This latency period very likely corresponds to the necessary time for the adaptive immune responses to be remobilized. In agreement, the dependence on adaptive immunity was distinctly demonstrated by the absence of anticancer effect when immunedeficient mice were used. Besides glycyrrhizin, RAP, A box and EP, a purified rabbit anti-HMGB1 antibody was also tested (online supplemental figure 14). Despite an in vitro neutralizing efficiency comparable to other HMGB1 inhibitors, and while a protective effect against sepsis lethality has previously been demonstrated,[33] the administration of an anti-HMGB1 antibody produced in rabbit was inefficient for reducing tumor growth. The different posologies/study designs used in our orthotopic models of cancer (injection of anti-HMGB1 antibody at 3-day intervals for 18 days) and those of murine sepsis (administration twice daily for 3 days and then monitoring for 10 days) are susceptible to explain the divergent results. Indeed, we cannot exclude that repeated doses for 3 weeks led to the generation of mouse antibodies against foreign epitopes, blocking ultimately the function of injected rabbit anti-HMGB1 antibody and/or shortening its half-life. Supporting this hypothesis, tumor-bearing mice were treated with a mouse anti-HMGB1 antibody and an important tumor growth inhibition (similar to that reported with the other tested HMGB1 inhibitors) was observed (online supplemental figure 14).

Without affecting the global number of $CD45^+$ cells (arguing against an 'alarmin' role of HMGB1 in cancer), we found that extracellular HMGB1 blockade alone elicited a drastic remodeling of tumor immune microenvironment. Overall, reduced proportions of immunosuppressive cells (especially MDSC but also M2 macrophages and Treg cells) associated with an increased activation of antigen-presenting cells (DC and pDC) were observed, indicating that targeting HMGB1 therapeutically enhances significantly local antitumor immune responses. Although the effector mechanism of HMGB1 inhibitors involves very likely several immune cell subtypes, the key role played by the reduction of intratumoral granulocytic MDSC was clearly demonstrated in anti-Ly6G-mediated depletion experiments. Confirming our observations on human samples (lower densities of both $Foxp3^+$ and $CD206^+$ cells within tumor microenvironment of nuclear HMGB1-positive cancers compared with their counterparts displaying a

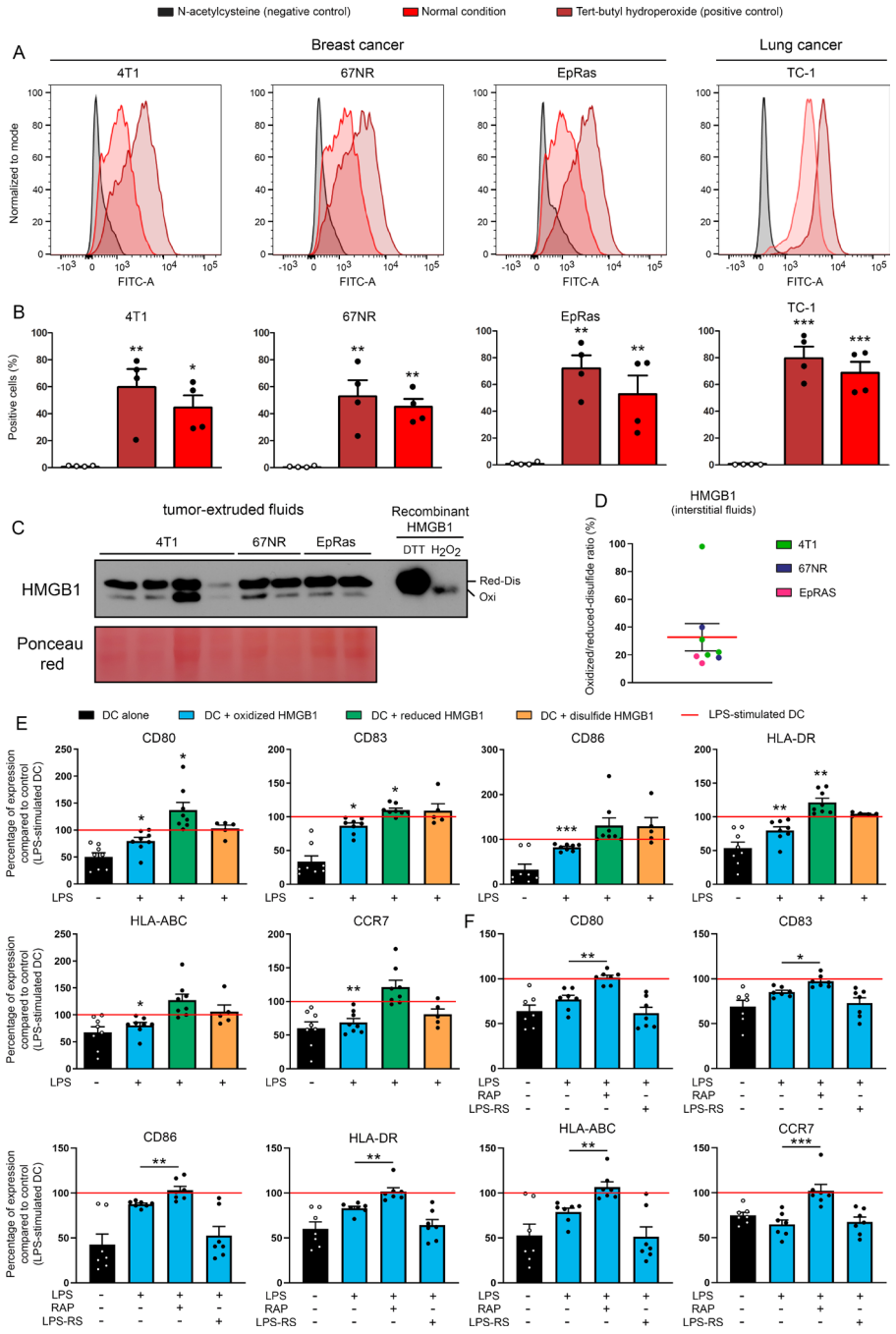

Figure 6 A significant fraction of HMGB1 contained in tumor-extruded fluids is in its oxidized form and displays RAGE-dependent tolerogenic properties. (A, B) The ROS accumulation in both breast (4T1, 67NR, EpRas) and lung (TC-1) cancer cells used in the present study was assessed by flow cytometry. N-acetylcysteine (5 mM) and tert-butyl hydroperoxide (100 µM) were used as negative and positive controls, respectively. Results represent the means±SEM of four independent experiments (each individual data point is shown). (C) The redox state of extracellular HMGB1 contained in tumor-extruded fluids was analyzed by Western blot. All samples were directly alkylated in order to 'freeze' the redox state of HMGB1 molecules. Recombinant HMGB1 (0.5 µg) incubated with either H_2O_2 or DTT (and then alkylated) were used as controls. (D) Oxidized/reduced-disulfide HMGB1 ratio (%) was calculated from the Western blot bands using ImageJ software. (E) DCs were incubated with terminally oxidized, fully reduced or disulfide HMGB1 for 24 hours before being stimulated with LPS for 24 hours. The expression of cell-surface molecules (CD80, CD83, CD86, HLA-DR, HLA-ABC and CCR7) was then measured by flow cytometry. All data were normalized to LPS-stimulated DC. Data represent the relative mean fluorescent intensity (MFI)±SEM of at least five independent experiments (each individual data point is shown). (F) DCs were incubated with terminally oxidized HMGB1 for 24 hours before being stimulated with LPS for 24 hours. When indicated, an inhibitor of RAGE (10 µM RAP) or TLR4 (2 µM LPS-RS) was added in the cell culture. The expression of DC activation markers was determined by flow cytometry. All data were normalized to LPS-stimulated DC. The relative MFI±SEM of 7 independent experiments are shown. Asterisks indicate statistically significant differences (*p<0.05, **p<0.01, ***p<0.001). P values were determined using one-way ANOVA, followed by Dunnett's multiple comparison post-test (A, B, E, F). ANOVA, analysis of variance; DC, dendritic cell; HMGB1, high-mobility group box 1.

cytoplasmic immunoreactivity), the improvement/activation of T cell immune response following HMGB1 inhibition was further supported by the increased number of apoptotic (cleaved caspase 3^+) tumor cells in treated cancers compared with control groups. Although the vast majority of studies focusing on HMGB1 did not pay attention to its redox state, it is intriguing to notice that, when an immune suppression (through promoting tolerogenic functionalities by DC/pDC, enhancing suppressive activities of MDSC or stimulating M2 polarization of macrophages) was reported in vitro,[55–57] the authors consistently used recombinant HMGB1 produced in cancer cell lines (g, myeloma (NS0)) and not in bacteria. Therefore, as extensively discussed below, it is reasonable to think that cysteine residues within the protein were mostly oxidized due to the high endogenous oxidative stress displayed by almost all tumors.

Given the numerous immunosuppressive molecules which can be encountered within tumor microenvironment, it is unrealistic to believe that treatment regimens using only one drug (eg, humanized anti-PD-1 or PD-L1 antibody) will display therapeutic efficacy in all patients with cancer. Therefore, both treatment personalization and the combinatorial targeting of several tumor-induced immune defects make sense intuitively for improving the efficacy of future therapies. Here, we showed that concurrent HMGB1 inhibition plus anti-PD-1 antibody resulted in significantly higher tumor growth inhibitions than did anti-PD-1 alone. Similarly to most studies analyzing the efficacy of immune checkpoint inhibitors in preclinical mouse models, it is important to emphasize that a quite high interindividual variability in anti-PD-1 therapeutic response was observed (online supplemental figure 10). Although still not completely understood, this latter phenomenon is very likely multifactorial (eg, differences in gut microbiota, upregulation/downregulation of the targeted proteins during treatment, expression of other immunosuppressive factors constituting compensatory mechanisms). Regarding the combination therapy using anti-PD-L1 antibody, the benefit was relatively modest (with 4T1 tumor cells) or absent (67NR). Displaying over 20% PD-L1$^+$ inflammatory and/or cancer cells, the 'super responder' profile of both models to anti-PD-L1 monotherapy is likely to explain these latter results. Altogether, the oversecretion of HMGB1 by cancer cells, its immunosuppressive/protumor activity as well as both the absence of toxicity and the long-standing use of some HMGB1 inhibitors in the context of other diseases (eg, glycyrrhizin in chronic hepatitis C patients)[58 59] make it a very promising target for cancer treatment. Furthermore, blocking extracellular HMGB1 with humanized antibodies or antagonists is unlikely to alter the beneficial nuclear functions (replication, DNA repair, genome stability) of the protein.

It is well established that tumor cells produce higher levels of ROS compared with normal/non-transformed cells. Still commonly called 'free radicals', these oxygen-containing chemically reactive molecules cause the oxidation of proteins, DNA and lipids, promoting ultimately many aspects of cancer progression.[60 61] To the best of our knowledge, this report provides the first evidence that HMGB1 is encountered on its oxidized form in cancer microenvironment/interstitial fluids (at least one third of total extracellular HMGB1) and acts as a tolerogenic signal on antigen-presenting cells in a RAGE-dependent manner. Based on our in vivo results, there is little doubt that the overall effect of HMGB1 in cancer is largely dictated by this latter form. Interestingly, without having identified the involved receptor, the induction of immunological tolerance by oxidized HMGB1 was previously proposed in the context of programmed cell death (apoptosis).[11] However, by lack of use of in vitro/in vivo models allowing the assessment of acquired immunotolerance development, most authors are still only focusing on the chemotactic/proinflammatory activities of HMGB1, and therefore, are considering its oxidized form as inactive.

In case of injury or pathogen infection, as a damage-associated molecular pattern molecule, extracellular reduced/disulfide HMGB1 stimulates innate immune cell chemotaxis and activation, mediating immunogenic cell death and triggering acute inflammatory responses. However, within the highly oxidative cancer microenvironment, the dark side of HMGB1 is revealed. Similarly to other secreted immunosuppressive molecules, the oxidation of HMGB1 is likely to be essential during the inflammation resolution but the persistence/chronicity of its tolerogenic activity is noxious and could be therapeutically targeted.

Author affiliations
[1]Laboratory of Experimental Pathology, GIGA-Cancer, University of Liege, Liege, Belgium
[2]Laboratory of Immunophysiology, GIGA-I3, University of Liege, Liege, Belgium
[3]Faculty of Veterinary Medicine, University of Liege, Liege, Belgium
[4]Metastasis Research Laboratory, GIGA-Cancer, University of Liege, Liege, Belgium
[5]Department of Pathology, University Hospital Center of Liege, Liege, Belgium

Acknowledgements The authors thank the Biobank of the University of Liege as well as the GIGA-Immunohistochemistry and in vitro imaging facilities (University of Liege) for their assistance. We are also grateful to Dr Stephanie Gofflot, Raphael Thonon, Kamilia El Kandoussi and Laurence Poma for their technical assistance.

Contributors PH and MH designed the study; PH, PR, SD, CP, MA, CR, TL, DB, AL, CR, MM, EH, OP and MH performed experiments; PH, SD, M-JN, OP and MH interpreted the data; PD provided resources; PH and MH generated the figures; MH wrote the manuscript. All authors discussed the results and commented on the manuscript.

Funding This work was supported in part by the University of Liege (Fonds spéciaux de la recherche and credits sectoriels), the Belgian Fund for Scientific Research (FNRS, MIS F.4520.20), the Televie (PDR 7.8507.19 and 7.4577.19), the Leon Fredericq Foundation and the Belgian Foundation against Cancer.

Competing interests None declared.

Patient consent for publication Not required.

Ethics approval All procedures and animal experiments were initially reviewed and approved by the institutional ethics committee of the University of Liege (#13-1572). All cancer specimens used in the present study were retrieved from the Tissue Biobank of the University Hospital Center of Liege (Belgium) with the approval of the local ethics committee (#2015-68).

Provenance and peer review Not commissioned; externally peer reviewed.

Data availability statement All data relevant to the study are included in the article or uploaded as online supplemental information. Any further information about resources and reagents should be directly requested to the corresponding author and will be fulfilled on reasonable request.

ORCID iD

Michael Herfs http://orcid.org/0000-0002-4382-8997

REFERENCES

1 Goodwin GH, Sanders C, Johns EW. A new group of chromatin-associated proteins with a high content of acidic and basic amino acids. *Eur J Biochem* 1973;38:14–19.
2 Wang H, Bloom O, Zhang M, *et al*. HMG-1 as a late mediator of endotoxin lethality in mice. *Science* 1999;285:248–51.
3 Pullerits R, Jonsson I-M, Verdrengh M, *et al*. High mobility group box chromosomal protein 1, a DNA binding cytokine, induces arthritis. *Arthritis Rheum* 2003;48:1693–700.
4 Popovic K, Ek M, Espinosa A, *et al*. Increased expression of the novel proinflammatory cytokine high mobility group box chromosomal protein 1 in skin lesions of patients with lupus erythematosus. *Arthritis Rheum* 2005;52:3639–45.
5 Zong M, Bruton JD, Grundtman C, *et al*. TLR4 as receptor for HMGB1 induced muscle dysfunction in myositis. *Ann Rheum Dis* 2013;72:1390–9.
6 Park JS, Svetkauskaite D, He Q, *et al*. Involvement of toll-like receptors 2 and 4 in cellular activation by high mobility group box 1 protein. *J Biol Chem* 2004;279:7370–7.
7 Andersson U, Wang H, Palmblad K, *et al*. High mobility group 1 protein (HMG-1) stimulates proinflammatory cytokine synthesis in human monocytes. *J Exp Med* 2000;192:565–70.
8 Yang D, Chen Q, Yang H, *et al*. High mobility group box-1 protein induces the migration and activation of human dendritic cells and acts as an alarmin. *J Leukoc Biol* 2007;81:59–66.
9 Yang S, Xu L, Yang T, *et al*. High-mobility group box-1 and its role in angiogenesis. *J Leukoc Biol* 2014;95:563–74.
10 Fang P, Schachner M, Shen Y-Q. HMGB1 in development and diseases of the central nervous system. *Mol Neurobiol* 2012;45:499–506.
11 Kazama H, Ricci J-E, Herndon JM, *et al*. Induction of immunological tolerance by apoptotic cells requires caspase-dependent oxidation of high-mobility group box-1 protein. *Immunity* 2008;29:21–32.
12 Yang H, Lundbäck P, Ottosson L, *et al*. Redox modification of cysteine residues regulates the cytokine activity of high mobility group box-1 (HMGB1). *Mol Med* 2012;18:250–9.
13 Venereau E, Casalgrandi M, Schiraldi M, *et al*. Mutually exclusive redox forms of HMGB1 promote cell recruitment or proinflammatory cytokine release. *J Exp Med* 2012;209:1519–28.
14 Yang H, Hreggvidsdottir HS, Palmblad K, *et al*. A critical cysteine is required for HMGB1 binding to Toll-like receptor 4 and activation of macrophage cytokine release. *Proc Natl Acad Sci U S A* 2010;107:11942–7.
15 Huang J, Ni J, Liu K, *et al*. HMGB1 promotes drug resistance in osteosarcoma. *Cancer Res* 2012;72:230–8.
16 Yan W, Chang Y, Liang X, *et al*. High-mobility group box 1 activates caspase-1 and promotes hepatocellular carcinoma invasiveness and metastases. *Hepatology* 2012;55:1863–75.
17 Lv D-J, Song X-L, Huang B, *et al*. Hmgb1 promotes prostate cancer development and metastasis by interacting with Brahma-related gene 1 and activating the Akt signaling pathway. *Theranostics* 2019;9:5166–82.
18 He S, Cheng J, Sun L, *et al*. HMGB1 released by irradiated tumor cells promotes living tumor cell proliferation via paracrine effect. *Cell Death Dis* 2018;9:648.
19 Zheng H, Chen J-N, Yu X, *et al*. Hmgb1 enhances drug resistance and promotes in vivo tumor growth of lung cancer cells. *DNA Cell Biol* 2016;35:622–7.
20 Li B, Song T-N, Wang F-R, *et al*. Tumor-derived exosomal HMGB1 promotes esophageal squamous cell carcinoma progression through inducing PD1$^+$ TAM expansion. *Oncogenesis* 2019;8:17.
21 Yamazaki T, Hannani D, Poirier-Colame V, *et al*. Defective immunogenic cell death of HMGB1-deficient tumors: compensatory therapy with TLR4 agonists. *Cell Death Differ* 2014;21:69–78.
22 Tesniere A, Schlemmer F, Boige V, *et al*. Immunogenic death of colon cancer cells treated with oxaliplatin. *Oncogene* 2010;29:482–91.
23 Kang R, Zhang Q, Zeh HJ, *et al*. Hmgb1 in cancer: good, bad, or both? *Clin Cancer Res* 2013;19:4046–57.
24 Haslam A, Prasad V. Estimation of the percentage of US patients with cancer who are eligible for and respond to checkpoint inhibitor immunotherapy drugs. *JAMA Netw Open* 2019;2:e192535.
25 Liu Z, Li M, Jiang Z, *et al*. A comprehensive immunologic portrait of triple-negative breast cancer. *Transl Oncol* 2018;11:311–29.
26 Nanda R, Chow LQM, Dees EC, *et al*. Pembrolizumab in patients with advanced triple-negative breast cancer: phase Ib KEYNOTE-012 study. *J Clin Oncol* 2016;34:2460–7.
27 Dirix LY, Takacs I, Jerusalem G, *et al*. Avelumab, an anti-PD-L1 antibody, in patients with locally advanced or metastatic breast cancer: a phase 1B javelin solid tumor study. *Breast Cancer Res Treat* 2018;167:671–86.
28 Zitvogel L, Kroemer G. Targeting PD-1/PD-L1 interactions for cancer immunotherapy. *Oncoimmunology* 2012;1:1223–5.
29 Gandhi L, Rodríguez-Abreu D, Gadgeel S, *et al*. Pembrolizumab plus chemotherapy in metastatic non-small-cell lung cancer. *N Engl J Med* 2018;378:2078–92.
30 Schmid P, Adams S, Rugo HS, *et al*. Atezolizumab and nab-paclitaxel in advanced triple-negative breast cancer. *N Engl J Med* 2018;379:2108–21.
31 Rotte A. Combination of CTLA-4 and PD-1 blockers for treatment of cancer. *J Exp Clin Cancer Res* 2019;38:255.
32 Shrimali RK, Ahmad S, Verma V, *et al*. Concurrent PD-1 blockade negates the effects of OX40 agonist antibody in combination immunotherapy through inducing T-cell apoptosis. *Cancer Immunol Res* 2017;5:755–66.
33 Yang H, Ochani M, Li J, *et al*. Reversing established sepsis with antagonists of endogenous high-mobility group box 1. *Proc Natl Acad Sci U S A* 2004;101:296–301.
34 Boivin G, Faget J, Ancey P-B, *et al*. Durable and controlled depletion of neutrophils in mice. *Nat Commun* 2020;11:2762.
35 Herfs M, Herman L, Hubert P, *et al*. High expression of PGE2 enzymatic pathways in cervical (pre)neoplastic lesions and functional consequences for antigen-presenting cells. *Cancer Immunol Immunother* 2009;58:603–14.
36 Herfs M, Vargas SO, Yamamoto Y, *et al*. A novel blueprint for 'top down' differentiation defines the cervical squamocolumnar junction during development, reproductive life, and neoplasia. *J Pathol* 2013;229:460–8.
37 Herfs M, Roncarati P, Koopmansch B, *et al*. A dualistic model of primary anal canal adenocarcinoma with distinct cellular origins, etiologies, inflammatory microenvironments and mutational signatures: implications for personalised medicine. *Br J Cancer* 2018;118:1302–12.
38 Bankhead P, Loughrey MB, Fernández JA, *et al*. QuPath: open source software for digital pathology image analysis. *Sci Rep* 2017;7:16878.
39 Bruyere D, Monnien F, Colpart P, *et al*. Treatment algorithm and prognostic factors for patients with stage I-III carcinoma of the anal canal: a 20-year multicenter study. *Mod Pathol* 2021;34:116–30.
40 Kim K, Watson PA, Lebdai S, *et al*. Androgen deprivation therapy potentiates the efficacy of vascular targeted photodynamic therapy of prostate cancer xenografts. *Clin Cancer Res* 2018;24:2408–16.
41 Demoulin SA, Somja J, Duray A, *et al*. Cervical (pre)neoplastic microenvironment promotes the emergence of tolerogenic dendritic cells via RANKL secretion. *Oncoimmunology* 2015;4:e1008334.
42 Demoulin S, Roncarati P, Delvenne P, *et al*. Production of large numbers of plasmacytoid dendritic cells with functional activities from CD34(+) hematopoietic progenitor cells: use of interleukin-3. *Exp Hematol* 2012;40:268–78.
43 Costanza B, Turtoi A, Bellahcène A, *et al*. Innovative methodology for the identification of soluble biomarkers in fresh tissues. *Oncotarget* 2018;9:10665–80.

44 Curtis C, Shah SP, Chin S-F, *et al*. The genomic and transcriptomic architecture of 2,000 breast tumours reveals novel subgroups. *Nature* 2012;486:346–52.
45 Pereira B, Chin S-F, Rueda OM, *et al*. The somatic mutation profiles of 2,433 breast cancers refines their genomic and transcriptomic landscapes. *Nat Commun* 2016;7:11479.
46 Rademaker G, Hennequière V, Brohée L, *et al*. Myoferlin controls mitochondrial structure and activity in pancreatic ductal adenocarcinoma, and affects tumor aggressiveness. *Oncogene* 2018;37:4398–412.
47 Arumugam T, Ramachandran V, Gomez SB, *et al*. S100P-derived RAGE antagonistic peptide reduces tumor growth and metastasis. *Clin Cancer Res* 2012;18:4356–64.
48 Mollica L, De Marchis F, Spitaleri A, *et al*. Glycyrrhizin binds to high-mobility group box 1 protein and inhibits its cytokine activities. *Chem Biol* 2007;14:431–41.
49 Davé SH, Tilstra JS, Matsuoka K, *et al*. Ethyl pyruvate decreases HMGB1 release and ameliorates murine colitis. *J Leukoc Biol* 2009;86:633–43.
50 Kim YM, Park EJ, Kim JH, *et al*. Ethyl pyruvate inhibits the acetylation and release of HMGB1 via effects on SIRT1/STAT signaling in LPS-activated RAW264.7 cells and peritoneal macrophages. *Int Immunopharmacol* 2016;41:98–105.
51 Mall C, Sckisel GD, Proia DA, *et al*. Repeated PD-1/PD-L1 monoclonal antibody administration induces fatal xenogeneic hypersensitivity reactions in a murine model of breast cancer. *Oncoimmunology* 2016;5:e1075114.
52 Szatrowski TP, Nathan CF. Production of large amounts of hydrogen peroxide by human tumor cells. *Cancer Res* 1991;51:794–8.
53 Lu B, Antoine DJ, Kwan K, *et al*. Jak/Stat1 signaling promotes HMGB1 hyperacetylation and nuclear translocation. *Proc Natl Acad Sci U S A* 2014;111:3068–73.
54 Gardella S, Andrei C, Ferrera D, *et al*. The nuclear protein HMGB1 is secreted by monocytes via a non-classical, vesicle-mediated secretory pathway. *EMBO Rep* 2002;3:995–1001.
55 Demoulin S, Herfs M, Somja J, *et al*. Hmgb1 secretion during cervical carcinogenesis promotes the acquisition of a tolerogenic functionality by plasmacytoid dendritic cells. *Int J Cancer* 2015;137:345–58.
56 Parker KH, Sinha P, Horn LA, *et al*. Hmgb1 enhances immune suppression by facilitating the differentiation and suppressive activity of myeloid-derived suppressor cells. *Cancer Res* 2014;74:5723–33.
57 Rojas A, Delgado-López F, Perez-Castro R, *et al*. Hmgb1 enhances the protumoral activities of M2 macrophages by a RAGE-dependent mechanism. *Tumour Biol* 2016;37:3321–9.
58 Arase Y, Ikeda K, Murashima N, *et al*. The long term efficacy of glycyrrhizin in chronic hepatitis C patients. *Cancer* 1997;79:1494–500.
59 Ikeda K. Glycyrrhizin injection therapy prevents hepatocellular carcinogenesis in patients with interferon-resistant active chronic hepatitis C. *Hepatol Res* 2007;37 Suppl 2:S287–93.
60 Liou G-Y, Storz P. Reactive oxygen species in cancer. *Free Radic Res* 2010;44:479–96.
61 Aggarwal V, Tuli HS, Varol A, *et al*. Role of reactive oxygen species in cancer progression: molecular mechanisms and recent advancements. *Biomolecules* 2019;9:735.

nature COMMUNICATIONS

ARTICLE

https://doi.org/10.1038/s41467-022-28724-8 OPEN

HPV infection alters vaginal microbiome through down-regulating host mucosal innate peptides used by *Lactobacilli* as amino acid sources

Alizee Lebeau[1,14], Diane Bruyere[1,14], Patrick Roncarati[1], Paul Peixoto[2,3], Eric Hervouet[2,3], Gael Cobraiville[4], Bernard Taminiau[5], Murielle Masson[6], Carmen Gallego[7], Gabriel Mazzucchelli[8], Nicolas Smargiasso[8], Maximilien Fleron[8,9], Dominique Baiwir[8,9], Elodie Hendrick[1], Charlotte Pilard[1], Thomas Lerho[1], Celia Reynders[1], Marie Ancion[1], Roland Greimers[10], Jean-Claude Twizere[11], Georges Daube[5], Geraldine Schlecht-Louf[7], Françoise Bachelerie[7], Jean-Damien Combes[12], Pierrette Melin[13], Marianne Fillet[4], Philippe Delvenne[1,10], Pascale Hubert[1] & Michael Herfs[1]✉

Despite the high prevalence of both cervico-vaginal human papillomavirus (HPV) infection and bacterial vaginosis (BV) worldwide, their causal relationship remains unclear. While BV has been presumed to be a risk factor for HPV acquisition and related carcinogenesis for a long time, here, supported by both a large retrospective follow-up study ($n = 6,085$) and extensive in vivo data using the K14-HPV16 transgenic mouse model, we report a novel blueprint in which the opposite association also exists. Mechanistically, by interacting with several core members (NEMO, CK1 and β-TrCP) of both NF-κB and Wnt/β-catenin signaling pathways, we show that HPV E7 oncoprotein greatly inhibits host defense peptide expression. Physiologically secreted by the squamous mucosa lining the lower female genital tract, we demonstrate that some of these latter are fundamental factors governing host-microbial interactions. More specifically, several innate molecules down-regulated in case of HPV infection are hydrolyzed, internalized and used by the predominant *Lactobacillus* species as amino acid source sustaining their growth/survival. Collectively, this study reveals a new viral immune evasion strategy which, by its persistent/negative impact on lactic acid bacteria, ultimately causes the dysbiosis of vaginal microbiota.

[1] Laboratory of Experimental Pathology, GIGA-Cancer, University of Liege, Liege, Belgium. [2] INSERM, EFS BFC, UMR 1098, Interactions Hôte-Greffon-Tumeur/Ingénierie Cellulaire et Génique, University of Bourgogne Franche-Comté, Besançon, France. [3] EPIGENEXP platform, University of Bourgogne Franche-Comté, Besançon, France. [4] Laboratory for the Analysis of Medicines, Center for Interdisciplinary Research on Medicines (CIRM), University of Liege, Liege, Belgium. [5] Department of Food Sciences-Microbiology, Fundamental and Applied Research for Animals and Health (FARAH), Faculty of Veterinary Medicine, University of Liege, Liege, Belgium. [6] Ecole Supérieure de Biotechnologie Strasbourg, UMR 7242, CNRS, University of Strasbourg, Illkirch, France. [7] INSERM UMR 996, Inflammation Microbiome and Immunosurveillance, University of Paris-Saclay, Clamart, France. [8] Laboratory of Mass Spectrometry, Department of Chemistry, University of Liege, Liege, Belgium. [9] GIGA Proteomic Facility, University of Liege, Liege, Belgium. [10] Department of Pathology, University Hospital Center of Liege, Liege, Belgium. [11] Laboratory of Signaling and Protein Interactions, GIGA-Molecular Biology of Diseases, University of Liege, Liege, Belgium. [12] Infections and Cancer Epidemiology Group, International Agency for Research on Cancer, World Health Organization, Lyon, France. [13] Department of Clinical Microbiology, University Hospital Center of Liege, Liege, Belgium. [14] These authors contributed equally: Alizee Lebeau, Diane Bruyere. ✉email: M.Herfs@uliege.be

Affecting at any point of time more than 300 million individuals worldwide, human papillomavirus (HPV) is the most common sexually transmitted infection[1]. To date, over 225 genotypes have been fully characterized and about one fifth, belonging to the alpha genus, can be detected in the anogenital mucosa. Although most infections are cleared or maintained in an asymptomatic or latent state by the immune system, carcinogenic (high-risk) HPV strains (most notably HPV16 and 18) cause virtually all squamous intraepithelial lesions [low-grade (LSIL) and high-grade (HSIL)] and cell carcinoma (SCC) arising from the uterine cervix as well as a large fraction (~50%) of vaginal/vulvar (pre)cancers. In total, HPV infections account for ~5% of the worldwide cancer burden with an estimated 550,000 new cases diagnosed annually in the lower genital tract[2,3]. The persistence of an active infection for years or decades indicates that these viruses have evolved a number of mechanisms to escape both innate and adaptive immune responses. Indeed, by directly interacting with some core proteins or by indirectly altering their activity (post-translational modifications) or their gene expression pattern (promoter hypermethylation and histone modifications), viral E6 and E7 oncoproteins have been especially shown to antagonize the cGAS-STING DNA sensing pathway[4], to suppress the interferon secretion and signaling[5–7], to impair Toll-like receptor 9 and major histocompatibility complex class I transcription[8,9] and to reduce chemotactic and proinflammatory gene expression[10].

In contrast to the skin and the gut which are colonized by a complex microbiome, the human vaginal ecosystem is associated with a low microbial diversity largely dominated (>90%) by a few *Lactobacillus* species (mainly *L. crispatus*, *L. jensenii* and *L. iners*)[11–13]. Characterized by the replacement of the normally dominant lactic acid bacteria by a more diverse bacterial mixture predominated by *Gardnerella vaginalis* and other anaerobic bacteria (e.g., *Atopobium vaginae, Prevotella_ge*, *Mobiluncus_ge*, *Sneathia_ge*,…)[14], bacterial vaginosis (BV) is a common vaginal disorder among women of reproductive age. Although at least 50% of women with BV are asymptomatic, this microbial imbalance (also called dysbiosis) can manifest clinically by a vaginal discharge, the presence of clue cells (recognized by cytologic review) and a "fishy" odor related to the production of volatile amines by anaerobes[15]. Three decades of epidemiologic studies reported the multiplicity of sexual partners, African descent, vaginal douching and cigarette smoking as risk factors for the acquisition of BV[15]. However, none of these latter on their own can reliably explain the prevalence of this condition and the etiopathogenesis of BV remains unclear[15,16]. Most likely, this imbalance in the vaginal flora is multifactorial and involves complex interactions between extrinsic factors, the different species of bacteria constituting the endogenous vaginal microbiome and the host mucosa.

In addition to causing symptoms for some women, BV has been shown to increase the risk of preterm delivery[17] as well as gynecologic complications such as endometritis, cervicitis and postoperative pelvic infections[18]. Moreover, both the rise in the vaginal pH and the reduced level of hydrogen peroxide (H_2O_2) resulting from the low abundance of *Lactobacilli* is presumed to promote the acquisition of both bacterial (e.g., *Chlamydia trachomatis* and *Neisseria gonorrhoeae*) and viral (e.g., herpes simplex virus type 2, HIV and HPV) sexually transmitted pathogens[19–22]. The degradation of the protective mucus barrier through the sialidase activity of anaerobic micro-organisms could also contribute to this latter susceptibility for developing infections in the lower genital tract[23]. Regarding HPV infections, besides favoring their acquisition, it is generally considered that the oxidative stress resulting from microbial dysbiosis also promotes the subsequent progression of HPV-positive (pre) neoplastic lesions. In agreement, recent evidence has shown that an anaerobic vaginal microbiome composition is associated with a lower regression rate of HPV-related diseases[24]. Despite these important findings, the interplay/association between BV and HPV infection is still unclear. Indeed, while longitudinal studies clearly reported increased rates of incident HPV among BV-positive women (for a meta-analysis, see[25]), the risk of BV occurrence following HPV infection has not been systematically pursued/calculated. Overall, data related to the influence of HPV on vaginal microbiome are limited and, as mentioned in several review articles[26,27], when BV and HPV coexist, we cannot exclude that, in a significant proportion of women, the viral infection preceded in time and, by altering the host mucosa secretome, ultimately caused BV development.

The present multi-approach study shows a causal relationship between HPV infection and BV. Mechanistically, the drastic down-regulation of host defense peptides, related to the interactions of HPV E7 oncoprotein with several key proteins (NEMO, CK1, β-TrCP) involved in both NF-kB and Wnt/β-catenin signaling pathways, has been shown to be instrumental in this process. Indeed, we unexpectedly uncovered that the innate molecules most secreted by the vaginal/cervical mucosa do not display any antimicrobial activity on *Lactobacillus* species but rather, are cleaved and used as amino acid source by these lactic acid bacteria, sustaining their growth/survival. The accumulating (retrospective clinical and in vitro) data have been finally confirmed in vivo using the K14-HPV16 transgenic mouse model in which (pre)cancer development was associated with a vaginal dysbiosis.

Results

A large retrospective follow-up analysis including over 6,000 patients identifies a two-way interaction between HPV infection and BV development. In the last decade, several systematic reviews of the literature (and meta-analysis) clearly indicated that HPV infection and BV are epidemiologically related[25,26,28]. However, some uncertainties still exist concerning the temporal sequence between these two pathological conditions. Indeed, while BV has been considered as a risk factor for HPV acquisition/persistence for a long time, the inverse relationship remains unclear. To address this important issue, a retrospective cohort study including women who underwent at least 2 Pap smear screenings over an 8-year period was performed. At each visit, complete data related to a potential abnormal cytology result (Bethesda classification), the existence of BV (Hay/Ison grading system) and high-risk HPV infection (Abbott RealTime HPV assay) were available for all enrolled patients. At the first visit, 3,481 out of 6,085 (57.2%) patients did not display any evidence of HPV infection and/or BV. A mixed bacterial flora (associated or not with the presence of clue cells) was reported in about one third (2,053/6,085, 33.7%) of patients with normal cytology (HPV negative). Single or multiple HPV infection was detected in 262 (4.3%) patients with a morphologically normal cervico-vaginal flora. At last, 289 (4.8%) patients were simultaneously positive for high-risk HPV and BV. The general characteristics of the four defined groups and the geographic repartition of patients are summarized in Fig. 1a and Supplementary Fig. 1, respectively. Of note, patients' age (distribution) was not significantly different between the groups. No obvious difference in terms of geographic distribution of patients was noticed either. Overall, 12,390 follow-up visits were completed by the selected women (median follow-up time: 66.3 months) and, in order to precisely determine the temporal relationship between BV and genital HPV infection, the probability of acquiring one condition when the other one was already present or not was estimated. During follow-up visits, a positive HPV test (associated with cytological abnormalities)

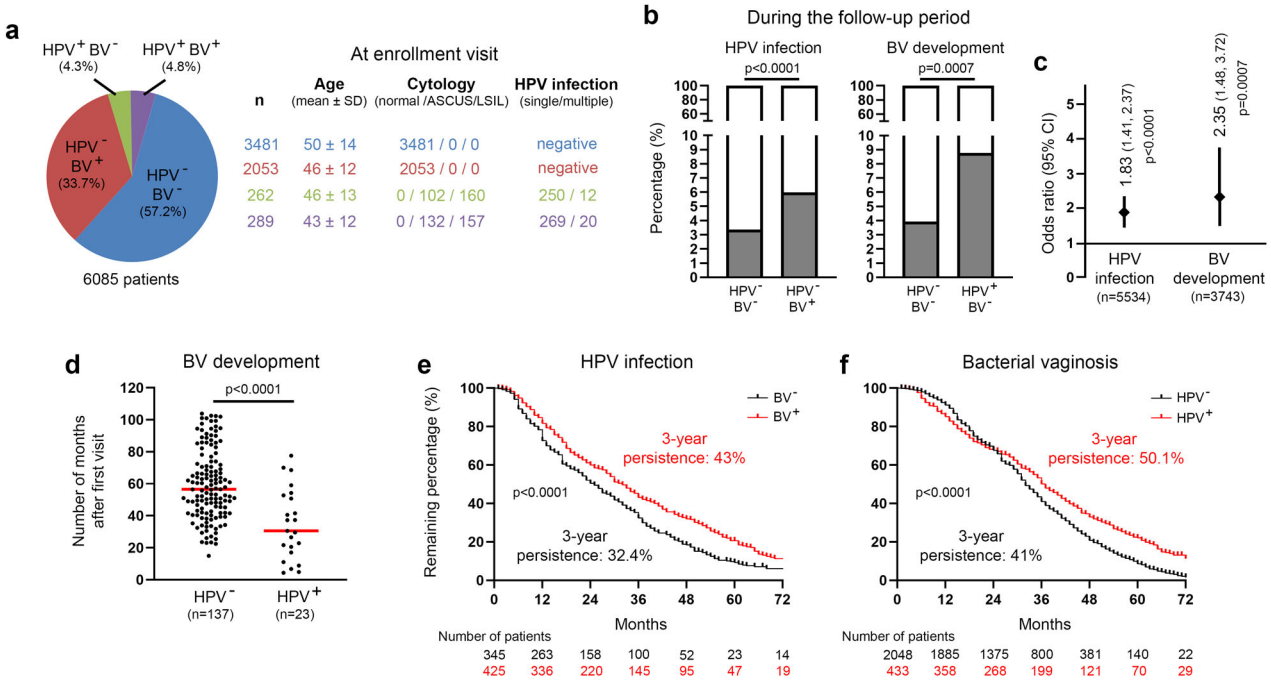

Fig. 1 Retrospective clinical follow-up analysis evaluating the relationship between genital HPV infection and BV occurrence/persistence. a General characteristics of the study population ($n = 6,085$). **b** Probability of high-risk HPV infection or BV development during the follow-up period according to the status for the other gynecological disorder at first (enrollment) visit. **c** Forest plot showing the odds ratio (OR) and 95% confidence intervals (CI) for developing one pathological condition when the other one was preceding in time [HPV infection (OR: 1.83, 95% CI: 1.41–2.37); BV development (OR: 2.35, 95% CI: 1.48–3.72)]. **d** Number of months for BV occurrence in HPV-positive and -negative patients. **e** Kaplan-Meier estimates for the persistence of HPV infection according to the BV status (negative *versus* positive). The clearance of HPV infections was ascertained by both cytology (Bethesda system) and PCR-based HPV test (Abbott High-risk HPV assay). **f** Kaplan–Meier curve for the persistence of BV according to the HPV status. Two consecutive negative results (using Hay/Ison grading system) at least 12 months apart were required to consider a patient really/durably cured of BV. *P* values were determined using two-sided Fisher's exact test **b**, **c**, two-sided unpaired *t*-tests (**d**) and log-rank (Mantel-Cox) test **e**, **f**. Source data are provided as a Source Data file.

and BV was observed in 117 (117/3,481, 3.4%) and 137 (137/3,481, 3.9%) control women (negative for HPV and BV at first visit), respectively. Eight patients were positive for both HPV and BV at the same follow-up visit. Importantly, the development of each disorder was significantly more frequently diagnosed when the other one was preceding in time [HPV: 123/2,053, 6% (OR: 1.83, $p < 0.0001$); BV: 23/262, 8.8% (OR: 2.35, $p < 0.001$)] (Fig. 1b, c). These latter results were not adjusted for age, race, or other potential confounders [e.g., socioeconomic status of patients or number of sex partners (due to the lack of available information)]. In parallel, the median time for BV occurrence in HPV-infected and -uninfected women was investigated and, interestingly, a significant difference (34.53 months *versus* 59.44, $p < 0.0001$) was observed (Fig. 1d). To further evaluate the interplay between HPV and BV, the persistence of HPV infection according to the BV status (Fig. 1e) as well as the inverse evaluation (Fig. 1f) were determined. Out of 791 HPV-positive patients (diagnosed at first visit or during follow-up), 21 (2.7%) were excluded from the present longitudinal analysis because they underwent examinations in a different hospital following HPV diagnosis and, therefore, no data allowing to assess the persistence of the viral infection were available in our records. For a similar reason, 0.8% (21/2,502) of BV-positive patients were not taken into consideration either. As shown in Fig. 1e, the duration of HPV infections was significantly longer in BV-positive women compared to their counterparts displaying a normal vaginal microbiome dominated by *Lactobacillus spp* (persistent infections after 3 years: 43% *versus* 32.4%, $p < 0.0001$). Remarkably, the opposite observation was also made (Fig. 1f). Indeed, the 3-year BV persistence was 50.1% for HPV-positive patients, as opposed to 41% for uninfected individuals ($p < 0.0001$).

HPV oncoproteins impair innate (antimicrobial) peptide expression in vaginal/cervical squamous mucosa. By the constitutive or inducible production of soluble molecules (especially innate peptides), the host mucosa actively participates to the regulation of bacterial flora. These complex host-microbiota interactions are still the subject of intense investigations and are very likely specific for each organ as suggested by the important disparities between each microbiome and mucosal surface (skin, gut, oral, vaginal). According to the antimicrobial peptide database (http://aps.unms.edu), the squamous epithelial cells (keratinocytes) lining the lower part of the gynecologic tract secrete a dozen of innate (antimicrobial) peptides[29,30]. By laser capture microdissection, 44 independent frozen human tissue specimens (11 normal squamous epithelia, 10 LSIL, 10 HSIL, and 13 SCC) were sampled. In order to avoid bias related to HPV status, all (pre)neoplastic lesions displayed diffuse (basal or full-thickness) $p16^{INK4a}$ immunoreactivity in keeping with carcinogenic HPV infection. To allow the comparison of the expression level of all analyzed host defense peptides, the amplification efficiency of each qPCR reaction was determined (Fig. 2a). As shown in Fig. 2b, c, with the exception of HβD3, all antimicrobial peptides were down-regulated in HPV-positive lesions compared to normal squamous vaginal/ectocervical epithelium. The inhibition of "defensin-like" peptides (mainly S100A7 and elafin) was especially considered as essential given that, in normal/uninfected conditions, these latter were up to 1000 fold (>10 Ct) more expressed than the epithelial members of the defensin family. Similar reduced expressions of both defensins and "defensin-like" peptides in HPV-positive (pre)neoplastic lesions were also observed at the protein level, as shown by immunohistochemical

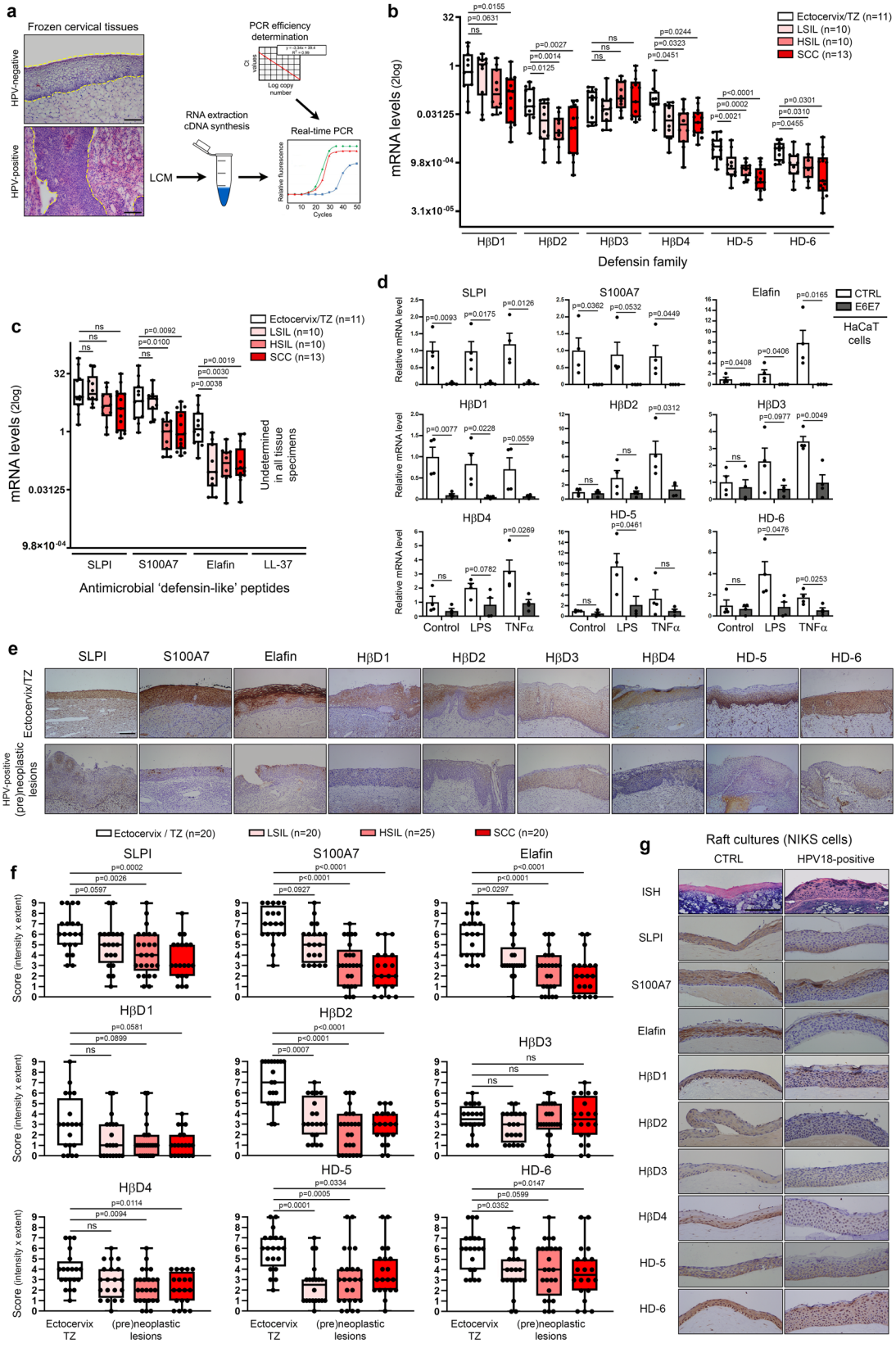

experiments (Fig. 2e, f). Regarding LL-37, this cathelicidin-related antimicrobial peptide was undetectable both at the mRNA and protein levels (Fig. 2c and Supplementary Fig. 2). It is interesting to notice that the morphologically normal ($p16^{INK4a}$-negative) squamous epithelium adjacent to HPV-positive (pre)neoplastic lesions also displayed a significantly reduced expression of several innate peptides (S100A7, elafin, HβD2, HβD4 and HD-5) (Supplementary Fig. 3). In order to determine whether or not HPV (and its viral oncoproteins) is directly responsible for the down-regulation of defensin(-like) peptides observed in (pre)neoplastic lesions, human keratinocytes were stably transduced with HPV16 E6E7 oncogenes and the expression level of each defense peptide

Fig. 2 HPV oncoproteins impair both the constitutive and inducible innate (antimicrobial) peptide expression. a Schematic illustration of the steps involved in gene expression analysis using microdissected frozen specimens. mRNA expression of epithelial-specific members of the defensin **b** and "defensin-like" **c** families was measured by RT-qPCR in HPV-positive (pre)neoplastic lesions (LSIL, $n = 10$; HSIL, $n = 10$; SCC, $n = 13$). Uninfected squamous samples [ectocervix, vagina, transformation zone (TZ)] ($n = 11$) were used as control. Gene expression was normalized using four calibrator genes (HPRT, GAPDH, 18S and TBP). Box limits: 25th to 75th percentiles; line: median; whiskers: minimum to maximum. **d** RT-qPCR analysis of SLPI, S100A7, elafin, HβD1-4 and HD-5/6 expression in immortalized keratinocytes stably transduced or not with HPV16 E6/E7 oncoproteins and stimulated with TNFα or LPS. Each experiment was normalized to the amount of HPRT mRNA from the same sample. Results represent the means ± SEM of four independent experiments. **e** HPV-negative and positive tissue specimens stained for antimicrobial peptides expressed by the squamous epithelium lining the lower part of the female reproductive tract. A reduced immunoreactivity for most of these innate factors was clearly observed in HPV-infected (pre)neoplastic lesions. **f** Semi-quantitative evaluation of innate peptide expression (intensity and extent of the immunostainings) in both normal epithelium from HPV-negative samples ($n = 20$) and (pre)neoplastic lesions (LSIL, $n = 20$; HSIL, $n = 25$; SCC, $n = 20$). Box limits: 25th to 75th percentiles; line: median; whiskers: minimum to maximum. **g** Representative control and HPV18-positive organotypic raft culture sections stained for all analyzed host defense (antimicrobial) peptides. As a control, HPV DNA was detected by in situ hybridization and, consistent with an episomal infection, a diffuse punctate pattern was observed. Images are representative of three independent experiments. The scale bar represents 100 μm. *P* values were determined using one-way ANOVA followed by Dunnett's multiple comparison post-hoc test **b**, **c**, two-sided unpaired *t*-tests **d** and ANOVA Kruskal–Wallis test followed by Dunn post-hoc test **f**. ns: not significant ($p > 0.1$). Source data are provided as a Source Data file.

potentially expressed by the squamous mucosa and being part of the innate immune barrier of the female lower genital tract was investigated (Fig. 2d). HβD2-4 expression was shown to be highly stimulated by TNFα whereas LPS was more efficient to induce HD-5/6 expression. Significantly, not only did the presence of viral oncoproteins greatly impair (up to 7 Ct, 128 fold) the expression of so called "constitutive" peptides (SLPI, S100A7, elafin and HβD1), but also the induction of HβD2-4 as well as HD-5/6 following the exposure to TNFα/LPS was significantly altered. A drastic reduced secretion of "constitutive" peptides in case of HPV16 E6E7 transduction was also reported in cell supernatants (ELISA) (Supplementary Fig. 4). In parallel, we utilized a second in vitro model mimicking more closely the early steps of the natural infection with carcinogenic HPV (Fig. 2g). Using organotypic raft cultures, keratinocytes maintaining episomal HPV18 genome displayed weaker immunoreactivities for SLPI, S100A7, elafin, HβD2 and HβD4 compared to uninfected cells. The other analyzed peptides were down-regulated at a lower extent.

HPV impairs TNFα/LPS-induced innate peptide expression through E7-dependent NEMO degradation and subsequent suppression of NF-κB activation. Proinflammatory factors such as TNFα, IL-1β and LPS have been previously shown to induce the expression of elafin as well as several members of the defensin family[31–33]. Given these results and the identification of putative NF-κB/p65 binding sites within the promoters of *DEFB2-4*, *DEFA5-6* and *PI3* (elafin) genes [estimations made using the Eukaryotic promoter database[34]], we first evaluated the requirement of NF-κB signaling pathway activation in TNFα/LPS-induced innate peptide expression. As expected, knockdown of p65 with siRNA or indirectly via blockade of the degradation of IκBα (BAY 11-7082) resulted in a significant decrease of defensin/elafin mRNA levels in normal/uninfected keratinocytes (Fig. 3a, b). To evaluate the potential alteration of NF-κB in case of HPV infection as well as the role of each individual viral oncoprotein, the occupancy of NF-κB binding sites on both *PI3/elafin* and *DEFB2* promoters was analyzed by ChIP in keratinocytes stably transduced with HPV16 E6 or E7. As shown in Fig. 3c, upon TNFα stimulation, a weaker occupancy of both gene promoters by p65 was reported in E7-positive cells. E6 viral oncoprotein did not seem to disrupt NF-κB signaling pathway. In order to determine the mechanism underlying E7-dependent alteration of NF-κB activation, the presence of both TNFα (TNFR1-2) and LPS (CD14 and TLR4) receptors at the cell membrane was first analyzed by flow cytometry. No significant difference was observed between cells transduced or not with HPV E6/E7 viral oncogenes (Fig. 3d). IκBα degradation and p65 nuclear translocation upon TNFα stimulation were then assessed. Interestingly, the presence of E7 oncoproteins strongly reduced IκBα degradation (Fig. 3e), explaining the cytoplasmic sequestration of p65 (Fig. 3f, g). Further confirming these data, the percentage of epithelial cells displaying nuclear p65 immunoreactivity was significantly lower in HPV-positive cancers compared to their viral-unrelated counterparts (Fig. 3h). Based on these clear-cut results, the direct interaction of HPV16 E7 oncoprotein with each protein members of the IKK kinase complex was evaluated using *Gaussia princeps* luciferase complementation assay (GPCA). Strikingly, a strong interaction between HPV16 E7 and NEMO was highlighted and confirmed by co-IP in both directions (Fig. 3i–j and Supplementary Fig. 5). Similar results were obtained with HPV E7 from several other genotypes (high-risk alpha: HPV18, 33 and 39; beta: HPV8, 38 and 49) (Supplementary Fig. 6). In order to further characterize this interaction between E7 and IKK regulatory subunit (NEMO), three truncated/mutated forms of HPV16 E7 were also tested: the CR1 + CR2 region (consisting of 1–36 amino acids), the C-terminal domain (37–98 amino acids) and the C24G/E26G construct mutated within the LxCxE motif. As shown in Fig. 3k, the GPCA signal was drastically reduced with the CR1 + CR2 construct, supporting that NEMO interacts with the C-terminal region of E7. Finally, protein stability/half-life was measured in cultured cells after treatment with a protein synthesis inhibitor (cycloheximide). In contrast to the high NEMO stability observed in normal cells, HPV16 E7 oncoprotein led to a marked degradation of this latter protein (Fig. 3l).

HPV E7 oncoprotein inhibits constitutive expression of both elafin and S100A7 through promoting β-catenin stabilization/signaling and subsequent up-regulation of c-myc. Based on data collected by several approaches (e.g., microarray gene expression profiling or ChIP-sequencing), it is estimated that ~15% of all human genes are regulated (positively or negatively) by the oncogenic protein c-myc[35]. Interestingly, both elafin and S100A7, which are drastically down-regulated in HPV-infected tissues, are listed within the high-affinity group of c-myc targets[36]. These latter results obtained by high-throughput screening were, however, never confirmed/validated. Highlighting the involvement of this transcriptional factor in elafin/S100A7 repression, by silencing c-myc (Fig. 4a) or chemically repressing its dimerization with Max (Fig. 4b), we significantly and strongly restored both elafin and S100A7 expression in E6E7-transduced cells. Importantly, close results were observed by using siRNA targeting β-catenin (Fig. 4a), a key factor involved in the Wnt signaling pathway and well-known to activate c-myc transcription[37]. In order to evaluate the potential impact of

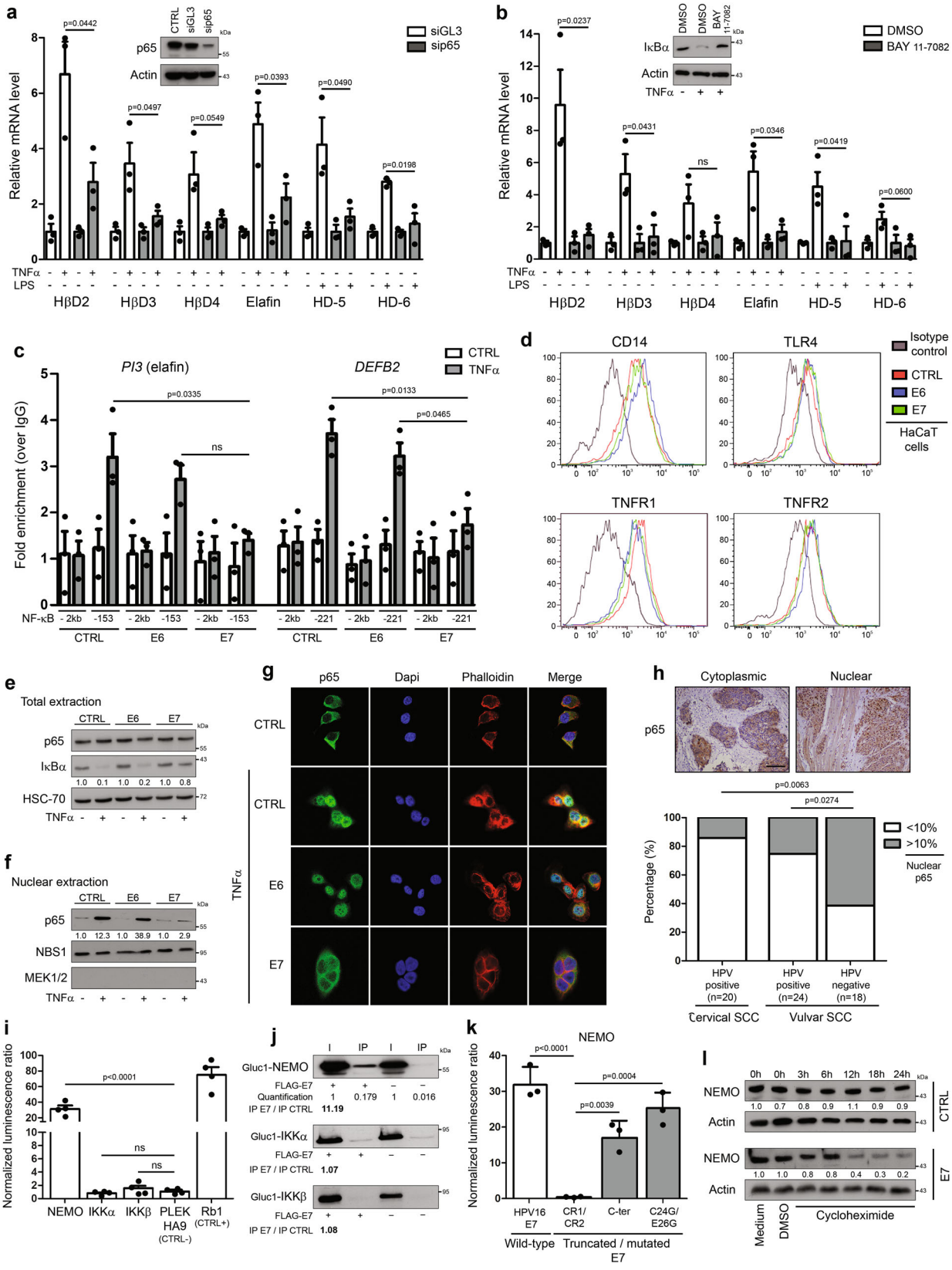

each individual viral oncoprotein on c-myc expression, its mRNA level was investigated in HPV16 E6 or E7-transduced keratinocytes. Compared to control cells, a significant increase in c-myc transcripts was only detected in HPV16 E7-positive cells (Fig. 4c) and the requirement of β-catenin in this up-regulation was highlighted (Fig. 4d). Confirming these data, an increased nuclear c-myc immunoreactivity was clearly observed in HPV18-positive organotypic raft cultures, E7-transduced keratinocytes as well as in HPV-positive (pre)neoplastic lesions compared to respective controls (Fig. 4e, f, i). Exclusively detected at the cell membrane in uninfected cells/tissues, an intense cytoplasmic/nuclear β-catenin immunoreactivity was reported in case of HPV infection/E7 transduction

Fig. 3 E7 viral oncoprotein reduces drastically TNFα/LPS-induced innate peptide expression through inducing NEMO degradation and impairing subsequent p65 nuclear translocation. TNFα/LPS-induced defensin/elafin expression was analyzed by RT-qPCR in non-infected cells transfected with siRNA targeting p65 **a** or treated with 5 μM BAY 11-7082 **b**. Cells transfected with control siRNA (siGL3) or treated with DMSO were used as negative controls. Each experiment was normalized to the amount of HPRT mRNA from the same sample. Results represent the means ± SEM of three independent experiments. **c** Occupancy of NF-κB binding sites on *PI3* (-153 bp) and *DEFB2* (-221 bp) promoters was evaluated by ChIP in control, HPV16 E6-positive and E7-positive cells. Primers targeting a region with no putative NF-κB sites (-2 kb) in both promoters served as negative controls. Results represent the means ± SEM of three independent experiments. **d** Analysis of cell surface expression of TNFα (TNFR1-2) and LPS (CD14 and TLR4) receptors by control, HPV16 E6 and E7-transduced cells using flow cytometry. Keratinocytes stably transduced or not with HPV16 E6 or E7 were first treated with TNFα and both the degradation of IκBα **e** and the nuclear translocation of p65 was then analyzed by Western blot **f** or immunofluorescence **g**. The absence of colocalization between p65 and DAPI in E7-transduced cells (cytoplasmic sequestration of p65) should be noticed. **h** Anti-p65 immunostaining in both HPV-positive ($n = 44$) and negative SCC ($n = 18$). Low densities of epithelial cells displaying a nuclear p65 immunoreactivity were observed in virus-related tumors. Of note, tissue specimens of vulvar cancer were included due to the impossibility of analyzing HPV-negative SCC arising from the uterine cervix. **i** Binding of protein members of the IKK kinase complex with HPV16 E7 oncoprotein assessed by *Gaussia princeps* luciferase complementation assay (GPCA). Retinoblastoma-associated protein (Rb1) and PLEKHA9 were used as positive and negative control, respectively. Results represent the means ± SEM of four independent experiments. **j** Co-IP of NEMO, IKKα and IKKβ with HPV16 E7 oncoprotein. **k** GPCA analyzing the binding of truncated/mutated forms of HPV16 E7 with NEMO. Results represent the means ± SEM of three independent experiments. **l** NEMO stability in both control and HPV16 E7-transduced cells following treatment with 100 μM cycloheximide. The scale bar represents 100 μm. *P* values were determined using two-sided unpaired *t*-tests **a**, **b**, one-way ANOVA followed by Dunnett's multiple comparison post-hoc test **c**, **i**, Fisher's exact test **h** and one-way ANOVA followed by Bonferroni post-hoc test **k**. ns: not significant ($p > 0.1$). The Western blot and co-IP analyses were independently performed three times and twice, respectively. One representative experiment is shown. Source data are provided as a Source Data file.

(Fig. 4e, f, h). As shown in Fig. 4f, E6 viral oncoprotein modified neither β-catenin cellular localization nor c-myc protein level. As β-catenin is well-known to interact with the cytoplasmic tail of E-cadherin in normal conditions, we then analyzed the expression of this latter protein in our in vitro/in situ models. Reduced anti-E-cadherin immunostainings were observed in the large majority (>75%) of HSIL and cervical cancers (Fig. 4g) as well as in HPV-positive raft cultures (Fig. 4e) and E7-transduced cells (Fig. 4f). The patchy E-cadherin immunoreactivity observed in both E7-positive cells (Fig. 4f) and most tissue specimens guided our choice to analyze the methylation status of E-cadherin gene (*CDH1*). As expected, *CDH1* promoter displayed more methylated CpG islands in E7-transduced cells compared to both control and E6-positive cells (Fig. 4j). The reactivation of silenced *CDH1* gene following 5-aza-deoxycytidine treatment further supported the implication of DNA methylation in E-cadherin down-regulation observed in case of HPV infection (Fig. 4k).

As extensively discussed by Jeanes et al.[38], the loss of E-cadherin alone (without concomitant alteration of the β-catenin degradation complex) does not increase β-catenin stabilization/signaling. Given the intense cytoplasmic/nuclear β-catenin immunoreactivity observed in vitro/in situ (Fig. 4e, f, h), the potential interactions between HPV16 E7 oncoprotein and members of the β-catenin degradation pathway were investigated by GPCA. Importantly, high (positive) GPCA signals were obtained with the alpha and gamma (γ1-3) isoforms of Casein Kinase 1 (CK1), the ubiquitin E3 ligase β-TrCP and GSK3β (Fig. 4l). Confirmed by co-IP in both directions, both E7-CK1 and E7-β-TrCP interactions required the C-terminal region of the viral oncoprotein (Fig. 4m, n, Supplementary Figs. 5 and 7). Regarding the interaction between HPV E7 and GSK3β, no clear confirmation by co-IP was obtained arguing that it is likely a false positive of the GPCA screening method (Supplementary Fig. 8). The interactions with both alpha and gamma isoforms of CK1 as well as with β-TrCP were also reported with E7 oncoprotein from other HPV genotypes (high-risk alpha: HPV18, 33 and 39; beta: HPV8, 38 and 49) (Supplementary Fig. 9). Finally, compared to control cells, a marked degradation of CK1 (associated with a stabilization of β-catenin) was observed in HPV16 E7-transduced cells following cycloheximide treatment (Fig. 4o). Further confirming all these latter results, the CK1-dependent phosphorylation of β-catenin (ser45) (first step of the β-catenin ubiquitination-dependent proteolysis) was drastically inhibited by HPV16 E7 (Fig. 4p).

Innate peptides predominantly and constitutively secreted by the cervical/vaginal mucosa promote Lactobacillus survival. In order to determine the antimicrobial activity of each host innate peptide down-regulated in case of HPV infection, the predominant *Lactobacillus* species constituting the vaginal microbiome (*L. crispatus, L. jensenii and L. iners*) as well as *Gardnerella vaginalis* were incubated with several concentrations of each peptide for 6 h. The bacterial suspensions were then plated on Columbia Blood agar plates for 24 or 48 h and the percentage of surviving colonies was finally quantified by computerized counts and verified by manual counting (Fig. 5a). Similar to data reported with commensal gut bacteria[39], the influence of each individual peptide was specific and varied according to each bacterial strain (Fig. 5b). Despite these observed variations, three main observations were made: (1) defensins (most notably HβD2-4 and HD-5) inhibit the growth of all tested bacteria, (2) all peptides (except HβD1) exhibit an antimicrobial activity on *Gardnerella vaginalis* and (3) unexpectedly, the constitutive and most expressed peptides by the cervical/vaginal squamous mucosa show a positive effect on *Lactobacillus* survival. Given that the redox potential may vary within the vaginal lumen and that this parameter has been previously shown to modify the activity of some defensins (especially HβD1) against a few bacterial species[39,40], the defense peptides were first incubated with DTT (2 mM) before reproducing our systematic analysis. The chemical peptide synthesis, the purity as well as the reduction of disulfide bridges following DTT addition were validated by MALDI mass spectrometry (Supplementary Fig. 10). As shown in Fig. 5c, the antimicrobial activity of β-defensins was globally unchanged in a reducing environment (with the exception of a slight increase in the antibacterial activity of HβD3 against *L. crispatus*) and the significant protective effect displayed by both elafin and S100A7 on *Lactobacilli* was still observed. Changing buffer (sodium to potassium phosphate buffer) or pH from 7.4 to 5.8 did not modify the positive effect of these latter peptides on *Lactobacillus* survival either (Fig. 5d–e).

Host defense peptides promoting Lactobacillus survival are cleaved, internalized and used as amino acid source. In order to determine whether the beneficial effect of innate peptides constitutively expressed by the vaginal/cervical mucosa appears

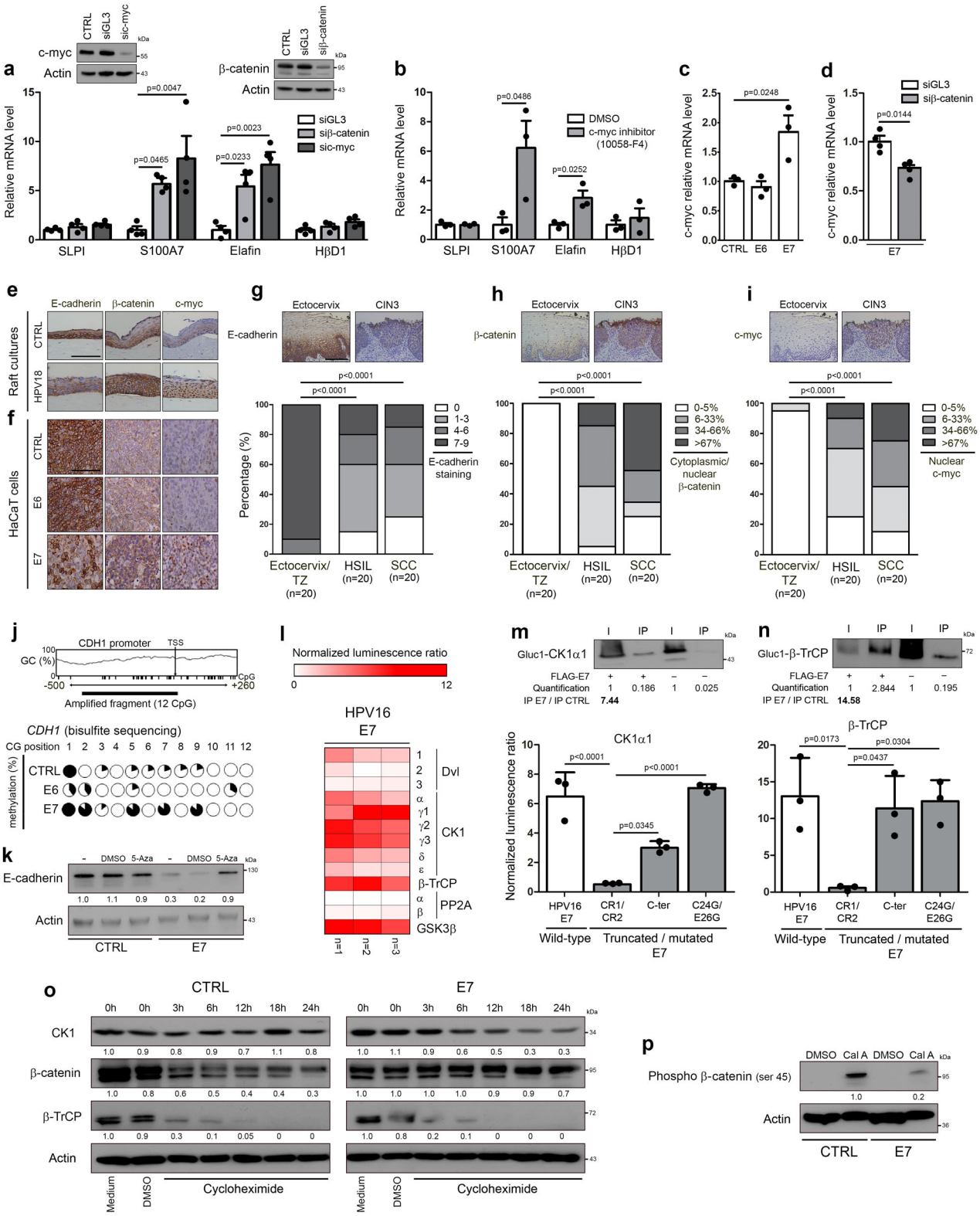

directly or needs some latency, elafin and S100A7 were added to lactic acid bacteria and several time points were investigated. Importantly, for all *Lactobacillus* species, a significant increased percentage of surviving colonies was only detected after 3 or 6 h of incubation (Fig. 6a). As commonly practiced for both eliminating variables and focusing on the compounds of interest, no nutrient (serum) was added during the incubation (starvation assay), explaining why the number of surviving colonies was decreasing over the time. By mass spectrometry, we then evaluated the ability of these dominant cervico-vaginal lactic acid bacteria to convert proteins/peptides present in their environment to smaller peptides and ultimately to free amino acids. Strikingly, almost all (>80%) of native elafin and S100A7 had disappeared after 6 h, indicating their proteolysis. (Fig. 6b and Supplementary Fig. 11). By flow cytometry, we also showed an internalization of fluorescent-labeled peptides (or more precisely

Fig. 4 E7 viral oncoprotein inhibits constitutive innate peptide expression (elafin and S100A7) through promoting β-catenin stabilization/signaling and subsequent c-myc expression. The reactivation of so called "constitutive" peptide (SLPI, S100A7, elafin and HβD1) expression was analyzed by RT-qPCR in HPV16 E6E7-positive cells transfected with siRNA targeting c-myc or β-catenin **a** or treated with 40 μM 10058-F4 **b**. Cells transfected with control siRNA (siGL3) or treated with DMSO were used as negative controls. Each experiment was normalized to the amount of HPRT mRNA from the same sample. Results represent the means ± SEM of three **b** or four **a** independent experiments. The level of c-myc mRNA was determined by RT-qPCR in control, HPV16 E6 and E7-transduced cells **c**. Results represent the means ± SEM of three independent experiments. The effect of knockdown of β-catenin on c-myc expression in HPV16 E7-positive cells was assessed by RT-qPCR **d**. Results represent the means ± SEM of four independent experiments. **e** Representative pictures of control and HPV18-positive organotypic raft culture sections stained for E-cadherin, β-catenin and c-myc. **f** Representative examples of anti-E-cadherin, β-catenin and c-myc immunoreactivities displayed by control, E6-positive and E7-positive keratinocytes. Anti-E-cadherin **g**, anti-β-catenin **h** and anti-c-myc immunostainings **i** in both HPV-negative specimens [ectocervix/transformation zone (TZ), $n = 20$] and HPV-positive (pre)neoplastic lesions (HSIL, $n = 20$; SCC, $n = 20$). Note the reduced expression of E-cadherin associated with cytoplasmic/nuclear β-catenin immunoreactivity observed in HPV-positive tissues. Regarding c-myc, its expression was almost exclusively detected in HPV-positive (pre)neoplastic lesions. **j** The methylation status of E-cadherin gene (*CDH1*) promoter in control, HPV16 E6 and E7-transduced cells was assessed by bisulfite genomic sequencing. The variation in GC content within *CDH1* promoter as well as the percentage of methylation of each individual CpG island contained in the PCR fragment analyzed by bisulfite sequencing are shown. **k** The reactivation of hypermethylated *CDH1* gene was determined by Western blot following 5-aza-deoxycytidine (5-Aza, 5 μM) treatment. **l** Binding of protein members of the β-catenin degradation complex with HPV16 E7 oncoprotein was assessed by *Gaussia princeps* luciferase complementation assay (GPCA). Heatmap representing the score (normalized luminescence ratio) of each analyzed protein for potential interaction with HPV E7 is shown. Three independent experiments were performed. The interactions between HPV16 E7 oncoprotein and CK1α1 **m** or β-TrCP **n** were validated by both Co-IP and GPCA using the truncated/mutated forms of E7. Results represent the means ± SEM of three independent experiments. **o** CK1, β-catenin and β-TrCP stability in both control and HPV16 E7-transduced cells following treatment with cycloheximide (100 μM). **p** CK1-dependent phosphorylation of β-catenin (ser45) in both control and E7-positive cells following treatment with calyculin A (50 nM). The scale bar represents 100 μm. *P* values were determined using one-way ANOVA followed by Dunnett's multiple comparison post-hoc test **a**, **c**, two-sided unpaired *t*-tests **b**, **d**, χ^2 test **g**, **h**, **i** and one-way ANOVA followed by Bonferroni post-hoc test **m**, **n**. The Western blot and co-IP analyses were independently performed three times and twice, respectively. One representative experiment is shown. Source data are provided as a Source Data file.

their hydrolyzed products) within the cytoplasm of bacteria as soon as 1h30 following peptide additions (Fig. 6c). Using synthetized elafin fragments containing $^{13}C_6{}^{15}N_2$-labeled lysines, we analyzed whether these latter were found in the amino acid sequence of some bacterial proteins. In total, 20,100 peptides (*L. crispatus*: 8,221; *L. jensenii*: 10,855; *L. iners*: 1,024 peptides), corresponding to 2,088 proteins (*L. crispatus*: 816; *L. jensenii*: 1,016; *L. iners*: 256 proteins), were identified by mass spectrometry. Importantly, 52 bacterial peptides that had incorporated $^{13}C_6{}^{15}N_2$-labeled lysines (from exogenous elafin) were detected (Supplementary Data 1). As shown in Fig. 6e, STRING analysis of positive proteins for $^{13}C_6{}^{15}N_2$-labeled lysines highlighted enrichments among several pathways (most notably ribonucleoprotein and protein biosynthesis as well as energy metabolism). Although the statistical significance was not reached in all conditions, an increase of ATP production was finally reported in bacteria cultured with elafin or S100A7 (Fig. 6d), indicating even more a metabolization of innate peptides into amino acids which are essential for bacterial survival/growth.

The development of cervical/vaginal HPV-associated neoplasia in the K14-HPV16 transgenic mouse model is associated with both reduced innate peptide expression and vaginal dysbiosis. In order to validate in vivo the physiological relevance of our in vitro data (and to further confirm our retrospective clinical results in patients who underwent routine cytology/HPV testing), squamous carcinogenesis within the lower genital tract of K14-HPV16 transgenic mice was first induced by chronic estrogen treatment. A similar procedure (use of a subcutaneous 17β-estradiol implant) was done with control (FVB/n) mice. After 12 weeks of treatment, 11 out of 12 (91.7%) K14-HPV16 mice displayed histological evidence of intraepithelial neoplasia (5 LSIL and 6 HSIL), in keeping with both the increased proliferative index and the thickening of the squamous epithelium lining the external part of the cervix, vagina and vulva (Fig. 7a). A cervical/vaginal hyperplasia was detected in the latest transgenic mouse (1/12, 8.3%). No sign of preneoplastic lesion was observed in the control group. The squamous mucosa was microdissected and the mRNA level of mouse orthologs of human defensin(-like) peptides was determined. Of note, there is no mouse ortholog for the human *PI3/elafin* and *DEFB4* genes. As shown in Fig. 7b and, similarly to our results collected with human tissue specimens (Fig. 2b, c), all (excepted mβD4) antimicrobial peptides were significantly down-regulated in HPV16-expressing epithelia compared to their normal (uninfected) counterparts. Mouse βD12 was undetectable in all HPV-positive as well as in 7 out of 10 control samples. In parallel to these transcriptional analyses, cervico-vaginal lavage samples were collected in both K14-HPV16 and control mice at week 0 and after 12 weeks of estrogen treatment. In order to avoid bias related to reproductive cycling status of mice, vaginal microbiota was always taken during estrous. Following DNA extraction, V5-V6 hypervariable regions of the 16S rRNA gene were amplified by standard PCR and sequencing was performed (Illumina MiSeq). From 5,266,888 raw sequencing reads, 4,782,589 reads were retained after data cleaning and chimera removal, with a mean read length of 281 nucleotides. In total, 4,619 operational taxonomic units (OTUs) were obtained when a clustering distance of 0.03 was used. The ecological indices (intrinsic diversity, richness and evenness) of microbial populations detected in the lavage samples were first assessed at both the genus and species levels (Fig. 7c and Supplementary Fig. 12) and no significant difference was detected between the four defined groups [FVB / n (week 0 *versus* week 12) and K14-HPV16 (week 0 *versus* week 12)]. It is interesting to notice that the composition of murine vaginal microbiota was not altered by long-term estrogen treatment (Supplementary Figure 13). Strikingly, when data reported in K14-HPV16 mice were separated depending on the grade of (pre)neoplastic lesions observed within the lower genital tract, a significant increase in bacterial richness was detected in mice displaying a high-grade precancer (HSIL). Concurrently, both the bacterial α-diversity and evenness were reduced (Fig. 7d and Supplementary Fig. 12), meaning that, despite a higher global number of genera/species, the distribution of these latter (relative abundance) in vaginal lumen is less uniform in mice with histologically-proven HSIL compared to their control (week 0) counterparts or those diagnosed with hyperplasia/LSIL. As revealed by AMOVA-based

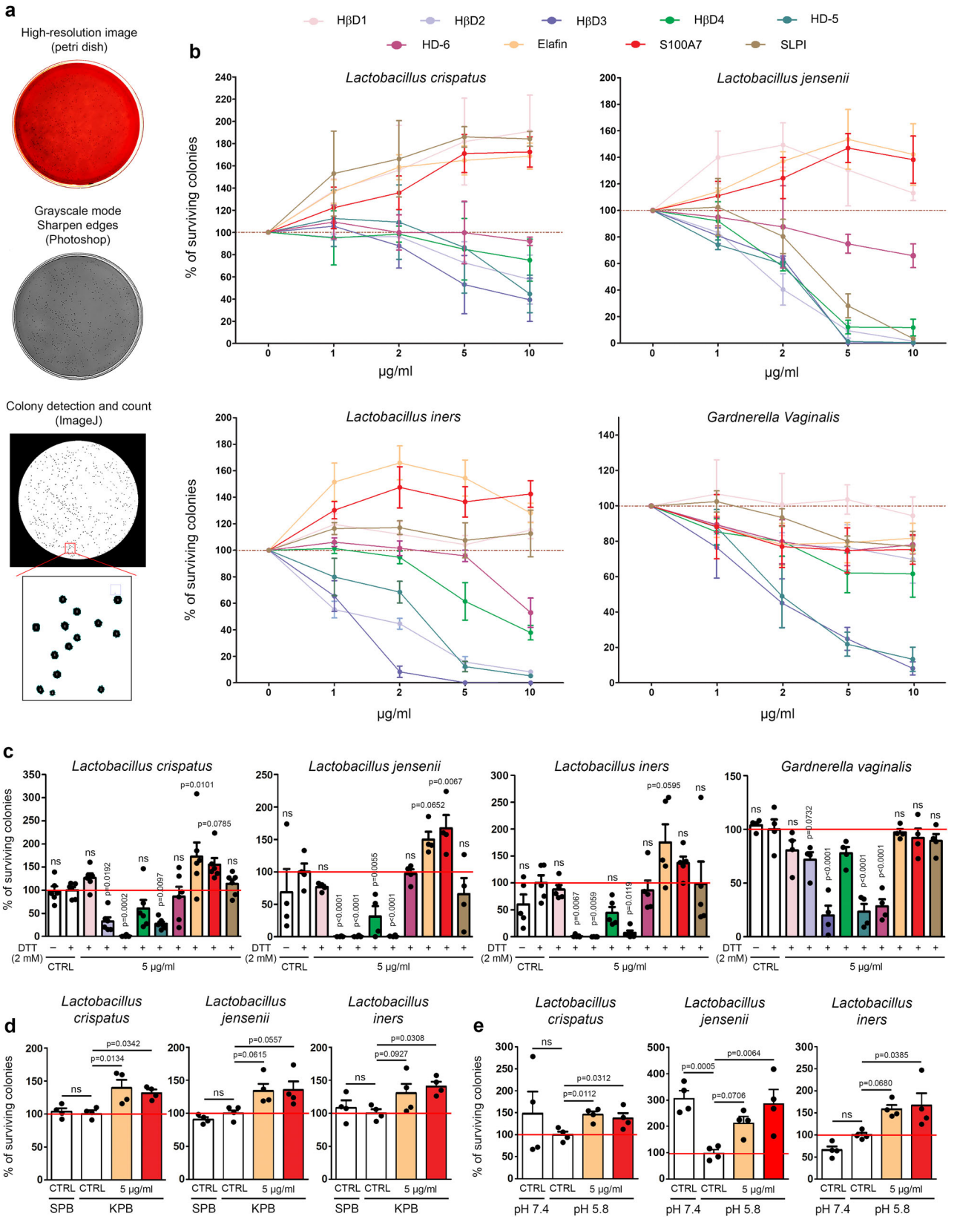

group clustering and clearly illustrated by the β-diversity plot (Fig. 7e), the microbial profiles detected in HSIL-positive K14-HPV16 mice were significantly distinct to those from hyperplasia/LSIL-positive ($p = 0.002$) or control mice ($p = 0.0005$). In addition, the homogeneity in the cervico-vaginal microflora tended to be different in mice diagnosed with a precancerous lesion compared to the control group, as indicated by HOMOVA testing (HSIL *versus* control, $p = 0.09$; hyperplasia/LSIL *versus* control, $p = 0.08$). The distribution of the twelve main bacterial orders and their relative abundance in the four groups of mice are shown in Fig. 7f. Accounting for over 90% of the total microbial community in the vast majority of samples (44/48, 91.7%), the

Fig. 5 Innate peptides abundantly and constitutively secreted by the squamous mucosa lining the lower gynecologic tract exhibit a positive effect on *Lactobacillus* survival. a Schematic illustration of the different steps involved in bacterial colony detection and count. **b** Systematic analysis of both defensin and "defensin-like" peptide activity on predominant bacterial species detected in normal (*L. crispatus, L. jensenii and L. iners*) and pathological (BV) (*G. vaginalis*) conditions. Results represent the means ± SEM of three (*L. crispatus, L. jensenii and L. iners*) or five (*G. vaginalis*) independent experiments. **c** Effect of reducing environment on antimicrobial/protective activity of tested innate peptides. Results represent the means ± SEM of four (*L. jensenii and G. vaginalis*), five (*L. iners*) or six (*L. crispatus*) independent experiments. The positive effect on *Lactobacillus* survival displayed by the most abundant innate peptides secreted by cervical/vaginal mucosa (elafin and S100A7) was also assessed in both potassium phosphate buffer (KPB) (**d**) and acidic (pH 5.8) conditions (**e**). For each experiment, peptides were incubated with bacteria for 6 h. Results represent the means ± SEM of four independent experiments. *P* values were determined using one-way ANOVA followed by Dunnett's multiple comparison post-hoc test (**c**, **e**). ns: not significant ($p > 0.1$). Source data are provided as a Source Data file.

bacteria belonging to the order of Lactobacillales or Pasteurellales were clearly predominant in the cervix/vagina of our mouse models, regardless of the HPV status. Whereas no statistical difference was observed in the FVB/n (HPV-negative) group, interestingly, (pre)cancer development in the K14-HPV16 transgenic mice was associated with a significant increase in the abundance of genera (especially *Rodentibacter_ge*) from the *Pasteurellaceae* family (Fig. 7g). When paired lavage samples were compared (week 0 *versus* week 12), a marked augmentation was detected in all animals (6/6, 100%) displaying a HSIL. In the opposite, the relative abundance of genera (especially *Lactobacillus_ge* and *Streptococcus_ge*) from the Lactobacillales order has been shown to drastically decrease in HPV16-expressing mice with a high-grade/extended (pre)neoplastic lesion (Fig. 7h).

Discussion

The development of HPV-related (pre)neoplastic lesions within the lower genital tract and BV are two common conditions among women of reproductive age. With a risk increasing with the multiplicity of sexual partners, both disorders have incidence rates peaking among women aged between 25 and 50 and then dropping gradually. In the last 20 years, many studies have been focused on both high-risk HPV genotypes and BV and, most of the time, an epidemiological link, characterized by higher rates of HPV infection (and persistence) among patients with BV, was reported[25,26,28]. In the opposite, and although suggested in a few recent publications[41–43], it remains unclear whether or not HPV can exert a critical influence on vaginal microbiome. To address this essential issue, a large retrospective follow-up study was conducted. Although a few sources of potential imprecision exist (e.g., the lack of data about the socioeconomic status of patients) that could slightly impact the collected results, remarkably, a bi-directional association was clearly reported. Indeed, each individual pathological disorder was more frequently diagnosed when the other one was preceding in time. Similarly to previous longitudinal measurements[25], an overall odds ratio of 1.83 (95% CI: 1.41–2.37, $p < 0.0001$) was obtained for HPV infection among BV-positive women. As for BV development, a 2.35-fold increased risk (95% CI: 1.48–3.72, $p < 0.0007$) was observed in case of prior HPV infection. Of interest, whatever their HPV status, BV women were typically treated with antibiotics (metronidazole or clindamycin) and the follow-up of HPV-positive patients did not differ by BV status. Taken together, this supports that these findings cannot be explained by differences in management between defined groups. Actually, these results are consistent with recent 16S rRNA sequencing studies that reported both higher vaginal microbial diversity and reduced relative abundance of *Lactobacillus* species in HPV-positive women compared to uninfected individuals[44–46]. Furthermore, the levels of both *L. crispatus* and *L. jensenii* have been shown to progressively decrease with preneoplastic disease severity, irrespective of the detected HPV genotypes[46]. Although the collected data are highly significant, an odds ratio of 2.35 with a cohort including over 6,000 patients may seem quite modest. It is, however, important to mention that not all HPV infections can substantially alter the vaginal microbiome. Indeed, a substantial proportion of HPV infections (even those implicating high-risk genotypes) are asymptomatic and/or spontaneously regressive within a few months. It is reasonable to think that these latter only modestly influence the vaginal ecosystem and, consequently, reduce the acquired odds ratio. In agreement, in our in vivo model, an imbalance in the vaginal flora was only detected in HPV16-expressing mice that had developed high-grade intraepithelial neoplasia. In addition to an increased risk of occurrence, strikingly, a significant effect on disease persistence was also clearly detected. Of note, the consensus guidelines recommend repeated cytology/HPV testing every 6 months for HPV-positive women while intervals of 3 years are usually acceptable in case of HPV negativity[47]. This difference likely explains why the positive impact of HPV infection on BV persistence was only detected after a 2.5-year period and then increased over the time (bias of follow-up frequency between patient groups). Therefore, besides the higher risk of HPV infection, viral persistence and related carcinogenesis following BV development, persistent/symptomatic HPV infection may also induce changes within the vaginal lumen that would ultimately disrupt the microbial balance. Despite bacterial diversity differences between humans and mice (more particularly, in normal condition, human vaginal microbiome is largely dominated by *Lactobacillus* species whereas, in rodents, higher abundances of *Proteobacteria* and *Actinobacteria* are encountered), the dysbiosis of vaginal microbiome detected following HPV-related carcinogenesis in the K14-HPV16 transgenic mouse model further supports the retrospective clinical data and, overall, this novel paradigm.

Using a large number of tissue specimens as well as several in vitro 2D/3D models, we here showed that HPV leads to a drastic reduction of innate peptide expression, mostly resulting of the interaction of E7 oncoprotein with several key members of both NF-κB and Wnt/β-catenin signaling cascades. Indeed, with the exception of HβD3 which has been recently shown to have a dual regulation by NF-κB and p53[48], all constitutive or inducible defense peptides normally secreted by the squamous epithelium lining both the vagina and the outer part of the uterine cervix were down-regulated in case of HPV positivity. In contrast to all the other peptides, we reported that SLPI and HβD1 were affected neither by NF-κB nor by the Wnt/β-catenin pathway. Targets of interferon regulatory factors (IRF) (IRF-1 and IRF-7)[49], their impaired expression detected in HPV-positive cells is very likely related to the well-characterized (direct or via TLR9 suppression) abrogation of these latter proteins by HPV oncoproteins[50,51]. Overall, we can reasonably speculate that the virus impairs the production of epithelial-specific members of the defensin and "defensin-like" families as early as the first steps of infection/(pre) cancer development as part of a broad effort to suppress the inflammatory response. As recently highlighted[52,53], the host defense peptides display properties which extend well beyond

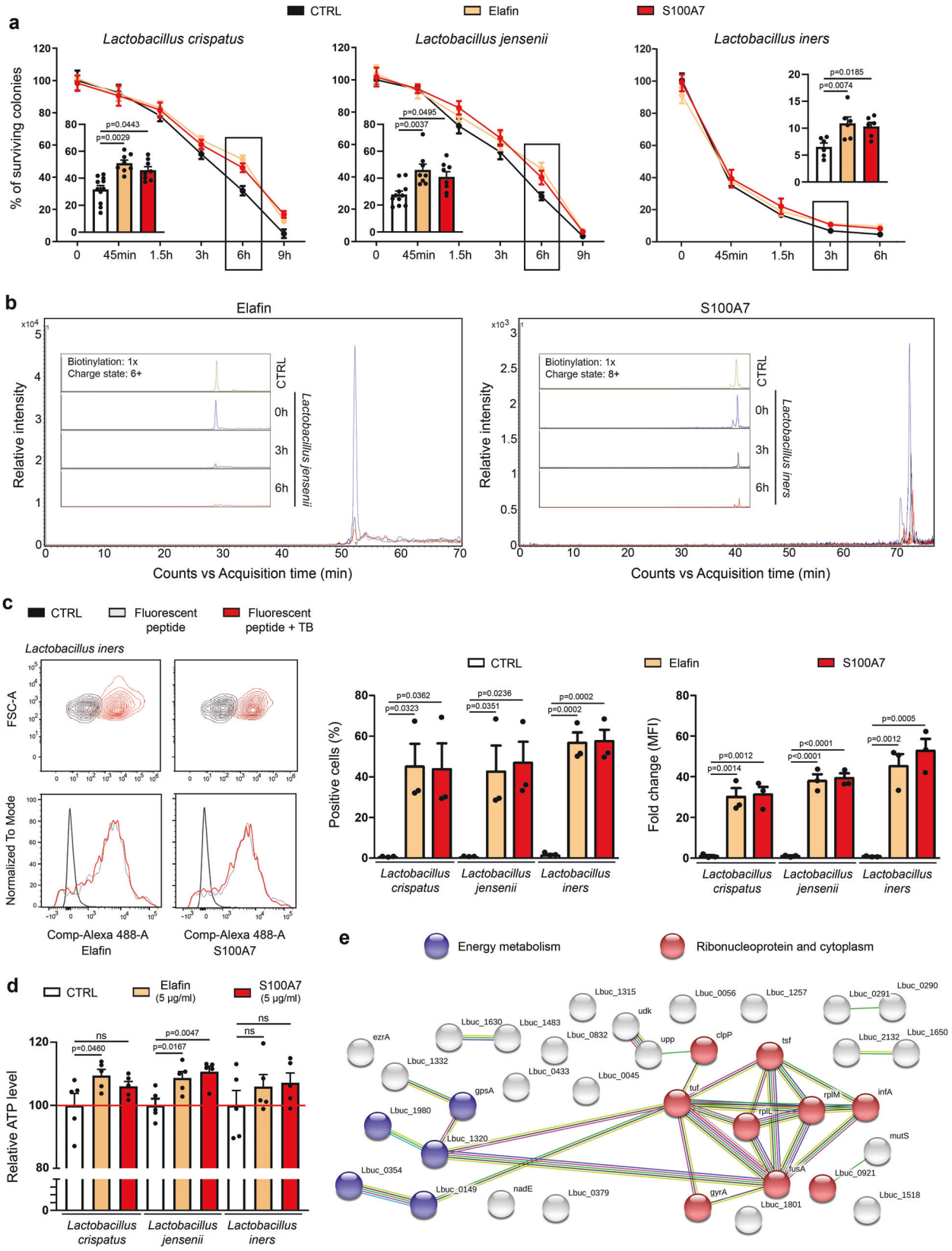

their antimicrobial activity. For example, defensin(-like) peptides (e.g., HβD2, HD-5, and S100A7) have a well-documented chemotactic capacity for lymphocytes, monocytes and dendritic cells and their reduced secretion would greatly help the virus to escape the host immunity[54–56]. Further promoting a tolerogenic environment, the lack of HβDs would also disrupt the activation and maturation of antigen-presenting cells[57]. Moreover, some defensins (most notably HD-5) have been demonstrated to block HPV infection via various mechanisms[58,59]. Therefore, the low HD-5 expression detected in infected epithelial cells could be particularly beneficial for the virus during the productive replication stage. Last but not least, this global decrease in innate peptide

Fig. 6 Host defense peptides are metabolized and used as amino acid source by *Lactobacillus* species. a Elafin and S100A7 were incubated with *Lactobacillus* species for 45 min to 9 h in the absence of nutrients (starvation assay) and the percentage of surviving colonies was determined. Results (each time point) represent the means ± SEM of six (*L. iners*: CTRL, elafin and S100A7), eight (*L. crispatus/L. jensenii*: elafin and S100A7) or eleven (*L. crispatus/L. jensenii*: CTRL) independent experiments. **b** The hydrolysis of host defense peptides (elafin and S100A7) by the dominant *Lactobacillus* species constituting the vaginal microbiome was evaluated at different time points (0 h, 3 h and 6 h) by mass spectrometry. Note the disappearance of native proteins after 3 to 6 h. **c** The internalization of fluorescent-labeled peptides within the cytoplasm of bacteria was then assessed by flow cytometry. Both the percentage of positive cells and mean fluorescence intensity (MFI) are shown. Results represent the means ± SEM of three independent experiments. **d** ATP production after 6 h of incubation between peptides and bacteria. Results represent the means ± SEM of five independent experiments. **e** STRING analysis of the bacterial proteins that have incorporated $^{13}C_6{}^{15}N_2$-labeled lysines (from exogenous elafin). All proteins identified by mass spectrometry in *L. crispatus, L. jensenii* or *L. iners* were pooled. *P* values were determined using two-way ANOVA followed by Bonferroni post-hoc test **a** and one-way ANOVA followed by Dunnett's multiple comparison post-hoc test **c**, **d**. ns: not significant ($p > 0.1$). Source data are provided as a Source Data file.

expression was not only detected in HPV-infected cells but also in the morphologically normal squamous epithelium adjacent to HPV-positive (pre)neoplastic lesions. The concomitant down-regulation of pro-inflammatory cytokines (e.g., TNFα, IL-1β) resulting from both NF-κB and Wnt/β-catenin signaling impairment is very likely to explain the extension of this immunosuppressive effect in the lesional (micro)environment (absence of paracrine stimulation).

We originally postulated that the altered antimicrobial peptide secretion profile of the host mucosa following HPV infection could differently impact *Lactobacillus* and anaerobic bacteria species constituting the vaginal microbiome. However, we were far to expect that defense peptides such as elafin and S100A7, which are very highly expressed by vaginal/cervical keratinocytes, do not display any antimicrobial activities on lactic acid bacteria but, rather, can be cleaved, internalized and used by these latter as amino acid source sustaining their survival. Changing the redox state of peptides, environment (buffer) or pH did not impact this positive effect on *Lactobacilli*. The citation "what doesn't kill you, makes you stronger" seems particularly adapted in the present context. Essential to compensate their inability to synthesize amino acids (auxotrophy), the interest for the hydrolytic capacities of *Lactobacilli* has largely risen during the last few years. Originally characterized on *L. casei*, *L. helveticus* and *L. delbrueckii* which are involved in the manufacture of cheeses, yogurts and fermented milks, the proteolytic system of *Lactobacillus* species not only supplies amino acids to the bacteria, but also produces bioactive peptides with health-protective effects[60]. As demonstrated by mass spectrometry, the dominant cervico-vaginal lactic acid bacteria have also developed the capability to hydrolyze proteins into free amino acids which are required for their growth. Interestingly, several studies reported important variations in caseinolytic properties between different *L. helveticus* strains used in food science and nutrition[61]. Whether disparities in protein hydrolysis patterns could explain the differential protective abilities displayed by cervico-vaginal *Lactobacillus* species (e.g., *L. crispatus versus L. iners*) or whether some cleaved products have beneficial properties for the host is still unknown but merits further investigations.

With the aim of persisting, replicating and escaping the immunity, oncogenic viruses developed multiple strategies for subverting host signaling cascades. Among these latter, both NF-κB and Wnt/β-catenin signaling pathways play critical roles in proliferation/apoptosis, inflammation and differentiation and are, therefore, considered as preferential targets for viral oncoproteins. To the best of our knowledge, this study provides the first evidence of interactions between HPV E7 oncoprotein and NEMO, CK1 and β-TrCP. Collectively, the results obtained by GPCA support that these three host proteins very likely interact directly to the C-terminal region of the viral oncoprotein. Interestingly, NEMO, CK1 and β-TrCP not only interacted with E7 from high-risk alpha HPVs (HPV16, 18, 33 and 39), but also with E7 from beta HPV genotypes (HPV8, 38 and 49) which have recently emerged as "facilitators" in UV-related cutaneous SCC development[62]. Altogether, our findings indicate the importance of these newly discovered targets for viral persistence/carcinogenesis and add to other mechanisms (e.g., impairment of p65 acetylation[63]) used by HPV for hijacking both NF-κB and canonical Wnt pathways. Essential to direct IKKβ activity towards IκBα[64], it is interesting to note that small T antigen of Merkel cell polyomavirus has also been shown to target the NEMO adaptor protein to inhibit NF-κB-dependent inflammatory/antiviral responses[65]. In agreement with previous studies reporting alterations of host DNA methylome in HPV E7 and hepatitis B virus (HBV) X protein-positive cells[66,67], altered E-cadherin expression (related to *CDH1* promoter hypermethylation) was observed both in vitro and in situ. Regarding the β-catenin degradation complex, we demonstrated that E7 interacts with CK1, inducing its degradation. As a result, both reduced phosphorylation (ser45) and stabilization of β-catenin were observed with, ultimately, the up-regulation of its targeted genes (e.g., c-myc). Finally, the interaction between the ubiquitin E3 ligase β-TrCP and HPV E7 oncoprotein could not only increase β-catenin half-life but also participate in NF-κB inhibition due to the fact that this latter protein is involved in ubiquitination and degradation of both β-catenin and IκBα[68,69]. Interestingly, the sequence of HPV E7 does not contain a putative $DSG(X)_{2+n}S$ motif (a common characteristic of protein targets for β-TrCP)[70], supporting that the viral oncoprotein is actually not a substrate for β-TrCP but, in the opposite, E7 binds to this host protein, impeding its activity.

Taken together, our findings indicate that HPV inhibits basal and pro-inflammatory-induced host defense peptide expression through subverting NF-κB and Wnt/β-catenin signaling cascades. As a consequence/side effect of HPV immune evasion, the amino acid source sustaining the survival of *Lactobacillus* species is greatly reduced, promoting an imbalance in the vaginal flora (Fig. 8). The oxidative stress resulting from BV establishment/persistence would then promote the progression of HPV-related (pre)neoplastic lesions supporting that the association between HPV and BV is complex and bi-directional.

Methods

All experiments performed in this study adhere to all relevant ethical regulations.

Retrospective cohort analysis. All women who underwent at least 2 routine cervical Pap smear during the period 2010–2018 at the University Hospital of Liege (Belgium) or at its associated regional hospitals [Citadelle Regional Hospital (Liege, Belgium), ND Bruyeres (Chenee, Belgium), Regional Hospital of Huy (Huy, Belgium), Bois de l'abbaye Hospital (Seraing, Belgium)] were eligible for the present retrospective research which aimed at analyzing the temporal relationship between BV and genital HPV infections. All samples were daily centralized at University Hospital of Liege where both HPV testing and microscopic examinations were performed. The exclusion criteria were as follows: patients younger than 21 years of age; absence of HPV testing in case of abnormal cytological findings (e.g., ASC-US, ASC-H); lack of data related to vaginal bacterial flora; immunosuppressive

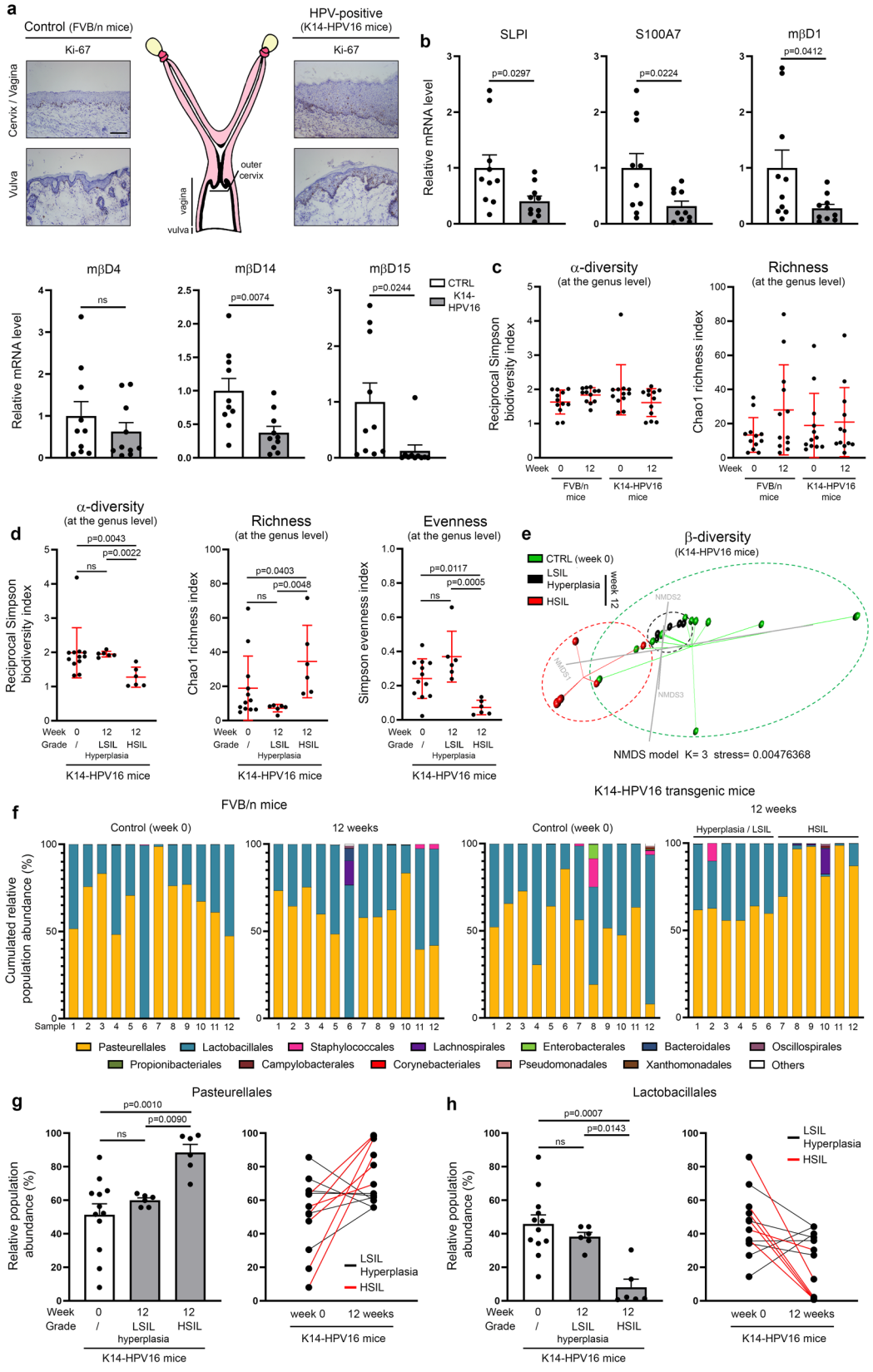

conditions. In total, six thousand one hundred seventeen women [mean age: 48 ± 13 years (range, 21–84)] were selected. Thirty-two patients (32/6,117, 0.52%) were excluded for missing data (incomplete viral-cytological information) during the follow-up period. Mean number of visits was 3 (range, 2–13). All Pap smear samples were analyzed by experienced cytopathologists according to the Bethesda system for reporting cervical cytology. HPV testing from residual liquid-based cytology specimens was performed using the Abbott RealTime High-Risk HPV assay (Abbott, Wiesbaden, Germany) which enables simultaneous detection of all WHO/IARC-classified carcinogenic (high-risk) HPV types (HPV16, 18, 31, 33, 35, 39, 45, 51, 52, 56, 58, 59, 66, and 68). The vaginal bacterial flora was systematically assessed for all patients during the entire study period and BV was diagnosed using the Hay/Ison grading system, a simpler version of Nugent's score displaying the same high performance for BV diagnosis[71,72]. First described in 2002[71], this method evaluates a shift from a vaginal flora rich in *Lactobacilli* to a polymicrobial

Fig. 7 Estrogen-induced cervical/vaginal carcinogenesis in transgenic mice expressing HPV16 induces an imbalance in the vaginal microflora. a Schematic representation of the mouse reproductive tract. The morphology of the squamous epithelium lining the cervix/vagina and vulva in K14-HPV16 and control (FVB/n) mice is shown. Both the increased percentage of proliferative (Ki-67-positive) cells and the thickening of the epithelium in case of HPV16 oncogene expression should be noticed. **b** mRNA level of SLPI, S100A7, mouse orthologs of HβD1-3 (mβD1, mβD4, mβD14) and HD-5/6 (mβD12, mβD15) was measured by RT-qPCR. Microdissected frozen squamous epithelia from FVB/n and K14-HPV16 mice were analyzed. Each experiment was normalized to the amount of both HPRT and GAPDH mRNAs from the same sample. Results represent the means ± SEM of ten independent experiments. **c** Bacterial intrinsic diversity (reciprocal Simpson biodiversity index) and richness (deduced from Chao1 index). The reported values (at the genus level) for each individual mouse in the four defined groups [FVB/n (week 0 *versus* week 12) and K14-HPV16 (week 0 *versus* week 12)] are shown (n = 12 per group). The means ± SD are represented. **d** Bacterial α-diversity, genus richness and evenness (Simpson index) for K14-HPV16 mice. Data were separated depending on 17β-estradiol treatment duration [week 0 ($n = 12$) *versus* week 12 ($n = 12$)] and preneoplastic lesion grade [hyperplasia/LSIL (n = 6) *versus* HSIL ($n = 6$)]. The means ± SD are represented. **e** β-diversity of the vaginal microbial profile in K14-HPV16 mice was visualized using a Bray-Curtis dissimilarity matrix-based non-parametric dimensional scaling (NMDS) model (three dimensions). **f** Stacked bar charts depicting the relative abundance of the twelve main bacterial orders detected in control (FVB/n) and K14-HPV16 mice by 16 S V5-V6 amplicon sequencing. Relative abundance of bacteria belonging to the order of Pasteurellales **g** and Lactobacillales **h** in K14-HPV16 mice depending on 17β-estradiol treatment duration [week 0 ($n = 12$) *versus* week 12 ($n = 12$)] and HPV-related lesion grade [hyperplasia/LSIL ($n = 6$) *versus* HSIL ($n = 6$)]. The means ± SEM are represented. The comparison of relative abundance of bacteria in paired (week 0 *versus* week 12) lavage samples is also shown. The scale bar represents 100 µm. *P* values were determined using two-sided unpaired t-tests **b** and non-parametric Kruskal-Wallis test corrected with a two-stage linear step-up procedure of Benjamini, Krieger and Yekutieli **c**, **d**, **g**, **h**. ns: not significant ($p > 0.1$). Source data are provided as a Source Data file.

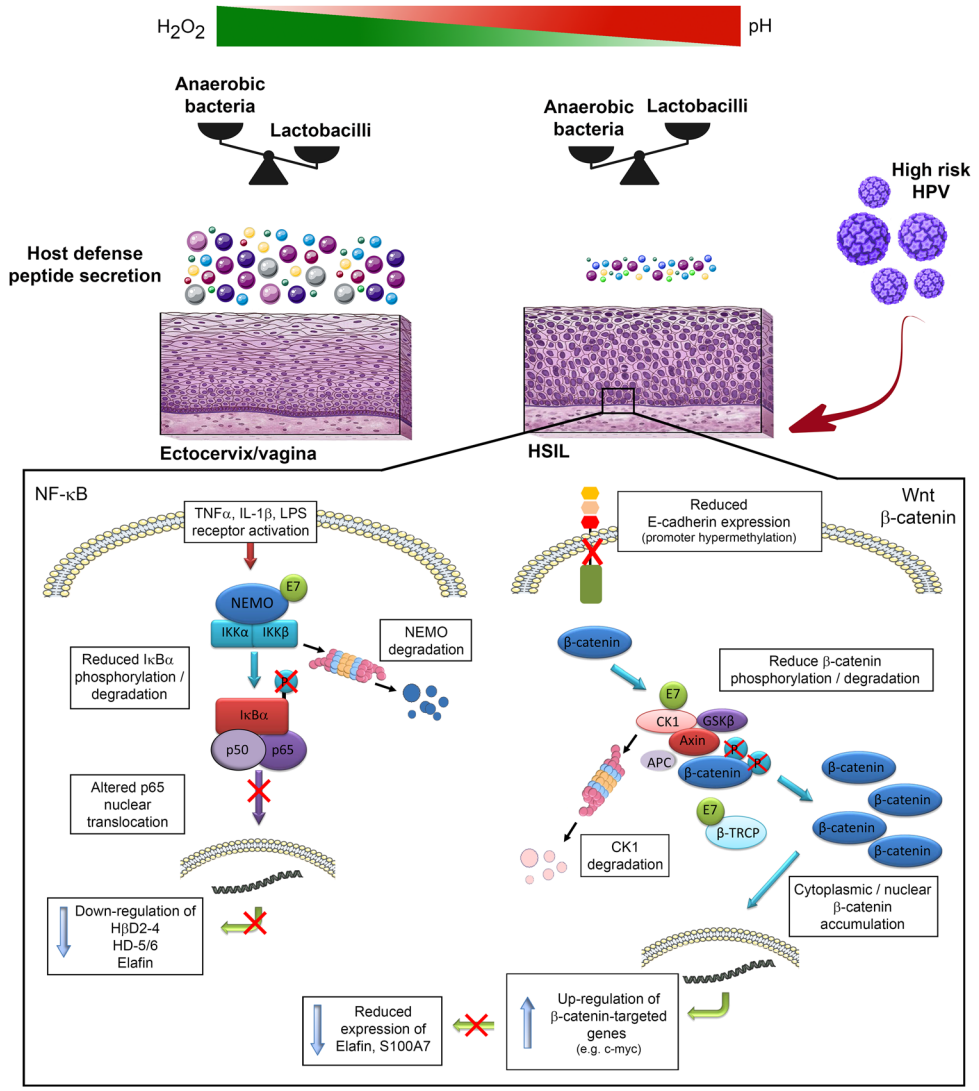

Fig. 8 Schematic representation of the proposed model. Left In HPV-positive cells, E7 oncoprotein impairs pro-inflammatory-induced innate peptide expression through inducing NEMO degradation and subsequent p65 cytoplasmic sequestration. Right In parallel, E7 reduces E-cadherin expression and alters β-catenin degradation complex by interacting with both CK1 and β-TrCP. As a result, defense peptides (e.g., elafin and S100A7) which are used by *Lactobacillus* species as amino acid source are greatly down-regulated by the β-catenin target gene c-myc. An imbalance in the vaginal flora is, therefore, achieved as a consequence of HPV persistence and subsequent immune evasion.

(anaerobic) microbiome and divides smears into three categories: Grade I (normal, *lactobacillus spp*. morphotype only), Grade II (intermediate, reduced *lactobacillus spp*. morphotype and equal amount of mixed bacterial morphotypes) and Grade III (BV, mixed bacterial morphotypes with few or absent *lactobacillus spp*. morphotype). Considering the previous studies reporting that most (>90%) smears assessed as Grade II are actually classified as normal when Nugent's or Amsel's criteria are used as well as the very high specificity (>95%) of clue cells for BV diagnosis[71–74], Grade II patients without clue cells were, therefore, routinely classified as normal whereas their counterparts exhibiting clue cells were considered as BV-positive (similarly to Grade III patients). Overall, the STROBE (STrengthening the Reporting of OBservational studies in Epidemiology) guidelines has been followed as accurately as possible. The data collection from personal health records was approved by the Ethics Committee of the University Hospital of Liege (#2021-117).

Human tissue samples, classification and laser capture microdissection. A total of 44 frozen and 127 paraffin-embedded cervical/vulvar specimens were retrieved from the Tissue Biobank of the University Hospital Center of Liege (Belgium). All patients underwent a surgical procedure between 2011 and 2015. An informed consent was obtained from all participants and the protocol was approved by the local ethics committee. These tissue samples included 31 normal squamous tissues (ectocervix/TZ), 65 dysplastic lesions (30 LSIL and 35 HSIL) and 75 primary invasive squamous cell carcinomas (SCC) (33 cervical and 42 vulvar cancers). The original diagnoses were re-examined by senior histopathologists and, to avoid misclassification, both the proliferative index (nuclear Ki67 staining) and $p16^{INK4a}$ expression of each specimen were determined by immunohistochemistry. In order to perform our transcriptional analyses on "pure" populations of epithelial cells (and to avoid any contamination with stromal structures), several serial sections (6 µm thick) of each frozen cervical specimen were microdissected using a Leica LMD7000 system (Leica, Wetzlar, Germany) (GIGA in vitro Imaging platform, University of Liege). To obtain sufficient RNA concentrations, microdissected squamous cell populations from different slides but from the same tissue sample were pooled.

Transgenic mouse model and hormone treatment. FVB/n mice expressing HPV16 under the control of the keratin 14 promoter (K14-HPV16 transgenic mice) were obtained from the National Cancer Institute Mouse Repository. Given that (pre)cancer development within the lower genital tract has been previously shown to be hormone-dependent in this model[75,76], 6 to 8-week-old female mice ($n = 12$ per condition) were subcutaneously implanted with a Belma's E2 implant (E2-M/90, Belma Technologies, Liege, Belgium), allowing reproducible long-term release of 17β-estradiol (1–2 µg/24 h) for 90 days[77]. A similar procedure was performed with control (FVB/n) mice. Mice were euthanized after 12 weeks of treatment and reproductive tracts were retrieved, embedded in Tissue-Tek® OCT compound (Sakura Finetek, Torrance, CA, USA) prior to cryosectioning and subsequent transcriptional and immunohistochemical evaluations. The protocol was approved by the Institutional Ethics Committee of the University of Liege (#2019-60).

Sample collection/preparation, estrous determination, 16S-based metagenomics and sequence analysis. Mice were randomly distributed in cages and housed under standard conditions [12 h light/12 h dark cycle, ad libitum access to food and water, constant temperature (19–21 °C) and humidity (40–50%)] in the GIGA-Mouse facility platform (University of Liege) during the entire course of the study. The gynecological tract of both control (FVB/n) and K14-HPV16 transgenic mice was colonized naturally (mother's impact at birth and the environment). Vaginal microbiome was not influenced by the investigators. In order to avoid environmental contaminations by soil bacteria, a sterilized recycled paper litter was preferred to the wood pellets. Before collecting vaginal microbiota (2 ×50 µl PBS lavage samples collected in sequence using gel-loading pipette tips and pooled), the perineal region of each individual mouse was carefully cleaned with an alcohol swab. The previous steps were performed with sterile materials in a laminar flow hood. Seven µl from each samples were spread on a glass slide, fixed/stained using Diff-Quick reagents (Medion Diagnostics, Düdingen, Switzerland) and the estrous cycle stage was determined using established criteria[78].

DNA was isolated from cervico-vaginal lavage samples using NucleoSpin Tissue kit (Macherey Nagel, Düren, Germany). Amplicon library preparation and sequencing were then performed in the GIGA-Genomics platform (University of Liege) according to the Illumina metagenomics workflow (https://support.illumina.com). Primers targeting the V5-V6 hypervariable regions of the 16S rRNA gene were used for standard PCR amplification. The primer sequences are listed in Supplementary Table 1. Of note, 7 random nucleotides were added to the 5′ region of forward primer to increase complexity and, therefore, improve sequence read quality. The Quant-iT PicoGreen dsDNA Kit (Invitrogen) and the KAPA Library Quantification Kit for Illumina platforms (KapaBiosystems, Wilmington, MA, USA) were used to normalize the DNA libraries and to determine the pooled library concentration, respectively. Pair-end sequencing (2×300 cycles) was done on the Illumina MiSeq platform. As previously described[79,80], both the alignment and taxonomical assignment (from phylum to species) of post-sequencing data were performed using the MOTHUR software package (v141.1), based on the SILVA database (v1.38) of full-length 16S rDNA sequences. Potentially chimeric sequences were detected using the VSEARCH algorithm. For each sample, a subsampling dataset containing 10,000 representative cleaned reads was retained and used to generate OTUs (cut off: 0.03) as well as to evaluate several ecological indicators. The validity of the process was confirmed by a Good's coverage at the genus level of at least 99.8% in all samples and no statistical difference between the defined groups. The bacterial α-diversity and richness of the samples were deduced from the inverse Simpson index and Chao1 index, respectively. The Simpson-derived evenness was also determined. Measuring the diversity between different communities, the β-diversity was estimated using a Bray-Curtis dissimilarity matrix.

Cell culture and stable clones. Immortalized human keratinocytes (HaCaT cells) cells expressing HPV16 E6 and/or E7 or green fluorescent protein (control cells) were generated by using lentiviral vectors (GIGA-Viral Vectors, University of Liege). Briefly, HPV16 E6 and E7 coding sequences were synthetized and cloned into the pLV-EF1a-IRES Luciferase plasmid (VectorBuilder, Chicago, IL, USA). Lentiviral particles were obtained by co-transfecting each lentivector with pSPAX2 (Addgene, Watertown, MA, USA), a VSV-G-encoding vector, into Lenti-X 293 T cells (Clontech, Mountain View, CA, USA). As previously described[81,82], viral supernatants were then collected 48 h and 72 h post-transfection, filtrated and concentrated by ultracentrifugation. Before cell transduction, the qPCR Lentivirus Titration kit (ABM, Richmond, BC, Canada) was used for titrating the lentiviral vectors. Positively transduced cells were selected with 100 µg/ml hygromycin B or 10 µg/ml blasticidin (InvivoGen, San Diego, CA, USA) and were grown in Dulbecco's modified Eagle's medium containing 10% fetal calf serum and supplied with 1% sodium pyruvate and 1% nonessential amino acid (Gibco, Thermo Fisher Scientific, Waltham, MA, USA).

Organotypic raft cultures. Spontaneously immortalized human keratinocytes (NIKS cells) and foreskin fibroblasts (kindly provided by Prof. Paul F. Lambert, University of Wisconsin School of Medicine and Public Health, Madison, WI, USA) were routinely cultured in incomplete F medium on mitomycin C-treated J2 3T3 feeder cells and in Ham's F12 medium containing 10% fetal bovine serum, respectively. All supplements added in culture media were previously described[83,84]. Before being used in organotypic cultures, 2.5×10^6 NIKS cells were transfected with both recircularized HPV18 DNA (2 µg) and pcDNA6 plasmid (0.5 µg) using Effectene Transfection Reagent (Qiagen, Hilden, Germany). After blasticidin selection (7 µg/ml) for 6 days, 1.5×10^6 HPV18-positive cells were seeded onto a dermal equivalent composed of rat-tail type 1 collagen (Sigma Aldrich, Saint Louis, MI, USA) and 1×10^6 human foreskin fibroblasts. The daily procedure allowing the production of a pluristratified epithelium using this organotypic culturing approach was extensively detailed previously[83,84]. After 18 days, rafts were fixed in formalin and embedded in paraffin for both immunohistochemical and in situ hybridization analyses.

Bacterial cultures and antimicrobial assays. Bacterial strains *Lactobacillus crispatus* DSM 20356, *Lactobacillus iners* CIP 105923 and *Garnerella vaginalis* CCUG 43336 were kindly provided by the Department of Clinical Microbiology at University Hospital Center of Liege. *Lactobacillus jensenii* LMG 6414 was obtained from BCCM/LMG Bacteria Collection (University of Gent, Belgium). Log-phase bacteria were grown on Columbia agar with 5% sheep blood (Becton Dickinson, Franklin Lakes, NJ, USA) at 37 °C in a humidified CO_2 atmosphere (*Lactobacilli*) or in anaerobic jars (*G. vaginalis*). To analyze the antimicrobial effect of innate peptides expressed by vaginal/cervical mucosa, 5×10^4 colony-forming unit (CFU)/ml were mixed with different peptides (concentration range: 1–10 µg/ml) in 10 mM sodium phosphate buffer (SPB) (final volume 100 µl) and incubated for 45 min to 9 h at 37 °C. Where indicated, the peptides were incubated with 2 mM dithiothreitol (DTT) (Invitrogen, Carlsbad, CA, USA) for 30 min at 37 °C before adding the bacteria. In indicated experiments, incubation was carried out in potassium phosphate buffer (KPB) (pH: 7.4, 10 mM). The following peptides were tested: HβD1 (PeptaNova, Sandhausen, Germany), HβD2 (PeptaNova), HβD3 (PeptaNova), HβD4 (PeptaNova), HD-5 (PeptaNova), HD-6 (PeptaNova), elafin (PeptaNova), S100A7 (Abnova, Taipei City, Taiwan) and SLPI (R&D Systems, Minneapolis, MI, USA). Bacterial suspensions were then plated on Columbia Blood agar plates for 24–48 h to determine CFU. High-resolution images for each condition were taken. Colony detection and counts were finally performed using ImageJ software (NIH, Bethesda, MD, USA) and verified by manual counting.

Matrix-assisted laser desorption/ionization (MALDI) mass spectrometry. The different innate peptides were incubated with or without DTT (2 mM, pH 7.4) for 30 min at 37 °C and then alkylated with 20 mM iodoacetamide for 30 min at 25 °C. The peptides were deposited on MALDI plate with α-cyano-4-hydroxy cinnamic acid (HCCA) saturated solution for co-crystallization (equal volume). The spectra were acquired with a rapifleX TOF/TOF instrument (Bruker, Bremen, Germany) in linear positive mode.

Flow cytometry. Cells were scraped and washed twice with PBS before staining reaction (30 min at 4 °C). After washing/centrifugation, cells were fixed with 1%

paraformaldehyde. Flow cytometry analyses were performed with a FACSCanto II flow cytometer and data (mean fluorescence intensity and positive cell percentages) were acquired using FACSDiva software (version 8.0.1, BD Biosciences, San Jose, CA, USA). Results were analyzed with FlowJo (version 10.5.3, TreeStar, Ashland, OR, USA). The following antibodies were used: anti-CD14 Phycoerythrin (PE) (1/33, clone TUK4, Dako, Glostrup, Denmark), anti-TLR4 PE (1/33, FAB6248P, R&D systems), anti-TNFR1 PE (1/33, clone W15099A, Biolegend, San Diego, CA, USA) and anti-TNFR2 PE (1/33, clone 3G7A02, Biolegend). The gating strategy is detailed in Supplementary Fig. 14.

To determine the incorporation of selected peptides (or their hydrolyzed products) within the cytoplasm of several bacterial species, free amine groups (lysine residues and N-terminus) were first conjugated with Atto 488 dye according to manufacturer's recommendations (Atto 488 protein labeling kit, Sigma Aldrich). A total 5×10^4 colony-forming unit (CFU)/ml were then mixed with fluorescent labeled peptides (5 µg/ml) in 10 mM sodium phosphate buffer (final volume 100 µl) and incubated for 1 h30 at 37 °C before being analyzed by flow cytometry. Where indicated, trypan blue was added before the analysis in order to exclusively consider cytoplasmic fluorescence.

Mass spectrometry (MS). To determine the hydrolysis of innate peptides by the different *Lactobacillus* species present in the female reproductive tract, free amine groups were first biotinylated and labeled peptides (5 µg/ml) were incubated with 5×10^4 CFU/ml for 3 h or 6 h at 37 °C in 10 mM SPB. Both labeled peptides and their hydrolyzed product were then purified using NeutrAvidin Agarose beads according to manufacturer's recommendations (cell surface protein isolation kit, ThermoFisher Scientific). MS experiments were performed with a 6560 Ion mobility Q-TOF system (Agilent Technologies, Waldbronn, Germany). The LC-chip was interfaced to the MS via the ChipCube interface (Agilent Technologies). The separation was achieved on a large capacity chip integrating a 160 nl enrichment column and a 150 mm × 75 µm ID analytical column (both packed with a Zorbax C_{18} phase) in 1 h gradient time. Other operational conditions as well as data-dependent acquisition settings were previously described[85]. Datafiles were opened using MassHunter Qualitative Analysis software (version 7.0, Agilent Technologies) and individual extracted ion chromatograms were generated at the MS level for each m/z value of interest.

To precisely verify whether the innate peptides highly secreted by the vaginal/cervical mucosa can be used by the predominant *Lactobacillus* species as amino acid source, two elafin fragments (H-AQEPVK*GPVSTK*PGSCPII-OH and H-PGIK*K*CCEGSCGMACFVPQ-OH), each containing two $^{13}C_6{}^{15}N_2$-labeled lysines, were synthesized (Pepscan, Lelystad, The Netherlands). Five µg/ml of each peptide were incubated with 6×10^8 CFU/ml for 6 h at 37 °C in 10 mM SPB. Following two steps of washing, bacterial cells were suspended in 20 µl of Tris-HCl (50 mM, pH 8) containing urea (8 M) and then sonicated for 15 min using a Bioruptor Plus (Diagenode, Seraing, Belgium). The supernatants were retrieved and the samples were successively reduced [5 mM dithiothreitol (DTT), 30 min at 37 °C], alkylated [15 mM iodoacetamide (IAA), 30 min at room temperature] and digested in 2 steps at 37 °C [a mixture of trypsin-Lys-C (Promega, Madison, WI, USA) for 4 h in initial buffer at a ratio enzymes/proteins of 1/25 (w/w) followed by 16 h after dilution to 1 M urea with 50 mM Tris HCl buffer]. Liquid chromatography-tandem MS were then performed using an Acquity M-Class UPLC (Waters Corporation, Milford, MA, USA) coupled to a Q Exactive Plus Hybrid Quadrupole-Orbitrap MS (Thermo Fisher Scientific). The positive ion mode nanoelectrospray was utilized. Symmetry C18 5 µm (180 µm × 20 mm) and HSS T3 C18 1.8 µm (75 µm × 250 mm) were used as trap and analytical column, respectively (Waters). The digested peptides were loaded on the trap column in 98% water 0.1% formic acid (solvent A) (flow rate: 20 µl/min) during 3 min and subsequently separated on the analytical column. The flow rate was constant (600 nL/min) with the following linear gradient: initial conditions 2% acetonitrile 0.1% formic acid (solvent B), at 5 min: 7% solvent B, at 135 min: 30% solvent B, at 150 min: 40% solvent B, at 154 min: 90% solvent B until 158 min and then back in the initial conditions at 162 min until 177 min. The total analytical run time was 180 min. The TopN-MS/MS method was used and N was set to 12. The resolution was set to 70,000 for full MS spectrum acquisition (range 400 to 1600 *m/z*) and 17,500 for MS/MS. The automatic gain control target was set to 1×10^6 and 1×10^5 for MS and MS/MS, respectively. A 2 *m/z* isolation window was used, the maximum injection time was 50 ms and a normalized collision energy of 28 was utilized for the activation of ions. Data analysis/protein identification was performed using SEQUEST HT search engine and Proteome Discoverer 2.1 software (Thermo Scientific). Databases were downloaded from Uniprot for each bacterial strain of interest (*L. jensenii*: 3763 sequences; *L. crispatus*: 5120 sequences; *L. iners*: 1872 sequences). The parameters for the search were as follows: maximum 2 miss-cleavages and cysteine carbamidomethylation as fixed modification and deamidation (asparagine, glutamine), oxidation (methionine) and label $^{13}C_6{}^{15}N_2$ of Lysine as variable modifications. The tolerances of precursor and fragment mass were 5 ppm and 0.02 Da, respectively. Percolator node was used to select peptides with a Target FDR set at maximum 1%.

ELISA. 1×10^6 cells/well of a six-well plate were seeded in appropriate growth medium. After 48 h, the secretions of constitutive innate peptides (elafin, S100A7, SLPI and HβD1) by control (HaCat) and HPV16 E6E7-transduced cells were quantified by ELISA using the following commercially available kits: human S100A7 ELISA kit (Biorbyt, Cambridge, UK), human Trappin-2/elafin ELISA kit (Sigma Aldrich), human SLPI ELISA kit (MyBioSource, San Diego, CA, USA) and human HβD1 ELISA kit (MyBioSource).

ATP measurement. ATP level in bacteria was determined using the BacTiter-Glo Microbial Cell Viability Assay (Promega) according to manufacturer's recommendations. For each bacterial species, 6×10^7 CFU/ml were mixed with elafin or S100A7 (5 µg) in 10 mM SPB and incubated 6 h at 37 °C. One hundred µl of bacterial-peptide solution were then mixed with an equal volume of BacTiter-Glo reagent and incubated for 5 min at room temperature. Luminescence was measured using a Centro LB960 microplate luminometer (Berthold Technologies, Bad Wildbad, Germany).

RNA interference and inhibitors. Immortalized keratinocytes (1.5×10^5 cells per well of a six-well plate) were transfected with ON-TARGETplus SMARTpool siRNAs targeting p65, β-catenin or c-Myc (Dharmacon, Lafayette, CO, USA) using Oligofectamine Transfection Reagent (Invitrogen). Oligos targeting the firefly luciferase gene (siGL2) were used as control. For each experiment, siRNA (40 nM) and 6 µl of Oligofectamine were diluted in 1 ml of Optimem (Invitrogen). The cells were incubated with the mixture for 4 h at 37 °C. Twenty-four hours after transfection, cells were either harvested or stimulated with LPS (2 µg/ml) or TNFα (20 ng/ml) and experiments were performed. For the chemical inhibition of NF-kB or c-Myc, BAY 11-7082 (5 µM, Sigma Aldrich) or 10058-F4 (40 µM, Selleckchem, Houston, TX, USA) was added to cell cultures before RNA expression analyses. In order to determine the stability of a given protein, monolayer cultures were pretreated with 100 µM cycloheximide (Sigma Aldrich). Where indicated, DNA methyltransferases were inhibited with 5 µM 5-aza-deoxycytidine (Sigma Aldrich). To analyze the CK1-dependent phosphorylation of β-catenin (ser45), cells were treated with 50 nM calyculin A (Sigma Aldrich) for 30 min before protein extraction.

Immunohistochemistry, immunofluorescence and in situ hybridization. Immunohistochemical/fluorescence analyses were performed using standard protocols previously described[86,87] and included the following primary antibodies: anti-SLPI (1/400, NBP1-76803, Novus Biologicals, Centennial, CO, USA), anti-S100A7 (1/500, HPA006997, Atlas Antibodies, Bromma, Sweden), anti-elafin (1/150, clone FL-117, Santa Cruz Biotechnology, Dallas, TX, USA), anti-LL37/CAMP (1/1000, HPA029874, Atlas Antibodies), anti-HβD1 (1/50, PA5-51286, Thermo Fisher Scientific), anti-HβD2 (1/100, ab63982, Abcam, Cambridge, MA, USA), anti-HβD3 (1/300, NB200-117, Novus Biologicals), anti-HβD4 (1/100, clone L13-10-D1, Abcam), anti-HD-5 (1/200, HPA015775, Atlas Antibodies), anti-HD-6 (1/50, NBP1-84281, Novus Biologicals), anti-p65 (1/500, clone D14E12, Cell Signaling Technology, Danvers, MA, USA), anti-E-cadherin (ready to use, clone 36, Ventana Medical Systems, Tucson, AZ, USA), anti-β-catenin (1/100, clone E247, Abcam), anti-c-Myc (1/100, ab32072, Abcam), anti-$p16^{INK4a}$ (1/300, clone JC8; Santa Cruz Biotechnology) and anti-ki67 (ready to use, clone 30-9; Ventana Medical Systems). Immunoperoxidase staining was performed using the mouse or rabbit Envision detection system (Dako) according to manufacturer's instructions. In immunofluorescence, the Alexa Fluor® 488 anti-rabbit antibody (Invitrogen) was used for the secondary reaction and pictures were taken with a Leica SP5 confocal microscope (GIGA in vitro Imaging platform, University of Liege). The actin filaments and nuclei were selectively stained with Alexa Fluor® 568 phalloidin (Invitrogen) and 4,6-diamidino-2-phenylindole (DAPI), respectively. Mouse and rabbit control IgGs (Santa Cruz Biotechnology) were used as negative controls.

In paraffin-embedded tissues/rafts, the detection of HPV DNA by in situ hybridization was performed using the Ventana INFORM HPV III family 16 probe (Ventana Medical Systems) according to the supplier's recommendations.

Immunohistochemical assessment. All immunolabelled tissues were evaluated independently by experienced histopathologists. E-cadherin and antimicrobial peptide expressions were assessed by using a semi-quantitative score of the immunoreactivity. As previously described[55,88], an arbitrary scale of the staining intensity (0: undetectable, 1: low, 2: moderate, 3: strong) and extent (0: <5% positive cells, 1: 6–33%, 2: 34–66%, 3: >67%) was used. A global score for each tissue specimen (ranged between 0 and 9) was yielded by multiplying the results obtained with these two scales. The percentage of cells displaying cytoplasmic/nuclear β-catenin immunoreactivity was also evaluated. Scoring of c-Myc was based on nuclear staining in the epithelial cells. Collected results were stratified as follows: 0–5%, 6–33%, 34–66%, 51–75% and > 67%. Regarding p65, the percentage (<10% *versus* > 10%) of cells exhibiting a nuclear immunoractivity was determined.

Bisulfite genomic sequencing. Freshly extracted genomic DNA (500 ng) was processed using Bisulfite Conversion kit (Active Motif, La Hulpe, Belgium) according to supplier's recommendations. Conversed *CDH1* (E-cadherin) promoter was amplified using the specific primers listed in Supplementary Table 1. These latter were designed with the Methprimer software (https://www.urogene.org/methprimer/). PCR products were cloned into pJET1.2 vector using CloneJET PCR cloning kit (Thermo Fisher Scientific) and then ligation products were transformed into competent JM109 bacteria using heat shock. Resistant colonies were isolated and recombinant plasmids were

purified (NucleoSpin Plasmid kit, Macherey Nagel). Finally, at least 6 independent plasmids for each condition were sequenced using Sanger method.

RT-qPCR. Total RNA was extracted and purified using NucleoSpin RNA isolation kit (Macherey Nagel) according to manufacturer's instructions. The ReliaPrep RNA Miniprep system (Promega) was used for both human and mouse micro-dissected samples. One microgram was reverse transcribed using RevertAid Reverse Transcriptase and oligo dT primers (Thermo Scientific). Quantitative PCR was performed using the FastStart Universal SYBR Green Master mix (Roche, Basel, Switzerland). Both human and mouse primer sequences used for PCR analysis are listed in Supplementary Table 1. The public database PrimerBank was used for the retrieval of most of these sequences[89]. The experiments were performed in triplicate and threshold cycle numbers (Ct) were determined using the ABI-Prism 7900HT Sequence Detection System (Applied Biosystems, Foster City, CA, USA). The relative amounts of mRNA per sample were finally calculated using the ΔΔCt method. Four calibrator genes (HPRT, GAPDH, 18S and TBP) were used to compare the relative quantities of mRNAs between tissue specimens from different patients. With tissue samples from different mice, the expression of 2 housekeeping genes (HPRT and GAPDH) was determined. In vitro experiments (with the same cell line) were normalized to the amount of HPRT mRNA. Where indicated, the amplification efficiency of qPCR reactions was determined using the qPCR efficiency calculator software (Thermo Fisher Scientific).

Western blotting analysis. After extraction in 1% SDS buffer (total extraction) containing protease and phosphatase inhibitors (Roche) and quantification (BCA protein assay kit; Pierce, Rockford, IL, USA), twenty micrograms of proteins were separated on 10% SDS-PAGE and transferred to PVDF membranes (Roche). For the extraction of separate protein fractions, the cytoplasmic (20 mM HEPES pH 7.9, 0.1 Mm EDTA, 2 mM MgCl2, 10 mM KCl, 0.2% Nonidet P-40) and nuclear (20 mM HEPES pH 7.9, 0.2 mM EDTA, 1.5 mM MgCl2, 0.63 mM NaCl, 25% glycerol) buffers were used. Blocking was subsequently performed with 5% skim milk in TBS-Tween 0.1% for 1 h and the membranes were then incubated overnight at 4 °C with the following primary antibodies: anti-p65 (1/1000, clone D14E12, Cell Signaling Technology), anti-IκBα (1/1000, clone L35A5, Cell Signaling Technology), anti-NEMO (1/1000, clone FL-419, Santa Cruz Biotechnology), anti-c-Myc (1/1000, ab32072, Abcam), anti-E-cadherin (1/1000, clone 36, BD Biosciences), anti-β-catenin (1/1000, clone E247, Abcam), anti-CK1 (1/1000, #2655, Cell Signaling Technology), anti-β-TrCP (1/1000, #11984, Cell Signaling Technology), anti-phospho-β-catenin (1/1000, Ser45, #9564, Cell Signaling Technology), anti-actin (1/2000, clone AC-15, Sigma Aldrich), anti-HSC-70 (1/2000, clone B-6, Santa Cruz Biotechnology), anti-NBS-1 (1/1000, BD Biosciences) and anti-MEK2 (1/1000, #9125, Cell Signaling Technology). The protein bands were detected using an enhanced chemiluminescence system (Westar ECL-Sun, Cyanagen, Bologna, Italy) and finally quantified by densitometry using ImageJ software. Actin, HSC-70, or NBS-1 was used for the normalization. For uncropped blots, see the Source Data file.

Gaussia princeps luciferase complementation assay (GPCA). The coding (or mutated/truncated) sequences of HPV E7 from several alpha and beta genotypes (alpha: HPV16, 18, 33, and 39; beta: HPV8, 38, and 49) were transferred into Gateway-compatible GPCA destination vector pSPICA-N2. The open reading frames (ORFs) encoding proteins involved in IKK or β-catenin destruction complex were obtained from the human ORFeome v7.1 and 8.1 (Dana-Farber Cancer Institute, Boston, MA, USA) and were transferred into pSPICA-N1 plasmid. GPCA expression vectors (pSPICA-N1 and N2) allow the expression of two complementary fragments of the *G. princeps* luciferase (Gluc1 or Gluc2) linked to the N-terminal ends of tested proteins. All constructions were controlled by Sanger sequencing (GIGA-Genomics platform, University of Liege). GPCA experiments were then performed as extensively described previously[90,91]. Briefly, HEK-293T cells were simultaneously transfected with 100 ng of pSPICA-N1-IKK or β-catenin destruction complex proteins and 100 ng of pSPICA-N2-E7 using PEI Max (Polysciences, Warrington, PA, USA). After 24 h, cells were washed, lysed and luciferase enzymatic activity was measured for 10 seconds using a Centro LB960 microplate luminometer (Berthold Technologies, Bad Wildbad, Germany). The luciferase assay system was purchased from Promega. As previously described[90], results were expressed as a luminescence value normalized over the sum of controls [normalized luminescence ratio (NLR)].

Co-immunoprecipitation. The detailed procedure for co-immunoprecipitation was previously described[90]. Briefly, the coding sequence of HPV E7 (from alpha HPV16 and 18 as well as beta HPV8) was first cloned into the pCineo-3xFLAG plasmid. HEK 293 T cells were then transfected (PEI Max) with 1.5 µg of FLAG-HPV E7 plasmid or empty vector and 1.5 µg of pSPICA-N1 plasmid expressing proteins involved in IKK or β-catenin destruction complex fused to the Gluc1 fragments of the *G. princeps* luciferase (used in GPCA experiments). After 24 h, cells were lysed, centrifugated at 16,000 g for 20 min and the lysate was incubated overnight at 4 °C with anti-FLAG M2 magnetic beads (ready to use, Sigma Aldrich). After several washes, IP proteins as well as total proteins (input corresponding to 5%) were analyzed by Western blot. The anti-GLuc (1/1000, *#E8023, New England Biolabs*, Ipswich, MA, USA) was used as primary antibody. For the novel E7 targets highlighted in the present study, the experiments were also reproduced in the inverse direction. To do so, the immunoprecipitation step was performed using magnetic beads (Cell Signaling) and the following antibodies: anti-NEMO (1/50, ab178872, Abcam), anti-CK1α1 (1/30, ab206652, Abcam) and anti- β-TrCP (1/200, clone D13F10, Cell Signaling). The anti-FLAG antibody (1/2000, clone M2, Sigma Aldrich) was then used for detecting FLAG-E7. Band intensities in the IP lanes were normalized according to intensities in the input lanes and IP (HPV E7)/IP (control) ratio was calculated.

Chromatin immunoprecipitation (ChIP). ChIP assays were performed as previously described[92]. Briefly, nuclei were lysed with a buffer containing 50 mM Tris/HCl pH8, 10 mM EDTA, 0.5% SDS and protease/phosphatase inhibitor (Roche). Each sample was sonicated for 10 min using a Diagenode Bioruptor (Diagenode) and then centrifugated at 14,000 g for 15 min. Supernatant (isolated chromatin) was incubated overnight at 4 °C with either anti-p65 antibody (1/50, clone D14E12, Cell Signaling Technology) or control rabbit IgG (C15410206, Diagenode) in ChIP dilution buffer (0.01% SDS, 1.1% Triton X-100, 1.1 mM EDTA, 20 mM Tris/HCl pH8, 167 mM NaCl, protease inhibitor). Protein G magnetic beads (prepared as previously described) were then added in each sample and incubated for 4 h under rotation at 4 °C. After washing and reversal of crosslinking, immunoprecipitated DNA was purified (phenol/chloroform extraction) and subjected to qPCR using *PI3/elafin* and *HβD2* promoter NF-kB binding site specific primers. Sequences targeting a more distal region (-2 kb) on both promoters were used as negative control (Supplementary Table 1).

Statistical analysis. Statistical analysis was performed using the GraphPad Prism 8 software (San Diego, CA, USA). For normally distributed variables, two group comparisons were performed using unpaired *t*-tests. One-way or two-way ANOVA was applied to determine the statistical significance of differences between more than two groups/conditions. Dunnett's or Bonferroni post-hoc test was used for multiple comparisons. In the case of discrete (staining scores for assessing innate peptide expression) or non-normally distributed (bacterial population abundances) variables, a Mann-Whitney or Kruskal-Wallis test was performed according to the number of groups. The comparison of phenotypic/immunohistochemical variables (0–5%, 6–33%, 34–66%, and >67% of cells displaying a nuclear c-myc/p65 immunoreactivity or membrane *versus* cytoplasmic/nuclear β-catenin localization) between independent groups was performed using a Fisher's exact test or a χ^2 test according to the number of variables. For the different microbial population ecological indices (α-diversity, richness, evenness), the differences between defined groups were evaluated using a non-parametric Kruskal–Wallis test followed by a two-stage linear step-up procedure of Benjamini, Krieger and Yekutieli. Using the MOTHUR software, sample clustering and beta-dispersion were assessed in a Bray–Curtis dissimilarity matrix with AMOVA (analysis of molecular variance) and HOMOVA (homogeneity of molecular variance) tests, respectively. Regarding the retrospective follow-up study assessing the interplay between HPV infection and BV, both odds ratios and corresponding 95% confidence intervals were calculated using a Fisher's exact test (contingency table) and the results were visualized in a Forest plot. The persistence of each pathological disorder in the presence or absence of the other one was compared using a log-rank (Mantel-Cox) test and the results were presented as Kaplan–Meier plots.

Reporting summary. Further information on research design is available in the Nature Research Reporting Summary linked to this article.

Data availability

Raw amplicon sequencing libraries have been deposited in the NCBI Sequence Read Archive (SRA) repository with the accession code: PRJNA670165. Both the alignment and taxonomical assignment (from phylum to species) of post-sequencing data were performed, based on the SILVA database (v1.38). The proteomics data have been deposited at the ProteomeXchange Consortium via the PRIDE partner repository with the following dataset identifier: PXD022113. Source data for all Figures are provided with this paper. Source data are provided with this paper.

Received: 10 April 2020; Accepted: 3 February 2022;
Published online: 28 February 2022

References

1. de Sanjose, S. et al. Worldwide prevalence and genotype distribution of cervical human papillomavirus DNA in women with normal cytology: a meta-analysis. *Lancet Infect. Dis.* **7**, 453–459 (2007).
2. de Martel, C., Plummer, M., Vignat, J. & Franceschi, S. Worldwide burden of cancer attributable to HPV by site, country and HPV type. *International journal of cancer. J. Int. du cancer* **141**, 664–670 (2017).
3. Schiffman, M. et al. Carcinogenic human papillomavirus infection. *Nat. Rev. Dis. Prim.* **2**, 16086 (2016).
4. Luo, X. et al. HPV16 drives cancer immune escape via NLRX1-mediated degradation of STING. *J. Clin. Investig.* **130**, 1635–1652 (2020).

5. Chang, Y. E. & Laimins, L. A. Microarray analysis identifies interferon-inducible genes and Stat-1 as major transcriptional targets of human papillomavirus type 31. *J. Virol.* **74**, 4174–4182 (2000).
6. Reiser, J. et al. High-risk human papillomaviruses repress constitutive kappa interferon transcription via E6 to prevent pathogen recognition receptor and antiviral-gene expression. *J. Virol.* **85**, 11372–11380 (2011).
7. Ronco, L. V., Karpova, A. Y., Vidal, M. & Howley, P. M. Human papillomavirus 16 E6 oncoprotein binds to interferon regulatory factor-3 and inhibits its transcriptional activity. *Genes Dev.* **12**, 2061–2072 (1998).
8. Bottley, G. et al. High-risk human papillomavirus E7 expression reduces cell-surface MHC class I molecules and increases susceptibility to natural killer cells. *Oncogene* **27**, 1794–1799 (2008).
9. Hasan, U. A. et al. TLR9 expression and function is abolished by the cervical cancer-associated human papillomavirus type 16. *J. Immunol.* **178**, 3186–3197 (2007).
10. Karim, R. et al. Human papillomavirus deregulates the response of a cellular network comprising of chemotactic and proinflammatory genes. *PLoS ONE* **6**, e17848 (2011).
11. Human Microbiome Project, C. Structure, function and diversity of the healthy human microbiome. *Nature* **486**, 207–214 (2012).
12. Zhou, X. et al. Characterization of vaginal microbial communities in adult healthy women using cultivation-independent methods. *Microbiology* **150**, 2565–2573 (2004).
13. Anahtar, M. N., Gootenberg, D. B., Mitchell, C. M. & Kwon, D. S. Cervicovaginal microbiota and reproductive health: the virtue of simplicity. *Cell host microbe* **23**, 159–168 (2018).
14. Onderdonk, A. B., Delaney, M. L. & Fichorova, R. N. The human microbiome during bacterial vaginosis. *Clin. Microbiol. Rev.* **29**, 223–238 (2016).
15. Turovskiy, Y., Sutyak Noll, K. & Chikindas, M. L. The aetiology of bacterial vaginosis. *J. Appl. Microbiol.* **110**, 1105–1128 (2011).
16. Muzny, C. A. & Schwebke, J. R. Pathogenesis of bacterial vaginosis: discussion of current hypotheses. *J. Infect. Dis.* **214**, S1–S5 (2016).
17. Leitich, H. et al. Bacterial vaginosis as a risk factor for preterm delivery: a meta-analysis. *Am. J. Obstet. Gynecol.* **189**, 139–147 (2003).
18. Sweet, R. L. Gynecologic conditions and bacterial vaginosis: implications for the non-pregnant patient. *Infect. Dis. Obstet. Gynecol.* **8**, 184–190 (2000).
19. Cherpes, T. L., Meyn, L. A., Krohn, M. A., Lurie, J. G. & Hillier, S. L. Association between acquisition of herpes simplex virus type 2 in women and bacterial vaginosis. *Clin. Infect. Dis.: Off. Publ. Infect. Dis. Soc. Am.* **37**, 319–325 (2003).
20. Cohen, C. R. et al. Bacterial vaginosis associated with increased risk of female-to-male HIV-1 transmission: a prospective cohort analysis among African couples. *PLoS Med.* **9**, e1001251 (2012).
21. Wiesenfeld, H. C., Hillier, S. L., Krohn, M. A., Landers, D. V. & Sweet, R. L. Bacterial vaginosis is a strong predictor of Neisseria gonorrhoeae and Chlamydia trachomatis infection. *Clin. Infect. Dis.: Off. Publ. Infect. Dis. Soc. Am.* **36**, 663–668 (2003).
22. Brotman, R. M. et al. Interplay between the temporal dynamics of the vaginal microbiota and human papillomavirus detection. *J. Infect. Dis.* **210**, 1723–1733 (2014).
23. Briselden, A. M., Moncla, B. J., Stevens, C. E. & Hillier, S. L. Sialidases (neuraminidases) in bacterial vaginosis and bacterial vaginosis-associated microflora. *J. Clin. Microbiol.* **30**, 663–666 (1992).
24. Mitra, A. et al. The vaginal microbiota associates with the regression of untreated cervical intraepithelial neoplasia 2 lesions. *Nat. Commun.* **11**, 1999 (2020).
25. Brusselaers, N., Shrestha, S., van de Wijgert, J. & Verstraelen, H. Vaginal dysbiosis and the risk of human papillomavirus and cervical cancer: systematic review and meta-analysis. *Am. J. Obstet. Gynecol.* **221**, 9–18 e18 (2019).
26. Gillet, E. et al. Bacterial vaginosis is associated with uterine cervical human papillomavirus infection: a meta-analysis. *BMC Infect. Dis.* **11**, 10 (2011).
27. Kyrgiou, M., Mitra, A. & Moscicki, A. B. Does the vaginal microbiota play a role in the development of cervical cancer? *Transl. Res.: J. Lab. Clin. Med.* **179**, 168–182 (2017).
28. Liang, Y., Chen, M., Qin, L., Wan, B. & Wang, H. A meta-analysis of the relationship between vaginal microecology, human papillomavirus infection and cervical intraepithelial neoplasia. *Infect. agents cancer* **14**, 29 (2019).
29. Yarbrough, V. L., Winkle, S. & Herbst-Kralovetz, M. M. Antimicrobial peptides in the female reproductive tract: a critical component of the mucosal immune barrier with physiological and clinical implications. *Hum. Reprod. Update* **21**, 353–377 (2015).
30. Wang, G., Li, X. & Wang, Z. APD3: the antimicrobial peptide database as a tool for research and education. *Nucleic Acids Res.* **44**, D1087–D1093 (2016).
31. Tsutsumi-Ishii, Y. & Nagaoka, I. NF-kappa B-mediated transcriptional regulation of human beta-defensin-2 gene following lipopolysaccharide stimulation. *J. Leukoc. Biol.* **71**, 154–162 (2002).
32. Johansen, C., Bertelsen, T., Ljungberg, C., Mose, M. & Iversen, L. Characterization of TNF-alpha- and IL-17A-mediated synergistic induction of DEFB4 gene expression in human keratinocytes through IkappaBzeta. *J. Investig. Dermatol.* **136**, 1608–1616 (2016).
33. Clauss, A. et al. Overexpression of elafin in ovarian carcinoma is driven by genomic gains and activation of the nuclear factor kappaB pathway and is associated with poor overall survival. *Neoplasia* **12**, 161–172 (2010).
34. Dreos, R., Ambrosini, G., Perier, R. C. & Bucher, P. The Eukaryotic Promoter Database: expansion of EPDnew and new promoter analysis tools. *Nucleic acids Res.* **43**, D92–D96 (2015).
35. Dang, C. V. et al. The c-Myc target gene network. *Semin. cancer Biol.* **16**, 253–264 (2006).
36. Fernandez, P. C. et al. Genomic targets of the human c-Myc protein. *Genes Dev.* **17**, 1115–1129 (2003).
37. He, T. C. et al. Identification of c-MYC as a target of the APC pathway. *Science* **281**, 1509–1512 (1998).
38. Jeanes, A., Gottardi, C. J. & Yap, A. S. Cadherins and cancer: how does cadherin dysfunction promote tumor progression? *Oncogene* **27**, 6920–6929 (2008).
39. Schroeder, B. O. et al. Paneth cell alpha-defensin 6 (HD-6) is an antimicrobial peptide. *Mucosal Immunol.* **8**, 661–671 (2015).
40. Schroeder, B. O. et al. Reduction of disulphide bonds unmasks potent antimicrobial activity of human beta-defensin 1. *Nature* **469**, 419–423 (2011).
41. Torcia, M. G. Interplay among vaginal microbiome, immune response and sexually transmitted viral infections. *Int. J. Mol. Sci.* **20**, (2019).
42. Lu, H. et al. Characteristics of bacterial vaginosis infection in cervical lesions with high risk human papillomavirus infection. *Int J. Clin. Exp. Med.* **8**, 21080–21088 (2015).
43. Moscicki, A. B., Shi, B., Huang, H., Barnard, E. & Li, H. Cervical-vaginal microbiome and associated cytokine profiles in a prospective study of HPV 16 acquisition, persistence, and clearance. *Front Cell Infect. Microbiol.* **10**, 569022 (2020).
44. Cheng, L. et al. Vaginal microbiota and human papillomavirus infection among young Swedish women. *NPJ Biofilms Microbiomes* **6**, 39 (2020).
45. Lee, J. E. et al. Association of the vaginal microbiota with human papillomavirus infection in a Korean twin cohort. *PLoS ONE* **8**, e63514 (2013).
46. Mitra, A. et al. Cervical intraepithelial neoplasia disease progression is associated with increased vaginal microbiome diversity. *Sci. Rep.* **5**, 16865 (2015).
47. Perkins, R. B. et al. 2019 ASCCP risk-based management consensus guidelines for abnormal cervical cancer screening tests and cancer precursors. *J. Low. Genit. Trac. Dis.* **24**, 102–131 (2020).
48. DasGupta, T. et al. Human papillomavirus oncogenic E6 protein regulates human beta-defensin 3 (hBD3) expression via the tumor suppressor protein p53. *Oncotarget* **7**, 27430–27444 (2016).
49. Nguyen, H., Teskey, L., Lin, R. & Hiscott, J. Identification of the secretory leukocyte protease inhibitor (SLPI) as a target of IRF-1 regulation. *Oncogene* **18**, 5455–5463 (1999).
50. Um, S. J. et al. Abrogation of IRF-1 response by high-risk HPV E7 protein in vivo. *Cancer Lett.* **179**, 205–212 (2002).
51. Hasan, U. A. et al. The human papillomavirus type 16 E7 oncoprotein induces a transcriptional repressor complex on the Toll-like receptor 9 promoter. *J. Exp. Med.* **210**, 1369–1387 (2013).
52. Suarez-Carmona, M., Hubert, P., Delvenne, P. & Herfs, M. Defensins: "Simple" antimicrobial peptides or broad-spectrum molecules? *Cytokine growth factor Rev.* **26**, 361–370 (2015).
53. Hancock, R. E., Haney, E. F. & Gill, E. E. The immunology of host defence peptides: beyond antimicrobial activity. *Nat. Rev. Immunol.* **16**, 321–334 (2016).
54. Hubert, P. et al. Defensins induce the recruitment of dendritic cells in cervical human papillomavirus-associated (pre)neoplastic lesions formed in vitro and transplanted in vivo. *FASEB J.: Off. Publ. Federation Am. Societies Exp. Biol.* **21**, 2765–2775 (2007).
55. Hubert, P. et al. Altered alpha-defensin 5 expression in cervical squamocolumnar junction: implication in the formation of a viral/tumour-permissive microenvironment. *J. Pathol.* **234**, 464–477 (2014).
56. Wolf, R. et al. Chemotactic activity of S100A7 (Psoriasin) is mediated by the receptor for advanced glycation end products and potentiates inflammation with highly homologous but functionally distinct S100A15. *J. Immunol.* **181**, 1499–1506 (2008).
57. Presicce, P., Giannelli, S., Taddeo, A., Villa, M. L. & Della Bella, S. Human defensins activate monocyte-derived dendritic cells, promote the production of proinflammatory cytokines, and up-regulate the surface expression of CD91. *J. Leukoc. Biol.* **86**, 941–948 (2009).
58. Wiens, M. E. & Smith, J. G. Alpha-defensin HD5 inhibits furin cleavage of human papillomavirus 16 L2 to block infection. *J. Virol.* **89**, 2866–2874 (2015).
59. Wiens, M. E. & Smith, J. G. alpha-Defensin HD5 inhibits human papillomavirus 16 infection via capsid stabilization and redirection to the lysosome. *mBio* **8**, e02304-16 (2017).
60. Raveschot, C. et al. Production of bioactive peptides by lactobacillus species: from gene to application. *Front. Microbiol.* **9**, 2354 (2018).

61. Sadat-Mekmene, L., Genay, M., Atlan, D., Lortal, S. & Gagnaire, V. Original features of cell-envelope proteinases of Lactobacillus helveticus: a review. *Int. J. Food Microbiol.* **146**, 1–13 (2011).
62. Rollison, D. E., Viarisio, D., Amorrortu, R. P., Gheit, T. & Tommasino, M. An emerging issue in oncogenic virology: the role of beta human papillomavirus types in the development of cutaneous squamous cell carcinoma. *J. Virol.* **93**, e01003–18 (2019).
63. Tummers, B. et al. The interferon-related developmental regulator 1 is used by human papillomavirus to suppress NFkappaB activation. *Nat. Commun.* **6**, 6537 (2015).
64. Schrofelbauer, B., Polley, S., Behar, M., Ghosh, G. & Hoffmann, A. NEMO ensures signaling specificity of the pleiotropic IKKbeta by directing its kinase activity toward IkappaBalpha. *Mol. Cell* **47**, 111–121 (2012).
65. Griffiths, D. A. et al. Merkel cell polyomavirus small T antigen targets the NEMO adaptor protein to disrupt inflammatory signaling. *J. Virol.* **87**, 13853–13867 (2013).
66. Cicchini, L. et al. High-risk human papillomavirus E7 alters host DNA methylome and represses HLA-E expression in human keratinocytes. *Sci. Rep.* **7**, 3633 (2017).
67. Lee, J. O. et al. Hepatitis B virus X protein represses E-cadherin expression via activation of DNA methyltransferase 1. *Oncogene* **24**, 6617–6625 (2005).
68. Kanarek, N. & Ben-Neriah, Y. Regulation of NF-kappaB by ubiquitination and degradation of the IkappaBs. *Immunological Rev.* **246**, 77–94 (2012).
69. Liu, C. et al. beta-Trcp couples beta-catenin phosphorylation-degradation and regulates Xenopus axis formation. *Proc. Natl Acad. Sci. USA* **96**, 6273–6278 (1999).
70. Busino, L. et al. Degradation of Cdc25A by beta-TrCP during S phase and in response to DNA damage. *Nature* **426**, 87–91 (2003).
71. Ison, C. A. & Hay, P. E. Validation of a simplified grading of Gram stained vaginal smears for use in genitourinary medicine clinics. *Sexually transmitted Infect.* **78**, 413–415 (2002).
72. Chawla, R., Bhalla, P., Chadha, S., Grover, S. & Garg, S. Comparison of Hay's criteria with Nugent's scoring system for diagnosis of bacterial vaginosis. *BioMed. Res. Int.* **2013**, 365194 (2013).
73. Bhujel, R., Mishra, S. K., Yadav, S. K., Bista, K. D. & Parajuli, K. Comparative study of Amsel's criteria and Nugent scoring for diagnosis of bacterial vaginosis in a tertiary care hospital, Nepal. *BMC Infect. Dis.* **21**, 825 (2021).
74. Sha, B. E. et al. Utility of Amsel criteria, Nugent score, and quantitative PCR for Gardnerella vaginalis, Mycoplasma hominis, and Lactobacillus spp. for diagnosis of bacterial vaginosis in human immunodeficiency virus-infected women. *J. Clin. Microbiol.* **43**, 4607–4612 (2005).
75. Arbeit, J. M., Howley, P. M. & Hanahan, D. Chronic estrogen-induced cervical and vaginal squamous carcinogenesis in human papillomavirus type 16 transgenic mice. *Proc. Natl Acad. Sci. USA* **93**, 2930–2935 (1996).
76. Elson, D. A. et al. Sensitivity of the cervical transformation zone to estrogen-induced squamous carcinogenesis. *Cancer Res.* **60**, 1267–1275 (2000).
77. Gerard, C. et al. Accurate Control of 17beta-estradiol long-term release increases reliability and reproducibility of preclinical animal studies. *J. mammary gland Biol. neoplasia* **22**, 1–11 (2017).
78. Goldman, J. M., Murr, A. S. & Cooper, R. L. The rodent estrous cycle: characterization of vaginal cytology and its utility in toxicological studies. *Birth defects Res. Part B, Dev. Reprod. Toxicol.* **80**, 84–97 (2007).
79. Wimmer-Scherr, C., et al. Comparison of fecal microbiota of horses suffering from atypical myopathy and healthy co-grazers. *Animals (Basel)* **11**, 506 (2021).
80. Cerri, S. et al. Effect of oral administration of omeprazole on the microbiota of the gastric glandular mucosa and feces of healthy horses. *J. Vet. Intern Med.* **34**, 2727–2737 (2020).
81. Fettweis, G. et al. RIP3 antagonizes a TSC2-mediated pro-survival pathway in glioblastoma cell death. *Biochimica et. Biophysica Acta Mol. Cell Res.* **1864**, 113–124 (2017).
82. Blomme, A. et al. Myoferlin regulates cellular lipid metabolism and promotes metastases in triple-negative breast cancer. *Oncogene* **36**, 2116–2130 (2017).
83. Lambert, P. F. et al. Using an immortalized cell line to study the HPV life cycle in organotypic "raft" cultures. *Methods Mol. Med.* **119**, 141–155 (2005).
84. Meuris, F. et al. The CXCL12/CXCR4 signaling pathway: a new susceptibility factor in human papillomavirus pathogenesis. *PLoS Pathog.* **12**, e1006039 (2016).
85. Nys, G., Cobraiville, G. & Fillet, M. Multidimensional performance assessment of micro pillar array column chromatography combined to ion mobility-mass spectrometry for proteome research. *Analytica Chim. Acta* **1086**, 1–13 (2019).
86. Herfs, M. et al. A dualistic model of primary anal canal adenocarcinoma with distinct cellular origins, etiologies, inflammatory microenvironments and mutational signatures: implications for personalised medicine. *Br. J. Cancer* **118**, 1302–1312 (2018).
87. Herfs, M. et al. A novel blueprint for 'top down' differentiation defines the cervical squamocolumnar junction during development, reproductive life, and neoplasia. *J. Pathol.* **229**, 460–468 (2013).
88. Herfs, M. et al. Transforming growth factor-beta1-mediated Slug and Snail transcription factor up-regulation reduces the density of Langerhans cells in epithelial metaplasia by affecting E-cadherin expression. *Am. J. Pathol.* **172**, 1391–1402 (2008).
89. Wang, X., Spandidos, A., Wang, H. & Seed, B. PrimerBank: a PCR primer database for quantitative gene expression analysis, 2012 update. *Nucleic Acids Res.* **40**, D1144–D1149 (2012).
90. Poirson, J. et al. Mapping the interactome of HPV E6 and E7 oncoproteins with the ubiquitin-proteasome system. *FEBS J.* **284**, 3171–3201 (2017).
91. Cassonnet, P. et al. Benchmarking a luciferase complementation assay for detecting protein complexes. *Nat. Methods* **8**, 990–992 (2011).
92. Nokin, M. J., et al. Methylglyoxal, a glycolysis side-product, induces Hsp90 glycation and YAP-mediated tumor growth and metastasis. *eLife* **5**, e19375 (2016).

Acknowledgements

We thank the Biobank of the University of Liege, the Laboratory of Clinical Microbiology as well as the GIGA-Immunohistochemistry, in vitro imaging, genomics and viral vectors facilities (University of Liege) for their assistance. We are also grateful to Dr Stephanie Gofflot, Dr Wouter Coppieters, Dr Emmanuel Di Valentin, Manon Deckers, Latifa Karim, Cecile Meex, Raphael Thonon, Kamilia El Kandoussi, and Nancy Rosiere for their technical assistance. We sincerely thank Prof Bernard Joris and Dr Ana Amoroso (Laboratory of Bacterial Physiology and Genetics, University of Liege), Prof Christine Jacobs-Wagner (Microbial Sciences Institute, Yale University) as well as Dr Olivier Peulen (Metastasis Research Laboratory, University of Liege) for helpful discussions. This work was supported in part by the University of Liege [Crédits Sectoriels de Recherche en Sciences de la Santé 2018-2020 (M.H.)], the Belgian Fund for Scientific Research [FNRS; MIS F.4520.20, CDR J.0088.21 (M.H.)], the Televie [PDR Televie 7.8507.19 (M.H.)], the Léon Frédéricq Foundation and the Seventh Framework Program for Research and Technological Development [European Commission: Infect-ERA 2015 (HPV-Motiva)]. C.P., T.L., C.R., and M.A. are Televie/FRIA fellows. A.L., D.B., and EloH are postdoctoral researchers. MH is a Research Associate at the FNRS.

Author contributions

M.H. designed the study; A.L., D.B., P.R., P.P., E.H., G.C., C.G., G.M., N.S., DomiB, EloH, C.P., T.L., C.R., M.A., P.H., and M.H. performed experiments; R.G. and P.D. collected retrospective clinical follow-up data; A.L., D.B., G.C., B.T., G.M., N.S., M.F., DomiB., G.D., J.-D.C., M.F., P.H., and M.H. interpreted the data; M.M., J.-C.T., G.S.-L., F.B., P.M., and P.D. provided resources; A.L., D.B., and M.H. generated the figures; M.H. wrote the manuscript. All authors discussed the results and commented on the manuscript.

Competing interests

The authors declare no competing interests.

Additional information

Supplementary information The online version contains supplementary material available at https://doi.org/10.1038/s41467-022-28724-8.

Correspondence and requests for materials should be addressed to Michael Herfs.

Peer review information *Nature Communications* thanks Robert Quinn, and the other, anonymous, reviewer(s) for their contribution to the peer review of this work. Peer reviewer reports are available.

Reprints and permission information is available at http://www.nature.com/reprints

Publisher's note Springer Nature remains neutral with regard to jurisdictional claims in published maps and institutional affiliations.

IVYSPRING INTERNATIONAL PUBLISHER

Theranostics

2023; 13(3): 1130-1149. doi: 10.7150/thno.78091

Research Paper

Human papillomavirus E6/E7 oncoproteins promote radiotherapy-mediated tumor suppression by globally hijacking host DNA damage repair

Diane Bruyere[1], Patrick Roncarati[1], Alizee Lebeau[1], Thomas Lerho[1], Florian Poulain[2], Elodie Hendrick[1], Charlotte Pilard[1], Celia Reynders[1], Marie Ancion[1], Margaux Luyckx[1], Michael Renard[1], Yves Jacob[3], Jean-Claude Twizere[4], Raphael Peiffer[5], Olivier Peulen[5], Philippe Delvenne[1,6], Pascale Hubert[1], Alison McBride[7], Nicolas Gillet[2], Murielle Masson[8], and Michael Herfs[1]✉

1. Laboratory of Experimental Pathology, GIGA-Cancer, University of Liege, 4000 Liege, Belgium.
2. Namur Research Institute for Life Sciences (NARILIS), Integrated Veterinary Research Unit (URVI), University of Namur, Namur, Belgium.
3. Unit of Molecular Genetics of RNA Viruses, UMR 3569, CNRS, Pasteur Institute, University of Paris Diderot, 75015 Paris, France.
4. Laboratory of Signaling and Protein Interactions, GIGA-Molecular Biology of Diseases, University of Liege, 4000 Liege, Belgium.
5. Metastasis Research Laboratory, GIGA-Cancer, University of Liege, 4000 Liege, Belgium.
6. Department of Pathology, University Hospital of Liege, 4000 Liege, Belgium.
7. Laboratory of Viral Diseases, National Institute of Allergy and Infectious Diseases, National Institutes of Health, Bethesda, MD, 20892, USA.
8. Biothechnology Superior School, UMR 7242, CNRS, University of Strasbourg, 67412 Illkirch, France.

✉ Corresponding author: Michael Herfs, PhD Laboratory of Experimental Pathology, GIGA-Cancer, B23 +4 University of Liege 4000 Liege Belgium Tel: (+32) 43664282 Email: M.Herfs@uliege.be

Received: 2022.08.17; Accepted: 2023.01.18; Published: 2023.01.31

Abstract

Rationale: Whatever the mucosa primary infected, HPV-positive cancers are traditionally associated with a favorable outcome, attributable to a high sensitivity to radiation therapy. However, the direct impact of viral E6/E7 oncoproteins on the intrinsic cellular radiosensitivity (and, globally, on host DNA repair) remains mostly speculative.

Methods: Using several isogenic cell models expressing HPV16 E6 and/or E7, the effect of viral oncoproteins on global DNA damage response was first investigated by *in vitro*/*in vivo* approaches. The binary interactome of each individual HPV oncoprotein with factors involved in the various host DNA damage/repair mechanisms was then precisely mapped by *Gaussia princeps* luciferase complementation assay (and validated by co-immunoprecipitation). The stability/half-life of protein targets for HPV E6 and/or E7 as well as their subcellular localizations were determined. At last, the host genome integrity following E6/E7 expression and the synergy between radiotherapy and compounds targeting DNA repair were analyzed.

Results: We first showed that the sole expression of one viral oncoprotein from HPV16 was able to significantly increase the sensitivity to irradiation of cells without affecting their basal viability parameters. In total, 10 novel targets (CHEK2, CLK2, CLK2/3, ERCC3, MNAT1, PER1, RMI1, RPA1, UVSSA and XRCC6) for E6 and 11 (ALKBH2, CHEK2, DNA2, DUT, ENDOV, ERCC3, PARP3, PMS1, PNKP, POLDIP2 and RBBP8) for E7 were identified. Importantly, not degraded following their interaction with E6 or E7, these proteins have been shown to be less linked to host DNA and to colocalize with HPV replication foci, denoting their crucial implication in viral life cycle. Finally, we found that E6/E7 oncoproteins globally jeopardize host genome integrity, increase the cellular sensitivity to DNA repair inhibitors and enhance their synergy with radiotherapy.

Conclusion: Taken together, our findings provide a molecular insight into the direct hijacking of host DNA damage/repair responses by HPV oncoproteins, demonstrate the significant impact of this phenomenon on both intrinsic cellular radiosensitivity and host DNA integrity and suggest novel connected therapeutic vulnerabilities.

Key words: human papillomavirus, DNA damage and repair, radiotherapy, protein-protein interactome.

Introduction

Although over 250 million doses of human papillomavirus (HPV) vaccine have already been distributed since its introduction 15 years ago, carcinogenic HPV genotypes (most notably HPV16) are still responsible for an estimated 690,000 cancers per year worldwide [1]. Diagnosed in the anogenital

and upper aero-digestive tracts, HPV-driven tumors are indisputably associated with a better outcome than their HPV-uninfected counterparts [2-6], which led to both the recent down-staging of patients with oropharyngeal HPV-positive squamous cell carcinoma (SCC) (AJCC, 8th edition) and the clinical evaluation of several de-intensification treatment strategies (e.g., reduced-dose radiotherapy) (for a review, see [7]). Whatever the primary site of infection, and despite the growing interest for targeted therapies or immune checkpoint inhibitors, the recommended first-line treatment modalities for HPV-related neoplasms still (in the large majority of cases) involves radiation therapy (fractionated exposure to 45-70 Gy), chemotherapy (most often with platinum-derived compounds) and surgical excision (when possible).

The main factors determining the success or failure of radiotherapy were first explained in the mid 70's by Prof. Rodney Withers in a seminal article entitled "The four R's of radiotherapy". The repopulation of surviving normal and tumor cells between dose fractions, redistribution of malignant cells in the G2/M cell cycle phase, reoxygenation of the hypoxic areas and repair of DNA damage induced by ionizing radiation were originally proposed. A few months later, the intrinsic radiosensitivity of irradiated cells was presented as the fifth "R". At last, a "6R" model has been recently suggested, adding the reactivation of immune responses to the five aforementioned R's [8]. In the context of HPV-positive cancers, three main parameters are commonly proposed to explain the favorable prognosis/ increased sensitivity to radiation therapy: the wild-type status of *TP53* [9], the elevated T-cell density detected within tumor microenvironment [10-12] and the low tumor hypoxia [13]. In parallel, data accumulated in the last few years indicate that HPV could also directly participate to this enhanced radiation sensitivity by disrupting DNA damage/ repair responses (particularly the canonical non-homologous end-joining, homologous recombination and Fanconi anemia DNA repair pathways) [14-17]. Still frequently disregarded by both clinicians and researchers, the primary goal of the virus is to complete its life cycle and not to promote carcinogenesis (which ultimately impedes its amplification and kills its host). To do so, and beside the requirement of sustaining keratinocyte proliferation, it becomes obvious that HPV must hijack the host signaling cascades to promote rapid repair and faithful replication of its genome. As a side effect, host DNA would become more vulnerable to the acquisition of genomic alterations, leading to (pre)cancer development. The molecular binding partners of viral oncoproteins involved in this process are, however, still mostly unknown. Of note, indirect mechanisms involving $p16^{ink4a}$ (a surrogate biomarker for HPV infection) or the defect of TGFβ signaling were also reported to explain the enhanced radiosensitivity of HPV-positive tumors. While the down-regulation of E3 ubiquitin ligase TRIP12 has been demonstrated to be essential in $p16^{ink4a}$-mediated repression of DNA damage/repair [18, 19], conflicting results exist regarding the HPV-TGFβ interplay and the subsequent miR-182-dependent inhibition of BRCA1, required for homologous recombination repair [20, 21].

Altogether, this context opens quite a few theoretical and translational questions. Could HPV-related "manipulation" of host DNA repair mechanisms represent the Achilles' heel of HPV-positive cancers? Are viral oncoproteins alone able to sensitize infected cells to irradiation-induced DNA single/double-strand breaks? Do E6 and E7 directly interact with key proteins involved in DNA damage repair pathways? Is the function, half-life and/or cellular localization of DNA repair proteins altered by viral oncoproteins? Could E6 and E7 oncoproteins enhance the sensitivity to DNA repair inhibitors and/or positively impact their synergy with radiotherapy? By using various *in vitro*/*in vivo* models as well as by mapping the interactome of HPV E6 and E7 oncoproteins with the different families of DNA repair proteins, the present study attempts to answer all these questions.

Materials and Methods

Human tissue specimens

A total of 59 oropharyngeal and 113 anal canal SCC were retrieved from pathology archives of the University Hospital of Liege (Belgium). Before selection, all cases were re-examined by experienced histopathologists. The paraffin-embedded specimens were processed and archived in the local Biobank throughout the project. For each specimen, the HPV status was determined by both immunohistochemistry (anti-$p16^{ink4a}$) and HPV DNA genotyping [Abbott RealTime High-Risk HPV assay (Abbott, Wiesbaden, Germany)]. The study was approved by the institutional review board at the University Hospital of Liege (#2021/25).

Cell lines and culture conditions

Eleven HPV-negative and 7 HPV-positive cell lines were maintained in Dulbecco's modified Eagle's medium (DMEM), Minimum Essential medium (MEM) or Roswell Park Memorial Institute (RPMI) 1640 medium (Gibco, Thermo Fisher Scientific, Waltham, MA, USA) supplemented with 10% fetal

calf serum and various additives. Precise cell culture conditions are detailed in Table S1. With the exception of U-2OS (osteosarcoma), HEK-293T (embryonic kidney) and HaCaT cells (immortalized keratinocytes), all cell lines were derived from the gynecologic or upper aerodigestive tracts. SiHa (HPV16), CaSki (HPV16), C4-II (HPV18), MDA-1483 (HPV18), HT-3 (HPV30), HeLa (HPV18), UPCI-SCC-154 (HPV16) as well as UPCI-SCC-40, UPCI-SCC-111, FaDu, SQ-20B, UD-SCC-1, CAL-27, CAL-33, BHY, A431, UPCI-SCC-036, UPCI-SCC-114 (HPV-negative) were obtained from ATCC or DSMZ (German collection of microorganisms and cell cultures). All cell lines used in this study have been regularly tested for potential mycoplasma contamination [MycoAlert Mycoplasma Detection kit (Lonza, Basel, Switzerland)] and were invariably found to be negative.

Isogenic cell models expressing HPV16 E6 and/or E7

HPV-negative malignant vulvar (A431), floor of mouth (UPCI-SCC-111) and osteosarcoma (U-2OS) cells (previously used as a model for studying HPV-related carcinogenesis [22, 23]) as well as immortalized/noncancerous keratinocytes (HaCaT) were stably transduced with HPV16 E6 and/or E7 or firefly luciferase (negative control) (GIGA-Viral Vectors, University of Liege). Using pSPAX2 (Addgene, Watertown, MA, USA), pLV-EF1a-IRES Luciferase plasmid (VectorBuilder, Chicago, USA), either empty or containing the coding sequence for HPV16 E6 or E7, was co-transfected with a VSV-G-encoding vector into Lenti-X 293T cells (Clontech, Mountain View, USA). Forty-eight and 72 h post-transfection, viral supernatants were collected, concentrated, purified and titrated (qPCR Lentivirus Titration kit; ABM, Richmond, Canada). Transduced cells were finally selected with 100 µg/ml hygromycin B or 10 µg/ml blasticidin (InvivoGen, San Diego, CA, USA).

In vivo mouse irradiation model

A431 Luc or A431 E6E7 cells ($7.5x10^5$ in 150-300 µl of DMEM) were subcutaneously injected (left flank) in Nude mice aged 4-6 weeks (n = 13 per condition). Throughout the experiment, tumor size was monitored every 2-3 days with a digital caliper (Thermo Fisher Scientific). When tumor volume [π /6 x (length × $width^2$)] reached 100-200 mm^3, a unique dose of 6 Gy was administrated using a small animal irradiator (X-RAD 225Cx; Precision X-Ray, North Branford, CT, USA). At day 9 after irradiation, the treated animals were anesthetized and 20 mg/kg luciferin (Promega) was injected intraperitoneally. Ten minutes later, mice were imaged using an IVIS® Lumina III *in vivo* Imaging System (PerkinElmer, Waltham, MA, USA). For ethical reasons, mice were euthanized when the average tumor volume exceeded 1000 mm^3 in the control group. All animals were purchased from Janvier Labs (Le Genest-Saint-Isle, France) and the authors strictly complied to the ethical recommendations established by the Federation of European Laboratory Animal Sciences Associations (FELASA). The procedures were initially reviewed and approved by the local ethics committee (#19-2109).

Immunohistochemistry and immunostaining assessment

Immunohistochemical experiments were performed as previously described [2, 24-26]. Briefly, slides were first deparaffinized in xylene, rehydrated in graded alcohol and endogenous peroxidases were inhibited using 4.5% H_2O_2 in methanol for 5 min. Antigens were retrieved in 10 mM citrate buffer (pH6) for 23 min at 100 °C. Before the primary reaction (1 h at room temperature), non-specific antigens were blocked using serum-free protein block reagent (Dako, Glostrup, Denmark) for 10 min. The following primary antibodies were used: anti-$p16^{ink4a}$ (1/100, ENZ-ABS377-0100, Enzo Life Sciences, Farmingdale, NY, USA) and anti-γH2AX (1/100, clone 20E3, Cell Signaling Technology, Danvers, MA, USA). For the immunoperoxidase staining, the rabbit EnVision detection kit (Dako) was used and positive cells were visualized using SignalStain DAB Substrate kit (Cell Signaling Technology).

All immunolabelled tissues were evaluated independently by two histopathologists. As previously described [2], $p16^{ink4a}$ staining was considered as positive when >75% cancer cells strongly expressed this surrogate biomarker for HPV infection. The number of γH2AX-positive tumor cells per mm^2 was precisely determined using QuPath 0.2.0 software for digital pathology image analysis (computerized counting) [27].

TP53 mutation analysis

Genomic DNA was extracted from cultured cells using the NucleoSpin Tissue kit (Macherey-Nagel, Düren, Germany). Exons 2 to 11 of *TP53* were amplified by classical PCR. The primer sequences were previously described [24]. The PCR products were then purified and sequenced using an ABI 3700 automated sequencer (Applied Biosystems, Foster City, CA, USA) (GIGA-Genomics platform, University of Liege).

Gene expression analysis (using public dataset)

The expression levels of *ALKBH2, BRCA1, BRCA2, CHEK2, CLK2, DNA2, DUT, ENDOV, ERCC3,*

H2AX, MNAT1, PARP3, PER1, PMS1, PNKP, POLDIP2, RAD51, RBBP8, RMI1, RPA1, UVSSA, XRCC1, XRCC2, XRCC3, XRCC4, XRCC5 and *XRCC6* in head and neck cancers were evaluated using The Cancer Genome Atlas (TCGA) public dataset through the cBioPortal interface [28]. This published dataset was also used to run a gene set enrichment analysis (GSEA) using both the KEGG pathways and GO database. GSEA was performed using RStudio v1.4.1 (clusterProfiler 4.0 package) [29, 30]. In parallel, data related to the overall survival were retrieved. All samples were separated according to their HPV status.

Quantitative reverse transcription PCR (RT-qPCR)

Total RNA was extracted and purified from cultured cells using the NucleoSpin RNA isolation kit (Macherey-Nagel). One µg was then reverse transcribed using RevertAid Reverse Transcriptase and oligodT primers (Thermo Fischer Scientific). qPCR experiments (QuantStudio 3, Applied Biosystems) were performed using the FastStart Universal SYBR Green Master mix (Roche, Basel, Switzerland) and the following primers sequences: HPV16 E6 forward: 5'-TGG AAT CTT TGC TTT TTG TCC-3'; E6 reverse: 5'-CTG CGA CGT GAG GTG TAT TAA C-3'; HPV16 E7 forward: 5'-GGT TAC AAT ATT GTA ATG GGC TC-3'; E7 reverse: 5'-AGC TCA GAG GAGGAG GAT GAA-3'; GAPDH forward: 5'-ACC AGG TGG TCT CCT CTG AC-3'; GAPDH reverse: 5'-TGC TGT AGC CAA ATT GGT TG-3'. Each experiment was performed in triplicate and normalized to the amount of GAPDH mRNA from the same sample.

Cell Proliferation

Cells were seeded in order to reach ~10% confluence. After cell adhesion, 24-well plates were incubated for 7 days in the IncuCyte S3 Live-Cell Analysis System (Sartorius, Göttingen, Germany). Every 12 h, pictures were taken (4 fields per well). Collected data were finally analyzed using the IncuCyte S3 software.

Apoptosis

The percentage of apoptotic cells was determined by flow cytometry (FACSCalibur flow cytometer, BD Biosciences, Franklin Lakes, NJ, USA), using annexin V-FITC and propidium iodide, according to the manufacturer's recommendations (BD Biosciences).

Cell cycle analysis

Cells were harvested using trypsin-EDTA solution, washed with PBS and fixed with iced cold 70% ethanol overnight at -20 °C. Fixed cells were then washed once with PBS and incubated for 30 min at room temperature with a solution containing RNase A (50 µg/ml, Macherey-Nagel, Germany) and propidium iodide (50 µg/ml, Invitrogen, Carlsbad, CA, USA). Cells were finally analyzed by flow cytometry (FACSCalibur flow cytometer, BD Biosciences).

Neutral comet assay

Cells were first irradiated with 40 Gy (Gammacell 40 Exactor, Best Theratronics, Vancouver, Canada) at room temperature and incubated for the indicated times (0 h, 1 h, 3 h and 6 h) at 37 °C in order to allow for DNA repair. Cells were then collected and processed for neutral comet assay as extensively described previously [31]. Briefly, OxiSelect comet slides (3-well slides, Cell Biolabs, San Diego, CA, USA) were used and cell lysis was performed overnight at 37 °C in a buffer containing 2% sarkosyl, 0.5M Na_2EDTA and 0.5 mg/ml proteinase K (pH 8.0). Electrophoresis was conducted for 25 min at 0.6 V/cm in a solution containing 90 mM Tris, 90 mM boric acid and 2 mM Na_2EDTA (pH 8.5). Following an incubation with Vista Green DNA dye for 20 min, comets were detected, photographed (6 fields per well) using a fluorescence microscope (Vanox AH BT3, Olympus, Tokyo, Japan) and quantified (CometScore 2.0 software). Tail length was used to estimate the degree of DNA damage (double-strand breaks) in each condition.

Cytokinesis-block micronucleus assay

Plated on a glass coverslip, 5 x 10^4 cancer cells transduced with HPV16 E6 and/or E7 or firefly luciferase (control) were exposed to 0, 2 or 4 Gy irradiation. After a 4 h recovery, cytochalasin B (3 µg/ml, Sigma Aldrich), a potent cytokinesis inhibitor, was added to the media for 18 h. The cells were then quickly washed with PBS, fixed with 4% paraformaldehyde (15 min at room temperature) and stained with 4',6-diamidino-2-phenylindole (DAPI). Micronucleus frequency was finally determined in once-divided binucleated cells according to previously described criteria [32].

Clonogenic growth analysis

HPV-negative and -positive cells were seeded in 6-well plates at a density comprised between 250 and 2,000 cells per well, depending on their growth rate. After 24h, cells were irradiated with 0, 1, 2, 4 or 6 Gy using a Gammacell 40 Exactor (Best Theratronics) and incubated for 10 days at 37 °C in a humidified 5% CO_2 atmosphere. Plates were then washed in PBS, fixed and colored for 45 min using a solution containing 5% glutaraldehyde (Acros Organics, Thermo Fischer

scientific) and 0,5% Crystal violet (Sigma-Aldrich, Saint Louis, MI, USA). After a washing step with deionized water, plates were dried, scanned (Epson Perfection V500 PHOTO, Epson, Nagano, Japan) and quantified using the ColonyArea ImageJ plugin (ImageJ software, National Institute of Health, Bethesda, MD, USA). Instead of the traditional manual counting, this standardized/computerized approach allows to determine the percentage of area covered by cell colonies [33].

Plasmid library generation

Both derived from pCiNeo vector, pSpica-N1 and pSpica-N2 plasmid vectors express Gluc1 and Gluc2, respectively. These complementary fragments of the *Gaussia princeps* luciferase are linked to the N-terminal ends of the proteins of interest through a 20-amino acid flexible hinge region. pSpica-N2 vectors expressing E6 or E7 from different high-risk (carcinogenic) HPV genotypes (HPV16, 18, 33 and 39) were previously generated [34]. Open reading frames (ORFs) encoding for proteins involved in DNA repair mechanisms were obtained from the human ORFeome collections v7.1 and 8.1 (Dana-Farber Cancer Institute, Boston, USA). Initially contained into a pDONR223 entry vector, the ORFs were transferred into the pSpica-N1 destination vector *via* Gateway cloning. In order to verify both the cloning step and the accuracy of all transferred sequences, resulting plasmids were sequenced (Sanger sequencing, GIGA-Genomics platform, University of Liege) using the following forward primer: 5'-CAG CTC TTA AGG CTA GAG TAC-3'. A library of 200 pSpica-N1 plasmids coding for 179 DNA damage and repair proteins (and 21 isoforms) was generated (Table S2).

Gaussia Princeps luciferase Complementation Assay (GPCA)

Twenty-four hours before transfection, $3x10^4$ HEK-293T cells were seeded per well of a Costar flat bottom white 96-well plate (Corning Life Sciences, Amsterdam, The Netherlands). Cells were transfected with 100 ng pSpica-N2-HPV E6 or E7 and 100 ng pSpica-N1 (from the DNA repair library) using PEImax (Polysciences, Warrington, PA, USA). Twenty-four hours post-transfection, cells were washed and then incubated for 30 min at room temperature with the Renilla lysis buffer (E2820, Promega, Madison, WI, USA). After injection of 50 µl of luciferase substrate reagent in each well, the luciferase activity was measured during 10 s using a Centro LB960 microplate luminometer (Berthold Technologies, Bad Wildbad, Germany). As previously described [34, 35], results were expressed as relative luminescence units (RLU) or as a normalized luminescence ratio (NLR). NLR was calculated by dividing the RLU by the sum of controls. NLR= (Gluc1-A and Gluc2-B) / [(Gluc1-empty and Gluc2-B) + (Gluc1-A and Gluc2-empty)].

Co-immunoprecipitation (co-IP)

HPV16 E6 or E7 sequence was first transferred into the pCineo-3xFLAG vector, allowing the expression of a 3xFLAG tag at the N-terminal end of the viral oncoproteins. The day before transfection, $4x10^5$ HEK-293T cells per well of a 6-well plate were seeded. Cells were transfected with 1.5 µg pCineo-3xFLAG (HPV16 E6, HPV16 E7 or empty) and 1.5 µg pSpica-N1 from our library using PEImax (Polysciences). Twenty-four hours post-transfection, cells were harvested and incubated for 30 min on ice in 100 µl lysis buffer (50 mM Tris-HCl pH7.4, 150 mM NaCl, 1 mM EDTA, 1%Triton X-100 and proteases inhibitors). After a centrifugation step (18,900 g for 30 min at 4 °C), 96 µl collected supernatant was incubated overnight with 30 µl anti-Flag M2 Magnetic Beads (Sigma-Aldrich). The 4 remaining µl represent the total fraction of the extraction. Total and immunoprecipitated proteins were analyzed by western blotting. The nitrocellulose membranes were incubated overnight at 4 °C with anti-*Gaussia luciferase* antibody (E8023, New England Biolabs, Ipswich, MA, USA). After several washings, the membranes were incubated for 1 h at room temperature with a secondary goat anti-rabbit antibody (G21234, Invitrogen). The protein bands were finally revealed using a chemiluminescence system (Pierce ECL substrate, Thermo Fisher Scientific).

Subcellular protein fractionation and western blotting

The harvested cells were first incubated in cytoplasmic buffer (HEPES pH 7.4 10 mM, KCl 10 mM, $MgCl_2$ 2 mM, EDTA 0.1 mM, NP-40 0.2%, DTT 1 mM and protease inhibitors) for 30 s. After centrifugation (4,000 g for 5 min at 4 °C), the cytoplasmic fraction (supernatant) was collected. The pellet was then washed 5 times (washing buffer: HEPES pH 7.4 10 mM, KCl 20 mM, $MgCl_2$ 2 mM, EDTA 0.1 mM, DTT 1 mM and protease inhibitors) before being lysed in buffer B (EDTA 3 mM, EGTA 0.2 mM, DTT 1 mM and protease inhibitors) for 30 min. The fraction corresponding to the nucleic acid-free proteins was collected after centrifugation (320 g for 7 min at 4 °C). Finally, the proteins linked to the chromatin were isolated after sonication (30 s) in Laemmli buffer (Tris-HCl pH8 62.5 mM, SDS 2%, glycerol 10% and protease inhibitors) at 4 °C. After quantification (BCA protein assay; Pierce, Rockford,

IL, USA), 30 µg of proteins were separated by electrophoresis (SDS-PAGE) and transferred onto PVDF membranes (Roche), that were blocked with 5% nonfat milk in TBS-tween 0.1%, before being incubated overnight at 4 °C with the primary antibodies (listed in Table S3). The membranes were then incubated with an anti-rabbit (G21234, Invitrogen) or anti-mouse (P0260, Dako) secondary antibody for 1 h. The protein bands were detected using an enhanced chemiluminescence system (Pierce ECL substrate, Thermo Fisher Scientific) and finally quantified by densitometric analysis (ImageJ software). To validate the fractionation method, anti-MEK2 (9125S; Cell Signaling), anti-YY1 (sc-7341; Santa Cruz Biotechnology, Dallas, TX, USA) and anti-HDAC2 (sc-9959; Santa Cruz Biotechnology) antibodies were used (positive controls).

Cycloheximide chase assay

HaCaT cells transduced with HPV16 E6, E7 or firefly luciferase (negative control) were treated with 100 µM Cycloheximide (Sigma Aldrich). The proteins were isolated in SDS buffer (SDS 1%, Tris-HCl pH 7.5 40 mM, EDTA 1 mM, protease inhibitors) at different time points (up to 24 h) and then quantified (BCA protein assay; Pierce). The level of given proteins was finally determined by western blot (see Table S3 for primary antibody specificities). Anti-actin (A5441; Sigma-Aldrich) and anti-HSC-70 (sc-7298; Santa Cruz Biotechnology) antibodies were used for normalization.

Recircularization of HPV16 genome

Full-length HPV16 DNA was first released from the pUC19 plasmid using FastDigest BamHI restriction enzyme, according to the manufacturer's instructions (Thermo Fisher Scientific). The linear genome was then recircularized by incubating 10 µg of the digested plasmid with 400 U of T4 ligase, 10X ligation reaction buffer and RNase free water (New England Biolabs, Ipswich, MA, USA) overnight at 16 °C. Finally, DNA was precipitated (NaCl 5 M and isopropanol at -20 °C), centrifuged (16 000 g for 30 min at 4 °C) and resuspended in TE buffer (Tris 10 mM, EDTA 1 mM).

HPV16 E1 and E2 transductions and immunofluorescence

HPV-negative malignant vulvar (A431) cells were stably transduced with HA-tagged HPV16 E1 and 3xFlag-tagged HPV16 E2 or mCherry (negative control) (GIGA-Viral Vectors, University of Liege), as described above (see Isogenic cell models expressing HPV16 E6 and/or E7). Given that the constitutive expression of E1 and E2 proteins is lethal for the cells, we used the Double-Floxed Inverted Open reading frame (DIO) technology to invert the Open Reading Frame (ORF). Therefore, the E1 and E2 genes are not expressed unless a Cre treatment is applied to the cell culture. Transduced cells were selected with 133 µg/ml hygromycin B or 0.33 µg/ml puromycin (InvivoGen).

Coverslips were coated with 0.1% poly-l-lysine (15 min at room temperature), sterilized using UV light and distributed in 6-well plates. Then, $1.25x10^5$ E1/E2-transduced cells were seeded per well. After 24 h, cells were transiently transfected with 0.5 µg of the recircularized HPV16 genome using FuGene 6 (Roche), according to the manufacturer's instructions. Six hours later, a non-integrative Cre lentivirus was added to the cell culture in order to induce the expression of HPV16 E1 and E2, by flipping the ORF to the right direction. Thirty-six hours after the Cre induction, the cells were quickly washed with PBS, fixed with 4% paraformaldehyde (15 min at room temperature), permeabilized with PBS-0.1% triton X-100 (15 min) and blocked with an animal-free blocking solution (cell signaling, 20 min). The cells were then incubated with the primary antibodies overnight at 4 °C [for additional information (e.g., clone numbers, dilutions), see Table S3]. After a washing step (PBS), the cells were incubated with conjugated (AlexaFluor 488 or AlexaFluor 647) anti-mouse and anti-rabbit secondary antibodies (1/1000) for 1 h at room temperature. Where indicated, 1h before the fixation step, the cells were treated with 10 µM 5-ethynyl-2'-deoxyuridine (EdU) (Click-iT™ Plus EdU Cell Proliferation Kit for Imaging, Thermo Fisher Scientific), a thymidine analog which is incorporated into DNA and used to evaluate DNA synthesis. EdU staining was performed according manufacturer's instructions. Finally, the coverslips were washed (PBS), mounted with Fluoromount-G™ Mounting Medium (Thermo Fischer Scientific) and visualized using a Nikon Eclispe Ti microscope (Magnification: X1000). Colocalization analysis was performed using the JACoP ImageJ plugin (ImageJ software).

Whole genome sequencing

HPV16 E6E7 isogenic cell pairs generated from immortalized keratinocytes (HaCaT) were grown (at 37 °C in a humidified 5% CO_2 atmosphere) until a ~80% confluence was reached. The cell culture medium and supplements are detailed in Table S1. At each passage, the cells were detached by adding 0.25% trypsin-EDTA (Gibco), counted and 1×10^6 cells were seeded into T75 flasks. At passage (P) 0, 10 and 20, expanded cells were harvested and genomic DNA was extracted using NucleoSpin Tissue kit (Macherey Nagel, Düren, Germany). DNA quantification

[Quant-iT PicoGreen dsDNA Kit (Invitrogen)], library preparation (Illumina DNA PCR-Free Library Prep Kit using 25 ng DNA) and quantification/ normalization [KAPA Library Quantification Kit (KapaBiosystems, Wilmington, MA, USA)] were then performed at the GIGA-Genomics platform (University of Liege). Sequencing (30X coverage) was conducted on the Illumina NovaSeq6000 platform (PE150 mode). Sequencing reads were aligned to the reference human genome (GRCh38) using the Burrows-Wheeler Alignment tool, with "bwa mem" settings [36]. Bam files were formulated using the set of utilities SAMtools.

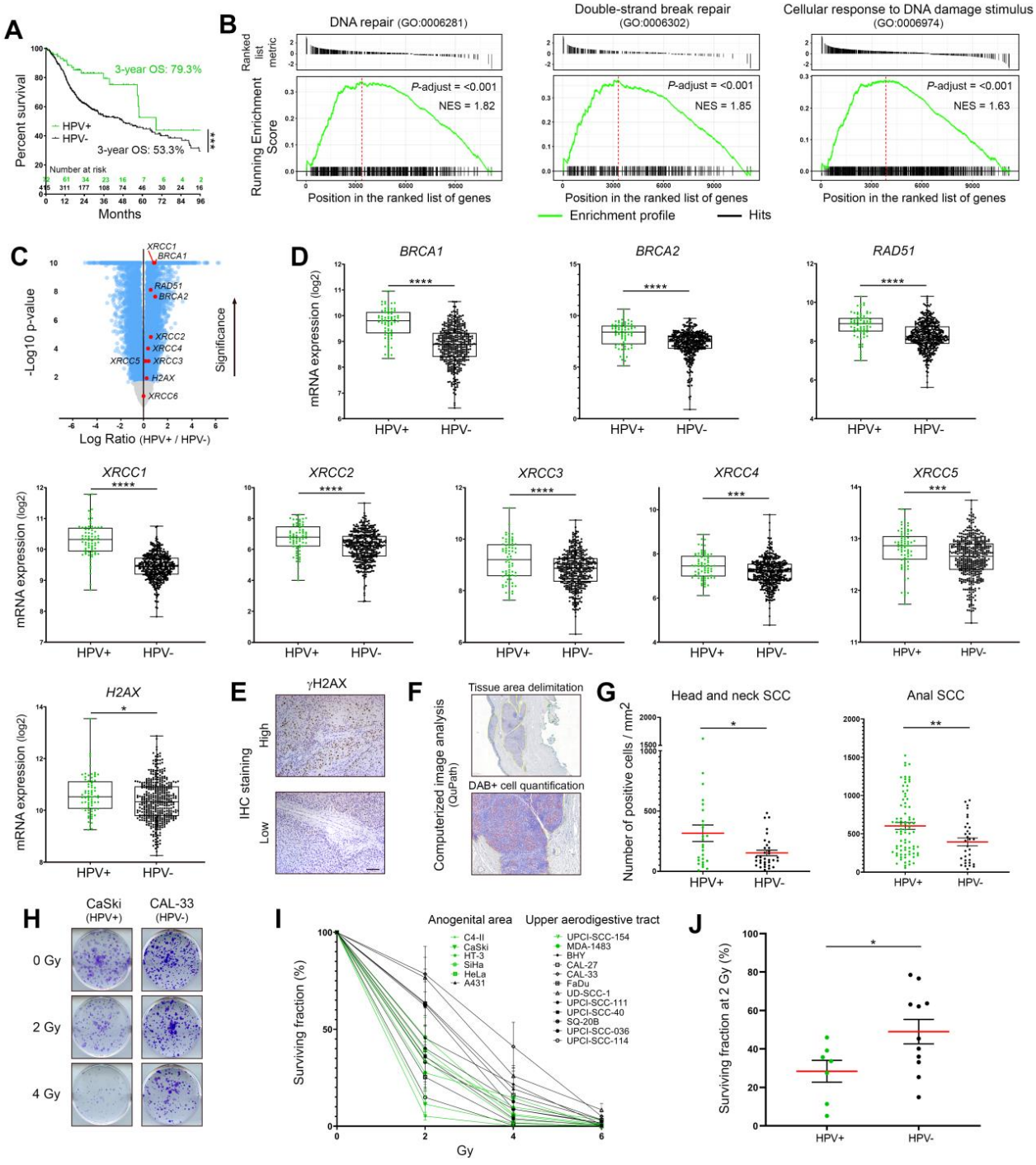

Figure 1. Expression profiles of DNA damage response factors and radiosensitivity of HPV-negative and -positive cancers. (A) Kaplan-Meier estimates of overall survival (OS) according to the HPV status (positive: n = 72; negative: n = 415). The TCGA dataset for head and neck neoplasms was used. **(B)** GSEA analyses of differentially expressed genes in HPV-positive *versus* HPV-negative tumors. The published dataset for head and neck tumors (TCGA) was used. NES: normalized enrichment score with adjusted *p*-value for each enrichment plots. **(C)** Volcano plot (x-axis: $\log_2$ HPV+/HPV- ratio; y-axis: $-\log_{10}$ *p*-value) showing the genes differentially expressed in HPV-positive SCC compared to their uninfected counterparts (blue dots, cut-off: $p < 0.01$). Standard DNA damage response biomarkers are highlighted in red. **(D)** *BRCA1*, *BRCA2*, *RAD51*, *XRCC1* to *5* and *H2AX* expression levels in head and neck cancers according to the HPV status. **(E)** Representative pictures of SCC displaying a high or low γH2AX expression. **(F)** Illustration of the computerized DAB-positive cell quantification (QuPath). **(G)** γH2AX-expressing cells were detected in each cancer tissue specimen (oropharyngeal or anal SCC) and the number of positive cells was reported to tumor area (mm^2). The mean (in red)

± SEM is shown. **(H)** Representative pictures (at day 10 post-irradiation) of crystal violet-stained CaSki (HPV16) and CAL-33 (HPV-negative) cell colonies irradiated with 0, 2 or 4 Gy. **(I)** Percentage of area covered by cell colonies from HPV-negative (black) and HPV-positive (green) cell lines following treatment with growing doses of irradiation (0-6 Gy). For each cell line, the non-irradiated condition (0 Gy) was used as control and set to 100%. Results represent the means ± SEM of at least three independent experiments. **(J)** Clonogenic growth analysis data at 2 Gy for each analyzed cell line. The means of at least three independent experiments are shown. Results were separated into two groups based on the HPV status of cancer cells. The scale bar represents 100 µm. Asterisks indicate statistically significant differences (*$p < 0.05$, **$p < 0.01$, ***$p < 0.001$, ****$p < 0.0001$). *P* values were determined using an unpaired t-test (D, G, J).

Variant calling and mutational signature analysis

Genomic variants have been assessed/detected using the open-source Strelka2 software, with default settings [37]. Both P10 and P20 samples were compared to the corresponding P0 read alignment sample. Only single nucleotide polymorphisms (SNPs) and insertions/deletions (InDels) filtered by Strelka2's empirical variant scoring (EVS) model were selected for both absolute/relative genomic alteration quantifications and mutational signatures analysis. The assignment of distinct mutational signatures reported in the Catalogue of Somatic Mutations in Cancer (COSMIC v3.3, June 2022) was performed using the SigProfilerExtractor package [38].

Drug response curves

Potent/selective inhibitors of PARP1/2 (Niraparib and Veliparib), RAD51 (RI-1), homology-dependent DNA repair (YU238259) and DNA topoisomerase I (Camptothecin) were purchased from Selleckchem (Houston, TX, USA). For IC_{50} determination, eleven dilutions of each compound were tested. The cells were seeded at 3,000 (A431), 5,000 (HaCaT) or 8,000 (UPCI-SCC-111) cells per well in 96-well plates containing working dilution of each DNA repair inhibitor and incubated for 72 h at 37 °C. Cell viability was assessed by MTT proliferation assay (Roche). The individual IC_{50} values of each drug against the HPV E6E7 isogenic cell pair were calculated using nonlinear regression analysis (GraphPad Prism 8 software, San Diego, CA, USA).

Combination treatments and synergy quantification

Both control and E6E7-trasnduced HaCaT cells (5,000 cells per well in 96-well plates) were exposed to growing doses of irradiation (0, 2, 4, 6, 8, 10 Gy) and/or to different concentrations (lower than IC50) of Niraparib, Veliparib, RI-1, Camptothecin or YU238259. After 72 h, cell viability was assessed by MTT proliferation assay (Roche). Synergy between radiotherapy and each DNA repair inhibitor was evaluated according to the Zero Interaction Potency (ZIP) method and using the open-source SynergyFinder 3.0 software [39, 40].

Statistical analysis

Statistical significance between 2 or more groups/conditions was assessed using GraphPad Prism 8 software (San Diego, CA, USA). Normal distribution was determined by both the skewness score and a D'Agostino and Pearson normality test. The outlier identification was performed using the ROUT method, with a Q=5% [41]. When two groups needed comparison, an unpaired t-test was performed whereas when more than two groups or conditions were compared, a one-way ANOVA was applied (followed by a Bonferroni post-test or by Dunnett's multiple comparison test). The comparison of cell cycle profiles (G1, S, G2/M) between independent groups was performed using a χ^2 test. *$p < 0.05$, **$p < 0.01$, ***$p < 0.001$ and ****p < 0.0001.

Results

HPV-positive cancers highly express DNA damage response factors and display an elevated sensitivity to radiation therapy

By using the TCGA public dataset for head and neck SCC, both the overall survival and the mRNA levels of the most frequently used DNA damage/repair biomarkers (BRCA1, BRCA2, RAD51, XRCC1 to 6 and H2AX) were first assessed. A pathway enrichment analysis (GSEA) was also performed. All collected data were separated according to the HPV status (positive: n = 72; negative: n = 415). As expected, [and reported in previous publications [4, 5], patients with HPV-positive neoplasms were associated with a favorable outcome (Figure 1A). Interestingly, GSEA analysis revealed the significant enrichments of various gene signatures directly related to DNA damage/repair mechanisms in HPV-positive cancers compared to their HPV-negative counterparts (Figure 1B and Table S4). Many other gene sets, secondarily linked to DNA repair/maintenance (e.g., DNA helicase activities, cell cycle checkpoints…) have also been found to be enriched in viral-related neoplasms (Table S4). Supporting these results, with the exception of XRCC6, all genes coding for "classical" biomarkers of DNA repair activation were significantly more expressed in HPV-related cancers (Figure 1C-D). The protein level of phosphorylated H2AX on its serine 139 [active form, also called γH2AX (sensitive marker of DNA double-strand breaks)] was also analyzed by immunohistochemistry and a similar significant up-regulation was detected in both anal and oropharyngeal HPV-driven tumors (Figure 1E-G). Clonogenic growth analyses were then performed to determine the radiosensitivity of many HPV-negative (n = 11) and -positive (n = 7) cell lines

from various origins (uterine cervix, vulva, head and neck). Ten days after being exposed to growing doses of irradiation (ranging from 0 to 6 Gy), the percentage of area covered by cell colonies was precisely determined by computerized counting. As shown in Figure 1H-J, despite some degree of heterogeneity within the two groups, overall, HPV-positive cells were significantly more radiosensitive than their HPV-unrelated counterparts. Containing about 600 copies of HPV16 per cell, it is interesting to notice that CaSki has been shown to be especially sensitive to radiation therapy (Figure 1H-I).

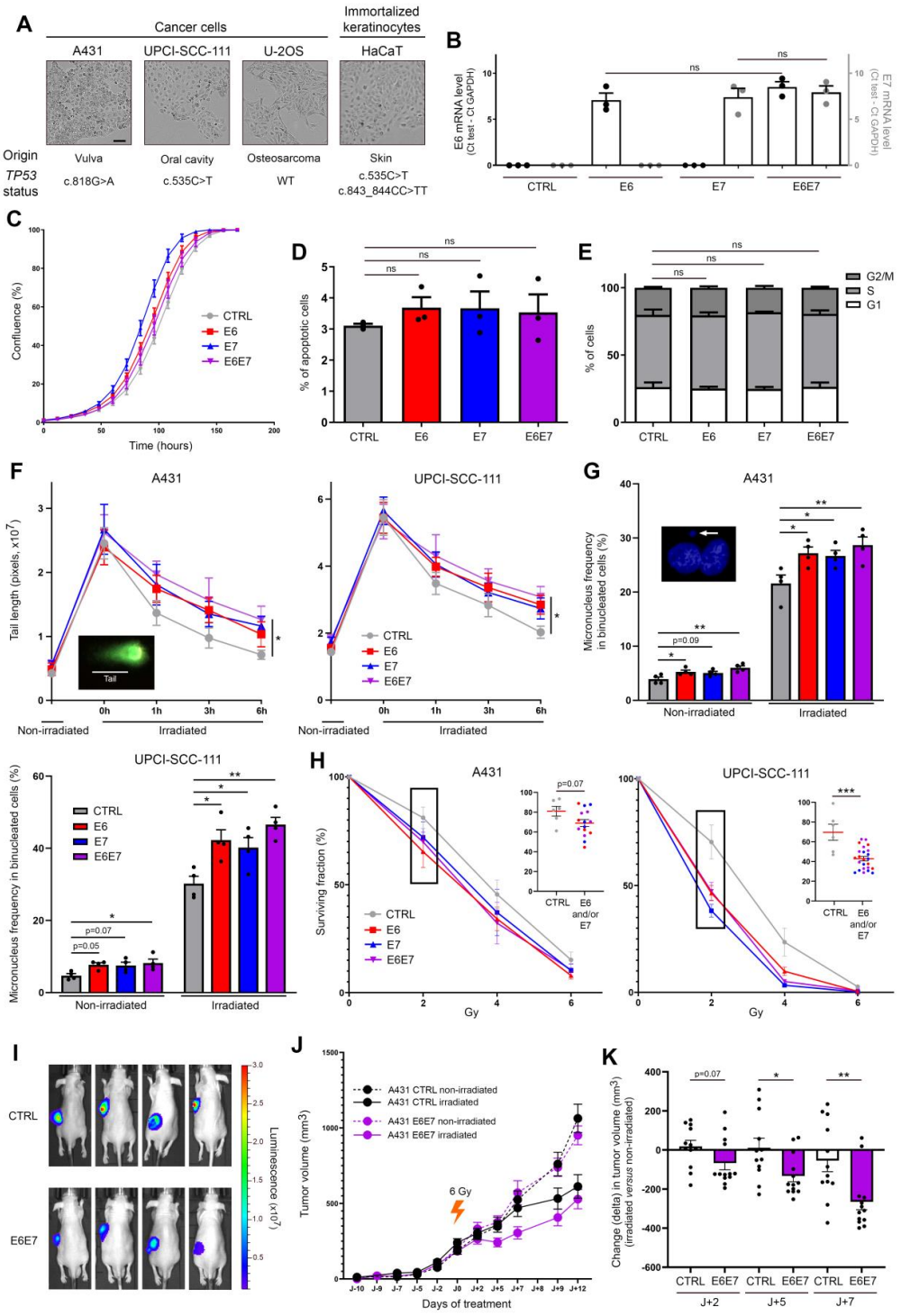

Figure 2. E6 and E7 viral oncoproteins increase cellular sensitivity to gamma irradiation. (A) Optical phase-contrast microscopy pictures of the cell lines used for the generation of isogenic models expressing HPV16 E6 and/or E7. The origin as well as the *TP53* mutation status (determined by DNA sequencing) of each cell line are also mentioned. **(B)** The mRNA level of HPV16 E6 (black dots, left y-axis) and/or E7 (grey dots, right y-axis) was determined by RT-qPCR in transduced A431 cells. No significant difference was observed between conditions. The proliferation **(C)**, apoptosis **(D)** and cell cycle **(E)** of A431 cells stably transfected or not with HPV16 E6 and/or E7 was assessed using the IncuCyte live cell analyzing system, annexin V-propidium iodide staining assay and propidium iodide incorporation, respectively. **(F)** Evaluation of DNA double-strand break repair by neutral comet assay. HPV16 E6 and/or E7-transduced A431 and UPCI-SCC-111 cell were exposed to 40 Gy irradiation. At different time points following irradiation (up to 6h), cells were collected and processed for neutral comet assay. To estimate the degree of DNA damage (double-strand breaks), the length of at least 30 comet's tails was measured in each condition. **(G)** Micronucleus frequencies in transduced A431 and

UPCI-SCC-111 cells at basal condition and following irradiation (4 Gy). For each independent experiment (n = 4), the presence of micronuclei was assessed in 250 binucleated cells. **(H)** Clonogenic growth analyses of transduced A431 and UPCI-SCC-111 cells following treatment with increasing doses of irradiation (0-6 Gy). At day 10, the percentage of area covered by cell colonies was determined by computerized counting (ColonyArea ImageJ plugin). For each cell line, the non-irradiated condition (0 Gy) was used as control and set to 100%. Results represent the means ± SEM of at least three independent experiments. Each individual data point at 2 Gy are also shown. **(I)** Representative bioluminescence images (at day 9 after irradiation) of A431 (CTRL/Luc and E6E7-transduced) tumor-bearing mice. **(J)** A431 Luc or A431 E6E7 cancer cells were subcutaneously injected in Nude mice. Tumor-bearing mice were then treated or not with a unique dose of 6 Gy. The mean tumor volumes ± SEM are represented. **(H)** Change (delta) in tumor volume between irradiated tumors and their relevant non-irradiated controls. The scale bars represent 100 µm. Asterisks indicate statistically significant differences (*$p < 0.05$, **$p < 0.01$, ***$p < 0.001$, **** $p < 0.0001$). ns: not significant. *P* values were determined using an ordinary one-way ANOVA (B), one-way ANOVA followed by a Dunnett's multiple comparison post-test (D, F, G), χ^2 test (E) and unpaired t-test (H, K).

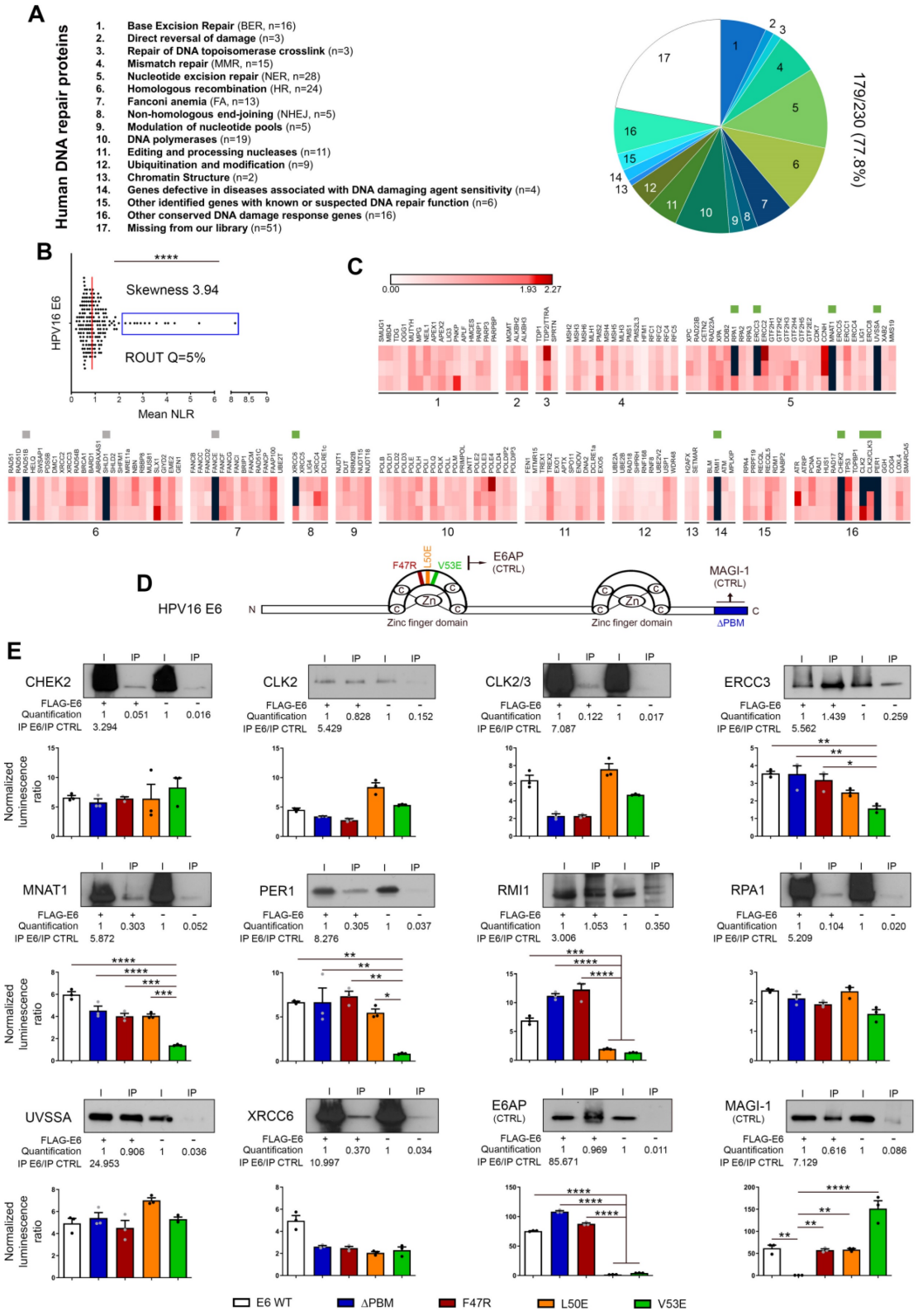

Figure 3. Bindings of HPV16 E6 with DNA damage/repair proteins: from large-scale screening to validation/characterization. (A) Pie chart representation of the DNA repair library generated from ORFs contained in the human ORFeome collections v7.1 and 8. According to the Human DNA Repair Gene Database, the 179-cDNA encoding for unique

proteins were divided into 16 sub-families. In total, about 80% (179/230, 77.8%) of the entire DNA damage/repair system is represented in the present library. **(B)** Scatter plot of the mean NLR values obtained by GPCA when the library was screened for direct interactions with E6 from HPV16. Confirmed by the skewness score of 3.94, the collected data were not normally distributed and outlier luminescence values (blue rectangle), representing potential interacting pairs, were detected using the ROUT method (with Q=5%). **(C)** Heatmap representing the NLR scores of each protein from the library tested for potential interaction with HPV16 E6. The black blocks represent values above the threshold set for outliers. Green and grey squares represent proteins identified as outliers and confirmed or not (false-positive) by co-IP, respectively. Three biological replicates were performed with each pSPICA-N1 plasmid of the library. The names of each family of DNA repair proteins are listed in the part A of the Figure. **(D)** Schematic representation of the 158 amino acids constituting HPV 16 E6 oncoprotein. In color, the parts that were either truncated (ΔPBM, blue) or mutated (F47R, red; L50E, orange and V53E, green) for the experiments presented in the next panel. **(E)** The protein targets for HPV16 E6 identified by GPCA and validated by co-IP are represented. To further characterize the uncovered interactions, GPCA experiments were also performed using truncated (ΔPBM) or mutated (F47R, L50E V53E) forms of HPV16 E6. E6AP and MAGI-1 were used as positive control for binding to the LxxLL motif and the PBM region, respectively. Results represent the means ± SEM of three independent experiments. Asterisks indicate statistically significant differences (*p < 0.05, **p < 0.01, ***p < 0.001, ****p < 0.0001). P values were determined using a D'Agostino and Pearson normality test (B) and one-way ANOVA followed by a Bonferroni post-test (E).

E6/E7 viral oncoproteins increase the intrinsic radiosensitivity of cells independently of affecting their basal viability parameters

In order to determine whether viral oncoproteins actively contribute to the elevated sensitivity of HPV-infected cells to radiation therapy, immortalized keratinocytes (HaCaT) and three cancer cell lines (A431, UPCI-SCC-111 and U-2OS) from different origins and displaying different *TP53* mutation statuses were transduced with HPV16 E6 and/or E7 (Figure 2A). As shown in Figure 2B and Figure S1A, the levels of viral mRNA were close in each isogenic cell model, allowing their further comparison. Moreover, the expression of E6 and E7 (alone or in combination) did not significantly change the cell proliferation, apoptosis and proportion of cells in different cell cycle phases (Figure 2C-E and Figure S1B-D). The cell morphology was not modified by viral oncoproteins either (data not shown). Given that DNA damage detection and repair capacity of irradiated tumor cells have been shown for a long time to contribute to their radiosensitivity, the impact of HPV16 E6 and E7 on DNA damage response was first assessed by neutral comet assay (Figure 2F and Figure S2). The average length of the comet tails predictably peaked immediately after irradiation. Importantly, the kinetics of DNA double-strand break repair was significantly impacted by E6 and/or E7 expression. Indeed, whereas the majority (~80%) of DNA damages seemed to be repaired 6h after irradiation in control condition, a significant delay in the rate of DNA repair was invariably observed in E6 and/or E7-expressing cells (whatever the analyzed isogenic model). In order to expand our DNA damage analysis in presence or absence of HPV oncoproteins, a cytokinesis-block micronucleus assay was carried out. As shown both in Figure 2G and Figure S2, E6- and, at a lesser extent, E7-transduced cells already displayed a slight increase of micronucleus formation compared to their corresponding control cells at basal (non-irradiated) condition. This increased frequency of micronuclei in binucleated cells was even more noticeable following irradiation. In parallel to these two tests directly measuring DNA damages, clonogenic growth analyses were also performed (Figure 2H and Figure S2). Although the statistical significance was not reached with the A431 isogenic models (p = 0.07), the expression of E6 and/or E7 viral oncoproteins was consistently associated with an increased cellular sensitivity to irradiation. Using this gold standard method for measuring long-term effects of radiotherapy, it is interesting to notice that a synergistic effect of E6 and E7 was only observed with wild-type *TP53* cells (U-2OS) (Figure S2). Finally, heterotopic tumor models were performed to further assess the radiosensitivity of HPV E6E7-transduced cells. To do so, cancer cells were subcutaneously injected in Nude mice. A431 tumor-bearing animals were then treated or not with a unique dose of 6 Gy when solid tumors (100–200 mm^3) were established. As shown in Figure 2I-K, following irradiation, the tumor growth delay was significantly more important in E6E7-transduced cancers compared to their control homologs, confirming our *in vitro* data. Of note, *in vivo* experiments using malignant UPCI-SCC-111 and U-2OS cells were also tried. Different cell numbers and conditions (e.g., with or without matrigel) were tested but their weak tumorigenicity (low capacity to develop palpable tumors *in vivo*) did not enable their use in mouse models.

Both high-throughput screening and co-IP experiments unequivocally reveal the direct interaction between E6/E7 viral oncoproteins and some key proteins involved in DNA damage and repair mechanisms

First, a library of cDNA encoding for DNA damage and repair factors was created from ORFs contained in the human ORFeome collections v7.1 and 8.1 (Dana-Farber Cancer Institute, Boston, USA). According to the Human DNA Repair Gene Database (created in 2001 and updated in June 2020, https://www.mdanderson.org/documents/Labs/Wood-Laboratory/human-dna-repair-genes.html), 230 proteins, divided into 16 different families, are directly (or indirectly) implicated in DNA repair mechanisms. As mentioned by the authors (Wood RD and Lowery M), it is important to notice that some proteins act in several pathways but, for the sake of simplicity, each ORF is only listed once (in its main family) in the present study (Figure 3A). The sequences of 18 DNA repair factors were not present in the different human ORFeome collections and, in

total, 212 cDNA encoding for unique proteins were cloned in the pSPICA-N1 vector (used subsequently in GPCA experiments). Due to sequence errors identified by Sanger sequencing, 33 cDNA constructs were excluded. Therefore, our library covers about 80% (179/230, 77.8%) of the entire DNA damage/repair response (Figure 3A, Table S2). Twenty-one cDNA encoding for protein isoforms were added in the final version of our library and this latter was used to perform a systematic high-throughput screening for binary interactions between DNA damage/repair proteins and E6/E7 viral oncoproteins. The findings collected with HPV16 E6 and E7 are shown in Figures 3 and 4, respectively. As demonstrated by a skewness score equal to 3.94 (for E6) and 2.44 (for E7), the luminescence values obtained by GPCA were not normally distributed, suggesting potential protein-protein interactions. Using the ROUT method (with a Q set to 5%) [41], 13 and 19 "outlier" luminescence values, representing potential interacting pairs, were highlighted for E6 and E7 oncoproteins, respectively (Figures 3B-C and 4A-B). In order to validate the data collected by the GPCA approach, co-IP experiments were then performed. Both assays were carried out using HEK-293T cells. Thus, as shown in Figure 3E, the interactions between HPV16 E6 and 10 DNA damage/repair proteins (CHEK2, CLK2, CLK2/3, ERCC3, MNAT1, PER1, RMI1, RPA1, UVSSA and XRCC6) were distinctly confirmed. In parallel, the bindings between E7 and ALKBH2, CHEK2, DNA2, DUT, ENDOV, ERCC3, PARP3, PMS1, PNKP, POLDIP2 and RBBP8 were also ascertained (Figure 4D). Intriguingly, ERCC3 and CHEK2 have been shown to interact with both E6 and E7 viral oncoproteins. Regarding the 11 other potential interacting pairs highlighted by GPCA, no clear confirmation by co-IP was obtained, arguing that they very likely represent false positive results of the screening method (Figure S3). When the 21 protein isoforms contained in our library were compared to their full-length homologs, 3 discriminant findings were observed. The isoform specificity of two interactions (PER1 with E6 and DUT with E7) was proved by co-IP (Figure S4). In order to further characterize all these newly uncovered/validated interactions, 4 truncated/mutated forms of HPV16 E6 [the F47R, L50E and V53E constructs containing point mutations within (or in close proximity to) the LxxLL-binding motif as well as an E6 construct truncated for 4 amino acids within the PDZ-binding motif (ΔPBM)] and 3 of HPV16 E7 [the CR1+CR2 region consisting of the 36 first amino acids, the C-terminal domain (37–98 amino acids) and a mutated construct within the LxCxE motif (C24G/E26G)] were also tested. While ERCC3, MNAT1, PER1 and RMI1 seem to interact with the LxxLL-binding motif of E6 (as demonstrated by the low GPCA signal obtained with the L50E and/or V53E construct), the interaction of the other proteins was unaffected by the mutations/deletions within both the LxxLL and PDZ-binding motifs (Figure 3E). Regarding all DNA damage/repair proteins interacting with E7, the GPCA signals were radically reduced when the CR1+CR2 construct was used, supporting their bindings with the C-terminal region of this viral oncoprotein (Figure 4D).

DNA damage/repair proteins are not degraded following their interaction with E6 or E7 but rather, are recruited to the E1/E2 (viral replication) foci

We next sought to determine whether the interaction with E6 or E7 modified the stability and/or cellular sublocalization of DNA damage/repair proteins. To do so, immortalized keratinocytes (HaCaT) transduced or not with HPV16 E6E7 were treated with a translation inhibitor (cycloheximide) and the level of each individual protein was monitored over a 24h period. In parallel, subcellular protein fractionations were performed (Figure 5A). Whereas no difference in term of protein turnover was detected (Figure 5B), the expression of viral oncoproteins has been shown to drastically alter the proportion of 9 proteins (CHEK2, DNA2, ENDOV, MNAT1, PARP3, PER1, RPA1, UVSSA and XRCC6) in the different subcellular fractions (Figure 5C). In particular, these proteins were strongly enriched in the S3 fraction corresponding to the nuclear proteins unbound to the host chromatin. Despite a greater nuclear presence of these proteins of interest at basal (E6E7-negative) condition, similar findings were obtained using cancer (UPCI-SCC-111) cells (Figure S5). To confirm these results (and to further characterize the hijacking of host DNA repair proteins by E6 and/or E7), immunofluorescence experiments were performed using malignant (A431) cells expressing both HA-HPV16 E1 and 3xFlag-E2 (following the addition of Cre lentivirus) and transfected with the complete HPV16 genome. As shown in Figure 5D, the coexpression of E1 and E2 resulted in the formation of defined nuclear E1/E2 foci. Both E1 and E2 proteins were invariably observed in fine granular nuclear patterns and the fluorescent signals were always more abundant/extended for E2.

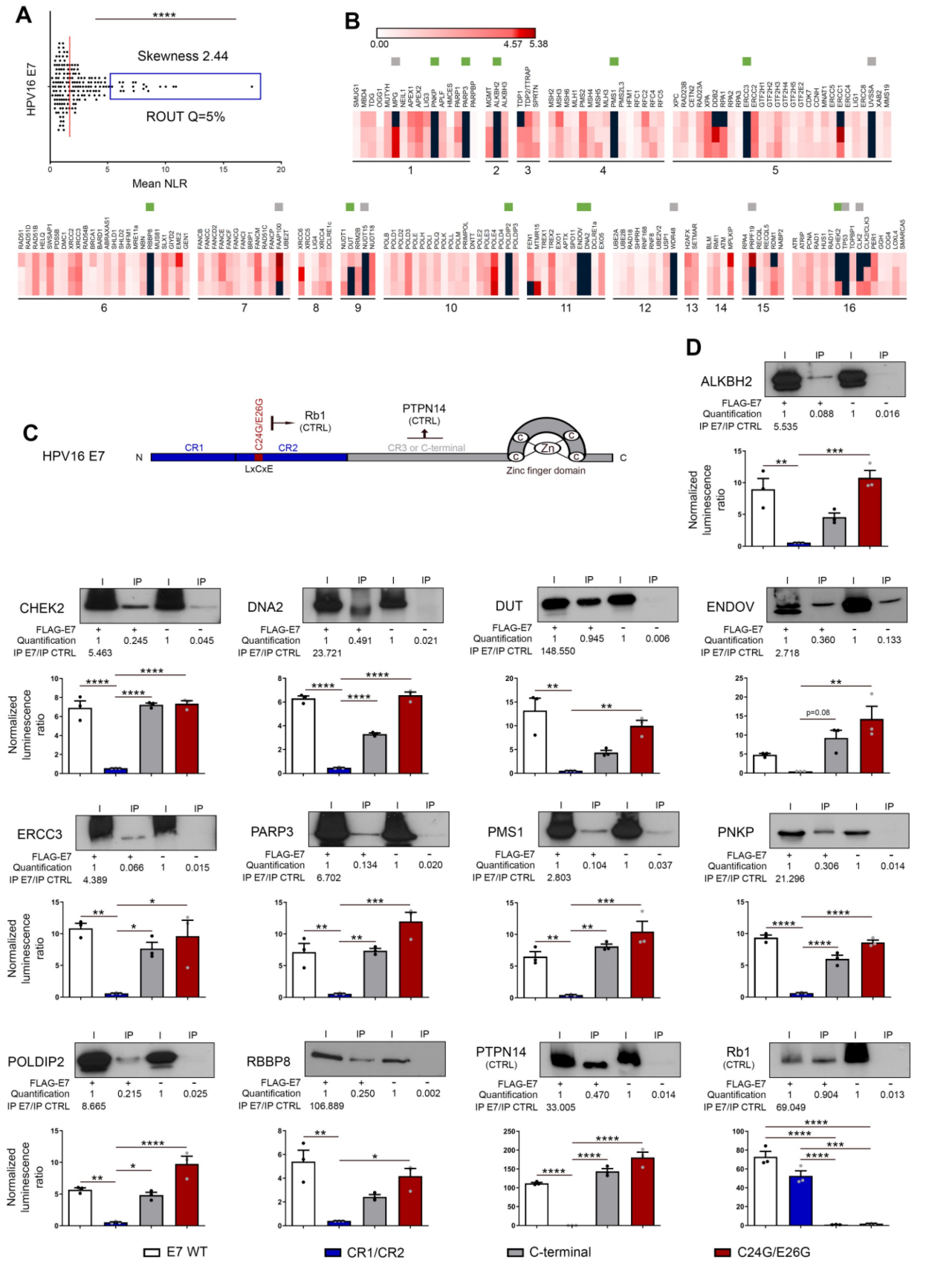

Figure 4. High-throughput screening and validation/characterization of DNA damage/repair proteins interacting with E7 oncoprotein from HPV16. (A) Scatter plot of the mean NLR values obtained by GPCA when the library of unique proteins (n = 179) was screened for direct interactions with HPV16 E7. The collected data were not normally distributed (skewness score=2.44) and 19 outlier luminescence values (blue rectangle), representing potential protein-protein interactions, were detected using the ROUT method (with Q=5%). **(B)** Heatmap representing the NLR scores of each protein from the library tested for potential interaction with HPV16 E7. The black blocks represent values above the threshold set for outliers. Green and grey squares represent proteins identified as outliers and confirmed or not (false-positive) by co-IP, respectively. Three biological replicates were performed with each pSPICA-N1 plasmid of the library. The names of each family of DNA repair proteins are listed in the panel A of the Figure 3. **(C)** Representation of the 98 amino acid constituting HPV16 E7 oncoprotein.

In color, the parts that were either truncated (CR1/CR2, blue; C-terminal, grey) or mutated (C24G/E26G, red) for the experiments presented in the next panel. **(D)** The protein targets for HPV16 E7 identified by GPCA and validated by co-IP are represented. To further characterize the uncovered interactions, GPCA experiments were also performed using truncated (CR1/CR2 and C-terminal) or mutated (C24G/E26G in the LxCxE region) forms of HPV16 E7. PTPN14 and Rb1 were used as positive control for binding to the c-terminal region and the LxCxE motif, respectively. Results represent the means ± SEM of three independent experiments. Asterisks indicate statistically significant differences (*$p < 0.05$, **$p < 0.01$, ***$p < 0.001$, ****$p < 0.0001$). *P* values were determined using a D'Agostino and Pearson normality test (A) and one-way ANOVA followed by a Bonferroni post-test (D).

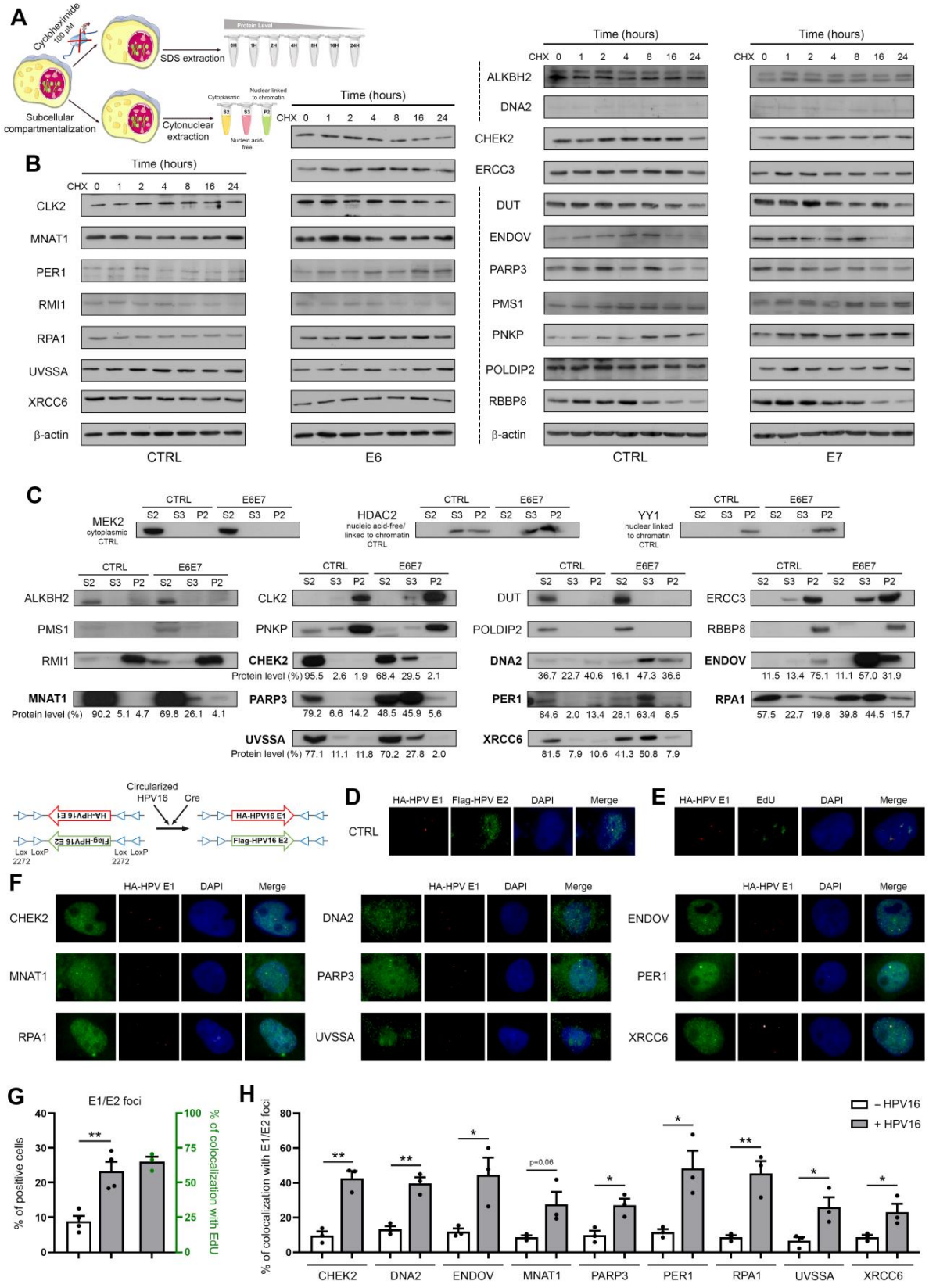

Figure 5. DNA damage/repair proteins targeted by HPV16 E6 and/or E7 are enriched in the nucleic acid-free protein fraction and partially colocalize with E1/E2 (viral replication) foci. (A) Schematic illustration of the steps involved in the cycloheximide chase assay and subcellular protein fractionation. **(B)** The isogenic models derived from immortalized

keratinocytes (HaCaT) were treated with 100 µM cycloheximide for the indicated times and the stability/half-life of protein targets for HPV16 E6 and/or E7 was determined. A representative immunoblot from at least 2 independent experiments is shown. **(C)** S2 (cytoplasmic), S3 (nucleic acid-free) and P2 (linked to chromatin) protein fractions were collected from HaCaT cells transduced or not with HPV16 viral oncoproteins. The proportions of each newly uncovered protein targets for E6 and/or E7 in S2, S3 and P2 fractions were then assessed by western blot. The protein bands were quantified by densitometric analysis (ImageJ software) and the sum of all three subcellular fractions was set to 100%. MEK2, HDAC2 and YY1 were used as purity control for S2, S3/P2 and P2 fractions, respectively. **(D)** Representative pictures of E1/E2 foci detected in A431 cells expressing both HA-HPV16 E1 and 3xFlag-E2 and transiently transfected with the complete HPV16 genome. To avoid long-term E1 and E2-dependent cellular lethality, the Double-Floxed Inverted Open reading frame technology was used, allowing the expression of both E1 and E2 only following the addition of Cre lentivirus. **(E)** Representative pictures of EdU staining in A431 cells expressing both HPV16 E1 and E2 and transiently transfected with the complete HPV16 genome. **(G)** Percentage of cells displaying E1/E2 foci in the absence or presence of HPV16 DNA (black dots, left y-axis) and percentage of colocalization with EdU (green dots, right y-axis). The significant increased proportion of positive cells in case of circularized HPV16 transfection as well as the frequent colocalization between E1/E2 foci and EdU staining confirm the active viral replication taking place in these cells. Results represent the means ± SEM of three/four independent experiments. For each replicate, at least 250 cells were analyzed. The colocalization between E1 foci and intense nuclear foci ("hot spots") for CHEK2, DNA2, ENDOV, MNAT1, PARP3, PER1, RPA1, UVSSA and XRCC6 was then analyzed by immunofluorescence **(F)** and quantified by computerized counting (JACoP ImageJ plugin) **(H)**. Results represent the means ± SEM of three independent experiments. For each replicate, colocalization analysis was performed with at least 100 HPV16 E1 foci. Asterisks indicate statistically significant differences (*$p < 0.05$, **$p < 0.01$). *P* values were determined using an unpaired t-test (G, H).

Importantly, the percentage of cells displaying E1/E2 foci (1 to 8 per cell) was 2.5-fold higher (23.35% *versus* 8.95, $p = 0.0035$) in the presence of HPV16 compared to the control condition lacking viral genome (Figure 5G), supporting that most of these latter are indeed active viral replication centers. The frequent colocalization (>65%) between EdU staining and E1/E2 foci indisputably validated the active viral replication occurring in these cells (Figures 5E and G). Determined by computerized counting, E1/E2 foci partially colocalized with "hot spots" (enriched immunolabellings) for the 9 aforementioned DNA damage/repair proteins and, strikingly, the percentages of colocalization were significantly higher in the presence of HPV16 DNA (Figures 5F and H). Altogether, these data argue for the E6/E7-dependent recruitment of these host proteins to the viral replication foci.

E6/E7 viral oncoproteins globally alter host genome integrity, enhance the cellular sensitivity to DNA repair inhibitors and positively influence their synergy with radiotherapy

In order to determine whether E6E7-dependent hijacking of DNA repair pathways jeopardizes host genome integrity, whole genome sequencing experiments were performed. Using HPV16 E6E7 and control isogenic cell pairs generated from immortalized keratinocytes (HaCaT), the number of SNPs and InDels was first estimated at different time intervals. In parallel, the COSMIC mutational signatures were extracted. As shown in Figures 6B and 6D, with the exception of the relatively modest emergence of the Single Base Substitution (SBS) Signature 1 (characterized by C>T mutations), the presence of viral oncoproteins modified neither the relative contribution of each distinct COSMIC signature to the overall mutational profile nor the InDel size distribution. No difference in terms of proportion of InDels/SNPs present in coding or non-coding regions was noticed either (Figure 6A and 6C). The features of extracted COSMIC reference signatures (SBS1, 5 and 40) are detailed in Figure 6E. In contrast, strikingly, E6E7 expression was associated with a substantial increase of both SNPs and InDels in host genome (Figures 6A and 6C), sustaining that the disruption of host DNA repair mechanisms by viral oncoproteins is not harmless for infected cells (and very likely participates to HPV-related carcinogenesis). Given the higher frequency of non-repaired genetic alterations detected following E6E7 expression, we decided to determine whether this feature can be exploited therapeutically. To do so, our HPV16 E6E7 isogenic cell pairs were first treated with several potent drugs targeting the DNA repair machinery [Niraparib and Veliparib (PARP1/2 inhibitors), RI-1 (RAD51 inhibitor), YU238259 (homology-dependent DNA repair inhibitor) and Camptothecin (DNA topoisomerase I inhibitor)]. Interestingly, E6E7-expressing cells were invariably associated with an increased sensitivity to these DNA repair inhibitors compared to their corresponding controls, as demonstrated by the 24 to 295% decrease of IC50 values in case of viral oncoprotein expression (Figure 6F). Despite some intercellular variations, the difference in sensitivity between E6E7-positive and -negative cells was especially noticeable with compounds targeting PARP or RAD51. The synergy between these compounds and radiotherapy was then evaluated in both control and E6E7-transduced keratinocytes (HaCaT cells). As shown in Figure 6G, some DNA repair inhibitors (Niraparib, Veliparib and YU238259) demonstrated clear synergistic effects with radiotherapy (as indicated by maximum ZIP scores >10) while others (especially RI-1) displayed relatively modest additive effects. Irrespective of these differences, strikingly, the calculated (average and maximum) synergy scores were consistently higher in cells expressing E6 and E7 viral oncoproteins compared to their control counterparts.

Discussion

In the last decades, multiple studies reported that HPV-positive cancers represent a distinct entity associated with a favorable prognosis. In addition, both the specific mutational signature and the elevated immune infiltration of HPV-driven neoplasms (compared to their HPV-unrelated counterparts) were described [42, 43]. Altogether,

these findings led to the recent recommendation of a clinical dualistic classification based on the HPV status (for oropharyngeal malignancies and proposed for invasive cancers arising from other anatomical sites). In parallel, the hijacking of DNA damage/repair mechanisms by HPV was proposed by several molecular virology research teams. Indeed, HPV proteins would activate and exploit host repair factors to ensure proper viral replication (for a review, see [17, 44]). Therefore, could this phenomenon participate to the high radiosensitivity of HPV-positive tumors and represent their Achilles' heel? The significant enrichments of various gene signatures related to DNA repair detected in HPV-positive cancers, the increase of DNA damage/repair biomarker expression detected at the mRNA and protein levels in infected tumor specimens (irrespective of their origin) as well as the results collected by clonogenic growth analysis using both HPV-related and -unrelated cell lines (18 in total) clearly support this hypothesis. These latter data are consistent with those reported by *in vitro* studies published in the past few years and using mainly oropharyngeal cancer cells [9, 45-48].

Playing a major role in viral replication, the implication of HPV E1/E2 in host DNA damage/repair response manipulation has been thoroughly studied [49-51]. In the present study, we focused our attention on both E6 and E7 oncoproteins given that, following viral integration into the host genome (occurring in ~70% cervical cancers and ~50% head and neck SCC), E1 and/or E2 genes are frequently disrupted or completely deleted. In parallel, the E2-dependent transcriptional repression of both E6 and E7 is traditionally impeded in HPV-positive (pre)cancer lesions through the methylation of E2-binding sites (E2BSs) in the viral upstream regulatory region (URR), leading to an enhanced/uncontrolled expression of viral E6 and E7 oncoproteins [52, 53]. Therefore, the impact of both E1 and E2 early proteins is presumably very limited and the sensitivity of invasive cancers to radiation therapy probably relies mainly on E6 and/or E7. Without affecting the cell proliferation, apoptosis and proportion of cells in the G2/M cell cycle phase, we showed that the sole addition/overexpression of one viral oncoprotein from HPV16 was able to increase intrinsic cancer cell radiosensitivity by 11% to 45% in three different isogenic cellular models. Very likely related to the pivotal function of p53 in both apoptosis and cell cycle arrest, a synergistic effect of E6 and E7 was only detected with tumor cells (U-2OS) displaying a wild-type *TP53* status. In parallel to clonogenic growth analyses, cytokinesis-block micronucleus assays demonstrated that both E6- and E7-transduced cells already displayed an increase of chromosome breakages compared to control cells at basal (non-irradiated) condition. These interesting observations (exacerbated following irradiation) are in agreement with recent studies analyzing the effect of viral oncoproteins from HPV16 as well as of E6 from cutaneous βHPV8 on genome instability [54, 55]. Finally, the significant slowing of DNA double-strand break repair kinetics observed in case of viral oncoprotein expression further supported the E6/E7-dependent increase of cellular radiosensitivity.

Given that neither E6 nor E7 possesses an intrinsic enzymatic activity, they act through their interactions with host proteins. Aiming at determining the interactome of HPV E6 and E7 oncoproteins with the different sub-families of DNA repair factors, a cDNA library covering about 80% of the entire DNA damage/repair responses was assembled and the GPCA was used as the high-throughput screening method. This luminescence-based technology represents a major improvement for the identification of binary protein-protein interaction. Indeed, compared to the currently more popular yeast two-hybrid which recovers less than 25% of total interactions [56], GPCA has been shown to be far more sensitive [57]. Moreover, by using mammalian cells (HEK-293T), the post-translational modifications of proteins are unaffected. However, GPCA only identifies direct binary interactions, leaving aside all the interactions requiring a tertiary partner (e.g., HPV E6/E6AP/p53). Detected by GPCA and then validated by co-IP, in total, 10 targets for HPV16 E6 and 11 for E7 were identified. It is interesting to notice that not all of these proteins act in the same signaling pathway, supporting that the virus requires various factors to ensure faithful replication of its genome and, therefore, globally hijacks host DNA damage repair. To the best of our knowledge, CHEK2 (which, like ERCC3, interacts with both E6 and E7) is the only host DNA damage/repair protein highlighted in the present study that had previously been reported as a potential HPV target [58]. Although the false-negative rate is presumed to be low, of course, we cannot exclude that a few other proteins have been missed by the GPCA screening approach. Interestingly, these 19 different host factors not only interacted with HPV16 E6 and/or E7 but also with the oncoproteins from other high-risk genotypes (HPV18, HPV33 and HPV39), pointing out the importance of these newly discovered targets for viral life cycle (and indirectly for HPV-related carcinogenesis) (Figure S6).

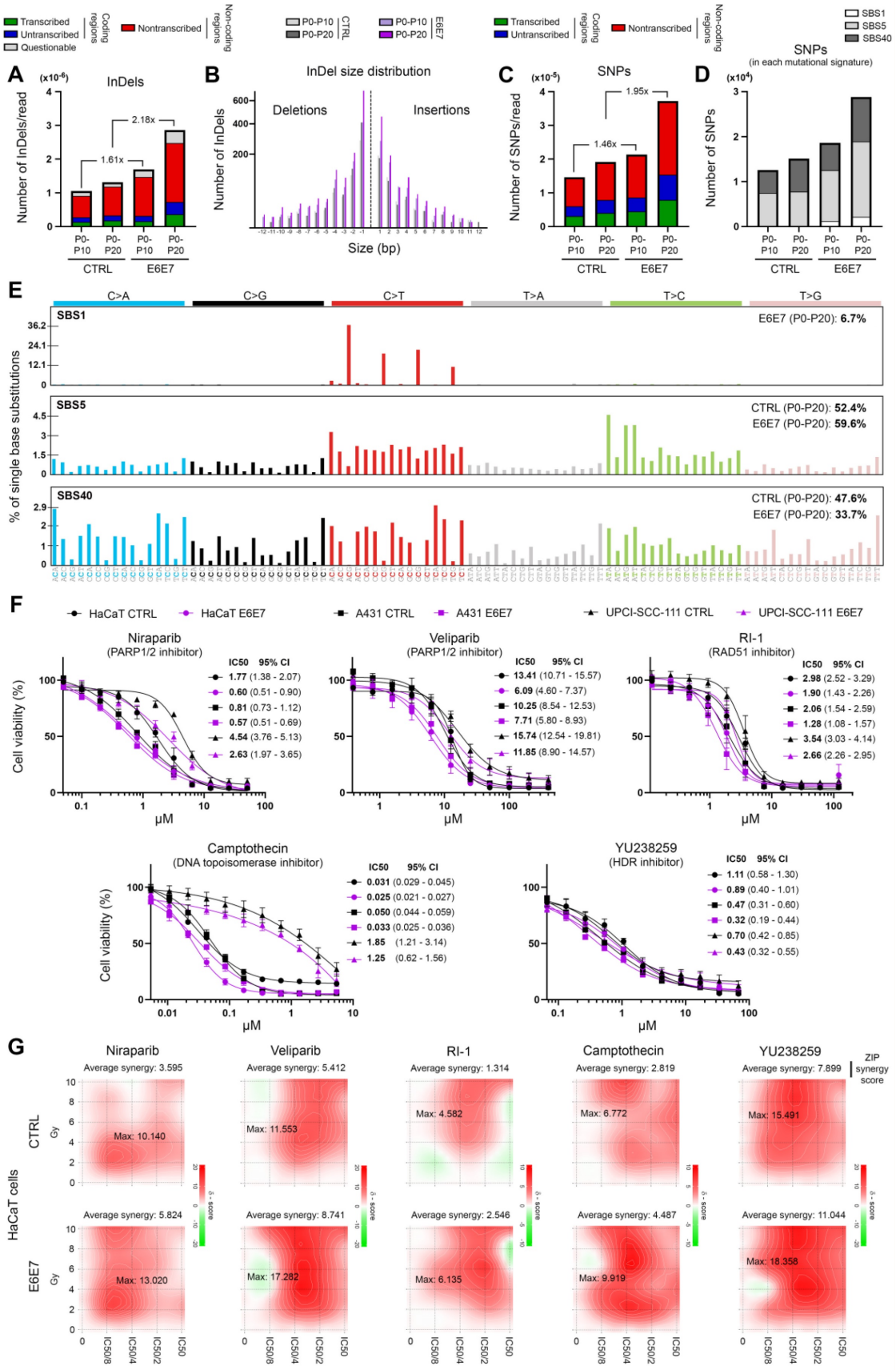

Figure 6. E6/E7 viral oncoproteins negatively affects host genome integrity and increases cellular sensitivity to various DNA repair inhibitors. Number of InDels **(A)** and SNPs **(C)** detected in DNA of immortalized keratinocytes (HaCaT) transduced or not with HPV16 E6 and E7. For each time interval (P0-P10 and P0-20), the values were normalized to the total number of sequencing reads. The proportions of InDels/SNPs present in coding or non-coding regions are also represented. Transcribed: the variant is on the transcribed strand. Untranscribed: the variant is on the untranscribed strand. Nontranscribed: the variant is in a non-coding region. **(B)** InDel size distribution (insertions: size >0; deletions: size <0). **(D)** Relative contribution of the different published SBS signatures (COSMIC v3.3) to the overall detected mutational profile. SBS5 (potentially associated to a deficiency of nucleotide excision repair and/or

aging) and 40 (unknown etiology) were responsible for >90% of the mutational burden. The COSMIC SBS1 signature (characterized by C>T mutations) exclusively detected in E6E7-transduced cells should be noticed. **(E)** Mutational spectrum of COSMIC signatures of interest (SBS1, 5 and 40). **(F)** Dose-response curves of several HPV E6E7 isogenic cell pairs treated with Niraparib or Veliparib (PARP1/2 inhibitors), RI-1 (RAD51 inhibitor), YU238259 (homology-dependent DNA repair inhibitor) and Camptothecin (DNA topoisomerase I inhibitor) for 72h. Results represent the means ± SEM of four independent experiments. The IC50 and 95% CI of each condition is also indicated. **(G)** 2D synergy maps highlighting synergistic dose regions (in red). The indicated average synergy score for a specific treatment combination was averaged over all the dose combination measurements. The means of three independent experiments were used to assess the synergy between radiotherapy and each DNA repair inhibitor according to the ZIP method.

This assumption was further supported by both the absence of degradation of these DNA repair proteins in presence of viral oncoproteins and their colocalization with E1/E2 foci. Of note, these protein recruitments to viral replication foci should no longer appear in invasive tumors displaying a pure integrated infection. However, given that the interactome of HPV E6/E7 with the DNA damage/repair system is not influenced by the viral status (episomal, mixed, full integrated) of infected cells (viral oncoproteins being still expressed), the negative impact for host DNA should occur in all HPV-related cancers. In order to further characterize the revealed interacting pairs, truncated or mutated forms of the relevant viral oncoproteins were tested. All identified targets of E7 exhibited negative GPCA signals with the CR1+CR2 construct (lacking the last 62 amino acids of E7), confirming that most E7-related interactions required the C-terminal region of the oncoprotein [34]. Regarding the protein interactions involving E6, 4 (ERCC3, MNAT1, PER1 and RMI1) were affected by L50E and/or V53E mutations directly in (or in the close vicinity of) the LxxLL-binding motif. The interactions of the 6 other DNA damage/repair proteins were not inhibited by any mutations/deletions within the LxxLL or PDZ-binding motifs.

In conclusion, viral E6 and E7 oncoproteins actively contribute to increase the intrinsic radiosensitivity of infected cells. Beside the high blood vessel and T-cell densities detected within tumor microenvironment, this latter parameter undoubtedly also contributes to the better response to radiation therapy of HPV-positive tumors. Even if all identified E6/E7-interacting DNA damage/repair proteins are not involved in signaling pathways directly activated in response to radiotherapy (e.g., base excision repair and non-homologous end-joining pathways), a DNA repair global weakness takes place in HPV-infected cells. Indeed, without drastically modifying the extracted/detected mutational signatures, the expression of viral oncoproteins was clearly associated with a substantial increase of SNPs/InDels in host genome. Therefore, despite an upregulation of multiple factors involved in various DNA repair mechanisms (Figure S7), these genomic data distinctly support that protein hijacking by both E6 and E7 is extremely efficient and the activation of host signaling pathways primarily benefits the viral genome (and not the cellular DNA). Very likely harmless for host genome in normal-appearing cells containing just a few copies of HPV DNA and "tolerated" by the (pre)cancerous cells harboring 100 to 2,000 episomal HPV copies (or in case of viral integration and subsequent uncontrolled E6/E7 expression), the perturbation/hijacking of many host factors by viral oncoproteins would ultimately lead to an increase of cell death following irradiation. This characteristic, not detected in HPV-unrelated cancers, supports the reduced-dose treatment regimens recently proposed in the context of oropharyngeal HPV-positive tumors [59]. Furthermore, the targeted inhibition of DNA repair machinery notably using PARP inhibitors (e.g., Niraparib, Veliparib and Olaparib, currently tested with BRCA1/2^{mut} breast, ovarian and prostate cancers [60, 61]) could be especially beneficial for treating HPV-positive cancer patients. Indeed, as demonstrated by the decreased IC50 values in case of E6 and E7 expression, viral oncoproteins (and their concomitant global alteration of host DNA repair) enhance the cellular sensitivity to these increasingly tested drugs. Remarkably, the synergy between DNA repair inhibitors and radiotherapy has also been shown to be positively influenced by E6 and E7. Given the over 300,000 deaths still attributable to HPV per year worldwide, such a strategy combining DNA repair inhibitors and radiotherapy certainly merits further study in a controlled clinical trial.

Abbreviations

DAPI: 4′,6-diamidino-2-phenylindole; DMEM: dulbecco's modified eagle's medium; EdU: 5-ethynyl-2′-deoxyuridine; EVS: empirical variant scoring; GPCA: *gaussia princeps* luciferase complementation assay; GSEA: gene set enrichment analysis; HPV: human papillomavirus; InDels: insertions/deletions; MEM: minimum essential medium; ORF: open reading frame; RLU: relative luminescence unit; RPMI: roswell park memorial institute; SBS: single base substitution; SCC: squamous cell carcinoma; SNPs: single nucleotide polymorphisms; URR: upstream regulatory region.

Supplementary Material

Supplementary figures, tables 1 and 3.
https://www.thno.org/v13p1130s1.pdf
Supplementary table 2.
https://www.thno.org/v13p1130s2.xlsx

Supplementary table 4.
https://www.thno.org/v13p1130s3.xlsx

Acknowledgements

The authors thank the Biobank of the University of Liege as well as the GIGA-Immunohistochemistry, *in vitro* imaging, genomics and viral vector platforms (University of Liege) for their assistance. We are also grateful to Dr Stephanie Gofflot, Dr Emmanuel Di Valentin, Dr Wouter Coppieters, Dr Natacha Leroi, Dr Alain Jung (University of Strasbourg), Dr Marie-Julie Nokin, Raphael Thonon, Kamilia El Kandoussi, Tiffany Di Salvo, Hülya Kocadag, Nadine Cambisano, Manon Deckers, François Giroulle, Majid Cherkaoui, Bartimée Galvan and Fabienne Perin for their technical assistance. The graphical abstract was created with BioRender.com (agreement number: AJ24WBV3N3). TL, CP, CR and MA are Televie/FRIA fellows. DB and EH are postdoctoral scientific collaborators at FRS/FNRS. MH is a Research Associate at the Belgian Fund for Scientific Research (FNRS).

Funding

This work was supported in part by the FNRS (MIS F.4520.20, CDR J.0088.21), the University of Liege (Crédits Sectoriels de Recherche en Sciences de la Santé 2018-2021), the Télévie (PDR Televie 7.8507.19) and the Leon Fredericq Foundation.

Author contributions

DB and MH designed the study; DB, PR, AL, TL, EH, CP, CR, MA, ML, MR and MH performed experiments; FP, RP, OP and NG performed bioinformatic analyses; DB, YJ, PH, MM and MH interpreted the data; YJ, J-CT, AM, PD and MM provided resources; DB and MH performed the statistical analysis; DB and MH generated the Figures; DB and MH wrote the paper. All authors had final approval of the submitted manuscript.

Data availability

All raw sequencing data have been deposited in the NCBI Sequence Read Archive (SRA) repository with the accession code: PRJNA863223.

Competing Interests

The authors have declared that no competing interest exists.

References

1. de Martel C, Plummer M, Vignat J, Franceschi S. Worldwide burden of cancer attributable to HPV by site, country and HPV type. Int J Cancer. 2017; 141: 664-70.
2. Bruyere D, Monnien F, Colpart P, Roncarati P, Vuitton L, Hendrick E, et al. Treatment algorithm and prognostic factors for patients with stage I-III carcinoma of the anal canal: a 20-year multicenter study. Mod Pathol. 2021; 34: 116-30.
3. Serup-Hansen E, Linnemann D, Skovrider-Ruminski W, Hogdall E, Geertsen PF, Havsteen H. Human papillomavirus genotyping and p16 expression as prognostic factors for patients with American Joint Committee on Cancer stages I to III carcinoma of the anal canal. J Clin Oncol. 2014; 32: 1812-7.
4. Ang KK, Harris J, Wheeler R, Weber R, Rosenthal DI, Nguyen-Tan PF, et al. Human papillomavirus and survival of patients with oropharyngeal cancer. N Engl J Med. 2010; 363: 24-35.
5. Ritchie JM, Smith EM, Summersgill KF, Hoffman HT, Wang D, Klussmann JP, et al. Human papillomavirus infection as a prognostic factor in carcinomas of the oral cavity and oropharynx. Int J Cancer. 2003; 104: 336-44.
6. Zhang J, Zhang Y, Zhang Z. Prevalence of human papillomavirus and its prognostic value in vulvar cancer: A systematic review and meta-analysis. PloS One. 2018; 13: e0204162.
7. Strohl MP, Wai KC, Ha PK. De-intensification strategies in HPV-related oropharyngeal squamous cell carcinoma-a narrative review. Ann Transl Med. 2020; 8: 1601.
8. Boustani J, Grapin M, Laurent PA, Apetoh L, Mirjolet C. The 6th R of Radiobiology: Reactivation of Anti-Tumor Immune Response. Cancers. 2019; 11.
9. Kimple RJ, Smith MA, Blitzer GC, Torres AD, Martin JA, Yang RZ, et al. Enhanced radiation sensitivity in HPV-positive head and neck cancer. Cancer Res. 2013; 73: 4791-800.
10. Jung AC, Guihard S, Krugell S, Ledrappier S, Brochot A, Dalstein V, et al. CD8-alpha T-cell infiltration in human papillomavirus-related oropharyngeal carcinoma correlates with improved patient prognosis. Int J Cancer. 2013; 132: E26-36.
11. Spanos WC, Nowicki P, Lee DW, Hoover A, Hostager B, Gupta A, et al. Immune response during therapy with cisplatin or radiation for human papillomavirus-related head and neck cancer. Arch Otolaryngol Head Neck Surg. 2009; 135: 1137-46.
12. Chen X, Yan B, Lou H, Shen Z, Tong F, Zhai A, et al. Immunological network analysis in HPV associated head and neck squamous cancer and implications for disease prognosis. Mol Immunol. 2018; 96: 28-36.
13. Hanns E, Job S, Coliat P, Wasylyk C, Ramolu L, Pencreach E, et al. Human Papillomavirus-related tumours of the oropharynx display a lower tumour hypoxia signature. Oral oncol. 2015; 51: 848-56.
14. Leeman JE, Li Y, Bell A, Hussain SS, Majumdar R, Rong-Mullins X, et al. Human papillomavirus 16 promotes microhomology-mediated end-joining. Proc Natl Acad Sci U S A. 2019; 116: 21573-9.
15. Wallace NA, Khanal S, Robinson KL, Wendel SO, Messer JJ, Galloway DA. High-Risk Alphapapillomavirus Oncogenes Impair the Homologous Recombination Pathway. J Virol. 2017; 91: e01084-17.
16. Khanal S, Galloway DA. High-risk human papillomavirus oncogenes disrupt the Fanconi anemia DNA repair pathway by impairing localization and de-ubiquitination of FancD2. PLoS Pathog. 2019; 15: e1007442.
17. Wallace NA. Catching HPV in the Homologous Recombination Cookie Jar. Trends Microbiol. 2020; 28: 191-201.
18. Molkentine DP, Molkentine JM, Bridges KA, Valdecanas DR, Dhawan A, Bahri R, et al. p16 Represses DNA Damage Repair via a Novel Ubiquitin-Dependent Signaling Cascade. Cancer Res. 2022; 82: 916-28.
19. Wang L, Zhang P, Molkentine DP, Chen C, Molkentine JM, Piao H, et al. TRIP12 as a mediator of human papillomavirus/p16-related radiation enhancement effects. Oncogene. 2017; 36: 820-8.
20. Liu Q, Ma L, Jones T, Palomero L, Pujana MA, Martinez-Ruiz H, et al. Subjugation of TGFbeta Signaling by Human Papilloma Virus in Head and Neck Squamous Cell Carcinoma Shifts DNA Repair from Homologous Recombination to Alternative End Joining. Clin Cancer Res. 2018; 24: 6001-14.
21. Chen J, Deng Y, Ao L, Song Y, Xu Y, Wang CC, et al. The high-risk HPV oncogene E7 upregulates miR-182 expression through the TGF-beta/Smad pathway in cervical cancer. Cancer lett. 2019; 460: 75-85.
22. Paget-Bailly P, Meznad K, Bruyere D, Perrard J, Herfs M, Jung AC, et al. Comparative RNA sequencing reveals that HPV16 E6 abrogates the effect of E6*I on ROS metabolism. Sci Rep. 2019; 9: 5938.
23. Isok-Paas H, Mannik A, Ustav E, Ustav M. The transcription map of HPV11 in U2OS cells adequately reflects the initial and stable replication phases of the viral genome. Virol J. 2015; 12: 59.
24. Herfs M, Longuespee R, Quick CM, Roncarati P, Suarez-Carmona M, Hubert P, et al. Proteomic signatures reveal a dualistic and clinically relevant classification of anal canal carcinoma. J Pathol. 2017; 241: 522-33.
25. Herfs M, Roncarati P, Koopmansch B, Peulen O, Bruyere D, Lebeau A, et al. A dualistic model of primary anal canal adenocarcinoma with distinct cellular origins, etiologies, inflammatory microenvironments and mutational signatures: implications for personalised medicine. Br J Cancer. 2018; 118: 1302-12.
26. Lebeau A, Bruyere D, Roncarati P, Peixoto P, Hervouet E, Cobraiville G, et al. HPV infection alters vaginal microbiome through down-regulating host mucosal innate peptides used by Lactobacilli as amino acid sources. Nat Commun. 2022; 13: 1076.
27. Bankhead P, Loughrey MB, Fernandez JA, Dombrowski Y, McArt DG, Dunne PD, et al. QuPath: Open source software for digital pathology image analysis. Sci Rep. 2017; 7: 16878.
28. Gao J, Aksoy BA, Dogrusoz U, Dresdner G, Gross B, Sumer SO, et al. Integrative analysis of complex cancer genomics and clinical profiles using the cBioPortal. Sci Signal. 2013; 6: pl1.

29. Wu T, Hu E, Xu S, Chen M, Guo P, Dai Z, et al. clusterProfiler 4.0: A universal enrichment tool for interpreting omics data. Innovation (Camb). 2021; 2: 100141.
30. Yu G, Wang LG, Han Y, He QY. clusterProfiler: an R package for comparing biological themes among gene clusters. OMICS. 2012; 16: 284-7.
31. Olive PL, Banath JP. The comet assay: a method to measure DNA damage in individual cells. Nat Protoc. 2006; 1: 23-9.
32. Fenech M. Cytokinesis-block micronucleus cytome assay. Nat Protoc. 2007; 2: 1084-104.
33. Guzman C, Bagga M, Kaur A, Westermarck J, Abankwa D. ColonyArea: an ImageJ plugin to automatically quantify colony formation in clonogenic assays. PloS One. 2014; 9: e92444.
34. Poirson J, Biquand E, Straub ML, Cassonnet P, Nomine Y, Jones L, et al. Mapping the interactome of HPV E6 and E7 oncoproteins with the ubiquitin-proteasome system. FEBS J. 2017; 284: 3171-201.
35. Cassonnet P, Rolloy C, Neveu G, Vidalain PO, Chantier T, Pellet J, et al. Benchmarking a luciferase complementation assay for detecting protein complexes. Nat methods. 2011; 8: 990-2.
36. Li H, Durbin R. Fast and accurate long-read alignment with Burrows-Wheeler transform. Bioinformatics. 2010; 26: 589-95.
37. Kim S, Scheffler K, Halpern AL, Bekritsky MA, Noh E, Kallberg M, et al. Strelka2: fast and accurate calling of germline and somatic variants. Nat methods. 2018; 15: 591-4.
38. Islam SMA, Díaz-Gay M, Wu Y, Barnes M, Vangara R, Bergstrom EN, et al. Uncovering novel mutational signatures by de novo extraction with SigProfilerExtractor. BioRxiv. 2022: 2020.12.13.422570.
39. Ianevski A, Giri AK, Aittokallio T. SynergyFinder 3.0: an interactive analysis and consensus interpretation of multi-drug synergies across multiple samples. Nucleic Acids Res. 2022; 50: 739-43.
40. Yadav B, Wennerberg K, Aittokallio T, Tang J. Searching for Drug Synergy in Complex Dose-Response Landscapes Using an Interaction Potency Model. Comput Struct Biotechnol J. 2015; 13: 504-13.
41. Motulsky HJ, Brown RE. Detecting outliers when fitting data with nonlinear regression - a new method based on robust nonlinear regression and the false discovery rate. BMC bioinformatics. 2006; 7: 123.
42. Wang J, Sun H, Zeng Q, Guo XJ, Wang H, Liu HH, et al. HPV-positive status associated with inflamed immune microenvironment and improved response to anti-PD-1 therapy in head and neck squamous cell carcinoma. Sci Rep. 2019; 9: 13404.
43. Seiwert TY, Zuo Z, Keck MK, Khattri A, Pedamallu CS, Stricker T, et al. Integrative and comparative genomic analysis of HPV-positive and HPV-negative head and neck squamous cell carcinomas. Clin Cancer Res. 2015; 21: 632-41.
44. Albert E, Laimins L. Regulation of the Human Papillomavirus Life Cycle by DNA Damage Repair Pathways and Epigenetic Factors. Viruses. 2020; 12: 744.
45. Gupta AK, Lee JH, Wilke WW, Quon H, Smith G, Maity A, et al. Radiation response in two HPV-infected head-and-neck cancer cell lines in comparison to a non-HPV-infected cell line and relationship to signaling through AKT. Int J Radiat Oncol Biol Phys. 2009; 74: 928-33.
46. Nickson CM, Moori P, Carter RJ, Rubbi CP, Parsons JL. Misregulation of DNA damage repair pathways in HPV-positive head and neck squamous cell carcinoma contributes to cellular radiosensitivity. Oncotarget. 2017; 8: 29963-75.
47. Rieckmann T, Tribius S, Grob TJ, Meyer F, Busch CJ, Petersen C, et al. HNSCC cell lines positive for HPV and p16 possess higher cellular radiosensitivity due to an impaired DSB repair capacity. Radiother Oncol. 2013; 107: 242-6.
48. Kono T, Hoover P, Poropatich K, Paunesku T, Mittal BB, Samant S, et al. Activation of DNA damage repair factors in HPV positive oropharyngeal cancers. Virology. 2020; 547: 27-34.
49. Jang MK, Shen K, McBride AA. Papillomavirus genomes associate with BRD4 to replicate at fragile sites in the host genome. PLoS Pathog. 2014; 10: e1004117.
50. Fradet-Turcotte A, Bergeron-Labrecque F, Moody CA, Lehoux M, Laimins LA, Archambault J. Nuclear accumulation of the papillomavirus E1 helicase blocks S-phase progression and triggers an ATM-dependent DNA damage response. J Virol. 2011; 85: 8996-9012.
51. Sakakibara N, Mitra R, McBride AA. The papillomavirus E1 helicase activates a cellular DNA damage response in viral replication foci. J Virol. 2011; 85: 8981-95.
52. Reuschenbach M, Huebbers CU, Prigge ES, Bermejo JL, Kalteis MS, Preuss SF, et al. Methylation status of HPV16 E2-binding sites classifies subtypes of HPV-associated oropharyngeal cancers. Cancer. 2015; 121: 1966-76.
53. Chaiwongkot A, Vinokurova S, Pientong C, Ekalaksananan T, Kongyingyoes B, Kleebkaow P, et al. Differential methylation of E2 binding sites in episomal and integrated HPV 16 genomes in preinvasive and invasive cervical lesions. Int J Cancer. 2013; 132: 2087-94.
54. Marullo R, Werner E, Zhang H, Chen GZ, Shin DM, Doetsch PW. HPV16 E6 and E7 proteins induce a chronic oxidative stress response via NOX2 that causes genomic instability and increased susceptibility to DNA damage in head and neck cancer cells. Carcinogenesis. 2015; 36: 1397-406.
55. Dacus D, Stancic S, Pollina SR, Rifrogiate E, Palinski R, Wallace NA. Beta Human Papillomavirus 8 E6 Induces Micronucleus Formation and Promotes Chromothripsis. J Virol. 2022; 96: e0101522.
56. Rual JF, Venkatesan K, Hao T, Hirozane-Kishikawa T, Dricot A, Li N, et al. Towards a proteome-scale map of the human protein-protein interaction network. Nature. 2005; 437: 1173-8.
57. Muller M, Cassonnet P, Favre M, Jacob Y, Demeret C. A comparative approach to characterize the landscape of host-pathogen protein-protein interactions. J Vis Exp. 2013: e50404.
58. Gillespie KA, Mehta KP, Laimins LA, Moody CA. Human papillomaviruses recruit cellular DNA repair and homologous recombination factors to viral replication centers. J Virol. 2012; 86: 9520-6.
59. Chen AM, Felix C, Wang PC, Hsu S, Basehart V, Garst J, et al. Reduced-dose radiotherapy for human papillomavirus-associated squamous-cell carcinoma of the oropharynx: a single-arm, phase 2 study. Lancet Oncol. 2017; 18: 803-11.
60. de Bono J, Mateo J, Fizazi K, Saad F, Shore N, Sandhu S, et al. Olaparib for Metastatic Castration-Resistant Prostate Cancer. N Engl J Med. 2020; 382: 2091-102.
61. Tutt ANJ, Garber JE, Kaufman B, Viale G, Fumagalli D, Rastogi P, et al. Adjuvant Olaparib for Patients with BRCA1- or BRCA2-Mutated Breast Cancer. N Engl J Med. 2021; 384: 2394-405.